EXPERIMENTAL AND NUMERICAL STUDIES OF THE RAYLEIGH-TAYLOR INSTABILITY FOR BOUNDED LIQUID FILMS WITH INJECTION THROUGH THE BOUNDARY

A Thesis
Presented to
The Academic Faculty

by

Fahd Fathi Abdelall

In Partial Fulfillment
of the Requirements for the Degree
Doctor of Philosophy in
The Woodruff School of Mechanical Engineering

Georgia Institute of Technology
March 2004

EXPERIMENTAL AND NUMERICAL STUDIES OF THE RAYLEIGH-TAYLOR INSTABILITY FOR BOUNDED LIQUID FILMS WITH INJECTION THROUGH THE BOUNDARY

Approved by:

Prof. Said I. Abdel-Khalik (Chair), ME

Prof. Minami Yoda (Co-Advisor), ME

Prof. S. Mostafa Ghiaasiaan, ME

Prof. Cyrus K. Aidun, ME

Prof. Donald Webster, CE

Prof. Roman Grigoriev, Physics

Date Approved by Chair: March 31, 2004

DEDICATION

To my Parents,
for their encouragement and magnanimous support throughout the years.
F. A.

ACKNOWLEDGEMENT

I would like to thank the chair of my PhD reading committee and the thesis advisor, Professor Abdel-Khalik for his guidance, helpful discussions, and insight into his field of the engineering frontier and the literature. I recognize the valuable contributions of Professors Yoda, Ghiaasiaan, Aidun, Webster and Grigoriev to the development of this thesis. I also wish to thank the members of the thermal-hydraulics laboratory directed by Eng. Sadowski. The financial support of Georgia Institute of Technology is gratefully acknowledged. The main contributors to the rewarding atmosphere of this project were my parents, and thus I would like to express my sincerest gratitude to them.

TABLE OF CONTENTS

LIST OF TABLES

LIST OF FIGURES

NOMENCLATURE

Symbols

A	Surface area, m^2
Bo	Bond Number, $\rho g h_o^2 / \sigma$
Ca	Capillary Number, $\left(U_o \mu \lambda^3\right) / \left(\sigma \left(2\pi h_o\right)^3\right)$
D	Equivalent diameter, m
F	Force, N
g	Gravitational acceleration, m/s^2
h_o	Liquid film mean thickness, m
I	Indicator heaviside function
k	Wave number
l	Length scale, $(\sigma/[g(\rho_L-\rho_G)])^{1/2}$, m
$\dot{m}''$	Mass flux from the gas to the liquid, kg/m^2s
n	Unit vector normal to the interface
P	Pressure, N/m^2
P_o	Pressure scale, $\rho_L U_o^2$, N/m^2
Q	Volume flow rate, m^3/s
Re	Reynolds Number, $\rho_L l U_o/\mu_L$
s	Growth rate of the perturbation, s^{-1}
T	Temperature, K
t	Time, s

t_o	Time scale, l/U_o, s
u	Fluid velocity vector
U_o	Velocity scale, $(gl)^{1/2}$, m/s
u, v, w	Fluid velocity components in Cartesian coordinates, m/s
V	Interface velocity vector
We	Weber Number, $\rho_L l U_o^2/\sigma$
x	Position vector
x, y, z	Cartesian coordinates, m
z_o	Initial liquid film thickness, m

Greek Letters

α	Property
β	Slip coefficient
γ	Specific weight, N/m^3
δ	Dirac delta function
ε_s	Amplitude of initial perturbation, m
θ	Inclination angle, degrees
κ	Twice the mean interface curvature
λ	Wavelength, m
μ	Dynamic viscosity, $N.s/m^2$
μ^*	Dynamic viscosity ratio, μ_G/μ_L
Π	External normal stress, Pa
ρ	Density, kg/m^3
ρ^*	Density ratio, ρ_G/ρ_L

σ	Surface tension coefficient, N/m; standard deviation, s
τ	External tangential stress, Pa
ϕ	Potential for conservative body forces, N/m^2

Subscripts

f	Quantity at interface
G	Gas phase
L	Liquid phase

Superscripts

*	Property ratio or nondimensional quantity
+	Nondimensional quantity

Acronyms

IFE	Inertial Fusion Energy
RT	Rayleigh-Taylor
VOF	Volume of Fluid

ABSTRACT

One of the most demanding engineering issues in Inertial Fusion Energy (IFE) reactors is the design of a reaction chamber that can withstand the intense photons, neutrons and charged particles due to the fusion event. Rapid pulsed deposition of energy within thin surface layers of the fusion reactor components such as the first wall may cause severe surface erosion due to ablation. One particularly innovative concept for the protection of IFE reactor cavity first walls from the direct energy deposition associated with soft X-rays and target debris is the thin liquid film protection scheme. In this concept, a thin film of molten liquid lead is fed through a silicon carbide first wall to protect it from the incident irradiations.

Numerous studies have been reported in the literature on the thermal response of the liquid film to the intermittent photon and ion irradiations, as well as on the fluid dynamics and stability of liquid films on vertical and upward-facing inclined surfaces. However, no investigation has heretofore been reported on the stability of thin liquid films on downward-facing solid surfaces with liquid injection through (i.e. normal to the surface of) the bounding wall. This flow models the injection of molten liquid lead over the upper end cap of the reactor chamber. The hydrodynamics of this flow can be interpreted as a variation of the Rayleigh-Taylor instability due to the effect of the bounding wall which is continuously fed with the heavier fluid.

In order to gain additional insight into the thin liquid film protection scheme, experiments have been conducted to investigate the critical issues associated with this concept. To this end, an experimental test facility has been designed and constructed to

simulate the hydrodynamics of thin liquid films injected normal to the surface of and through downward-facing flat walls. In this doctoral thesis, the effect of different design parameters (film thickness, liquid injection velocity, liquid properties and inclination angle) on liquid film stability has been examined. The results address the morphology of the film free surface, the frequency of droplet formation and detachment, the size and penetration depth of the detached droplets, and the interface wave number. These experimental data have been used to validate a novel mechanistic numerical code based on a level contour reconstruction front tracking method over a wide range of parameters.

The results of this investigation will allow designers of IFE power plants to identify appropriate "windows" for successful operation of the thin liquid film protection concept for different coolants.

CHAPTER 1
INTRODUCTION

The Rayleigh-Taylor instability takes place when a heavy fluid is situated above a light fluid in a gravitational field pointing toward the light fluid. The interface becomes unstable for certain perturbation wavelengths and these perturbations evolve into bubbles of light fluid and spikes of heavy fluid which penetrate into both fluids. The evolution of a Rayleigh-Taylor (RT) unstable interface is complex, involving phenomena such as the development of a Helmholtz instability on the side of the penetrating spikes, formation and detachment of droplets, competition and amalgamation among rising bubbles, entrainment and turbulent mixing in a region of fluid of finite thickness, and a possible chaotic limit with a fractalized interface. Therefore, the Rayleigh-Taylor instability is the prototype case for fluid mixing induced by unstable stratification, and as such, is of fundamental importance; it has been the subject of numerous experimental and numerical studies in fundamental research and practical applications such as multiphase hydrodynamics.

The Rayleigh-Taylor instability occurs in diverse applications, including: the electromagnetic implosion of a metal liner, the formation of high luminosity twin-exhaust jets in rotating gas clouds in an external gravitational potential, the overturn of the outer portion of the core of a massive star, and the laser implosion of deuterium-tritium fusion targets in inertial fusion systems. Rigorous understanding of these phenomena can be gained by investigating the Rayleigh-Taylor instability.

1.1 First Wall Protection Schemes in Fusion Energy Systems

The energy release from the exploding pellets of inertially confined fusion systems consists of energetic neutrons, photons, and ionized debris that eventually deposit their energies in the walls surrounding the reactor cavity. The energy deposition from the soft X-rays and charged particles takes place in an extremely thin surface layer, resulting in intense surface heating of vulnerable bare first walls. These incident photon and ion irradiations may cause excessive wall erosion that severely reduce the wall lifetime and therefore diminish reactor safety and economic attractiveness. First wall erosion takes place due to numerous mechanisms, including evaporation, spallation and macroscopic degradation resulting from shock wave destruction, high thermal stresses, and inter-granular pores explosion.

Numerous investigations of the thermal-mechanical response of inertial fusion energy (IFE) reactor first walls for several wall materials, target yields, target design (i.e. spectra), and repetition rates have been reported in the literature [1-8]. The findings of these studies emphasize the necessity of a wall protection scheme to assure wall survival at practical cavity sizes (i.e. wall loadings). One of the IFE first wall protection schemes is the wetted porous wall concept, originally proposed by Los Alamos in 1972 [9, 10] and later adopted by other conceptual reactor designs. Prometheus-L/H (Laser/Heavy ion driven) [11-13], Osirus [14] and Hiball [15] utilized the wetted wall concept, where a film a fraction of a millimeter thick is fed through a porous first wall. Table 1.1 and Figure 1.1 provide a summary of the design parameters utilized in the Prometheus-L/H conceptual reactor designs and a 3-D model of the original thin liquid film protection scheme, respectively. Thin liquid films injected at higher speeds in the form of jets were

also proposed as an alternative feeding mechanism. In the HYLIFE-II [16, 17] reactor design, a different shielding concept is presented based on a thick liquid protection scheme utilizing slab jets or liquid sheets at a speed of 12 m/s as illustrated in Figure 1.2.

Table 1.1 Comparison of the design parameters of the Prometheus-L/H conceptual reactor designs [11, 18-20].

Design Parameter	Prometheus-L	Prometheus-H
Total pellet yield, [MJ]	497	719
X-ray yield, [MJ]	31	46
Ionized debris yield, [MJ]	107	159
Repetition rate, [Hz]	5.6	3.6
Cavity radius, [m]	5	4.5
Cavity height, [m]	5	4.5
Cavity surface area, [m^2]	471	382
Cavity volume, [m^3]	916	668
Non-condensable gas pressure (273 K), [Pa]	1.5	1.5

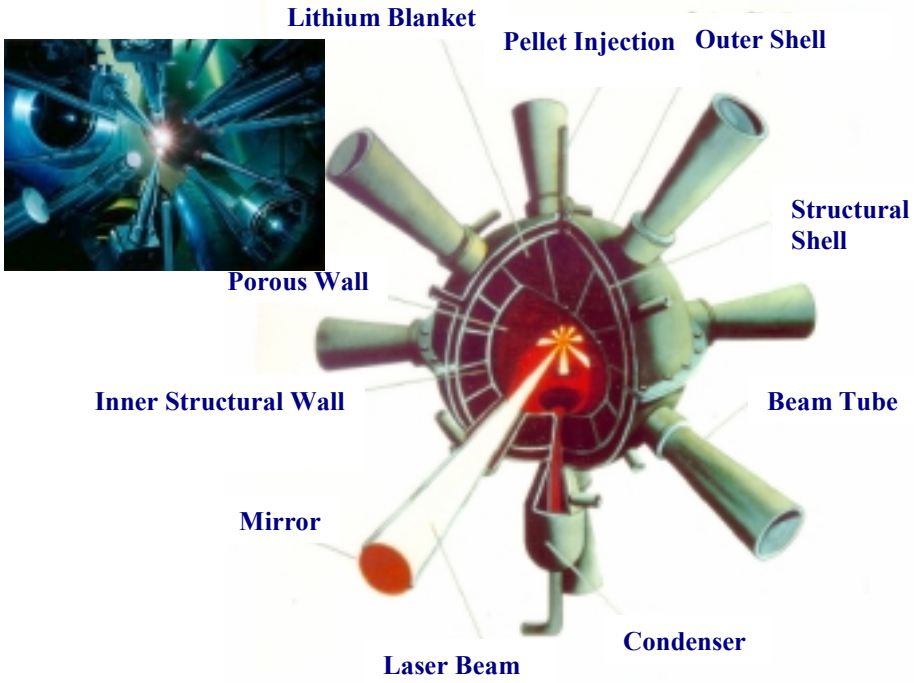

Figure 1.1 Conceptual 3-D model of the original thin liquid film protection scheme for the inertial fusion energy IFE system and close-up of the DT implosion process [9, 21].

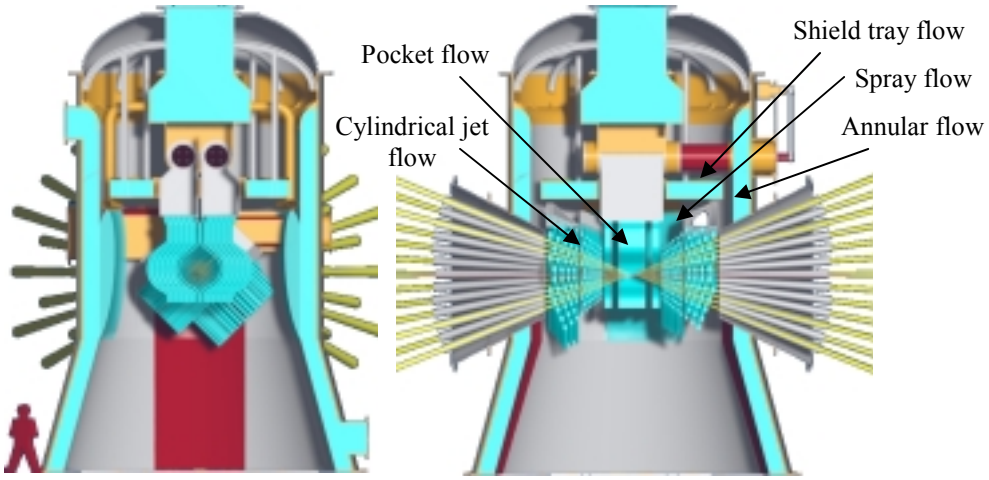

Figure 1.2 Conceptual 3-D model of the thick liquid protection scheme for the inertial fusion energy IFE system as visualized in the HYLIFE-II reactor design [22].

An essential element of IFE first wall protection schemes is the detailed characterization of the target yield and spectrum. Different target designs can be analyzed, including: direct-drive and indirect-drive target designs. Reactor chamber designs with dry walls subjected to the X-ray and charged particle spectra represent a reference for the required shielding by thin liquid film protection or thick liquid jets concept. Therefore, dry wall chambers with direct-drive targets were analyzed by investigating target heating which may lead to upper limits on chamber gas and chamber wall temperature. Incident energy and particle fluxes on the target wall were calculated and the thermal response was documented in several studies [1-8, 23, 24]. The detailed spectrum and temperature response of the direct-drive target is provided in Figures 1.3 and 1.4, respectively [23]. For indirect drive target designs, the penetration depth of the charged particles is thinner and thus the thermal response may exceed the limiting sublimation temperature for the selected wall materials such as carbon and tungsten. Figure 1.5 presents the attenuation of charged particles in carbon and tungsten targets for indirect-drive spectra without protective chamber gas [23].

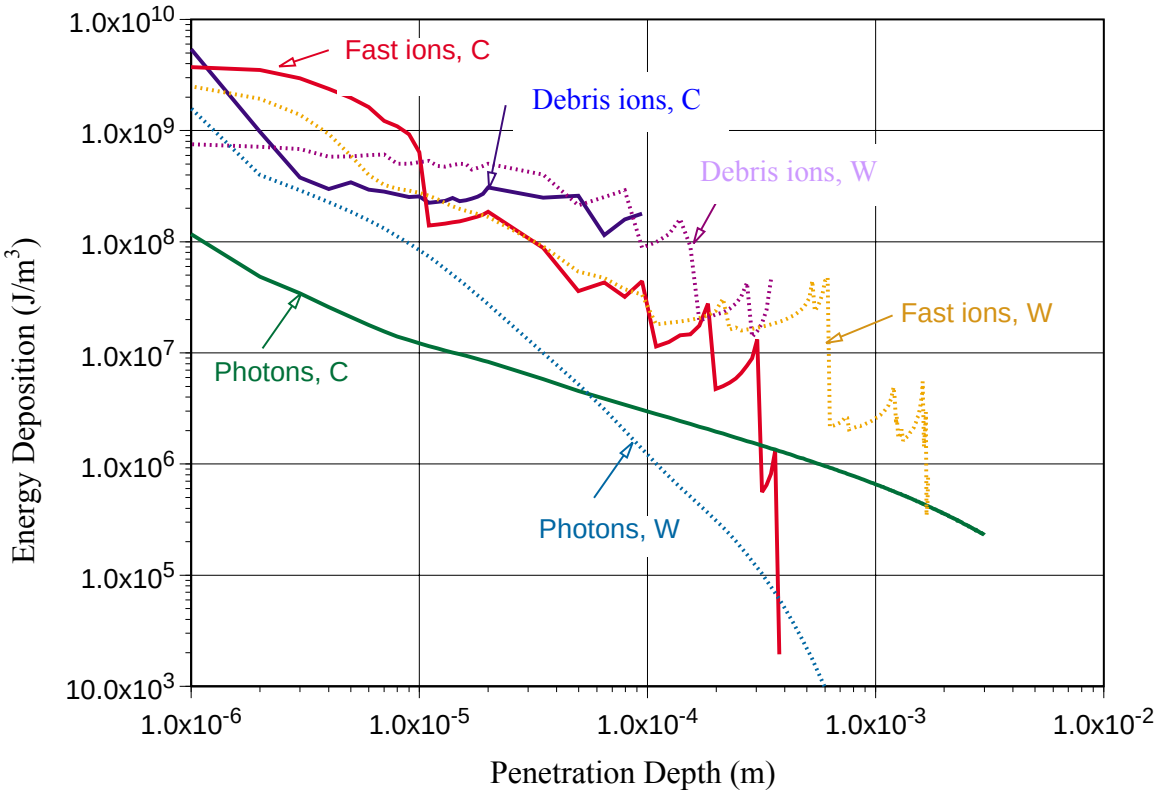

Figure 1.3 Photon and ion attenuation in carbon (C) and tungsten (W) for direct-drive spectra without protective chamber gas [23].

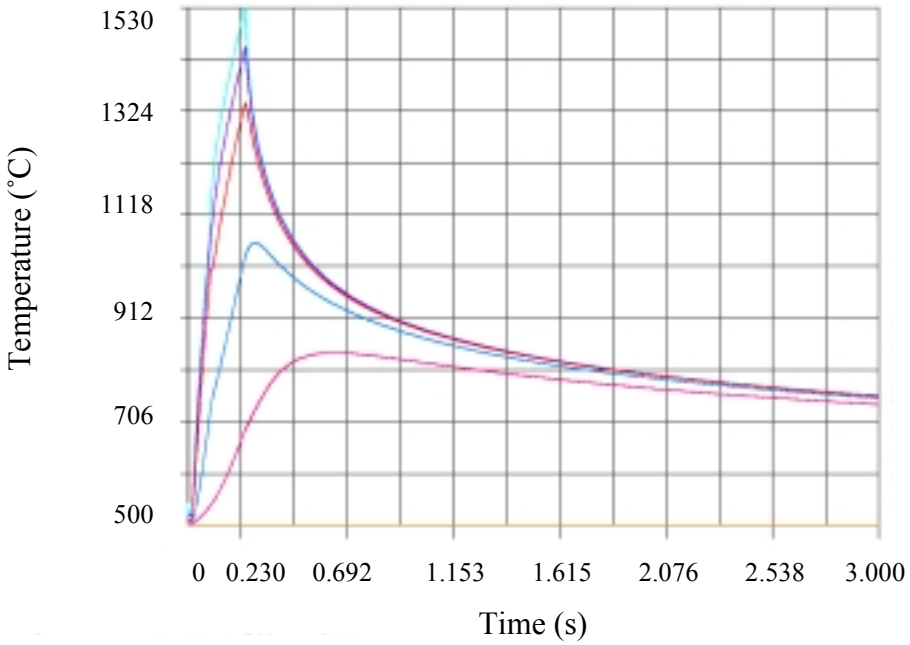

Figure 1.4 Temperature history for Carbon flat wall under energy deposition from direct-drive spectra without protective chamber gas [23].

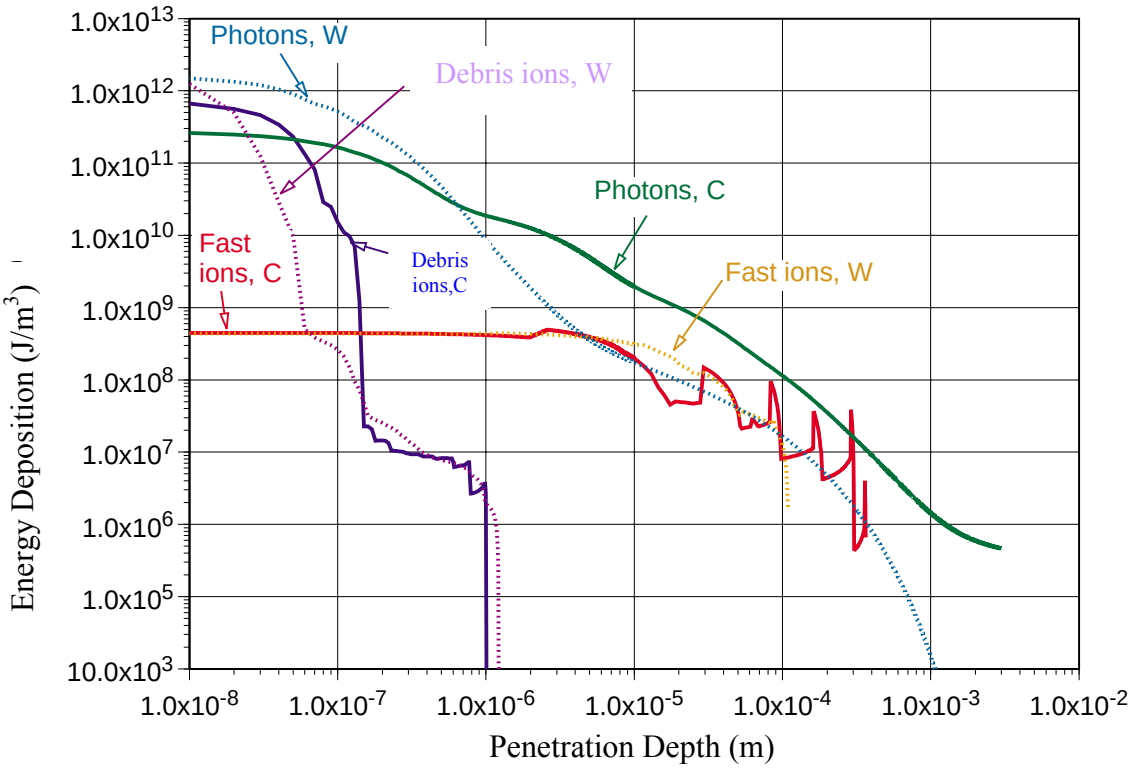

Figure 1.5 Photon and ion attenuation in carbon (C) and tungsten (W) for indirect-drive spectra without protective chamber gas [23].

Waganer, et al. [11] introduced in the Prometheus-L study a novel concept of a thin (0.4-0.6mm) film of liquid lead that is permitted to form on the surface of a porous silicon carbide first wall. Since liquid lead is a high-Z material, it is chosen as one of the alternative coolants used as efficient photon attenuators. The X-rays produced by the exploding targets deposit their energy (5-50 MJ with a pulse width of ~10 ns) in the thin liquid film, which prevents severe surface heating of the silicon carbide first wall. The partially vaporized liquid lead forms a protective cloud that expands toward the incoming ionic debris which arrives shortly (a few μs) thereafter. The ionized particles then deposit part of their energy into the vapor shield; the rest of the energy (20-200 MJ with a pulse width of ~1μs) is deposited into the remaining liquid film, thereby leading to further evaporation. Re-condensation of the vapor cloud allows the energy absorbed in the film

to be recovered prior to the next target disruption, albeit over a longer time period, hence limiting first wall heating, degradation and thermal stress. Therefore, the thin liquid film shielding scheme will provide adequate protection to assure reactor chamber survival at practical sizes. Figure 1.6 illustrates a conceptual three-dimensional model of the Prometheus-L fusion laser reactor chamber [25, 26].

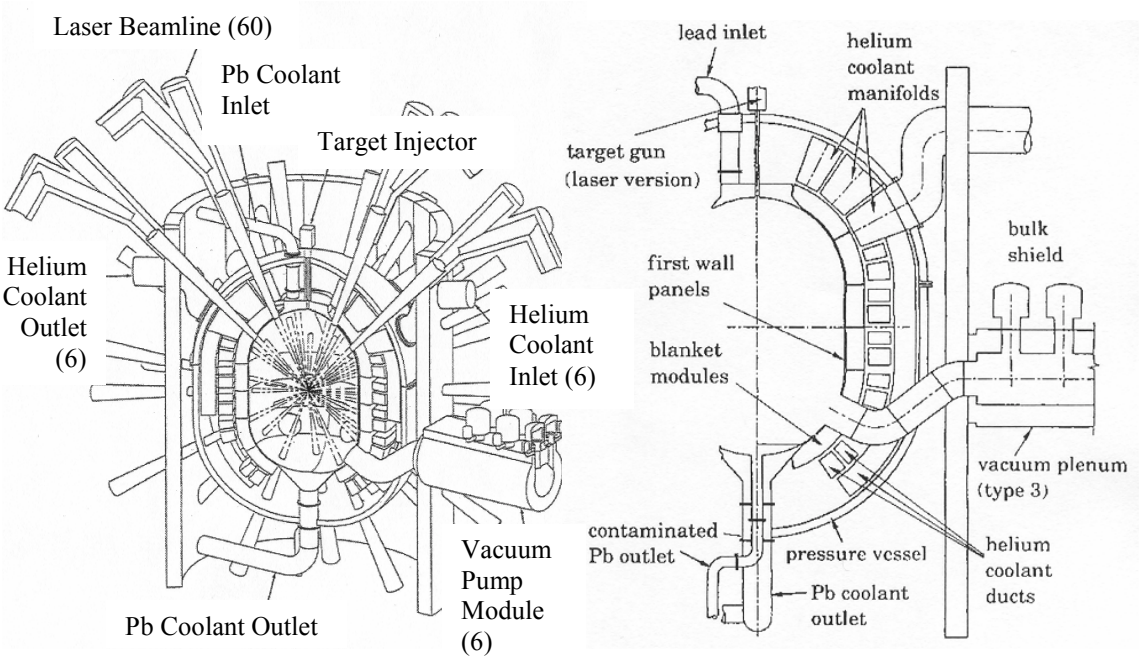

(a) (b)

Figure 1.6 Conceptual model of the Prometheus-L thin liquid protection scheme for the inertial fusion energy IFE system: (a) three-dimensional model, and (b) two dimensional section [25, 26].

Another approach to fusion power is the magnetic confinement approach. In magnetic fusion energy (MFE) systems, plasma facing components (PFCs) such as the first wall and the divertor are subjected to erosion and ablation during plasma instabilities such as disruptions, edge-localized modes and high power excursions [8, 27]. These technical considerations are essential for the design and development of the conceptual

International Thermonuclear Experimental Reactor (ITER) shown in Figure 1.7 [28, 29]. Liquid metal layer protection schemes provide shielding for the PFCs from the incident plasma particles (ions and electrons). These liquid metal films will be subjected to hydrodynamic instabilities during the thermal quench phase of a disruption from the plasma impact momentum at the liquid surface. A thin surface layer of the liquid metal film will be accelerated due to partial deposition of the plasma momentum. This mechanism will cause hydrodynamic instabilities such as the Rayleigh-Taylor and Kelvin-Helmholtz instabilities to transpire and form liquid droplets that will drift away by the plasma wind [30, 31].

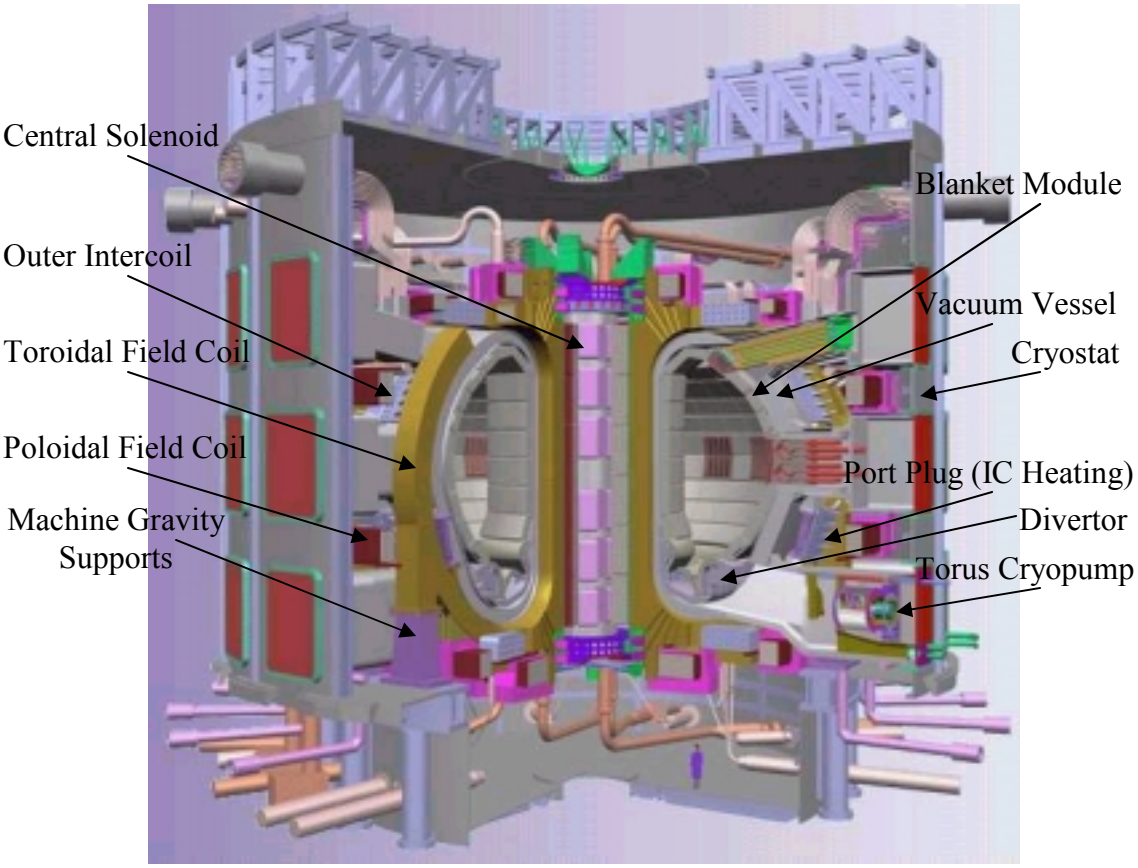

Figure 1.7 Conceptual 3-D model of the magnetic fusion energy system in the ITER [29].

1.2 Motivation and Design Requirements

Several studies have been carried out to investigate the thermal response of the liquid film to the intermittent ion and photon irradiations in inertial fusion reactors, as well as the thermal-mechanical response of the backing solid first wall [8, 11, 32, 33]. In the chemical engineering literature, several investigations have studied the fluid dynamics and stability of liquid films on vertical and upward-facing inclined surfaces [34-38]. These studies also included analytical representations of stable liquid rivulets and characteristic velocity distributions. Despite the host of studies undertaken by researchers, however, no work has heretofore been reported on the evolution and stability of thin liquid films on downward-facing surfaces with liquid injection through the wall.

In order to reduce the proposed thin film protection scheme to practice and to address its viability, several critical design issues need to be explored, including:

1- Can a stable liquid film be maintained on the upper section of the chamber?

2- Can the film be reestablished over the entire cavity surface prior to the next target explosion?

3- Can a minimum film thickness be maintained to provide adequate shielding during the next target blast?

To this end, an experimental investigation is proposed to examine the hydrodynamics of thin liquid films formed on the downward-facing surface of a porous wall with transpiration normal to the surface. The objective is to assess and determine the effect of different design and operational parameters (liquid injection velocity, film thickness, inclination angle, and liquid properties) on the liquid film stability between target explosions. The results of this investigation will address the effect of these design

parameters on the spatiotemporal evolution of the film free surface, the frequency of liquid droplet formation and subsequent detachment, the size of detached droplets, and the time history of the penetration depth. Figure 1.8 shows a schematic of the reactor cavity and the envisioned thin liquid film protection scheme as an application to the Rayleigh-Taylor instability.

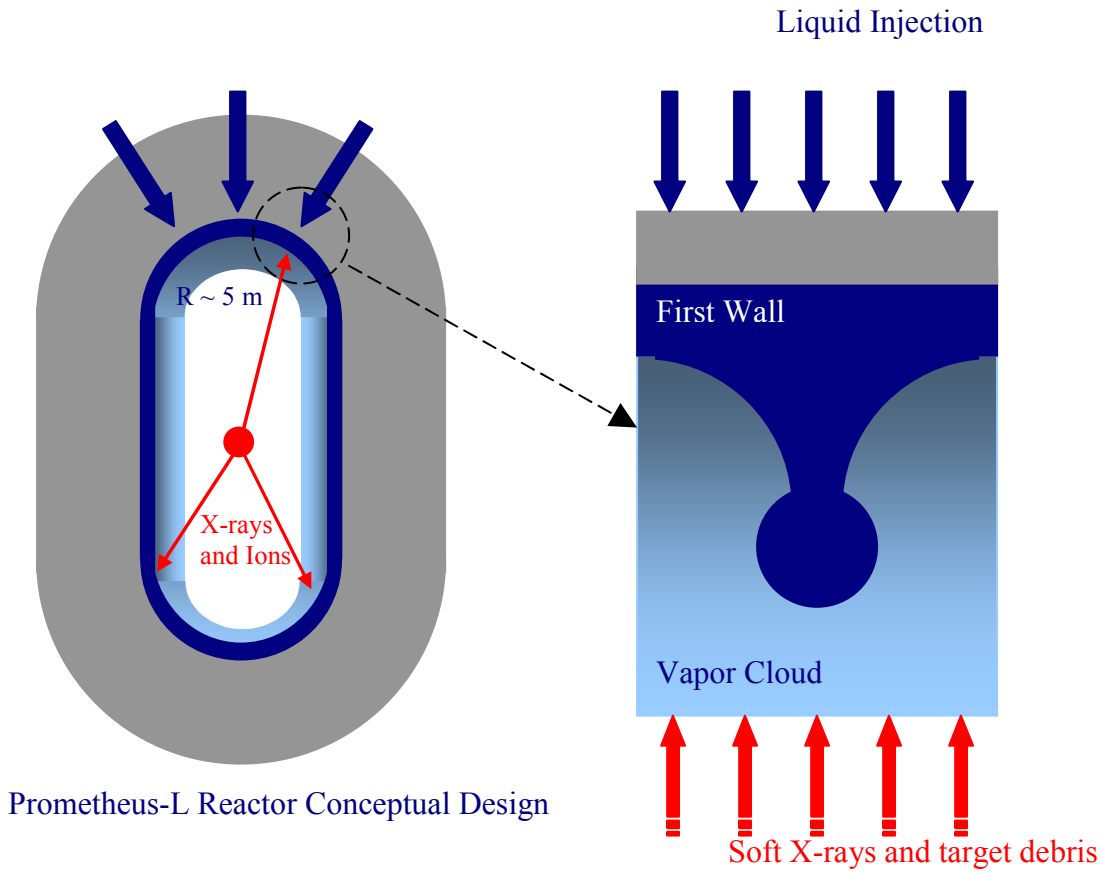

Figure 1.8 Schematic illustration of the IFE reactor cavity and the proposed thin liquid film protection concept.

The long-wave theory [36] which is based on the asymptotic reduction of the full set of governing equations and boundary conditions to a simplified highly nonlinear evolution equation is utilized in analyzing the hydrodynamics of the bounded Rayleigh-Taylor instability with transpiration through the boundary. A mathematical formulation is

derived that overcomes the complexity of the original free-boundary problem while preserving many of the essential aspects of its physics. Analogy with Reynolds theory of lubrication can also be drawn because the Reynolds number of the thin liquid film flow is not large. A discussion of the linear stability properties of the base-state solution and of the nonlinear spatiotemporal evolution of the interface is introduced in this analysis.

The experimental results obtained in this investigation are used to verify and validate over a wide range of parameters a novel numerical code which is based on a state-of-the-art level contour reconstruction front tracking technique [39-42]. This numerical code is designed to perform accurate 3D simulations of multiphase flows with complete transport and interface physics as well as with robust treatment of interface merging and breakup. Validation of this code will give designers of IFE systems a powerful tool to identify design and operational windows for successful operation of the thin liquid film protection system. Aside from its direct applicability to inertial fusion systems design, the experimental data in itself is valuable, inasmuch as it addresses a complex fluid dynamics problem, which has heretofore not been investigated, namely the bounded Rayleigh-Taylor instability with injection of the heavier fluid through the boundary surface.

1.3 Research Objectives

When applied to the downward-facing upper surface of the reactor cavity, the hydrodynamics of the wetted wall thin film protection scheme can be interpreted as a variation to the well-known Rayleigh-Taylor instability problem. Despite numerous investigations of the Rayleigh-Taylor instability, none of these studies was directed

towards examining the effect of a bounding solid wall through which the heavier fluid is continuously injected, as is the case in the porous wetted wall concept. Thus, the aim of this research is to expand the scope of RT instability applications and to enhance the exposition of physical principles by embarking on an experimental and numerical investigation of the thin liquid film protection scheme. This goal will be attained by achieving the following objectives:

1- Design and construct an experimental test facility that simulates the proposed thin liquid film protection scheme, while independently controlling several input parameters such as the unperturbed liquid film thickness and injection velocity through the bounding surface,

2- Measure the unperturbed local instantaneous liquid film thickness by using a non-intrusive technique,

3- Determine the effect of different design and operational parameters (liquid film thickness, liquid injection velocity through the boundary, inclination angle of the bounding surfaces, and liquid properties) on liquid film stability,

4- Obtain results pertaining to the conceptual design of the thin liquid film protection scheme, including:

    4.1- The frequency of liquid droplet formation,

    4.2- The size of detached droplets, and

    4.3- The time history of the penetration depth,

5- Verify over a wide range of design parameters an existing numerical code which is based on a state-of-the-art level contour reconstruction front tracking technique [39-42].

1.4 Preface and Outline

The combined research and pedagogical mission of this doctoral thesis is molded into a vertical approach in which chapters are designed to provide a deepening understanding of the bounded Rayleigh-Taylor instability with injection through the boundary. In chapter 2, literature review of the previous work on Rayleigh-Taylor instability is presented. This chapter provides comprehensive coverage of the experimental, theoretical and numerical investigations carried out on various aspects of the Rayleigh-Taylor instability as well as on the evolution and stability of thin liquid films. The essential elements of the theoretical and numerical investigation carried out in this research are conveyed in chapter 3. Linear stability analysis of confined thin liquid films developing on inverted surfaces is modified to include the effect of transpiration through the boundary. A level contour reconstruction front tracking technique is also discussed as the basis for the numerical investigation utilized in this work in order to analyze the effect of different design parameters (film thickness, liquid injection velocity, liquid properties and inclination angle) on the liquid film response and stability. Chapter 4 is a detailed presentation and description of the experimental investigation, including: the experimental test facility, instrumentation, data acquisition system and analysis techniques utilized in measuring the targeted flow field variables. Discussion of the results obtained from the theoretical, numerical and experimental studies is detailed in chapter 5; validation of the front tracking numerical technique introduced in chapter 3 and utilized in this research is conducted over a wide range of design and operational parameters. Chapter 6 provides the conclusions derived from the conducted theoretical,

numerical and experimental investigations, and outlines the recommendations for future work.

CHAPTER 2
LITERATURE REVIEW

The hydrodynamics of the wetted porous wall protection scheme, which is applied to the downward-facing upper surface of the IFE reactor cavity, can be viewed as a variation of the well-known Rayleigh-Taylor (henceforth RT) instability problem. RT instability transpires when a dense fluid lies above a lighter fluid in a gravitational field pointing toward the light fluid. The interface between the two fluids is inherently unstable to certain perturbation wavelengths. These perturbations evolve into bubbles of light fluid that mushroom into the heavy fluid, causing it to form spikes which penetrate into the lighter fluid. This classic form of Rayleigh-Taylor instability was first theoretically studied by Rayleigh [43] and Taylor [44]. Later, Chandresekhar [45] investigated the linear theory of RT instability for two infinite fluids with equal kinematic viscosities separated by an interface with surface tension. Fermi and von Neumann [46] also developed a model with the interface consisting of two horizontal and two vertical line segments per wave length. They then derived a model dynamical system with two degrees of freedom for the length of the vertical segment and for the length of the horizontal segment. The RT instability has subsequently been investigated in numerous studies, none of which however include the effect of a bounding solid wall through which the heavier fluid is continuously injected, as in the case of the porous wetted wall concept. Earlier experimental, theoretical and numerical investigations are nevertheless relevant to this work and are therefore briefly reviewed in the following sections.

2.1 Experimental Background

As stated by Sharp [47]: "*There is a clear need for more and **better experiments**. First, available experiments are still inadequate for modeling the very late stage of Rayleigh-Taylor instability. Second, experiments are needed to **benchmark codes** which compute Rayleigh-Taylor instability in circumstances where accurate special purpose codes do not exist for comparison. To be of most use, the experiments should be designed with two criteria in mind: They should be analyzable to produce quantitative data on the **time history** of the unstable interface. The quantitative data may well refer to appropriately chosen **statistical quantities** rather than to the detailed properties of a specific interface*" (emphasis added).

The RT instability can be divided into four stages [47] as depicted in Figure 2.1. The first stage is dominated by the small growth of a perturbation relative to its wavelength. As analyzed by the linear stability theory, the growth rate depends on the fluids' density ratio, viscosities, surface tension, and compressibility. The linear theory is no longer applicable after the perturbation grows to more than 10-40% of its wavelength. The second stage is characterized by the nonlinear perturbation growth forming bubbles of light fluid threading through the heavy fluid causing spikes to fall into the light fluid. During this stage, the nonlinear growth of perturbations is strongly influenced by the density ratio and three-dimensional effects. Interactions and amalgamations among the bubbles and the mushroom-shaped spikes are characteristics of the third stage. Finally, the interaction evolves into turbulent or chaotic mixing which dominates the fourth stage of the instability. In this final stage, phenomena such as the penetration of a bubble

through a slab of fluid of finite thickness, necking, breakup of the spikes by various mechanisms, and other complicated behavior are encountered.

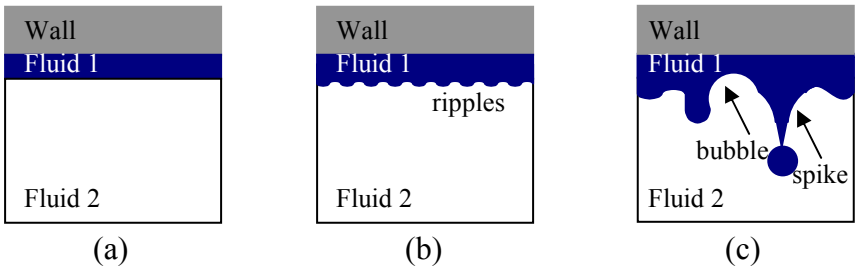

Figure 2.1 Schematic illustration of the Rayleigh-Taylor instability sequence.

Classic experiments on RT instability were performed by, among others, Lewis [48], Emmons, Chang and Watson [49], Duff, Harlow and Hirt [50], Ratafia [51], Popil and Curzon [52], and J. F. Barnes, et al. [53]. Lewis [48] conducted a Rayleigh-Taylor experiment by subjecting a column of water to a pressure difference by imposing different air pressures above and below the water column. He concluded from his experiments that the RT instability can be divided into three stages. The first is an exponential increase in amplitude followed by a transition stage which includes the formation of round ended columns of air threading through vertical columns of liquid. The final stage is a penetration through the liquid of air columns at a uniform velocity proportional to the square root of the gravitational acceleration. However, in this work (see Figure 16 of [48]) large scatter in the growth of the wave amplitude as a function of time is apparent for similar initial conditions.

Emmons, Chang and Watson [49] experimentally studied the RT instability of the accelerated interface between a liquid (methanol or carbon tetrachloride) and air. A frame containing the fluids, mounted on guide columns, was accelerated downwards by

stretched rubber tubing when a wire, which held the uppermost point in the frame, was electrically melted. At accelerations greater than that of gravity, the atmospheric air pressure plays the role of the lighter fluid being accelerated in the direction of the heavier fluid. Their results included the growth rates of the RT instability and the phenomenon of bubble competition which involves the growth of the large bubbles at the expense of the small ones. They showed (see Figures 1 and 14 of [49]) that in their system the unstable waves were three-, vs. two-dimensional, but nevertheless compared their experimental data with two-dimensional models. Duff, Harlow and Hirt [50] carried out a set of experiments focused on RT instability when an argon-bromine mixture falls under gravity into air or helium. In these experiments, a steel diaphragm was used to divide the experimental volume into two parts into which the desired gases were injected. The instability was investigated when the diaphragm was removed at different times after starting injection. They showed that including the diffusion effects in addition to viscosity accounts quite well for the experimental observations. The effectiveness of the diffusion considerations in explaining all features of early perturbation growth was demonstrated in the observed values of amplitude plotted with time and compared to the theoretical slopes with and without diffusion.

Ratafia [51] at Lawrence Livermore Laboratory investigated the RT instability using a two-fluid system of octyl alcohol and water. The alcohol initially above the water in a Pyrex container was perturbed and then forced into an unstable configuration by being accelerated downward with a magnitude greater than that of gravity. Oscillations of the fluids about an axis above the top of the container were employed to introduce a cyclic perturbation to the interface. The expected bubble and spike formation was

observed, and, for the first time, they imaged the flattening and curling of spikes in mushroom shapes. They found the foot to be growing with constant velocity and the foot amplitude to be proportional to the spike amplitude. Popil and Curzon [52] used a rectangular Lucite tank, which contained water, in their experiments. The tank was accelerated downward by the force provided by an air-driven piston which is linked to a reservoir of compressed air. The virtual acceleration experienced by the water surface is 1.5g in the vertical direction. To generate standing surface waves, horizontal electrodes were positioned over the water surface. They visually detected the instability by imaging the interface. The amplitude of the spikes measured from the initial water level was 12 cm, in contrast to the initial amplitude of 1.5 mm before the acceleration. They also showed that films of water cling to the tank walls and that these films are more common near the troughs of the growing waves. Their results demonstrated that reproducible RT instabilities can be achieved provided that the amplitude and phase of the initial perturbation are accurately measured at the onset of the acceleration of the tank. Barnes et al. [53] conducted a number of experiments on Rayleigh-Taylor instability in solids. They machined or pressed a sinusoidal perturbation on the surface of a flat metal plate. The plate surface was smoothly accelerated by expanding detonation products. The growth in the amplitude of the perturbation was captured by using x-ray shadowgraphs. The observed results were compared to an elastic-plastic numerical hydrodynamics code. They reached the conclusion that an amplitude threshold controls the onset of Taylor instability at a plane interface in a solid.

Recently, Lange et al. [54] examined the temporal evolution of a water-sand interface driven by gravity. A distilled water column rested on sand and both were placed

in a cell fixed to a frame. As sand, they used spherical glass particles (Würth Ballotini MGL) of different sizes with a density of 2.45 g/cm^3. A CCD camera and a neon tube were also linked to the frame to monitor the interface morphology. The frame was turned around a horizontal axis bearing during which the images were captured in the frame. Figure 2.2 shows the evolution of the water-sand interface [54]. They showed that the initial disturbances of the interface grow exponentially at the beginning of the pattern forming process. Their results established that the growth rate increases with increasing wave number.

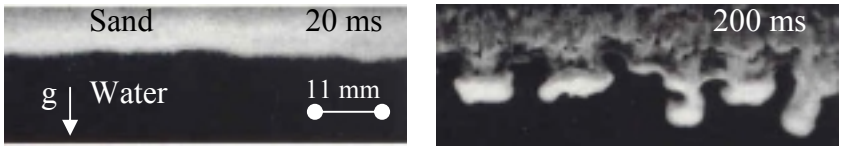

Figure 2.2 Transient evolution of water-sand interface [54].

Water droplets impacted on horizontal wire screens at isothermal conditions were studied by Hung and Yao [55]. Fine mesh stainless steel screens were used in the experiments. The screen has 100 × 100 meshes with a wire diameter of 0.14 mm and a 0.14 mm clear width of mesh opening. Droplets impacting the top surface of the screens pass through the fine mesh and form a thin liquid film at the bottom side of the screen. This liquid film builds up forming liquid ligaments from which droplets detach.

2.2 Theoretical and Numerical Background

The evolution of a single initial perturbation from small to large amplitude is now fairly well studied for two-dimensional or axisymmetric flows. Most of these calculations

have assumed inviscid flow or at least very small viscosities, neglected surface tension effects, and imposed a semi-infinite boundary for each fluid. Analytical and simple ordinary differential equations (ODE) solutions for perturbation growth during the first stage where linear theory is applicable have been well-established for some time. One means of analyzing the Rayleigh-Taylor instability is to investigate only the long-scale phenomena via lubrication or long-wave theory [36, 56-59]. Recently, volume of fluid (VOF) [60-63], front tracking [64], level set [65], and lattice Boltzmann [66] methods have been successfully used in two and three-dimensional computations of Rayleigh-Taylor instability.

Oron, Davis and Bankoff [36] present a review of the lubrication theory or long-wave theory approach which is based on the asymptotic reduction of the governing equations and boundary conditions to a simplified system consisting of a single nonlinear partial differential equation. This derived partial differential evolution equation is formulated in terms of the local thickness of the film. Functionals of the solution of that differential equation are then used to determine several field variables such as the fluid velocity. Although the notorious complexity of the original free boundary problem is reduced, a strong nonlinearity in the governing equation and higher-order spatial derivatives are present as a resulting penalty. This hindrance can be alleviated by using linear stability analysis based on the resulting evolution equation. Based on this approach, many hydrodynamic thin liquid film cases were analyzed and discussed, including: the evolution equation of a bounded film, flows in a cylindrical geometry, and flow on a rotating disc.

On the numerical side, Glimm, et al. [64] modeled the RT instability for two dimensional incompressible inviscid fluid flows using a front tracking technique. They carried out studies for statistically distributed heterogeneities in the initial perturbation and reached the conclusion that these heterogeneities can vary the flow characteristics. Tryggvason and Unverdi [67-69] solved the three-dimensional Navier-Stokes equations for weak stratification also using the front tracking method. They found that the amplitude increases with decreasing viscosity and thus leads to the formation of rolled-up vortices. They also obtained results showing that the inherent difference between 2D and 3D simulations is most evident in the vortex structure. For two-dimensional disturbances, the vortex remains at the original interface due to symmetry constraints whereas in 3D the vortex propagates away from the original interface causing the disturbance penetration to be much faster in 3D than in 2D calculations.

Glimm, et al. [70] studied bubble interactions in the RT instability of two compressible fluids and their influence on the statistical behavior and evolution of the bubble envelope using a front tracking method. In this study, they analyzed bubble dynamics and interaction with neighboring bubbles in a chaotic environment and acceleration of the overall bubble envelope. Youngs [71] examined a three-dimensional numerical simulation of turbulent mixing of miscible fluids by the RT instability, and concluded that two-dimensional calculations provide an adequate estimate of the overall growth of the mixing zone but cannot represent the fine scale details.

Li [72, 73] employed a level set approach to analyze three-dimensional RT instability in compressible fluids. A second-order Total Variation Diminishing (TVD) scheme with a fully parallelized algorithm was used to solve the 3D Euler equations. He

compared his results for terminal velocity, which is proportional to the square root of gravitational acceleration and bubble radius, with those of Taylor [44] and found both sets of results were in good agreement. He suggested that transition from constant velocity to constant acceleration was caused by bubble merger. Hecht, et al. [74] employed their custom built LEEOR3D code to investigate classical Rayleigh-Taylor instability growth in the nonlinear region. An arbitrary Lagrangian Eulerian (ALE) scheme in three-dimensions is used in LEEOR3D hydrocode. They analyzed Rayleigh-Taylor instability growth in diverse geometries such as 3D square and rectangular modes or in planar and cylindrical geometries. The effect of density ratio on the shape of the final stages was also demonstrated. Furthermore, they carried out an analysis on the growth of the Rayleigh-Taylor instability in a spherical geometry simulating the late deceleration stage of a typical inertially confined fusion pellet.

Elgowainy and Ashgriz [75] used a VOF method based on an accurate flux line segment model (FLAIR) to solve the two-dimensional incompressible Navier-Stokes equations for RT instability. This model simulated a finite thickness of the heavy fluid layer and accounted for surface tension and viscosity effects. They analyzed the effect of surface tension, viscosity, and initial perturbation characteristics on the evolution of RT instability in plane finite fluid layers. He, et al. [76, 77] used a novel lattice Boltzmann scheme for simulation of the RT instability in two and three dimensions.

Recently, Shin, Juric and Abdel-Khalik [39-42] developed a state-of-the-art level contour reconstruction technique in order to track the three dimensional evolution of the liquid film surface on a porous downward facing wall with different injection velocities. The technique enables front tracking methods to naturally, automatically, and robustly

model the merging and breakup of interfaces in three dimensional flows. This method is designed so that the interface is treated as a collection of physically linked but not logically connected surface elements. Thus, the Lagrangian tracking of interfaces is greatly simplified by eliminating the need to track logical connections between neighboring surface elements. This simplification is essential for 3D flows exhibiting topology change. Details of this numerical model will be discussed in chapter 3.

CHAPTER 3

THEORETICAL AND NUMERICAL INVESTIGATION

In order to achieve the previously stated objectives, theoretical and numerical studies of the bounded thin liquid film Rayleigh-Taylor instability with injection through the boundary as applied to the IFE reactor first wall protection scheme were conducted. Overviews of the theoretical and numerical components of the research are described in this chapter.

3.1 Theoretical Investigation

A discussion of the theoretical study carried out to analyze the bounded thin liquid film Rayleigh-Taylor instability with transpiration through the boundary is presented in this section. The theoretical technique employed in this investigation stems from the long-wave theory which relies on the asymptotic reduction of the original free-boundary problem to a nonlinear partial differential evolution equation formulated in terms of the local thickness of the film [36, 56-59]. This long-wave theory is utilized to analyze phenomena in which the disparity in scales results in more gradual field variations along the analyzed liquid film than those normal to the film. The resulting evolution equation is highly nonlinear with high order spatial derivatives. This complexity is solved by using linear stability analysis which provides stability curves for the perturbed liquid film.

3.1.1 Mathematical Formulation for the Evolution Equation

The analysis is unified into a framework from which the bounded Rayleigh-Taylor instability will emerge as a special case. The long-wave approximation as applied by Oron, Davis and Bankoff [36] is introduced in this section. The analysis is carried out for a viscous liquid film confined above by a liquid/gas interface and below by a horizontal solid boundary as depicted in Figure 3.1. External normal (Π) and tangential (τ) stresses as well as conservative body forces with potential (ϕ) are included in the analysis. The dimensional Navier-Stokes and continuity equations in two dimensions are expressed as:

$$\rho\left(\partial_t u + u\partial_x u + w\partial_z u\right) = -\partial_x p + \mu\nabla^2 u - \partial_x \phi \tag{3.1}$$

$$\rho\left(\partial_t w + u\partial_x w + w\partial_z w\right) = -\partial_z p + \mu\nabla^2 w - \partial_z \phi \tag{3.2}$$

$$\partial_x u + \partial_z w = 0 \tag{3.3}$$

where

u = velocity component in x-direction

w = velocity component in z-direction

ρ = liquid density

μ = dynamic viscosity

p = pressure

ϕ = potential for conservative body forces

The boundary conditions used includes relative motion slip at the solid boundary near contact lines, a kinematic boundary condition, and a balance of the stress tensor at the interface.

Solid boundary (z = 0):

$$u - \beta \partial_z u = 0 \quad \text{and} \quad \text{w} = 0 \tag{3.4}$$

Free boundary (z = $h(x,t)$):

$$w = \partial_t h + u \partial_x h \tag{3.5}$$

$$\mathbf{T} \cdot \mathbf{n} = -\kappa \sigma \mathbf{n} + \frac{\partial \sigma}{\partial s} \mathbf{t} + \mathbf{f} \tag{3.6}$$

where

β = slip coefficient

T = stress tensor of the liquid

n = unit vector normal to the interface

t = unit vector tangent to the interface

f = forcing at the interface including normal Π and tangential τ components

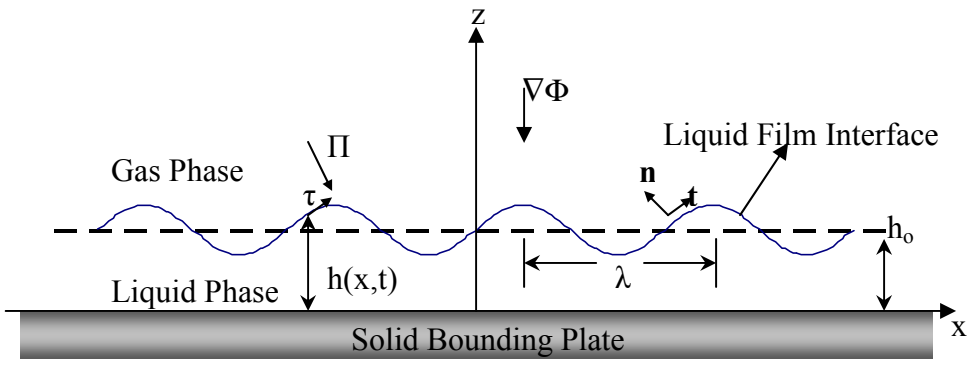

Figure 3.1 Evolution of a thin liquid film on a bounding surface.

The governing equations and boundary conditions are non-dimensionalized based on the assumption that the distortions are of long scale if:

$$\varepsilon = \frac{2\pi h_o}{\lambda} << 1 \tag{3.7}$$

where

h_o = liquid film mean thickness

λ = wavelength

The independent parameters and field variables in equations (3.1)-(3.3) are non-dimensionalized by relying on the assumption in (3.7) as follows:

$$X = \frac{x}{\lambda} = \frac{\varepsilon x}{2\pi h_o} \tag{3.8}$$

$$Z = \frac{z}{h_o} \tag{3.9}$$

$$U = \frac{u}{U_o} \tag{3.10}$$

$$W = \frac{w}{\varepsilon U_o} \tag{3.11}$$

$$T = \frac{\varepsilon U_o t}{h_o} \tag{3.12}$$

$$(\tau, \Pi) = \frac{h_o}{\mu U_o}(\tau_o, \varepsilon \Pi_o) \tag{3.13}$$

$$(\Phi, P) = \frac{\varepsilon h_o}{\mu U_o}(\phi, p) \tag{3.14}$$

where

U_o = characteristic velocity

The non-dimensional governing equations and boundary are obtained by applying the above scaling to nondimensionalize equations (3.1)-(3.3) leading to the following system of equations:

$$\partial_Z^2 U = \partial_X P + \partial_X \Phi \tag{3.15}$$

$$\partial_Z P + \partial_Z \Phi = 0 \tag{3.16}$$

$$\partial_T H + \partial_X \left(\int_0^H U dZ \right) = 0 \tag{3.17}$$

Solid boundary ($Z = 0$):

$$U - \beta_o \partial_Z U = 0 \tag{3.18}$$

Free boundary ($Z = H$):

$$\partial_Z U = \tau_o + \partial_X \Sigma \tag{3.19}$$

$$-\Pi_o - P = \frac{1}{\mathrm{Ca}} \partial_X^2 H \tag{3.20}$$

where

$$\mathrm{Ca} = \frac{U_o \mu}{\sigma \varepsilon^3} = \text{Capillary number} \tag{3.21}$$

σ = surface tension coefficient

The above set of non-dimensional equations is solved for the velocity field from which the evolution equation for the interface is obtained by utilizing the mass conservation condition of equation (3.17).

$$U = (\tau_o + \partial_X \Sigma)(Z + \beta_o) + \partial_X \overline{P} \left(\frac{1}{2} Z^2 - HZ - \beta_o H \right) \tag{3.22}$$

$$\partial_T H + \partial_X \left[(\tau_o + \partial_X \Sigma) \left(\frac{1}{2} H^2 + \beta_o H \right) \right] - \partial_X \left[\left(\frac{1}{3} H^3 + \beta_o H^2 \right) \partial_X \overline{P} \right] = 0 \tag{3.23}$$

where

$$\overline{P} = P + \Phi \tag{3.24}$$

Equation (3.23) is the non-dimensional evolution equation formulated in terms of the non-dimensional local thickness of the film H as presented by Oron, Davis and Bankoff [36]. In dimensional form, the evolution equation is written as:

$$\mu\partial_t h + \partial_x\left[\left(\tau + \partial_x\sigma\right)\left(\frac{1}{2}h^2 + \beta h\right)\right] - \partial_x\left[\left(\frac{1}{3}h^3 + \beta h^2\right)\times\partial_x\left(\phi_{z=h} - \sigma\partial_x^2 h - \Pi\right)\right] = 0 \quad (3.25)$$

3.1.2 Linear Stability Analysis for the Bounded Rayleigh-Taylor Instability

The thin liquid film evolution equation (3.25) is utilized to analyze the bounded Rayleigh-Taylor instability. In this analysis, surface tension is constant and gravity is applied in the opposite direction (positive z-direction is shown in Figures 3.1 and 3.2). The gas at the interface does not exert a drift stress. Thus, external forcing at the bottom edge of the liquid film is negligible indicating that $\tau = \Pi = 0$. Relative motion and slip are not applied at the boundary ($\beta = 0$). Furthermore, pressure variations are included $\left(P = \rho g h - \sigma\partial_x^2 h\right)$. In order to account for the injected liquid through the bounding solid surface, a transpiration term (μq) is introduced. This modification will extend the analysis carried out in previous studies [36, 56-59]. Based on these assumptions equation (3.25) reduces to:

$$\mu\partial_t h - \mu q + \frac{1}{3}\rho g\partial_x\left(h^3\partial_x h\right) + \frac{1}{3}\sigma\partial_x\left(h^3\partial_x^3 h\right) = 0 \quad (3.26)$$

where

$$q = \frac{Q}{A} \quad (3.27)$$

Q = volume flow rate through the solid boundary

A = plate surface area

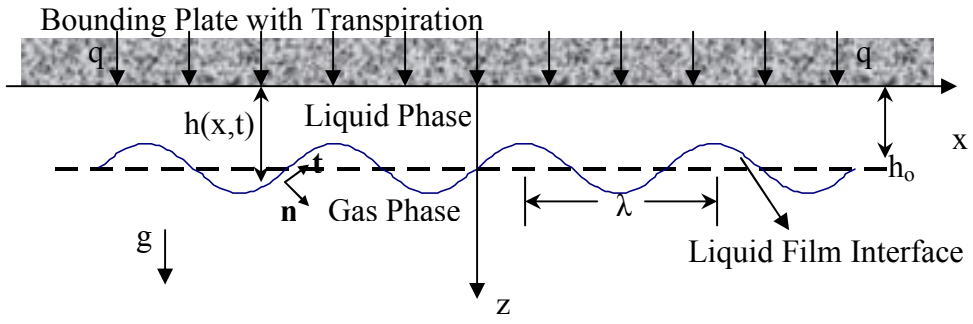

Figure 3.2 Bounded thin liquid film with transpiration through the boundary.

In order to investigate the response of the uniform film ($h = h_o$) to small disturbances, the liquid film is perturbed with a small disturbance h'.

$$h = h_o + qt + h' \tag{3.28}$$

where

$h' = h_o' f(t) e^{ikx}$, $f(t)$ = function of time

$k = \dfrac{2\pi}{\lambda}$ = wave number of the perturbed liquid film

λ = wavelength of the perturbed liquid film

The definitions of the liquid film thickness h and the imposed perturbation h' as give by (3.28) are substituted into the evolution equation (3.26). Linearization in primed quantities is carried out and the linear stability equation is obtained for h'.

$$f = f_o \exp\left[\frac{\rho g}{3\mu}\left(h_o^3 t + \frac{3}{2}h_o^2 q t^2 + \frac{2}{3}h_o q^2 t^3\right)k^2 - \frac{\sigma}{3\mu}\left(h_o^3 t + \frac{3}{2}h_o^2 q t^2 + \frac{2}{3}h_o q^2 t^3\right)k^4\right] \tag{3.29}$$

The exponent term inside the bracket in equation (3.29) can be rewritten in terms of the growth rate s and the wave number k. Let us define this exponent term as η:

$$\eta = \left(\gamma k^2 - \sigma k^4\right)\left(\frac{h_o^3}{3\mu}t + \frac{h_o^2}{2\mu}qt^2 + \frac{2}{9\mu}h_o q^2 t^3\right) \tag{3.30}$$

where

γ = specific weight of the liquid

Equation (3.30) characterizes the perturbation evolution for the case of the bounded Rayleigh-Taylor instability with injection through the boundary. In this formulation, the perturbation is driven by a common factor $\left(\gamma k^2 - \sigma k^4\right)$ including the effects of gravity and surface tension acting through a second order diffusion term and a fourth order dissipation term in the modified partial differential equation (3.26), respectively. If no transpiration is allowed through the boundary (q = 0), equation (3.30) is reduced to the original characteristic equation of the Rayleigh-Taylor instability:

$$\eta = \left(\gamma k^2 - \sigma k^2\right)\frac{h_o^3}{3\mu}t = st \tag{3.31}$$

where

s = growth rate of the perturbation

The liquid film perturbation can also be characterized in terms of the dimensionless growth rate s' and the dimensionless wave number k' by introducing the Bond number Bo through which the liquid film thickness controls the characteristic stability curves.

$$s' = k'^2 - \frac{k'^4}{\mathrm{Bo}} \tag{3.32}$$

where

$s' = \dfrac{3s\mu}{\rho g h_o}$ = non-dimensional growth rate of the perturbation

$k' = kh_o$ = non-dimensional wave number of the perturbation

$\text{Bo} = \frac{\rho g h_o^2}{\sigma}$ = Bond number

For inclined thin liquid films with transpiration through the boundary, the base state is obtained by solving the momentum and continuity equations and deriving the velocity distribution in the thin liquid film and the mass flow rate per unit width of the plate Γ.

$$u = \frac{(\rho_L - \rho_G)}{\mu_L} g \sin\theta \left(hz - \frac{z^2}{2} \right) \tag{3.33}$$

$$\Gamma = \frac{\rho_L (\rho_L - \rho_G) g h^3 \sin\theta}{3\mu_L} \tag{3.34}$$

3.1.3 Atomization Technique for Liquid Films

The quasi-static detachment of droplets from liquid films developing on the bottom side of flat horizontal surfaces can be formulated in a mechanistic model [55, 78]. An expression for the size of droplets can be derived based on a balance between gravitational and surface tension forces.

$$D_{theory} = 3.3 \left(\frac{\sigma}{\rho g} \right)^{0.5} \tag{3.35}$$

where

D = droplet diameter

This formulation for the size of droplets does not account for transpiration through the bounding surface. Thus, it can be utilized for predicting results pertaining to the original Rayleigh-Taylor instability ($q = 0$).

3.2 Numerical Investigation

In this section, the level contour reconstruction method developed in an investigation by Shin, Juric and Abdel-Khalik [39-42] will be delineated. The numerical technique employed in that investigation stems from Tryggvason's original finite difference/front tracking method developed for 2D and 3D isothermal multifluid flows [67-69].

3.2.1 Mathematical Formulation

This level contour reconstruction technique is a simplified front tracking method that eliminates logical connectivity and hence alleviate the associated algorithmic burden, while retaining the advantages and accuracy of explicit Lagrangian surface tracking. An essential advantage of this method is its ability to automatically and naturally handle interface merging and breakup in three-dimensional flows. The elements are meshed on a level contour of an indicator function. This characteristic indicator function is a Heaviside function which takes the value of unity in one fluid and zero in the other fluid. The operations of element addition, deletion and reconnection are carried out simultaneously in one step and without resorting to bookkeeping or element connectivity. Furthermore, once the elements are meshed, element areas and interface normals are automatically defined and thus surface tension forces are directly computed on the interface elements. This approach leads to the computation of as much of the interfacial physics as possible directly on the interface before providing this information to the stationary grid.

One set of transport equations valid for both fluids is used. Delta-function source terms, which act only at the interface, are used in the local single field formulation in order to incorporate the effect of the interface. The bulk fluids are assumed to be incompressible and thus the material properties are specified as constant, but not generally equal for both fluids. An indicator Heaviside function $I(\mathbf{x},t)$ is employed to define the material property fields for the entire domain. The local values of the material property field can then be given by

$$\alpha(\mathbf{x},t) = \alpha_1 + (\alpha_2 - \alpha_1) I(\mathbf{x},t) \tag{3.36}$$

where the subscripts 1 and 2 refer to the respective fluids, and α stands for either the density ρ or the dynamic viscosity μ. The indicator function $I(\mathbf{x},t)$ is found by solving the Poisson equation

$$\nabla^2 I = \nabla \cdot \int_{\Gamma(t)} \mathbf{n}\delta(\mathbf{x} - \mathbf{x}_f)\mathrm{ds} \tag{3.37}$$

where

$\mathbf{n}$ = unit normal to the interface

$\mathbf{x}_f = \mathbf{x}(s,t)$ = parameterization of the interface $\Gamma(t)$

$\delta(\mathbf{x}\text{-}\mathbf{x}_f)$ = three-dimensional delta function that is nonzero only when $\mathbf{x} = \mathbf{x}_f$

The interface is advected in a Lagrangian fashion by integrating:

$$\frac{d\mathbf{x}_f}{dt} \cdot \mathbf{n} = \mathbf{V} \cdot \mathbf{n} \tag{3.38}$$

where

$\mathbf{V} = \mathbf{u}_f = \mathbf{u}(\mathbf{x}_f)$ = the interface velocity vector

In the absence of phase change, the interface velocity will be equal to the fluid velocity at the interface. On the other hand, when phase change takes place, the interface velocity components in dimensional form are given by:

$$\frac{d\tilde{\mathbf{x}}_f}{dt} = \tilde{\mathbf{u}}_{\mathrm{L}} + \frac{\dot{m}''_f}{\rho_{\mathrm{L}}}\mathbf{n} \tag{3.39}$$

where

$\tilde{\mathbf{u}}_{\mathrm{L}}$ = heavier fluid (liquid) velocity at the interface

ρ_{L} = liquid density

$\dot{m}''_f$ = mass flux from the gas to the liquid at the interface

(positive for condensation and negative for evaporation)

Only the normal component of the interface motion is determined by the physics. The tangential motion is not; the interface and fluid at the interface are assumed to have the same tangential velocity component.

The momentum equation is written for the entire flow field and the forces due to surface tension are accounted for at the interface as body forces, which act only at the interface. In order to simulate the confined wall Rayleigh-Taylor instability with evaporation and condensation, mass exchange at the interface is parametrically accounted for, thereby eliminating the need to solve the energy equation. A single non-dimensional momentum equation can then be solved for both fluids. More importantly, by parametrically accounting for mass exchange at the interface, all the relevant physical phenomena can be addressed without restriction to specific target output spectra, chamber design, or fluid properties. Therefore, the dominant non-isothermal effects, i.e. evaporation and condensation at the interface, are analyzed by introducing a

parametrically specified interfacial mass flux $\dot{m}''_f$ as a source term in the conservation of mass and interface advection.

In non-dimensionalizing the governing equations and boundary conditions, the following scales are defined:

1- the length scale $l = (\sigma/[g(\rho_L-\rho_G)])^{1/2}$,

2- the velocity scale $U_o = (gl)^{1/2}$,

3- the pressure scale $P_o = \rho_L U_o^2$, and

4- the time scale $t_o = l/U_o$

Here, the subscript "L" refers to the film liquid injected through the bounding porous wall (heavy fluid), while the subscript "G" refers to the low pressure gas (vacuum) within the reactor cavity (light fluid). Hence, the governing non-dimensional momentum equation in conservative form can be expressed as:

$$\frac{\partial \rho^+ \mathbf{u}}{\partial t} + \nabla \cdot \left(\rho^+ \mathbf{u}\mathbf{u}\right) = -\nabla p + \rho^+ \mathbf{g} + \frac{1}{Re}\nabla \cdot \mu^+ \left(\nabla \mathbf{u} + \nabla \mathbf{u}^{\mathrm{T}}\right) + \int_A \frac{1}{\mathrm{We}} \kappa \mathbf{n} \delta\left(\mathbf{x} - \mathbf{x}_f\right) dA \quad (3.40)$$

where

$$\frac{\rho_G}{\rho_L} = \rho^*, \frac{\mu_G}{\mu_L} = \mu^* \quad (3.41)$$

$$\rho^+ \equiv \frac{\rho(\mathbf{x},t)}{\rho_L} = 1 + \left(\rho^* - 1\right) I(\mathbf{x},t) \quad (3.42)$$

$$\mu^+ \equiv \frac{\mu(\mathbf{x},t)}{\mu_L} = 1 + \left(\mu^* - 1\right) I(\mathbf{x},t) \quad (3.43)$$

$$\mathrm{Re} = \frac{\rho_L U_o l}{\mu_L}, \mathrm{We} = \frac{\rho_L U_o^2 l}{\sigma} = \frac{\rho_L}{\rho_L - \rho_G} \quad (3.44)$$

In this formulation, P is the pressure, $\mathbf{g}$ is the gravitational acceleration, σ is the surface tension coefficient, and κ is twice the mean interface curvature. The integral source term in equation (3.40) accounts for surface tension effects at the interface. The surface tension coefficient is assumed to be constant and thus, without loss of generality, the tangential variations in σ along the interface are ignored. Also, the light fluid (IFE chamber cavity gas) is assumed to be inviscid, so that the viscosity ratio defined in equation (3.41) is equal to zero. The selected definitions for the length and velocity scales make the Weber number We a function of only the density ratio as defined in equation (3.44); a density ratio of 20 corresponds to a Weber number of 1.05, while an infinite density ratio corresponds to a Weber number of unity. Values of the length, velocity, and time scales, along with the Reynolds number for different candidate fluids at different temperatures are given in Table 3.1.

By including condensation and evaporation as a source term at the interface, the non-dimensional conservation of mass equation can be rewritten as:

$$\nabla \cdot \rho^{+}\mathbf{u} = u \cdot \nabla \rho^{+} + \frac{2\left(\rho^{*}-1\right)}{\left(\rho^{*}+1\right)} \int_{A} \dot{m}_{f}^{+} \delta\left(\mathbf{x}-\mathbf{x}_{f}\right) dA \qquad (3.45)$$

where

$\dot{m}_{f}^{+}$ = non-dimensional mass flux scaled by $\rho_{\mathrm{L}} U_{\mathrm{o}}$

Table 3.1 Values of the scaling length, velocity, and time, along with the Reynolds number for various candidate coolants [79-82].

T (K)	Water, H_2O		Lead, Pb		Lithium, Li		Flibe, $LiF\text{-}BeF_2$		
	293	323	700	800	523	723	773	873	973
l (mm)	2.73	2.65	2.14	2.12	8.25	7.99	3.35	3.22	3.17
U_{o} (mm/s)	163.5	161.2	144.7	144.2	284.4	280	181.4	177.8	176.4
t_{o} (ms)	16.7	16.4	14.8	14.7	29	28.6	18.5	18.1	18
Re	445	771.2	1618	1831	1546	1775	81.8	130.8	195.3

3.2.2 Interface Tracking and Reconstruction

The original front tracking method is based on constructing two grids. One of the grids is a stationary finite difference mesh while the other grid is a discretized interface mesh employed to explicitly track the moving interface. The discretized interface is defined by Lagrangian computational points connected to form a two-dimensional surface for 3D geometries and a one-dimensional line for 2D geometries. This concept has been used in several numerical investigations, including: Sheth and Pozrikidis [83], Popinet and Zaleski [84], and Torres and Brackbill [85]. Figure 3.3 illustrates the two grids used in the standard concept of the front tracking method.

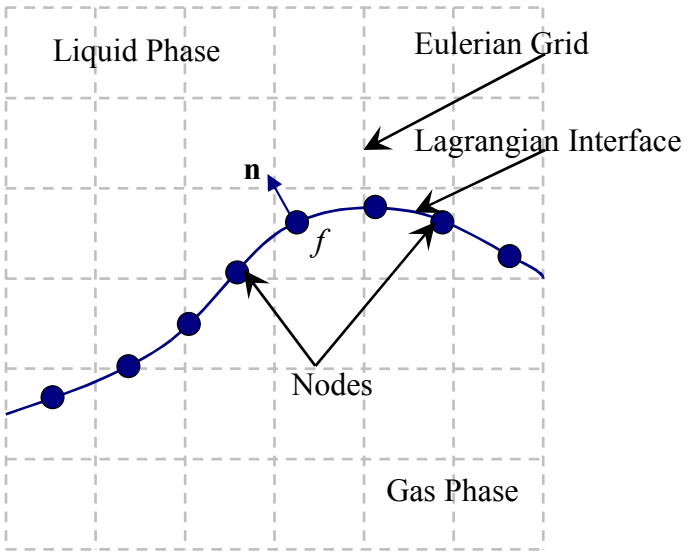

Figure 3.3 The Eulerian and Lagrangian grids utilized in the front tracking method.

In the original implementation of the front tracking method, the basic structural unit for a three-dimensional geometry is a triangular interface element consisting of three interface points. A line segment consisting of two adjacent points is used in two-

dimensional geometries. The interface elements are connected with each other such that each element keeps track of its nearest neighbor elements. The tracking of element neighbor connectivity is implemented in two-dimensional solutions by using linked lists. Interface elements must be added or deleted to maintain regularity while the interface moves and deforms. In the case of merging or breakup, interface elements are relinked to produce a change in topology.

The front tracking method used in this thesis relies on a novel implementation developed by Shin, Juric and Abdel-Khalik [39-42]. In this implementation, an interface reconstruction procedure is designed to eliminate the need for element connectivity while accurately defining interface geometry (normals and curvature) and automatically providing for element addition/deletion to effect topology change. There are two separate representations of the interface position: 1) the indicator function with a 0.5 contour level and 2) the explicitly tracked interface elements. Therefore, starting with interface elements, this technique solves the Poisson equation (3.37) for the indicator function. On the other hand, beginning with a given indicator function field we can deposit a set of interface elements on the 0.5 contour level.

In two-dimensional analysis, a temporal procedure is carried out. At the end of a time step, the tracked interface elements in the solution of equation (3.37) can be utilized to calculate the indicator function I at each grid point. The interface elements are then discarded and new ones are developed by tracing a contour level across each grid cell at the value of $I_f = 0.5$ using linear interpolation. Hence, one new interface element is constructed by the two endpoints of the contour line as depicted in Figure 3.4(a). Neighboring elements from adjacent cells must have the same endpoint locations because

linear interpolation is used. This will allow elements to always be connected since interface points that coexist at the same spatial location will have the same velocity. Therefore, neighboring interface elements are automatically linked and the need for explicit tracking of adjacent element connectivity is eliminated. In order for the interface elements to be properly oriented, the element normals must point toward the inside of the volume enclosed by the moving surface. This orientation procedure is carried out cell by cell such that the maximum cell indicator function lies to the right of the element tangent drawn from node 1 to node 2 as presented in Figure 3.4(b).

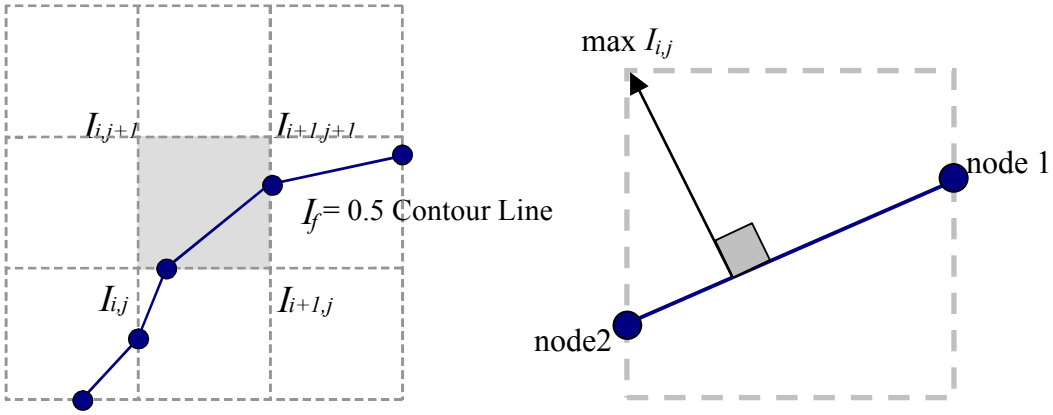

Figure 3.4 Interface reconstruction and orientation: (a) Linear approximation of the I_f = 0.5 contour in each grid cell, and (b) Element orientation conducted such that the maximum cell indicator function value is located to the right of the element tangent traced from node 1 to node 2.

The reconstruction step has obviated the need to add or delete elements individually. Thus, the method accounts for topology change naturally in a process

similar to using the distance function as carried out by the level set method [86, 87]. The frequency of the reconstruction can be prescribed as a multiple of the solution time step.

The level contour reconstruction procedure delineated above in solving two-dimensional models is extended to include three-dimensional solutions. In three-dimensional analysis, the reconstruction process is applied to the 6 faces of a rectangular parallelepiped (grid cell) as shown in Figure 3.5. Elements are formed by connecting individual line segments constructed on the $I_f = 0.5$ contour level. At the 6 cell faces at least 3 and at most 6 line segments can be constructed. A triangular element is formed by connecting 3 line segments while a polygon is constructed from 4, 5 or 6 line segments. In the case of a polygon, triangular elements are segmented from the centroid.

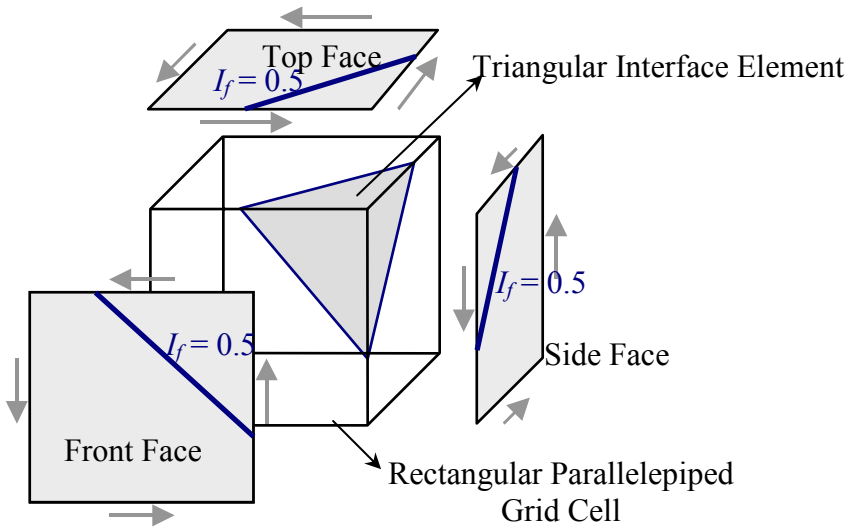

Figure 3.5 Three-dimensional representation of the level contour reconstruction method.

In order to preserve the global mass enclosed by the moving interface, the reconstruction procedure is modified by varying the value of the indicator function I_f at the interface. At very low grid resolution calculations, the linear reconstruction using $I_f =$

0.5 provides an inaccurate approximation of the exact surface contour. Mass redistribution or loss between two different size surfaces can occur using a constant I_f value. In some computations, the reconstruction step produces an interface which underestimates the actual tracked interface as presented in Figure 3.6. Therefore, in order to improve the reconstruction process, an optimum I_f value is defined based on the equality between the volume enclosed by the new surface and the volume before reconstruction. An analogous procedure would be in calculating the area of a discretized circle by using two-point Gauss quadrature versus trapezoidal rule integration. The optimum value for I_f reaches a value of nearly 0.5 as the computation resolution is increased.

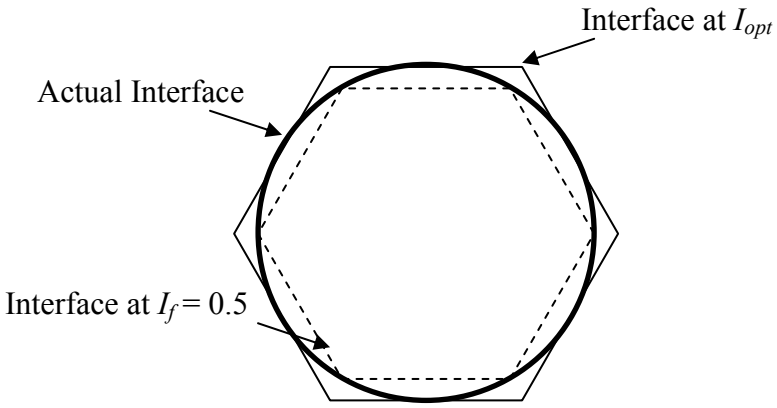

Figure 3.6 Representation for the optimum value of the indicator function I_f.

In the modified reconstruction procedure, several I_f values are obtained throughout the computation space at any surface element point. This localized indicator function value is then used to reconstruct the element at the cell which may have more than one element. Each computation cell is influenced by several elements $I_{p,i}$ with different areas ds_i as shown in Figure 3.7. At that location, the optimum value for the

indictor function $I_{opt}(i,j)$ which is used to reconstruct the surface in that cell is expressed as:

$$I_{opt}(i,j) = \frac{\sum I_{p,i} ds_i}{\sum ds_i} \tag{4.46}$$

Element merging and break up as in droplet detachment is carried out by utilizing a weighted value for I_{opt} rather than using the interpolated $I_{p,i}$ value discussed in the previous paragraph. In the case of spike necking , two adjacent surfaces approach each other and the distance between them *dl* is less than a specific value. In order for droplet detachment to occur, a value of $I_{opt} = 1$ is used for breaking while a value of $I_{opt} = 0.5$ is used in the case of connecting two surfaces. Figure 3.8 illustrates the detachment and merging procedure.

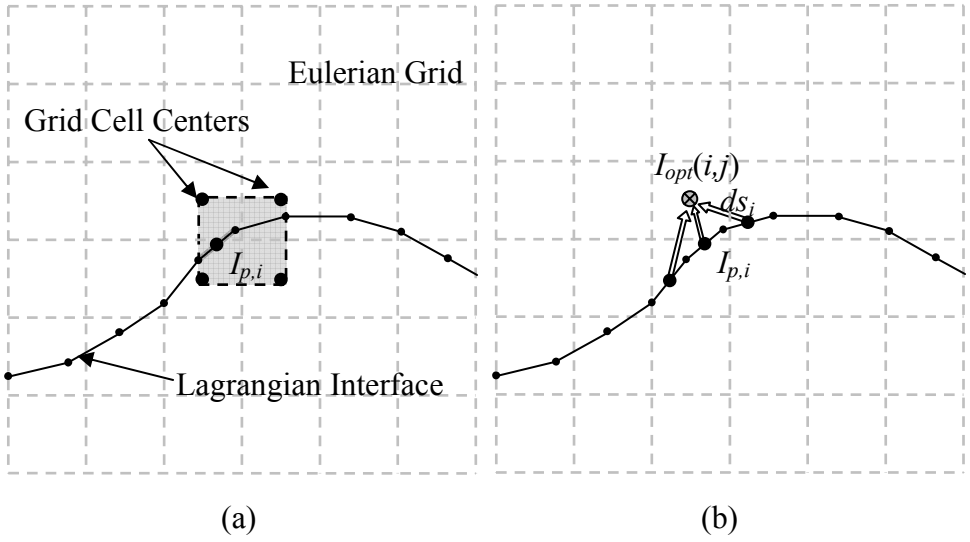

Figure 3.7 The localized optimum indicator function value I_{opt} used in the reconstruction method: (a) The indicator function value is interpolated at each element and then distributed to the adjacent cell centers , and (b) The area averaged value of I_{opt} is influenced by several elements.

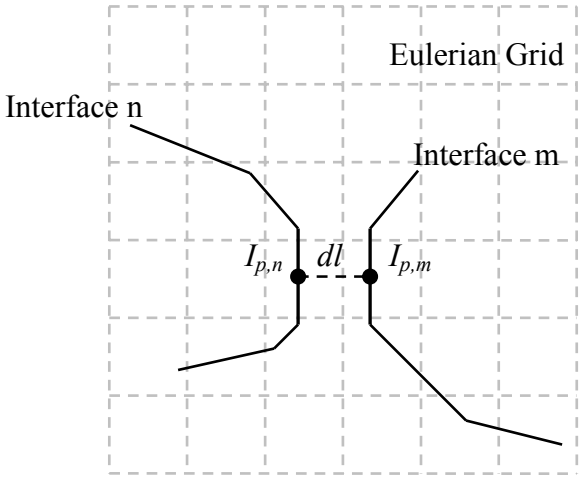

Figure 3.8 Detachment and merging of two adjacent interfaces based on the values of dl and I_{opt}.

3.2.3 Interface Advection

Interface advection with finite phase change expressed in equation (3.39) can be non-dimensionalized as:

$$\frac{d\mathbf{x}_f}{dt} = \mathbf{u}_{\mathrm{L}} + \dot{m}_f^+ \mathbf{n} \tag{3.47}$$

The non-dimensional mass flux $\dot{m}_f^+$ disappears for surfaces that do not undergo phase change. In this case, the interface follows the fluid velocity.

3.2.4 Transfer of Information between the Lagrangian Interface and Eulerian Grid

Information is transferred between the moving interface and the fixed grid using the immersed boundary method. This method accounts for the situation when the Eulerian grid points $\mathbf{x}_{ij}$ do not coincide with the Lagrangian interface points $\mathbf{x}_p$. A smooth distribution function is utilized in spreading sources at the interface over several grid points adjacent to the interface. Interpolation of the field variables from the fixed

Eulerian grid to the moving interface is also carried out by using the same distribution function. At a specific interface point $\mathbf{x}_p = (x_p, y_p)$, a distribution function is expressed as:

$$\mathrm{D}_{ij}\left(\mathbf{x}_p\right) = \frac{\delta\left(x_p/h_x - i\right)\delta\left(y_p/h_y - j\right)}{h_x h_y} \tag{3.48}$$

where

$$\delta(r) = \begin{Bmatrix} \delta_1(r) & |r| \le 1 \\ \frac{1}{2} - \delta_1\left(2 - |r|\right) & 1 < |r| < 2 \\ 0 & |r| \ge 2 \end{Bmatrix} \tag{3.49}$$

$$\delta_1(r) = \frac{3 - 2|r| + \sqrt{1 + 4|r| - 4r^2}}{8} \tag{3.50}$$

This distribution function D_{ij} is used to approximate the Dirac function in the source term integrals which are part of the governing equations (3.37) and (3.40). The source terms can be expressed in general form as:

$$\Phi = \int_{\Gamma(t)} \varphi\delta\left(\mathbf{x} - \mathbf{x}_f\right) ds \tag{3.51}$$

This general form of the source terms can be discretized with the discrete interface sources φ_p distributed to the stationary grid and the discrete field variables R_{ij} interpolated to the moving interface.

$$\Phi_{ij} = \sum_p \varphi_p \mathrm{D}_{ij}\left(\mathbf{x}_p\right)\Delta s \tag{3.52}$$

$$\mathrm{R}_p = \sum_{ij} h_x h_y \mathrm{R}_{ij} \mathrm{D}_{ij}\left(\mathbf{x}_p\right) \tag{3.53}$$

where

Δs = the element length in 2D or element area in 3D computations

The formulation of D_{ij} presented above is extended to three-dimensions to carry out 3D computations.

In the Poisson equation (3.37), the normal and area *ds* are readily defined for each element as presented in Figure 3.9. The source term is then distributed by using the immersed boundary method discussed above. Another source term for surface tension appears in the momentum equation (3.40). The conservative approach provided by Tryggvason et al. [88] is utilized to compute the surface tension source term. In two-dimensional computations, the force on a segment of the front is expressed as:

$$\delta F_e = \int_{\Delta s} \sigma \kappa \mathbf{n} \delta \mathrm{d}s \tag{3.54}$$

The Frenet relation $\kappa \mathbf{n} = d\mathbf{t}/ds$ is then used to rewrite equation (3.54) as:

$$\delta F_e = \int_A^B \sigma \frac{\partial \mathbf{t}}{\partial s} \mathrm{d}s = \sigma \left(\mathbf{t}_B - \mathbf{t}_A \right) \tag{3.55}$$

where

σ = surface tension coefficient

κ = twice the mean interface curvature

$\mathbf{t}$ = a vector tangent to the edge of the element

$\mathbf{n}$ = a vector normal to the surface

Since the tangent at each element is known, the force is applied at the end points of each element. The resultant force at each endpoint is directed inward. Thus, the total force on any closed surface in a two-dimensional model analysis is zero because the forces on the two endpoints of every element exactly cancel. This process provides a conservation property avoiding a fictitious net force on an interface due to the possible accumulation of errors in the surface tension computation while marching in time.

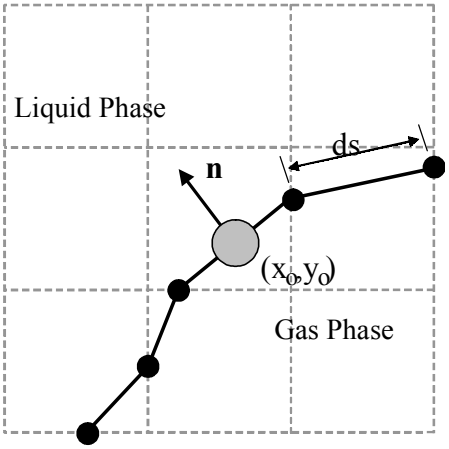

Figure 3.9 Definition of the normal vector **n** and area ds for each element as utilized in the Poisson equation (3.37).

The surface tension computation described above is extended to three-dimensional analysis in which the surface tension force on a surface element is defined as:

$$\delta F_e = \sigma \oint_S \mathbf{t} \times \mathbf{n} ds \tag{3.56}$$

Equation (3.56) is then discretized and applied to each triangular surface element in the three-dimensional model construction numerical grid. In this numerical computation approach, the element normal and tangent is provided to each of the three edges of the triangular grid element. The surface tension force is then applied at the middle of each edge with the resultant force at each edge of the triangular element pointing inward. Figure 3.10 illustrates the three-dimensional conservative surface tension applied to a triangular element. Based on this approach, the total surface force is locally and globally conservative. This is due to the fact that whether the analysis is carried out for two-dimensional or three-dimensional numerical models, the total surface tension force on a closed surface will vanish.

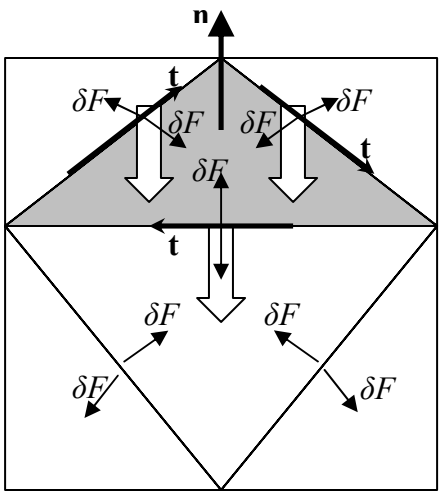

Figure 3.10 The three-dimensional surface tension force on each side of the triangular element is in the direction of $\mathbf{t} \times \mathbf{n}$ leading to a conservative resultant force.

3.2.5 Finite Difference Technique

The fluid variables **u** and P are computed by employing a projection method (see, for example, Chorin [89], and Juric and Tryggvason [90]) using a first order forward Euler time integration. Using the projection method, equations (3.40) and (3.45) is reduced to a generic form:

$$\frac{\mathbf{w}^{n+1} - \mathbf{w}^{n}}{\Delta t} = \mathbf{A}^{n} + \mathbf{F}^{n+1} - \nabla_h P \tag{3.57}$$

$$\nabla_h \cdot \mathbf{w}^{n+1} = R^{n+1} \tag{3.58}$$

where **w** = ρ**u** is the fluid mass flux

A = a lumped parameter which includes the advection, diffusion and gravitational terms in equation (3.40)

F = the surface integral which includes the surface tension forces in equation (3.40)

R = the right side of equation (3.45)

The momentum equation is then split into two parts based on Chorin's projection method [89]. Thus, equation (3.57) is divided into:

$$\frac{\tilde{\mathbf{w}} - \mathbf{w}^n}{\Delta t} = \mathbf{A}^n + \mathbf{F}^{n+1} \tag{3.59}$$

$$\frac{\mathbf{w}^{n+1} - \tilde{\mathbf{w}}}{\Delta t} = -\nabla_h P \tag{3.60}$$

where $\tilde{\mathbf{w}}$ = the fluid mass flux obtained by deleting the effect of pressure

Equation (3.59) is used to obtain the fluid mass flux $\tilde{\mathbf{w}}$ while the pressure is attained by using equation (3.58) and applying the divergence of equation (3.60). A standard fast Poisson solver is then utilized to solve for P in the following equation:

$$\nabla^2 P = \frac{\nabla \cdot \tilde{\mathbf{w}} - R^{n+1}}{\Delta t} \tag{3.61}$$

Employing the fluid mass flux $\tilde{\mathbf{w}}$ and the pressure P obtained by solving equations (3.59) and (3.61), the mass flux $\tilde{\mathbf{w}}^{n+1}$ at the next time step is found using equation (3.60). The updated velocity $\mathbf{u}^{n+1}$ is then found as follows:

$$\mathbf{u}^{n+1} = \frac{\mathbf{w}^{n+1}}{\rho^{n+1}} \tag{3.62}$$

For the spatial discretization, the staggered mesh marker and cell (MAC) method of Harlow and Welch [91] is used. The (x, y, z) components of velocity are located at the faces while the pressure and indicator function are located at the cell centers. All spatial derivatives are approximated by standard second-order centered differences. A simple first-order upwind scheme is used for the convective term in the momentum equation. Figures 3.11 and 3.12 illustrate the spatial discretization and staggered mesh used in the numerical analysis.

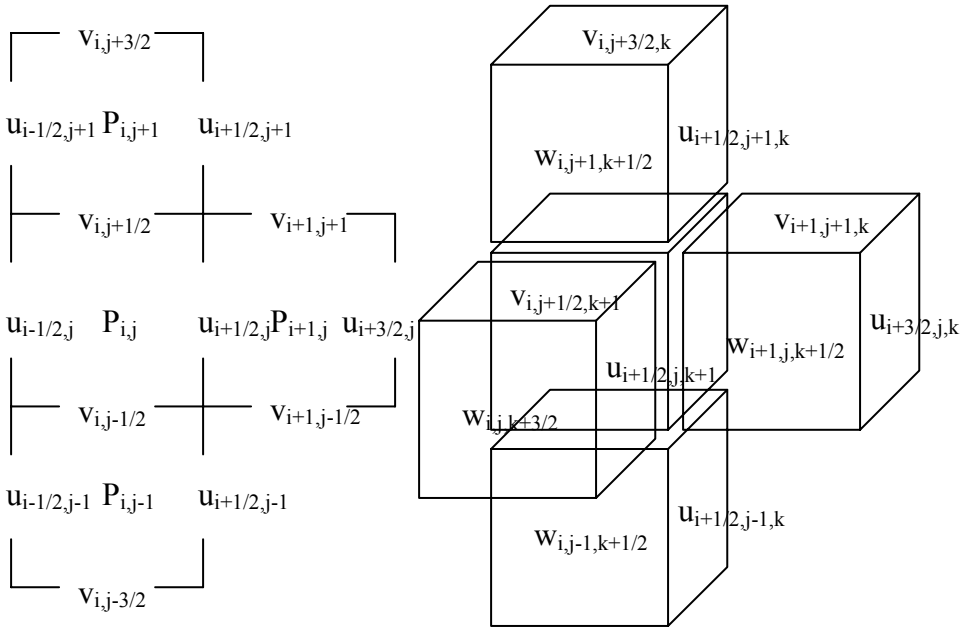

(a) (b)

Figure 3.11 Staggered grid utilized for the spatial discretization: (a) two-dimensional, and (b) three-dimensional.

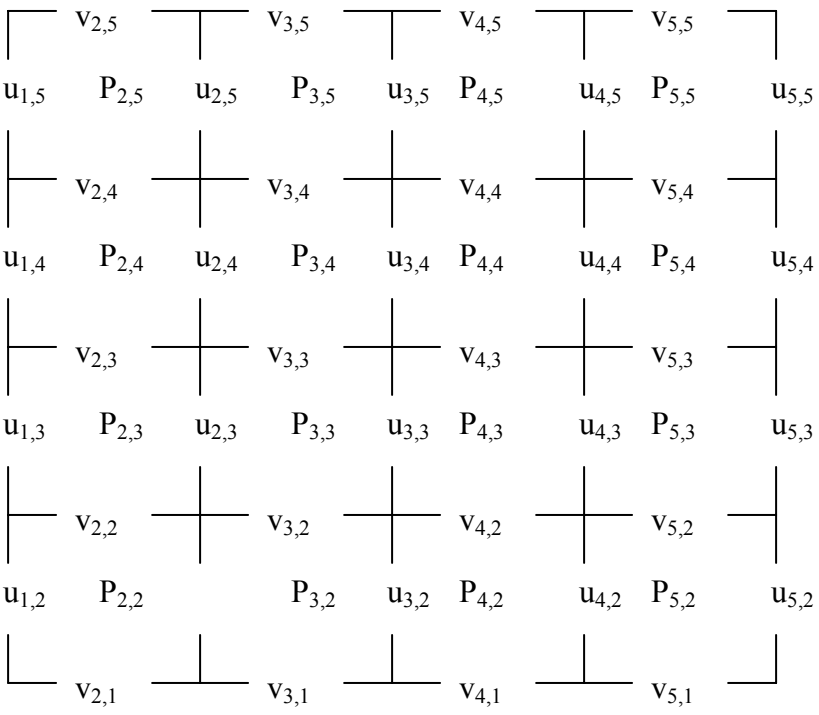

Figure 3.12 Staggered grid for 4×4 computational domain.

3.2.6 Geometry and Boundary Conditions

The calculation geometry and boundary conditions used to model horizontal, downward facing surfaces with liquid injection through the wall surface is depicted in Figure 3.13. This corresponds to the uppermost point in the reactor cavity inner surface. Liquid is injected at a specified normal velocity at the upper solid boundary, while an open boundary condition is used at the bottom surface.

For cases where the surface is inclined at an angle θ with respect to the horizontal, the computation geometry and boundary conditions are modified. The initial surface consists of one peak perturbation on one side of the calculation domain and the other side is flat without any disturbance as shown in Figure 3.14. This inclined case models sectors near the uppermost point in the reactor cavity inner surface. As in the horizontal case, no slip conditions with transpiration are applied on the upper boundary, while the bottom surface represents an open boundary condition. Rather than using periodic boundary conditions in the horizontal directions, Neumann conditions for velocity and hydrostatic pressure gradients are applied along the x and y directions.

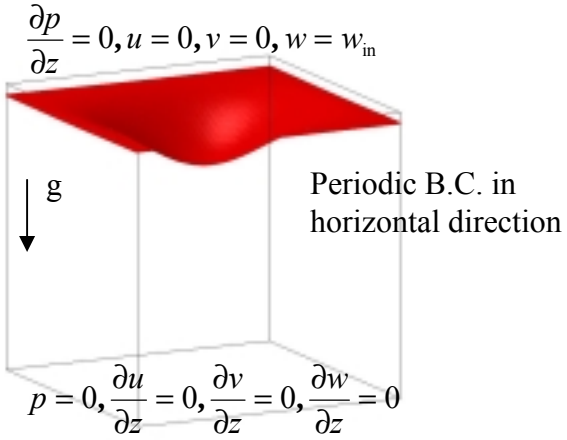

Figure 3.13 Initial surface configuration and boundary conditions used to model horizontal downward-facing surfaces with liquid injection through the wall surface.

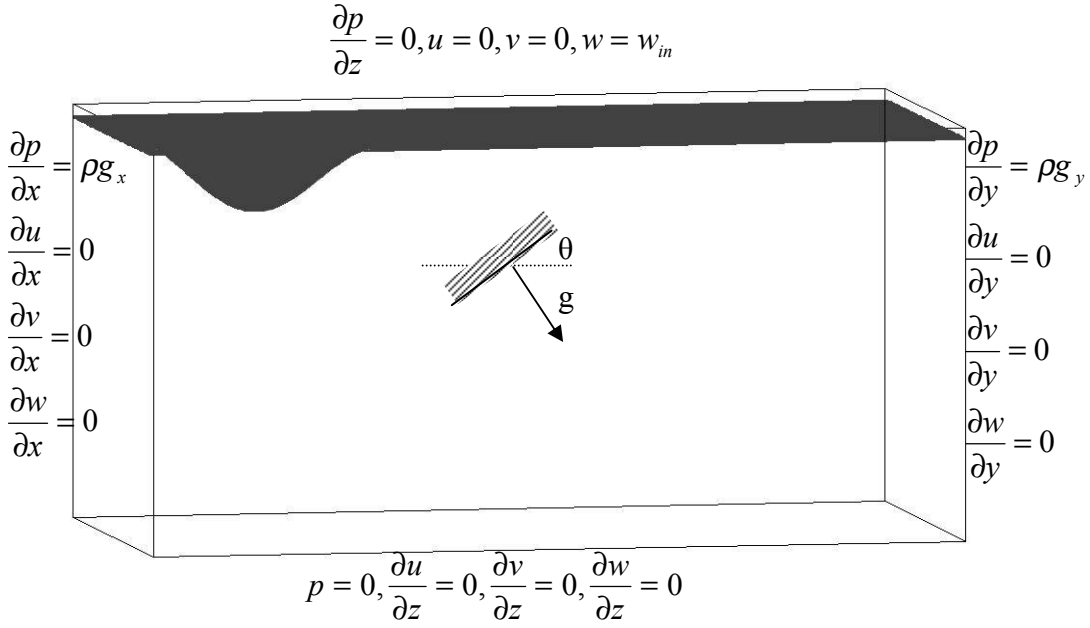

Figure 3.14 Initial surface configuration and boundary conditions utilized in modeling inclined downward-facing surfaces with liquid injection through the bounding wall surface.

3.2.7 Determination of Field Variables

The data extracted by conducting the numerical runs consist of several sequences showing how the surface evolves from the initially perturbed interface to the fully developed spike penetrating through the lighter fluid and necking to form droplets that detach at the pinch off point. The growth patterns and the sequences are processed and analyzed to calculate several field parameters, including: the frequency of liquid droplet formation and detachment, the volume and size of detached droplets, and the time history of the penetration depth for the developing spikes. Figure 3.15 depicts the triangular grid elements utilized in the Rayleigh-Taylor instability numerical simulation at pinch off or detachment for horizontal and inclined bounding surfaces with transpiration through the boundary.

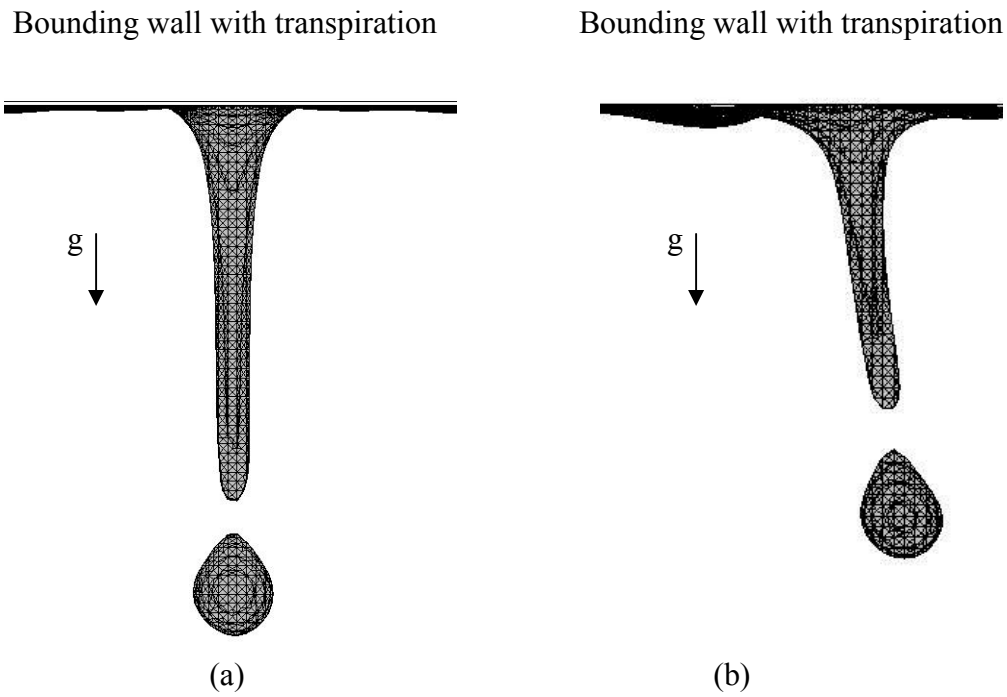

Figure 3.15 Configuration of the grid elements for the bounded Rayleigh-Taylor instability numerical simulation at detachment utilized in modeling inclined downward-facing surfaces with liquid injection through the wall surface: (a) horizontal bounding surface, and (b) inclined bounding surface ($\theta = 2.5^{\circ}$).

The detachment time was calculated by following the evolution of the surface to the pinch-off point where droplet formation transpires. The detached droplet was then isolated in order to determine the liquid volume enclosed by the constructed surface. This computed numerical volume is utilized in obtaining an equivalent droplet diameter based on the definition of the standard sphere volume $\left(D_{\text{equivalent}} = \sqrt[3]{\left(6\text{Volume}_{\text{numerical}}\right)/\pi}\right)$. In order to trace the time history of the penetration depth, the maximum vertical distance from the plate surface to the lowermost tip point of the developing spike or the detached droplet is stored in a temporal array. These numerical computations for the field variables were carried out for all the numerical runs utilized in simulating the confined Rayleigh-

Taylor instability with liquid transpiration through horizontal and inclined bounding surfaces.

CHAPTER 4
EXPERIMENTAL INVESTIGATION

In order to attain a more comprehensive understanding of the thin liquid film protection scheme, an experiment has been designed to investigate the critical issues associated with this concept. This chapter provides a detailed description of the experimental test facility, the instrumentation, the data acquisition system and the analysis techniques.

4.1 Experimental Test Facility

This section details the essential components of the experimental test facility utilized to carry out the experimental investigation. The following paragraphs include a discussion of the experimental apparatus, the test section and the experimental procedure used to investigate various design and operational parameters.

4.1.1 Experimental Setup and Test Section

A recirculating experimental test facility is designed and constructed to study the hydrodynamics of thin liquid films injected through downward-facing porous walls. The flow is started by forcing the working fluid through flexible tubing up from a reservoir into a constant-head supply tank using a sump pump placed in the reservoir. The constant-head tank is placed at different heights above the test section to obtain a range of inlet pressures, i.e. flow rates, and hence transpiration velocities. The fluid from the

constant-head tank is allowed to flow continuously through a porous Type 316L stainless steel rectangular plate which serves as the test section. The injected liquid forms a thin film on the underside of this porous plate; the film then grows downwards and forms spikes that "neck" and detach as droplets, which fall into the light fluid (ambient air). The droplets ultimately fall into the reservoir, where they are then recirculated back into the constant-head tank. Figure 4.1 and Table 4.1 illustrate and list the components of the experimental test facility.

The test section is a porous Type 316L stainless steel rectangular plate (thickness ~ 1.6 mm) fed by a stainless steel plenum. Plates with different porosities in micron grades ranging from 0.2μm to 20μm are used as test sections. The plate dimensions (~12 × 18 cm) are considerably larger than the characteristic length scale of the flow (see Table 3.1) and are therefore expected to adequately model the behavior of the much larger surfaces expected in an IFE reactor chamber (radius ~5 m). A rectangular cutout in the stainless steel plenum, machined by using wire electro-discharge machining (EDM), holds the plate. The porous plate is attached to the plenum with an ultra-strength aerospace grade epoxy adhesive (Hysol, LOCTITE E-120HP 29353). A polycarbonate plate (thickness ~12.7 mm) is used to cap the plenum by means of forced fit bolting.

The test liquid supply line from the constant-head tank is connected to the stainless steel plenum through an intermediate shutoff valve. In order to provide uniform pressure distribution on the inner surface of the porous plate, baffles are installed underneath the supply inlet in the plenum cap. Different supply tank levels are used to produce wide ranges of injection velocity and film thickness. The film thickness and injection velocity may be independently varied by using plates with different porosities.

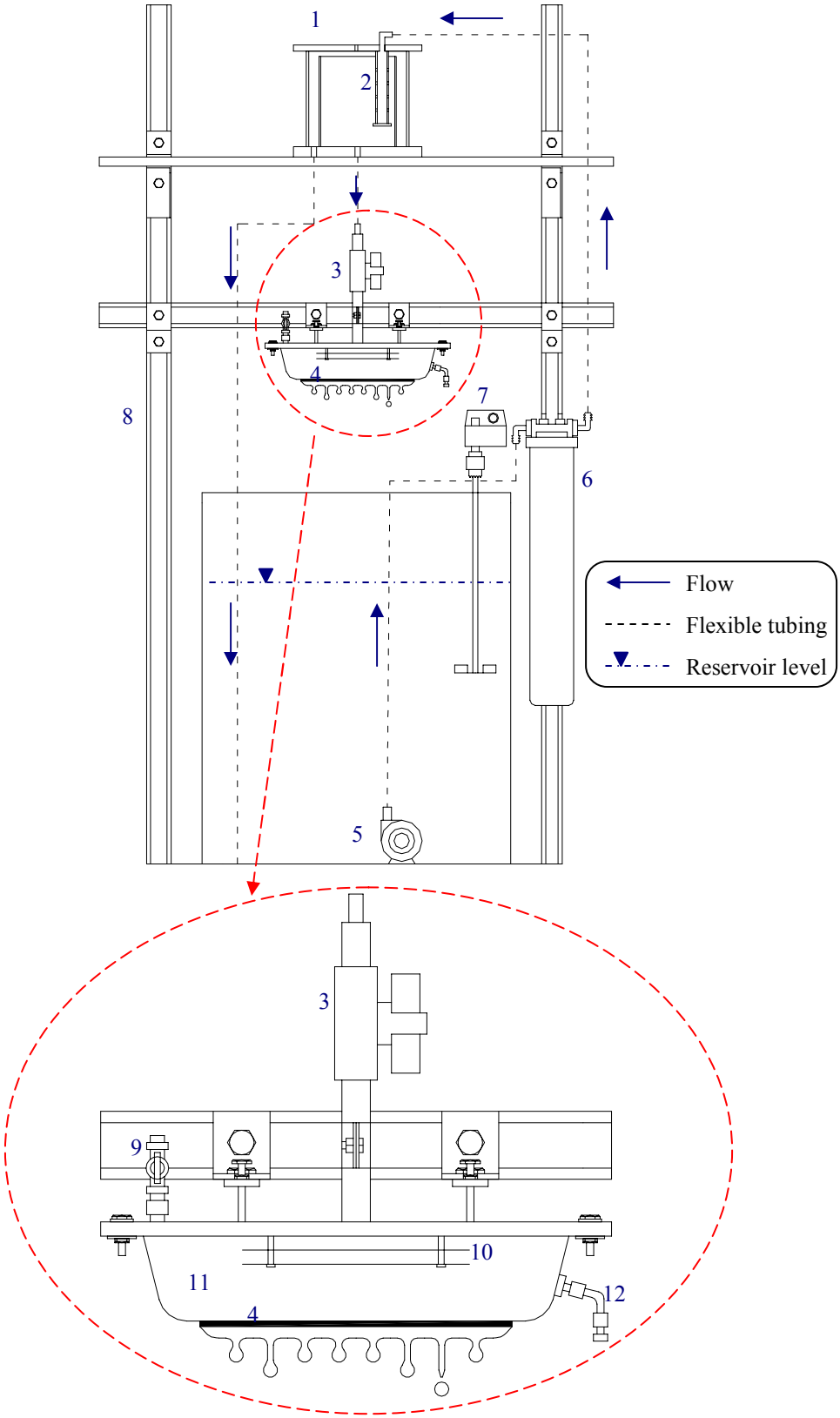

Figure 4.1 Experimental setup (top) and closeup of test section (bottom).

Table 4.1 List of numbered hardware components in the experimental setup.

Number	Description	Manufacturer	Model
1	Constant-head supply tank w/var. height	In house construction	-
2	Perforated tube	In house construction	-
3	Shutoff valve	-	-
4	Test section porous plate, 316L SS	Mott Industrial	1100-W-L-T-μGrade
5	Sump pump	Little Giant	4E-34NR
6	Sub-micron filter	Gelman Sciences	960822
7	Fast stirrer	Fisher Scientific	SL600
8	Unistrut frame	In house construction	-
9	Air relief valve	-	-
10	Baffles	In house construction	-
11	Porous plate plenum	In house construction	-
12	Draining valve	-	-

4.1.2 Experimental Procedure and Design Parameters

System preparation and control procedures were conducted prior to each experiment in order to provide different experimental setups and flow configurations. Several experimental runs were carried out to assess and determine the effect of different design and operational parameters (liquid injection velocity, film thickness, inclination angle, and liquid properties) on the liquid film stability between target explosions.

A range of liquid injection velocities through the porous plate were obtained by varying the constant-head tank levels leading to different inlet pressures, and thus flow rates. Figure 4.2 depicts the hydraulic head variation procedure used in providing different transpiration velocities. For a given constant-head tank level and porous plate grade, the average injection velocity through the plate was determined by collecting the injected fluid during a specified period of time. In order for a continuous liquid film to develop forming spikes from which droplets detach, liquid injection velocities of 0.9-2.1 mm/s were utilized in the experimental runs as listed in Table 4.2. The testing facility is designed to reach higher injection velocities; however, the developed liquid film forms continuous columns that do not neck or detach as droplets at injection velocities higher

than 2.1 mm/s. On the lower end of the injection velocity range ($w_{in} << 0.9$ mm/s), a discontinuous liquid film develops and droplets are separated by dry spots. Figure 4.3 shows the two limiting cases of continuous columns and dry spots. An alternative approach to independently vary the liquid film thickness and injection velocities was carried out by utilizing plates with different porosities in micron grades ranging from 0.2μm to 20μm representing a solid volume percentage of 80% to 55%.

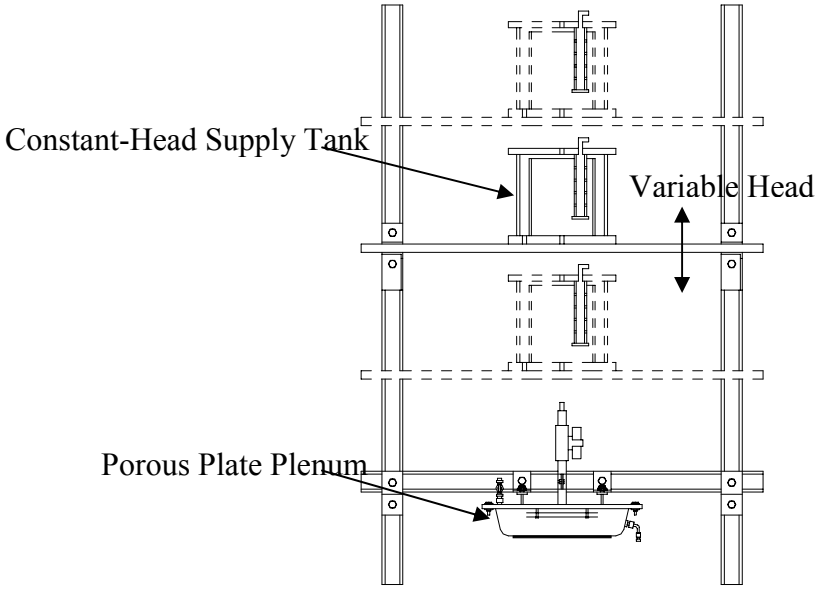

Figure 4.2 Hydraulic head variation procedure utilized in adjusting the transpiration velocity w_{in}.

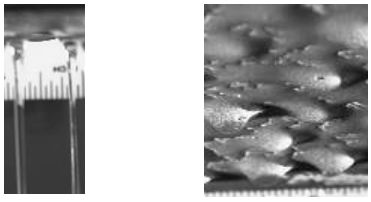

(a) (b)

Figure 4.3 Limiting conditions for the transpiration velocity w_{in}: (a) continuous liquid columns for $w_{in} > 2.1$ mm/s, and (b) dry spots for $w_{in} < 0.9$ mm/s.

Table 4.2 Liquid mass flow rates and injection velocities for different experimental runs, including: water (W) and 20% glycerol (G) as working fluids.

Time, [sec]	$M_{W0.9}$, [kg]	$M_{G0.9}$, [kg]	$M_{W1.4}$, [kg]	$M_{W1.7}$, [kg]	$M_{G1.7}$, [kg]	$M_{W1.9}$, [kg]	$M_{W2.1}$, [kg]
5	0.120	0.128	0.208	0.222	0.284	0.247	0.249
10	0.226	0.289	0.304	0.400	0.467	0.488	0.548
15	0.378	0.394	0.548	0.682	0.698	0.762	0.849
20	0.482	0.486	0.750	0.900	0.904	1.011	1.105
25	0.592	0.587	0.900	1.133	1.149	1.324	1.398
30	0.711	0.798	1.131	1.359	1.354	1.487	1.642
35	0.814	0.844	1.308	1.580	1.598	1.714	1.989
40	0.972	0.948	1.509	1.802	1.799	1.971	2.288
45	1.020	1.049	1.622	2.082	2.089	2.224	2.499
50	1.177	1.102	1.883	2.244	2.279	2.479	2.782
$\dot{m}_{av}$, [kg/s]	0.024	0.025	0.037	0.045	0.047	0.049	0.055
$\dot{V}_{av}$, [mm^3/s]	23747	23719	36919	44763	44795	50023	55330
$w_{in,av}$, [mm/s]	0.903	0.902	1.404	1.702	1.703	1.902	2.104

The stability and evolution of the liquid film on downward facing surfaces with liquid injection through the boundary were studied on horizontal and finite inclination surfaces. These experimental runs correspond to the uppermost point and adjacent sectors in the IFE reactor cavity inner surface. Figure 4.4 illustrates the test section configuration for the inclined case study. Inclination angles of 0° and 2.5° were utilized to investigate the effect of shear stress and liquid film drift on the stability and detachment response. In order to accurately tilt the test section to the required angle of inclination θ_y, an electronic level was employed to measure the inclination angle directly on the plate. The angle measurement resolution is 0.1°. An inclination angle of 2.5° emerged as a limiting condition since higher angles of inclination produced high liquid film velocities on the downward facing surface which caused the film to flow along the entire test section length without droplet detachment as shown in Figure 4.5.

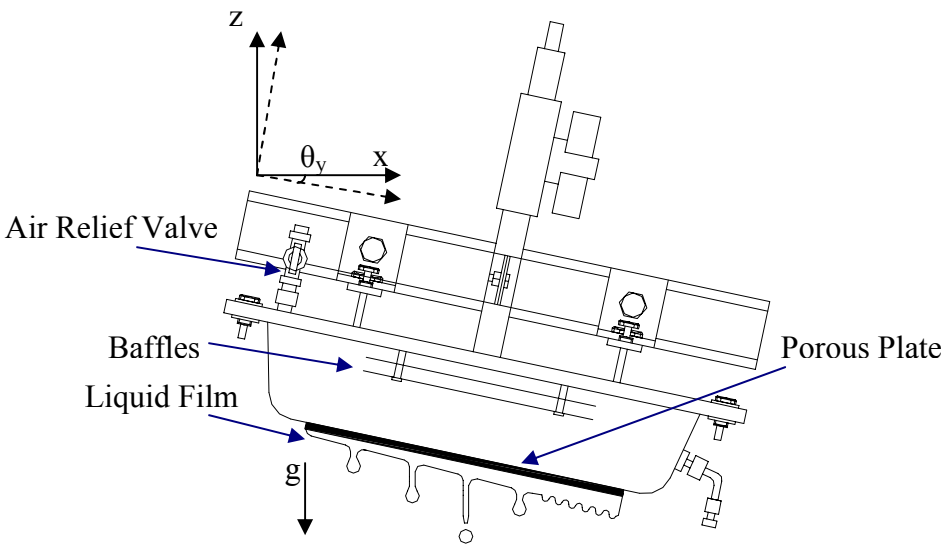

Figure 4.4 Experimental test section setup for an inclined downward facing surface with transpiration through the boundary.

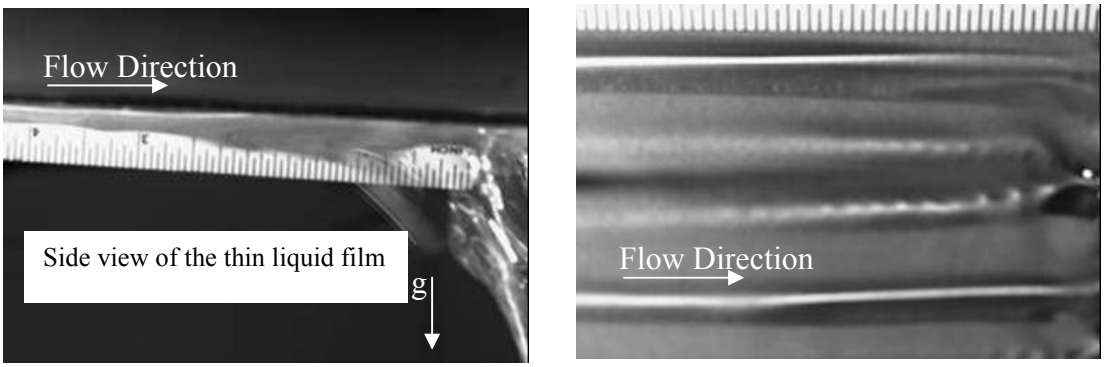

(a) (b)

Figure 4.5 Thin liquid film development on inclined surfaces with an angle of inclination 5°: (a) side view of the inclined surface, (b) bottom view of the inclined surface.

Water, glycerol and mixtures of the two are used as working fluids to provide a wide range of parameters to enable extensive comparison between the experiments and the numerical model. A glycerol-water solution was prepared from the pure fluids so that their compositions by weight were accurately known. In order to provide a Reynolds

number value which is approximately 50% of that for pure water, a concentration of 20% glycerol was used in the aqueous solution. Table 4.3 lists values of the scaling parameters and Reynolds numbers for the working fluids. The surface tension coefficient values used to determine the scaling parameters were obtained from the literature on the properties of the working fluids [79-82]. These working fluids were selected in the experimental and numerical runs such that the Reynolds numbers for water and 20% glycerol at room temperature (T ~293 K) fall within the range of interest for most IFE reactor coolants (see Table 3.1). Hence, this selection of working fluids renders the experimental and numerical investigations applicable to the thin liquid film shielding scheme in IFE reactors. Two type-T thermocouples were utilized in the experiment to measure the working fluid temperature. The fluid properties were determined based on the measured temperature. One thermocouple was mounted in the center of the upper constant-head tank before entrance to the test section plenum while the other thermocouple was placed inside the reservoir. These thermocouples were calibrated using a platinum resistance thermometer RTD (OMEGA PRP-2) to provide a reference scale utilized in developing a calibration equation. The calibration process and data for the calibrated thermocouple mounted in the constant-head tank are presented in Figures 4.6 and 4.7.

Table 4.3 Values of the scaling length, velocity, and time, along with the Reynolds number for various working fluids.

T (K)	Water, H_2O		20% Glycerol	
	293	323	293	323
l (mm)	2.73	2.65	2.62	2.56
U_o (mm/s)	163.5	161.2	160.5	158.6
t_o (ms)	16.7	16.4	16.4	16.2
Re	445	771.2	250	777.8

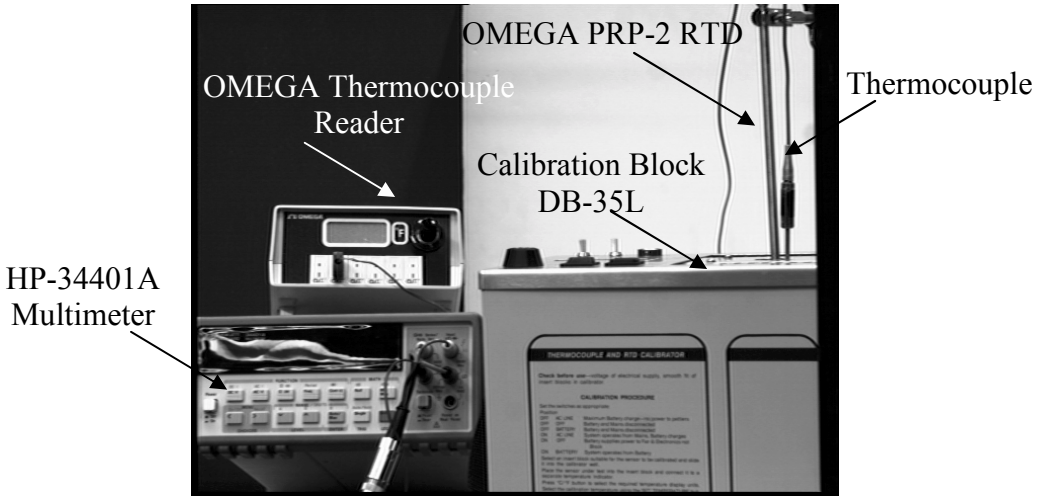

Figure 4.6 Thermocouple and RTD calibration procedure carried out prior to temperature measurement.

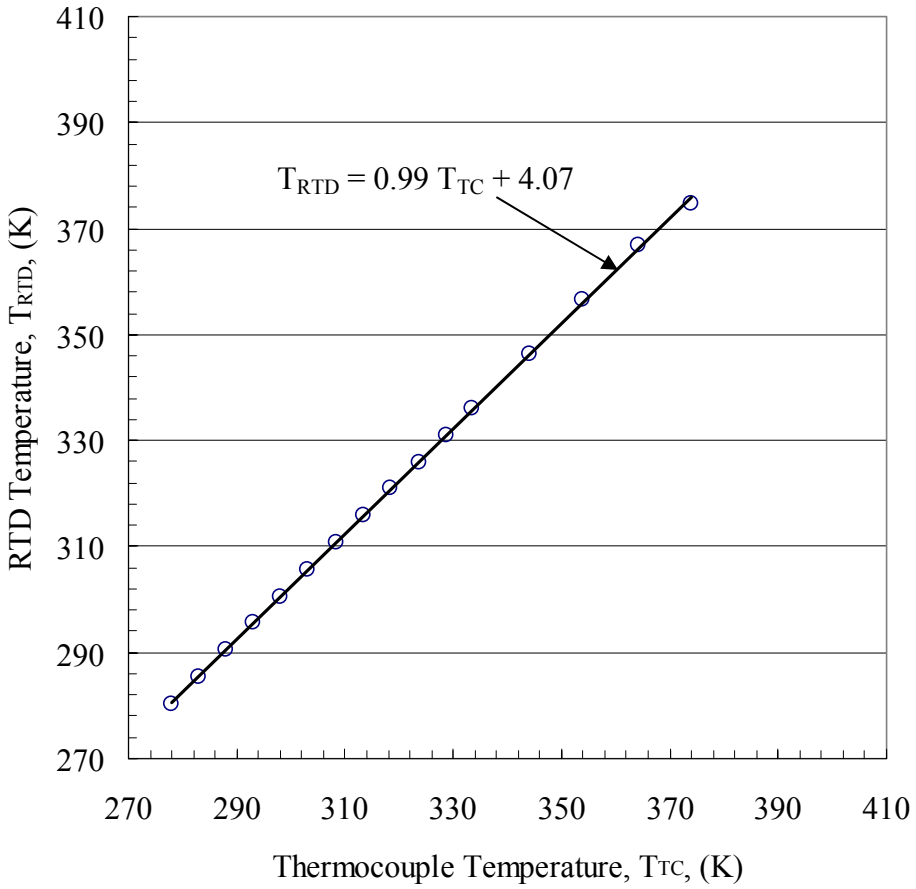

Figure 4.7 Calibration curve for the thermocouple mounted in the center of the upper constant-head tank.

4.2 Instrumentation and Data Acquisition System

The experimental test facility is instrumented with a set of equipment in order to determine and measure several design variables such as the instantaneous liquid film thickness. The objective is to interrogate the test section and carry out the required measurements without disturbing or intruding upon the developed thin liquid film. Image capture and analysis supported by a computer interface is utilized to extract different field parameters from the perturbed thin liquid film developing on the underside of the plate.

4.2.1 Measurement of Liquid Film Thickness

Precise measurement of the thickness of the "unperturbed" liquid film is necessary to provide an accurate comparison with the numerical model predictions obtained by utilizing the front tracking technique detailed in Chapter 3. In order to monitor and measure the liquid film thickness, a non-intrusive technique based on a laser displacement measurement was employed. This measurement was carried out using a laser system manufactured by Keyence (LT-8110). The LT calculates displacement from the focal point that transmits the maximum quantity of light. The non-contact laser measurement principle is detailed in the following steps:

1- A 20 μW laser beam operated at 670 nm wavelength is focused on the target liquid film surface through a lens that is vibrated by a tuning fork. To measure nominal film thickness, the laser beam is focused upon a smooth spot on the film free surface (i.e. away from spikes or droplets),

2- The laser beam is reflected off the target liquid film surface and back into the sensor and is redirected by means of half-mirrors to converge precisely on a pinhole over a

light-receiving element. A detection signal is generated when the lens is precisely positioned for maximum light reception, and

3- The sensor detects and determines the tuning fork's exact position when the laser beam focuses on the target liquid film surface. The distance to the target liquid film surface is then calculated. The measurement resolution is 0.2 μm.

These stages are preceded by a calibration step where the laser beam was focused on the dry plate surface to give an absolute position reference. Figure 4.8 traces the optical path of the laser beam.

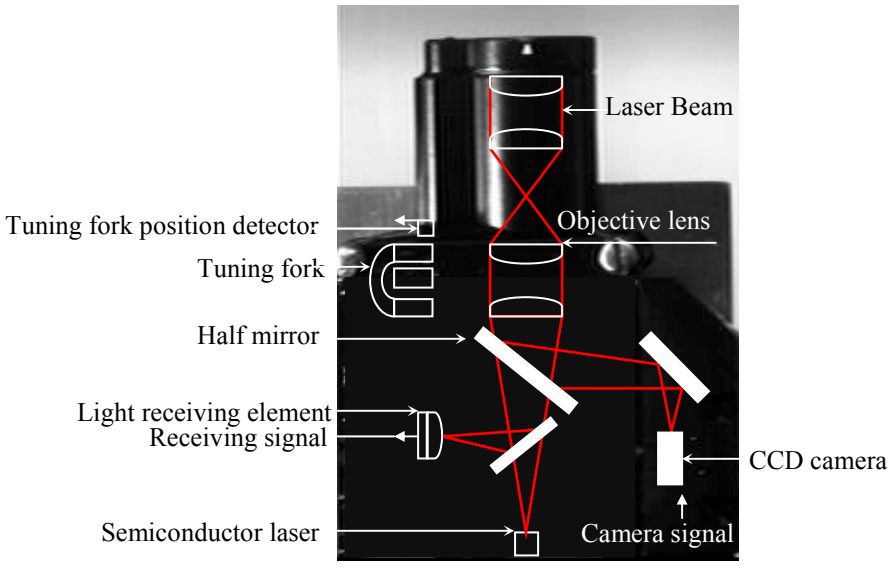

Figure 4.8 Optical path for the laser beam involved in the non-intrusive experimental measurement of the unperturbed liquid film thickness.

The liquid film thickness measurement was conducted for horizontal and inclined test sections. In the horizontal setup, the laser sensor head was mounted under the developing liquid film and near the center of the rectangular porous plate. For every

experimental run, 100 consecutive equally spaced measurements were acquired over 10 seconds. The instrumentation and data acquisition system used for the horizontal configuration are depicted and listed in Figure 4.9 and Table 4.4.

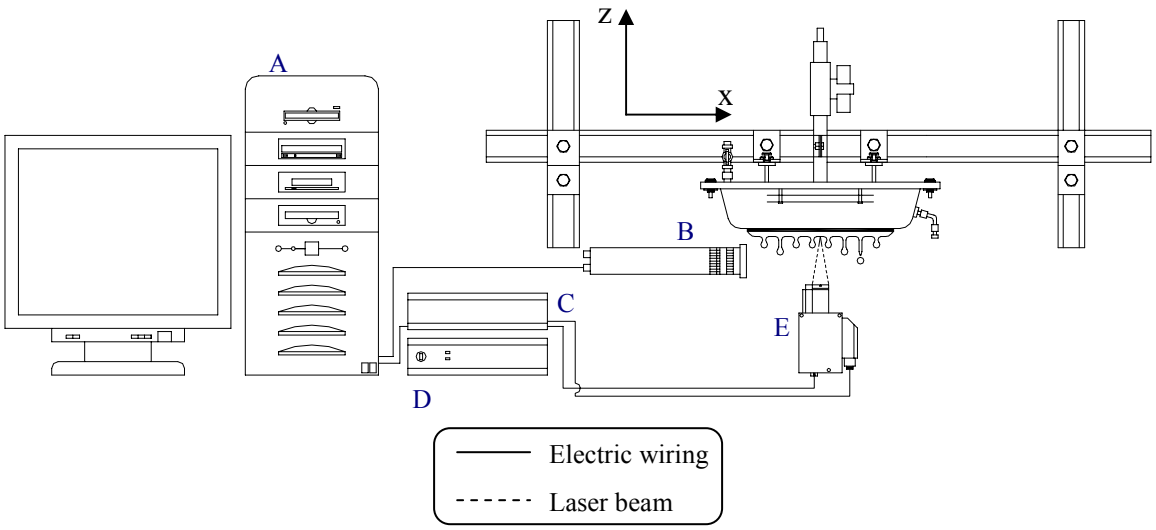

Figure 4.9 Experimental instrumentation and data acquisition system for the horizontal plate setup.

Table 4.4 Listing of instrumentation used in conjunction with the experimental setup.

Label	Description	Manufacturer	Model
A	Workstation PC	Dell	Precision 410
B	CCD camera	Pulnix	TM-6710
C	Laser camera unit	Keyence	LT-V201
D	Laser controller	Keyence	LT-8106
E	Laser sensor head	Keyence	LT-8110

In the inclined plate setup, the thickness of the advected liquid film increases along the length of the plate from the uppermost point to the lowermost edge because of the continuous transpiration through the porous plate and the delayed droplet formation and detachment. The flow starts at the top edge of the inclined plate with a fluid motion

that is highly ordered with identifiable streamlines along which impending droplets drift. Fluid fluctuations at the liquid-gas interface then begin to develop in a transition wavy region which is characterized by the formation of spikes and detachment of droplets. The fluid film drifting towards the lower edge of the bounding plate eventually becomes completely turbulent in the sense that it is dominated by chaotic mixing, competing bubbles, impacting droplets and random movement of relatively large parcels of fluid. Figure 4.10 illustrates the Rayleigh-Taylor instability spatiotemporal sequence for an inclined plate configuration.

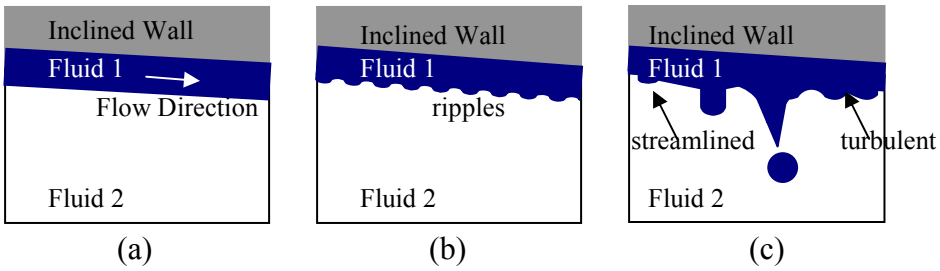

Figure 4.10 Schematic illustration of the Rayleigh-Taylor instability sequence for an inclined plate: (a) streamlined flow, (b) wavy rippling flow, and (c) flow dominated by spike formation and droplet detachment.

In order to accurately characterize and measure the spatiotemporally varying thickness of the liquid film in the inclined configuration, four equally spaced measurements were conducted along the centerline of the bounding rectangular plate in the flow direction. The first measurement was taken 20 mm from the top edge of the plate and then the next three measurements were conducted 10 mm away from the previous measurement location. The positions of the laser sensor head were juxtaposed in a stepped motion maintaining a constant vertical distance from the plate as depicted in

Figure 4.11. At each of the four selected positions, 100 consecutive liquid film thickness measurements were obtained over 10 sec equally incremented by 0.1 sec. This procedure was carried out for each experimental run investigating an inclined plate configuration.

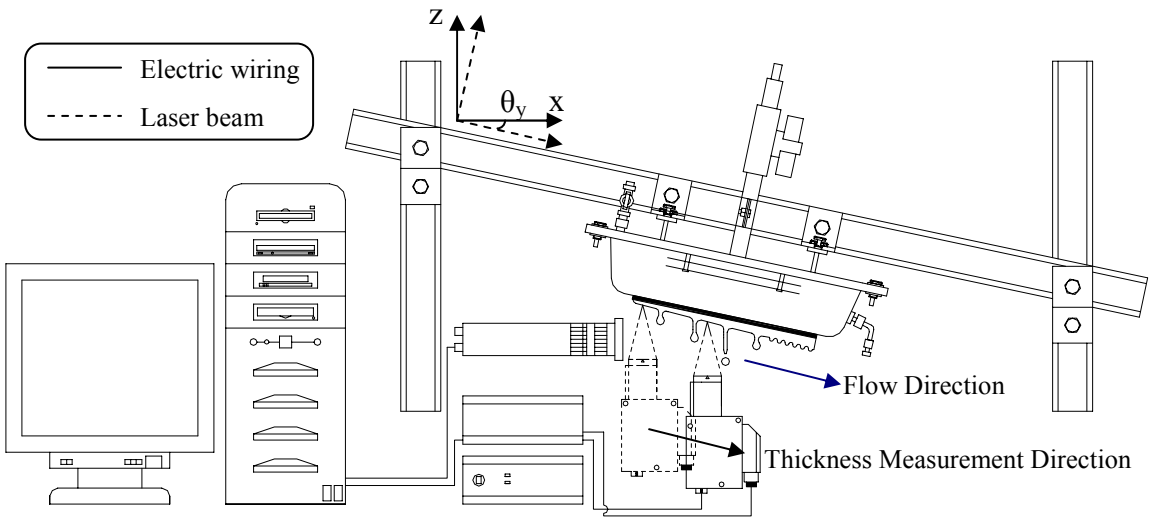

Figure 4.11 Experimental instrumentation and data acquisition system for the inclined plate setup.

Reliable and consistent measurement of the varying liquid film thickness for the horizontal and inclined configurations depends on the stability of the laser sensor head. The positioning and aligning of the laser sensor head were carried out accurately using a four degree of freedom positioning system mounted on the test facility frame. This aligning system was utilized to tune the position of the laser sensor head by allowing three linear motions in x, y and z directions as well as one angular motion θ_x around the x-axis. Figure 4.12 illustrates the mounting and aligning of the laser sensor head using an assembled multislide positioning system.

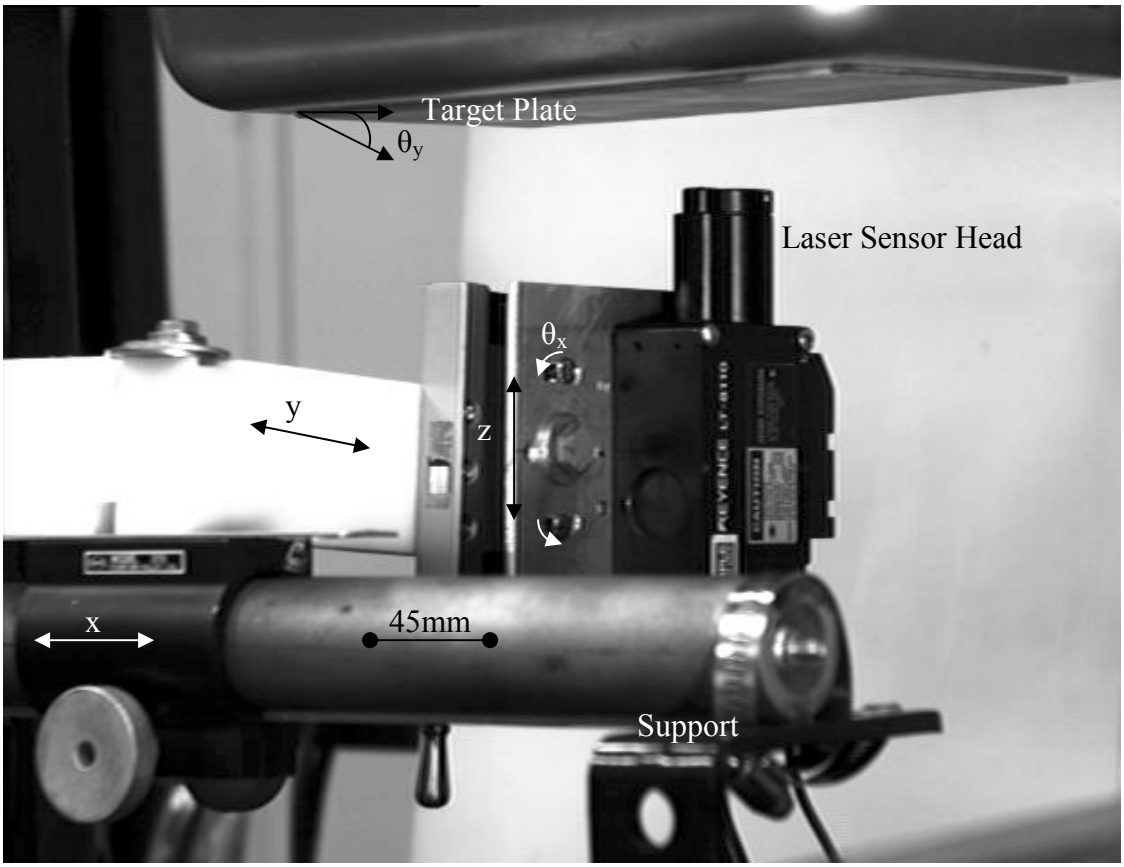

Figure 4.12 Multislide positioning and aligning system utilized in mounting the laser sensor head.

As indicated previously, the laser beam was focused upon a smooth spot on the perturbed liquid film free surface away from spikes or droplets in order to measure the nominal liquid film thickness accurately. This essential positioning requirement was achieved using the multislide aligning system. By following this procedure, the laser-emitting/-receiving surface was maintained dry by avoiding the working fluid developing spikes and impacting droplets, and thus preventing possible beam refraction which may cause an artifact in the monitored optical focal point leading to liquid film thickness measurement errors. Figure 4.13 illustrates the non-intrusive liquid film thickness

measurement for a specific experimental run carried out for a horizontal downward facing bounding plate configuration.

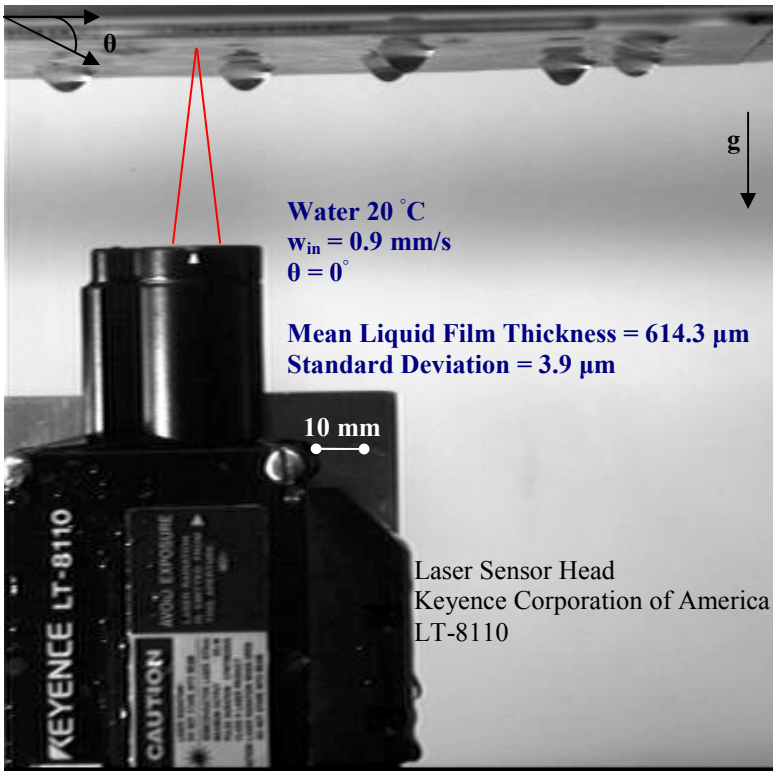

Figure 4.13 Experimental measurement of the unperturbed liquid film thickness utilizing a non-intrusive measurement technique.

4.2.2 Image Capturing and Computer Interface

The droplet formation and detachment were imaged over time using a progressive scanning high speed digital output charge-coupled device CCD camera (Pulnix TM-6710). The signal from the CCD camera is sent to a computer framegrabber card (the Road Runner Camera Link board R3-PCI-CL-23-L manufactured by BitFlow Inc.) installed in a PC (DELL Precision 410). Different scanning modes are provided by the CCD camera. The experimental runs were carried out utilizing a non-interlace quad speed

scanning mode. The framing rate is 120 Hz with an exposure time of 8.33 ms and 648 × 484 spatial resolution. The images were captured sequentially and saved to disk in JPG format. The frequency of liquid droplet formation, the size of detached droplets, and the time history of the penetration depth were extracted from the set of saved images for each conducted experimental run.

4.3 Image Processing and Data Analysis

The data extracted by carrying out the experimental runs consist of several sets of temporal sequential images from the initially perturbed interface to the fully developed spike penetrating through the lighter fluid and necking to form droplets that detach at the pinch off point. These images were saved in JPG format, processed and analyzed using an edge identification and detection technique in order to measure a myriad of flow field parameters, including: the frequency of liquid droplet formation and detachment, the size of detached droplets, the time history of the penetration depth for the developing spikes, and the wave number of the perturbed liquid-gas interface. These experimentally measured field variables are then utilized in the validation of and comparison with the numerical model results attained using the level contour reconstruction front tracking technique detailed in chapter 3.

4.3.1 Determination of Defining Edges

In order to detect the defining edges in each captured image, the sequential images were loaded into MATLAB as a set of intensity images. Then, an image processing code was developed in order to convert the intensity images into edge detected contours. Figures 4.14 and 4.15 depict the image acquisition and processing of

the formation of spikes and droplets from developing liquid films on horizontal and inclined bounding surfaces, respectively.

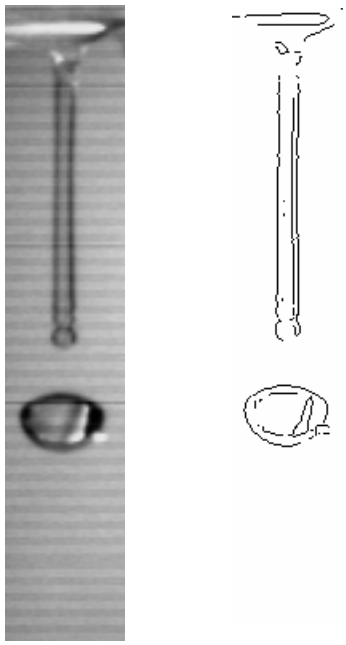

(a) (b)

Figure 4.14 Image acquisition and processing of developing spikes and detaching droplets from perturbed thin liquid films on horizontal downward facing surfaces: (a) original intensity image, (b) detected edge image.

Each intensity image was supplied as an input to the developed code and a binary image of the same size was produced as an output. The binary image consists of values of unity where edges are found and values of zero elsewhere in the image domain. The edges were found by using the local maxima of the gradients in the intensity image. The gradients were calculated using the derivative of a Gaussian filter. The required flow field parameters were then extracted from the detected edge images.

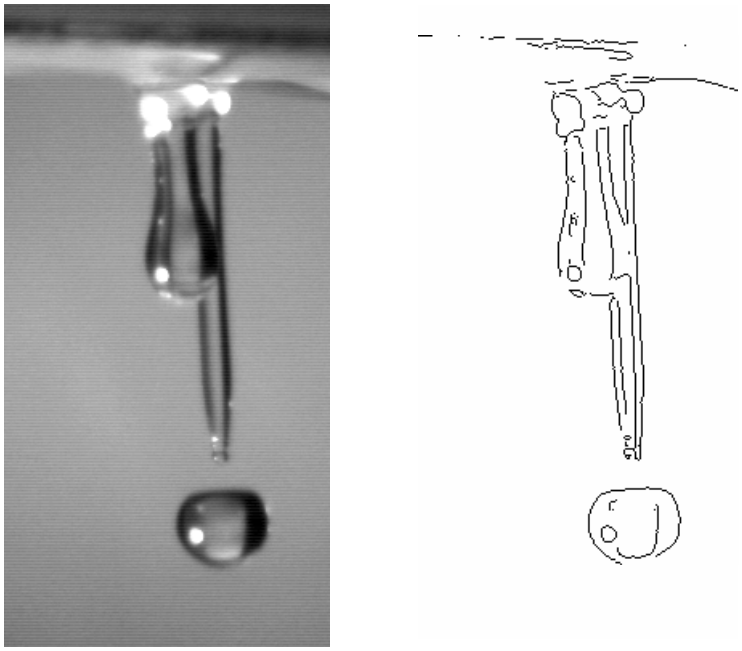

(a) (b)

Figure 4.15 Image acquisition and processing of developing spikes and detaching droplets for perturbed thin liquid films on inclined downward facing surfaces: (a) original intensity image, (b) detected edge image.

4.3.2 Measurement of Field Parameters

Each set of detected edge images were analyzed to measure the desired flow field variables. The droplet detachment time was measured by tracking the sequential evolutions of the contoured edges to the pinch off point where droplets separate from the developing spikes. The resolution of these time steps is 8.33 ms as given by the CCD camera framing rate of 120 Hz. The detached droplets were then extracted to a confined geometrical domain in order to measure an equivalent value of the droplets diameter. As illustrated in Figures 4.14 and 4.15, the detaching droplets are not exactly spherical, but they can be approximated as prolate spheroids with a major axis (a) and a minor axis (b).

The length of these axes was extracted and measured using the sharp detected edges defining the droplet surface. An equivalent droplet diameter of a prolate spheroid was obtained by equating the droplet geometrical volume to the equivalent volume of a standard sphere $\left((4\pi/3)(a/2)(b/2)^2 = (\pi/6)(D_{\text{equivalent}})^3\right)$. Therefore, by measuring both a and b, the equivalent droplet diameter is defined as $\left(D_{\text{equivalent}} = \sqrt[3]{ab^2}\right)$. This formulation was utilized and verified experimentally for measuring the diameter of droplets detaching from fine mesh screens [48]. The wavelength values defining the perturbed liquid-gas interface were also experimentally measured as illustrated in Figure 4.16.

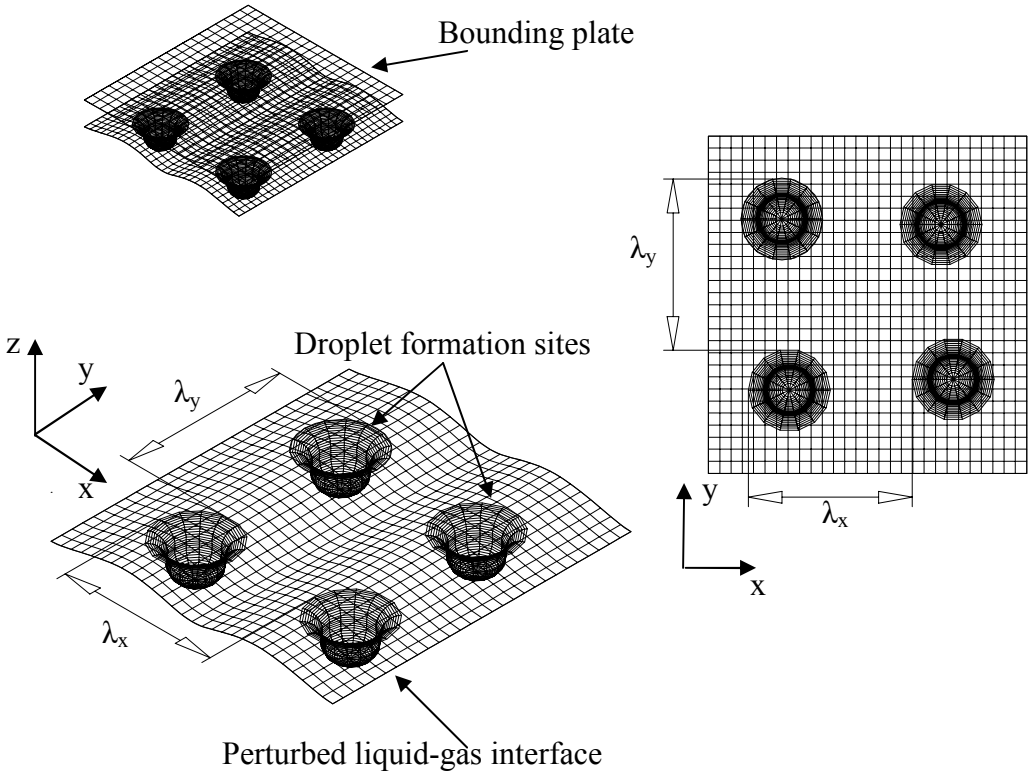

Figure 4.16 Schematic illustration of the perturbed liquid-gas interface and the definition of the wave length between impending droplet formation sites: (a) three-dimensional view, (b) two-dimensional view.

A set of images capturing the bottom view of the perturbed liquid-gas interface was obtained to measure the defining wave length values. This measurement was carried out using the edge detection technique described in section 4.3.1. Two values of the wave length λ_x and λ_y were measured due to the three-dimensionality of the evolving interface. In order to trace the time history of the penetration depth, the maximum vertical distance from the plate surface to the lowermost tip point of the developing spike or the detached droplet was measured while marching in time. These experimental measurements for the flow field variables were carried out for the conducted experimental runs utilized in simulating the confined Rayleigh-Taylor instability with liquid transpiration through horizontal and inclined bounding surfaces.

CHAPTER 5
RESULTS AND DISCUSSION

In this chapter experimental, theoretical and numerical results on the characteristic flow field variables for the bounded Rayleigh-Taylor instability with injection through the bounding surface are reported. These results are discussed and categorized into several sections, including: evolution of liquid film thickness, liquid film surface perturbation geometry, liquid droplet formation and detachment time, equivalent size for detached droplets, time history of the penetration depth, interface wave length and characteristic time scales, and evaporation and condensation effects on bounded liquid films. In these sections, the theoretical and numerical predictions are compared with the experimental results for a wide range of design parameters (liquid film thickness, liquid injection velocity through the boundary, inclination angle, and liquid properties) representing horizontal and inclined bounding surface configurations.

5.1 Evolution of the Liquid Film Thickness

Precise measurement of the thickness of the "unperturbed" liquid film is necessary to provide an accurate comparison with the numerical model predictions attained by using the front tracking technique detailed in Chapter 3. Thus, a non-contact measurement of the liquid film thickness was done using a thickness measurement laser system. This system was described in section 4.2 of chapter 4. The liquid film thickness measurement was carried out for films developing on horizontal and inclined surfaces.

5.1.1 Developing Liquid Films for Horizontal Surfaces

The experimental runs were carried out using water and glycerol as the working fluids. The Reynolds number for water and 20% glycerol at room temperature ($T \approx 293$ K) falls within the range of interest for most IFE reactor coolants (see Tables 3.1 and 4.3). Each experimental run with a unique combination of test fluid, injection velocity, and inclination angle is given a specific letter-number designation in the presented results. In a generic run, the letter-number designation is W090, where W refers to the working fluid (water), 09 refers to the injection velocity ($w_{in} = 0.9$ mm/s), and the trailing 0 refers to the inclination angle ($\theta = 0^{\circ}$). Table 5.1 lists the experimental and numerical runs carried out for horizontal and inclined bounding surfaces. Runs W090, W0925, W210, and W2125 are selected as representative samples of these runs to be presented and detailed in this chapter while data for the other runs are provided in the appendices.

Table 5.1 Letter-number designation of the conducted experimental and numerical runs for horizontal and inclined surfaces.

Experiment Runs	Working Fluid	Injection Velocity, w, [mm/s]	Surface Inclination Angle, θ
W090	Water	0.9	0°
G090	20% Glycerol	0.9	0°
W0925	Water	0.9	2.5°
G0925	20% Glycerol	0.9	2.5°
W140	Water	1.4	0°
W1425	Water	1.4	2.5°
W170	Water	1.7	0°
G170	20% Glycerol	1.7	0°
W1725	Water	1.7	2.5°
G1725	20% Glycerol	1.7	2.5°
W190	Water	1.9	0°
W1925	Water	1.9	2.5°
W210	Water	2.1	0°
W2125	Water	2.1	2.5°

In the horizontal surface configuration, the non-intrusive liquid film thickness measurements were conducted under the developing liquid film and near the center of the rectangular porous plate. In each experimental run, 100 sequential measurements were carried out over a time period of 10 seconds equally incremented by 0.1 seconds. The dimensional and nondimensional measured mean (h_o) and standard deviation (σ) values of the unperturbed liquid film thickness are detailed in Table 5.2. These liquid film thickness values were nondimensionalized using the Laplace length scale (l) for the appropriate working fluid as given by Table 4.3 for water and 20% glycerol at a temperature of 293 K. Based on the data presented in Table 5.2, the unperturbed liquid film thickness increases by providing a higher injection velocity through the bounding plate. For example, a percentage increase in the experimental mean liquid film thickness of approximately 28% and 145% is measured when the transpiration velocity of water increases from 0.9 mm/s to 1.7 mm/s and 2.1 mm/s, respectively. These higher injection velocities were obtained by increasing the head and/or by using higher porosity bounding plates.

Using 20% glycerol (Re = 250 at 293K) as compared to water (Re = 445 at 293K) results in an increase in the measured liquid film thickness at the same transpiration velocity which requires providing a higher head for the 20% glycerol experimental run. This working fluid effect is dominant at higher injection velocities with an increase of 28% in the experimental mean liquid film thickness at a transpiration velocity of 1.7 mm/s as compared to an increase of 12% at an injection velocity of 0.9 mm/s. Liquid film thickness data obtained using 20% glycerol (Re = 250 at 293 K) provide an essential tool to predict the liquid film response when using Flibe (Re = 195.3 at 973K) as a candidate

coolant for first wall shielding in IFE reactors. Dimensional and nondimensional results showing the evolution of the unperturbed liquid film thickness are shown in Figures 5.1 and 5.2 for experimental runs W090 and W210.

Table 5.2 Dimensional and nondimensional experimental mean (h_o) and standard deviation (σ) values of the unperturbed liquid film thickness for the experimental runs conducted using horizontal surfaces.

Experiment Runs	Dimensional Values		Nondimensional Values	
	Mean Value, h_o [μm]	σ [μm]	Mean Value, h_o^*	σ^*
W090	614.3	3.9	0.2252	0.0014
G090	686.2	32.5	0.2610	0.0123
W140	713.0	13.7	0.2614	0.0050
W170	787.7	63.1	0.2887	0.0231
G170	1009.2	23.4	0.3839	0.0088
W190	1131.8	105.4	0.4148	0.0386
W210	1506.4	16.1	0.5522	0.0058

5.1.2 Developing Liquid Films for Inclined Surfaces

In the inclined bounding surface configuration, the thickness of the advected liquid film increases along the axial direction of the plate from the uppermost point to the lowermost edge due to the continuous injection and the deferred droplet formation as will be explained in section 5.3.2. The spatiotemporal varying thickness of the liquid film in the inclined configuration was measured at four equally spaced locations carried out along the centerline of the bounding rectangular surface in the direction of the liquid film flow. The first measurement was taken 20 mm from the top edge of the plate and then the following three measurements were incremented by 10 mm at axial positions along the plate of 30, 40, and 50 mm. Tables 5.3 and 5.4 list the mean and standard deviation values for the liquid film thickness obtained for each experimental run. The detailed

dimensional and nondimensional transient variation of the unperturbed liquid film thickness for experimental runs W0925 and W2125 are presented in Figures 5.3-5.10.

As provided by the data in tables 5.3 and 5.4, the mean liquid film thickness increases by 273% and 236% from x = 20 mm to x = 50 mm for experimental runs W0925 and W2125, respectively. Increasing the injection velocity or using 20% glycerol rather than water as the working fluid, causes the mean liquid film thickness value to increase at the same axial location in the x direction.

Table 5.3 Experimental mean (h_o) and standard deviation (σ) values of the unperturbed liquid film thickness at several axial positions (x) in the direction of the liquid film flow for the experimental runs conducted using inclined surfaces (θ =2.5˚).

Runs	x = 20 mm		x = 30 mm		x = 40 mm		x = 50 mm	
	h_o[μm]	σ [μm]	h_o[μm]	σ [μm]	h_o[μm]	σ [μm]	h_o[μm]	σ [μm]
W0925	217.8	21.4	324.1	21.2	419.1	12.7	812.5	16.8
G0925	268.4	8.5	350.4	26.2	500.9	14.8	924.8	21.0
W1425	293.3	6.1	441.1	4.5	622.0	26.5	917.1	59.4
W1725	316.8	9.4	491.2	2.8	757.7	53.1	986.0	26.4
G1725	400.4	65.2	520.9	57.2	826.2	41.6	1267.8	31.8
W1925	399.1	8.1	597.1	54.8	930.3	62.4	1251.3	147.8
W2125	456.0	31.2	705.6	29.4	1168.6	41.5	1533.7	17.4

Table 5.4 Nondimensional experimental mean (h_o^*) and standard deviation (σ^*) values of the unperturbed liquid film thickness at several axial positions (x^*) in the direction of the liquid film flow for the experimental runs conducted using inclined surfaces (θ =2.5˚).

Runs	x^* = 7.3		x^* = 10.9		x^* = 14.6		x^* = 18.3	
	h_o^*	σ^*	h_o^*	σ^*	h_o^*	σ^*	h_o^*	σ^*
W0925	0.0798	0.0078	0.1188	0.0078	0.1537	0.0047	0.2978	0.0062
W1425	0.1075	0.0023	0.1617	0.0017	0.2280	0.0097	0.3362	0.0218
W1725	0.1162	0.0034	0.1801	0.0011	0.2777	0.0194	0.3614	0.0096
W1925	0.1463	0.0029	0.2188	0.0201	0.3410	0.0229	0.4586	0.0542
W2125	0.1672	0.0114	0.2586	0.0107	0.4284	0.0152	0.5622	0.0064
Runs	x^* = 7.6		x^* = 11.4		x^* = 15.2		x^* = 19	
	h_o^*	σ^*	h_o^*	σ^*	h_o^*	σ^*	h_o^*	σ^*
G0925	0.1021	0.0032	0.1333	0.0099	0.1905	0.0056	0.3517	0.0079
G1725	0.1523	0.0248	0.1982	0.0218	0.3142	0.0158	0.4823	0.0121

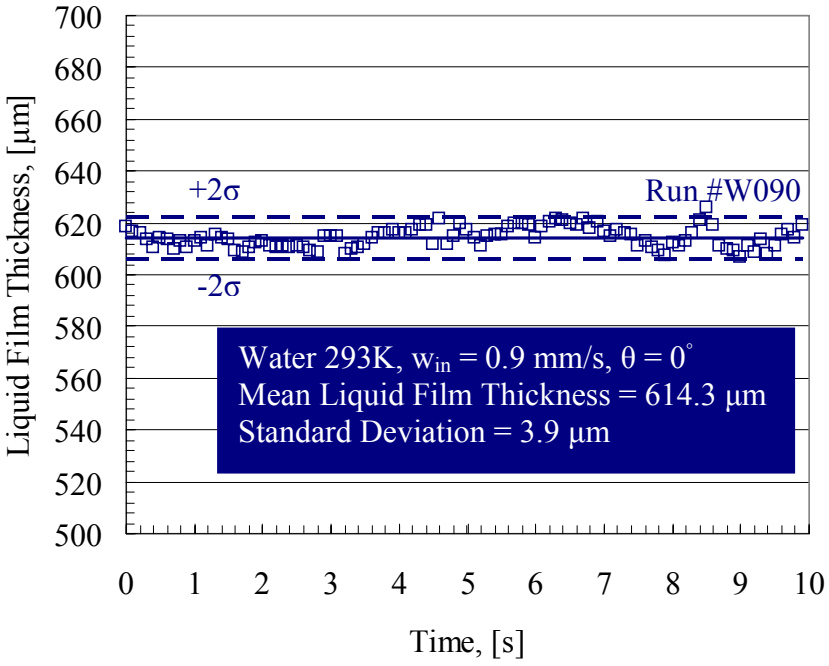

(a)

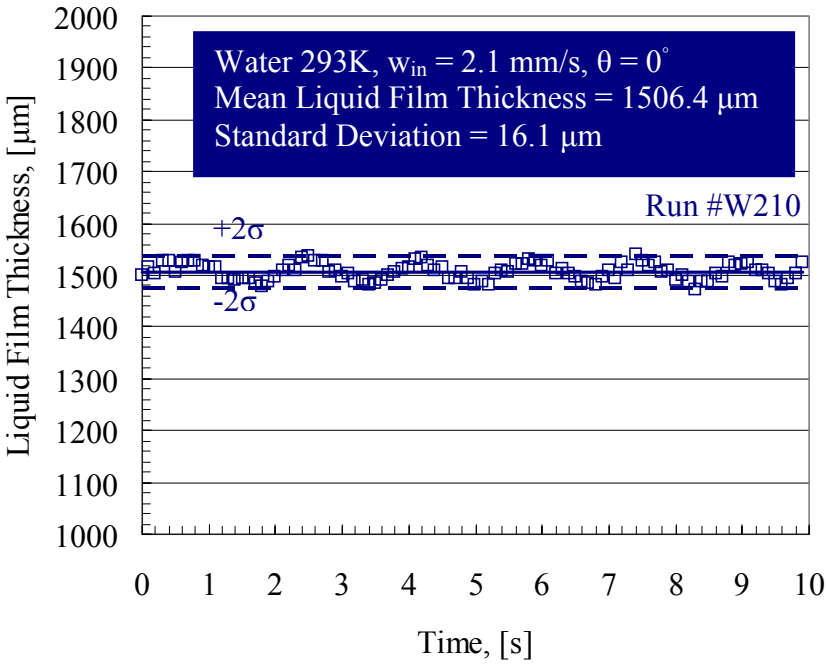

(b)

Figure 5.1 Transient variation of the unperturbed liquid film thickness: (a) Run #W090, and (b) Run #W210.

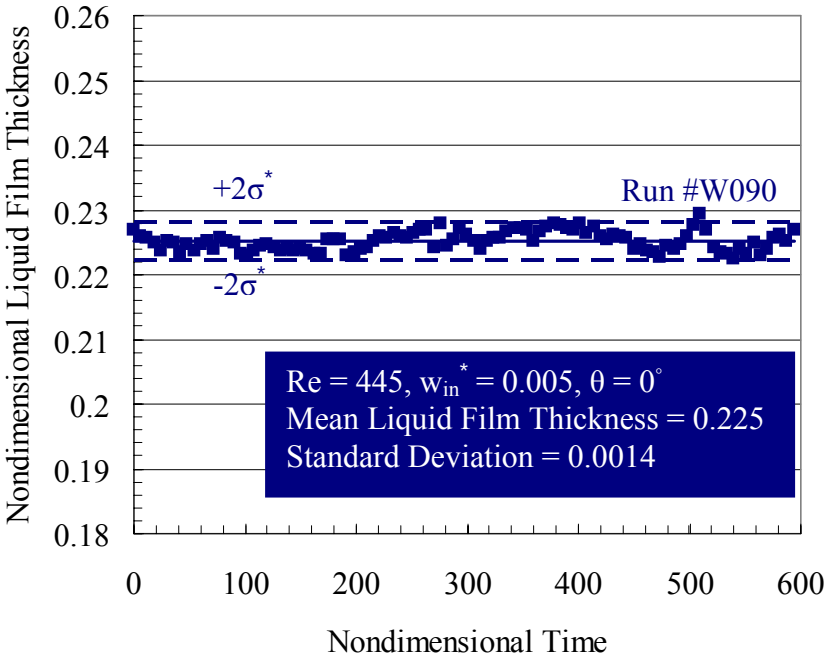

(a)

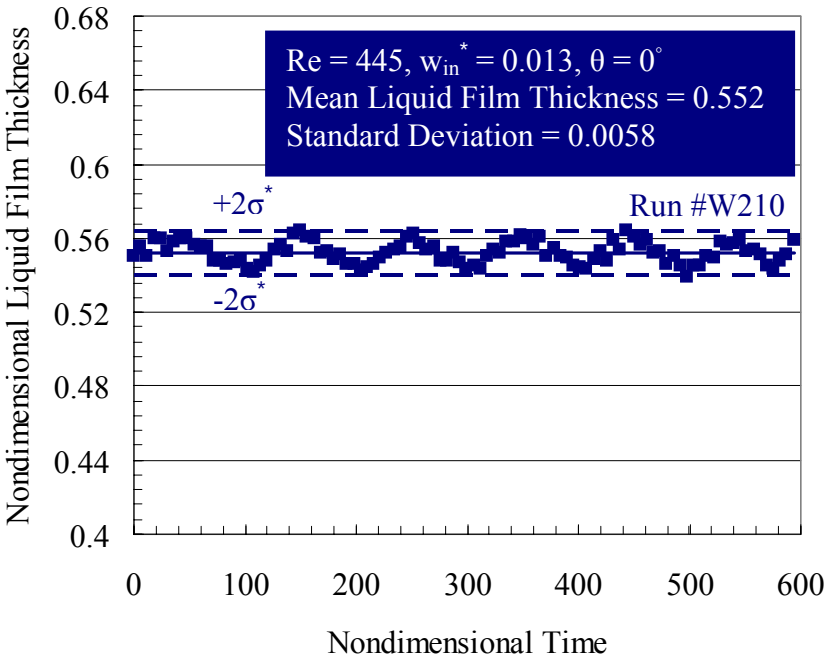

(b)

Figure 5.2 The unperturbed liquid film thickness normalized by l as a function of time normalized by t_o: (a) Run #W090, and (b) Run #W210.

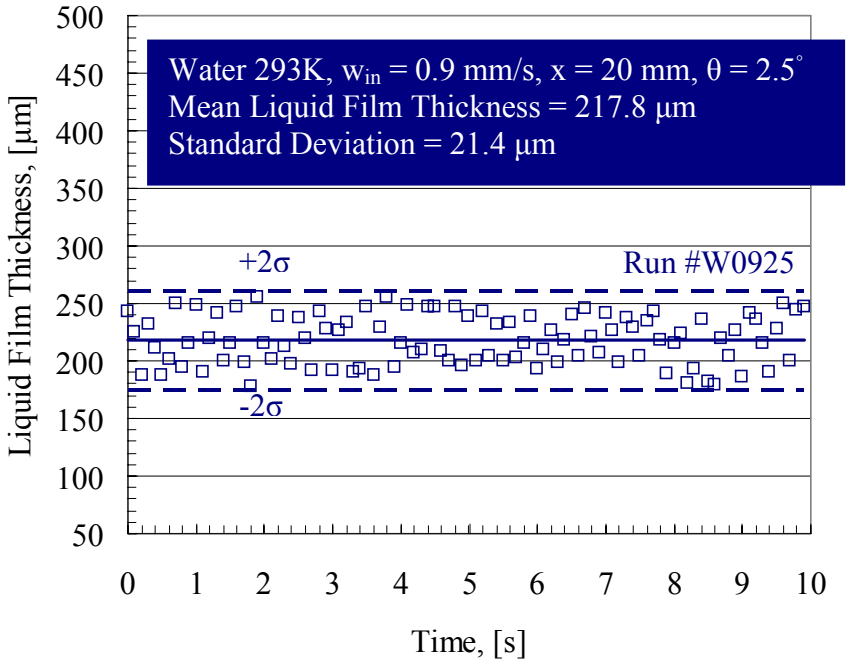

(a)

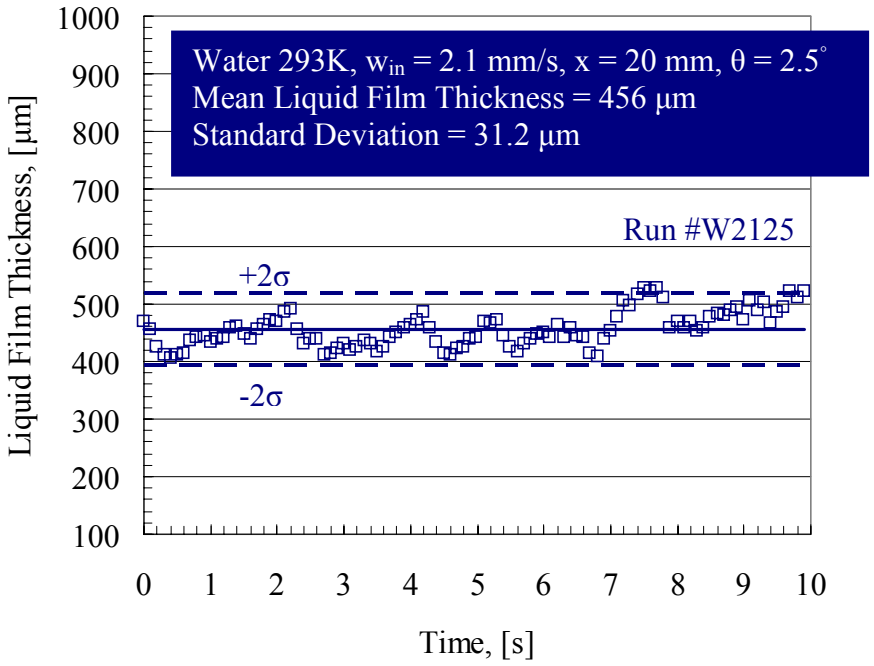

(b)

Figure 5.3 Transient variation of the unperturbed liquid film thickness measured at x = 20 mm: (a) Run #W0925, and (b) Run #W2125.

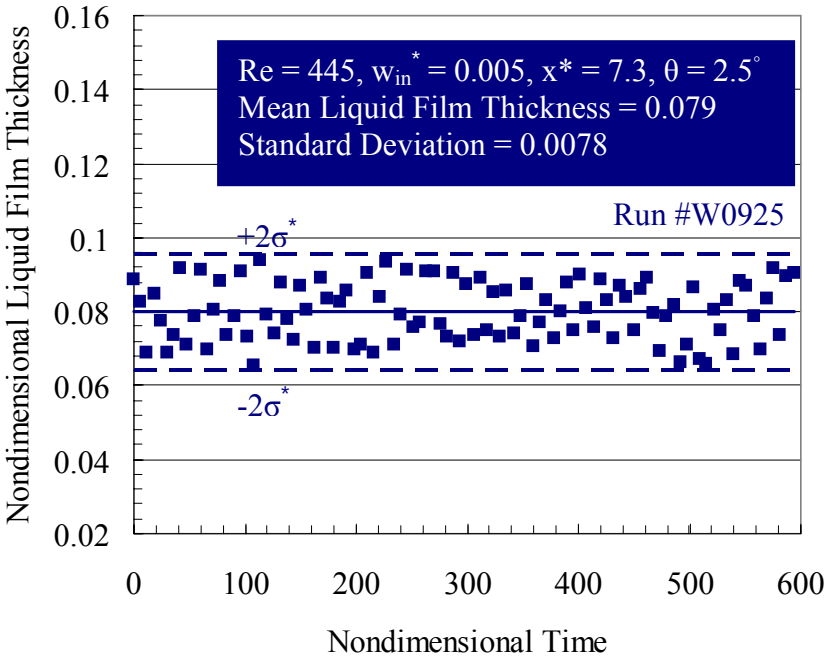

(a)

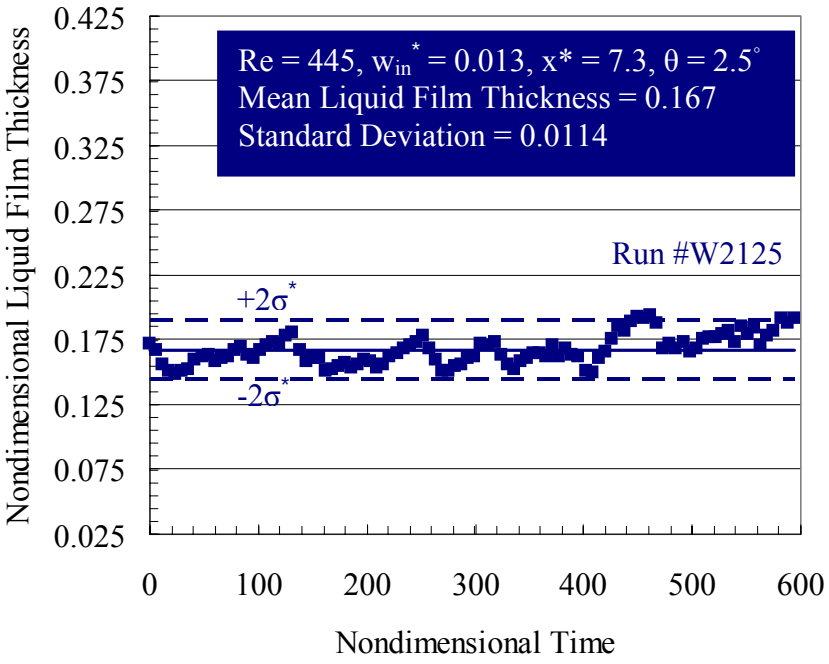

(b)

Figure 5.4 The unperturbed liquid film thickness normalized by l as a function of time normalized by t_o (at $x^* = 7.3$): (a) Run #W0925, and (b) Run #W2125.

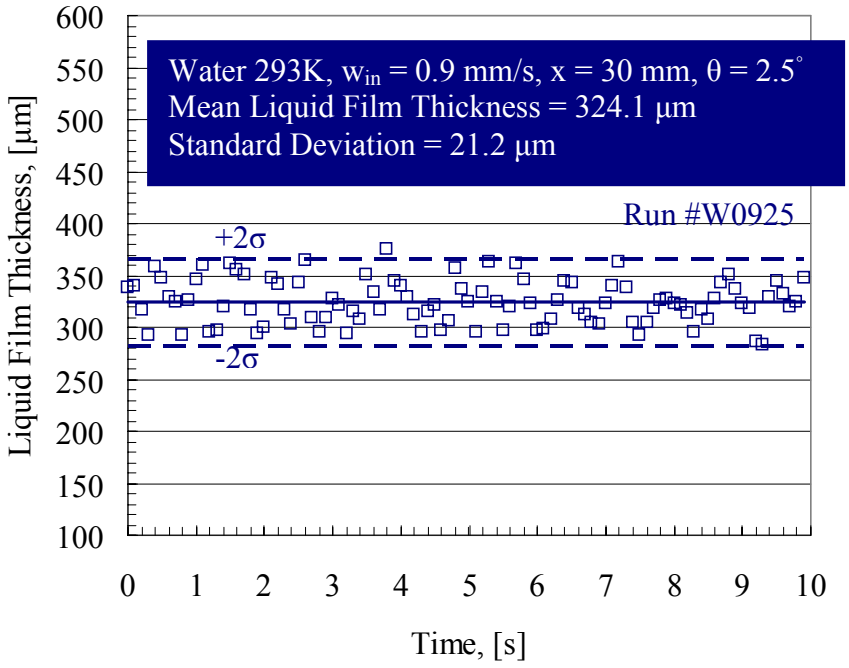

(a)

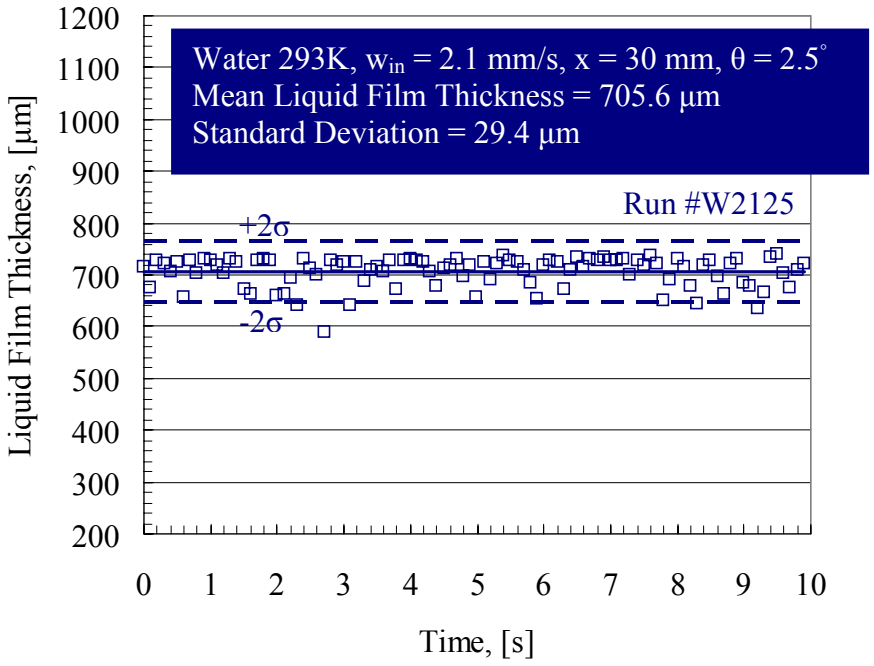

(b)

Figure 5.5 Transient variation of the unperturbed liquid film thickness measured at x = 30 mm: (a) Run #W0925, and (b) Run #W2125.

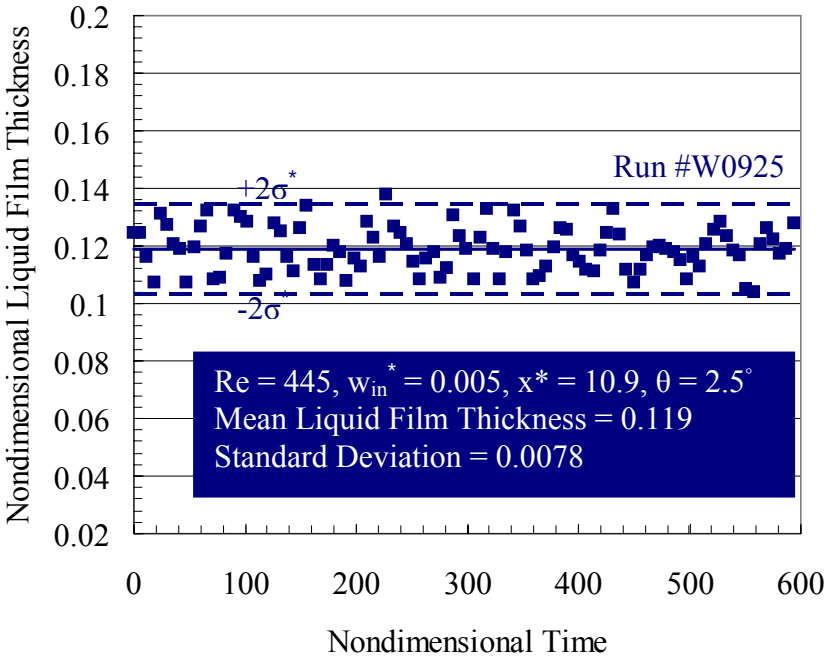

(a)

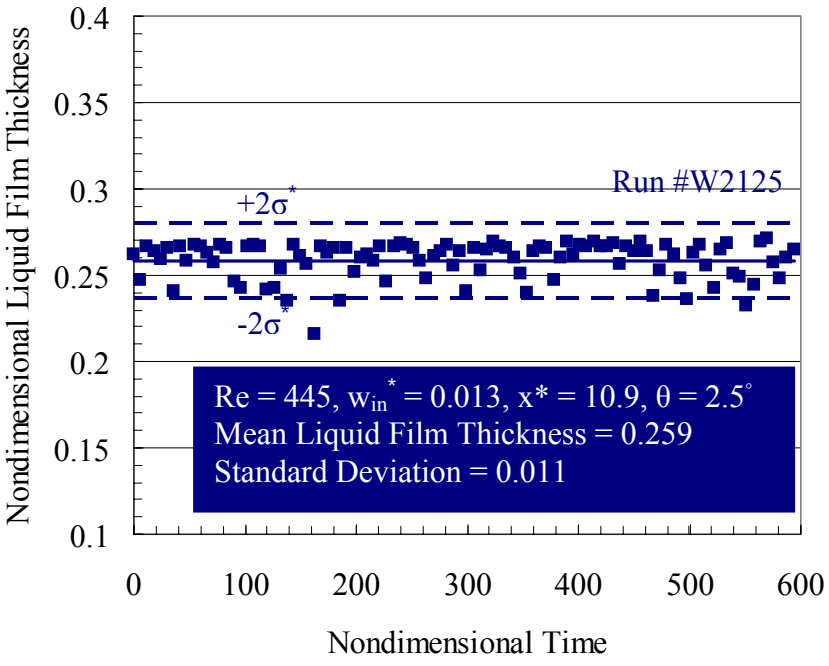

(b)

Figure 5.6 The unperturbed liquid film thickness normalized by l as a function of time normalized by t_o (at $x^* = 10.9$): (a) Run #W0925, and (b) Run #W2125.

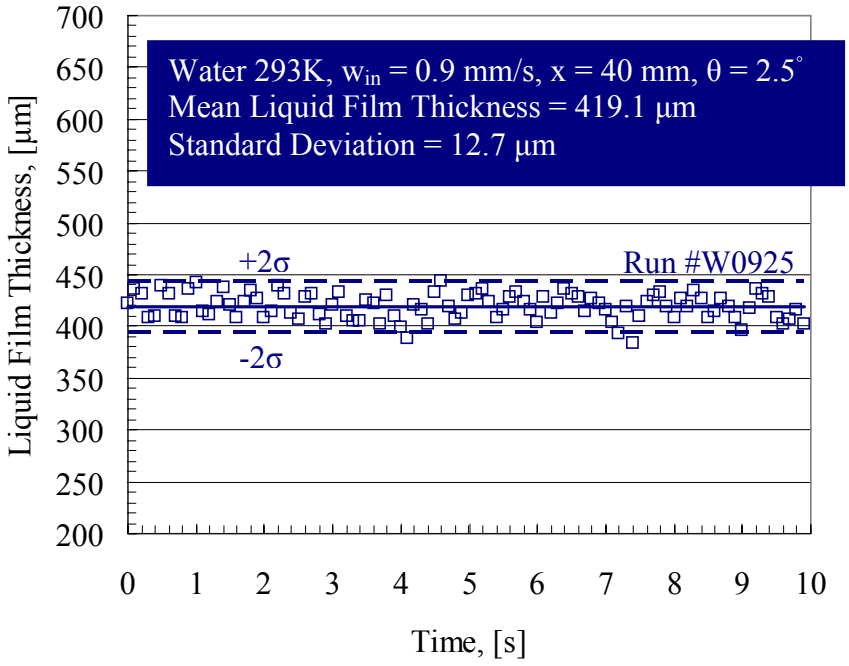

(a)

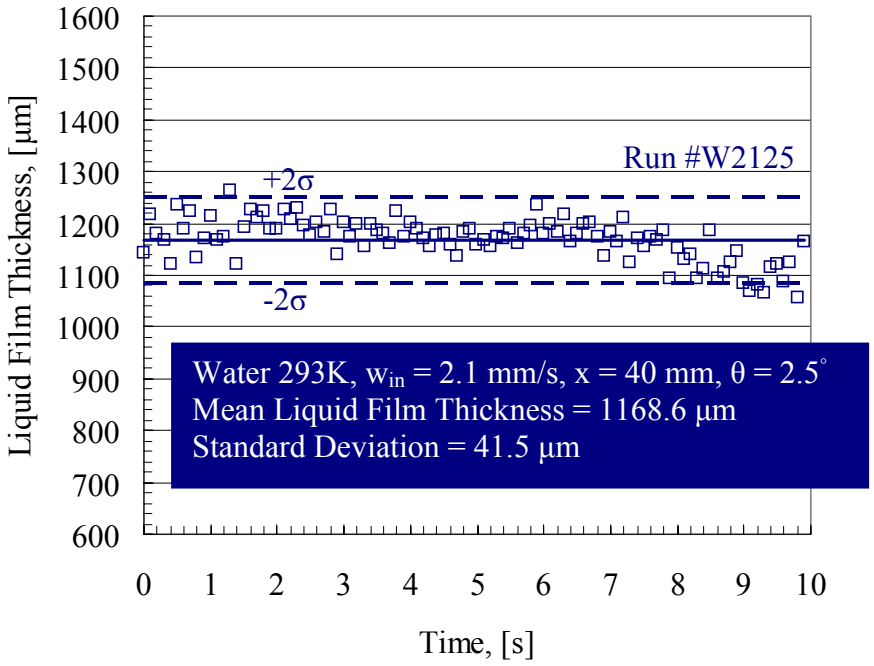

(b)

Figure 5.7 Transient variation of the unperturbed liquid film thickness measured at x = 40 mm: (a) Run #W0925, and (b) Run #W2125.

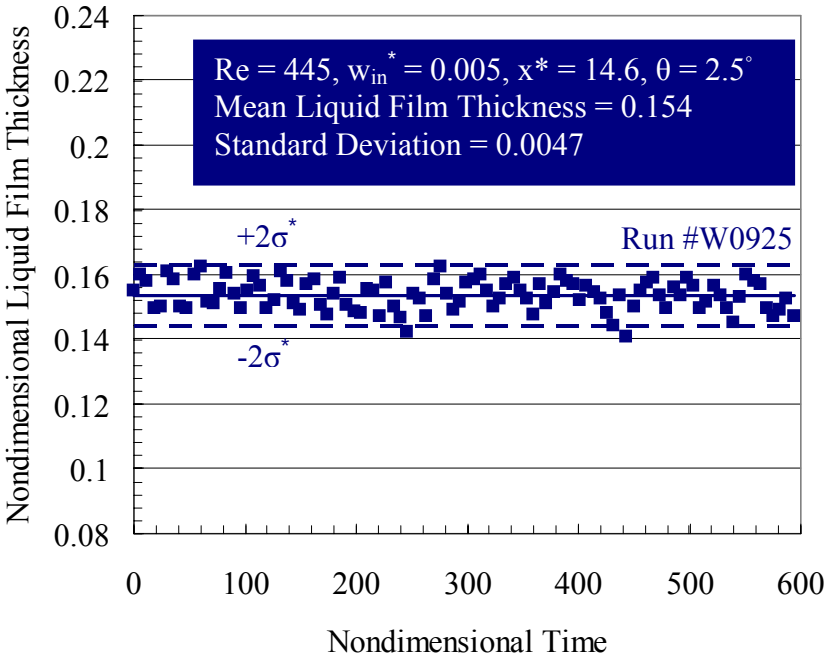

(a)

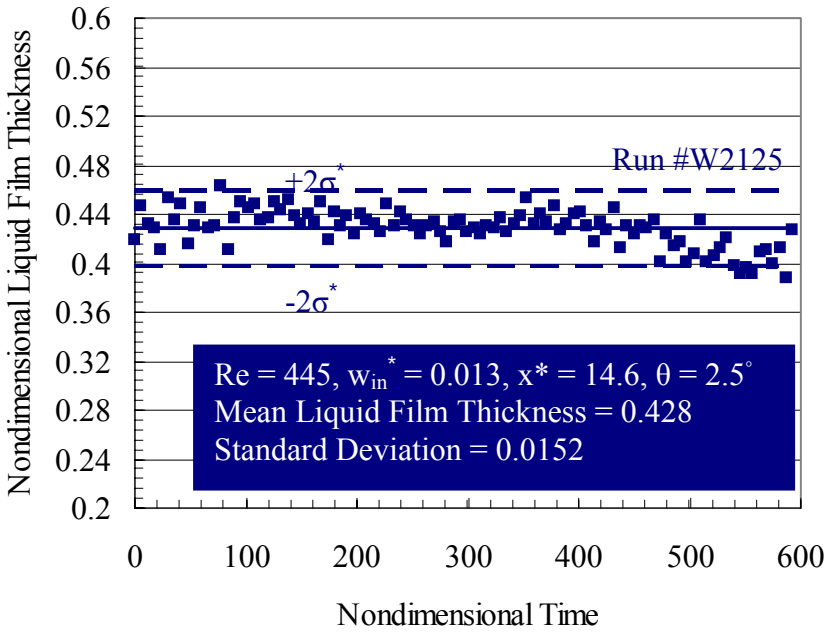

(b)

Figure 5.8 The unperturbed liquid film thickness normalized by l as a function of time normalized by t_o (at $x^* = 14.6$): (a) Run #W0925, and (b) Run #W2125.

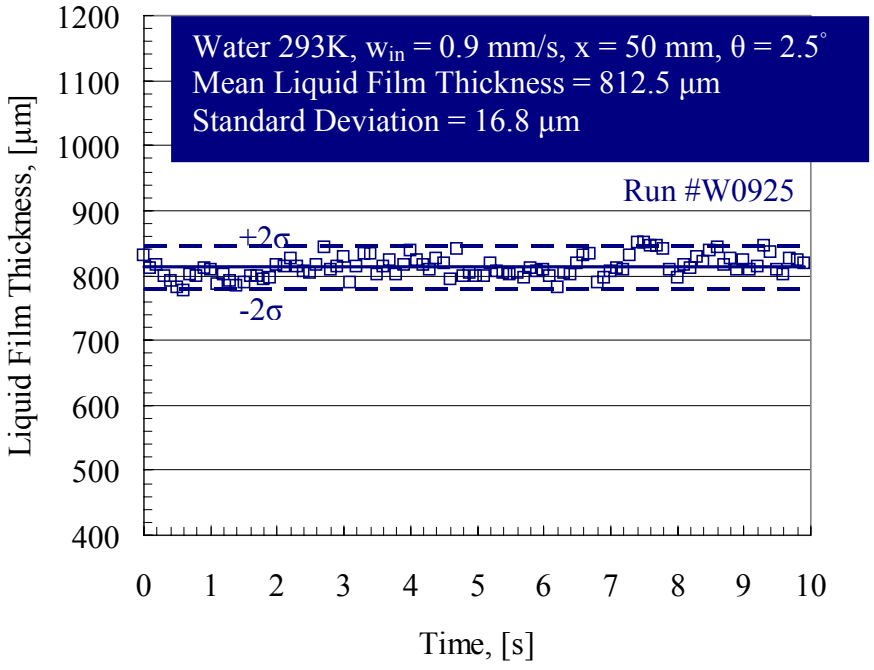

(a)

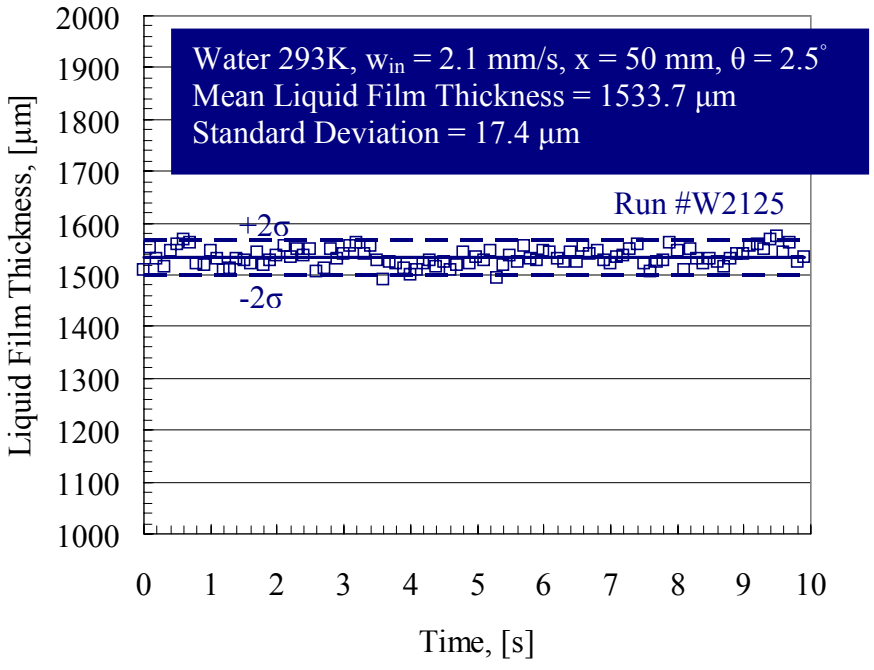

(b)

Figure 5.9 Transient variation of the unperturbed liquid film thickness measured at x = 50 mm: (a) Run #W0925, and (b) Run #W2125.

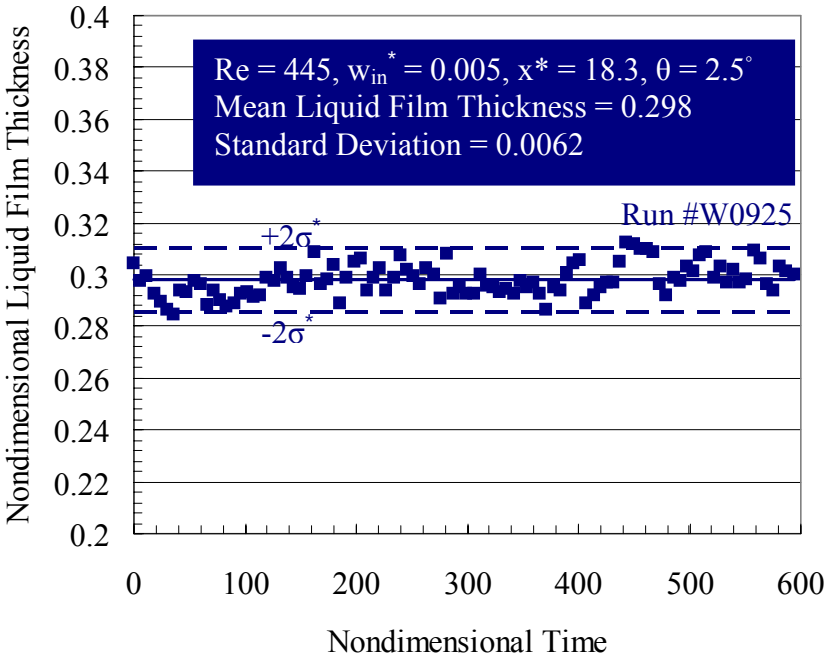

(a)

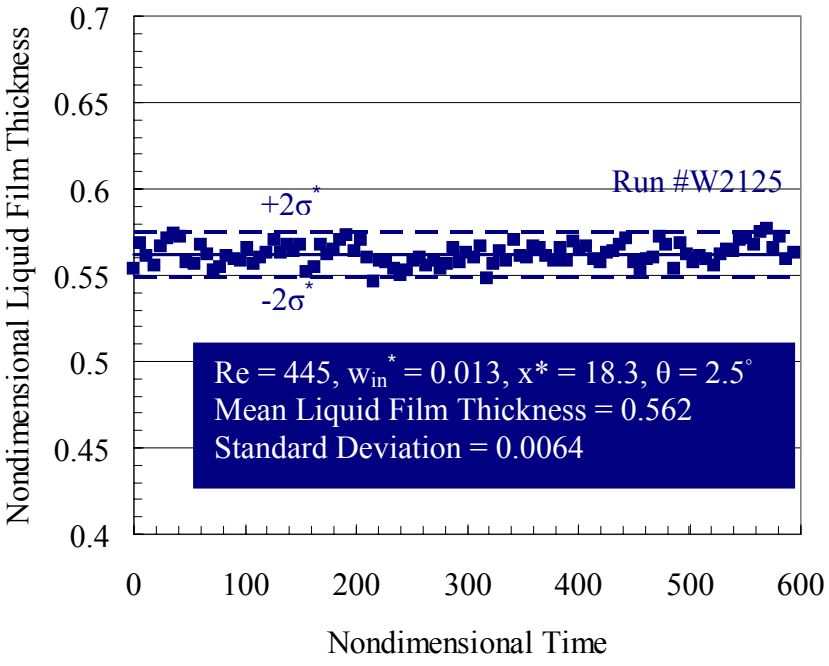

(b)

Figure 5.10 The unperturbed liquid film thickness normalized by l as a function of time normalized by t_o (at $x^* = 18.3$): (a) Run #W0925, and (b) Run #W2125.

5.2 Liquid Film Surface Perturbation Geometry

The initial liquid-gas interface geometry is essential in predicting the liquid film evolution, growth pattern and detachment time of the Rayleigh-Taylor instability. Thus, in the numerical analysis using the front tracking method, the effect of surface perturbation geometry and mode number on the evolution of the interface was examined. For mode number one, the perturbation wavelength is equal to the calculation box size in the x (L_x) and y (L_y) directions. The interface is defined using the following formulation:

$$z_s = z_o - \frac{\varepsilon_s}{4}\left(\cos\left(\frac{2\pi\left(x_s - L_x/2\right)}{L_x}\right)+1\right)\left(\cos\left(\frac{2\pi\left(y_s - L_y/2\right)}{L_y}\right)+1\right) \quad (6.1)$$

The random initial surface perturbation is, in essence, equivalent to higher mode number perturbations. Therefore, the effect of higher mode numbers (i.e. wavelength values) on the evolution of the free surface contours and droplet detachment time was also investigated as an initial test to determine the optimum mode number to be used in all the planned numerical runs. In this preliminary analysis, the standard run was a one mode perturbation with equal initial thickness z_o and perturbation ε_s ($z_o = \varepsilon_s = 0.5$ mm) and an injection velocity $w_{in} = 1$ mm/s imposed at the upper boundary within a 0.05 m^3 calculation box size. For higher mode numbers, the volume of liquid was kept the same as the standard mode number 1 run. These initial numerical calculations were conducted using a nodal resolution of $50\times50\times50$. The number of modes of perturbation was increased from 1 to 9 to 16. For the higher mode numbers the different nodes grow into spikes and detach into droplets at higher detachment times as compared to the mode number 1 perturbation. This delay in the pinch-off time is due to the perturbations interaction and interference with each other. This effect is more prominent when using

the 16-mode perturbation with the adjacent disturbances strongly interacting and damping out the small wavelength perturbations which were initially imposed on the interface. Fewer spikes evolve from the remaining disturbances and the detachment time is increased significantly. Therefore, the planned numerical runs were carried out utilizing the long wavelength (mode number 1) initial surface perturbations representing the conservative case with regard to the detachment time. Figure 5.11 depicts the effect of the surface geometry and mode number on the interface evolution for liquid lead at 700K.

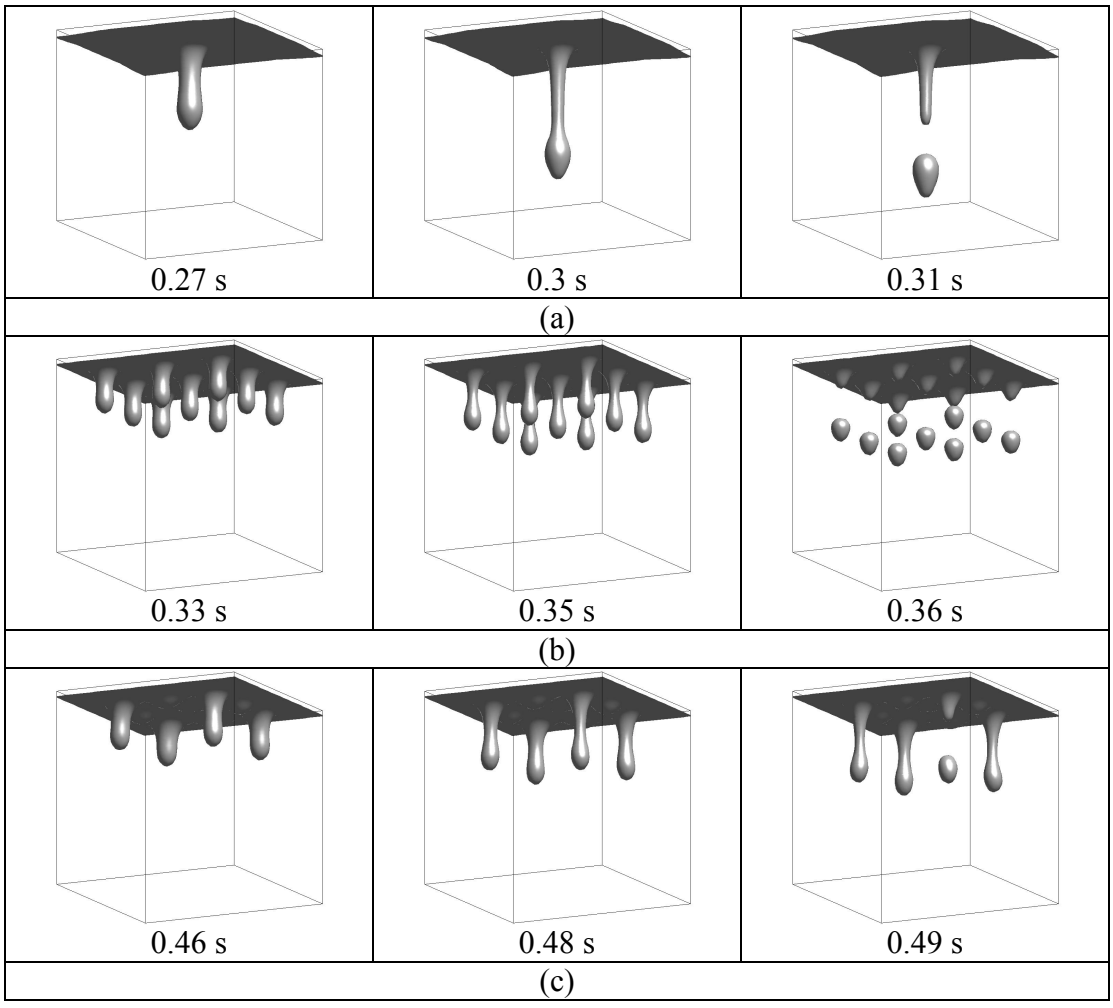

Figure 5.11 The effect of initial interface perturbation geometry on the film evolution: (a): 1 mode perturbation, (b) 9 modes perturbation, and (c) 16 modes perturbation.

5.3 Liquid Droplet Formation and Detachment Time

Results for the droplet detachment time from horizontal and inclined surfaces with several injection velocities using water and 20% glycerol as working fluids are given in this section. These data represent the distribution of measured values for 100 different droplets; the mean droplet detachment time and the standard deviation among the experimental measurements are provided. The distribution of droplet detachment times is a direct result of the random nature of surface perturbations in the conducted experiments. Clearly, in the relatively hostile environment following target explosion in IFE reactors, the morphology of the initial film surface would vary greatly. Thus, the sensitivity of the numerical results to normalized initial perturbation amplitude ε_s/z_o is tested by running the numerical front tracking code for a range of ε_s/z_o values namely: 0.1, 0.25, 0.5, 0.75 and 1. The initial liquid film thickness z_o is extracted from the experimental runs as the mean value provided by the transient variation of the unperturbed liquid film thickness ($z_o = h_o$) as provided in section 5.1. The numerical runs were performed by utilizing the long wave length (mode number 1) initial surface perturbations for a fine mesh (100×100×100).

5.3.1 Droplets Detaching from Horizontal Bounded Liquid Films

In the experiments carried out for horizontal bounded liquid films, the interface is subjected to the Rayleigh-Taylor instability with an influx Q_1 and an outflux Q_2 resulting in the formation and detachment of droplets as shown in Figure 5.12. The droplet detachment time was measured for the conducted experimental runs by tracking the sequential evolutions of the developing spikes using the CCD camera which has a

framing rate of 120 Hz as explained in section 4.3.2. In order to provide adequate comparison, the numerical runs were carried out using several normalized initial perturbation amplitudes ε_s/z_o as detailed in Tables 5.5 and 5.6. These tables provide the dimensional and nondimensional experimental mean (t_d), standard deviation (σ) and numerical prediction values of the detachment time for the experimental and numerical runs. The scaling parameters presented in Table 4.3 in section 4.1.2 were used to nondimensionalize the detachment time values. Figures 5.13 and 5.14 provide the experimental results for the statistical distributions of dimensional and nondimensional detachment times based on which the mean and standard deviation values were extracted for runs W090 and W210. The numerical and experimental results for the variation of the dimensional and nondimensional detachment time with the normalized initial perturbation amplitude carried out for run W090 and run W210 are presented in Figures 5.15 and 5.16. The detailed numerical and experimental results for the other test runs are given in the appendices.

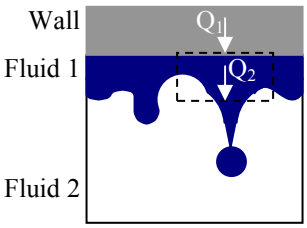

Figure 5.12 Schematic illustration of the volume flow rates passing through the depicted control surface for a developing liquid film on a horizontal bounding plate.

The results provided in Tables 5.5 and 5.6 indicate that the detachment time increases by either decreasing the transpiration velocity w_{in} which decreases the liquid film thickness or by using 20% glycerol rather than water at the same injection velocity.

For instance, the experimental mean detachment time increases by 93% when the transpiration velocity varies from 2.1 mm/s to 0.9 mm/s for water while an increase of 44.5% is attained by utilizing 20% glycerol rather than water as the working fluid at an injection velocity of 0.9 mm/s.

Table 5.5 Experimental mean (t_d), standard deviation (σ) and numerical prediction values of the detachment time in seconds for the experimental and numerical runs conducted using horizontal surfaces.

Runs	Experiment		Normalized Initial Perturbation Amplitude, ε_s/z_o				
	t_d, [s]	σ, [s]	0.1	0.25	0.5	0.75	1
W090	0.4652	0.0148	0.4992	0.4222	0.3634	0.3277	0.3042
G090	0.6724	0.0113	0.6784	0.5592	0.472	0.4234	0.3904
W140	0.4071	0.0091	0.4717	0.3999	0.3449	0.3124	0.2912
W170	0.3576	0.0085	0.4552	0.3872	0.3342	0.3037	0.2824
G170	0.5069	0.0105	0.5470	0.4564	0.3872	0.3531	0.3364
W190	0.3119	0.0106	0.4067	0.3442	0.2977	0.2732	0.2582
W210	0.2412	0.0140	0.3714	0.3179	0.2807	0.2604	0.2484

Table 5.6 Nondimensional experimental mean (t_d^*), standard deviation (σ^*) and numerical prediction values of the detachment time for the experimental and numerical runs conducted using horizontal surfaces.

Runs	Experiment		Normalized Initial Perturbation Amplitude, ε_s/z_o				
	t_d^*	σ^*	0.1	0.25	0.5	0.75	1
W090	27.90	0.88	29.93	25.31	21.79	19.65	18.24
G090	41.07	0.69	41.44	34.16	28.83	25.86	23.84
W140	24.41	0.54	28.28	23.98	20.68	18.73	17.46
W170	21.44	0.51	27.29	23.22	20.04	18.21	16.94
G170	30.97	0.64	33.41	27.88	23.65	21.57	20.54
W190	18.70	0.64	24.39	20.64	17.85	16.38	15.48
W210	14.46	0.84	22.27	19.07	16.83	15.62	14.89

The results also show that the numerical model predictions of droplet detachment times over the conducted wide range of perturbation amplitudes are essentially within two standard deviations (2σ) of the experimentally measured mean droplet detachment

times. For lower injection velocities, as in run W090, the numerical and experimental results closely agree at lower normalized initial perturbation amplitudes (ε_s/z_o = 0.1-0.25) due to the thinner liquid film thickness as compared to the thicker values at higher transpiration velocities as in run W210. In run W210, there is an adequate agreement between the numerical and experimental results at a higher normalized initial perturbation amplitude (ε_s/z_o = 1). In thick liquid films, spikes form and droplets detach from the preceding pinched off spike due to the backward reaction on the liquid film while in thinner liquid films leveling transpires after droplets detachment. This action results in a close agreement between the numerical and experimental results at higher normalized initial perturbation amplitude values ε_s/z_o for thick liquid films (higher w_{in}) and at lower values of ε_s/z_o for thin films (lower w_{in}).

5.3.2 Droplets Detaching from Inclined Bounded Liquid Films

An inclination angle of 2.5° was utilized to investigate the effect of shear stress and liquid film drift on the stability and detachment response. In this case, several normal and tangential flow rates characterize the flow field. Figure 5.17 illustrates the inflow and outflow rates through a control volume defining the spatiotemporal liquid film development for an inclined plate setup.

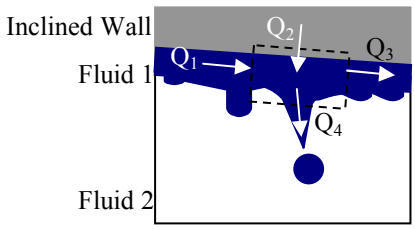

Figure 5.17 Schematic illustration of the volume flow rates passing through the defining control surface for a developing liquid film on an inclined bounding plate.

As discussed in section 5.1.2, the thickness of the advected liquid film increases along the length of the plate from the uppermost point to the lowermost edge because of the continuous transpiration through the porous plate and the delayed droplet formation. The numerical front tracking analysis was carried out using a constant liquid film thickness along the flow direction in the inclined plate setup. Thus, the numerical runs for water were conducted utilizing the measured liquid film thickness at x = 30 mm and then another calculation was executed using the measured thickness at x = 40 mm as given in Tables 5.7-5.10. For the 20% glycerol numerical runs the measured thickness values at x = 20 mm and x = 30 mm were utilized as provided in Tables 5.11 and 5.12.

Table 5.7 Experimental mean (t_d), standard deviation (σ) and numerical prediction values of the detachment time in seconds for the experimental and numerical runs conducted using inclined surfaces ($\theta = 2.5^\circ$) and the corresponding liquid film thickness at x = 30 mm for water at 293 K.

Runs	Experiment		Normalized Initial Perturbation Amplitude, ε_s/z_o				
	t_d, [s]	σ, [s]	0.1	0.25	0.5	0.75	1
W0925	0.5991	0.0114	0.6657	0.5541	0.4717	0.4232	0.3876
W1425	0.5155	0.0098	0.5582	0.4701	0.4041	0.3671	0.3407
W1725	0.4322	0.0094	0.5328	0.4498	0.3879	0.3519	0.3277
W1925	0.3641	0.0129	0.4989	0.4221	0.3638	0.3298	0.3074
W2125	0.2867	0.0108	0.4726	0.4002	0.3444	0.3128	0.2927

Table 5.8 Experimental mean (t_d), standard deviation (σ) and numerical prediction values of the detachment time in seconds for the experimental and numerical runs conducted using inclined surfaces ($\theta = 2.5^\circ$) and the corresponding liquid film thickness at x = 40 mm for water at 293 K.

Runs	Experiment		Normalized Initial Perturbation Amplitude, ε_s/z_o				
	t_d, [s]	σ, [s]	0.1	0.25	0.5	0.75	1
W0925	0.5991	0.0114	0.5874	0.4902	0.4171	0.3774	0.3477
W1425	0.5155	0.0098	0.4986	0.4186	0.3599	0.3262	0.3032
W1725	0.4322	0.0094	0.4658	0.3912	0.3378	0.3068	0.2853
W1925	0.3641	0.0129	0.4341	0.3657	0.3147	0.2866	0.2688
W2125	0.2867	0.0108	0.4009	0.3387	0.2922	0.2695	0.2545

Table 5.9 Nondimensional experimental mean (t_d^*), standard deviation (σ^*) and numerical prediction values of the detachment time for the experimental and numerical runs conducted using inclined surfaces ($\theta = 2.5^\circ$) and the corresponding liquid film thickness at $x^* = 10.9$ for water at 293 K (Re = 445).

Runs	Experiment		Normalized Initial Perturbation Amplitude, ε_s/z_o				
	t_d^*	σ^*	0.1	0.25	0.5	0.75	1
W0925	35.92	0.68	39.92	33.23	28.28	25.37	23.24
W1425	30.92	0.59	33.47	28.18	24.23	22.01	20.43
W1725	25.92	0.56	31.95	26.97	23.26	21.11	19.65
W1925	21.83	0.77	29.92	25.31	21.81	19.77	18.43
W2125	17.19	0.64	28.34	23.99	20.65	18.76	17.55

Table 5.10 Nondimensional experimental mean (t_d^*), standard deviation (σ^*) and numerical prediction values of the detachment time for the experimental and numerical runs conducted using inclined surfaces ($\theta = 2.5^\circ$) and the corresponding liquid film thickness at $x^* = 14.6$ for water at 293 K (Re = 445).

Runs	Experiment		Normalized Initial Perturbation Amplitude, ε_s/z_o				
	t_d^*	σ^*	0.1	0.25	0.5	0.75	1
W0925	35.92	0.68	35.22	29.39	25.01	22.64	20.85
W1425	30.92	0.59	29.89	25.10	21.58	19.56	18.18
W1725	25.92	0.56	27.93	23.45	20.25	18.40	17.11
W1925	21.83	0.77	26.02	21.93	18.87	17.19	16.12
W2125	17.19	0.64	20.04	20.31	17.51	16.15	15.25

Table 5.11 Dimensional and nondimensional experimental mean (t_d), standard deviation (σ) and numerical prediction values of the detachment time for the experimental and numerical runs conducted using inclined surfaces ($\theta = 2.5^\circ$) and the corresponding liquid film thickness at x = 20 mm ($x^* = 7.6$) for 20% glycerol at 293 K (Re = 250).

Runs	Experiment		Normalized Initial Perturbation Amplitude, ε_s/z_o				
	t_d, [s]	σ, [s]	0.05	0.25	0.5	0.75	1
G0925	0.8122	0.0127	0.8428	0.6516	0.5605	0.4987	0.4554
G1725	0.6449	0.0164	0.6781	0.5201	0.4472	0.4051	0.3754
Runs	Experiment		Normalized Initial Perturbation Amplitude, ε_s/z_o				
	t_d^*	σ^*	0.05	0.25	0.5	0.75	1
G0925	49.62	0.78	51.48	39.81	34.23	30.46	27.82
W1725	39.39	1.01	41.42	31.77	27.32	24.74	22.93

Table 5.12 Dimensional and nondimensional experimental mean (t_d), standard deviation (σ) and numerical prediction values of the detachment time for the experimental and numerical runs conducted using inclined surfaces ($\theta = 2.5^{\circ}$) and the corresponding liquid film thickness at x = 30 mm ($x^* = 11.4$) for 20% glycerol at 293 K (Re = 250).

Runs	Experiment		Normalized Initial Perturbation Amplitude, ε_s/z_o				
	t_d, [s]	σ, [s]	0.05	0.25	0.5	0.75	1
G0925	0.8122	0.0127	0.7984	0.5794	0.4860	0.4351	0.3991
G1725	0.6449	0.0164	0.6236	0.4774	0.4110	0.3714	0.3452
Runs	Experiment		Normalized Initial Perturbation Amplitude, ε_s/z_o				
	t_d^*	σ^*	0.05	0.25	0.5	0.75	1
G0925	49.62	0.78	48.77	35.39	29.68	26.58	24.38
W1725	39.39	1.01	38.09	29.16	25.11	22.68	21.08

The experimental data for the statistical distributions of dimensional and nondimensional detachment times based on which the mean and standard deviation values were obtained are presented in Figures 5.18 and 5.19 for runs W0925 and W2125. Due to the tangential acceleration, shear stress effect and liquid film drift, droplet formation is delayed for the inclined plate configuration as compared to the horizontal surface setup. Based on the results provided in Tables 5.7-5.12, the measured mean detachment time increased by 28.8% and 20.8% when using inclined bounding surfaces ($\theta = 2.5^{\circ}$) as compared to the horizontal bounding plate setup for runs W0925 and G0925, respectively.

In the inclined surface configuration, the droplet pinch-off times are also increased by decreasing the transpiration velocity w_{in} or by utilizing 20% glycerol as a working fluid compared to water for the same injection velocity. Using water as the working fluid, the detachment time decreases from 0.5991 to 0.2867 seconds by increasing the transpiration velocity through the inclined plate from 0.9 to 2.1 mm/s. The numerical and experimental data for the variation of the dimensional and nondimensional droplet detachment time with the normalized initial perturbation amplitude ε_s/z_o carried

out for runs W0925 and W2125 are depicted in Figures 5.20 and 5.21. The detailed numerical and experimental results for the other conducted runs are given in the appendices. These results cover a wide range of injection velocities using water and 20% glycerol as working fluids as provided in Table 5.1.

The numerical results extracted using two different liquid film thickness values corresponding to two different axial positions (x = 30 and 40 mm for water as the working fluid) along the plate indicate that for thinner liquid films (using the thickness at x = 30 mm) an increase in the detachment time is expected. For instance, the droplet detachment time increases by 17.8% when using the liquid film thickness at 30 mm as compared to the thickness value at 40 mm for run W2125 at a normalized initial perturbation amplitude $\varepsilon_s/z_o = 0.1$.

Similar to the horizontal surface runs, for higher injection velocities w_{in} the numerical and experimental results closely agree at higher normalized initial perturbation amplitudes ε_s/z_o as in run W2125 while they agree at lower ε_s/z_o values for lower transpiration velocity w_{in} values as in run W0925. The numerical and experimental evolution sequence for runs W090, W210, W0925 and W2125 corresponding to horizontal and inclined bounding surface configurations are provided in Figures 5.22-5.25. These numerical and experimental images are compared at the detachment or pinch-off point. In the horizontal bounding plate setup, the experimental images representing the spike evolution and droplet detachment were captured approximately at the center of the rectangular bounding plate. Droplets detaching from inclined surfaces were captured near the upper edge away from the turbulent liquid film domain defining the lower region of the inclined plate.

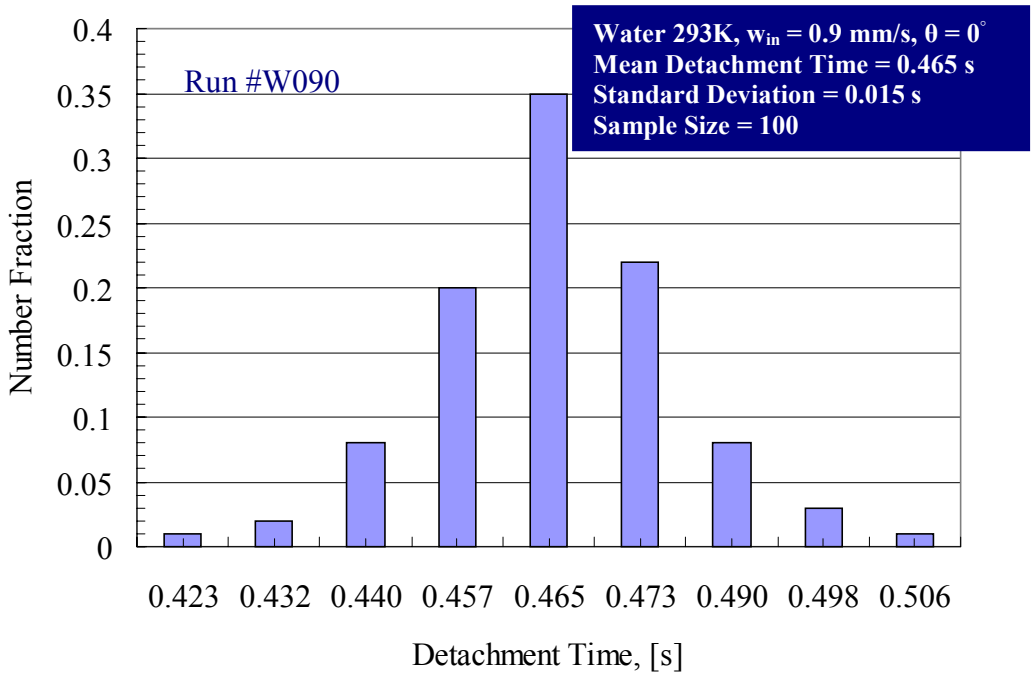

(a)

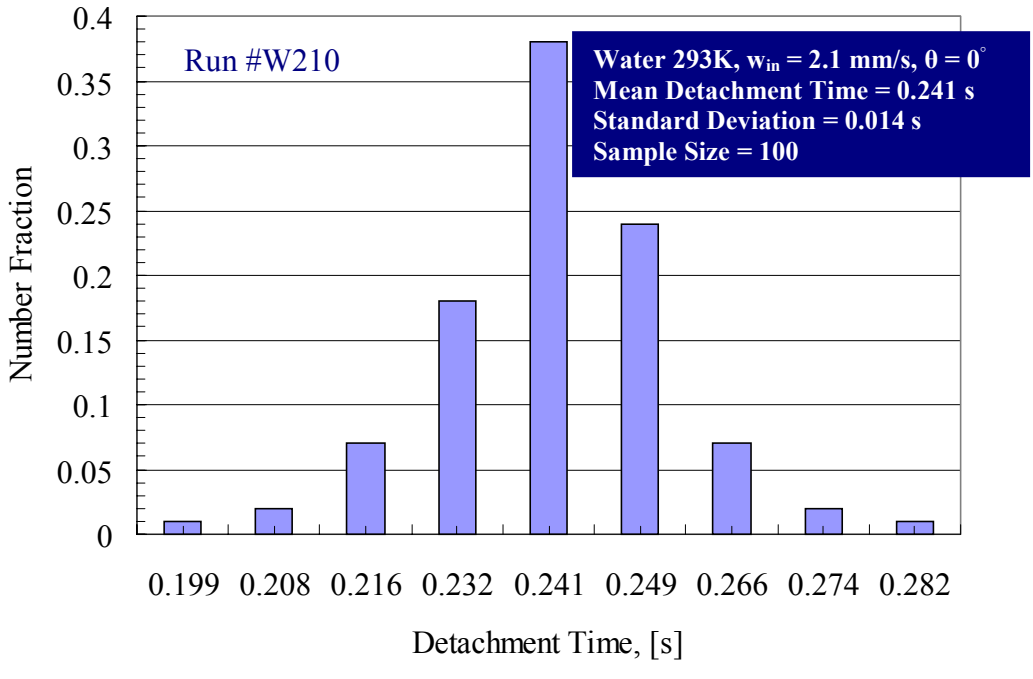

(b)

Figure 5.13 Experimental data for the distribution of the detachment times carried out for horizontal surfaces (θ = 0˚) : (a) Run #W090, and (b) Run #W210.

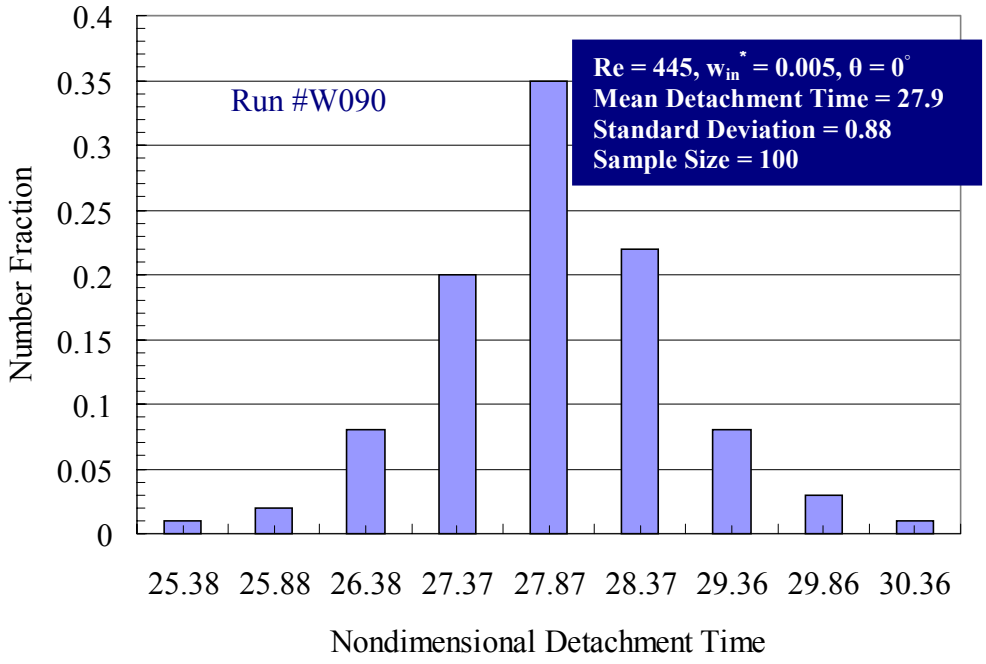

(a)

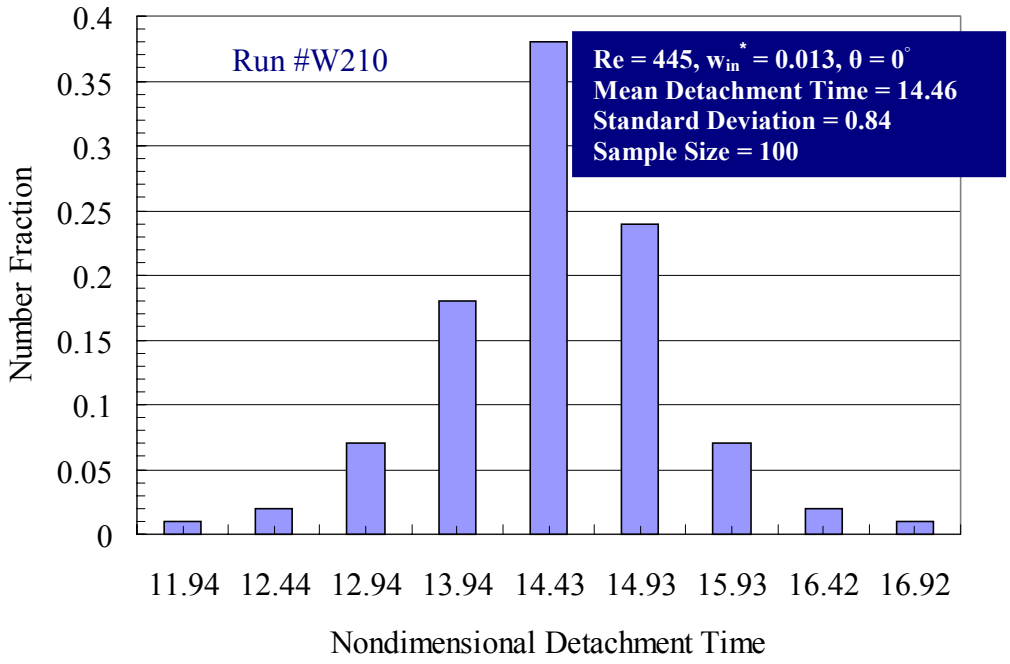

(b)

Figure 5.14 Experimental data for the distribution of the nondimensional detachment time carried out for horizontal surfaces (θ = 0˚): (a) Run #W090, and (b) Run #W210.

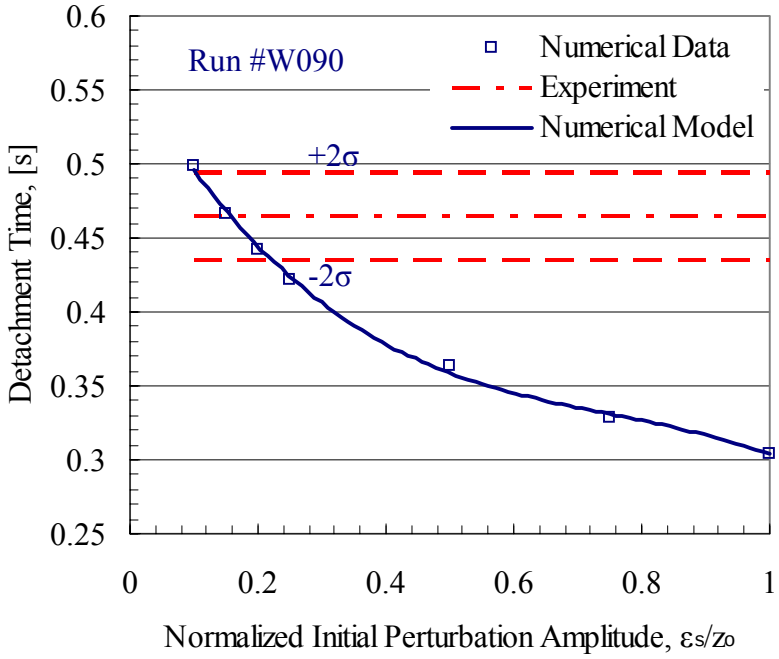

(a)

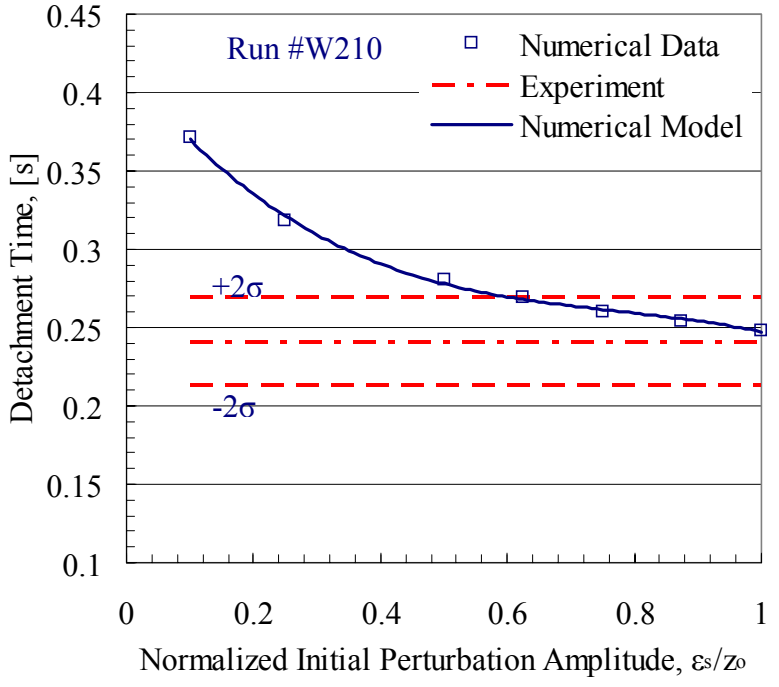

(b)

Figure 5.15 Numerical and experimental data for the variation of the detachment time with the normalized initial perturbation amplitude carried out for horizontal surfaces ($\theta = 0^{\circ}$): (a) Run #W090, and (b) Run #W210.

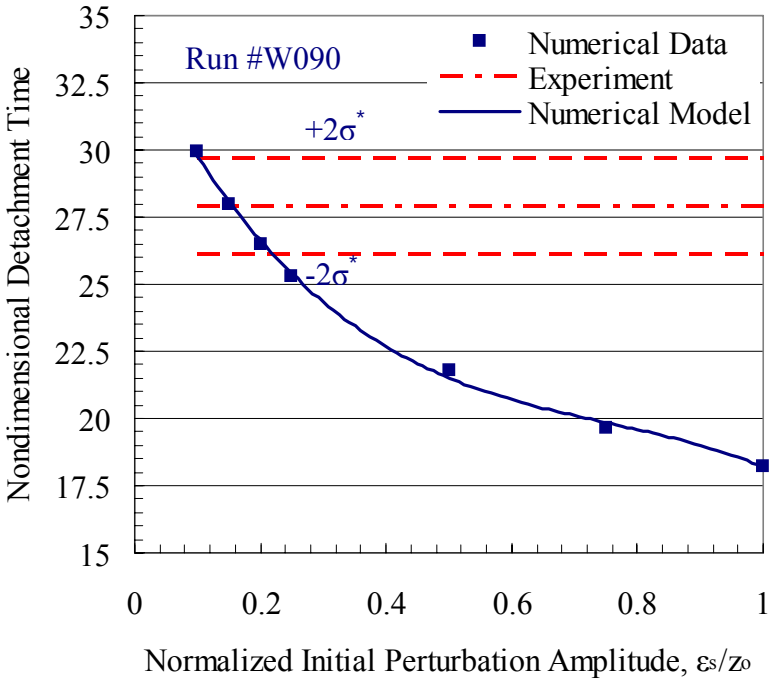

(a)

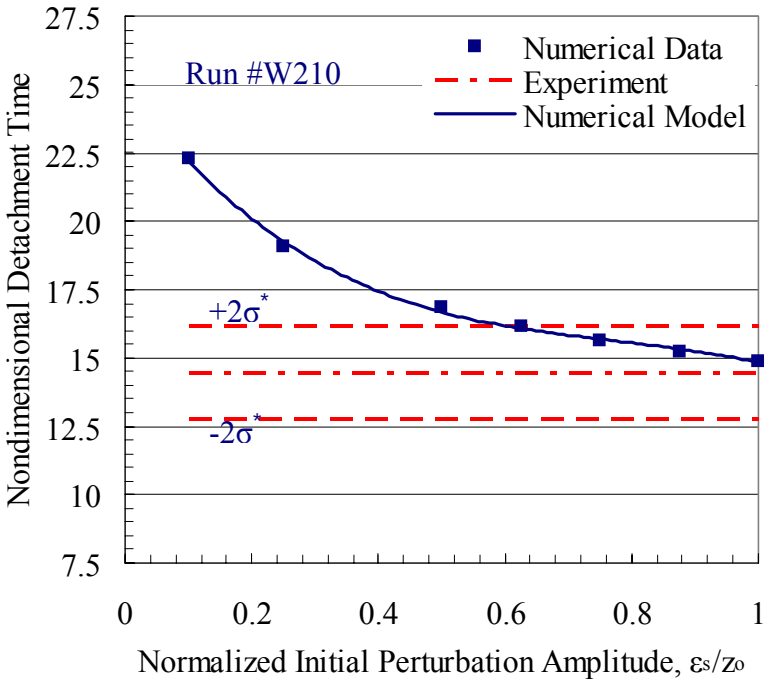

(b)

Figure 5.16 Numerical and experimental data for the variation of the nondimensional detachment time with the normalized initial perturbation amplitude carried out for horizontal surfaces ($\theta = 0^{\circ}$): (a) Run #W090, and (b) Run #W210.

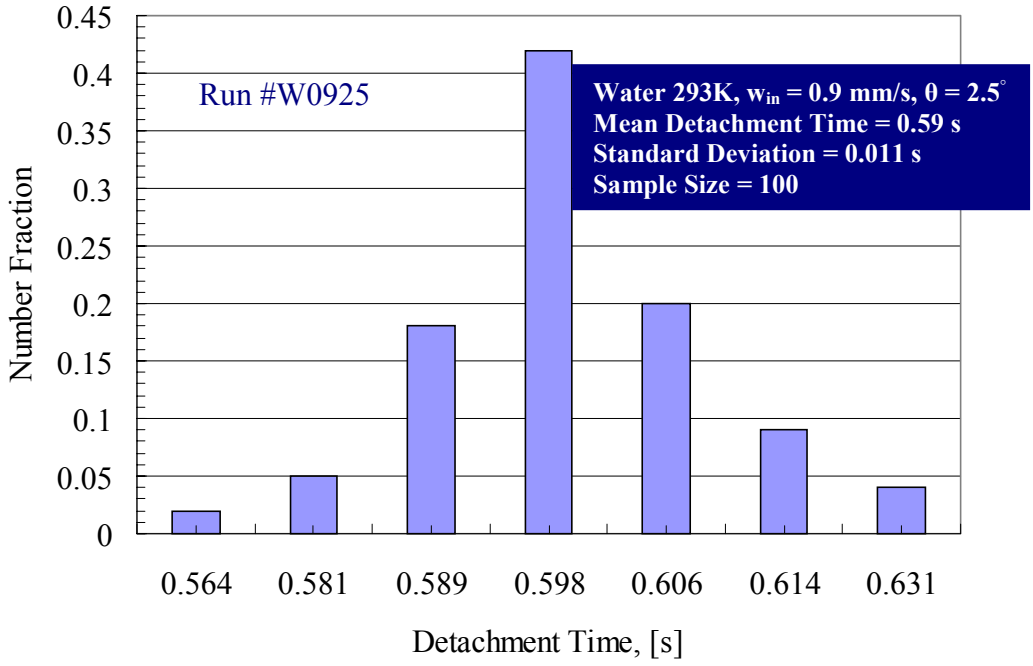

(a)

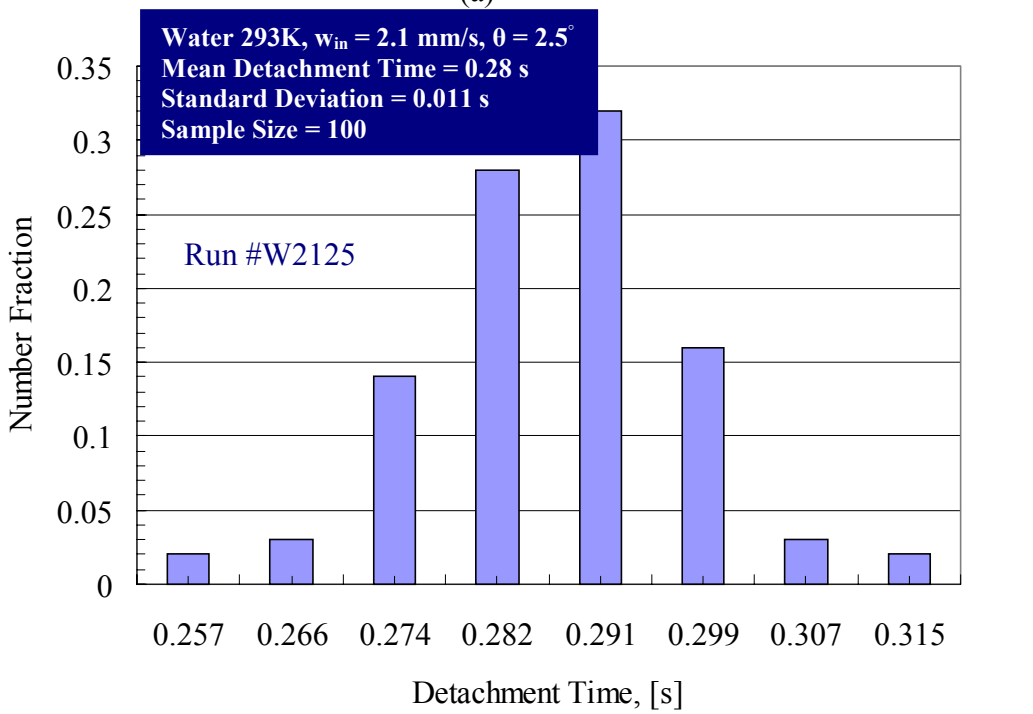

(b)

Figure 5.18 Experimental data for the distribution of the detachment times carried out for inclined surfaces (θ = 2.5˚): (a) Run #W0925, and (b) Run #W2125.

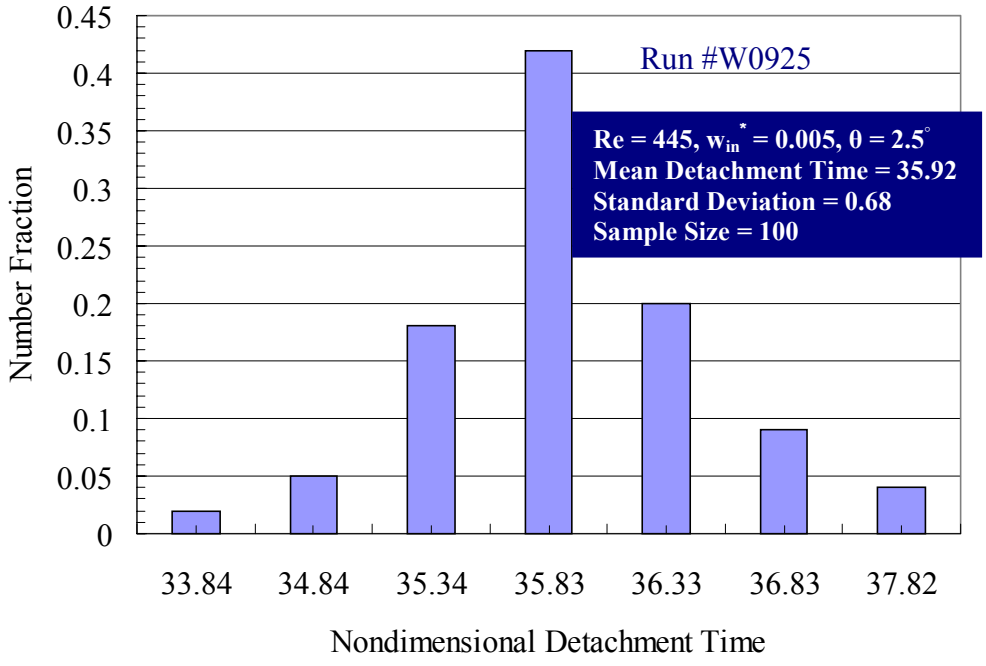

(a)

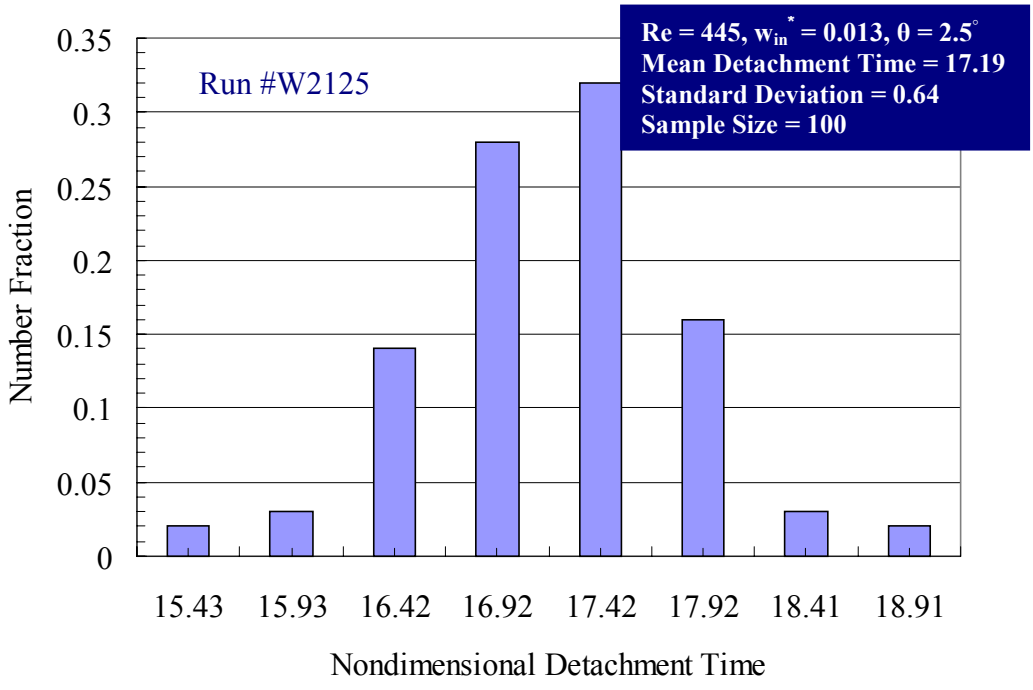

(b)

Figure 5.19 Experimental data for the distribution of the nondimensional detachment time carried out for inclined surfaces (θ = 2.5˚): (a) Run #W0925, and (b) Run #W2125.

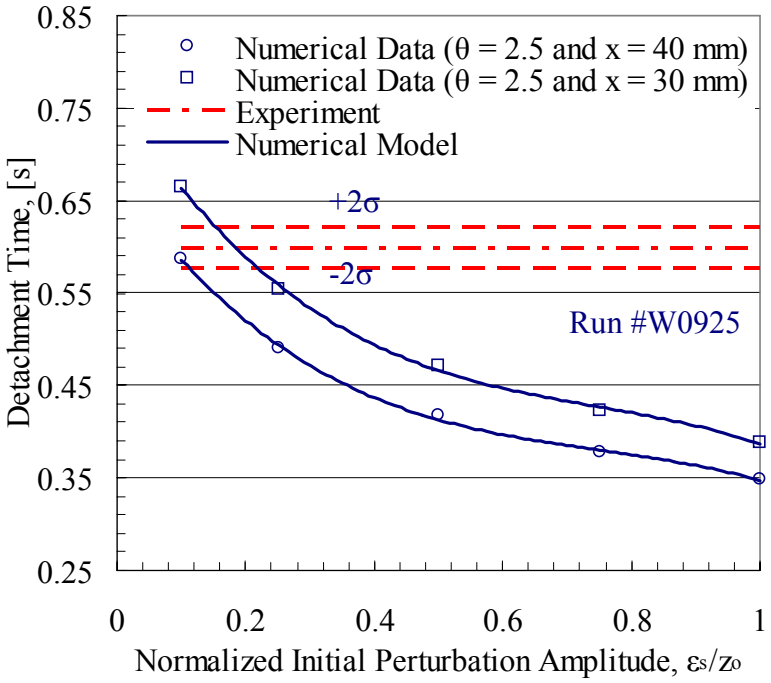

(a)

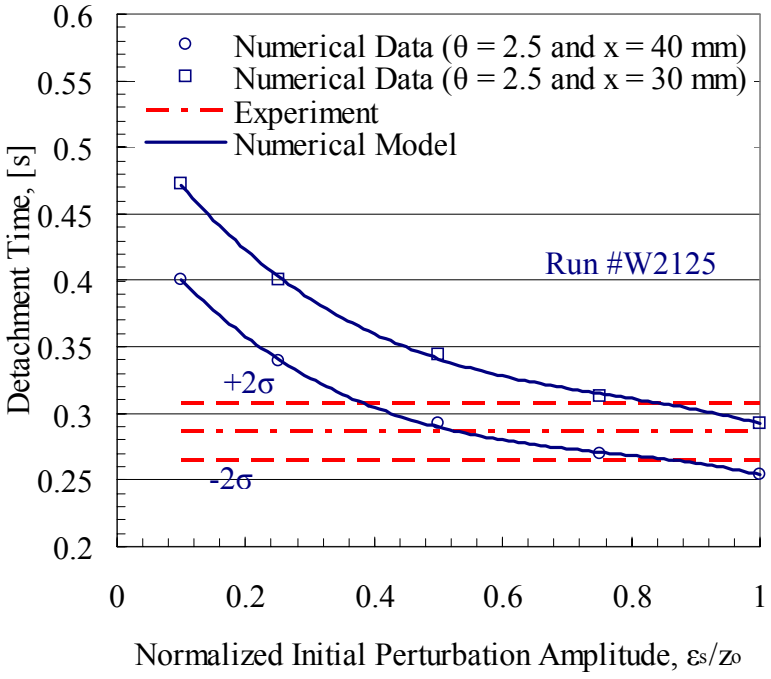

(b)

Figure 5.20 Numerical and experimental data for the variation of the detachment time with the normalized initial perturbation amplitude carried out for inclined surfaces (θ = 2.5˚): (a) Run #W0925, and (b) Run #W2125.

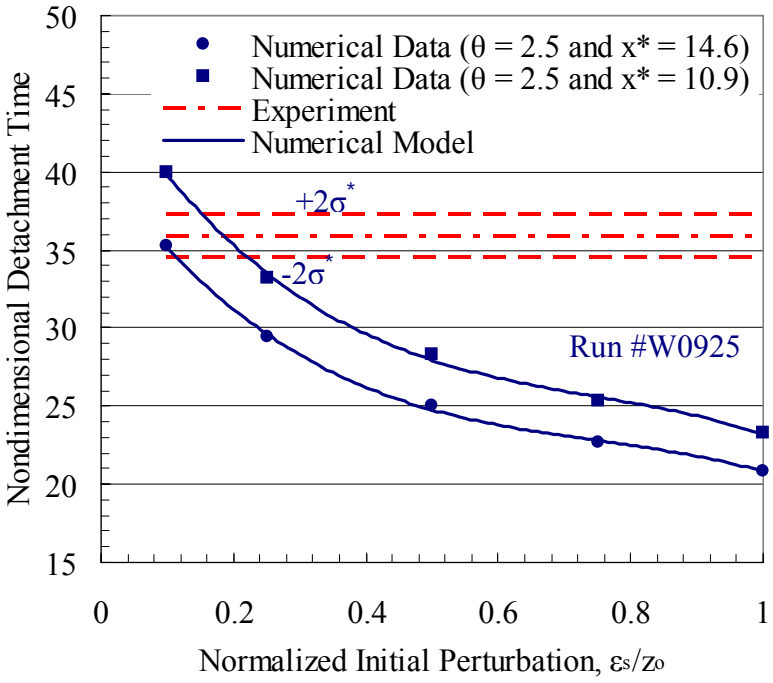

(a)

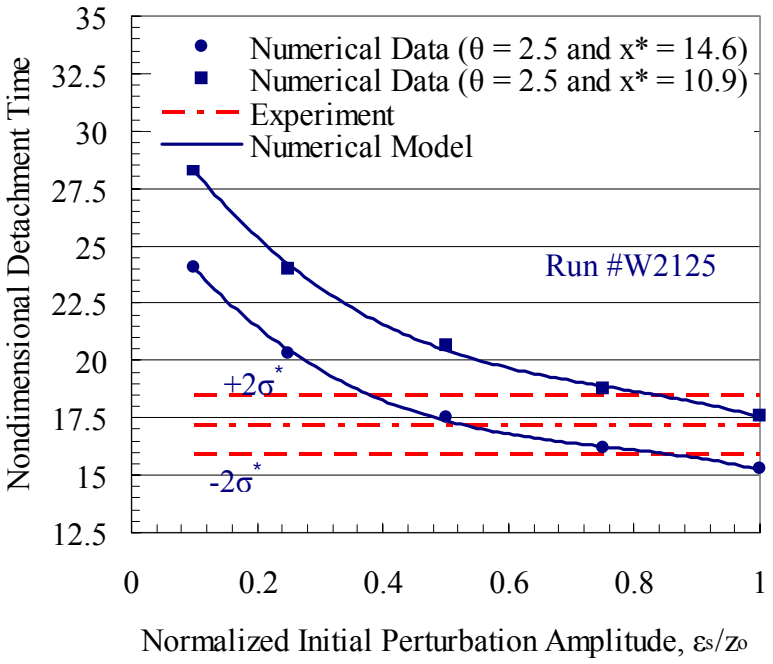

(b)

Figure 5.21 Numerical and experimental data for the variation of the nondimensional detachment time with the normalized initial perturbation amplitude carried out for inclined surfaces (θ = 2.5˚): (a) Run #W0925, and (b) Run #W2125.

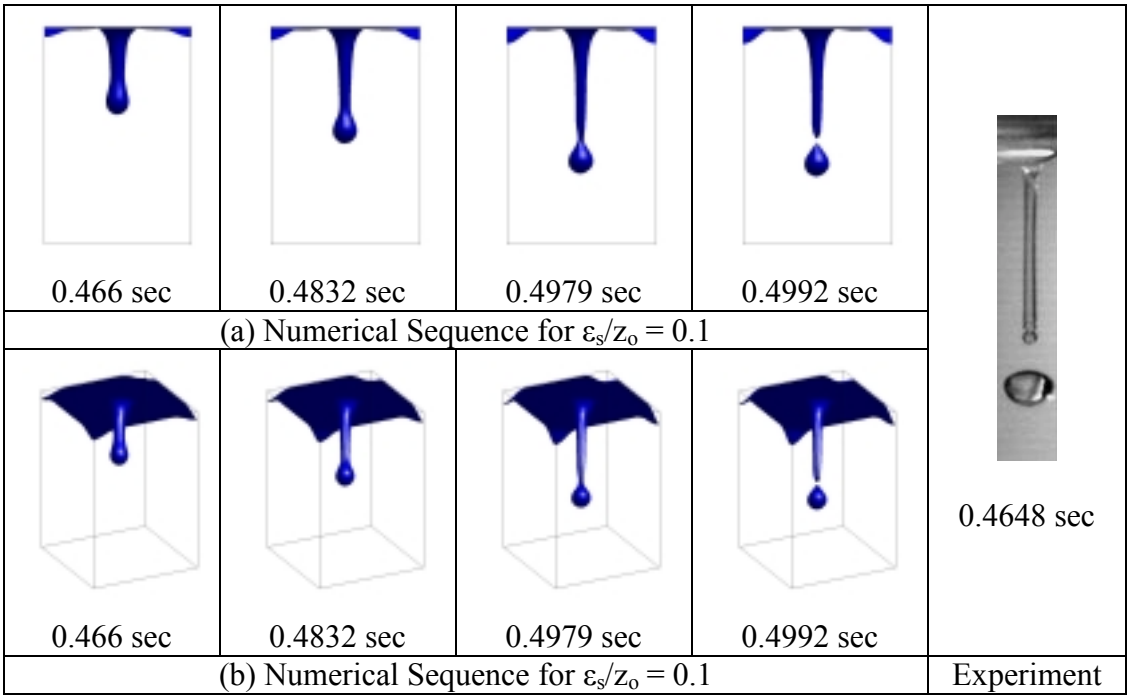

Figure 5.22 Numerical and experimental liquid film evolution and droplet detachment sequence for run #W090: (a) two-dimensional view, (b) three-dimensional view.

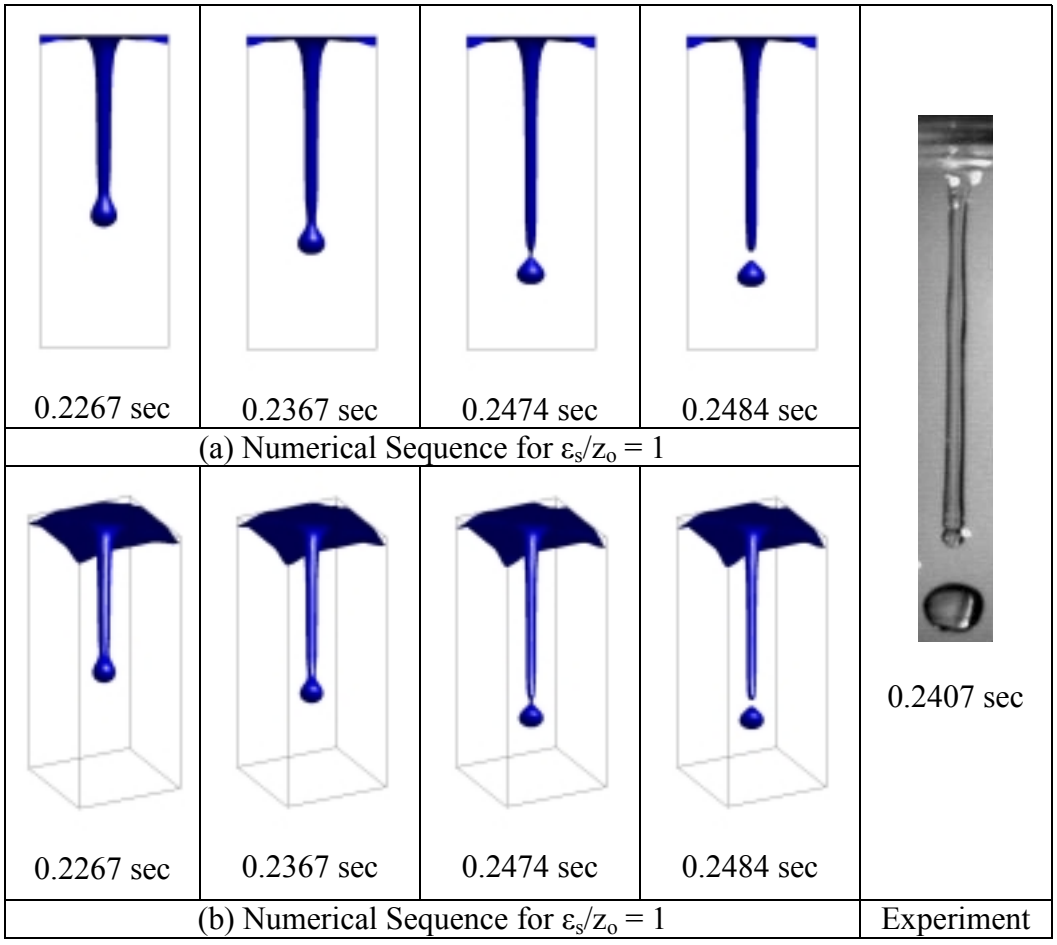

Figure 5.23 Numerical and experimental liquid film evolution and droplet detachment sequence for run #W210: (a) two-dimensional view, (b) three-dimensional view.

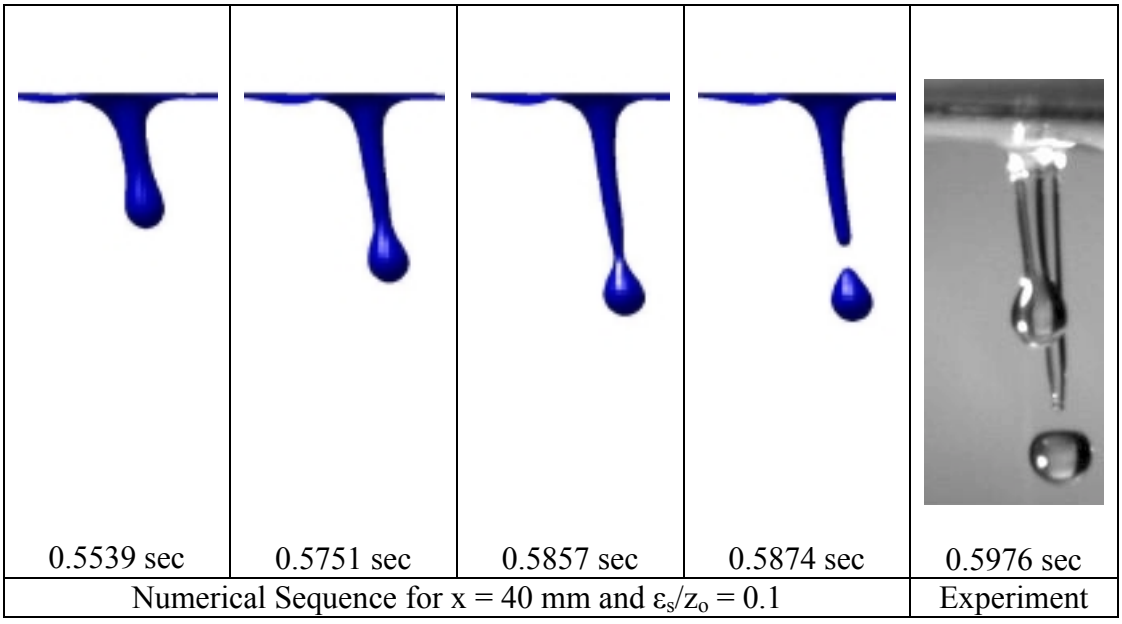

Figure 5.24 Numerical and experimental liquid film evolution and droplet detachment sequence for run #W0925 (θ = 2.5˚).

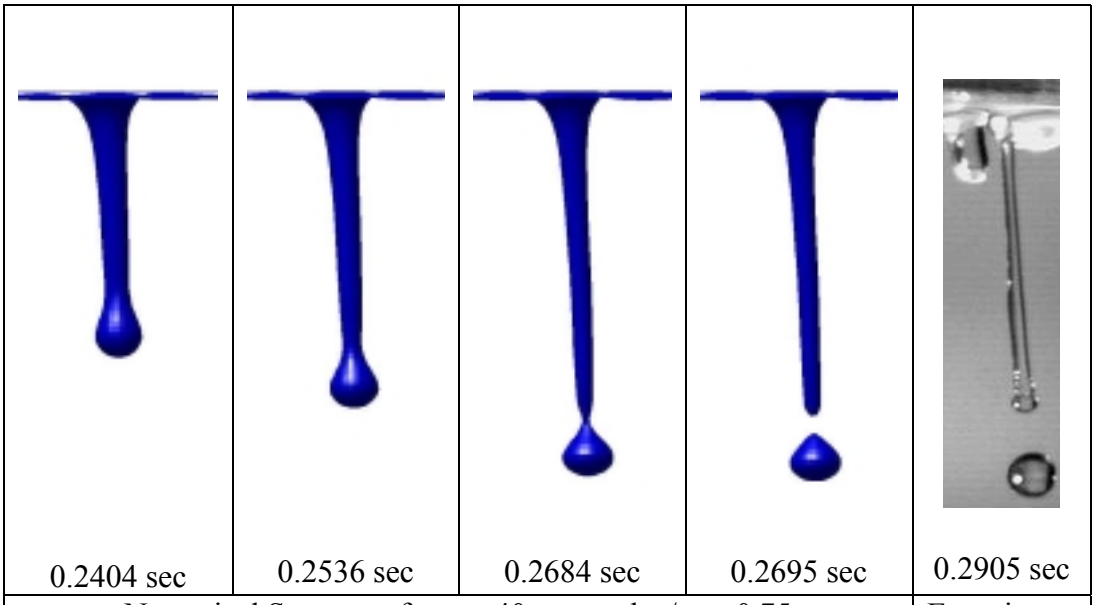

Figure 5.25 Numerical and experimental liquid film evolution and droplet detachment sequence for run #W2125 ($\theta = 2.5^{\circ}$).

5.4 Equivalent Size for Detached Droplets

The equivalent diameter results of droplets detaching from thin liquid films bounded by horizontal and inclined surfaces and subjected to different transpiration velocities using water and 20% glycerol as working fluids are provided in this section. These results are extracted from the distribution of measured equivalent diameter values with a sample size of 100 droplets. Using these distributions, the mean equivalent droplet diameter and the standard deviation among the conducted experimental measurements were obtained. The experimental results are compared with the theoretical predictions obtained using an atomization technique and with the numerical front tracking code results carried out for a range of normalized initial perturbation amplitude ε_s/z_o values from 0.1 to 1.

5.4.1 Equivalent Droplet Diameter for Horizontal Liquid Films

In order to measure the equivalent droplet diameter values for the conducted experiments, images of the detached droplets were captured and confined to a geometrical domain in which the defining edges were detected. As is explained in section 4.3.2 of chapter 4, the detaching droplets are not exactly spherical, but they can be approximated as prolate spheroids with a major axis (a) and a minor axis (b). Hence, by using the edge detection technique and measuring both a and b, the equivalent droplet diameter is defined as $\left(D_{\text{equivalent}} = \sqrt[3]{ab^2}\right)$. Tables 5.13 and 5.14 list the dimensional and nondimensional experimental mean (D), standard deviation (σ) and numerical prediction values of the equivalent droplet diameter for horizontal bounding surfaces conducted using different injection velocities and working fluids. The detailed experimental data for

the statistical distributions of dimensional and nondimensional equivalent droplet diameters for runs W090 and W210 are presented in Figures 5.26 and 5.27.

The atomization mechanistic model presented in section 3.1.3 of chapter 3 for the size of droplets based on a balance between gravitational and surface tension forces provides theoretical values for the droplet diameter as follows:

Using water at 293 K as the working fluid: $D_{theory} = 3.3\left(\frac{\sigma}{\rho g}\right)^{0.5} = 9.0$ mm

Using 20% glycerol at 293 K as the working fluid: $D_{theory} = 8.7$ mm

Based on the results provided in Tables 5.13 and 5.14, the equivalent droplet diameter increases when the transpiration velocity is increased or when 20% glycerol is used as a working fluid rather than water. This trend can be attributed to the development of thicker liquid films at higher injection velocities or when using 20% glycerol as compared to water at the same injection velocity. There is also a close agreement between the experimentally measured diameter and the theoretical droplet diameter value obtained using the atomization mechanistic model for a given working fluid. However, this mechanistic model predicts a smaller diameter value when 20% glycerol is used as compared to water (due to the higher surface tension and lower density of water). The theoretical model assumes a constant liquid film thickness for both working fluids and does not account for transpiration through the boundary.

Figures 5.28 and 5.29 compare the numerical and experimental results for the variation of the dimensional and nondimensional equivalent droplet diameter with the normalized initial perturbation amplitude for runs W090 and W210. The numerical

predictions are approximately constant for the entire range of normalized initial perturbation amplitude ε_s/z_o values from 0.1 to 1.

Table 5.13 Experimental mean (D), standard deviation (σ) and numerical prediction values of the equivalent droplet diameter in mm for the experimental and numerical runs conducted using horizontal surfaces.

Runs	Experiment		Normalized Initial Perturbation Amplitude, ε_s/z_o				
	D [mm]	σ [mm]	0.1	0.25	0.5	0.75	1
W090	8.2	0.2	8.6	8.5	8.6	8.7	8.7
G090	9.0	0.2	8.9	9.0	9.2	9.3	9.4
W140	8.6	0.1	8.8	8.8	8.8	8.9	9.0
W170	8.9	0.1	9.0	8.9	9.0	9.0	9.1
G170	9.9	0.2	9.5	9.5	9.6	9.9	10.2
W190	9.3	0.1	9.2	9.3	9.3	9.4	9.5
W210	9.6	0.2	9.6	9.7	9.8	9.9	10.0

Table 5.14 Nondimensional experimental mean (D^*), standard deviation (σ^*) and numerical prediction values of the equivalent droplet diameter for the experimental and numerical runs conducted using horizontal surfaces.

Runs	Experiment		Normalized Initial Perturbation Amplitude, ε_s/z_o				
	D^*	σ^*	0.1	0.25	0.5	0.75	1
W090	3.00	0.06	3.15	3.12	3.15	3.19	3.19
G090	3.43	0.07	3.39	3.42	3.49	3.54	3.58
W140	3.15	0.05	3.23	3.23	3.23	3.26	3.29
W170	3.26	0.05	3.29	3.26	3.29	3.29	3.34
G170	3.79	0.07	3.59	3.61	3.65	3.76	3.89
W190	3.42	0.05	3.37	3.41	3.41	3.45	3.48
W210	3.52	0.06	3.52	3.56	3.59	3.63	3.67

5.4.2 Equivalent Droplet Diameter for Inclined Liquid Films

The equivalent droplet diameter values for inclined surfaces with an inclination angle of 2.5° were measured for different design parameters. The dimensional and nondimensional experimental mean (D), standard deviation (σ) and numerical prediction values of the equivalent droplet diameter for the inclined surface configuration using

different injection velocities and working fluids are listed in Tables 5.15-5.20. The numerical runs were carried out using two liquid film thickness values corresponding to two axial positions along the inclined plate. The extracted results indicate that the droplet diameter increases for higher transpiration velocities and when 20% glycerol is used. This increasing trend is due to the increased liquid film thickness when providing more liquid through the bounding surface or when using 20% glycerol vs. water. Figures 5.30 and 5.31 present the detailed experimental data for the statistical distributions of dimensional and nondimensional equivalent droplet diameters for runs W0925 and W2125.

Table 5.15 Experimental mean (D), standard deviation (σ) and numerical prediction values of the equivalent droplet diameter in mm for the experimental and numerical runs conducted using inclined surfaces (θ = 2.5˚) and the corresponding liquid film thickness at x = 30 mm for water at 293 K.

Runs	Experiment		Normalized Initial Perturbation Amplitude, ε_s/z_o				
	D [mm]	σ [mm]	0.1	0.25	0.5	0.75	1
W0925	7.79	0.15	7.78	7.80	7.89	7.88	7.99
W1425	8.29	0.14	8.18	8.15	8.16	8.17	8.22
W1725	8.69	0.10	8.34	8.30	8.33	8.35	8.40
W1925	9.01	0.13	8.48	8.37	8.49	8.56	8.59
W2125	9.24	0.14	8.67	8.59	8.66	8.72	8.74

Table 5.16 Experimental mean (D), standard deviation (σ) and numerical prediction values of the equivalent droplet diameter in mm for the experimental and numerical runs conducted using inclined surfaces (θ = 2.5˚) and the corresponding liquid film thickness at x = 40 mm for water at 293 K.

Runs	Experiment		Normalized Initial Perturbation Amplitude, ε_s/z_o				
	D [mm]	σ [mm]	0.1	0.25	0.5	0.75	1
W0925	7.79	0.15	7.86	7.87	7.96	7.97	8.05
W1425	8.29	0.14	8.37	8.36	8.41	8.46	8.54
W1725	8.69	0.10	8.58	8.61	8.63	8.72	8.82
W1925	9.01	0.13	8.77	8.79	8.91	9.01	9.08
W2125	9.24	0.14	8.99	9.06	9.21	9.33	9.49

Table 5.17 Nondimensional experimental mean (D^*), standard deviation (σ^*) and numerical prediction values of the equivalent droplet diameter for the experimental and numerical runs conducted using inclined surfaces ($\theta = 2.5^\circ$) and the corresponding liquid film thickness at $x^* = 10.9$ for water at 293 K (Re = 445).

Runs	Experiment		Normalized Initial Perturbation Amplitude, ε_s/z_o				
	D^*	σ^*	0.1	0.25	0.5	0.75	1
W0925	2.86	0.05	2.85	2.86	2.89	2.89	2.93
W1425	3.04	0.05	2.99	2.99	2.99	2.99	3.01
W1725	3.18	0.04	3.06	3.04	3.05	3.06	3.08
W1925	3.30	0.05	3.11	3.07	3.11	3.14	3.15
W2125	3.39	0.05	3.18	3.15	3.17	3.19	3.20

Table 5.18 Nondimensional experimental mean (D^*), standard deviation (σ^*) and numerical prediction values of the equivalent droplet diameter for the experimental and numerical runs conducted using inclined surfaces ($\theta = 2.5^\circ$) and the corresponding liquid film thickness at $x^* = 14.6$ for water at 293 K (Re = 445).

Runs	Experiment		Normalized Initial Perturbation Amplitude, ε_s/z_o				
	D^*	σ^*	0.1	0.25	0.5	0.75	1
W0925	2.86	0.05	2.88	2.88	2.92	2.92	2.95
W1425	3.04	0.05	3.07	3.06	3.08	3.10	3.13
W1725	3.18	0.04	3.15	3.16	3.16	3.19	3.23
W1925	3.30	0.05	3.21	3.22	3.27	3.30	3.33
W2125	3.39	0.05	3.29	3.32	3.38	3.42	3.48

Table 5.19 Dimensional and nondimensional experimental mean (D), standard deviation (σ) and numerical prediction values of the equivalent droplet diameter for the experimental and numerical runs conducted using inclined surfaces ($\theta = 2.5^\circ$) and the corresponding liquid film thickness at x = 20 mm ($x^* = 7.6$) for 20% glycerol at 293 K (Re = 250).

Runs	Experiment		Normalized Initial Perturbation Amplitude, ε_s/z_o				
	D [mm]	σ [mm]	0.05	0.25	0.5	0.75	1
G0925	8.25	0.17	7.80	7.91	7.80	7.82	7.76
G1725	8.98	0.21	8.60	8.30	8.26	8.26	8.28
Runs	Experiment		Normalized Initial Perturbation Amplitude, ε_s/z_o				
	D^*	σ^*	0.05	0.25	0.5	0.75	1
G0925	3.14	0.06	2.97	3.01	2.97	2.97	2.95
W1725	3.41	0.08	3.27	3.16	3.14	3.14	3.15

Table 5.20 Dimensional and nondimensional experimental mean (D), standard deviation (σ) and numerical prediction values of the equivalent droplet diameter for the experimental and numerical runs conducted using inclined surfaces (θ = 2.5˚) and the corresponding liquid film thickness at x = 30 mm ($x^* = 11.4$) for 20% glycerol at 293 K (Re = 250).

Runs	Experiment		Normalized Initial Perturbation Amplitude, ε_s/z_o				
	D [mm]	σ [mm]	0.05	0.25	0.5	0.75	1
G0925	8.25	0.17	8.12	7.89	7.90	7.89	7.96
G1725	8.98	0.21	8.64	8.42	8.39	8.44	8.49
Runs	Experiment		Normalized Initial Perturbation Amplitude, ε_s/z_o				
	D^*	σ^*	0.05	0.25	0.5	0.75	1
G0925	3.14	0.06	3.09	3.00	3.01	3.00	3.03
W1725	3.41	0.08	3.29	3.20	3.19	3.21	3.23

Droplets detaching from horizontal liquid films have slightly larger equivalent diameter than droplets pinching off from inclined films. An inclination angle of 2.5˚ for a given transpiration velocity slightly reduces the measured mean equivalent diameter by approximately 5% and 8% for runs W0925 and G0925, respectively. Although the thickness of the advected liquid films increases along the length of the inclined surfaces, droplets pinch-off at axial locations corresponding to mean film thickness values smaller than those values measured for horizontal liquid films as listed in Tables 5.2 and 5.3. Thus, the volume of liquid feeding the detached droplets for horizontal surfaces is greater than the volume available at the detachment axial location for droplets pinching off from inclined surfaces. The numerical and experimental results for the variation of the dimensional and nondimensional equivalent droplet diameter with the normalized initial perturbation amplitude for runs W0925 and W2125 are provided in Figures 5.32 and 5.33. Based on these figures, the numerical model predictions of the equivalent droplet diameters are within two standard deviations (2σ) of the experimentally measured mean droplet diameter.

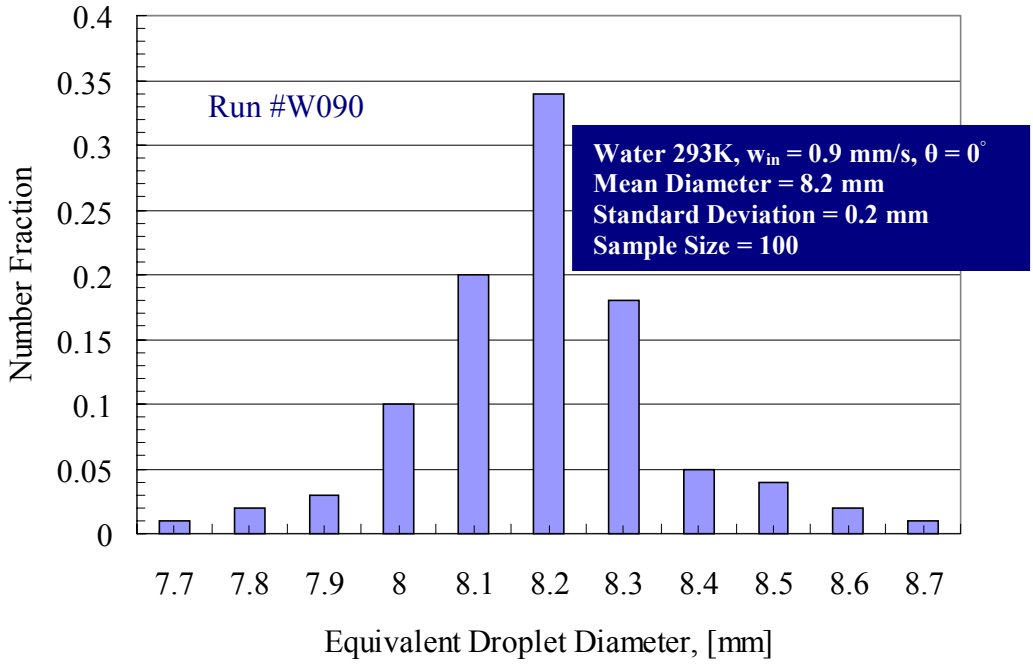

(a)

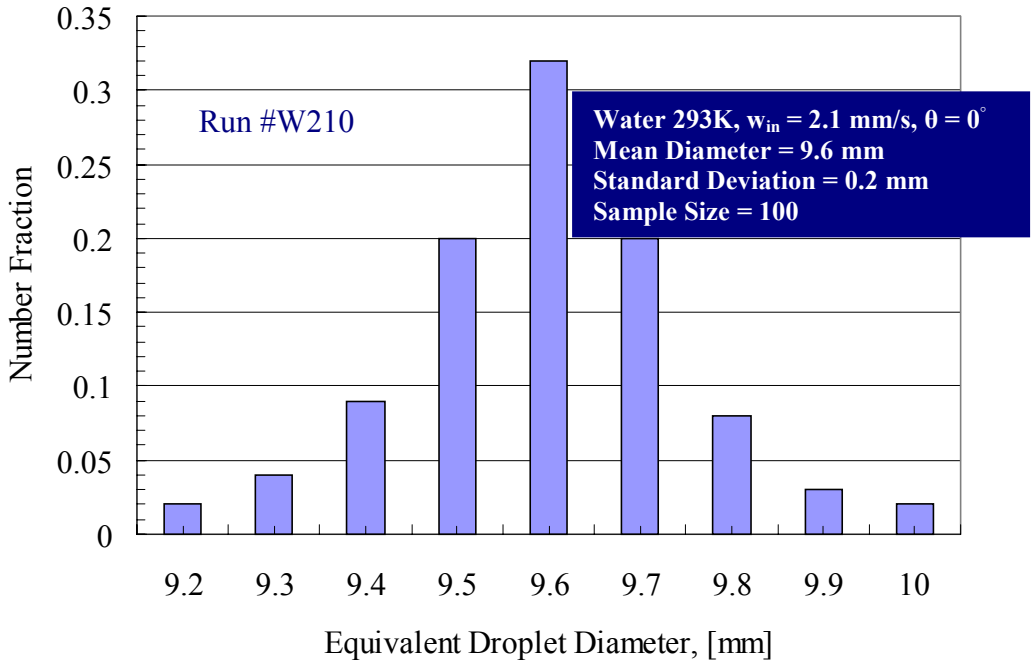

(b)

Figure 5.26 Experimental data for the distribution of the equivalent droplet diameter carried out for horizontal surfaces (θ = 0˚) : (a) Run #W090, and (b) Run #W210.

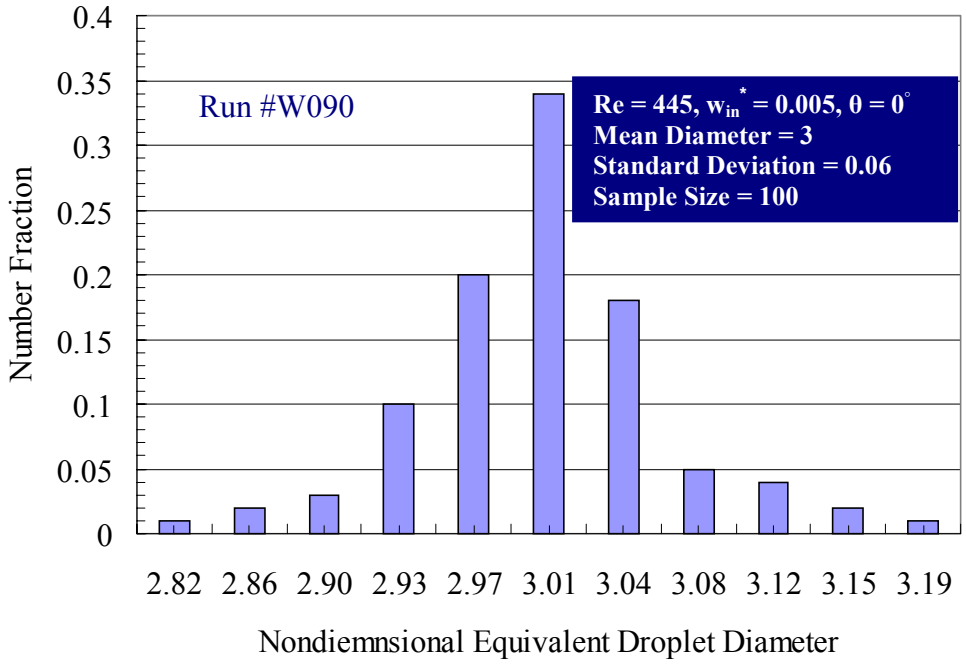

(a)

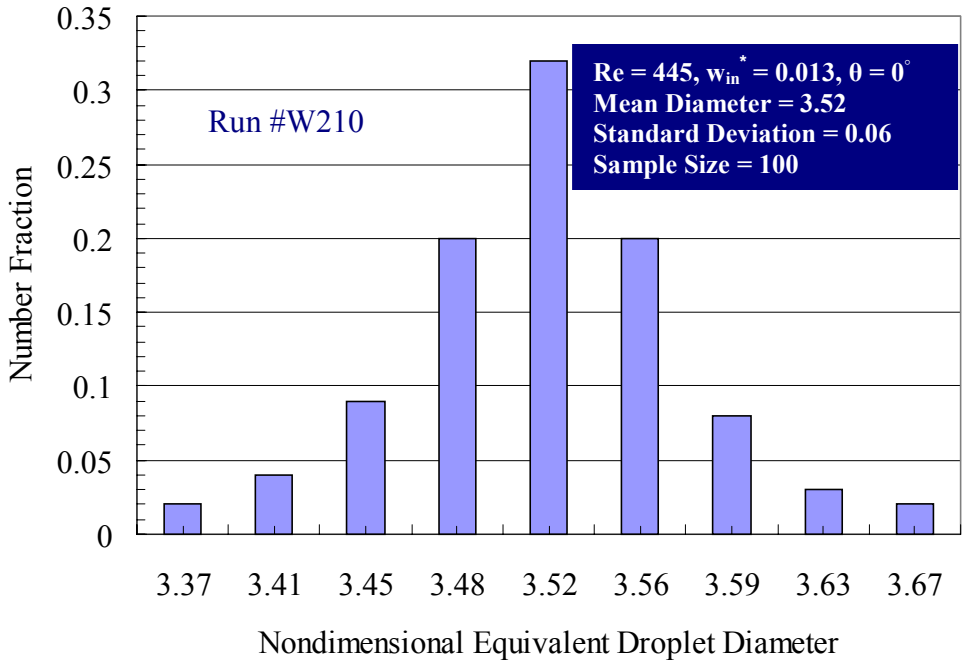

(b)

Figure 5.27 Experimental data for the distribution of the nondimensional equivalent droplet diameter carried out for horizontal surfaces (θ = 0˚): (a) Run #W090, and (b) Run #W210.

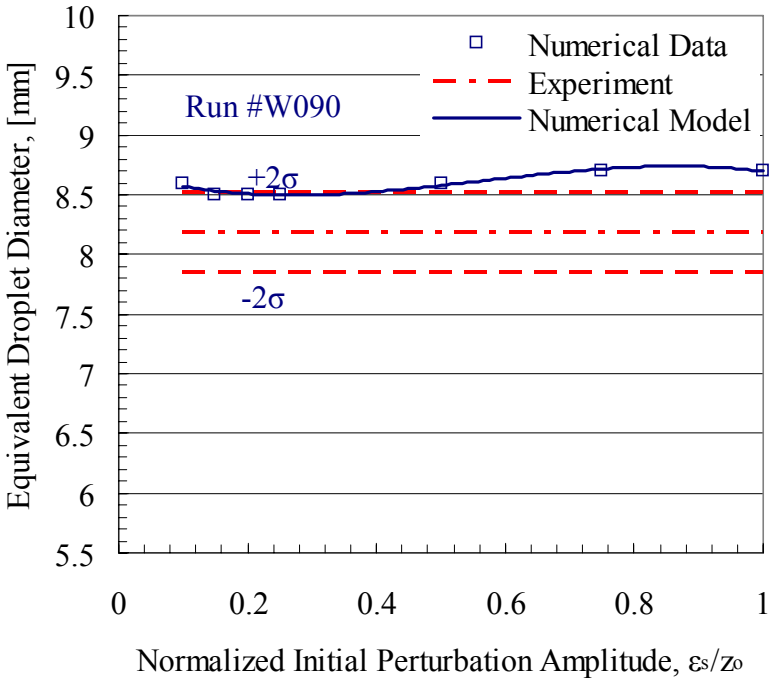

(a)

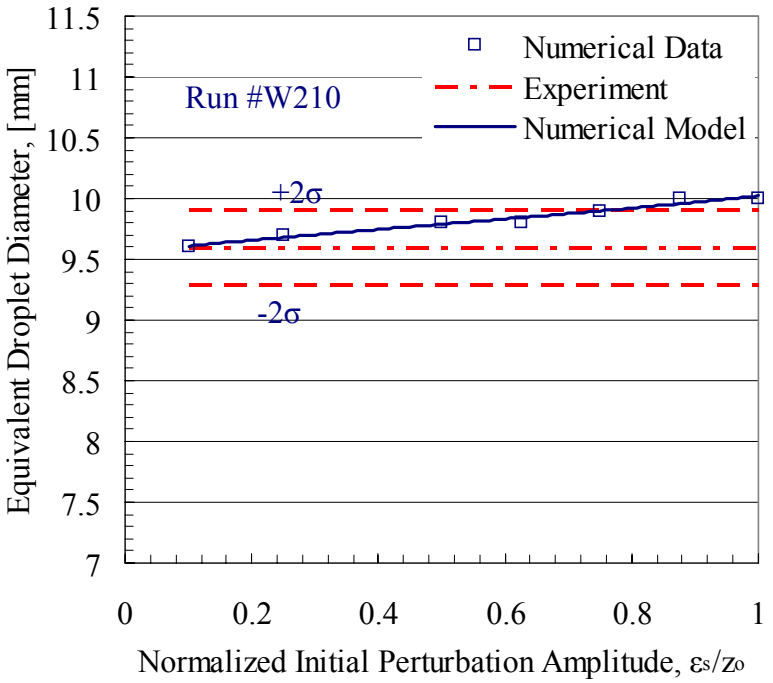

(b)

Figure 5.28 Numerical and experimental data for the variation of the equivalent droplet diameter with the normalized initial perturbation amplitude carried out for horizontal surfaces ($\theta = 0^{\circ}$): (a) Run #W090, and (b) Run #W210.

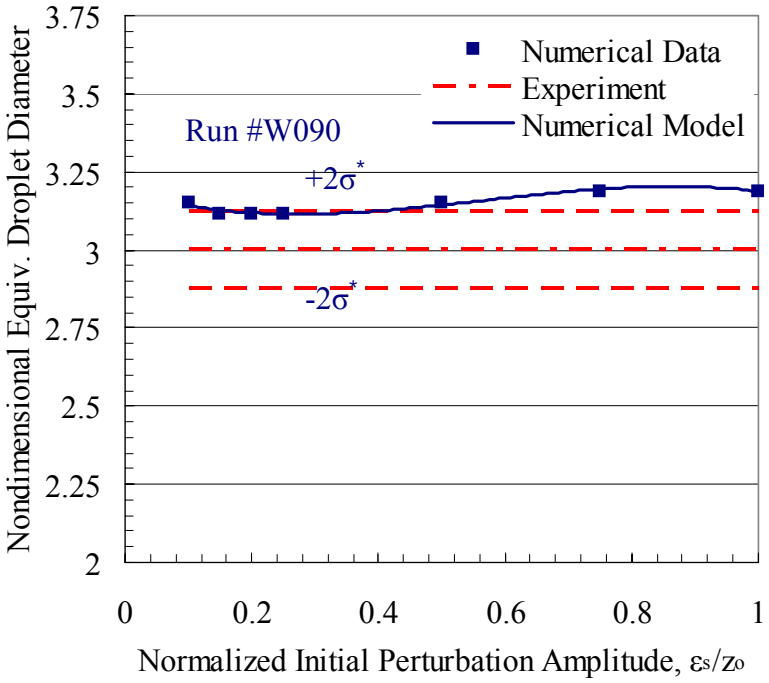

(a)

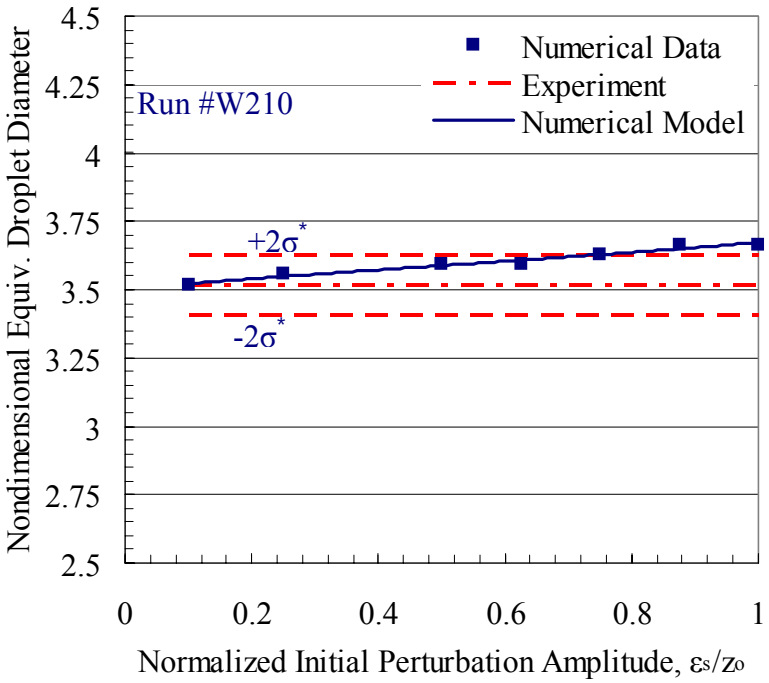

(b)

Figure 5.29 Numerical and experimental data for the variation of the nondimensional equivalent droplet diameter with the normalized initial perturbation amplitude carried out for horizontal surfaces ($\theta = 0^{\circ}$): (a) Run #W090, and (b) Run #W210.

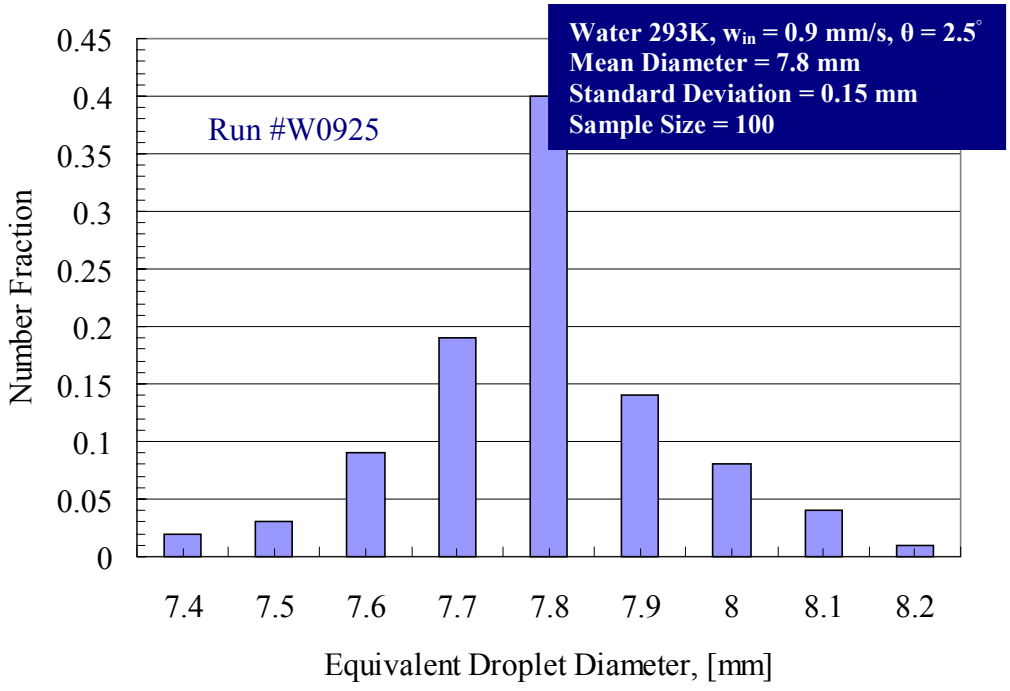

(a)

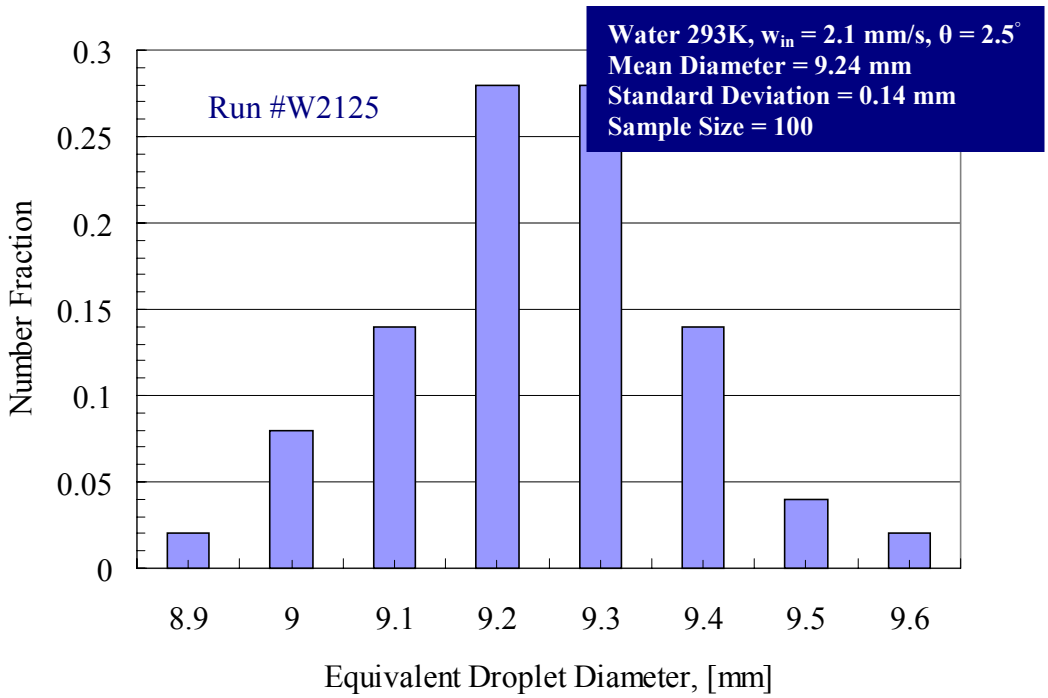

(b)

Figure 5.30 Experimental data for the distribution of the equivalent droplet diameter carried out for inclined surfaces (θ = 2.5˚): (a) Run #W0925, and (b) Run #W2125.

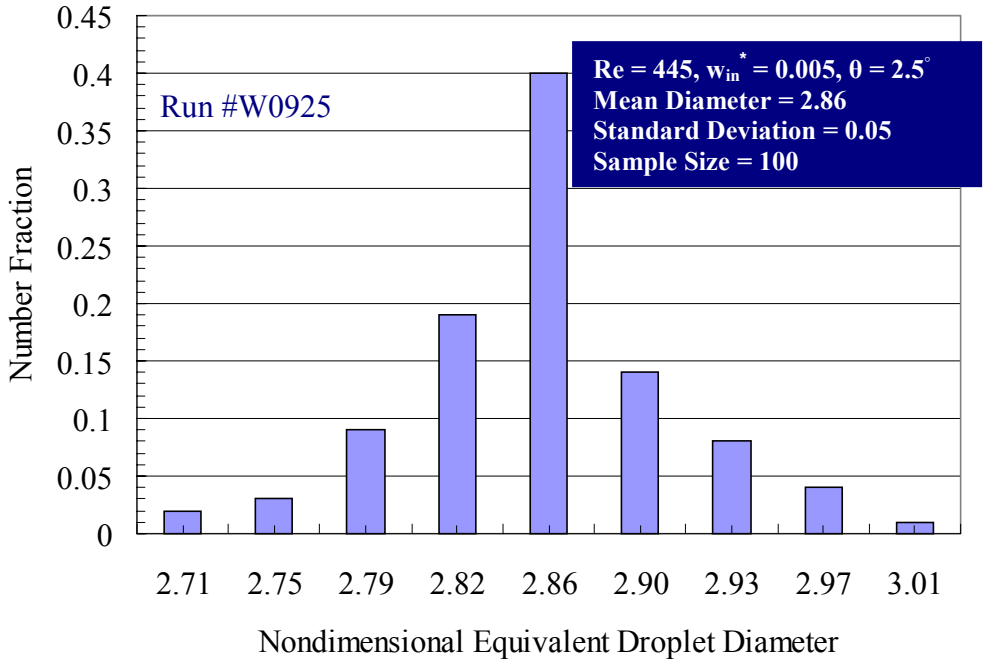

(a)

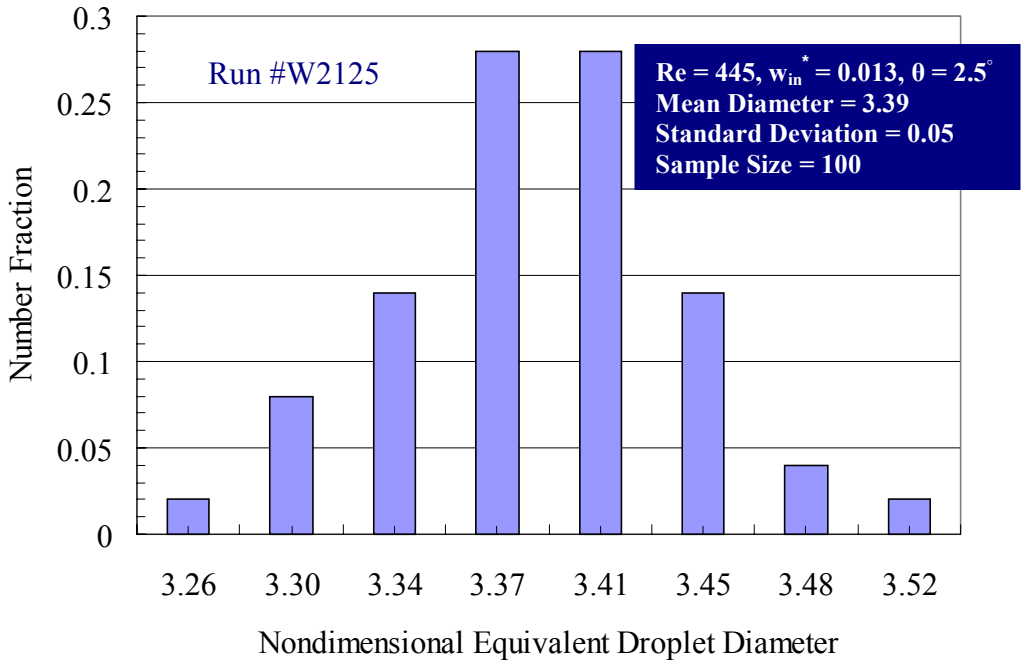

(b)

Figure 5.31 Experimental data for the distribution of the nondimensional equivalent droplet diameter carried out for inclined surfaces (θ = 2.5˚): (a) Run #W0925, and (b) Run #W2125.

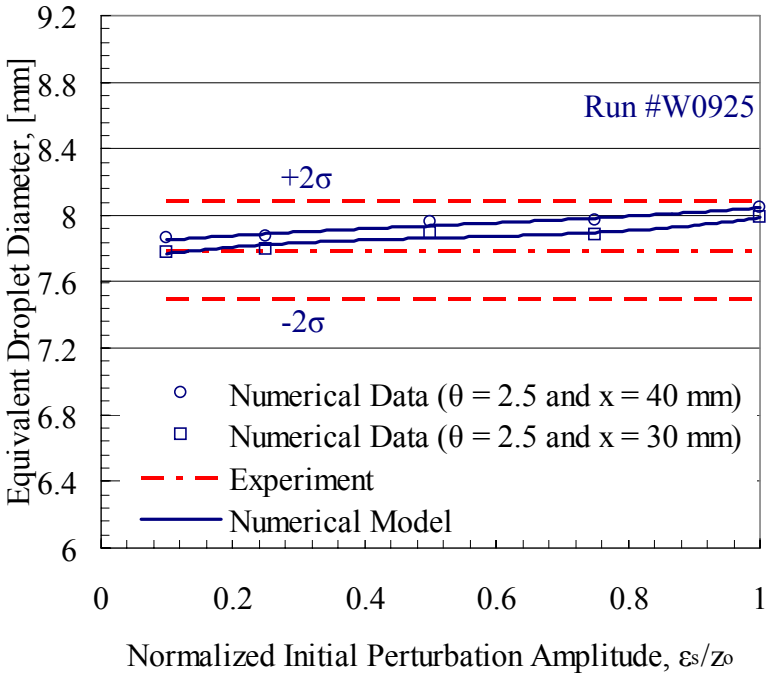

(a)

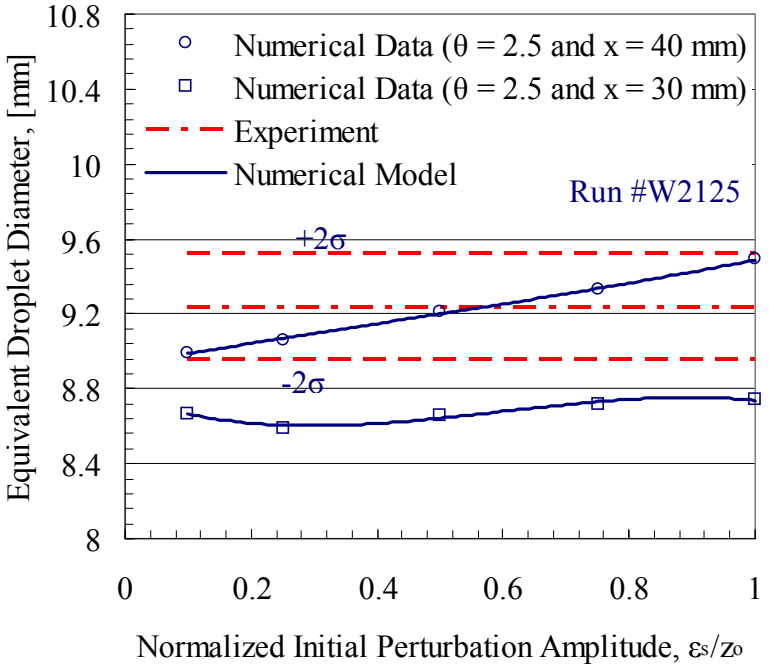

(b)

Figure 5.32 Numerical and experimental data for the variation of the equivalent droplet diameter with the normalized initial perturbation amplitude carried out for inclined surfaces (θ = 2.5˚): (a) Run #W0925, and (b) Run #W2125.

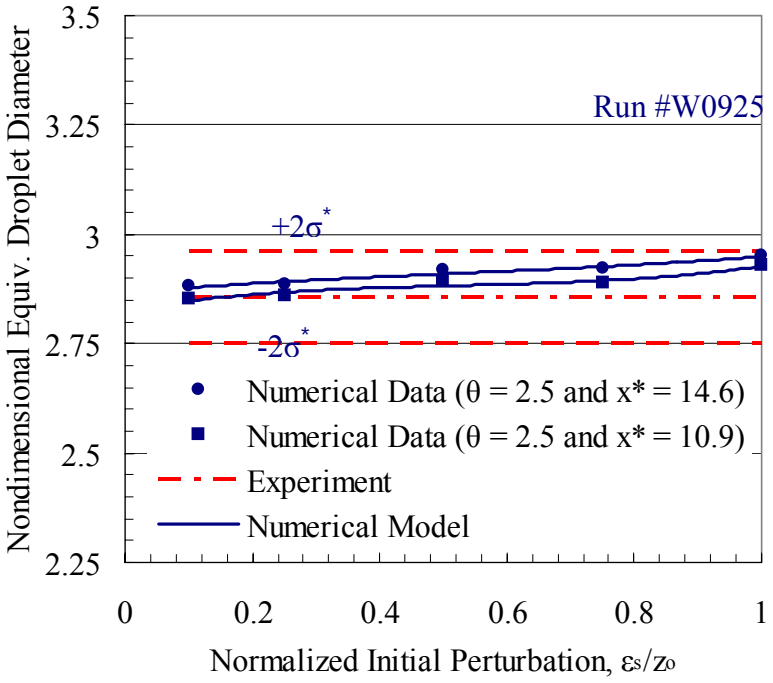

(a)

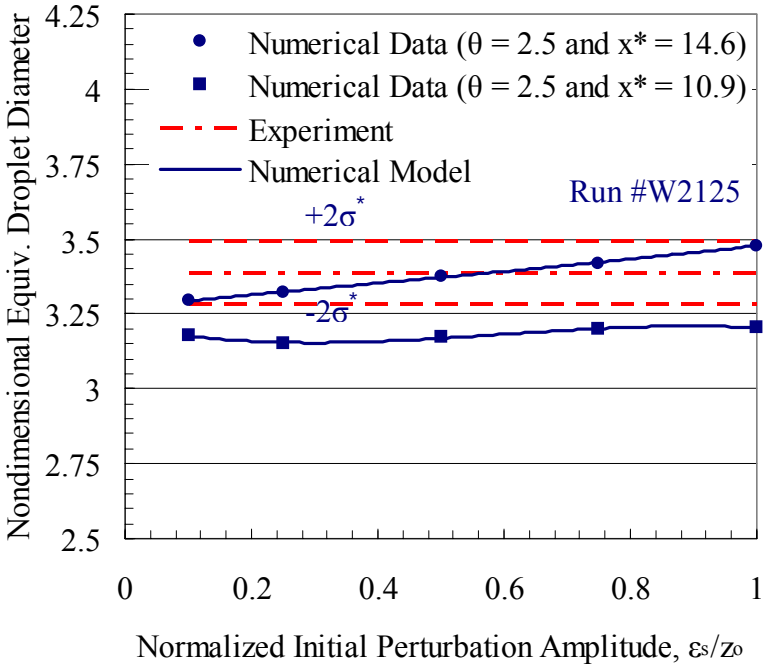

(b)

Figure 5.33 Numerical and experimental data for the variation of the nondimensional equivalent droplet diameter with the normalized initial perturbation amplitude carried out for inclined surfaces (θ = 2.5˚): (a) Run #W0925, and (b) Run #W2125.

5.5 Time History of the Penetration Depth

In this section, the time history of the penetration depth for spikes and droplets detaching from horizontal and inclined bounded thin liquid films is presented. The effect of different design parameters (liquid film thickness, liquid transpiration velocity, inclination angle, and liquid properties) on the penetration depth is studied. A sample size of 100 droplets was used to establish distributions of measured penetration depth values based on which the mean maximum penetration depth and the standard deviation values among the conducted experimental measurements were obtained. The numerical front tracking code predictions carried out for a range of normalized initial perturbation amplitude ε_s/z_o values are also verified using the experimental results.

5.5.1 Penetration Depth of Spikes for Horizontal Surfaces

In order to track the time history of the penetration depth, the maximum vertical distance from the horizontal plate surface to the lowermost tip point of the developing spike or the detached droplet was measured while marching in time. Tables 5.21 and 5.22 list the dimensional and nondimensional experimental mean (d), standard deviation (σ) and numerical prediction values of the maximum penetration depth for horizontal bounding surfaces carried out using several transpiration velocities and different working fluids. Based on the data provided in these tables, when the transpiration velocity increases or when 20% glycerol is used as a working fluid rather than water, the maximum penetration depth also increases. A percentage increase of approximately 72% in the experimental mean value of the maximum penetration depth is obtained when the injection velocity increases from 0.9 to 2.1 mm/s using water. At higher transpiration

velocities, the thickness (h_o) of the liquid film increases (h_{W090} = 0.614 mm and h_{W210} = 1.506 mm) providing more liquid to the developing spikes. The experimental data for the statistical distributions of the dimensional and nondimensional maximum penetration depth for runs W090 and W210 are given in Figures 5.34 and 5.35.

Table 5.21 Experimental mean (d), standard deviation (σ) and numerical prediction values of the maximum penetration depth in mm for the experimental and numerical runs conducted using horizontal surfaces.

Runs	Experiment		Normalized Initial Perturbation Amplitude, ε_s/z_o				
	d, [mm]	σ, [mm]	0.1	0.25	0.5	0.75	1
W090	51.25	2.68	51.70	51.60	53.70	54.60	56.90
G090	74.40	1.91	73.09	74.37	78.42	83.14	87.94
W140	62.33	1.37	59.36	58.50	59.71	60.99	63.48
W170	69.82	1.79	63.54	63.03	63.79	65.38	67.39
G170	86.32	2.59	89.74	91.08	94.62	102.39	114.00
W190	76.70	2.50	73.06	72.09	74.52	78.52	82.93
W210	87.87	3.41	84.44	85.06	89.18	94.01	100.00

Table 5.22 Nondimensional experimental mean (d^*), standard deviation (σ^*) and numerical prediction values of the maximum penetration depth for the experimental and numerical runs conducted using horizontal surfaces.

Runs	Experiment		Normalized Initial Perturbation Amplitude, ε_s/z_o				
	d^*	σ^*	0.1	0.25	0.5	0.75	1
W090	18.79	0.98	18.95	18.91	19.68	20.01	20.86
G090	28.29	0.73	27.80	28.29	29.83	31.62	33.45
W140	22.85	0.50	21.76	21.44	21.89	22.35	23.27
W170	25.59	0.66	23.29	23.10	23.38	23.97	24.70
G170	32.83	0.98	34.13	34.64	35.99	38.94	43.36
W190	28.12	0.92	26.78	26.42	27.32	28.78	30.40
W210	32.21	1.25	30.95	31.18	32.91	34.46	36.65

The experimental results and numerical predictions for how the dimensional and nondimensional maximum penetration depth vary with normalized initial perturbation amplitude are compared in Figures 5.36 and 5.37 for runs W090 and W210. The

comparison indicates that the numerical model predictions of the maximum penetration depth over the conducted wide range of perturbation amplitudes adequately agree within two standard deviations (2σ) of the experimentally measured mean value of the maximum penetration depth. The numerical and experimental data for the transient variation of the dimensional and nondimensional penetration depth carried out for runs W090 and W210 using selected values of the normalized initial perturbation amplitude is also presented in Figures 5.38 and 5.40. In these Figures, the numerical curves show an increasing trend in the penetration depth particularly in the last 0.1 sec before detachment. The experimental data points are qualitatively similar to the numerical curves in all runs. At lower values of w_{in}, the measured detachment times are similar to the numerical results corresponding to lower normalized perturbation amplitudes ε_s/z_o as represented by run W090. This can be attributed to the randomness of the perturbed interface in the experiment compared to the structured numerical perturbation. However, the experimental and numerical results are in reasonable agreement at higher injection velocities as in run W210. Figure 5.39 presents the numerical and experimental simulations of the detachment for horizontal surfaces for runs W090 and W210.

5.5.2 Penetration Depth of Spikes for Inclined Surfaces

In the inclined bounding surface configuration ($\theta = 2.5^{\circ}$), the penetration depth is also measured as the maximum vertical distance from the plate surface to the lowermost tip point of the developing spike or the detached droplet. The dimensional and nondimensional experimental mean (d), standard deviation (σ) and numerical prediction values of the maximum penetration depth carried out for inclined surfaces and using

different injection velocities and water and 20% glycerol as working fluids are detailed in Tables 5.23-5.28. The data given in these tables indicate that the maximum value of the penetration depth increases by increasing the transpiration velocity or by using 20% glycerol as a working fluid rather than water due to the development of thicker liquid films. Figures 5.41 and 5.42 present the experimental data for the statistical distributions of the dimensional and nondimensional maximum penetration depth for runs W0925 and W2125. The experimental and numerical results conducted for the variation of the dimensional and nondimensional maximum penetration depth with the normalized initial perturbation amplitude are given in Figures 5.43 and 5.44 for runs W0925 and W2125.

Table 5.23 Experimental mean (d), standard deviation (σ) and numerical prediction values of the maximum penetration depth in mm for the experimental and numerical runs conducted using inclined surfaces (θ = 2.5˚) and the corresponding liquid film thickness at x = 30 mm for water at 293 K.

Runs	Experiment		Normalized Initial Perturbation Amplitude, ε_s/z_o				
	d, [mm]	σ, [mm]	0.1	0.25	0.5	0.75	1
W0925	44.34	2.33	41.57	40.34	40.45	41.35	41.36
W1425	54.08	2.39	47.66	47.47	48.34	50.42	52.06
W1725	61.84	1.76	52.08	51.75	52.39	53.61	55.62
W1925	70.72	2.25	54.92	55.76	56.78	57.89	60.07
W2125	80.72	2.66	58.75	60.05	60.46	62.12	65.34

Table 5.24 Experimental mean (d), standard deviation (σ) and numerical prediction values of the maximum penetration depth in mm for the experimental and numerical runs conducted using inclined surfaces (θ = 2.5˚) and the corresponding liquid film thickness at x = 40 mm for water at 293 K.

Runs	Experiment		Normalized Initial Perturbation Amplitude, ε_s/z_o				
	d, [mm]	σ, [mm]	0.1	0.25	0.5	0.75	1
W0925	44.34	2.33	42.44	42.43	43.29	46.17	47.35
W1425	54.08	2.39	51.92	52.58	54.65	56.79	58.97
W1725	61.84	1.76	57.92	58.06	61.01	63.19	65.33
W1925	70.72	2.25	62.47	63.23	65.29	68.63	72.61
W2125	80.72	2.66	69.46	70.40	72.80	77.86	82.22

Table 5.25 Nondimensional experimental mean (d^*), standard deviation (σ^*) and numerical prediction values of the maximum penetration depth for the experimental and numerical runs conducted using inclined surfaces ($\theta = 2.5^\circ$) and the corresponding liquid film thickness at $x^* = 10.9$ for water at 293 K (Re = 445).

Runs	Experiment		Normalized Initial Perturbation Amplitude, ε_s/z_o				
	d^*	σ^*	0.1	0.25	0.5	0.75	1
W0925	16.25	0.85	15.23	14.78	14.82	15.15	15.16
W1425	19.82	0.88	17.47	17.40	17.72	18.48	19.08
W1725	22.66	0.64	19.09	18.97	19.20	19.65	20.39
W1925	25.92	0.82	20.13	20.44	20.81	21.22	22.02
W2125	29.59	0.98	21.53	22.01	22.16	22.77	23.95

Table 5.26 Nondimensional experimental mean (d^*), standard deviation (σ^*) and numerical prediction values of the maximum penetration depth for the experimental and numerical runs conducted using inclined surfaces ($\theta = 2.5^\circ$) and the corresponding liquid film thickness at $x^* = 14.6$ for water at 293 K (Re = 445).

Runs	Experiment		Normalized Initial Perturbation Amplitude, ε_s/z_o				
	d^*	σ^*	0.1	0.25	0.5	0.75	1
W0925	16.25	0.85	15.56	15.55	15.87	16.92	17.35
W1425	19.82	0.88	19.03	19.27	20.03	20.81	21.61
W1725	22.66	0.64	21.23	21.28	22.36	23.17	23.95
W1925	25.92	0.82	22.89	23.18	23.94	25.15	26.62
W2125	29.59	0.98	25.46	25.81	26.68	28.54	30.14

Table 5.27 Dimensional and nondimensional experimental mean (d), standard deviation (σ) and numerical prediction values of the maximum penetration depth for the experimental and numerical runs conducted using inclined surfaces ($\theta = 2.5^\circ$) and the corresponding liquid film thickness at x = 20 mm ($x^* = 7.6$) for 20% glycerol at 293 K (Re = 250).

Runs	Experiment		Normalized Initial Perturbation Amplitude, ε_s/z_o				
	d, [mm]	σ, [mm]	0.05	0.25	0.5	0.75	1
G0925	54.37	2.87	54.88	44.47	45.37	44.33	45.41
G1725	68.8	2.84	60.94	56.59	55.91	56.95	58.05
Runs	Experiment		Normalized Initial Perturbation Amplitude, ε_s/z_o				
	d^*	σ^*	0.05	0.25	0.5	0.75	1
G0925	20.68	1.09	20.88	16.92	17.26	16.86	17.27
W1725	26.17	1.08	23.18	21.52	21.27	21.66	22.08

Table 5.28 Dimensional and nondimensional experimental mean (d), standard deviation (σ) and numerical prediction values of the maximum penetration depth for the experimental and numerical runs conducted using inclined surfaces (θ = 2.5˚) and the corresponding liquid film thickness at x = 30 mm ($x^* = 11.4$) for 20% glycerol at 293 K (Re = 250).

Runs	Experiment		Normalized Initial Perturbation Amplitude, ε_s/z_o				
	d, [mm]	σ, [mm]	0.05	0.25	0.5	0.75	1
G0925	54.37	2.87	52.21	47.53	46.33	47.43	48.52
G1725	68.8	2.84	60.69	61.25	62.18	63.04	65.29
Runs	Experiment		Normalized Initial Perturbation Amplitude, ε_s/z_o				
	d^*	σ^*	0.05	0.25	0.5	0.75	1
G0925	20.68	1.09	19.86	18.08	17.62	18.04	18.45
W1725	26.17	1.08	23.08	23.29	23.65	23.98	24.83

Spikes developing from horizontal liquid films have higher values of the penetration depth when compared to spikes forming from inclined surfaces for the same transpiration velocity and working fluid. A percentage increase of approximately 15% in the experimentally measured mean value of the maximum penetration depth transpires when using a horizontal bounding plate in run W140 as compared to using an inclination angle of 2.5˚ for run W1425. The mean liquid film thickness value for horizontal films is higher than the local liquid thickness value at which droplets detach in the axial direction of inclined liquid films as given in Tables 5.2 and 5.3. This can be attributed to the tangential velocity component for the bounded inclined liquid films. Figures 5.45 and 5.47 present the numerical and experimental data for the transient variation of the dimensional and nondimensional penetration depth conducted for runs W0925 and W2125 using selected values of the normalized initial perturbation amplitude. The numerical and experimental simulations of the detachment for inclined surfaces for runs W0925 and W2125 are depicted in Figure 5.46.

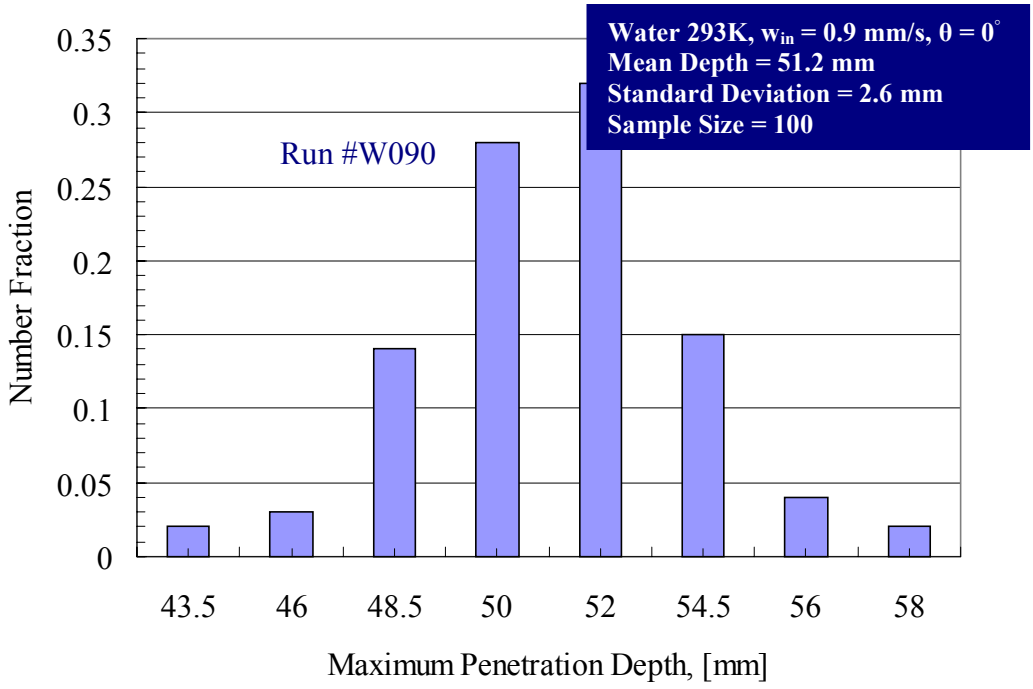

(a)

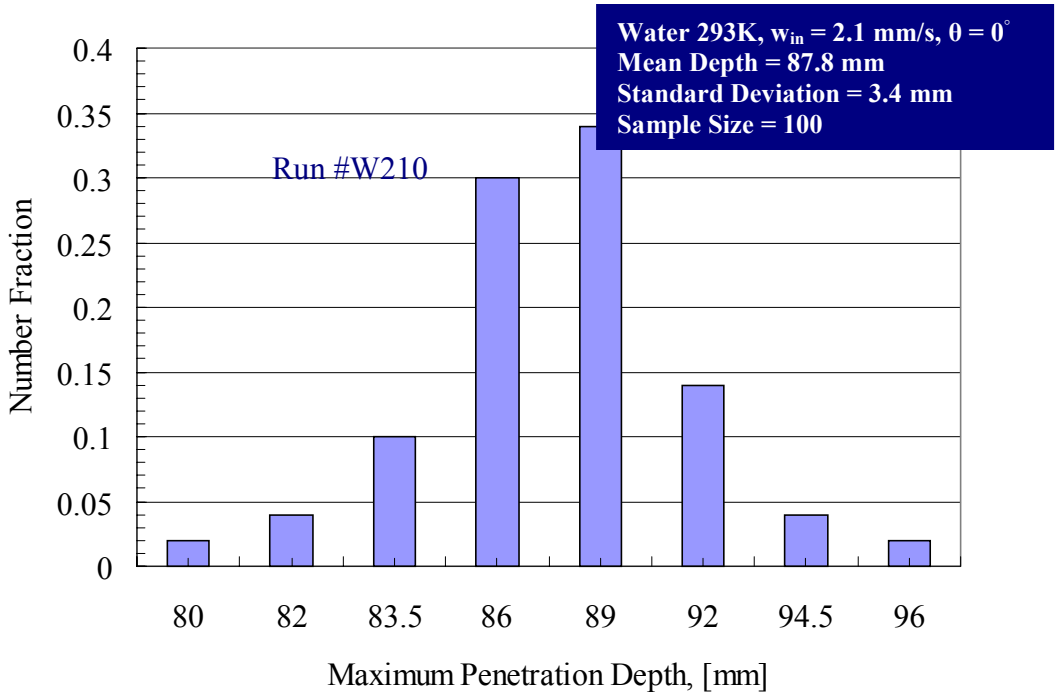

(b)

Figure 5.34 Experimental data for the distribution of the maximum penetration depth carried out for horizontal surfaces (θ = 0˚) : (a) Run #W090, and (b) Run #W210.

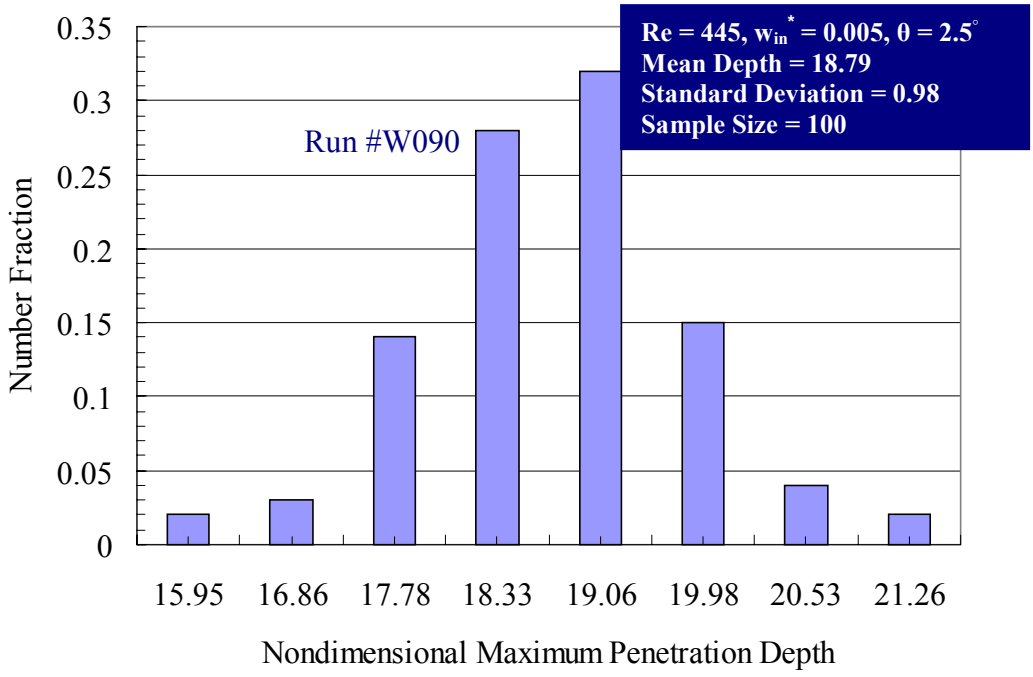

(a)

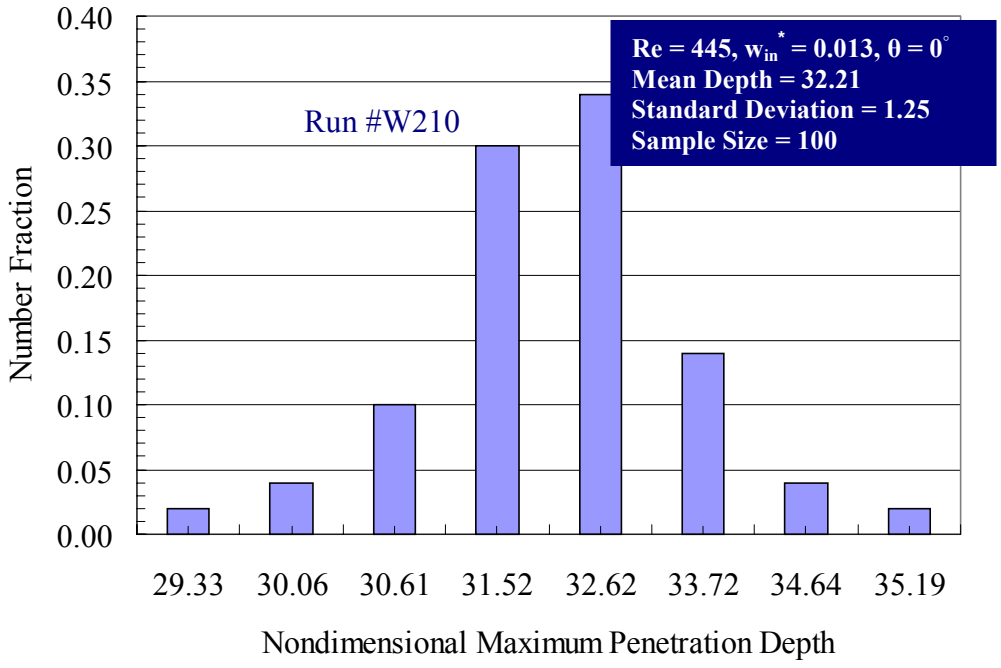

(b)

Figure 5.35 Experimental data for the distribution of the nondimensional maximum penetration depth carried out for horizontal surfaces (θ = 0°): (a) Run #W090, and (b) Run #W210.

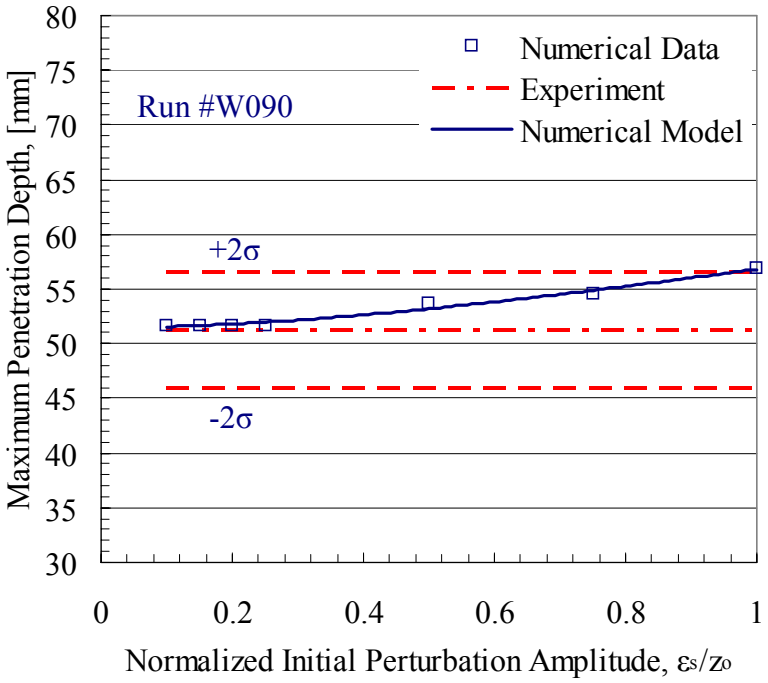

(a)

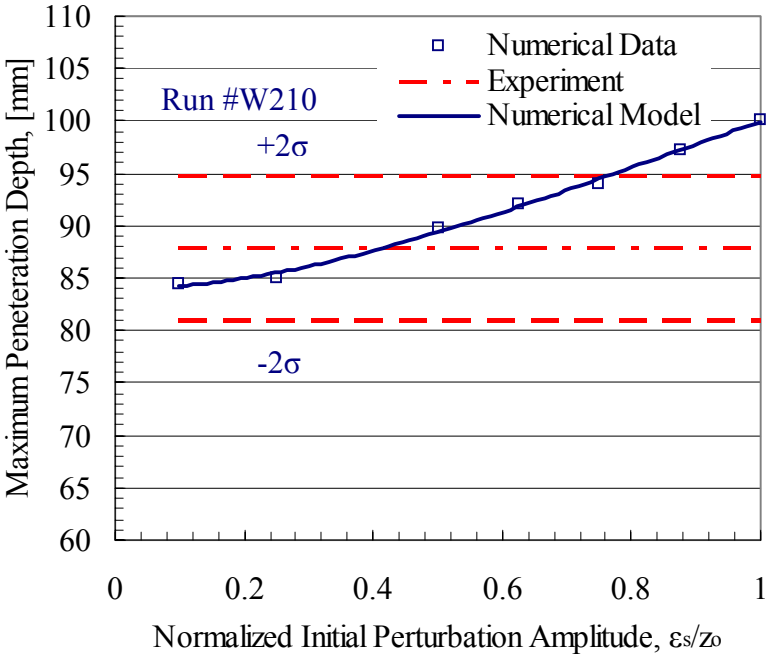

(b)

Figure 5.36 Numerical and experimental data for the variation of the maximum penetration depth with the normalized initial perturbation amplitude carried out for horizontal surfaces ($\theta = 0^{\circ}$): (a) Run #W090, and (b) Run #W210.

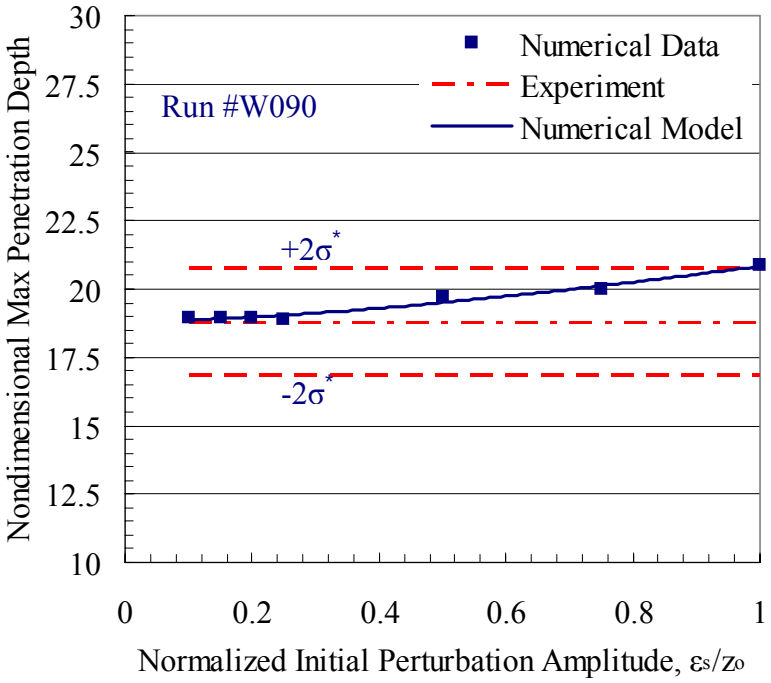

(a)

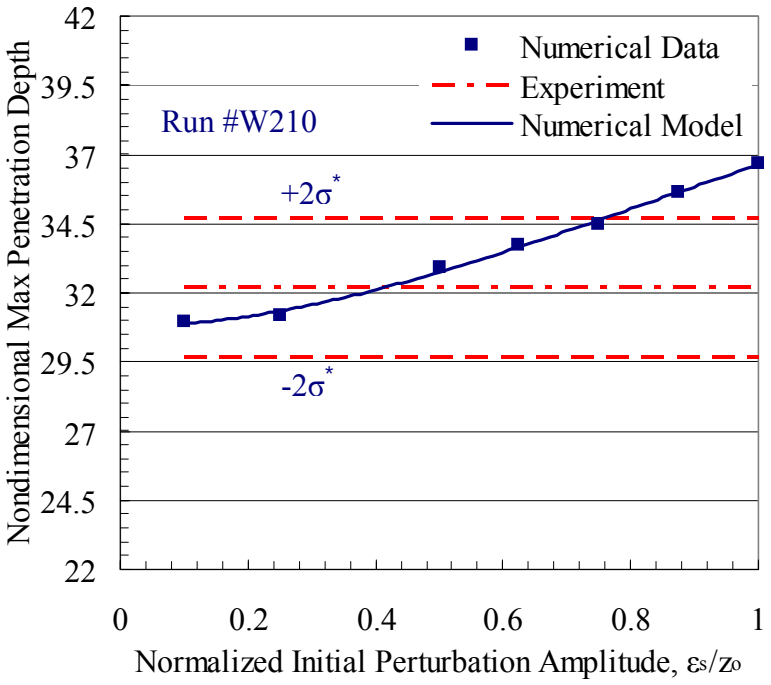

(b)

Figure 5.37 Numerical and experimental data for the variation of the nondimensional maximum penetration depth with the normalized initial perturbation amplitude carried out for horizontal surfaces ($\theta = 0^{\circ}$): (a) Run #W090, and (b) Run #W210.

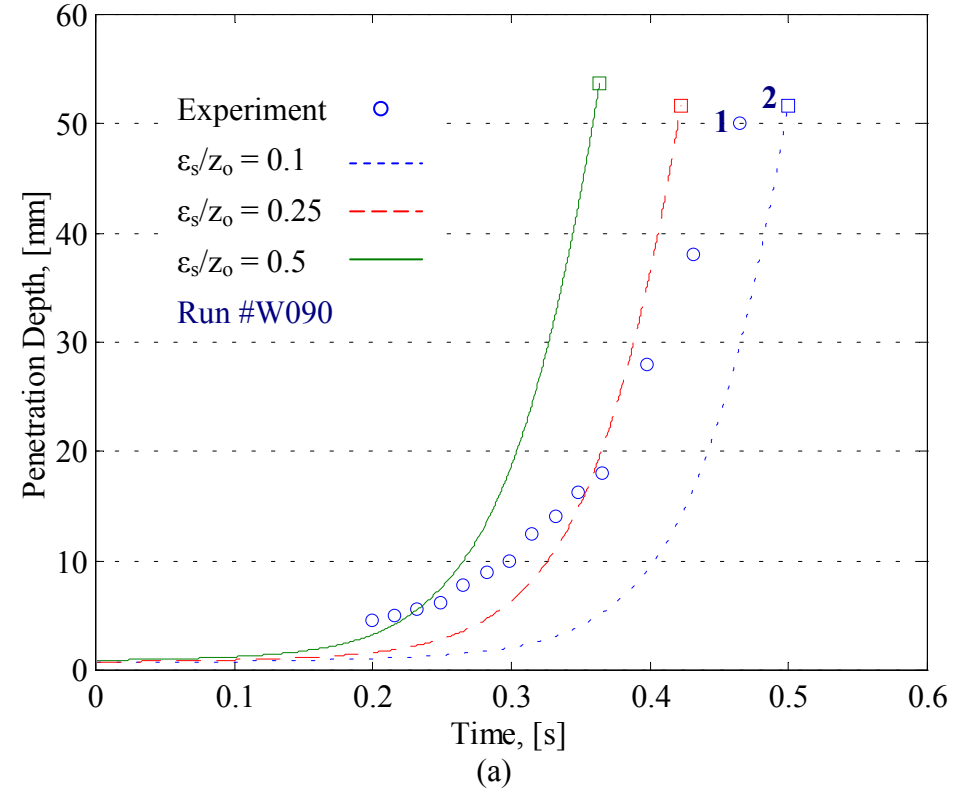

(a)

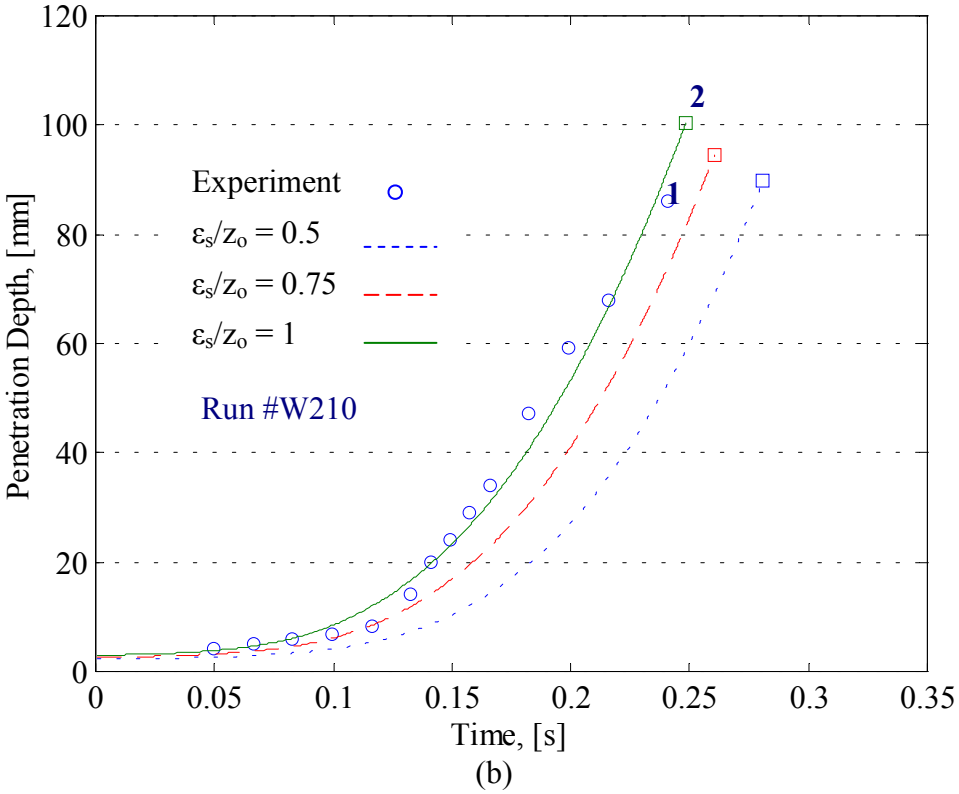

(b)

Figure 5.38 Numerical and experimental data for the transient variation of the penetration depth carried out for horizontal surfaces ($\theta = 0^{\circ}$): (a) Run #W090, and (b) Run #W210.

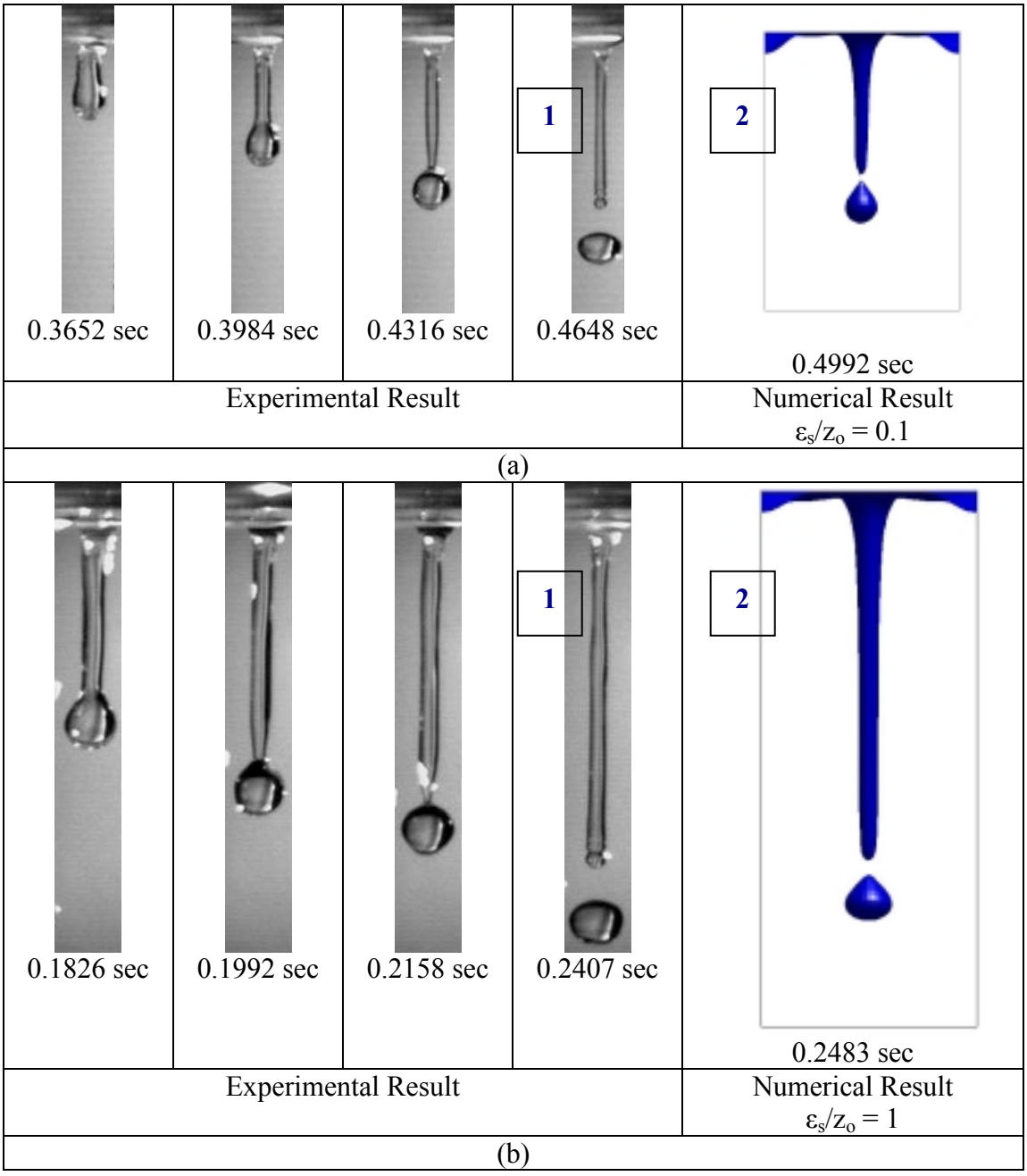

Figure 5.39 Numerical and experimental simulations of the detachment for horizontal surfaces ($\theta = 0^{\circ}$): (a) Run #W090 (Numbering refers to Figure 5.44(a)), and (b) Run #W210 (Numbering refers to Figure 5.44(b)).

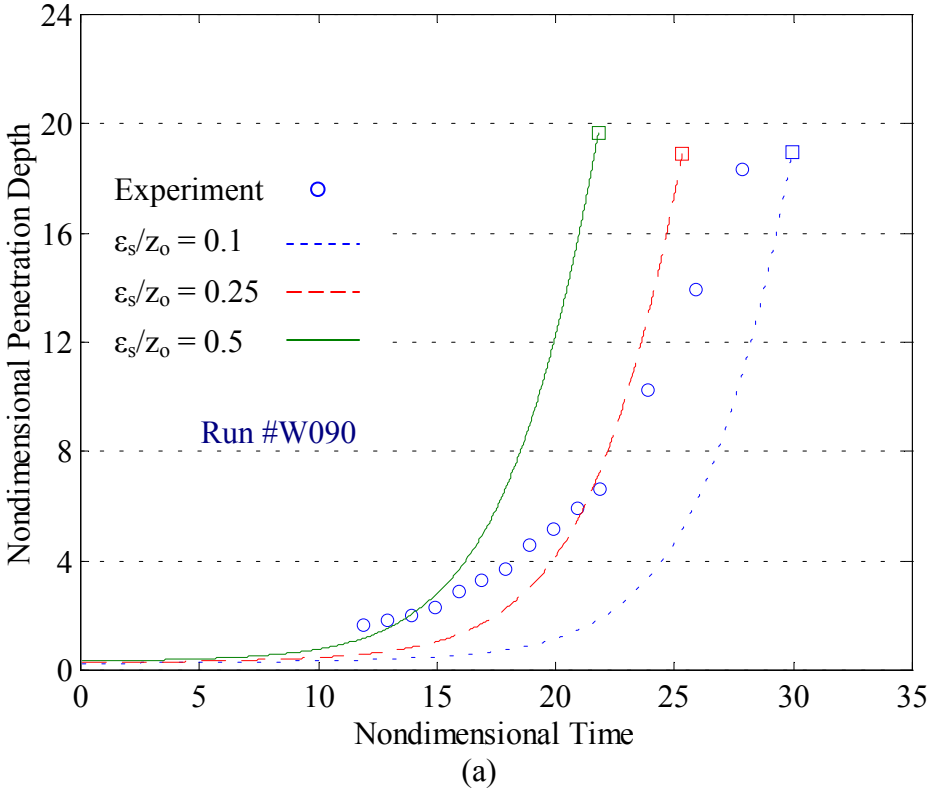

(a)

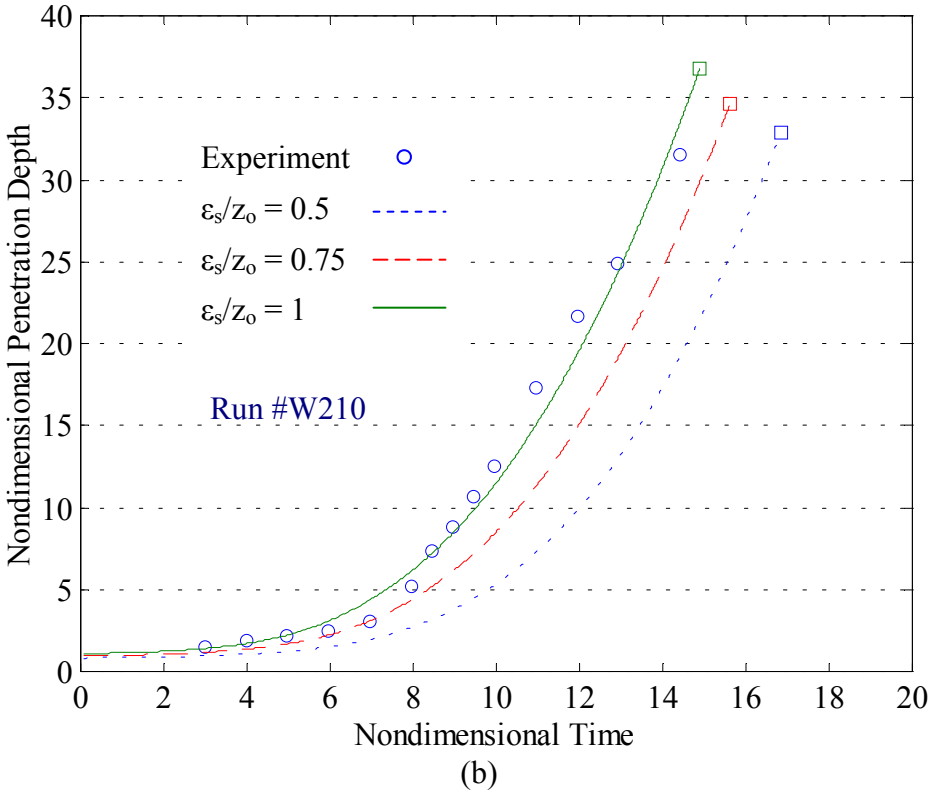

(b)

Figure 5.40 Numerical and experimental data for the transient variation of the nondimensional penetration depth carried out for horizontal surfaces ($\theta = 0^{\circ}$): (a) Run #W090, and (b) Run #W210.

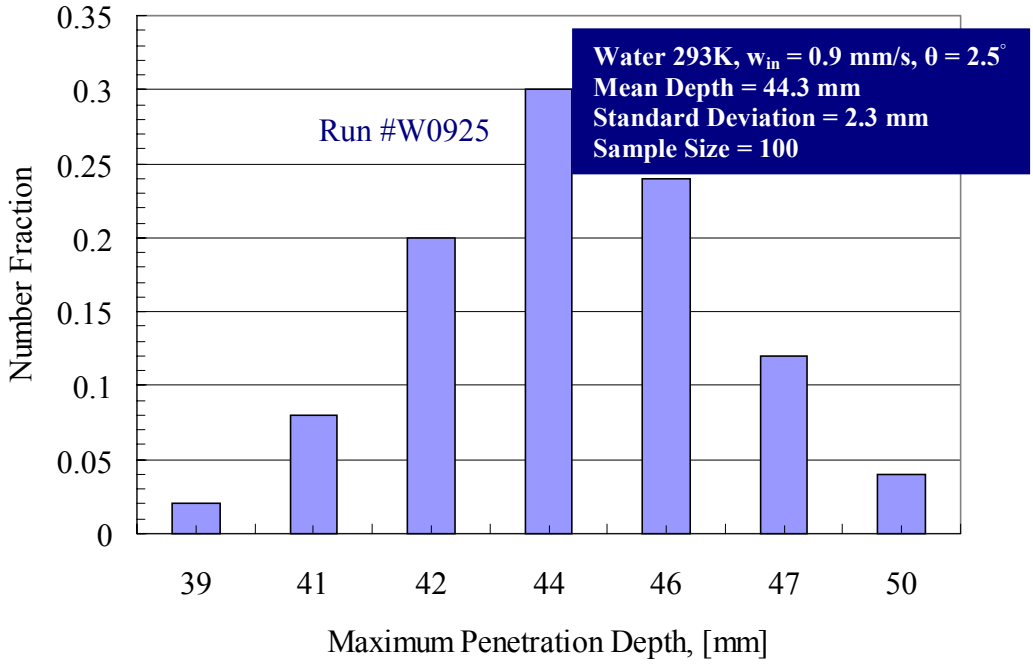

(a)

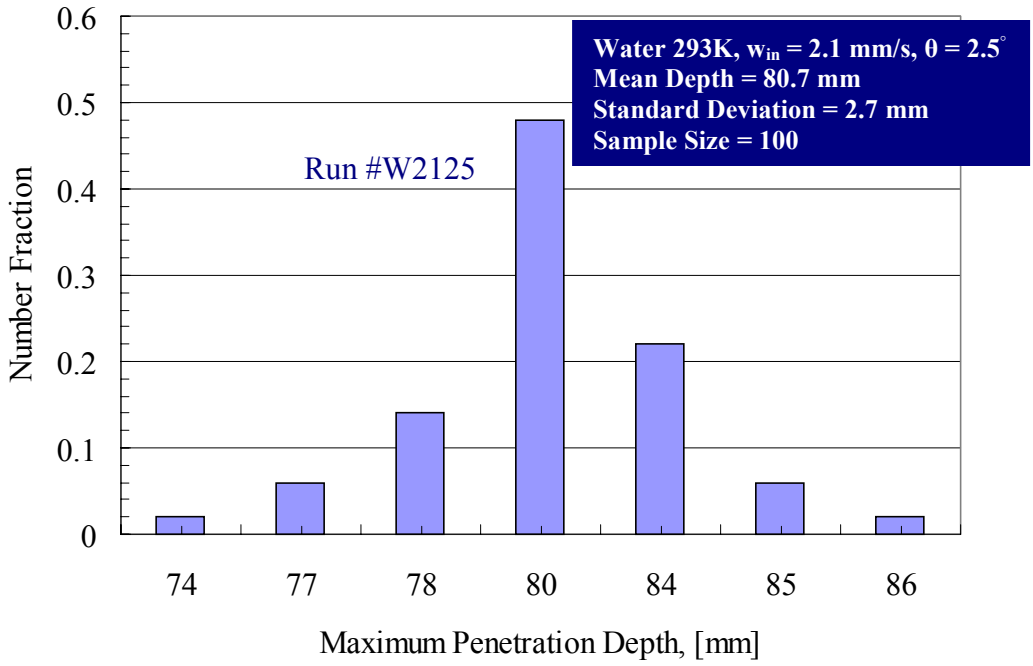

(b)

Figure 5.41 Experimental data for the distribution of the maximum penetration depth carried out for inclined surfaces (θ = 2.5˚): (a) Run #W0925, and (b) Run #W2125.

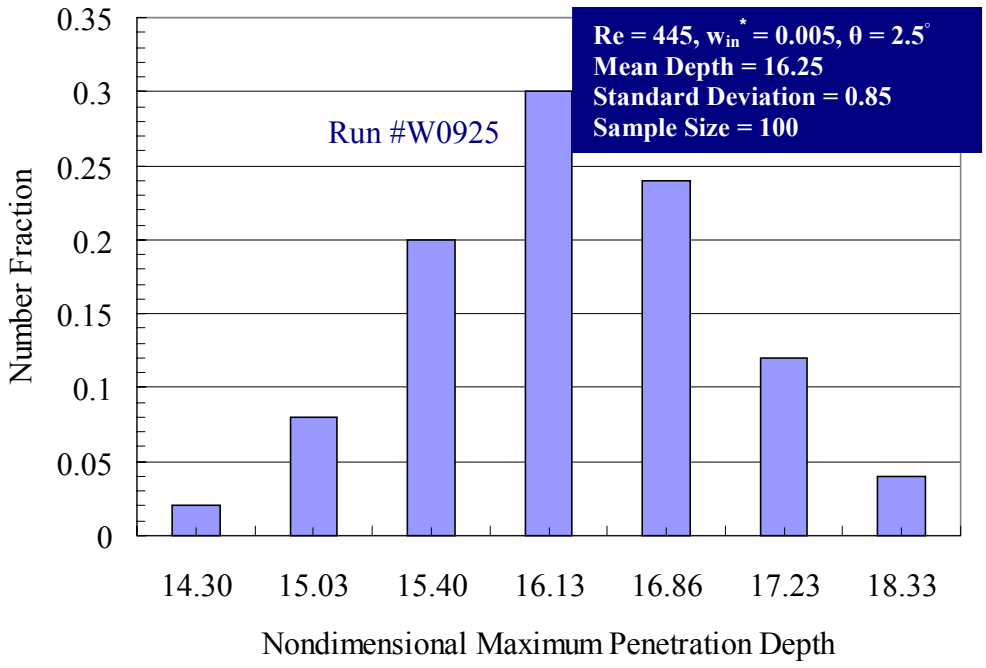

(a)

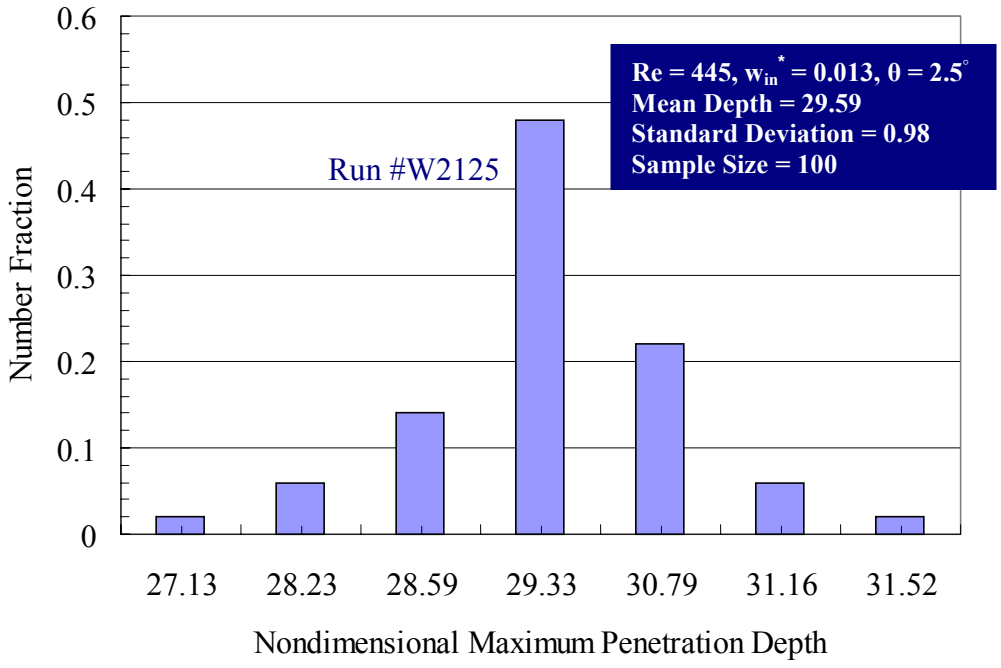

(b)

Figure 5.42 Experimental data for the distribution of the nondimensional maximum penetration depth carried out for inclined surfaces (θ = 2.5˚): (a) Run #W0925, and (b) Run #W2125.

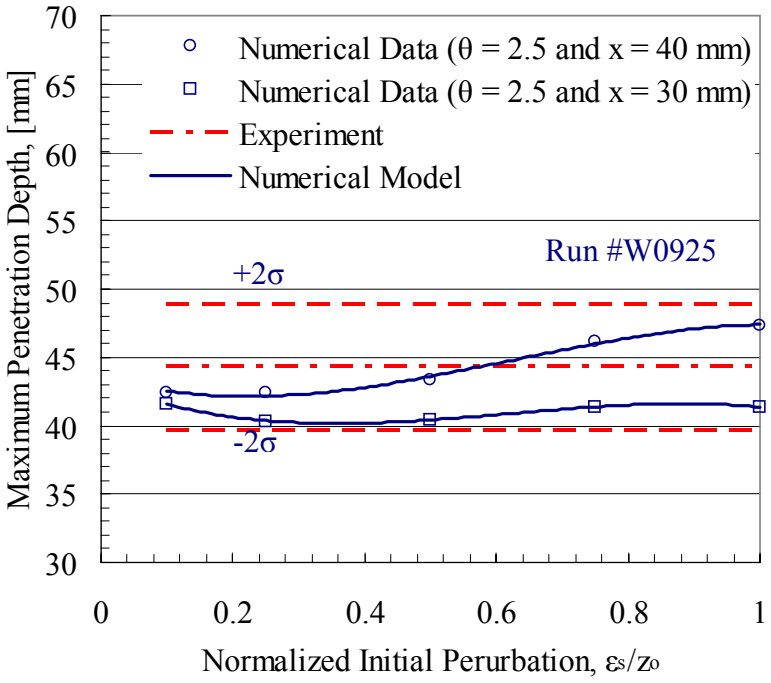

(a)

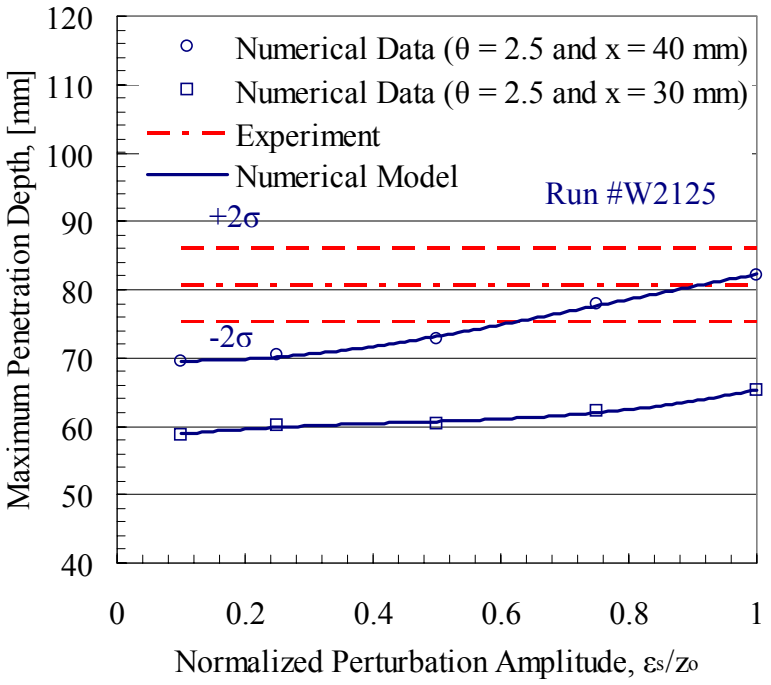

(b)

Figure 5.43 Numerical and experimental data for the variation of the maximum penetration depth with the normalized initial perturbation amplitude carried out for inclined surfaces (θ = 2.5˚): (a) Run #W0925, and (b) Run #W2125.

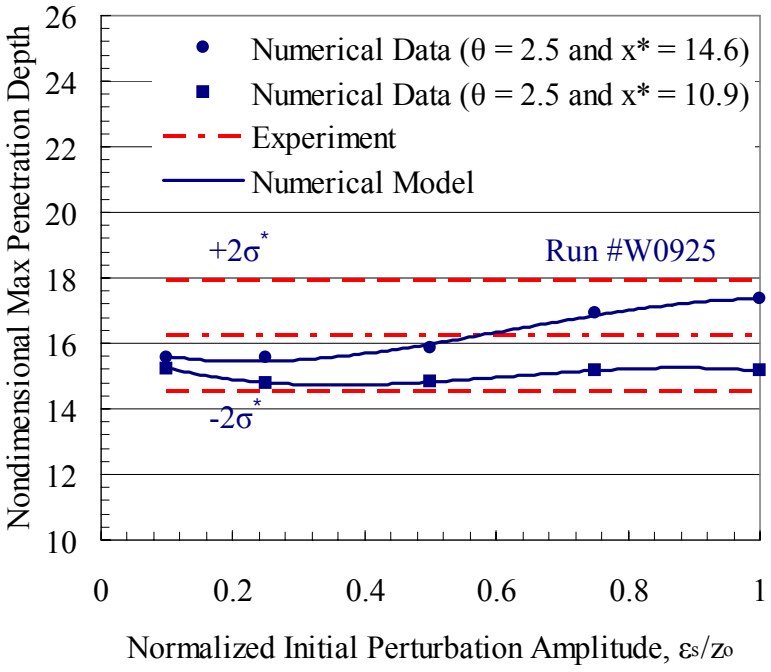

(a)

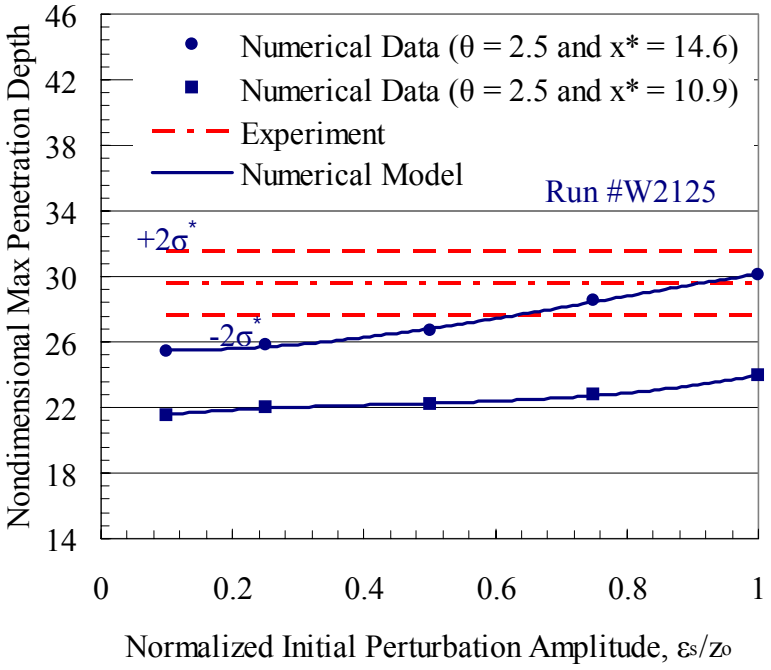

(b)

Figure 5.44 Numerical and experimental data for the variation of the nondimensional maximum penetration depth with the normalized initial perturbation amplitude carried out for inclined surfaces (θ = 2.5˚): (a) Run #W0925, and (b) Run #W2125.

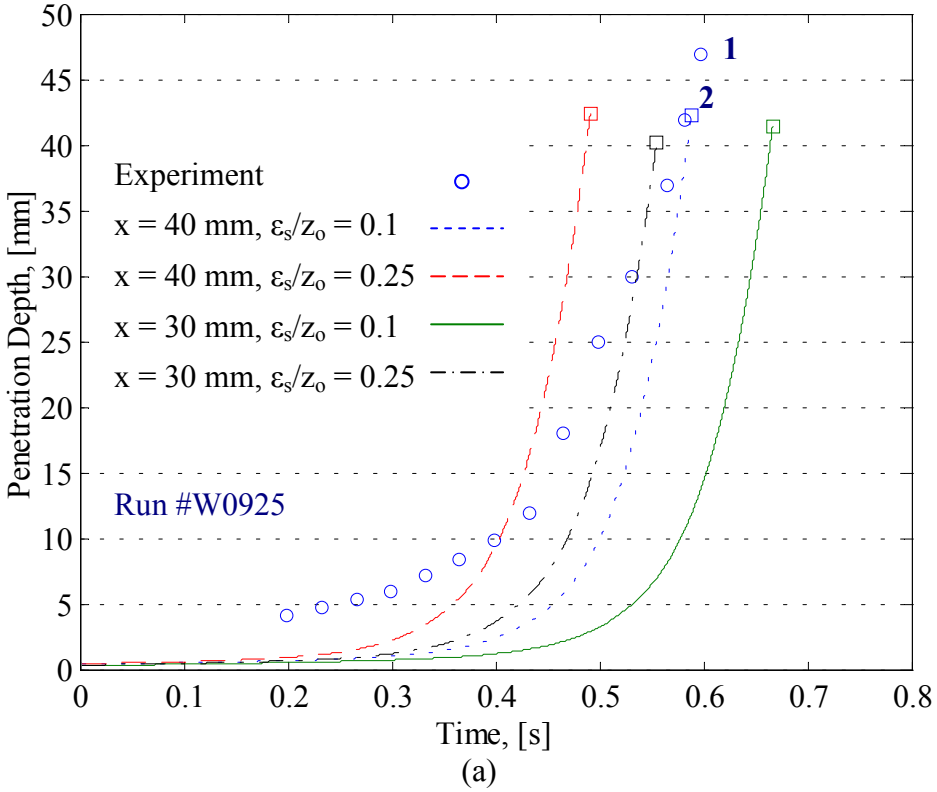

(a)

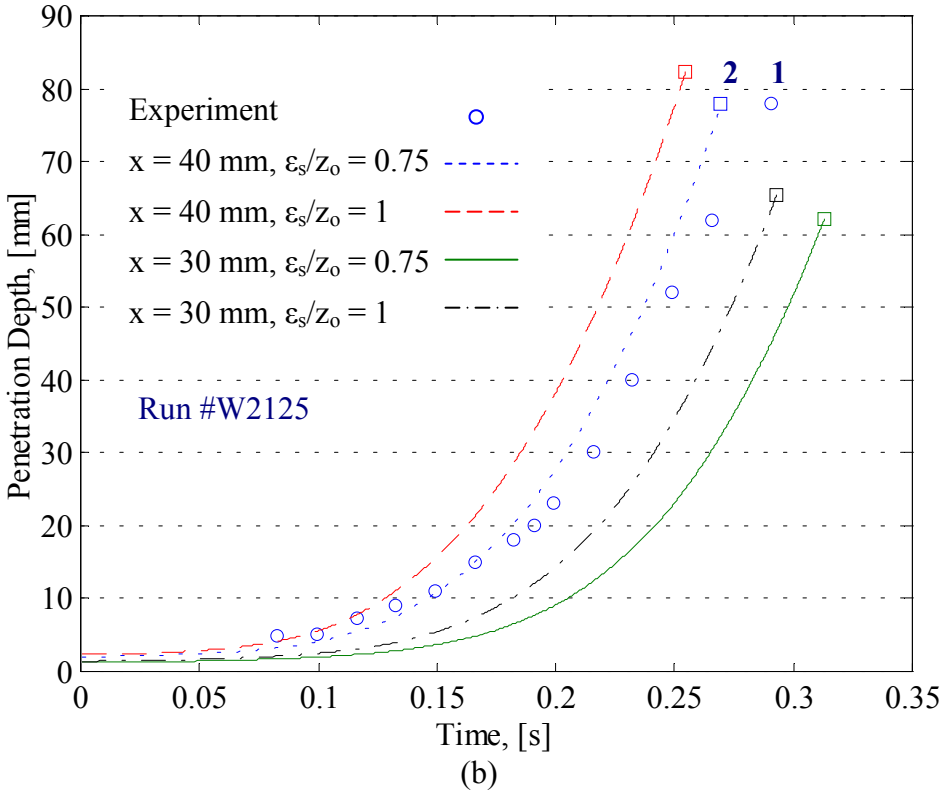

(b)

Figure 5.45 Numerical and experimental data for the transient variation of the penetration depth carried out for inclined surfaces (θ = 2.5˚): (a) Run #W0925, and (b) Run #W2125.

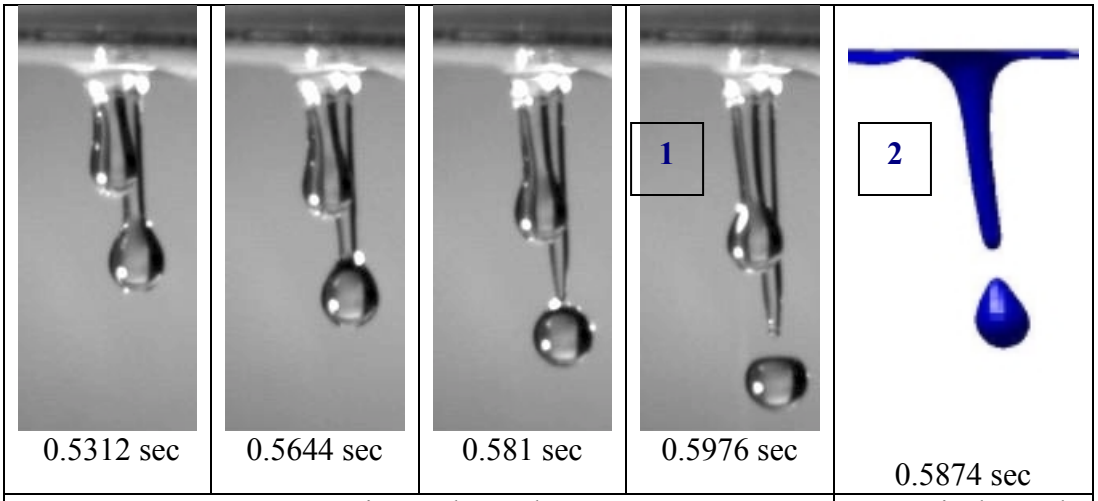

Figure 5.46 Numerical and experimental simulations of the detachment for inclined surfaces ($\theta = 2.5^{\circ}$): (a) Run #W0925 (Numbering refers to Figure 5.51(a)), and (b) Run #W2125 (Numbering refers to Figure 5.51(b)).

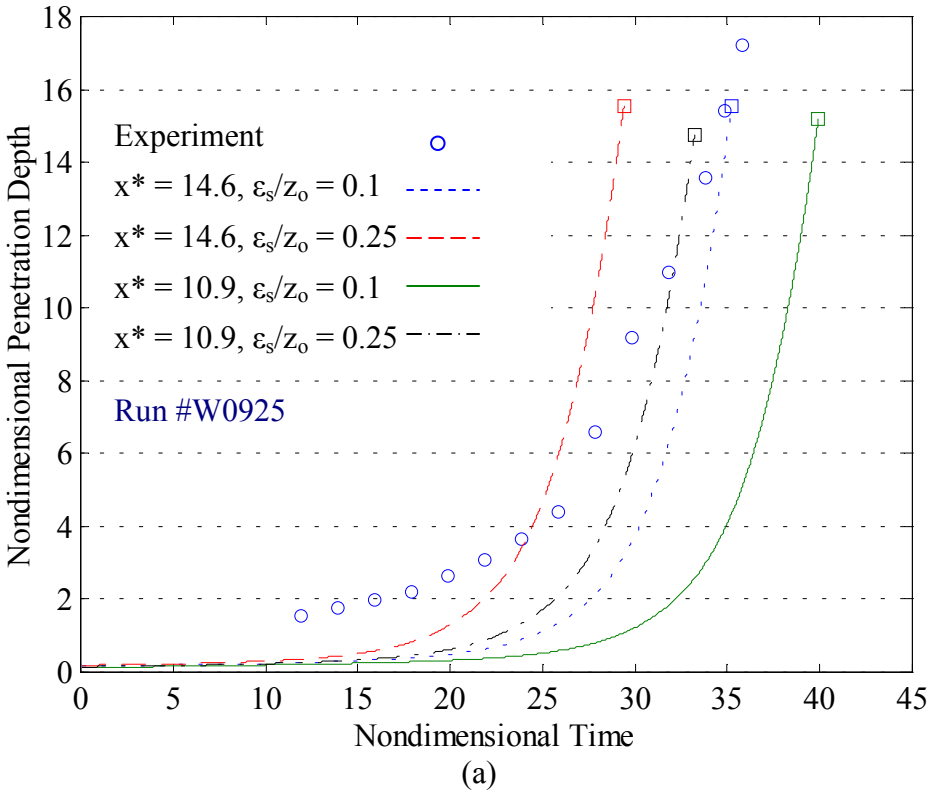

(a)

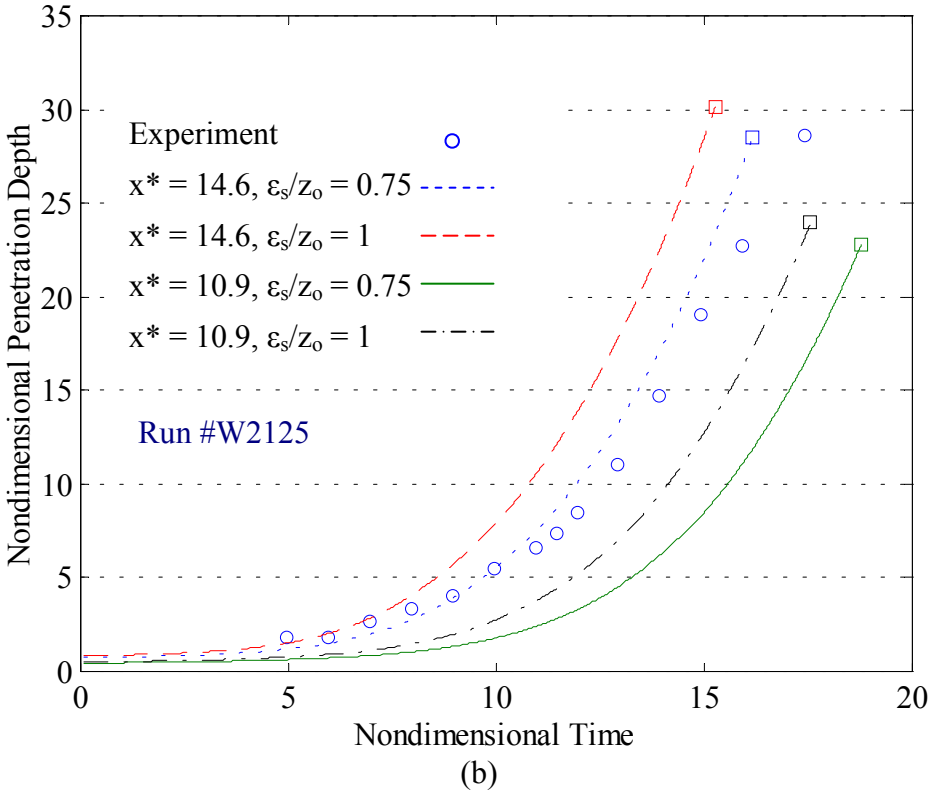

(b)

Figure 5.47 Numerical and experimental data for the transient variation of the nondimensional penetration depth carried out for inclined surfaces (θ = 2.5˚): (a) Run #W0925, and (b) Run #W2125.

5.6 Interface Wave Length and Characteristic Time Scales

The results presented in this section are based on the modified theoretical study conducted for the bounded thin liquid film Rayleigh-Taylor instability with transpiration through the boundary as presented in section 3.1 of chapter 3. This theoretical analysis was carried out for horizontal bounding surfaces. Using equation (3.32) which defines the nondimensional growth rate s' $\left(s' = 3s\mu/\rho g h_o\right)$ as a function of the nondimensional wave number k' $\left(2\pi h_o/\lambda\right)$ and the Bond number Bo $\left(\text{Bo} = \rho g h_o^2/\sigma\right)$, the dimensional and nondimensional characteristic stability curves of the bounded liquid films are plotted as shown in Figures 5.48-5.51 for different transpiration velocities using water and 20% glycerol. In these figures, each injection velocity results in a corresponding value of the Bond number (Bo) due to the difference in the liquid film thickness h_o at different transpiration velocities as was discussed in section 5.1.

In this analysis, the evolving liquid-gas interface is characterized using different time scales. The droplet detachment time characterized in section 5.3 as a statistical distribution with a mean value (t_d) and a standard deviation (σ) is used as a characteristic time scale for the droplets formation and pinch off. The volume flow rate through the bounding plate provides another time scale ($t_{\text{flow rate}}$) for the developing thin liquid film as follows:

$$t_{\text{flow rate}} = h_o/q \qquad (6.2)$$

where

$q = \dfrac{Q}{A}$ as defined in equation (3.27)

Based on Figures 5.48-5.51, the maximum value of the growth rate is utilized to obtain the corresponding theoretical time t_{theory} and wave length λ_{theory} which characterize the Rayleigh-Taylor instability. The experimental and theoretical time scales defining the bounded Rayleigh-Taylor instability are listed in Table 5.29. The theoretical time scale t_{theory} is lower than the detachment time and the flow rate based time scales which have the same order of magnitude. Thus, the long-wave analysis carried out for this experiment holds as a valid theoretical representation of the perturbed liquid-gas interface.

The extracted theoretical time scale t_{theory} increases by decreasing the transpiration velocity w_{in}. For instance, the theoretical time increases by approximately 110% when the transpiration velocity decreases from 1.7 mm/s to 0.9 mm/s using water. This is due to the decreased liquid film thickness at the lower transpiration velocity through the bounding surface as was presented in section 5.1. However, all the conducted runs for different injection velocities have approximately the same theoretical wave length (λ_{theory} = 24.5 mm for water at 293 K) corresponding to the maximum growth rate for the perturbed liquid-gas interface. In the experiment, two values of the wave length λ_x and λ_y were measured at each transpiration velocity w_{in} due to the three-dimensionality of the evolving liquid-gas interface. Figure 5.52 presents the theoretical and experimental wave length variation with the transpiration velocity using water at 293 K as the working fluid. The maximum measured difference in the wave length values λ_x and λ_y is 5.5 mm at an injection velocity of 2.1 mm/s while the minimum measured difference is 2 mm at a transpiration velocity of 1.7 mm/s. This disparity in the wave length values λ_x and λ_y can be attributed to the confining edge effects caused by the rectangular bounding plate

geometry (~12 × 18 cm). However, the bounding surface dimensions are considerably larger than the characteristic length scale of the flow field (see Table 3.1) and are therefore expected to adequately model the behavior of the much larger bounding surfaces expected in an inertial fusion energy IFE reactor chamber (radius ~5 m).

The experimental results for the wave length values λ_x and λ_y indicate a decreasing trend with higher transpiration velocities in a range from 0.9 to 2.1 mm/s. This empirical trend indicates that more droplet formation sites are present at larger injection velocities corresponding to thicker liquid films. However, as indicated in the previous paragraph the long-wave theory predicts an approximately constant wave length value of 24.5 mm for the different injection velocities. A discrepancy of approximately 42% and 58% at a transpiration velocity of 0.9 mm/s exists between the theoretical wave length value and the experimentally measured wave length values λ_x and λ_y, respectively. This disparity in the theoretical and experimental wave length values is reduced for higher injection velocities through the bounding surface with a very close agreement ($\lambda_x - \lambda_{theory}$ = 0.2 mm, i.e. 0.8% difference) at 1.9 mm/s.

The theoretical and experimental wave length values discrepancy can be attributed to the formation and propagation of capillary waves at the interface of the bounded thin liquid film as a reaction to droplets formation and detachment. Including the effect of capillary waves into the modified long-wave theory will provide a closer agreement with the conducted experiments. Figure 5.53 presents an experimental sequence for the formation and propagation of capillary waves at the liquid-gas interface as a result of a droplet pinch off using water at 293 K as the working fluid for experimental run W090.

Table 5.29 Experimental and theoretical characteristic time scales for the bounded Rayleigh-Taylor instability.

Runs	Experiment			Theory	
	t_d, [s]	$t_d+2\sigma$, [s]	$t_d-2\sigma$, [s]	t_{theory}, [s]	$t_{flow\ rate}$, [s]
W090	0.4652	0.4948	0.4356	0.0394	0.6804
G090	0.6724	0.6950	0.6498	0.0442	0.7609
W140	0.4071	0.4253	0.3889	0.0252	0.5079
W170	0.3576	0.3746	0.3406	0.0187	0.4628
G170	0.5069	0.5279	0.4859	0.0139	0.5926
W190	0.3119	0.3331	0.2907	0.0062	0.5951
W210	0.2412	0.2692	0.2132	0.0027	0.7162

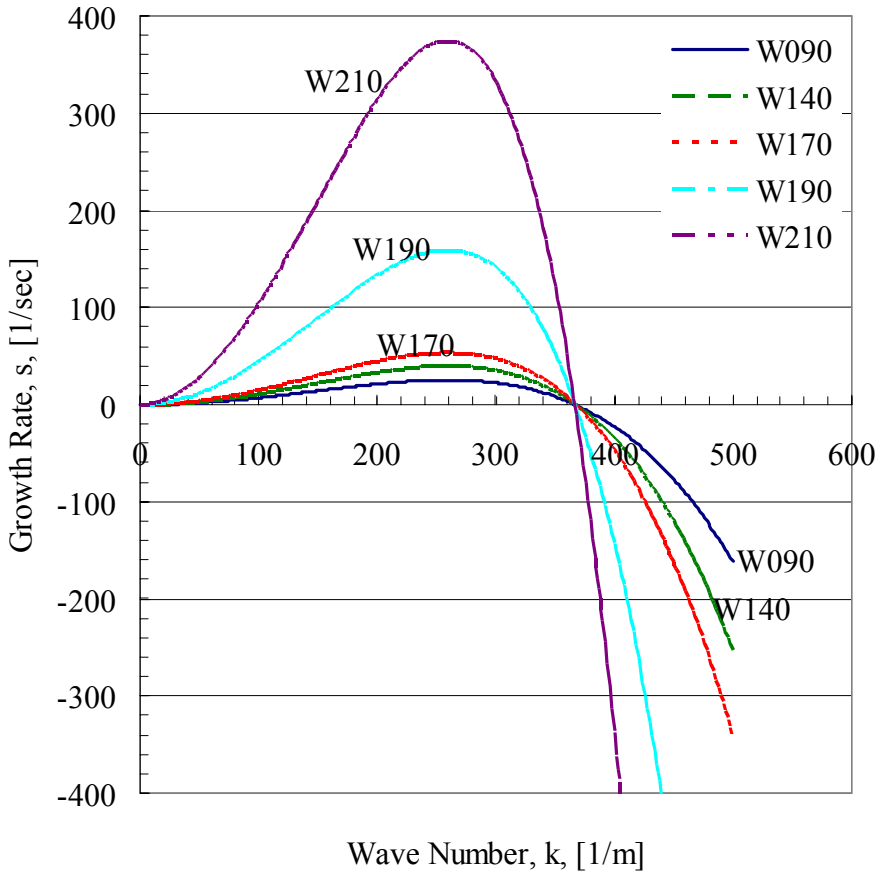

Figure 5.48 Characteristic stability curves of the growth rate of the perturbation with the dimensional wave number for different transpiration velocities using water at 293 K as the working fluid.

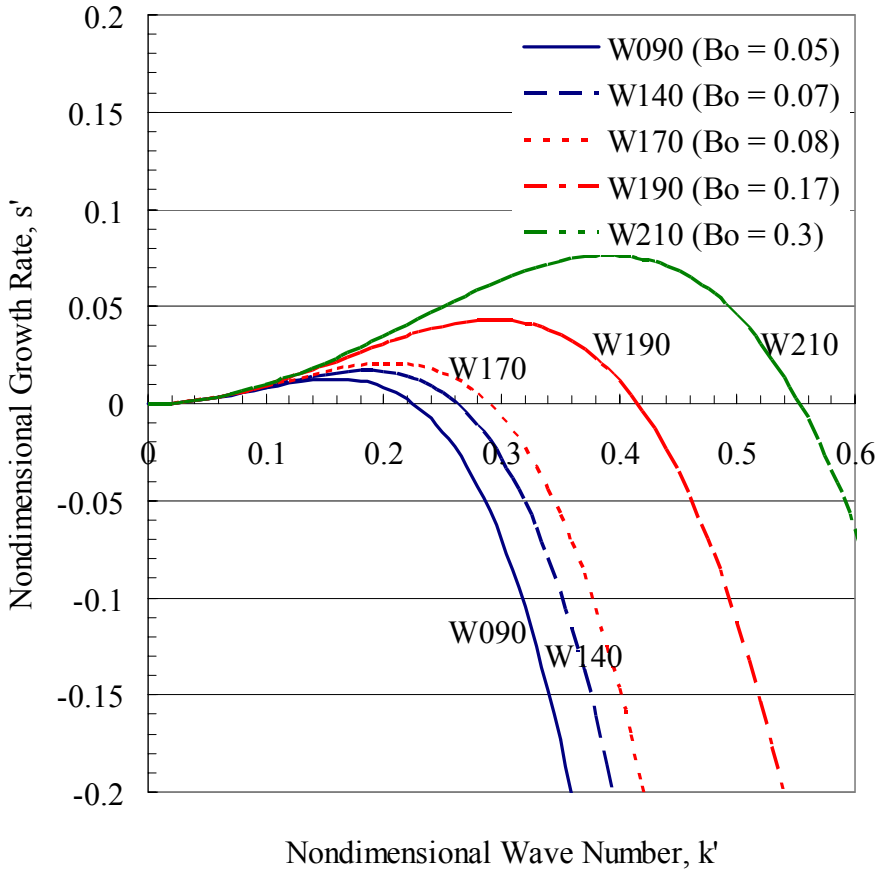

Figure 5.49 Characteristic stability curves of the nondimensional growth rate of the perturbation with the nondimensional wave number for different Bond numbers corresponding to various transpiration velocities.

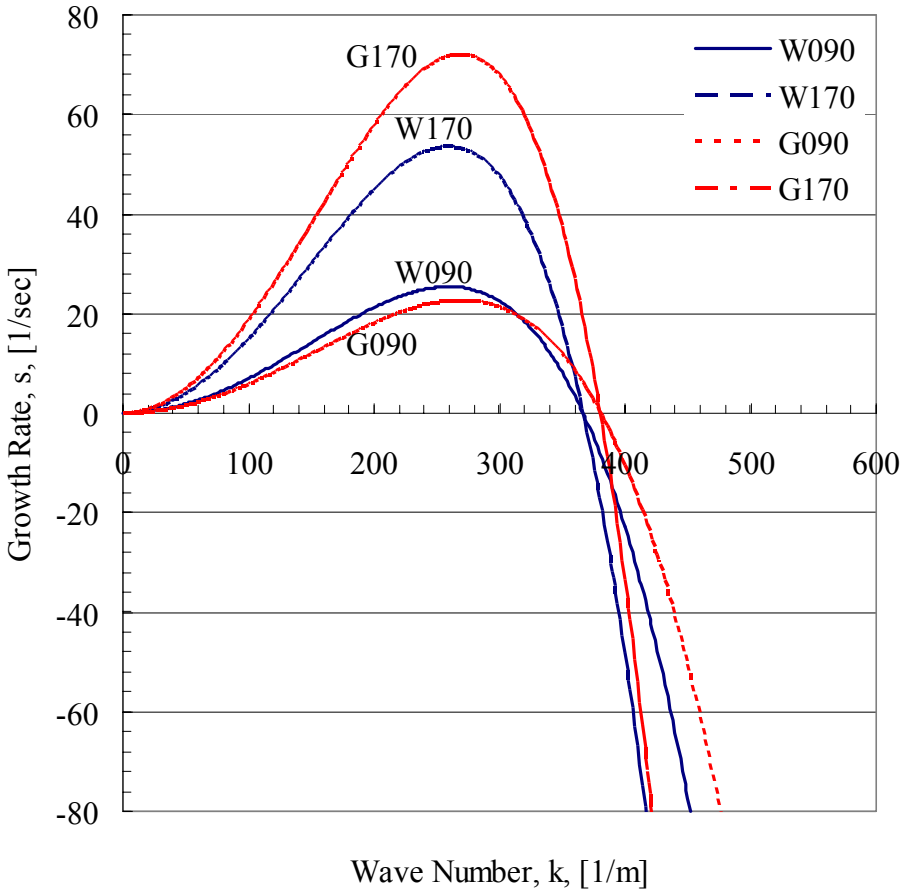

Figure 5.50 Characteristic stability curves of the growth rate of the perturbation with the dimensional wave number for different transpiration velocities using water and 20% glycerol at 293 K as the working fluids.

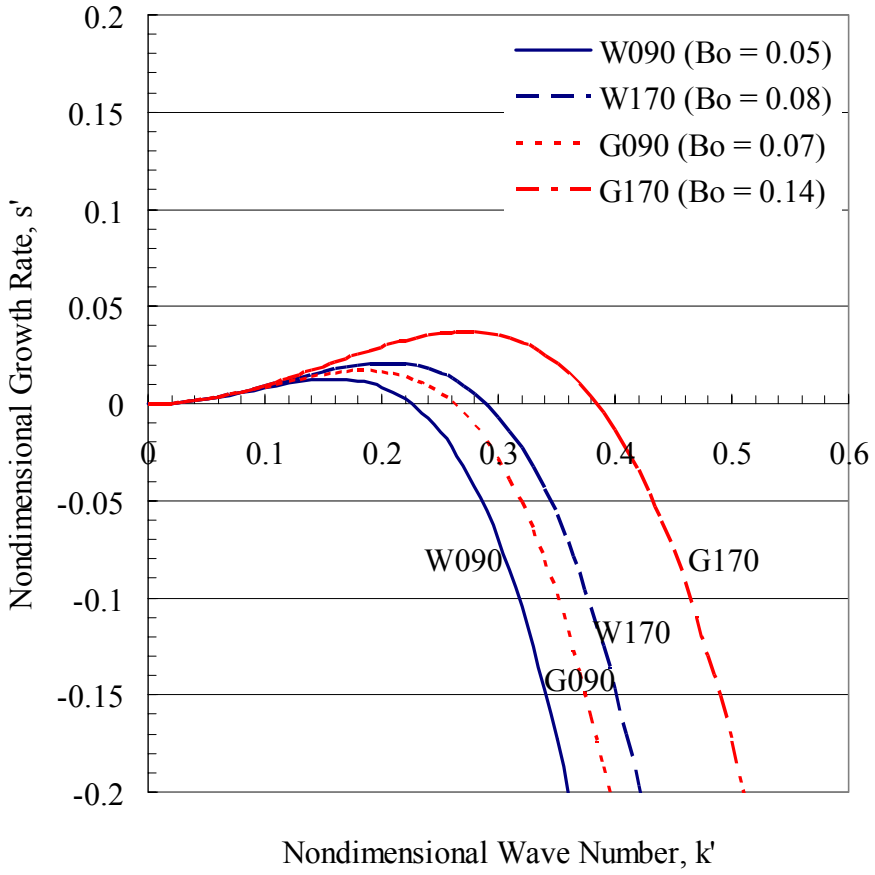

Figure 5.51 Characteristic stability curves of the nondimensional growth rate of the perturbation with the nondimensional wave number for Bond numbers corresponding to various working fluids and transpiration velocities.

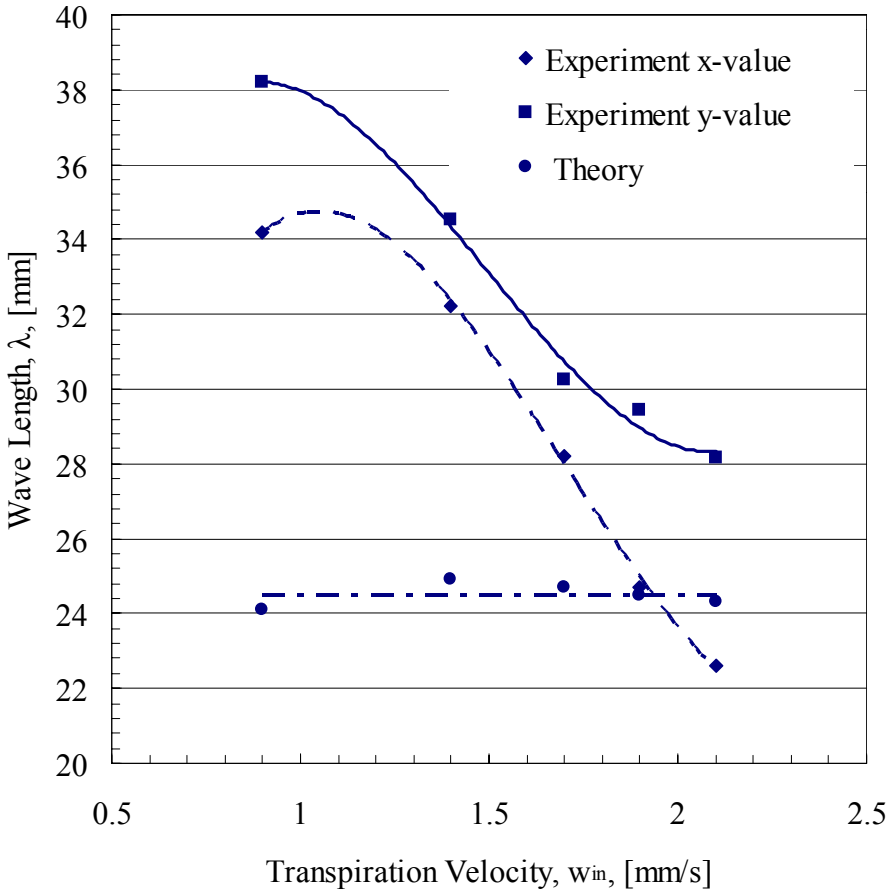

Figure 5.52 Theoretical and experimental wave length variation with the transpiration velocity through the bounding plate using water at 293 K as the working fluid.

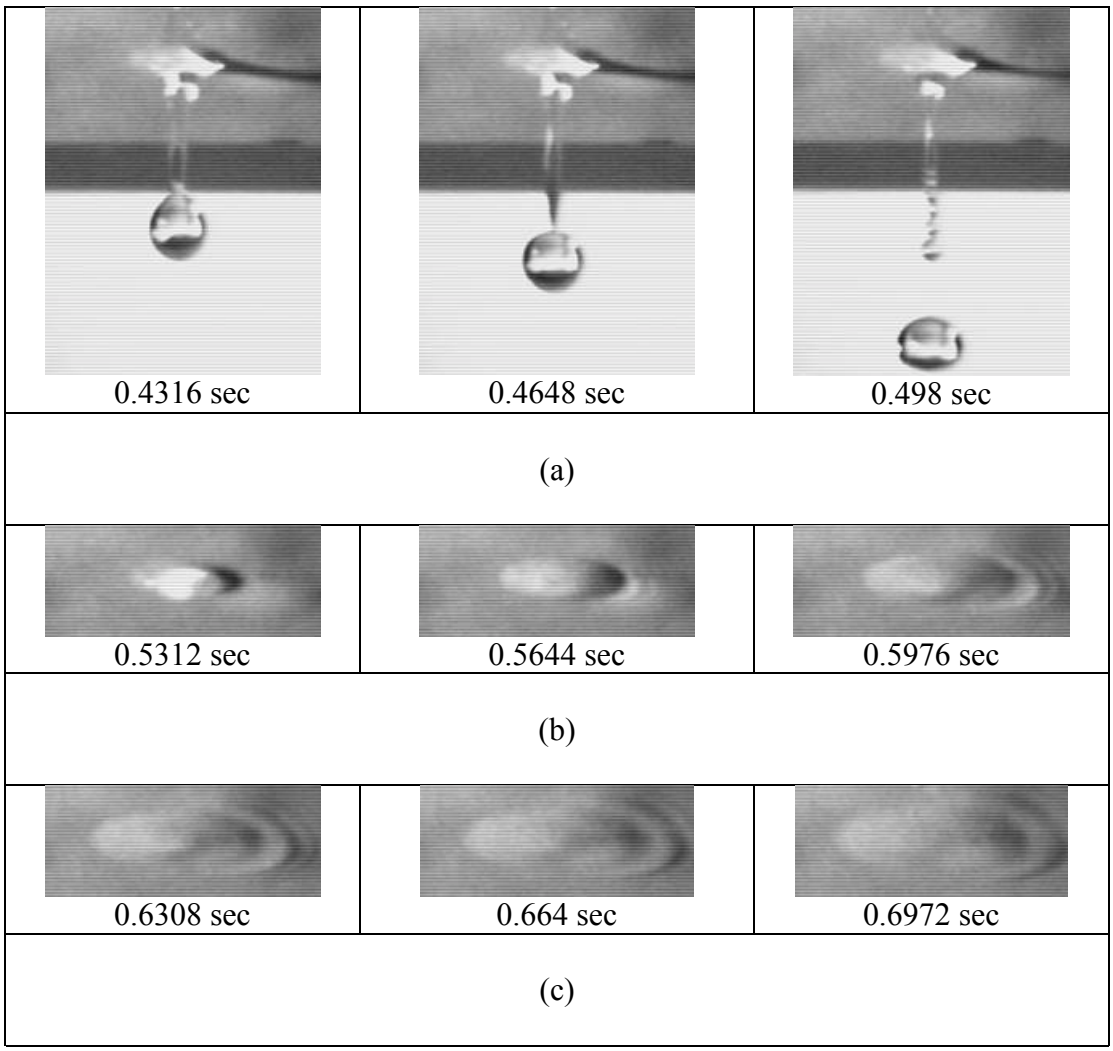

Figure 5.53 Formation and propagation of capillary waves of a bounded thin liquid film with transpiration through the boundary using water at 293 K as the working fluid for experimental run W090: (a) droplet detachment, (b) close-up of the wave formation domain, and (c) close-up of the wave propagation region.

5.7 Evaporation and Condensation Effects for Bounded Liquid Films

Evaporation and condensation at the liquid film free surface have a key role in the dynamics of liquid film flow. Mass exchange at the interface between the liquid film and the chamber gas in inertial fusion systems will directly impact the liquid film stability results, including: the free surface topology, the minimum film thickness between explosions, the frequency of liquid droplet formation and detachment, the equivalent diameter of detached droplets, the penetration depth, and the characteristic wave number. As indicated in chapter 3, the numerical front tracking code can parametrically account for mass exchange at the liquid-gas interface in the nondimensional momentum equation without the need to solve the energy equation. Therefore, all the relevant physical phenomena can be addressed without restriction to specific target output spectra as those provided in chapter 1. The dominant non-isothermal effects at the interface are analyzed by introducing a specified interfacial mass flux as a source term in the conservation of mass and interface advection equations.

The numerical code predictions indicate that evaporation at the interface delays while condensation expedites detachment compared to the reference analysis with no mass exchange at the interface. Figure 5.54 illustrates the liquid film development and droplet detachment for a nondimensional initial liquid film thickness of 0.1, transpiration velocity of 0.01 and nondimensional mass flux values of -0.005 (evaporation) and +0.01 (condensation). In inertial fusion energy applications, liquid lead has been proposed as a candidate coolant for the first wall shielding. Thus, when lead at 800 K is used as the working fluid, these values correspond to an initial liquid film thickness of 0.2 mm,

transpiration velocity of 1.4 mm/s and mass flux values of -7.6 kg/m^{2}s (evaporation) and +15.2 kg/m^{2}s (condensation).

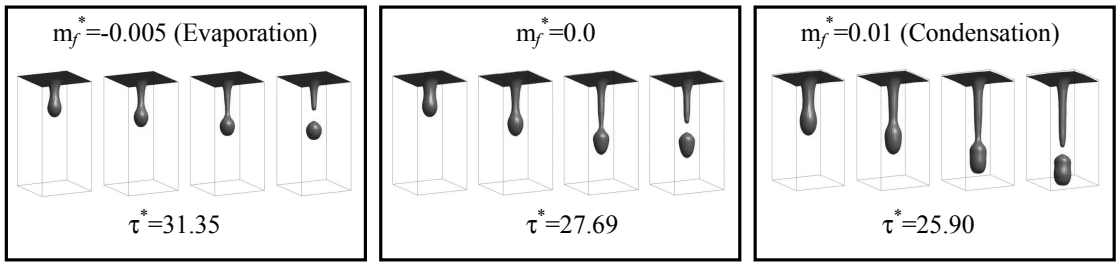

Figure 5.54 Numerical results for the effect of evaporation/condensation at the interface on the nondimensional detachment time for horizontal bounded thin liquid films (z_o^* = 0.1, w_{in}^* = 0.1, and Re = 2000).

The present experiment is not designed to control evaporation and/or condensation at the liquid film surface. The numerical code predictions can be validated by designing a bounded liquid film experiment that accounts for evaporation and condensation at the interface. In such experiment, an enclosure would be required to provide adequate control of the ambient gas. Indirect liquid film heating or cooling can be used to provide the required evaporation or condensation while independently controlling the mass flux at the interface. The effects of noncondensable gases on steam condensation under forced convection conditions are essential in understanding the dynamics of liquid film condensation [92]. Active or feedback control schemes based on the thermocapillary aspect of heated liquid films can also be used to verify the numerical code.

CHAPTER 6
CONCLUSIONS AND RECOMMENDATIONS

This chapter provides the conclusions derived from the conducted theoretical, numerical and experimental investigations of the Rayleigh-Taylor instability for bounded liquid films with injection through the boundary. The contributions of this research are emphasized as an expansion to the scope of the Rayleigh-Taylor instability applications and an enhancement to the exposition of physical principles involved in the thin liquid film protection scheme for fusion reactor first walls. The conclusions and contributions are categorized into several points, including: evolution of liquid film thickness, liquid film surface perturbation geometry, liquid droplet formation and detachment time, interface wave length and characteristic time scales, equivalent size for detached droplets, and time history of the penetration depth for bounded liquid films. This chapter also outlines the recommendations for future work.

6.1 Conclusions and Contributions

The conclusions obtained from this work are briefly listed in this section since they have been thoroughly detailed in the previous chapters. The outcome of this investigation and the primary conclusions that can be extracted from this thesis are:

1- Surface perturbation geometry and mode number have a major impact upon numerical simulations of the liquid film evolution and growth pattern for the Rayleigh-Taylor instability. The numerical front tracking code predicts higher

detachment times for higher mode number perturbations, and thus the longest wavelength (mode number 1) initial surface perturbation gives the conservative numerical estimate with regard to the detachment time.

2- The long-wave theory predictions are a reasonable theoretical representation of the perturbed liquid gas interface because the theoretical time scale is lower than the detachment time and the flow rate based time scales which have the same order of magnitude. A close concurrence between the theoretical predictions and the experimental measurements of the wavelength is obtained at higher injection velocities.

3- The liquid film injection velocity through the bounding surface affects several flow parameters. A higher injection velocity through the boundary increases the unperturbed liquid film thickness. Therefore, the equivalent droplet diameter of the detaching droplets and the maximum penetration depth of the developing spikes also increase in turn because of the corresponding increase in the liquid volume at higher transpiration velocities. However, the detachment time increases by decreasing the injection velocity due to the development of thinner liquid films.

4- The atomization mechanistic model predictions for the equivalent droplet diameter are in good agreement with the experimentally measured diameter for a given working fluid. However, when comparing the equivalent droplet diameters for water and glycerol solution (20%), the mechanistic model predicts a larger diameter value than that measured in the experiments for water. The theoretical atomization model does not account for the transpiration through the boundary and thus neglects

the effect of the unperturbed local instantaneous liquid film thickness on the equivalent droplet diameter.

5- Water and glycerol solution (20%) are used as working fluids to extend the fluid parameters and the range of comparison between the experiments and the numerical front tracking model. The glycerol solution (20%) runs have greater measured unperturbed liquid film thickness values than the corresponding water runs at the same transpiration velocity w_{in}, and hence larger equivalent droplet diameter and maximum penetration depth. However, utilizing glycerol solution (20%) as the working fluid caused a decrease in the detachment time because glycerol solution (20%) has a higher viscosity or lower Reynolds number than those of water.

6- Inclined (vs. horizontal) bounding surfaces provide a different behavior for the liquid film stability results. The thickness of the advected liquid film increases along the axial direction of the bounding surface due to the continuous injection and delayed droplet formation as a result of the tangential acceleration, the shear stress effects, and the liquid film drift. Droplets detaching from horizontal liquid films have larger values of the equivalent droplet diameter and penetration depth than those pinching off from inclined films. In inclined liquid films, droplets detach at axial locations corresponding to mean liquid film thickness values that are smaller than those measured for horizontal liquid films at a given injection velocity.

7- The effects of evaporation and condensation at the liquid film free surface is included in the numerical front tracking code by introducing a specified interfacial mass flux as a source term in the conservation of mass and interface advection equations. The numerical predictions establish that evaporation at the interface

delays while condensation expedites detachment compared to the baseline analysis with no mass exchange at the interface.

8- The effect of the normalized initial perturbation amplitude ε_s/z_o upon the numerical results was investigated by running the numerical front tracking code for a range of ε_s/z_o values of: 0.1, 0.25, 0.5, 0.75 and 1. The initial liquid film thickness z_o is extracted from the experimental runs as the mean value provided by the transient variation of the unperturbed liquid film thickness ($z_o = h_o$). In all runs, the numerical model predictions of detachment time, droplet diameter and penetration depth are within two standard deviations of the corresponding experimentally measured field variables.

The contributions of this theoretical, numerical and experimental study are valuable as a novel investigation of a variant of the Rayleigh-Taylor instability with a bounding wall with transpiration through the bounding surface. This work is the first in the available literature to investigate this aspect of the bounded Rayleigh-Taylor instability. The aim is extended by modifying the long wave theory and verifying the numerical front tracking model, and thus by doing so, a powerful tool is made available to designers of inertial fusion energy (IFE) systems which would help identify design windows for successful operation of the thin liquid film protection concept. The main contributions of this thesis are provided in the following points:

1- Designing and constructing an experimental test facility that simulates the thin liquid film protection scheme for horizontal and inclined bounding surfaces, while independently controlling several input parameters such as the unperturbed liquid film thickness and injection velocity through the bounding surface,

2- Measuring the unperturbed local instantaneous liquid film thickness by using a non-intrusive technique. The measurement was carried out for horizontal liquid films and along the axial direction of inclined films,

3- Determining the effect of different design and operational parameters (liquid film thickness, liquid injection velocity through the boundary, inclination angle of the bounding surfaces, and liquid properties) on liquid film stability,

4- Obtaining dimensional and nondimensional results from the conducted experiments pertaining to the conceptual design of the thin liquid film protection scheme for horizontal and inclined bounding surfaces, including:

    4.1- The frequency of liquid droplet formation,

    4.2- The size of detached droplets,

    4.3- The time history of the penetration depth, and

    4.4- The interface wave number,

5- Modifying and extending the long-wave theory in order to characterize and account for transpiration through the bounding surface, and thus determining the theoretical wave numbers and the characteristic time scales,

6- Validating over a wide range of design parameters a numerical code which is based on a state-of-the-art level contour reconstruction front tracking technique by comparing the numerical predictions with the experimental results, and

7- Establishing the design and technical requirements for the liquid film stability and survivability mandated for the robust and successful development of the thin liquid film shielding concept.

6.2 Recommendations and Future Work

The work presented in this doctoral thesis is the first theoretical, numerical and experimental investigation in the available literature to study the various aspects of the bounded Rayleigh-Taylor instability with injection through the boundary. The knowledge gained from this investigation paves the way for future work in the stability of thin liquid films. Therefore, the following investigation steps are recommended:

1- Design an experimental test facility that accounts for the non-isothermal effects such as evaporation and condensation at the bounded liquid film surface, while independently controlling the mass flux at the interface,

2- Investigate the thermocapillary effects on the continuity and stability of heated liquid films,

3- Modify the long-wave theory to characterize thin liquid films bounded by inclined surfaces and to account for capillary waves at the liquid film surface,

4- Account for the response of the liquid film to a specific target spectra by directly solving the energy and momentum equations in a coupled front tracking numerical code, and

5- Use parallel techniques in the numerical front tracking code in order to achieve the higher resolution simulations required to resolve the detailed characteristics of the thin liquid film flow.

APPENDICES

The appendices are provided as a continuation to the numerical and experimental results obtained for the characteristic flow field variables of the bounded Rayleigh-Taylor instability with injection through the bounding horizontal and inclined surfaces. They are categorized as follows:

Appendix A Error Analysis

Appendix B Numerical and Experimental Results for Horizontal Surfaces

Appendix C Numerical and Experimental Results for Inclined Surfaces

APPENDIX A
ERROR ANALYSIS

The error analysis and the uncertainty of a measurement is an essential consideration in the conducted experiments. Therefore, the uncertainty is estimated in this appendix for direct and indirect measurements, including: the mass flow rate, the working fluid temperature and Reynolds number, the image analysis, and the characteristic flow field variables.

A.1 Mass Flow Rate

Mass flow rates through the bounding surface were measured using a weighing tank process in which the working fluid was collected during a specified period of time. Table 4.2 in Chapter 4 lists the mass flow rates for different experimental runs. Hence, the mass flow rate was not measured directly but is obtained from two direct measurements involving the mass and time as independent variables. For an indirect measurement y which depends on N direct measurements x_i the following generic formula is used:

$$u^2 = \sum_{i=1}^{N} \frac{\partial y}{\partial x_i} u_i^2 \qquad \text{(A.1)}$$

where

$$y = y(x_1, x_2, ..., x_N)$$

u = standard uncertainty

The expanded uncertainty U is reported in this appendix for the conducted experimental runs, and thus it is given by:

$$U = k_c u \tag{A.2}$$

where U = expanded uncertainty

k_c = coverage factor = 2

The expanded uncertainty U is taken to be twice the standard uncertainty u based on the assumption that the experimental distribution is approximate to the normal distribution such that the uncertainty will include 95% of the possibilities. Applying equation (A.1) to the mass flow rate measurement results in the following formulation:

$$u_{\dot{m}}^2 = \left(\frac{u_m}{\Delta t}\right)^2 + \left(\frac{-m}{\Delta t^2} u_{\Delta t}\right)^2 \tag{A.3}$$

Based on equation (A.3) for the standard uncertainty u in the mass flow rate calculation and using the minimum time increment of 5 seconds as a limiting value, the maximum expanded uncertainty U for the conducted experimental runs in this investigation is 5×10^{-5} kg/s which translates to an expanded uncertainty of 0.18×10^{-5} m/s in the velocity.

A.2 Working Fluid Temperature

Measurement of the working fluid temperature is an essential component of the experimental process. Therefore, calibration of the thermocouples was carried out using a platinum resistance thermometer RTD (OMEGA PRP-2) to provide a reference scale. The measured temperature also affects the working fluid properties, and thus the calculated Reynolds number.

A.2.1 Calibration Curve

The calibration process and data for the calibrated thermocouple mounted in the constant-head tank are presented in Figures 4.6 and 4.7 of Chapter 4. The following calibration function was obtained:

$$T_{\mathrm{RTD}} = 0.99T_{\mathrm{TC}} + 4.07 \qquad \text{(A.4)}$$

where

T_{RTD} = RTD temperature in K

T_{TC} = thermocouple temperature in K

The expanded uncertainty U of the temperature calibration is taken as twice the standard error of estimate (SEE) obtained from the regression analysis. In this calibration, the expanded uncertainty U is 0.914 K.

A.2.2 Reynolds Number

The normalized results provided in this investigation are categorized using the Reynolds number as a characteristic parameter. The Reynolds number used in this investigation is defined in section 3.2 of Chapter 3 as follows:

$$\mathrm{Re} = \frac{\rho_{\mathrm{L}} U_o l}{\mu_{\mathrm{L}}} \qquad \text{(A.5)}$$

This definition of the Reynolds number can be reduced to be a function of the working fluid temperature:

$$\mathrm{Re} = \mathrm{Re}(T) \qquad \text{(A.6)}$$

Equation (A.6) can be derived by using the characteristic scales introduced in Chapter 3 and by including the correlations of the liquid properties as a function of the

working fluid temperature [79-82]. After manipulating equation (A.5), the Reynolds number dependence on temperature for water is given by:

$$\mathrm{Re} = \left(\frac{\left(0.132674 \left(1 - \frac{T}{647.1} \right)^{0.955} \right)^3 \left(347.1 \times 0.274^{-\left(1-\frac{T}{647.1}\right)^{0.2857}} \right)}{9.8 \left(\left(\frac{1}{1000} \right) 10^{\left(-10{,}2158 + \frac{1792.5}{T} + 0{,}01773T - 1{,}26\times10^{-5}T^2 \right)} \right)^4} \right)^{\frac{1}{4}} \qquad \text{(A.7)}$$

Equation (A.7) is plotted in Figure A.1 to trace the variation of the Reynolds number with the working fluid temperature.

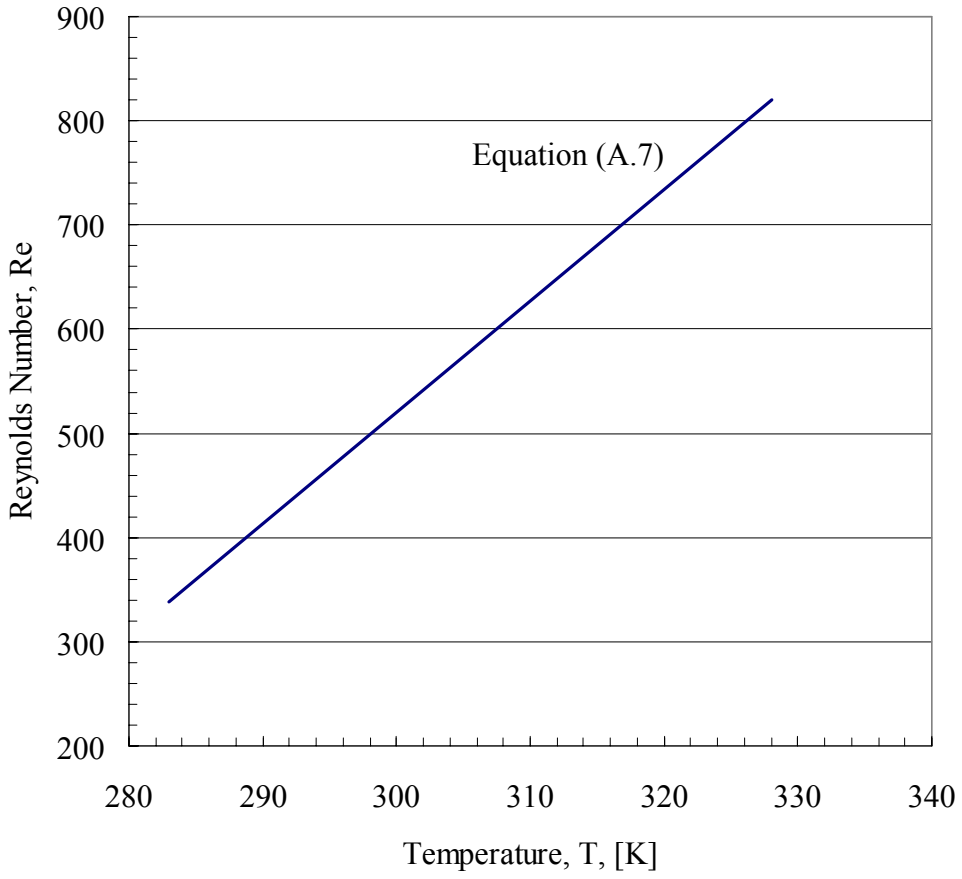

Figure A.1 Reynolds Number (Re) variation with the working fluid temperature.

A.3 Image Analysis

As is explained in Chapter 4, each set of detected edge images were analyzed to measure the flow field parameters. The droplet detachment time was measured by tracking the sequences of the contoured surface edges to the detachment point. The expanded uncertainty U for this measurement is given by the resolution of the time steps which is 8.33 ms as provided by the CCD camera framing rate of 120 Hz. Errors in the measured droplet diameter can be attributed to the axisymmetric geometry assumed for calculating an equivalent value of the diameter. Therefore, the actual droplet geometry may deviate from the used spheroid formulation.

A.4 Flow Field Variables

This section details the uncertainty associated with the statistical distributions obtained from the experimental runs for the flow field variables, including: the liquid film thickness, the droplet detachment time, the equivalent droplet diameter, and the maximum penetration depth. These statistical distributions were developed by gathering multiple data for the conducted experimental runs. Based on error propagation analysis, the standard uncertainty u of an average of N data is computed from the standard deviation of the sample as follows:

$$u = \frac{\sigma}{\sqrt{N}} \tag{A.8}$$

where

σ = standard deviation

N = number of measurements

The standard uncertainty, which is in these distributions a Type A uncertainty, is less than the sample standard deviation. For a large sample size, the uncertainty due to a random influence can be virtually eliminated. In order to investigate the accuracy and precision of the developed statistical distributions, the experimental run #W090 is conducted twice and the results for the experimental mean and expanded uncertainty values are compared in Tables A.1 and A.2. A close agreement between runs W090,1 and W090,2 is achieved.

Table A.1 Liquid mass flow rates and velocities for two experiments representing run #W090.

Time, [sec]	$M_{W0.9,1}$, [kg]	$M_{W0.9,2}$, [kg]
5	0.120	0.119
10	0.226	0.224
15	0.378	0.380
20	0.482	0.480
25	0.592	0.590
30	0.711	0.704
35	0.814	0.819
40	0.972	0.974
45	1.020	1.015
50	1.177	1.179
$\dot{m}_{av}$, [kg/s]	0.024	0.023
$\dot{V}_{av}$, [mm^3/s]	23747	23691
$w_{in,av}$, [mm/s]	0.903	0.901

Table A.2 Experimental mean and expanded uncertainty values of the detachment time (t_d), equivalent droplet diameter (D), and maximum penetration depth (d) for the two experiments representing run #W090.

Runs	Detachment Time		Equivalent Diameter		Max Penetration Depth	
	t_d, [s]	*U*, [s]	D, [mm]	*U*, [mm]	d, [mm]	*U*, [mm]
W090,1	0.4652	0.0029	8.2	0.04	51.25	0.54
W090,2	0.4826	0.0029	8.0	0.04	49.42	0.41

Tables A.3-A.6 provide the experimental mean and expanded uncertainty values of the liquid film thickness, detachment time, equivalent droplet diameter, and maximum penetration depth for the conducted experimental runs including horizontal and inclined surfaces.

Table A.3 Experimental mean (h_o) and expanded uncertainty (U) values of the unperturbed liquid film thickness for the experimental runs conducted using horizontal surfaces.

Runs	Mean Value, h_o, [μm]	U, [μm]
W090	614.3	0.8
W140	713.0	2.7
W170	787.7	12.6
W190	1131.8	21.1
W210	1506.4	3.2

Table A.4 Experimental mean (h_o) and expanded uncertainty (U) values of the unperturbed liquid film thickness at several axial positions (x) in the direction of the liquid film flow for the experimental runs conducted using inclined surfaces (θ =2.5˚).

Runs	x = 20 mm		x = 30 mm		x = 40 mm		x = 50 mm	
	h_o[μm]	U[μm]	h_o[μm]	U[μm]	h_o[μm]	U[μm]	h_o[μm]	U[μm]
W0925	217.8	4.3	324.1	4.2	419.1	2.5	812.5	3.4
W1425	293.3	1.2	441.1	0.9	622.0	5.3	917.1	11.9
W1725	316.8	1.9	491.2	0.6	757.7	10.6	986.0	5.3
W1925	399.1	1.6	597.1	10.9	930.3	12.5	1251.3	29.6
W2125	456.0	6.2	705.6	5.9	1168.6	8.3	1533.7	3.5

Table A.5 Experimental mean and expanded uncertainty values of the detachment time (t_d), equivalent droplet diameter (D), and maximum penetration depth (d) for the experimental runs conducted using horizontal surfaces.

Runs	Detachment Time		Equivalent Diameter		Max Penetration Depth	
	t_d, [s]	U, [s]	D, [mm]	U, [mm]	d, [mm]	U, [mm]
W090	0.4652	0.0029	8.2	0.04	51.25	0.54
W140	0.4071	0.0018	8.6	0.02	62.33	0.27
W170	0.3576	0.0017	8.9	0.02	69.82	0.35
W190	0.3119	0.0021	9.3	0.02	76.70	0.50
W210	0.2412	0.0028	9.6	0.04	87.87	0.68

Table A.6 Experimental mean and expanded uncertainty values of the detachment time (t_d), equivalent droplet diameter (D), and maximum penetration depth (d) for the experimental runs conducted using inclined surfaces.

Runs	Detachment Time		Equivalent Diameter		Max Penetration Depth	
	t_d, [s]	*U*, [s]	D, [mm]	*U*, [mm]	d, [mm]	*U*, [mm]
W090	0.5991	0.0023	7.79	0.03	44.34	0.47
W140	0.5155	0.0019	8.29	0.03	54.08	0.48
W170	0.4322	0.0019	8.69	0.02	61.84	0.35
W190	0.3641	0.0026	9.01	0.03	70.72	0.45
W210	0.2867	0.0022	9.24	0.03	80.72	0.53

The bounding plate surface uniformity condition may affect the distribution of the droplet formation sites at the liquid film surface. However, the plate media was assessed and rated using bubble point testing conducted by the manufacturer. The maximum expanded uncertainty *U* for the measured interface wave length values in the conducted experimental runs in this investigation is 0.2 mm.

APPENDIX B

NUMERICAL AND EXPERIMENTAL RESULTS FOR HORIZONTAL SURFACES

The numerical and experimental results obtained for the characteristic flow field variables of the bounded Rayleigh-Taylor instability with injection through the bounding horizontal surfaces are detailed in this appendix. These numerical and experimental runs are listed in Table B.1. Runs W090 and W210 are provided in Chapter 5 while the other runs are given in this appendix.

Table B.1 Letter-number designation of the conducted experimental and numerical runs for horizontal surfaces.

Experiment Runs	Working Fluid	Injection Velocity, w, [mm/s]	Surface Inclination Angle, θ
W090	Water	0.9	0˚
G090	20% Glycerol	0.9	0˚
W140	Water	1.4	0˚
W170	Water	1.7	0˚
G170	20% Glycerol	1.7	0˚
W190	Water	1.9	0˚
W210	Water	2.1	0˚

B.1 Numerical and Experimental Results for Run #G090

This section details the numerical and experimental results on the characteristic flow field variables for the bounded Rayleigh-Taylor instability with injection through the bounding horizontal surface for Run #G090. These results include: the evolution of the liquid film thickness, the liquid film surface perturbation geometry, the liquid droplet formation and detachment time, the equivalent size for detached droplets, and the time history of the penetration depth.

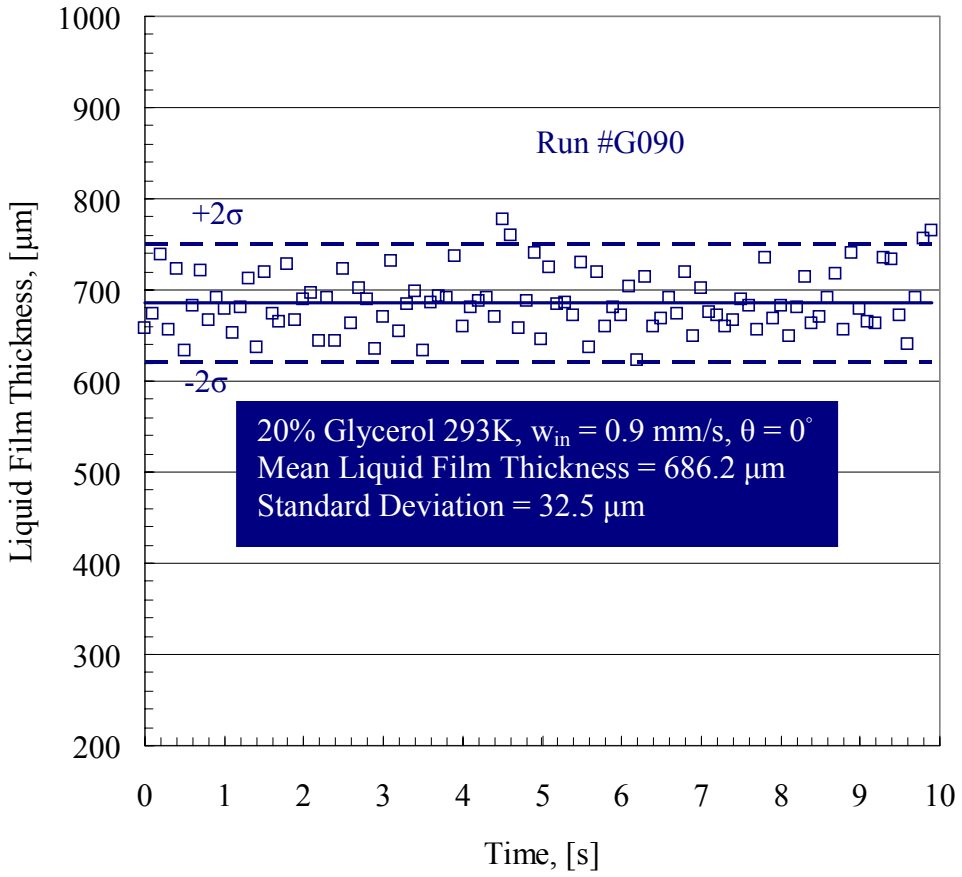

Figure B.1 Transient variation of the unperturbed liquid film thickness for Run #G090.

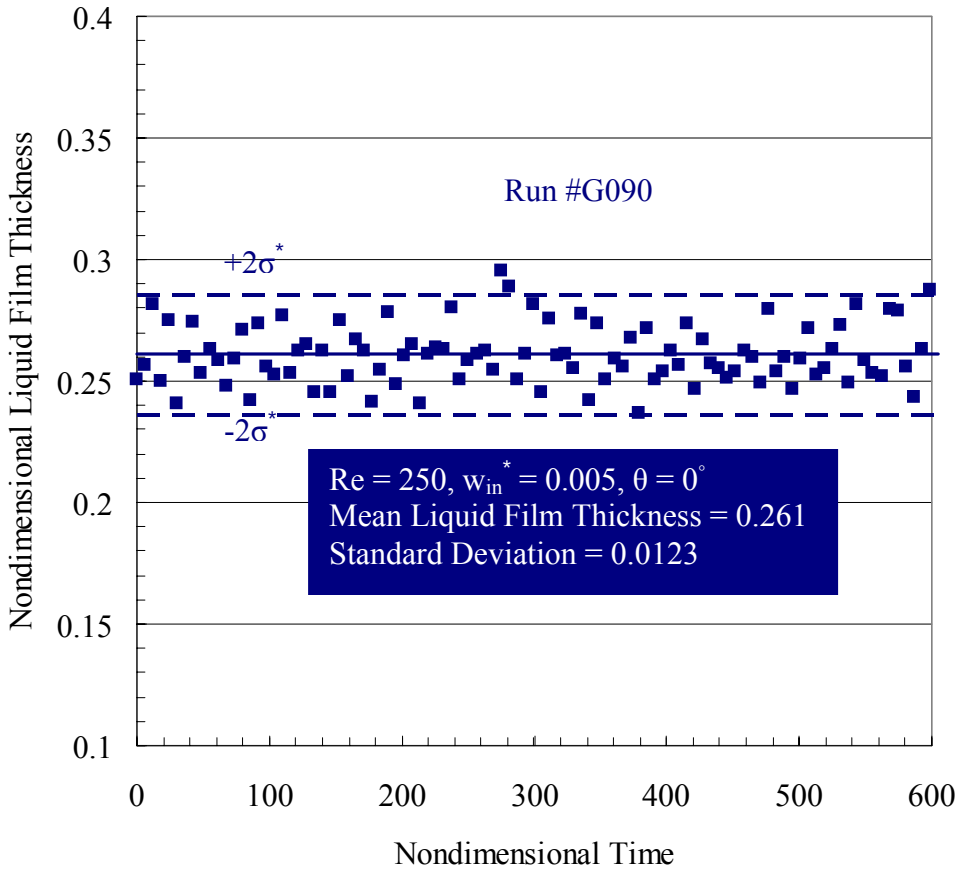

Figure B.2 The unperturbed liquid film thickness normalized by l as a function of time normalized by t_o for Run #G090.

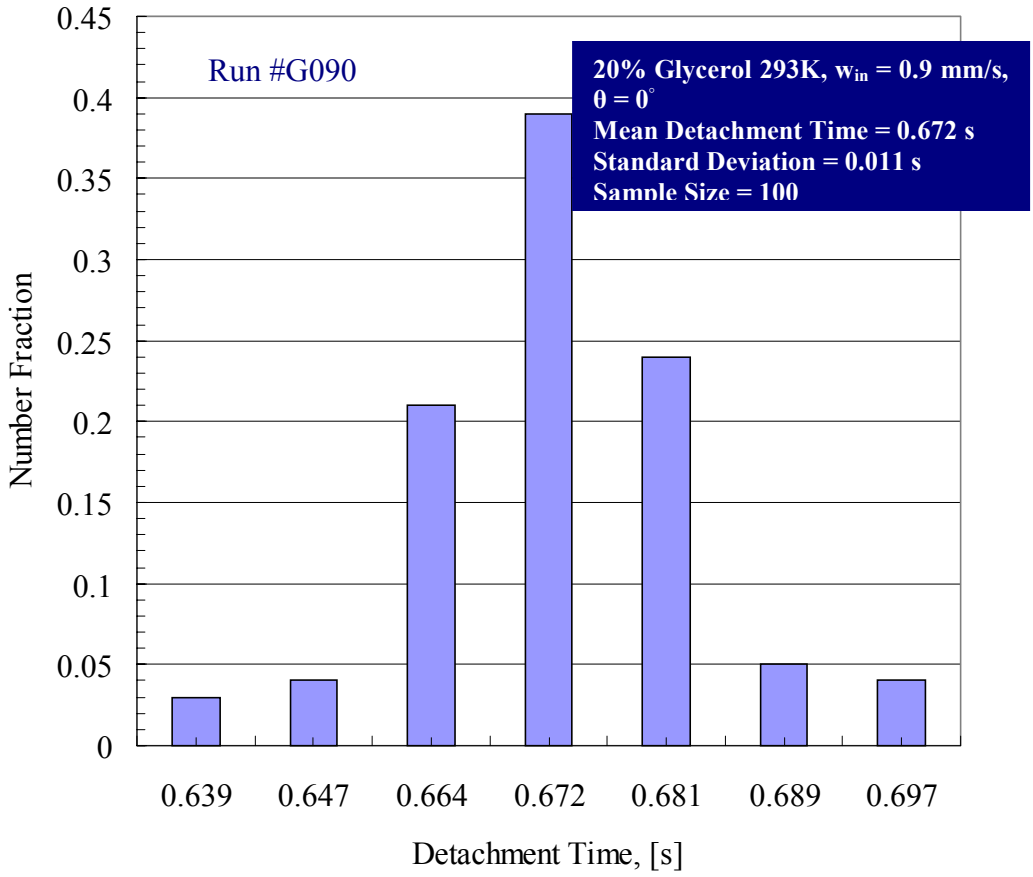

Figure B.3 Experimental data for the distribution of the detachment times carried out for a horizontal surface (Run #G090).

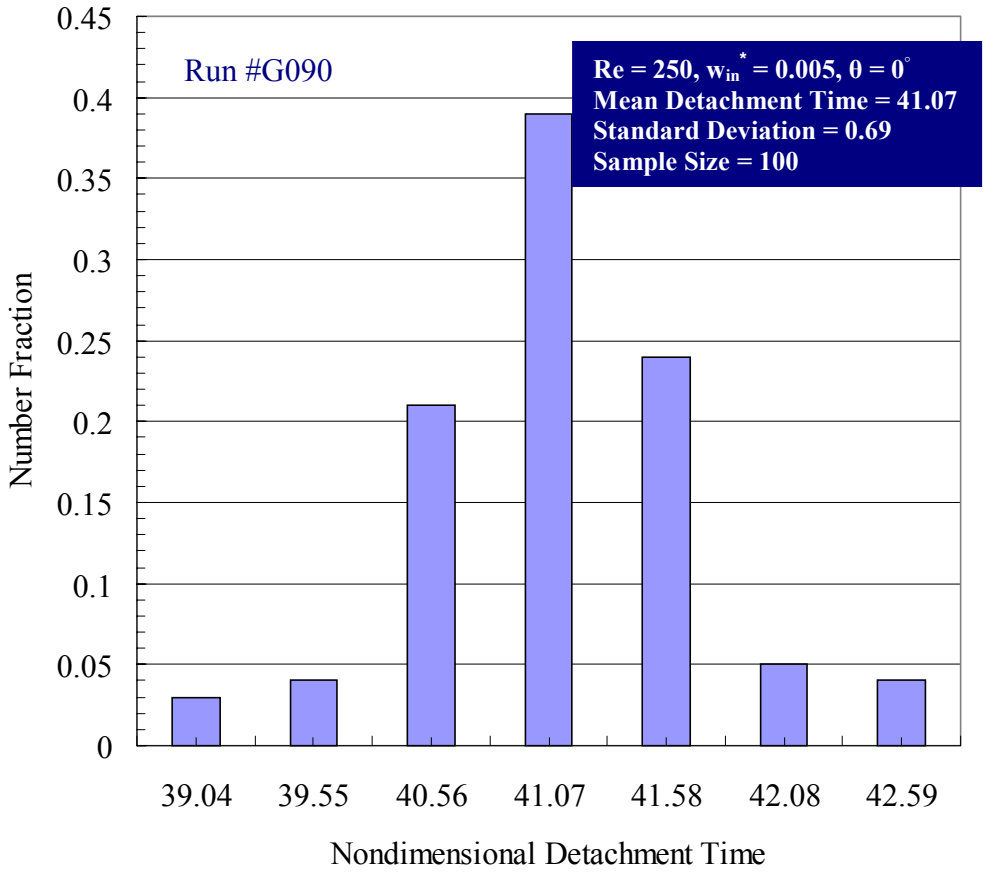

Figure B.4 Experimental data for the distribution of the nondimensional detachment time carried out for a horizontal surface (Run #G090).

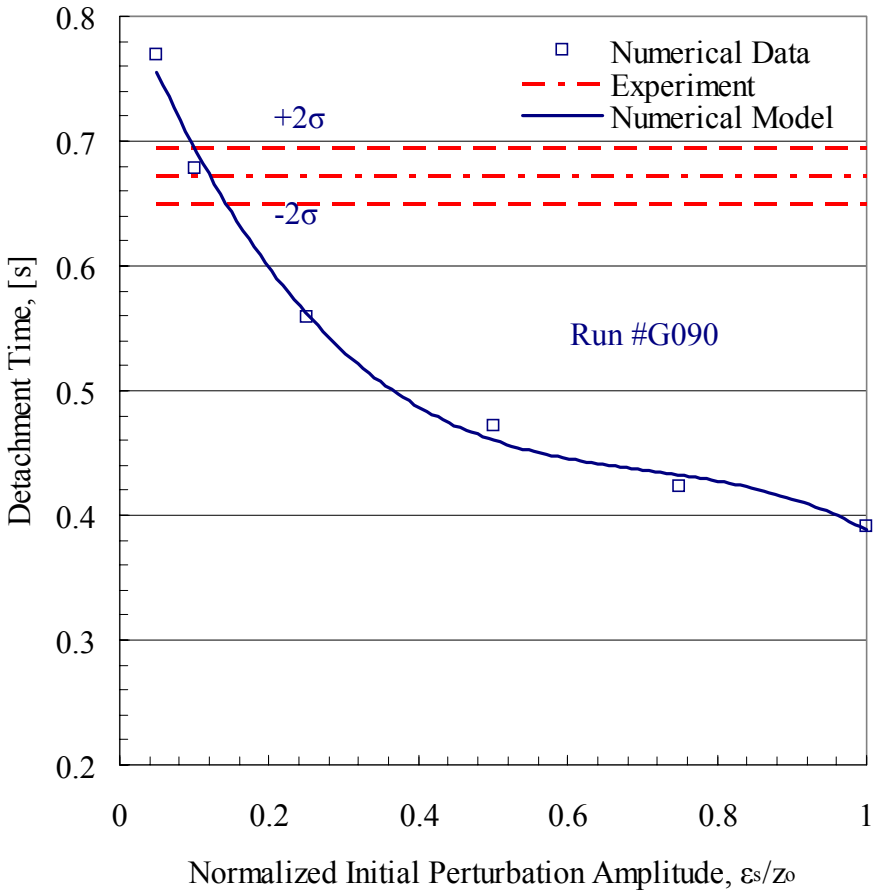

Figure B.5 Numerical and experimental data for the variation of the detachment time with the normalized initial perturbation amplitude carried out for a horizontal surface (Run #G090).

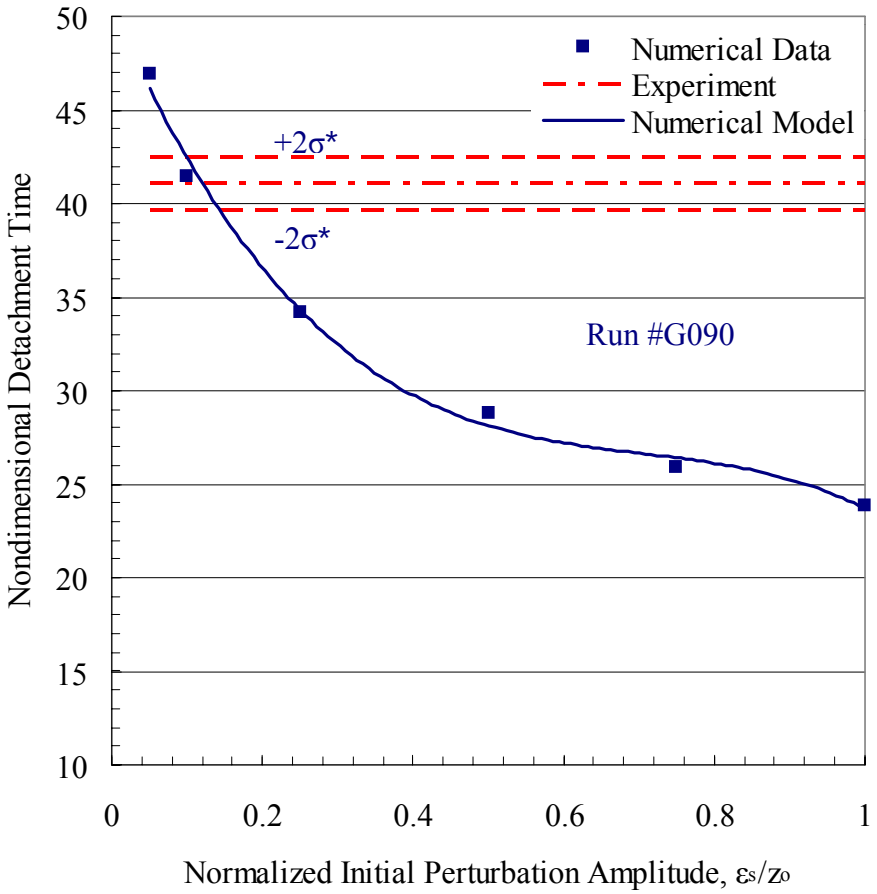

Figure B.6 Numerical and experimental data for the variation of the nondimensional detachment time with the normalized initial perturbation amplitude carried out for a horizontal surface (Run #G090).

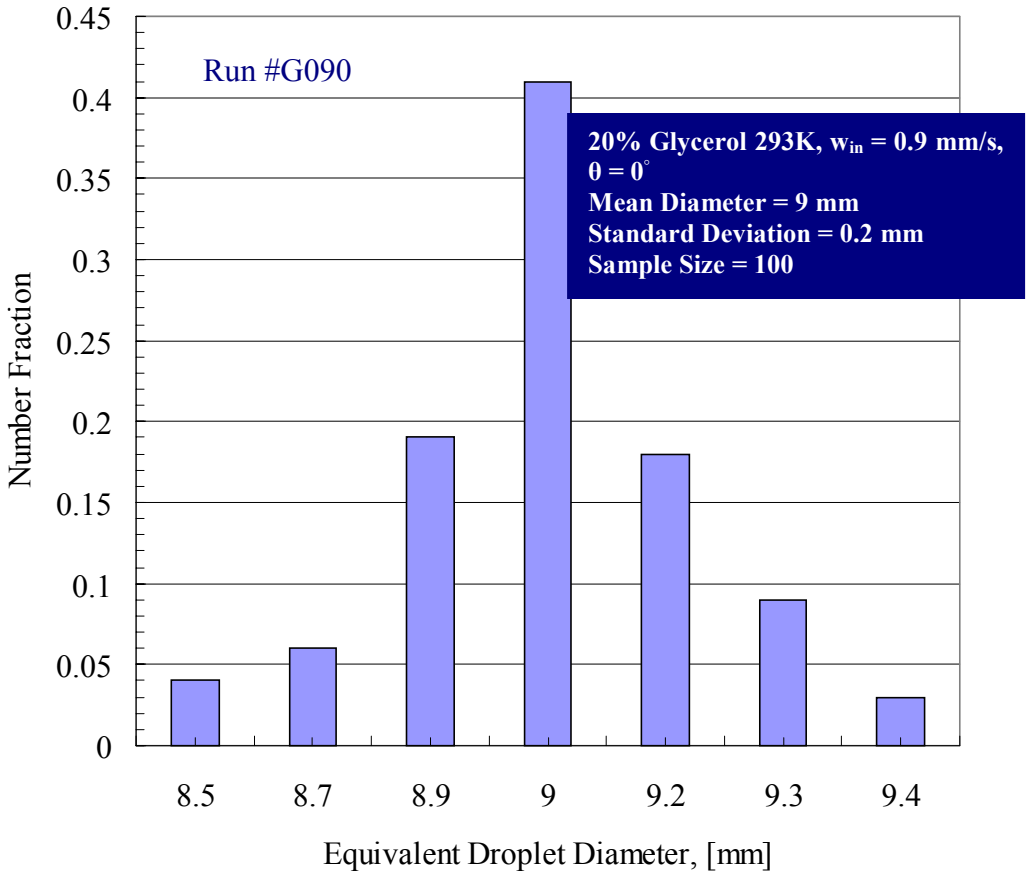

Figure B.7 Experimental data for the distribution of the equivalent droplet diameter carried out for a horizontal surface (Run #G090).

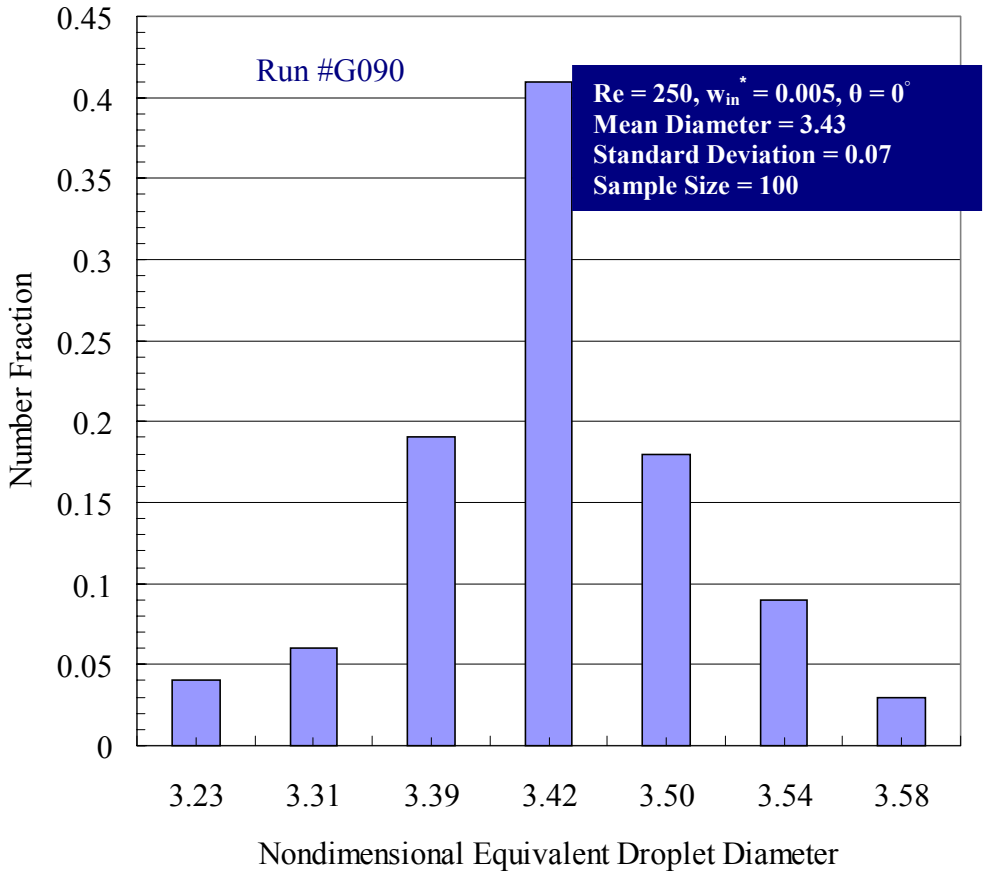

Figure B.8 Experimental data for the distribution of the nondimensional equivalent droplet diameter carried out for a horizontal surface (Run #G090).

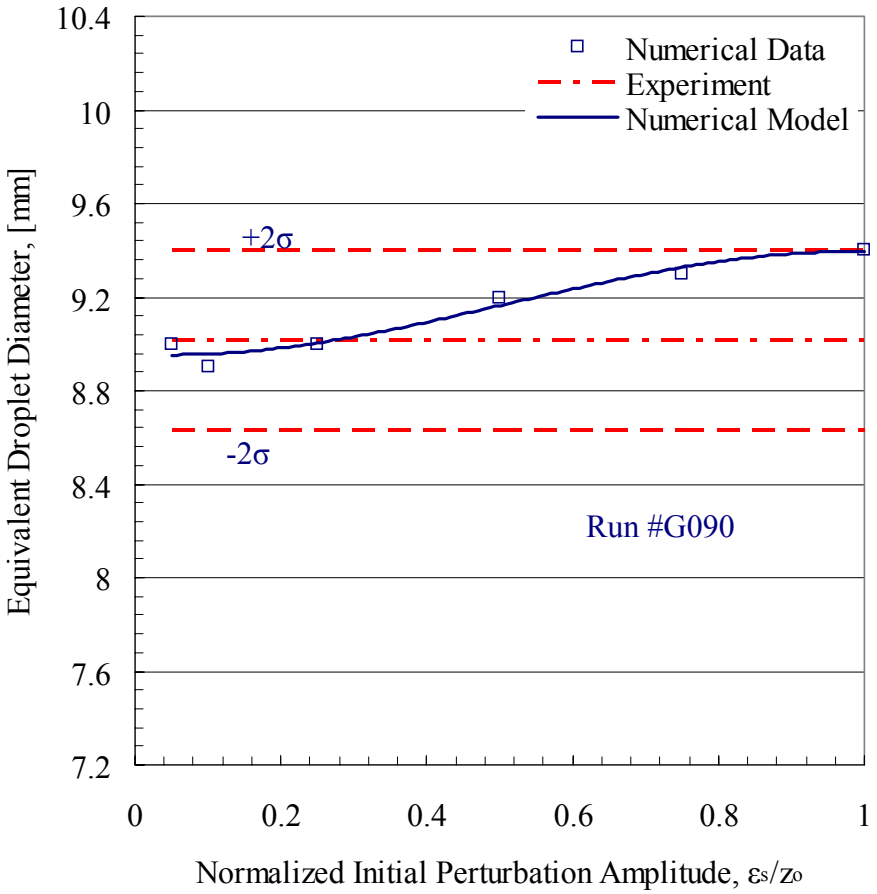

Figure B.9 Numerical and experimental data for the variation of the equivalent droplet diameter with the normalized initial perturbation amplitude carried out for a horizontal surface (Run #G090).

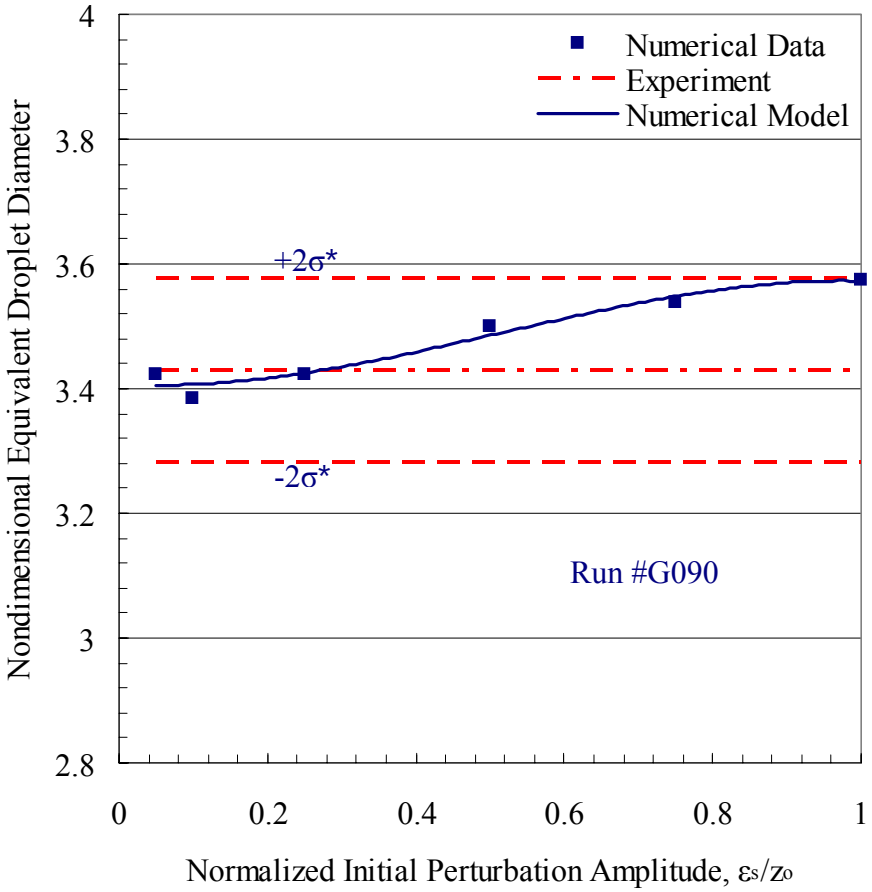

Figure B.10 Numerical and experimental data for the variation of the nondimensional equivalent droplet diameter with the normalized initial perturbation amplitude carried out for a horizontal surface (Run #G090).

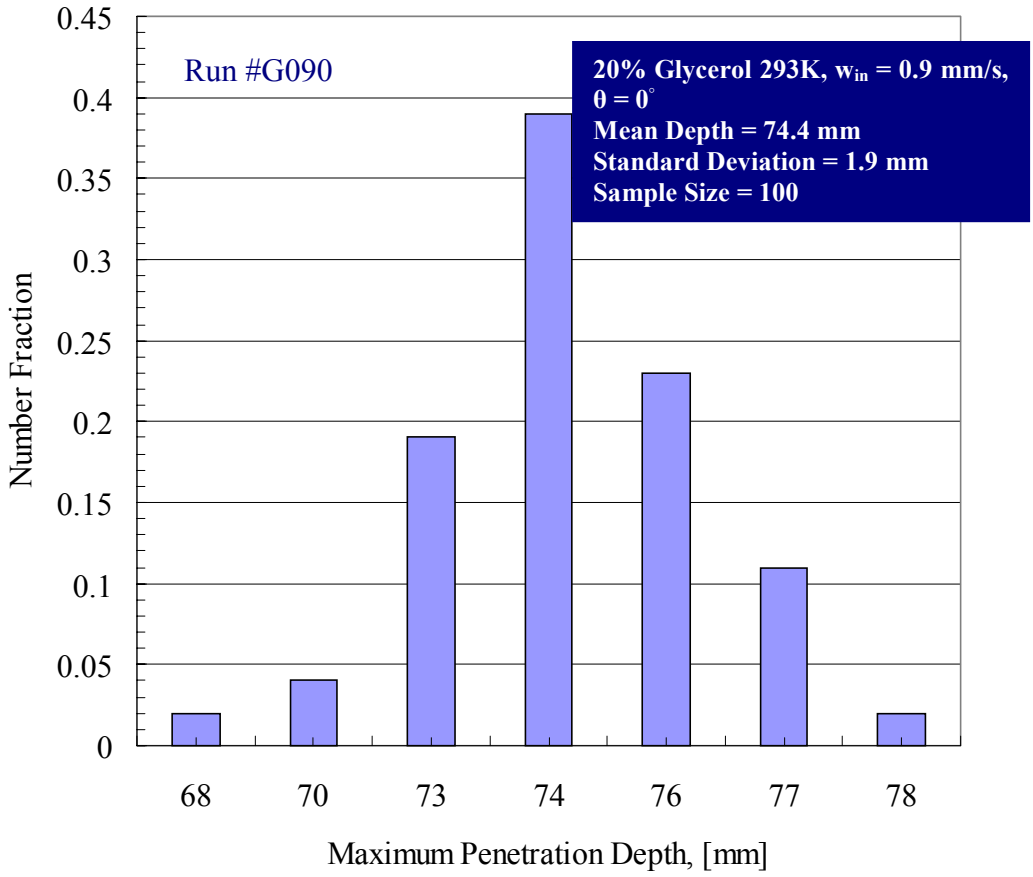

Figure B.11 Experimental data for the distribution of the maximum penetration depth carried out for a horizontal surface (Run #G090).

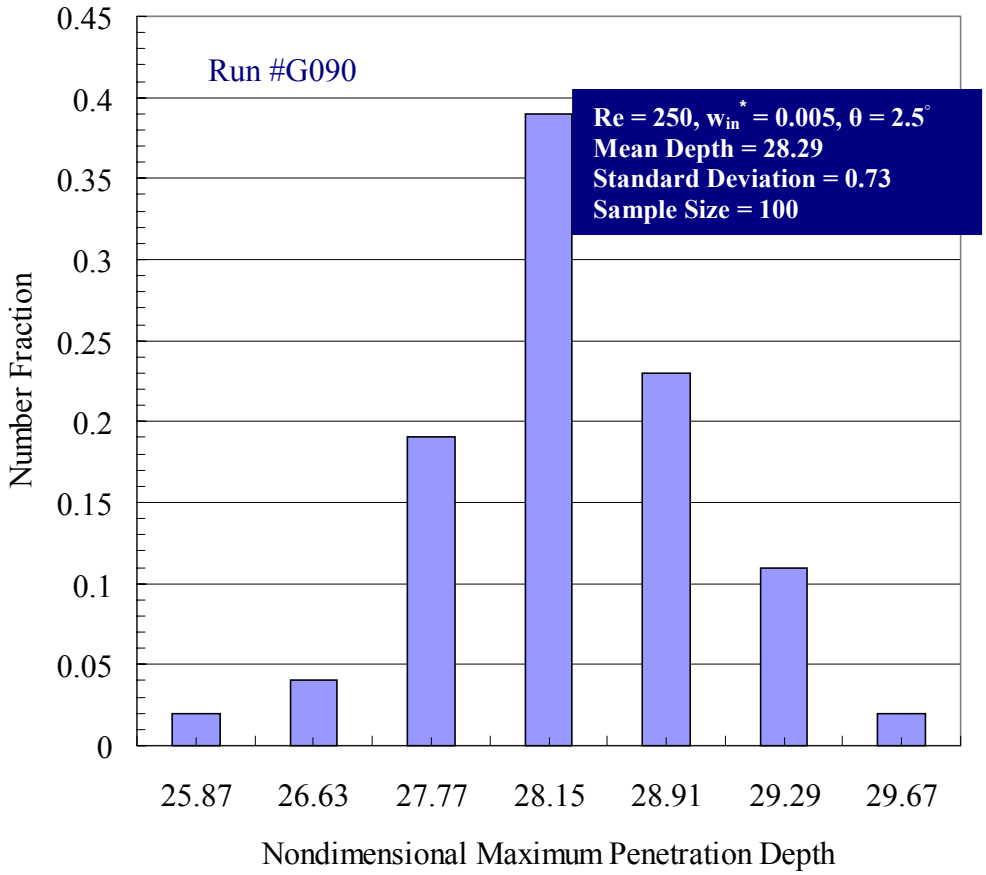

Figure B.12 Experimental data for the distribution of the nondimensional maximum penetration depth carried out for a horizontal surface (Run #G090).

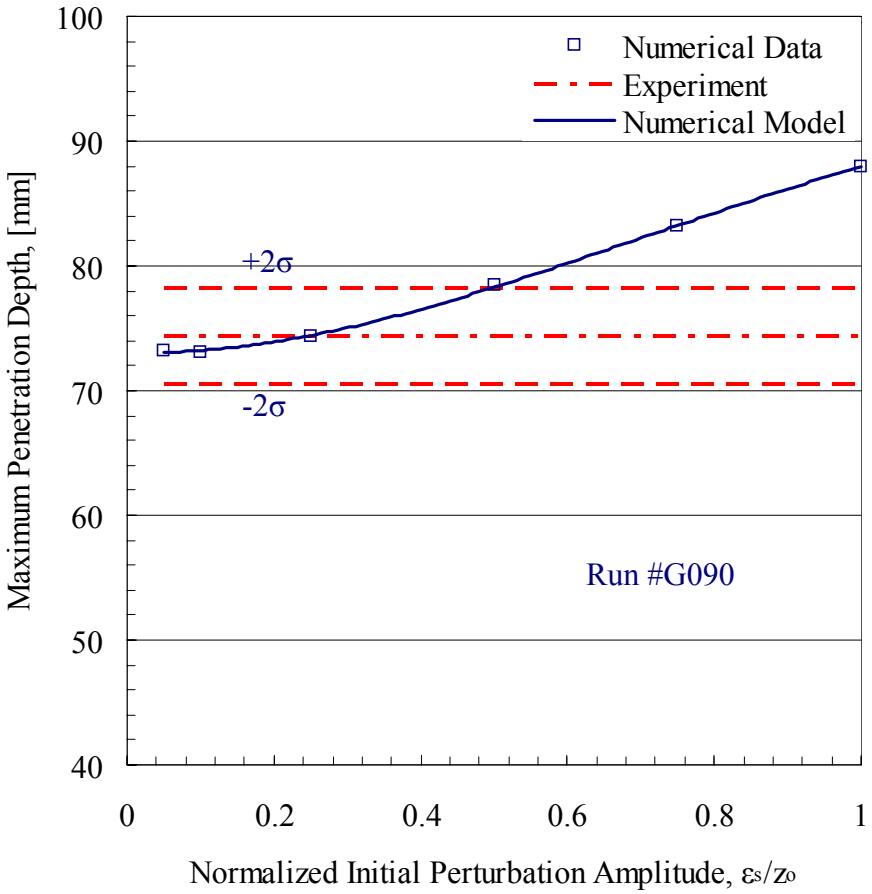

Figure B.13 Numerical and experimental data for the variation of the maximum penetration depth with the normalized initial perturbation amplitude carried out for a horizontal surface (Run #G090).

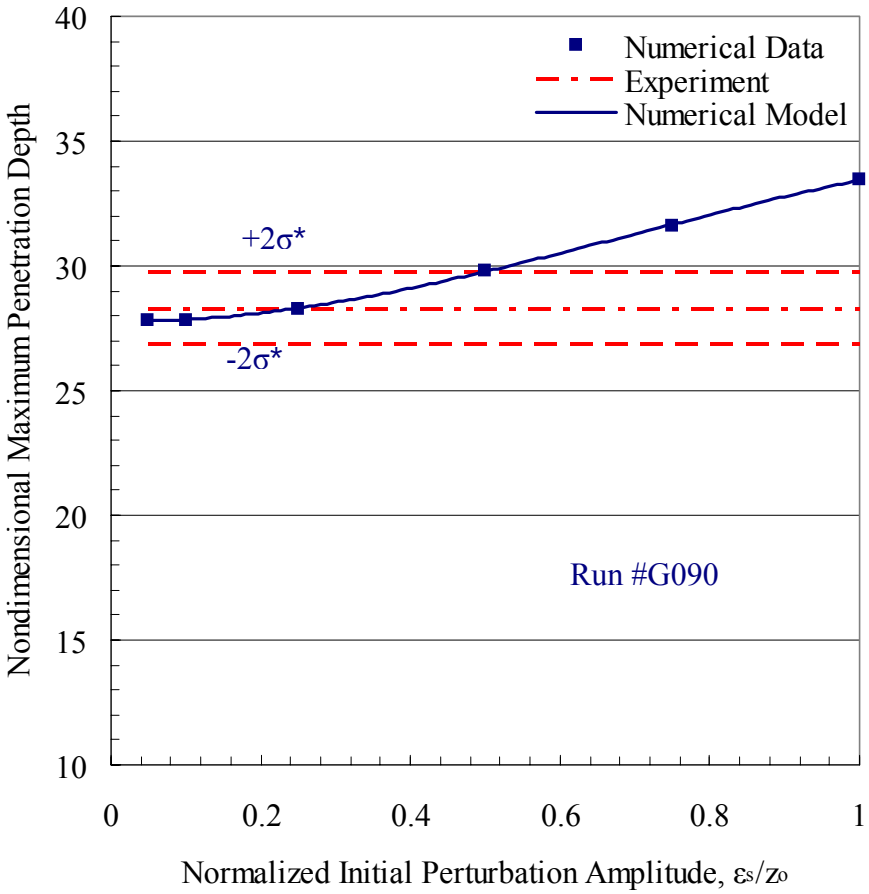

Figure B.14 Numerical and experimental data for the variation of the nondimensional maximum penetration depth with the normalized initial perturbation amplitude carried out for a horizontal surface (Run #G090).

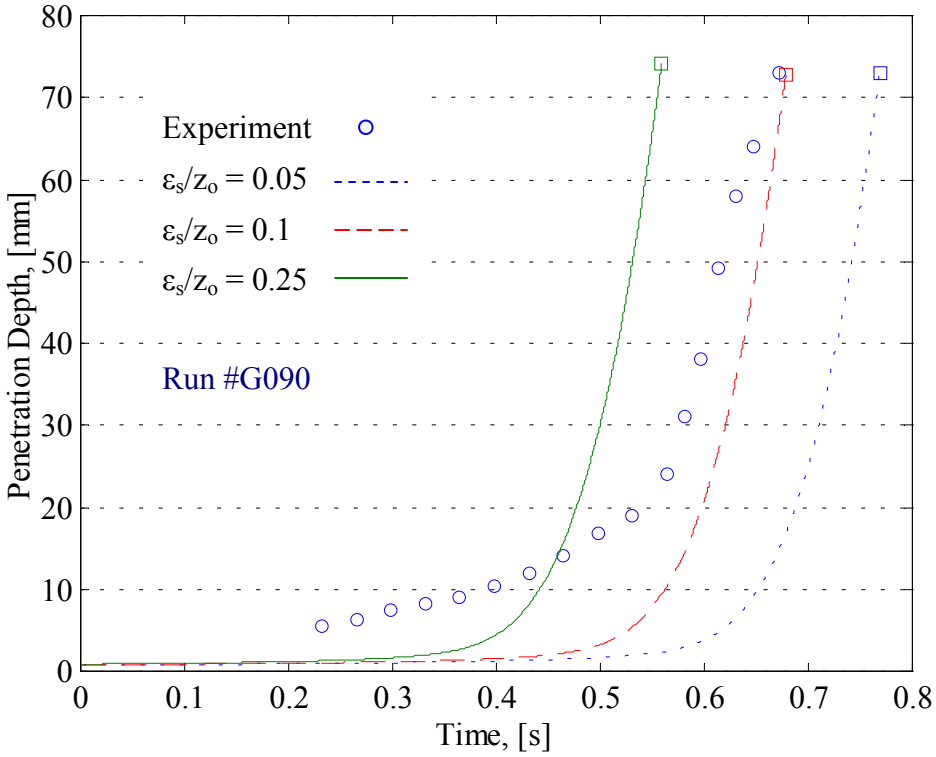

Figure B.15 Numerical and experimental data for the transient variation of the penetration depth carried out for a horizontal surface (Run #G090).

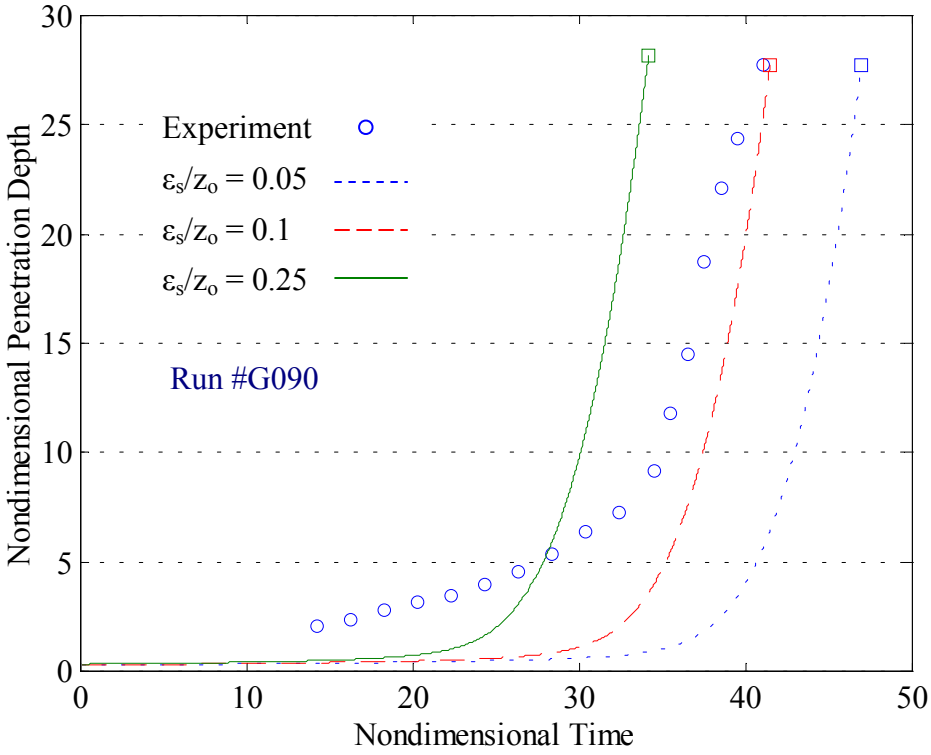

Figure B.16 Numerical and experimental data for the transient variation of the nondimensional penetration depth carried out for a horizontal surface (Run #G090).

B.2 Numerical and Experimental Results for Run #W140

This section details the numerical and experimental results on the characteristic flow field variables for the bounded Rayleigh-Taylor instability with injection through the bounding horizontal surface for Run #W140. These results include: the evolution of the liquid film thickness, the liquid film surface perturbation geometry, the liquid droplet formation and detachment time, the equivalent size for detached droplets, and the time history of the penetration depth.

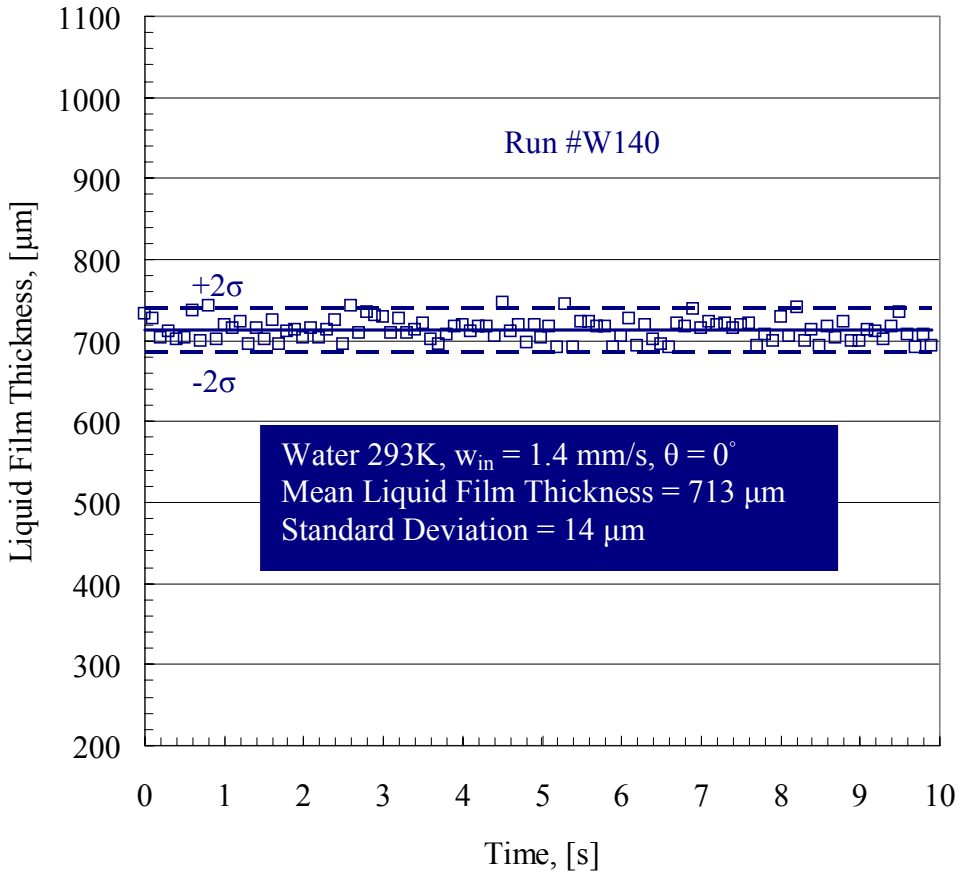

Figure B.17 Transient variation of the unperturbed liquid film thickness for Run #W140.

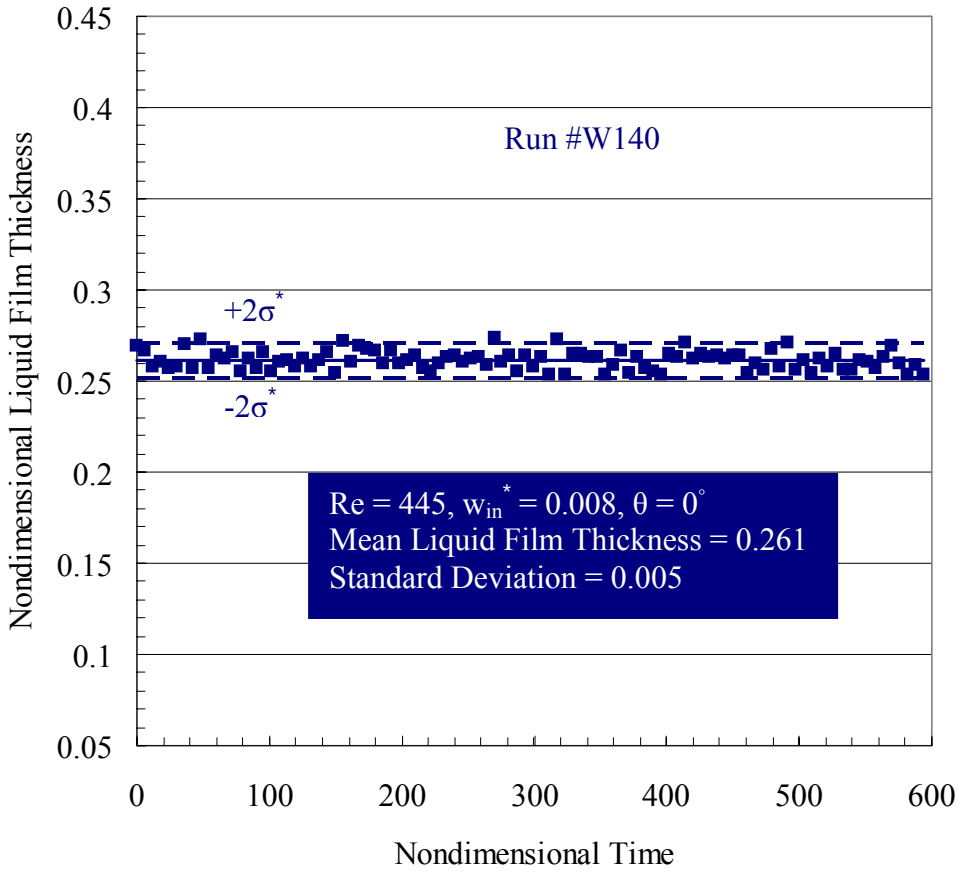

Figure B.18 The unperturbed liquid film thickness normalized by l as a function of time normalized by t_o for Run #W140.

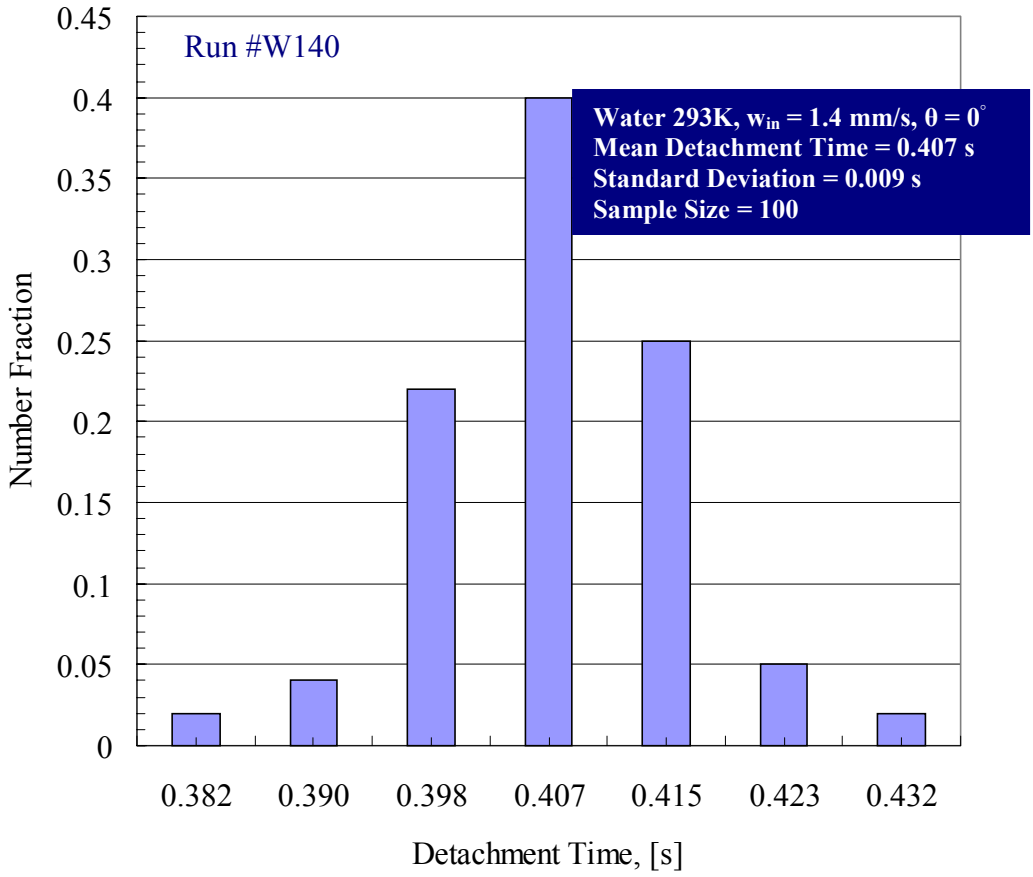

Figure B.19 Experimental data for the distribution of the detachment times carried out for a horizontal surface (Run #W140).

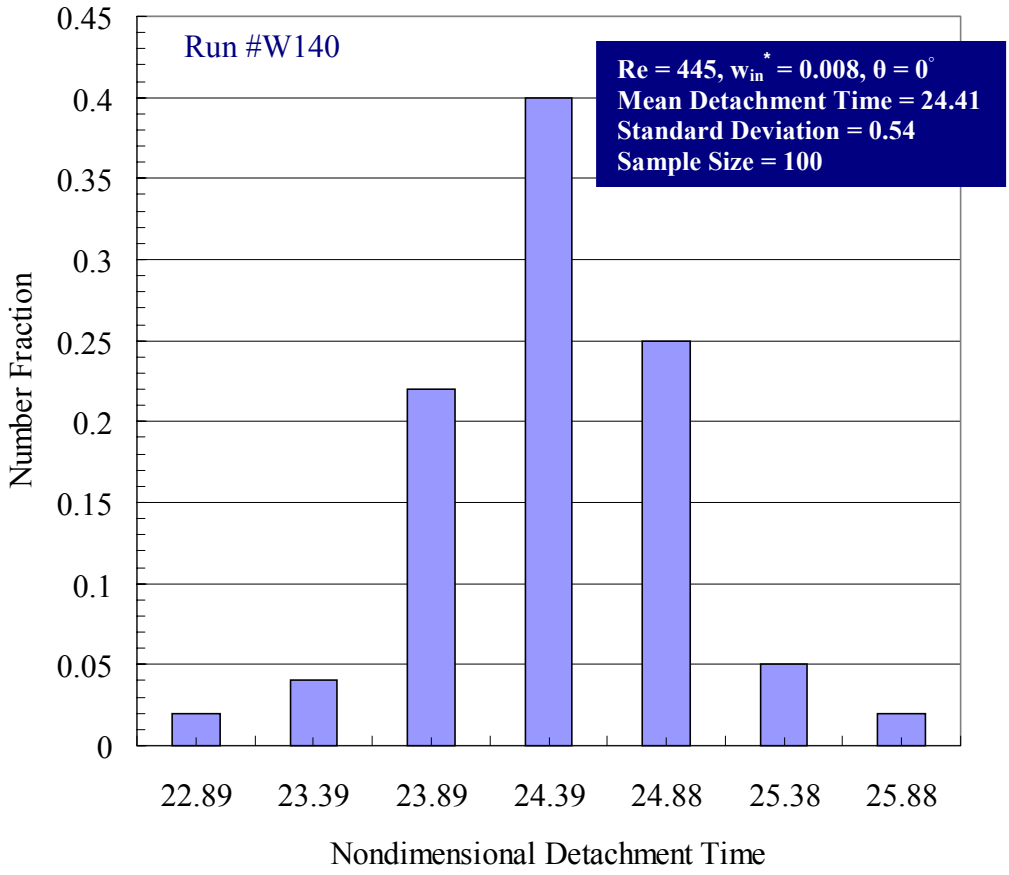

Figure B.20 Experimental data for the distribution of the nondimensional detachment time carried out for a horizontal surface (Run #W140).

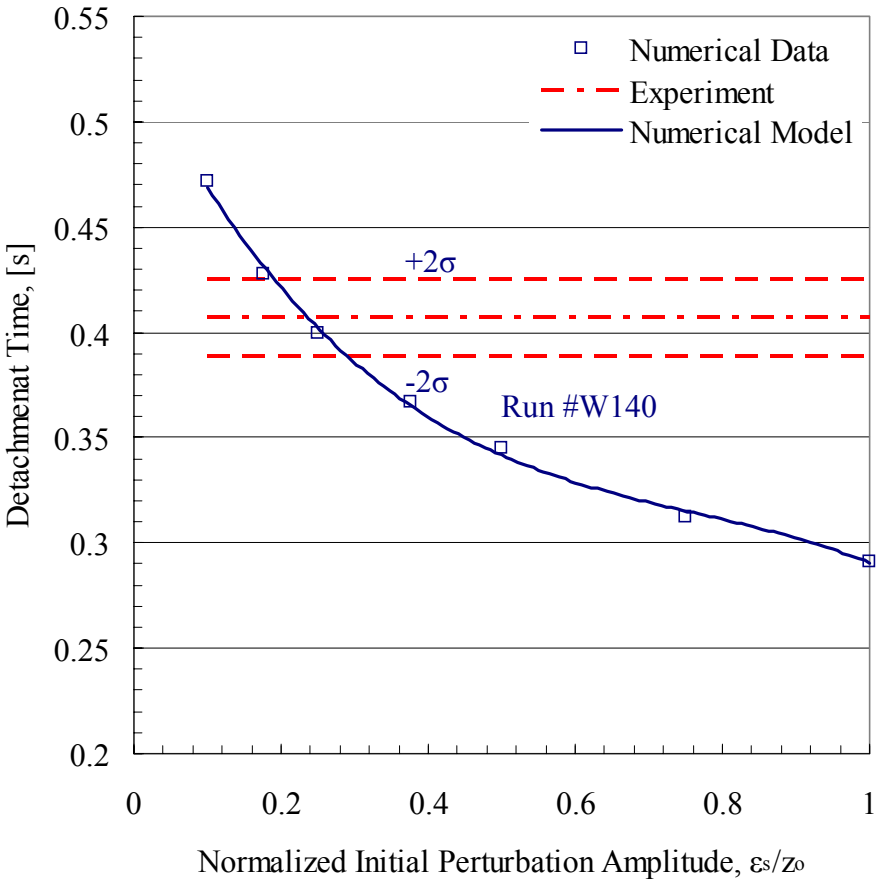

Figure B.21 Numerical and experimental data for the variation of the detachment time with the normalized initial perturbation amplitude carried out for a horizontal surface (Run #W140).

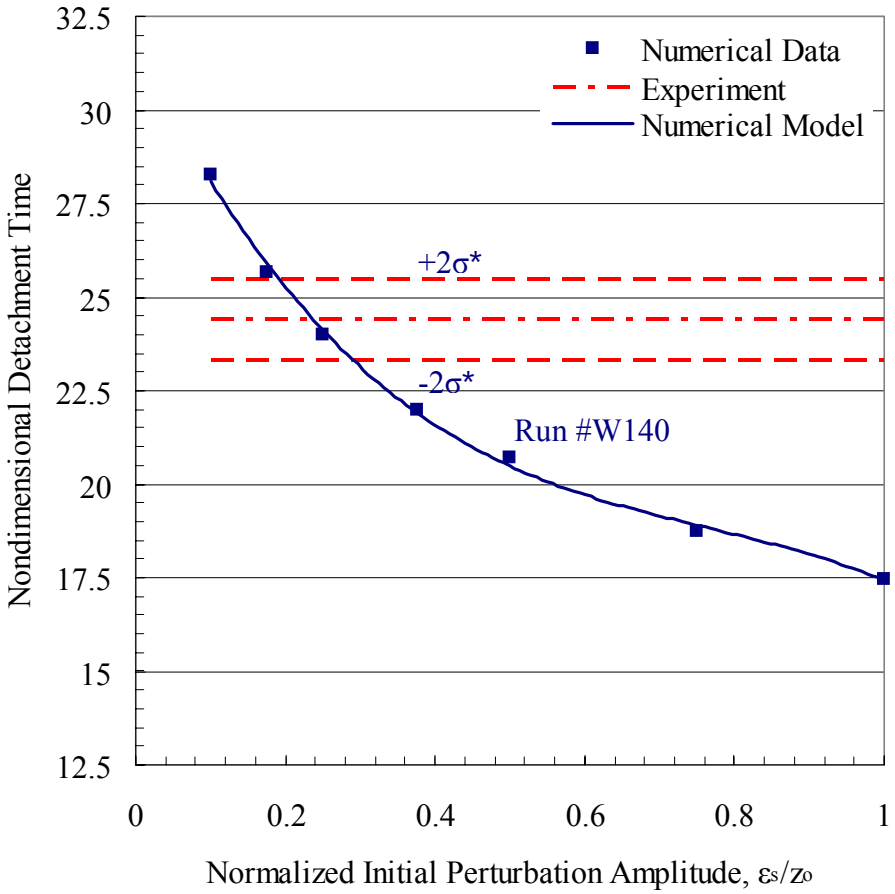

Figure B.22 Numerical and experimental data for the variation of the nondimensional detachment time with the normalized initial perturbation amplitude carried out for a horizontal surface (Run #W140).

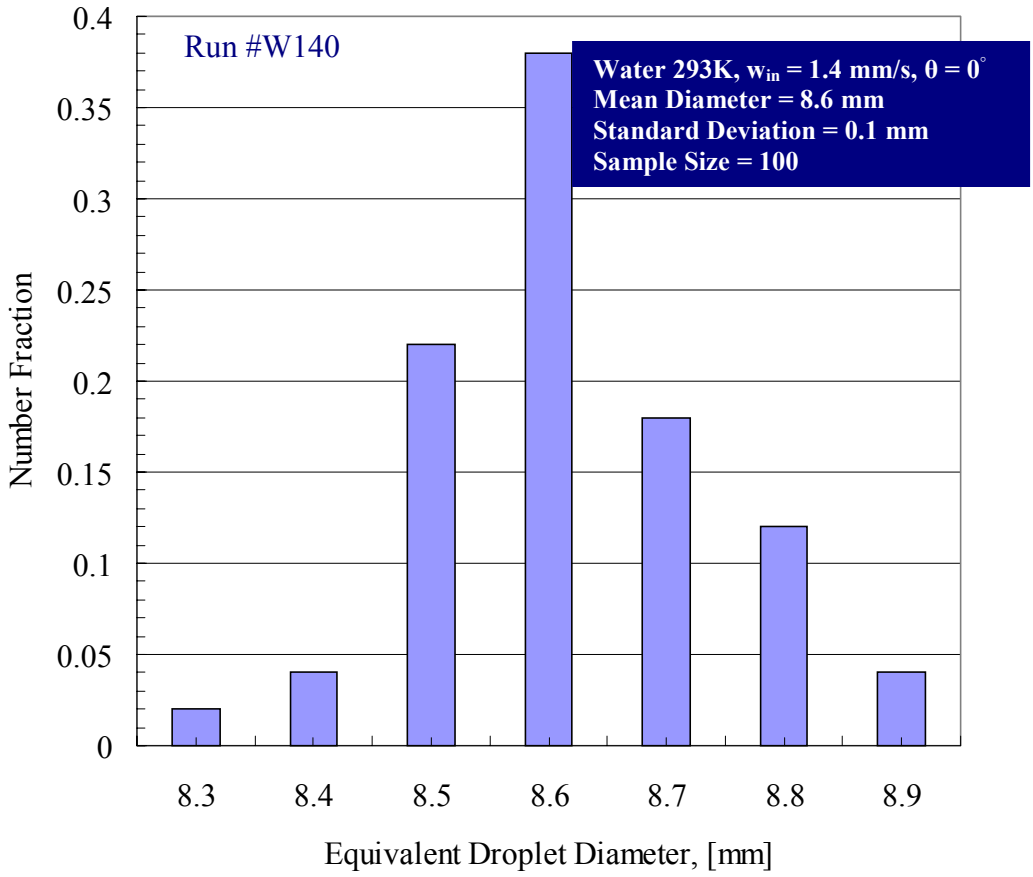

Figure B.23 Experimental data for the distribution of the equivalent droplet diameter carried out for a horizontal surface (Run #W140).

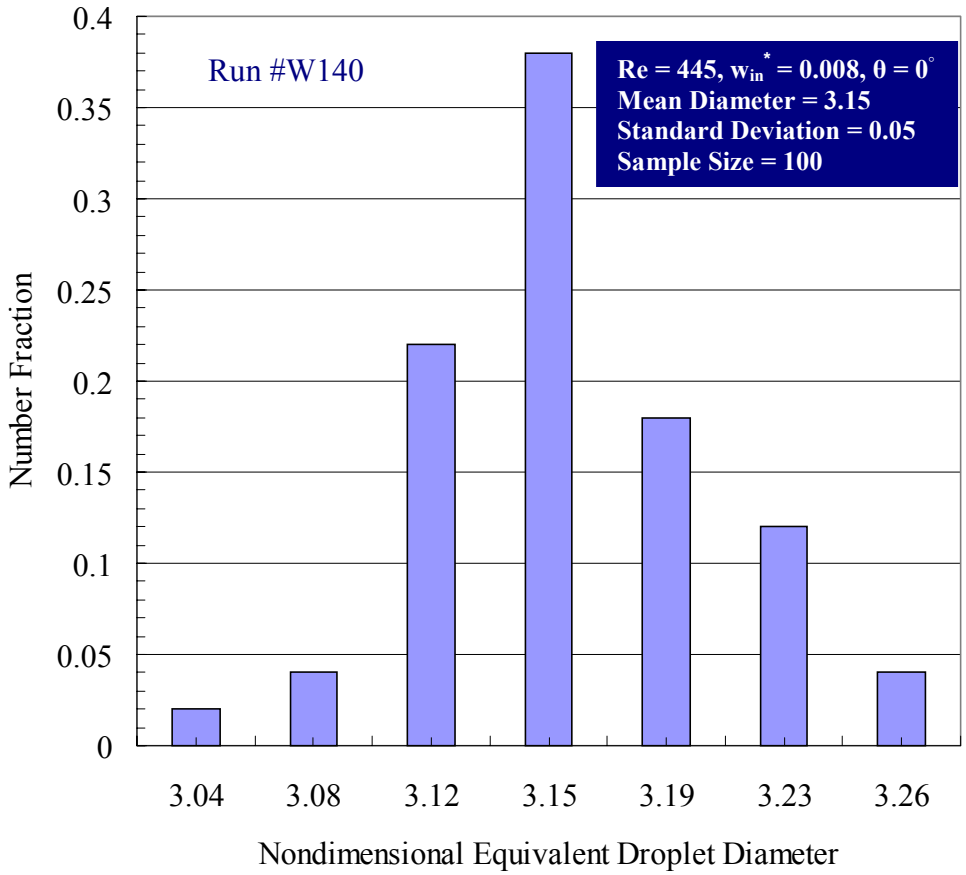

Figure B.24 Experimental data for the distribution of the nondimensional equivalent droplet diameter carried out for a horizontal surface (Run #W140).

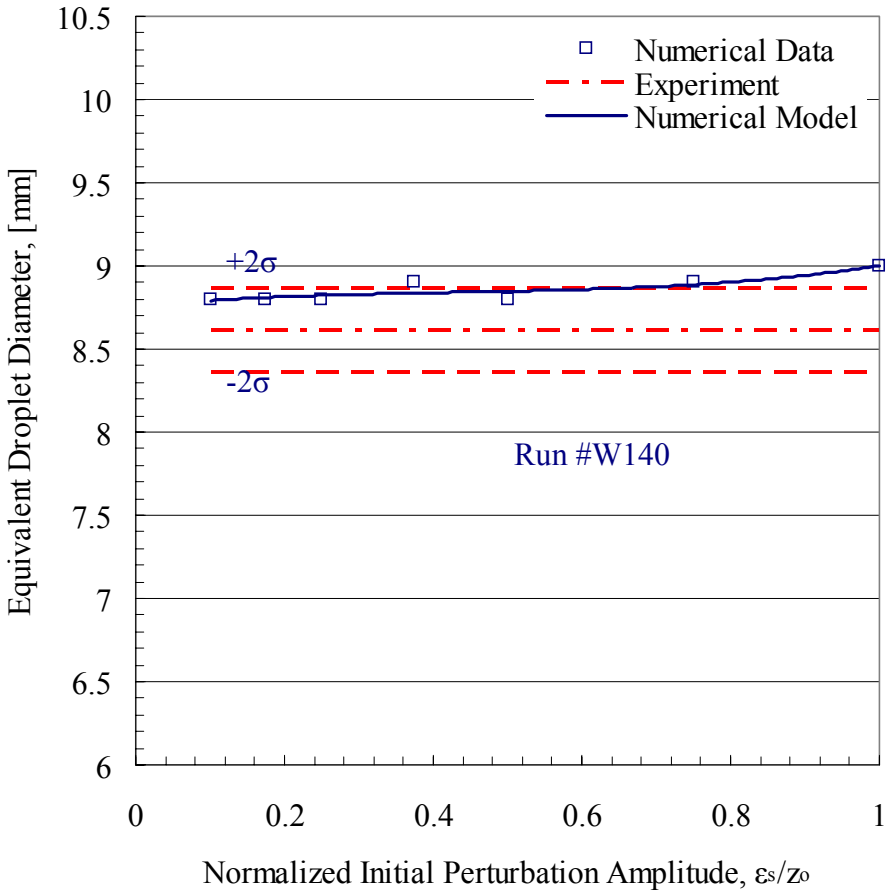

Figure B.25 Numerical and experimental data for the variation of the equivalent droplet diameter with the normalized initial perturbation amplitude carried out for a horizontal surface (Run #W140).

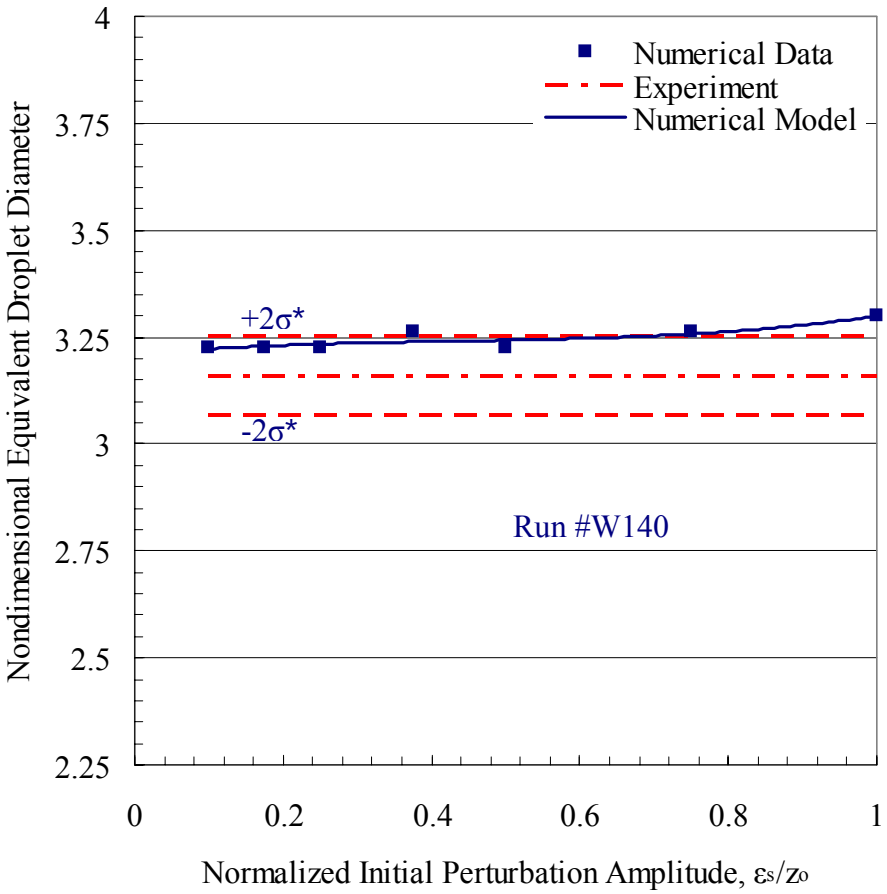

Figure B.26 Numerical and experimental data for the variation of the nondimensional equivalent droplet diameter with the normalized initial perturbation amplitude carried out for a horizontal surface (Run #W140).

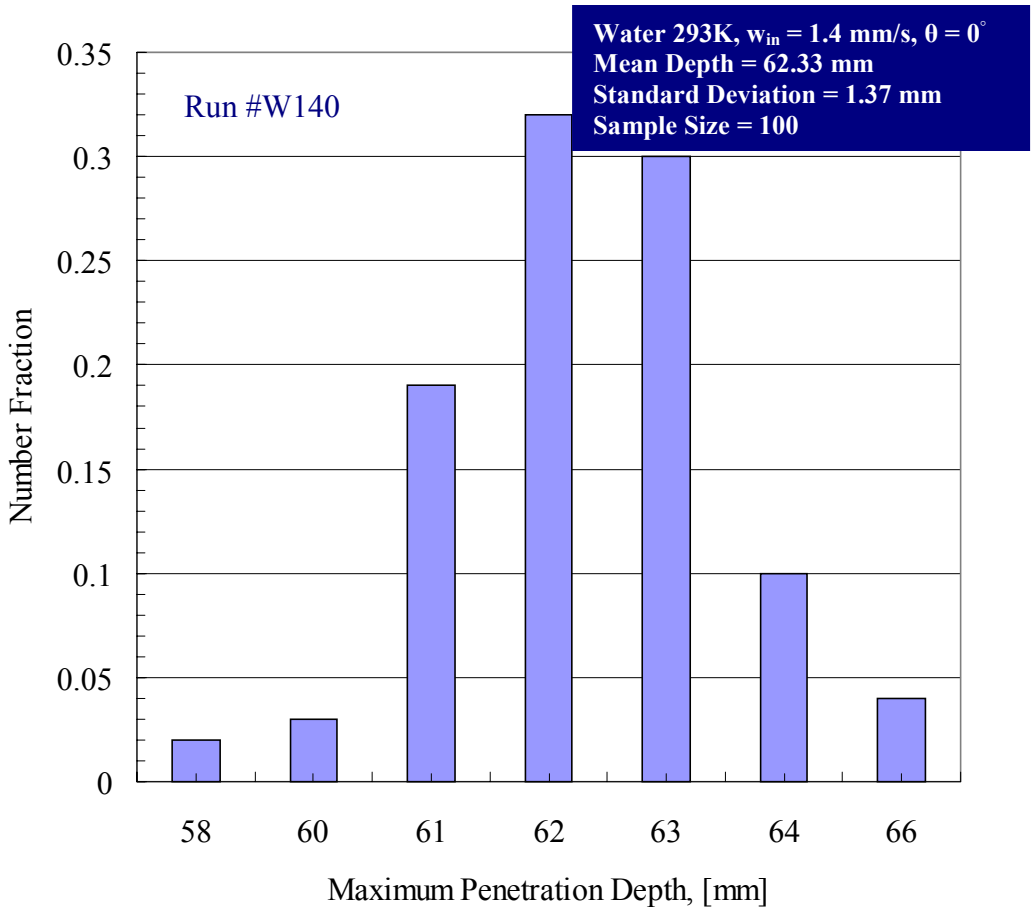

Figure B.27 Experimental data for the distribution of the maximum penetration depth carried out for a horizontal surface (Run #W140).

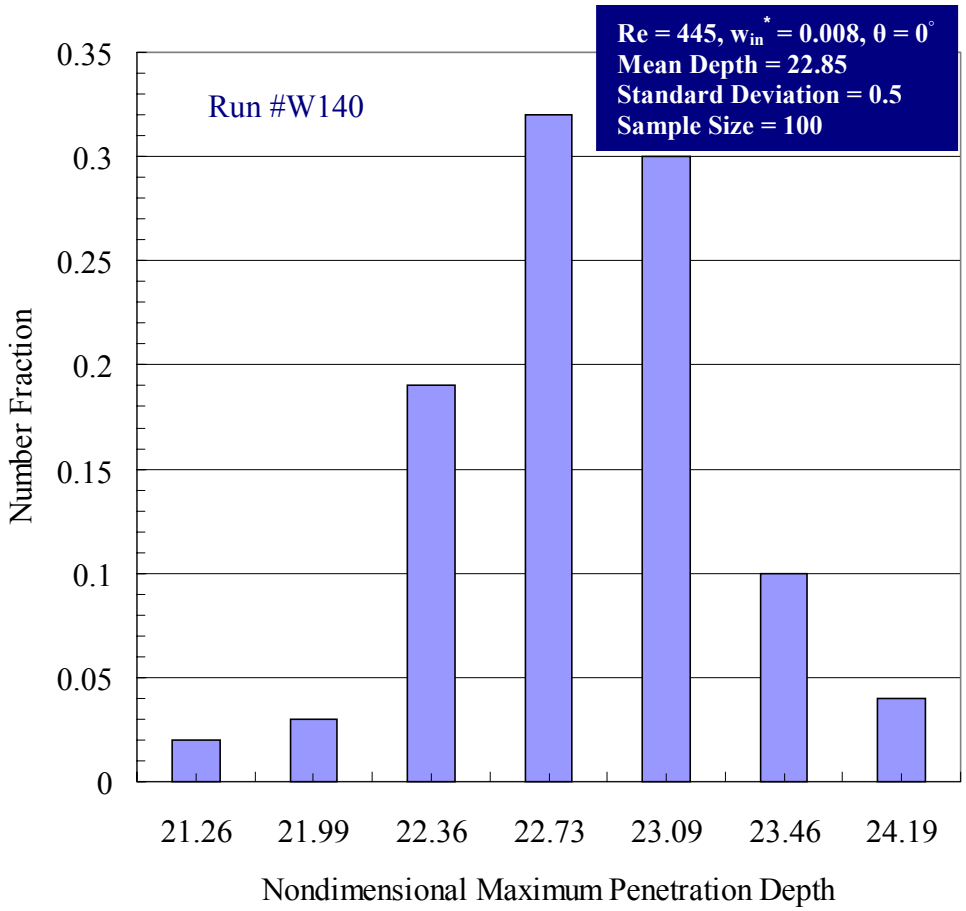

Figure B.28 Experimental data for the distribution of the nondimensional maximum penetration depth carried out for a horizontal surface (Run #W140).

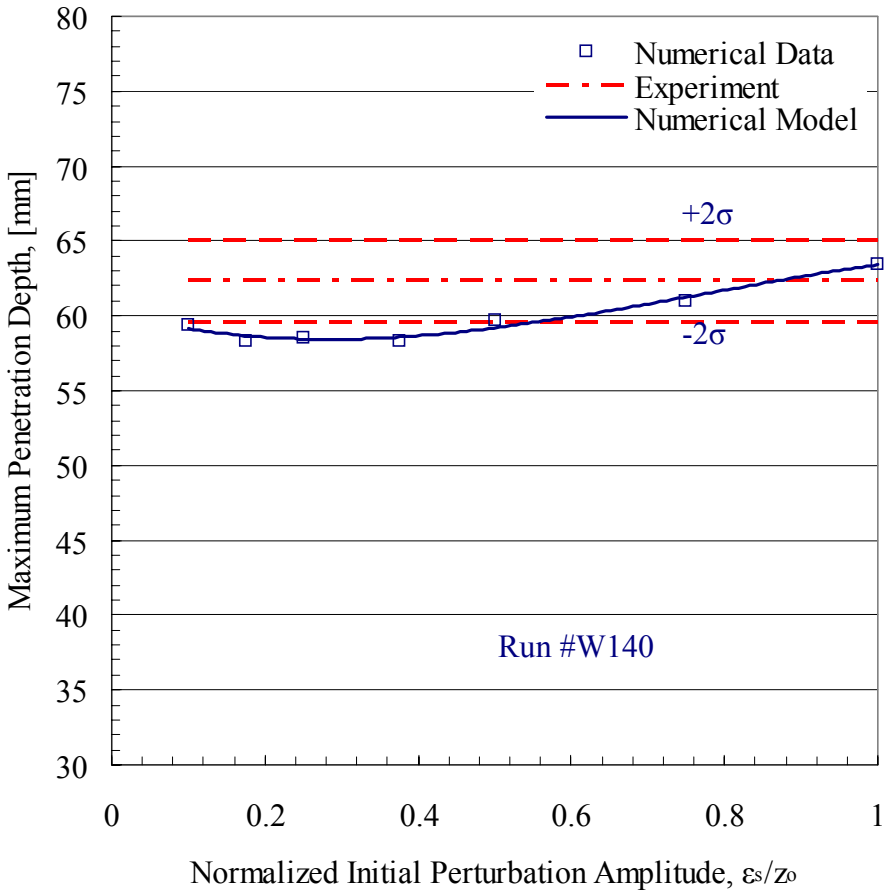

Figure B.29 Numerical and experimental data for the variation of the maximum penetration depth with the normalized initial perturbation amplitude carried out for a horizontal surface (Run #W140).

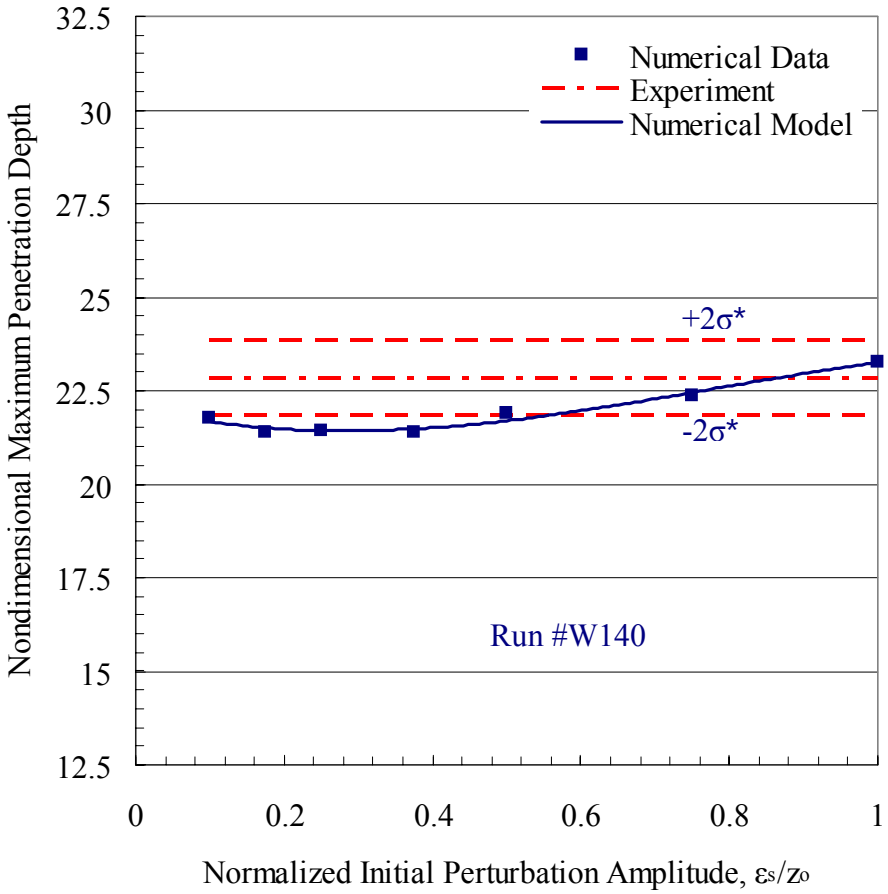

Figure B.30 Numerical and experimental data for the variation of the nondimensional maximum penetration depth with the normalized initial perturbation amplitude carried out for a horizontal surface (Run #W140).

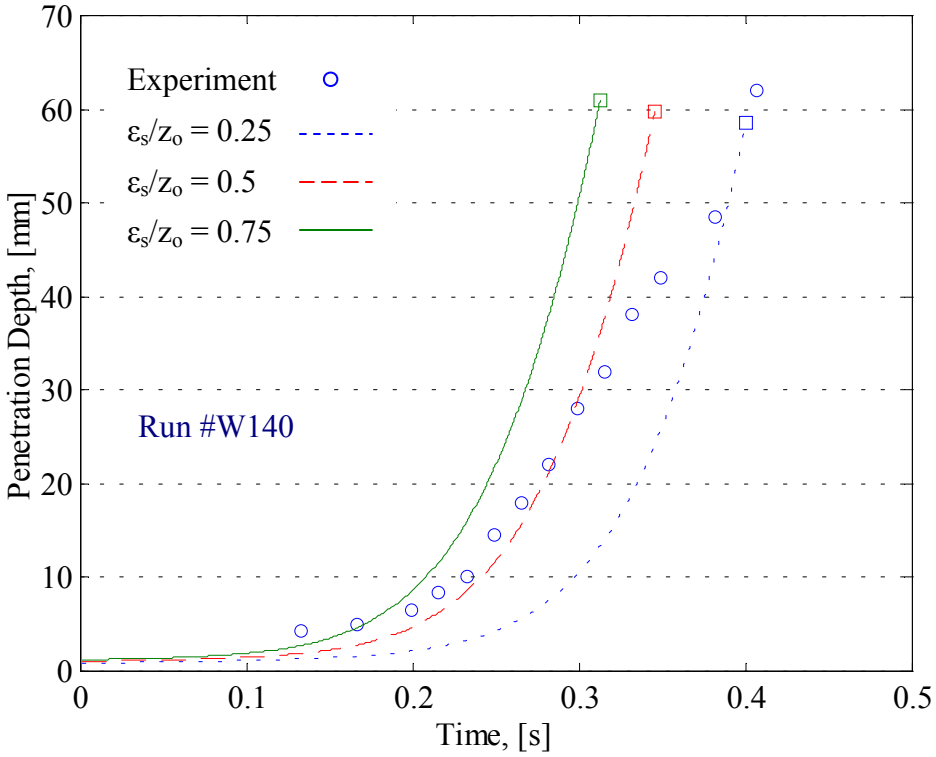

Figure B.31 Numerical and experimental data for the transient variation of the penetration depth carried out for a horizontal surface (Run #W140).

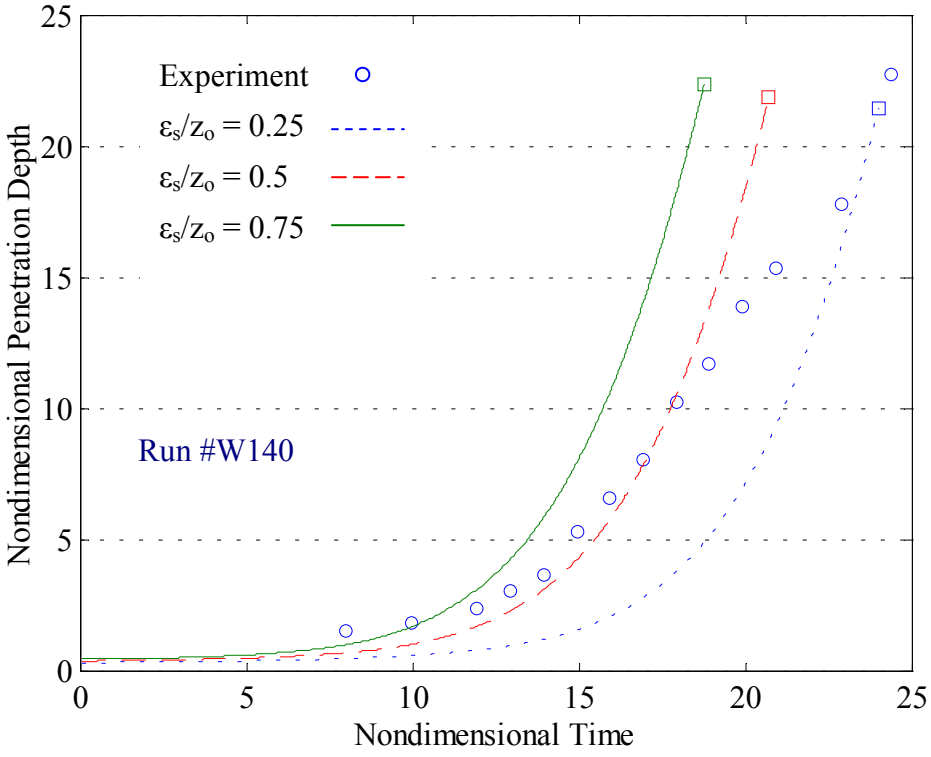

Figure B.32 Numerical and experimental data for the transient variation of the nondimensional penetration depth carried out for a horizontal surface (Run #W140).

B.3 Numerical and Experimental Results for Run #W170

This section details the numerical and experimental results on the characteristic flow field variables for the bounded Rayleigh-Taylor instability with injection through the bounding horizontal surface for Run #W170. These results include: the evolution of the liquid film thickness, the liquid film surface perturbation geometry, the liquid droplet formation and detachment time, the equivalent size for detached droplets, and the time history of the penetration depth.

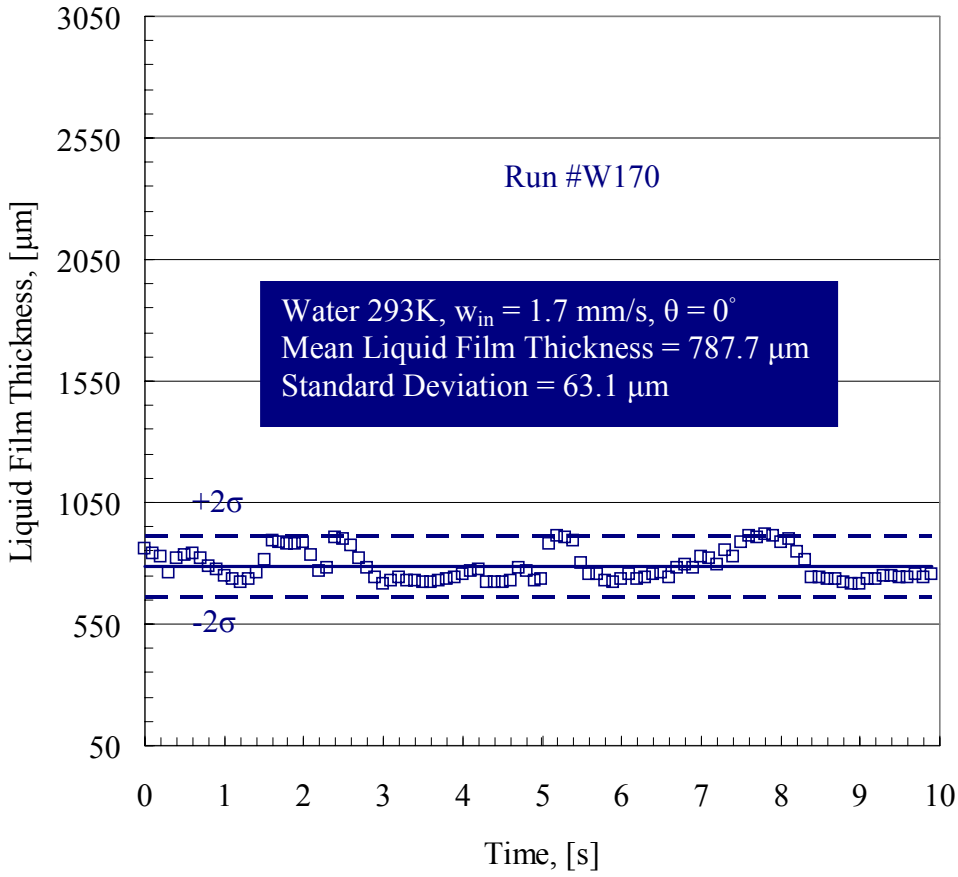

Figure B.33 Transient variation of the unperturbed liquid film thickness for Run #W170.

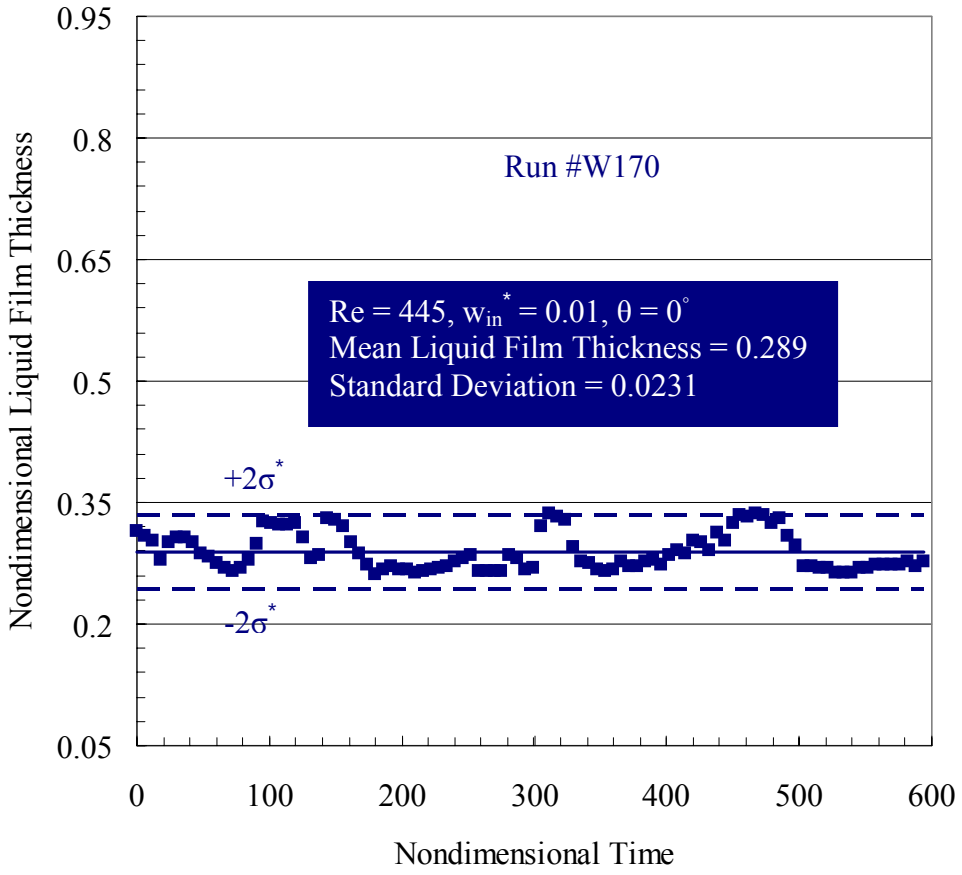

Figure B.34 The unperturbed liquid film thickness normalized by l as a function of time normalized by t_o for Run #W170.

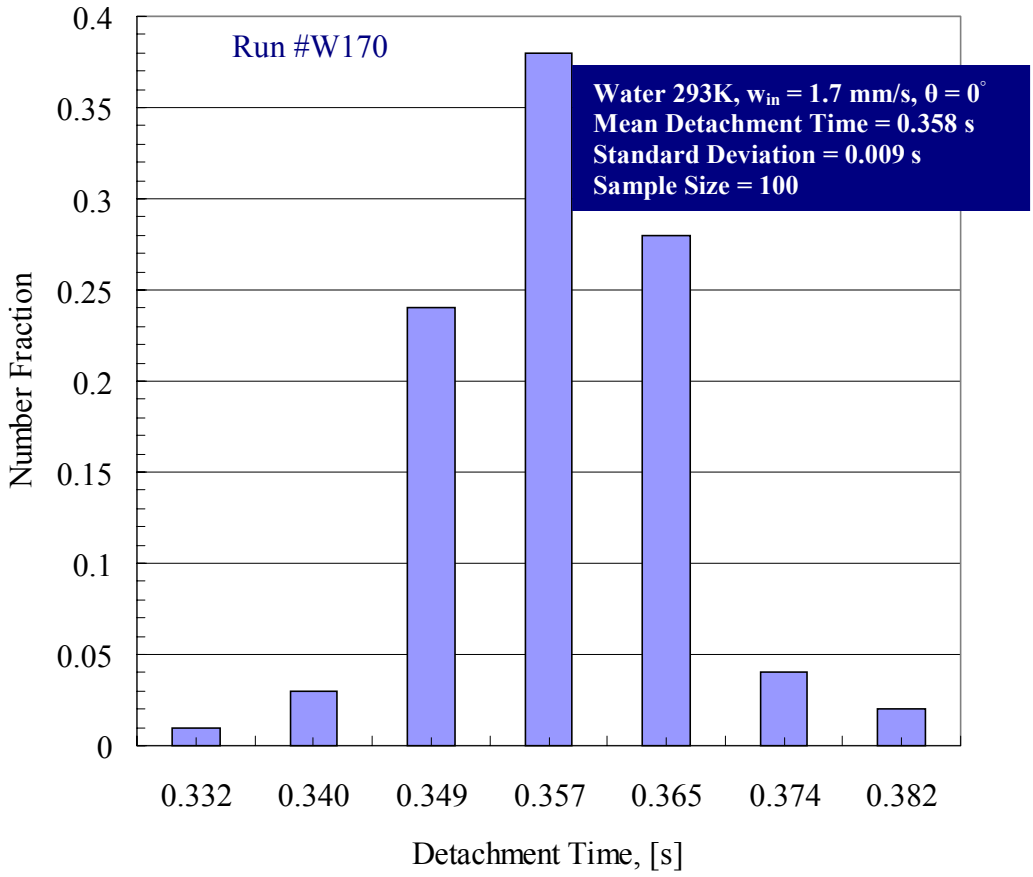

Figure B.35 Experimental data for the distribution of the detachment times carried out for a horizontal surface (Run #W170).

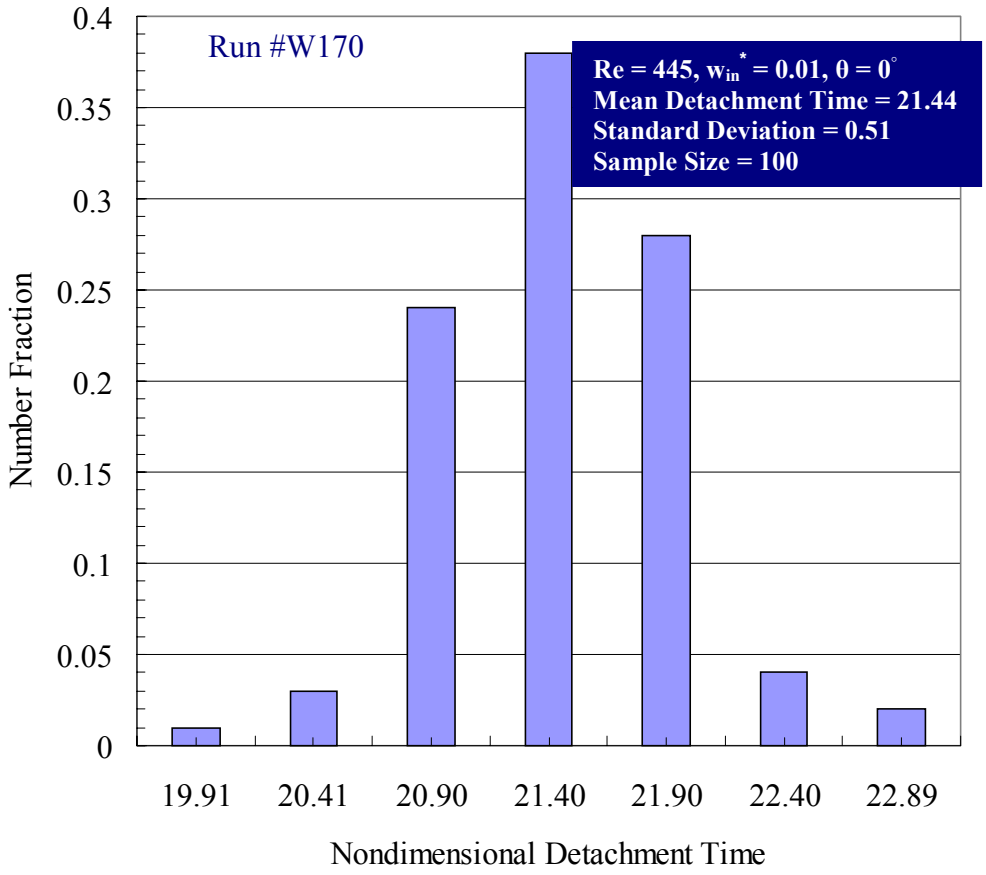

Figure B.36 Experimental data for the distribution of the nondimensional detachment time carried out for a horizontal surface (Run #W170).

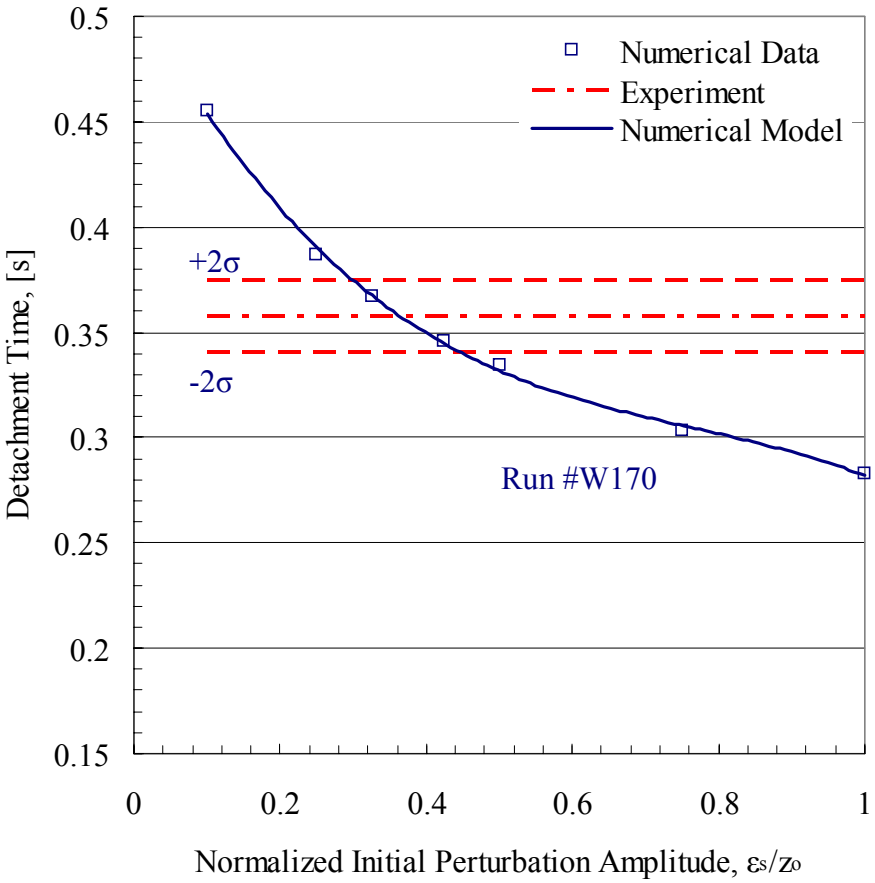

Figure B.37 Numerical and experimental data for the variation of the detachment time with the normalized initial perturbation amplitude carried out for a horizontal surface (Run #W170).

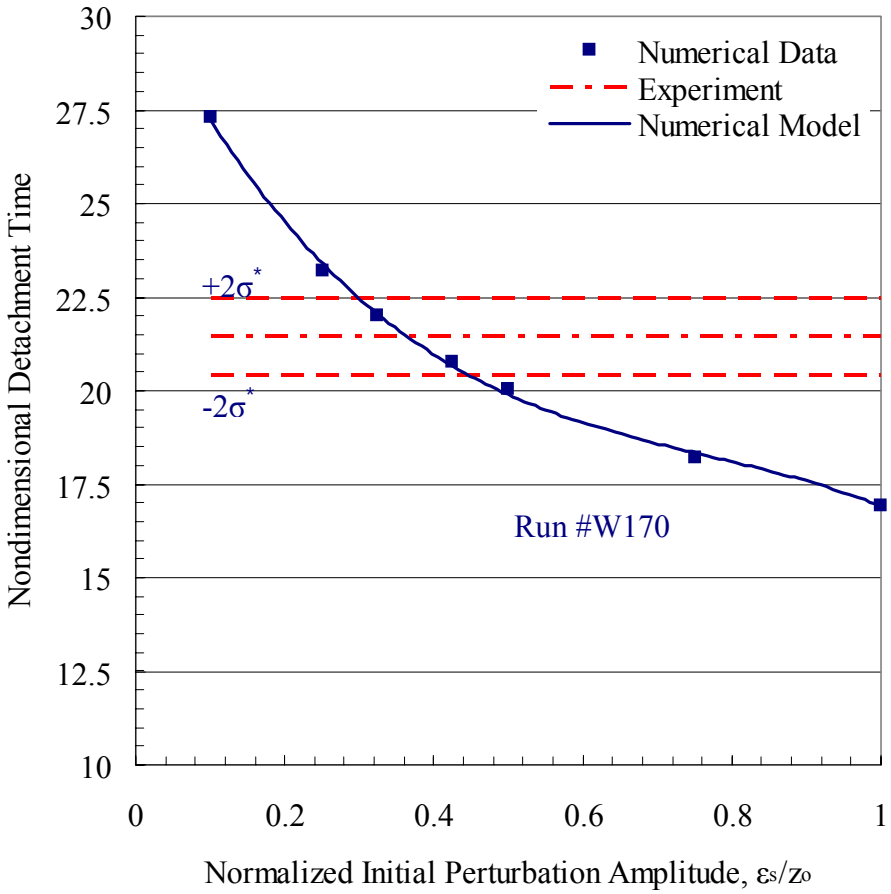

Figure B.38 Numerical and experimental data for the variation of the nondimensional detachment time with the normalized initial perturbation amplitude carried out for a horizontal surface (Run #W170).

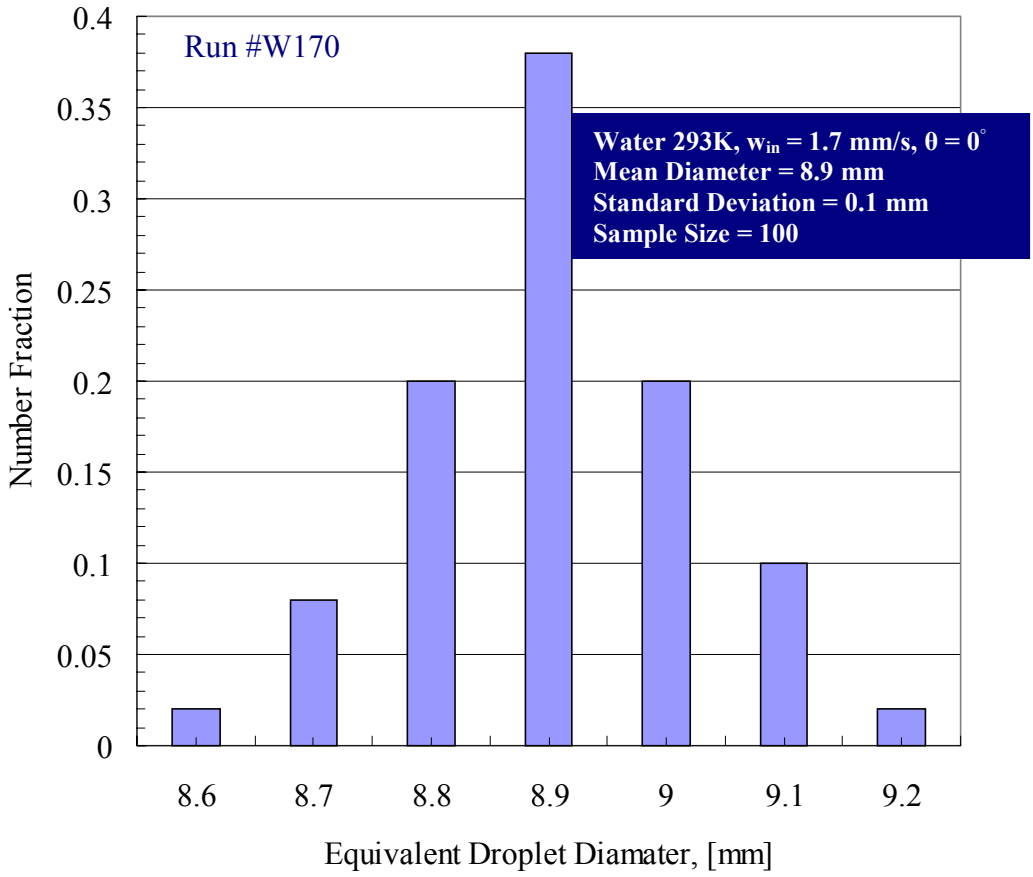

Figure B.39 Experimental data for the distribution of the equivalent droplet diameter carried out for a horizontal surface (Run #W170).

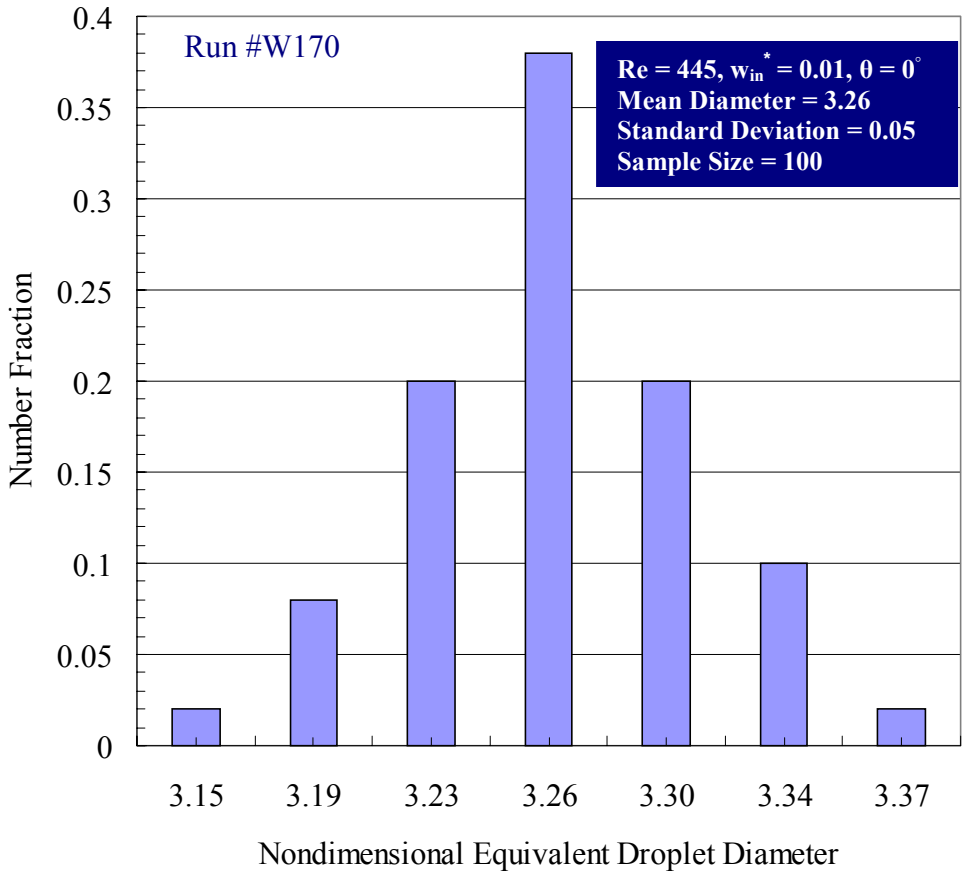

Figure B.40 Experimental data for the distribution of the nondimensional equivalent droplet diameter carried out for a horizontal surface (Run #W170).

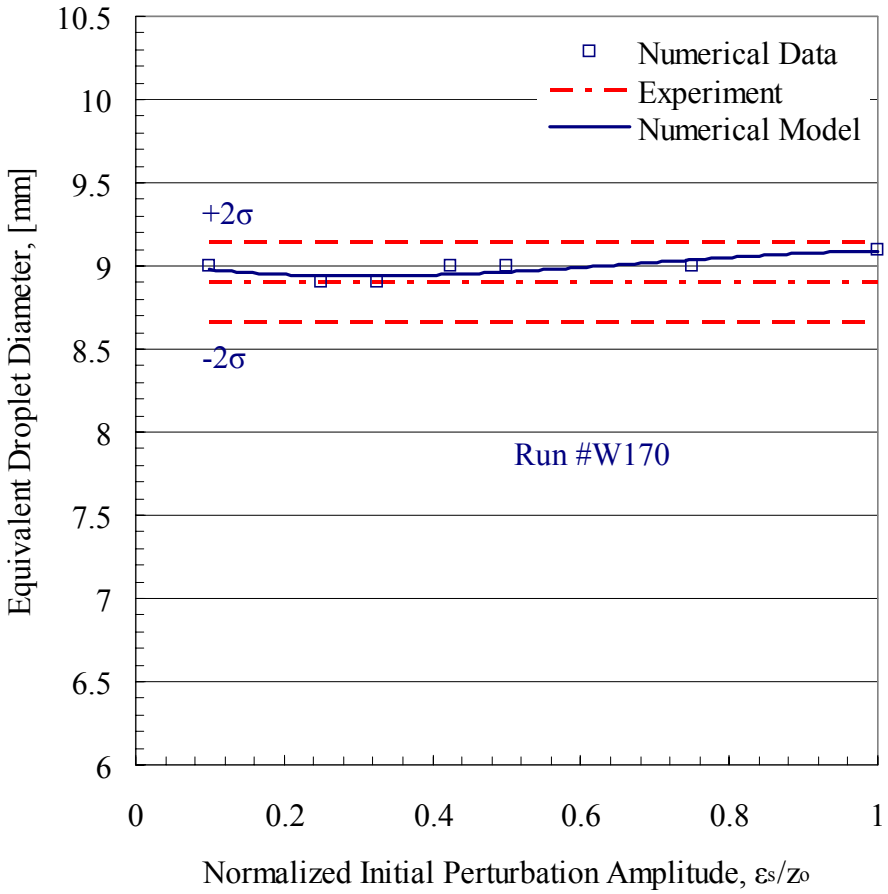

Figure B.41 Numerical and experimental data for the variation of the equivalent droplet diameter with the normalized initial perturbation amplitude carried out for a horizontal surface (Run #W170).

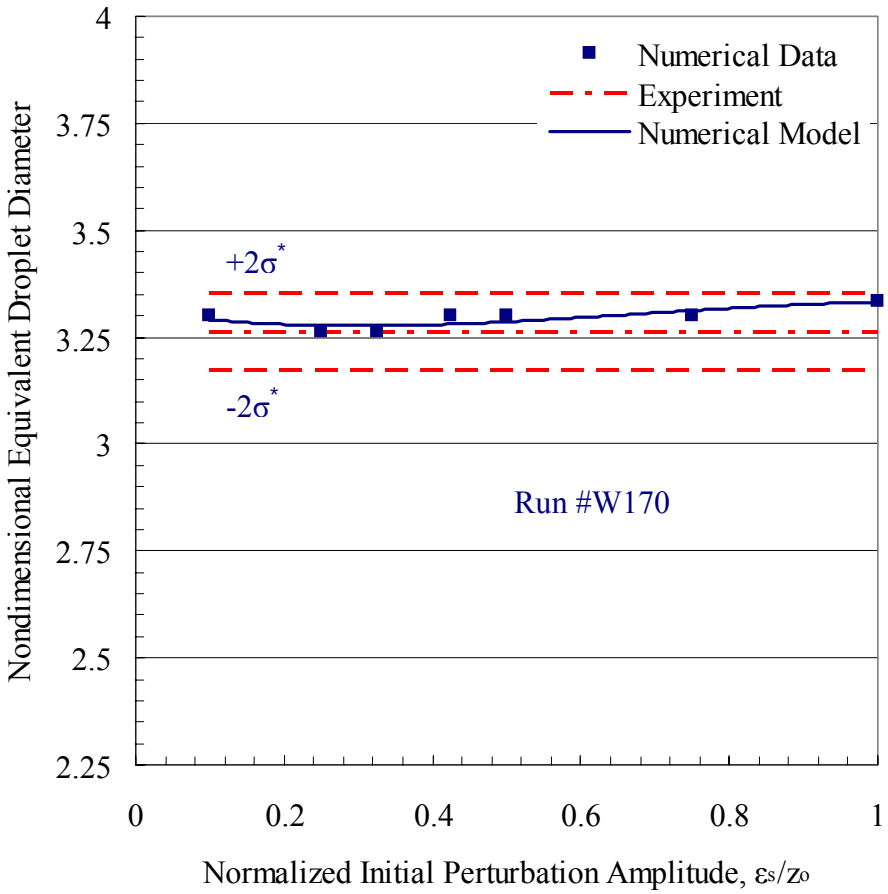

Figure B.42 Numerical and experimental data for the variation of the nondimensional equivalent droplet diameter with the normalized initial perturbation amplitude carried out for a horizontal surface (Run #W170).

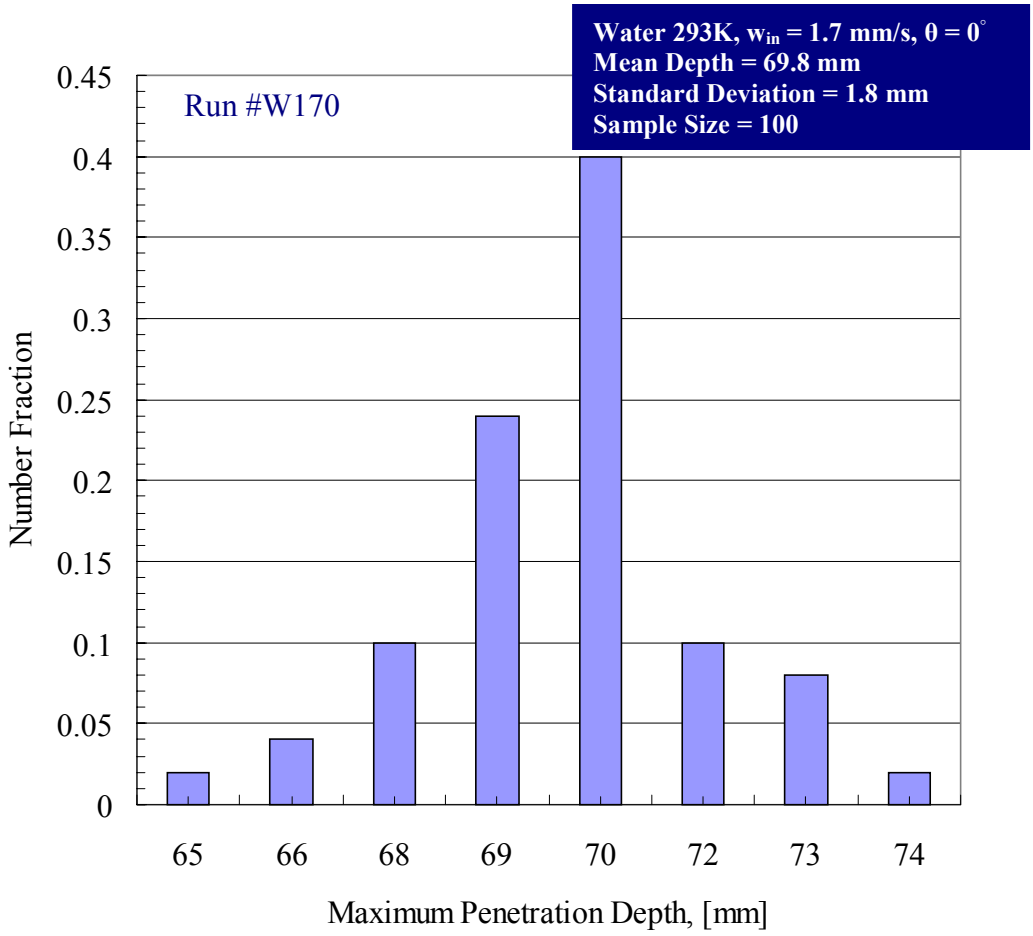

Figure B.43 Experimental data for the distribution of the maximum penetration depth carried out for a horizontal surface (Run #W170).

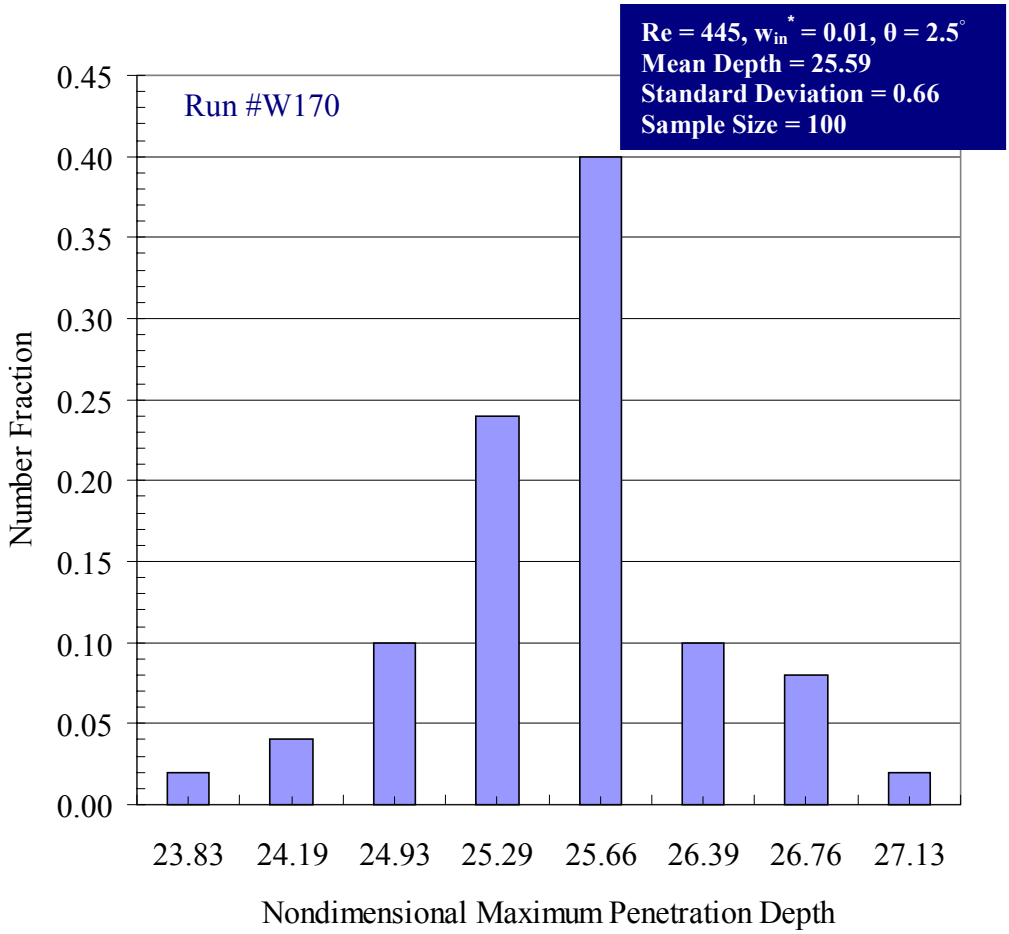

Figure B.44 Experimental data for the distribution of the nondimensional maximum penetration depth carried out for a horizontal surface (Run #W170).

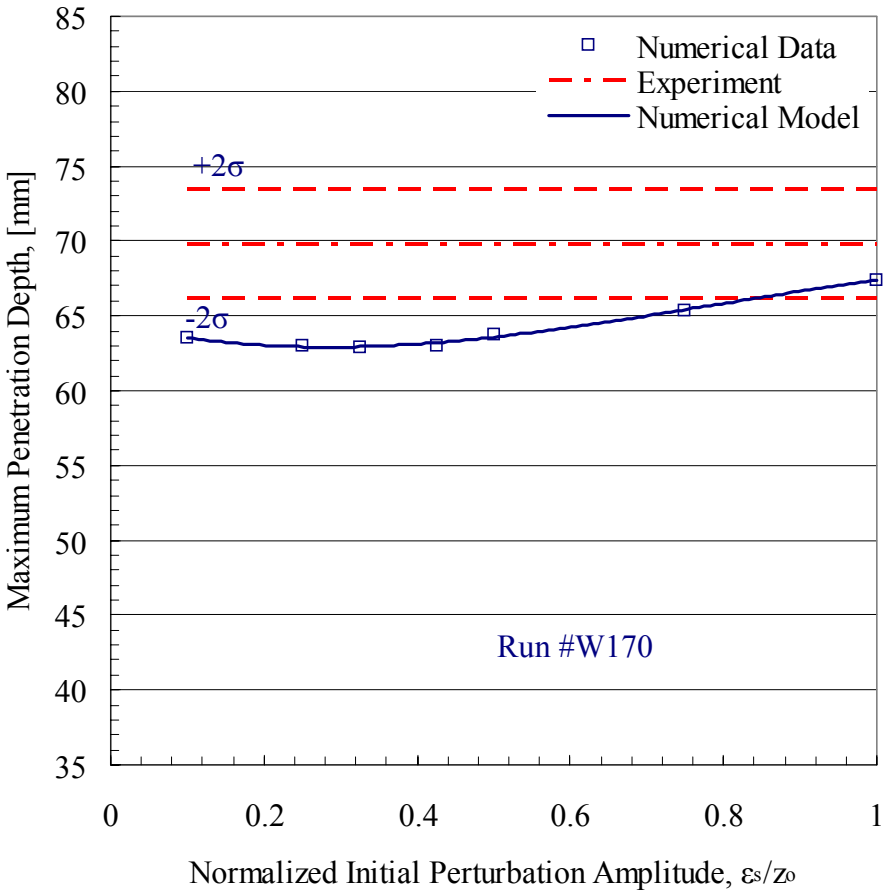

Figure B.45 Numerical and experimental data for the variation of the maximum penetration depth with the normalized initial perturbation amplitude carried out for a horizontal surface (Run #W170).

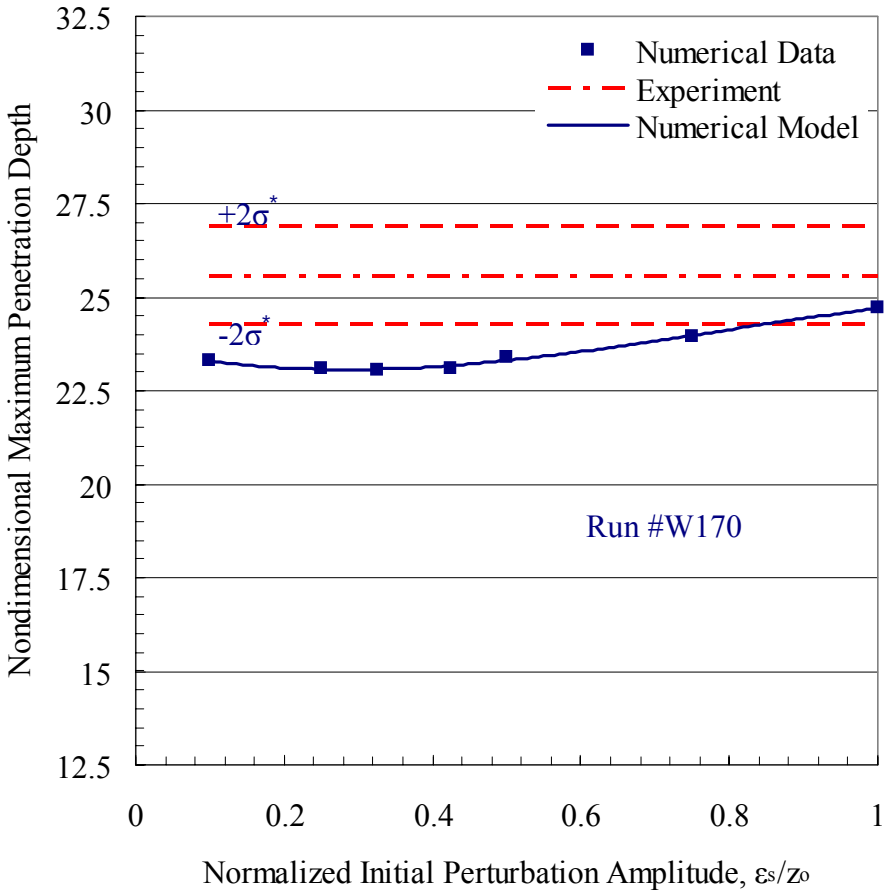

Figure B.46 Numerical and experimental data for the variation of the nondimensional maximum penetration depth with the normalized initial perturbation amplitude carried out for a horizontal surface (Run #W170).

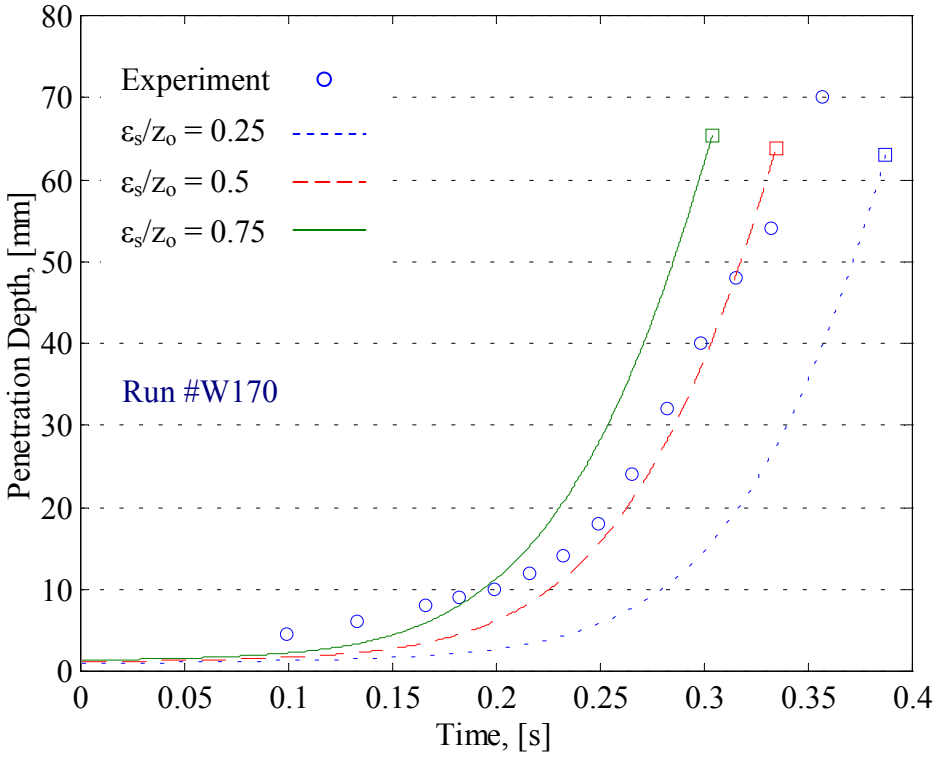

Figure B.47 Numerical and experimental data for the transient variation of the penetration depth carried out for a horizontal surface (Run #W170).

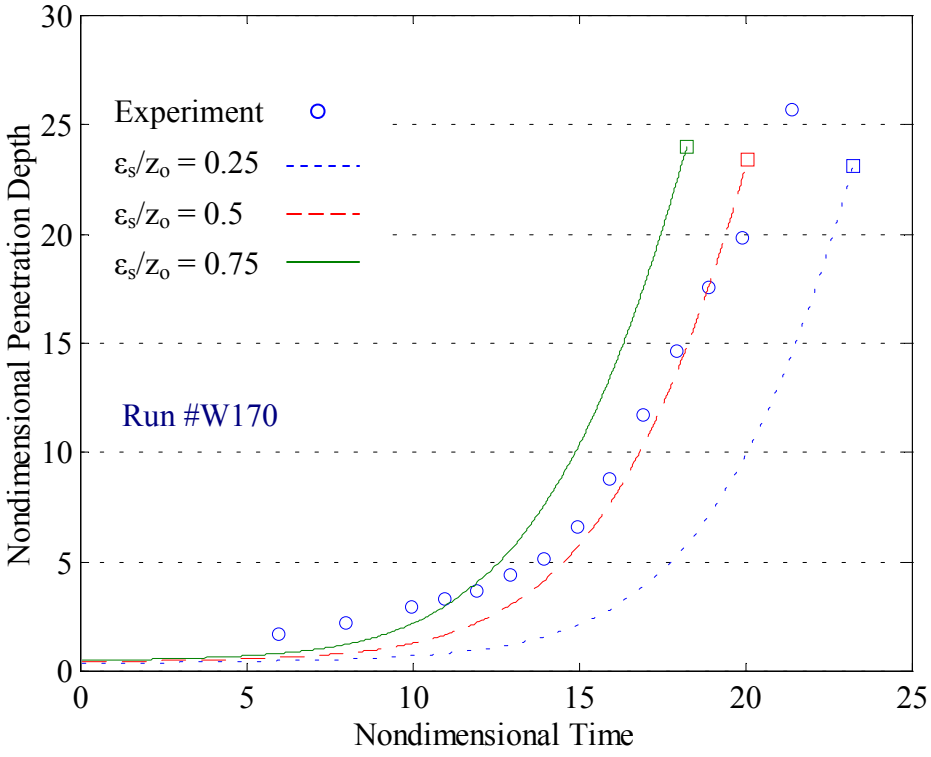

Figure B.48 Numerical and experimental data for the transient variation of the nondimensional penetration depth carried out for a horizontal surface (Run #W170).

B.4 Numerical and Experimental Results for Run #G170

This section details the numerical and experimental results on the characteristic flow field variables for the bounded Rayleigh-Taylor instability with injection through the bounding horizontal surface for Run #G170. These results include: the evolution of the liquid film thickness, the liquid film surface perturbation geometry, the liquid droplet formation and detachment time, the equivalent size for detached droplets, and the time history of the penetration depth.

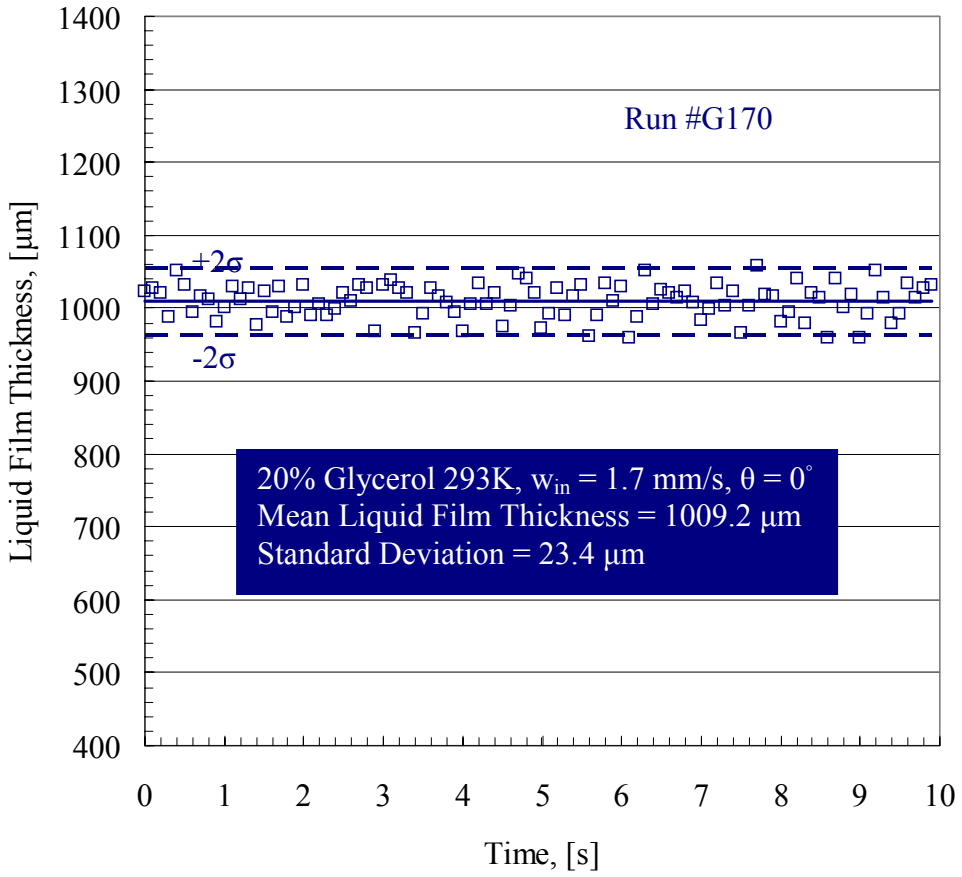

Figure B.49 Transient variation of the unperturbed liquid film thickness for Run #G170.

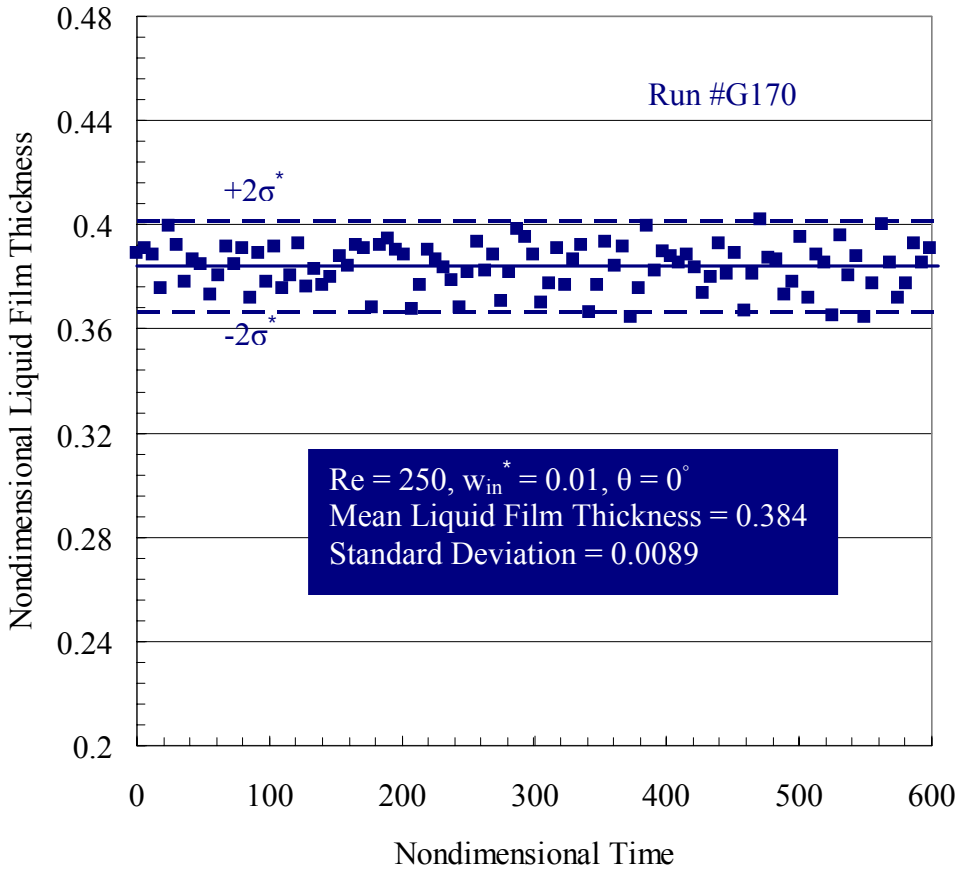

Figure B.50 The unperturbed liquid film thickness normalized by l as a function of time normalized by t_o for Run #G170.

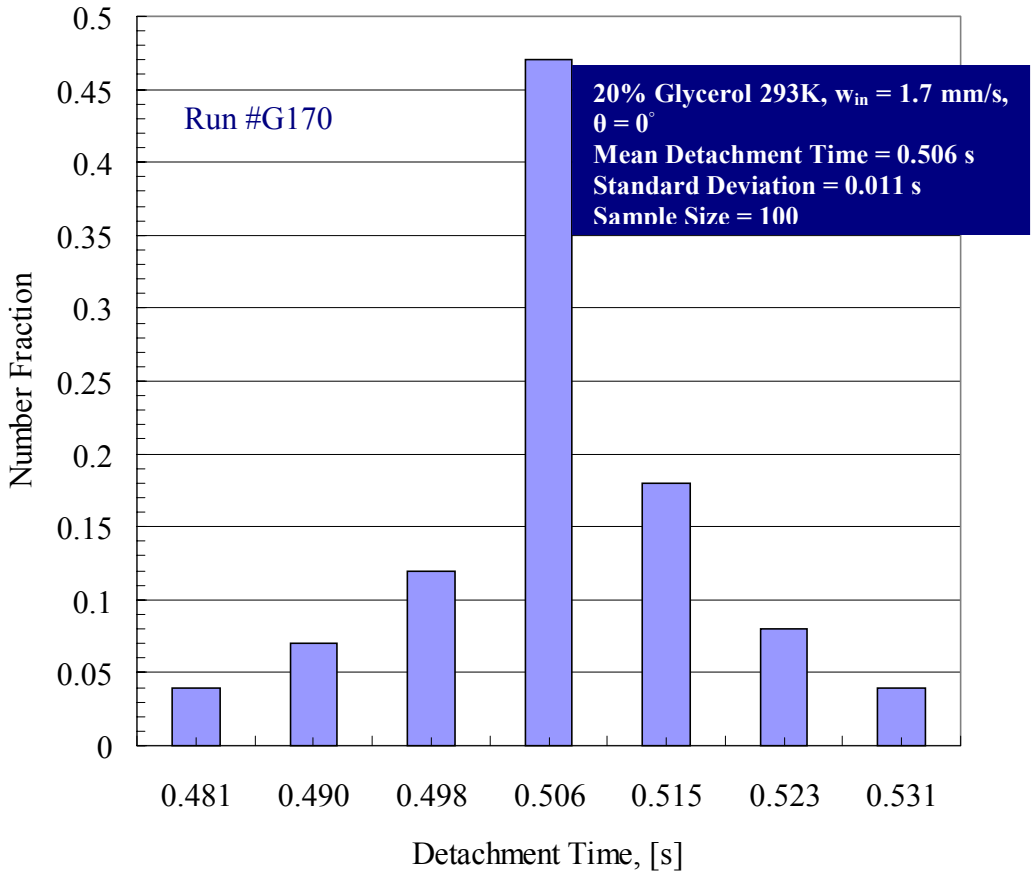

Figure B.51 Experimental data for the distribution of the detachment times carried out for a horizontal surface (Run #G170).

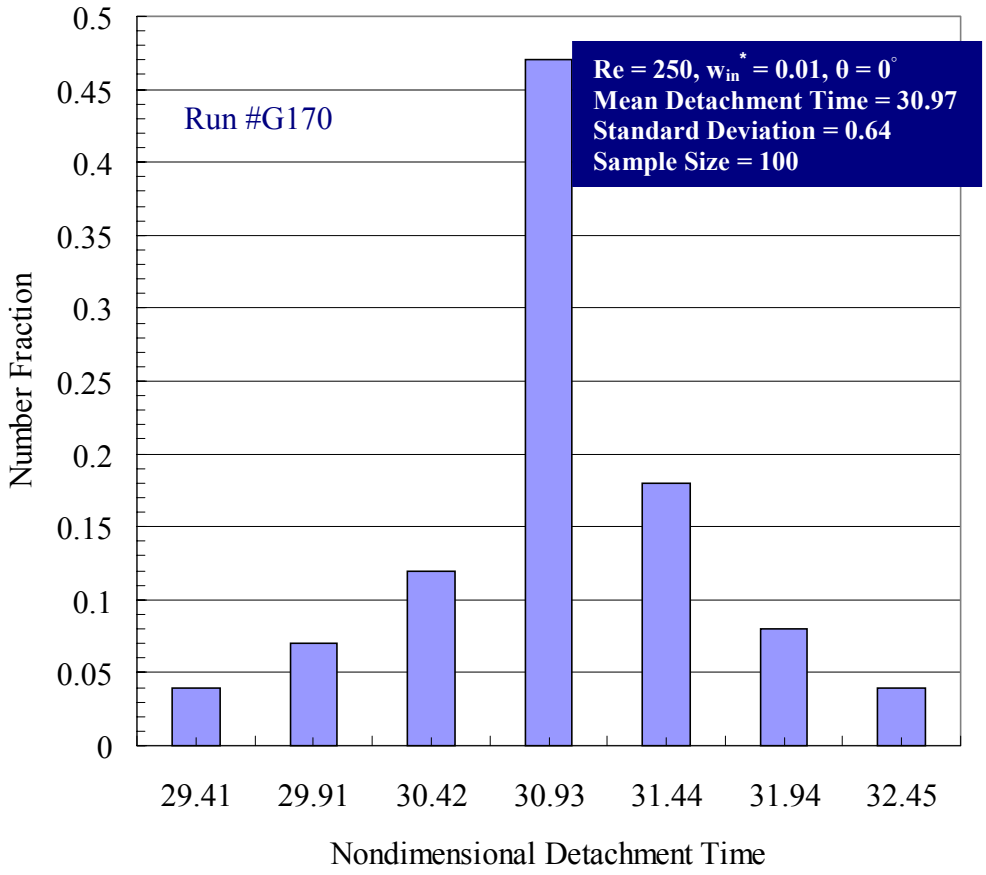

Figure B.52 Experimental data for the distribution of the nondimensional detachment time carried out for a horizontal surface (Run #G170).

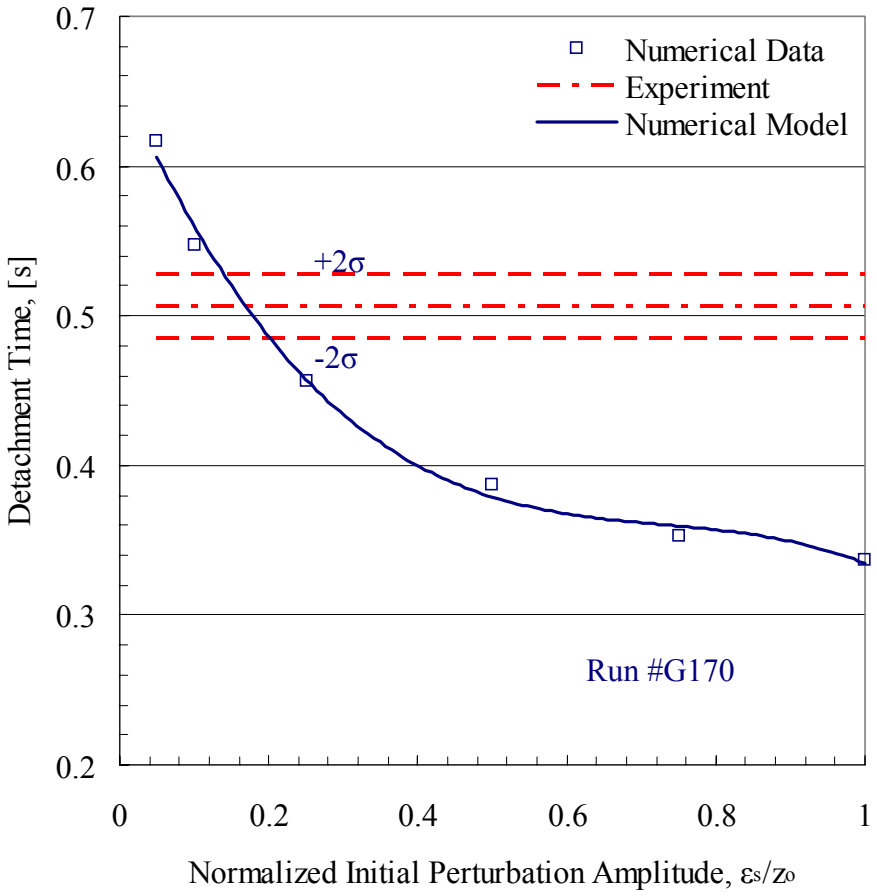

Figure B.53 Numerical and experimental data for the variation of the detachment time with the normalized initial perturbation amplitude carried out for a horizontal surface (Run #G170).

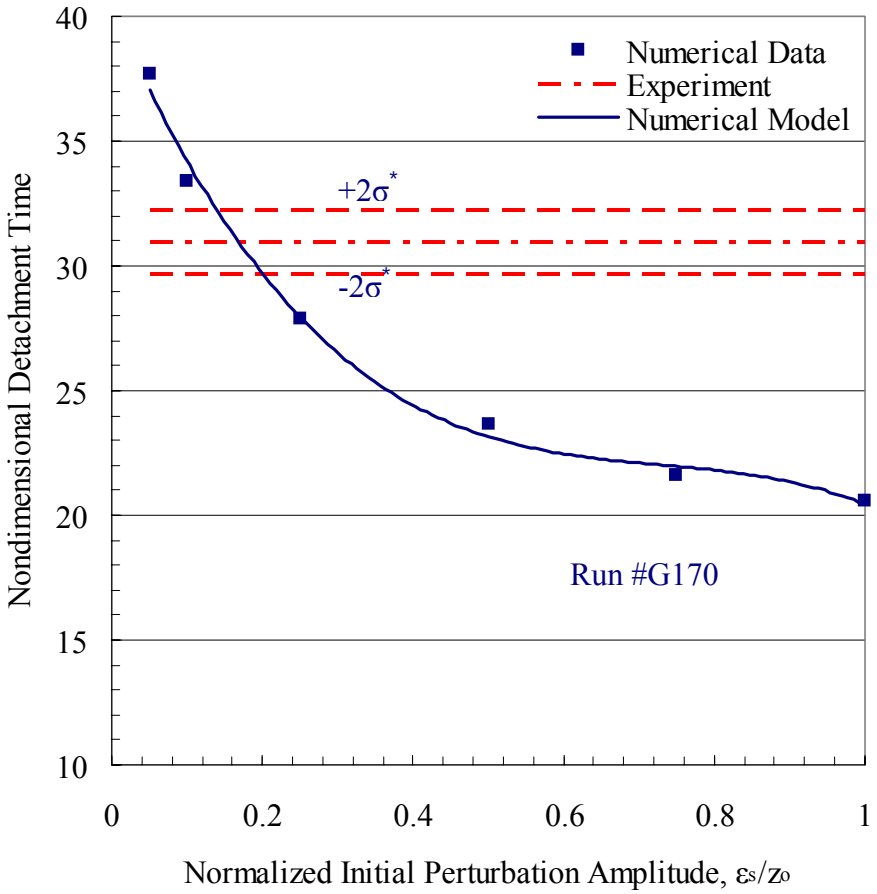

Figure B.54 Numerical and experimental data for the variation of the nondimensional detachment time with the normalized initial perturbation amplitude carried out for a horizontal surface (Run #G170).

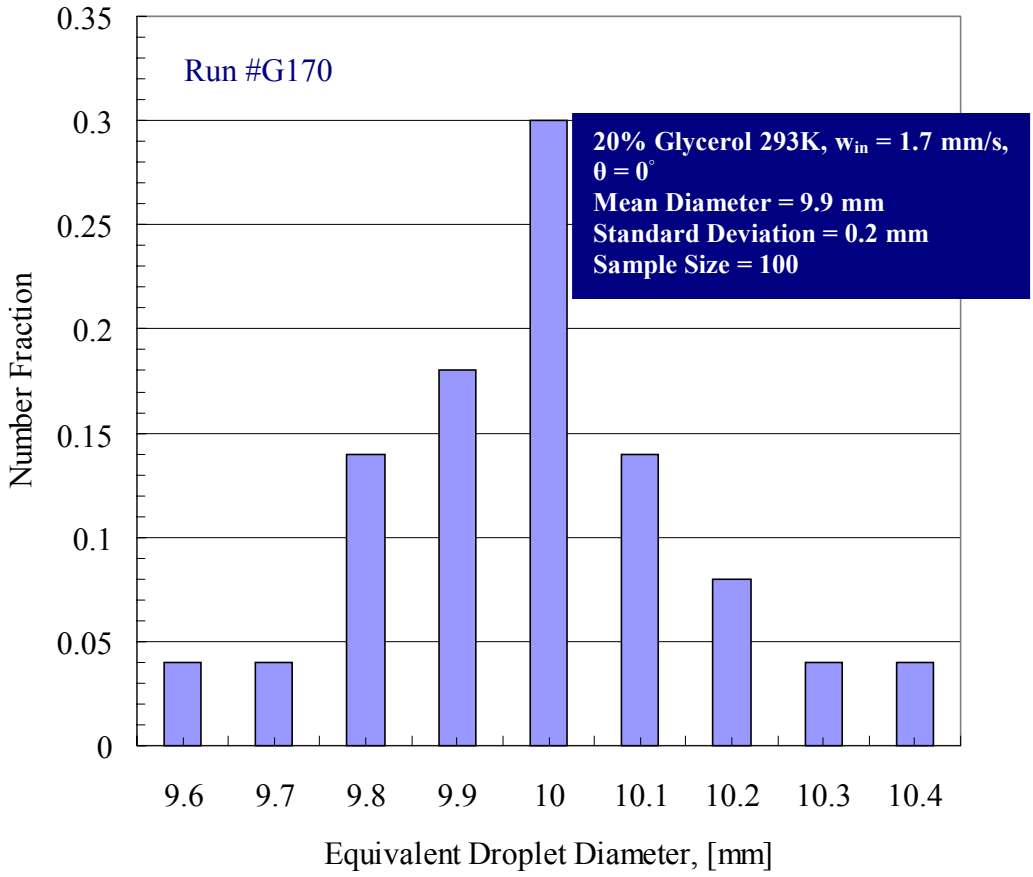

Figure B.55 Experimental data for the distribution of the equivalent droplet diameter carried out for a horizontal surface (Run #G170).

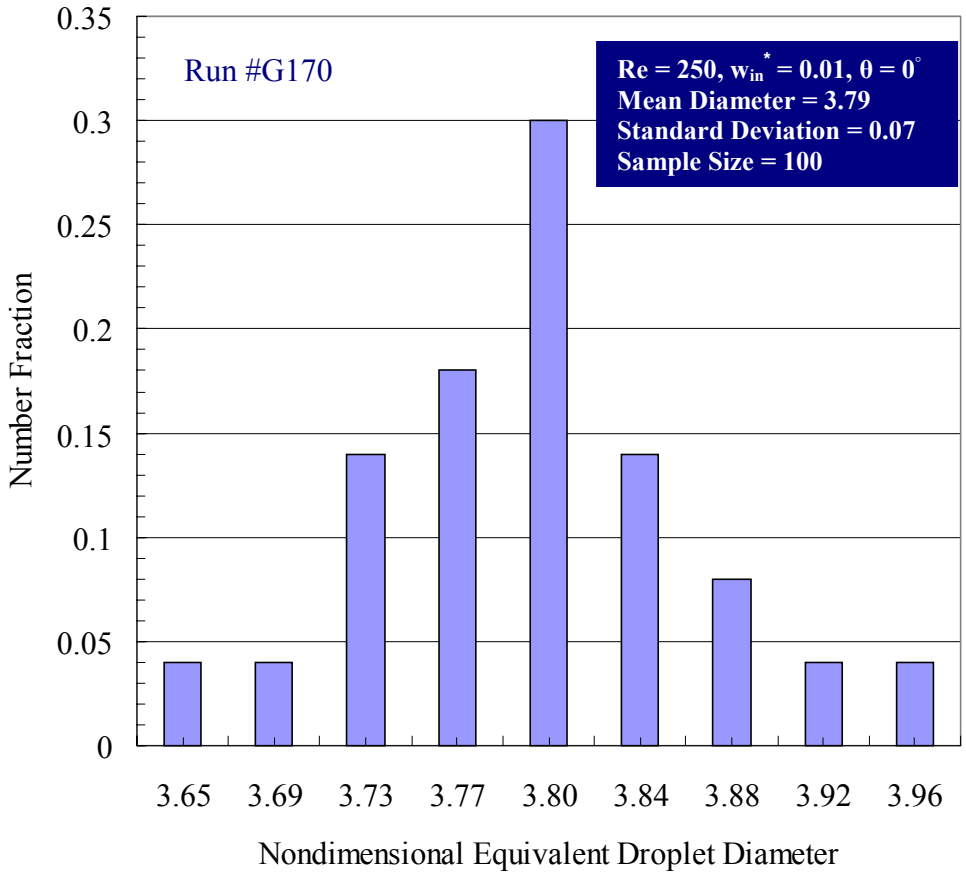

Figure B.56 Experimental data for the distribution of the nondimensional equivalent droplet diameter carried out for a horizontal surface (Run #G170).

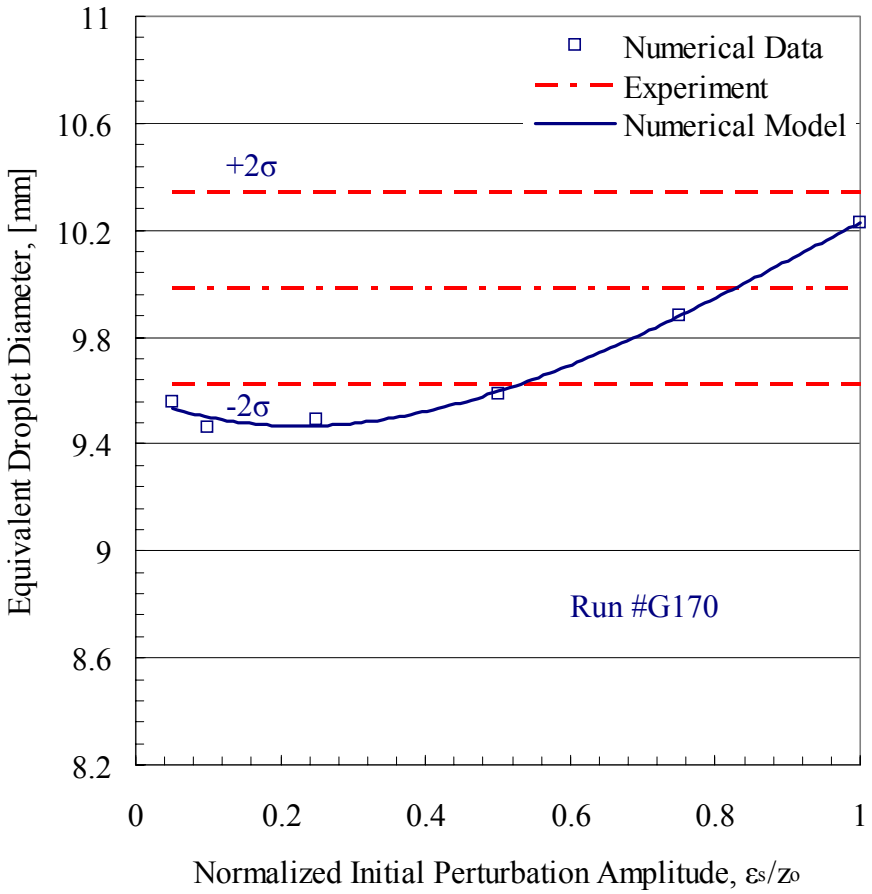

Figure B.57 Numerical and experimental data for the variation of the equivalent droplet diameter with the normalized initial perturbation amplitude carried out for a horizontal surface (Run #G170).

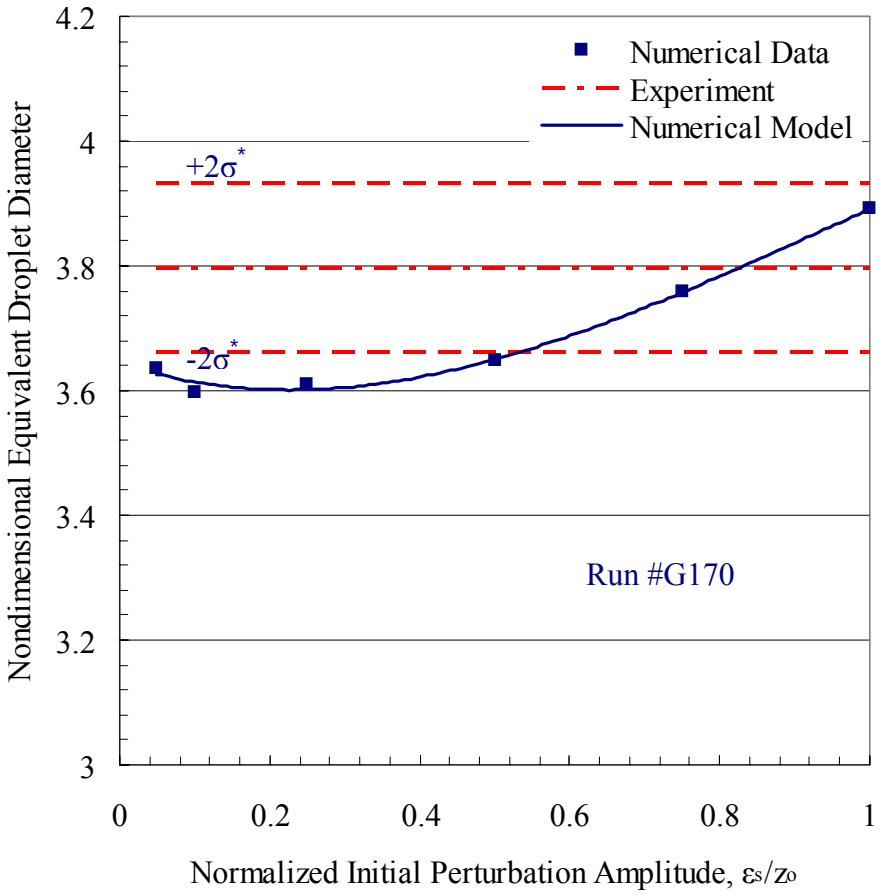

Figure B.58 Numerical and experimental data for the variation of the nondimensional equivalent droplet diameter with the normalized initial perturbation amplitude carried out for a horizontal surface (Run #G170).

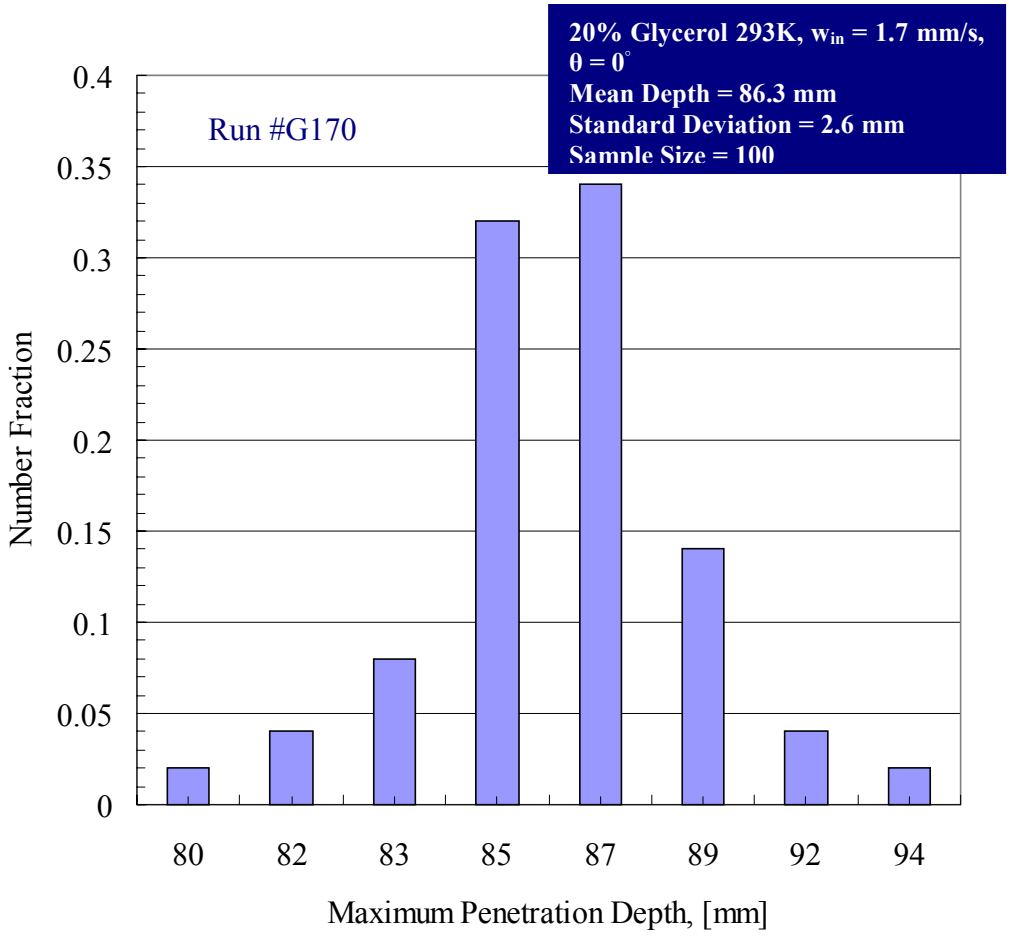

Figure B.59 Experimental data for the distribution of the maximum penetration depth carried out for a horizontal surface (Run #G170).

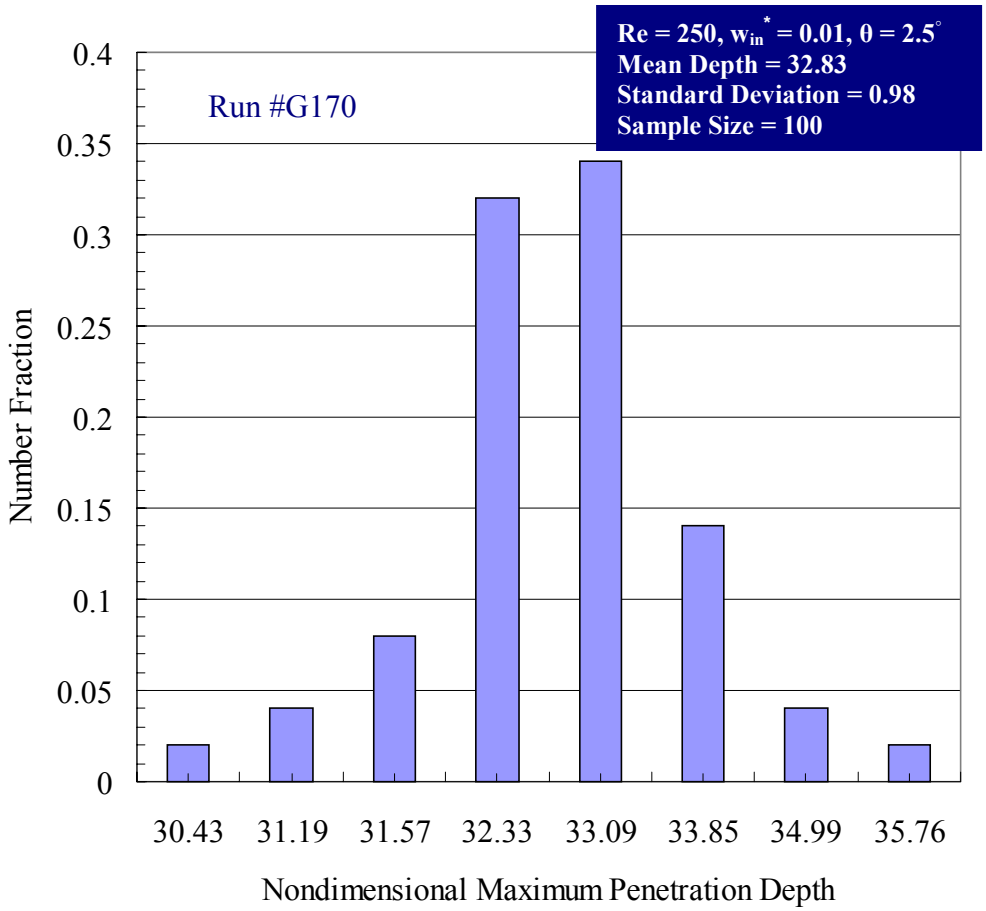

Figure B.60 Experimental data for the distribution of the nondimensional maximum penetration depth carried out for a horizontal surface (Run #G170).

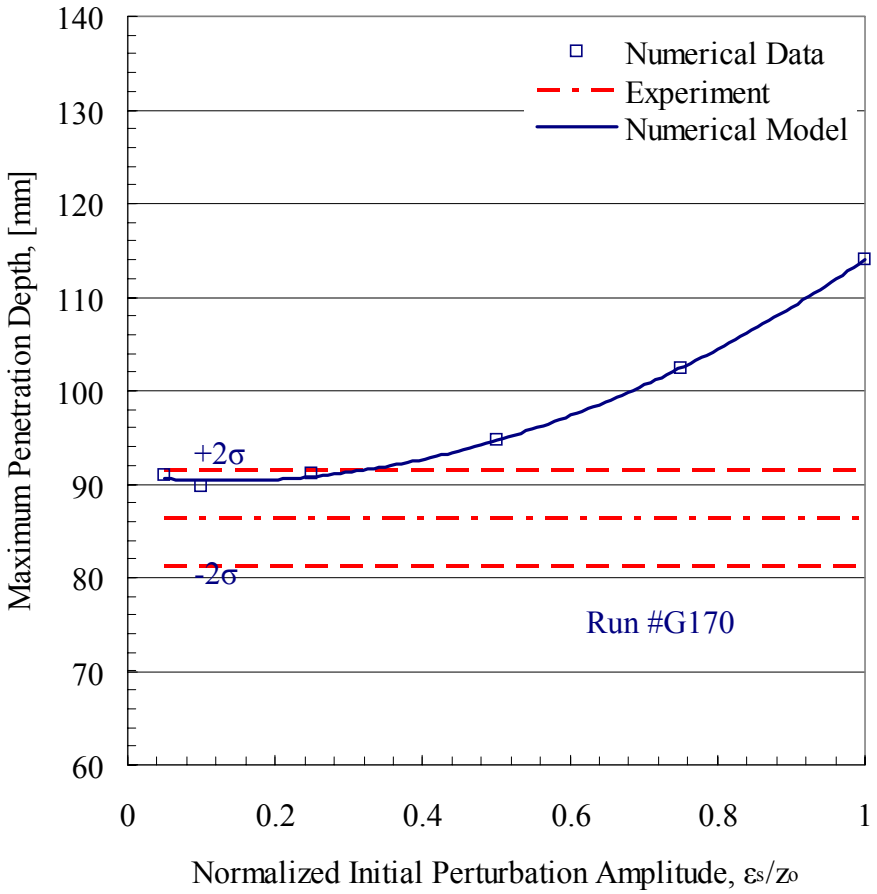

Figure B.61 Numerical and experimental data for the variation of the maximum penetration depth with the normalized initial perturbation amplitude carried out for a horizontal surface (Run #G170).

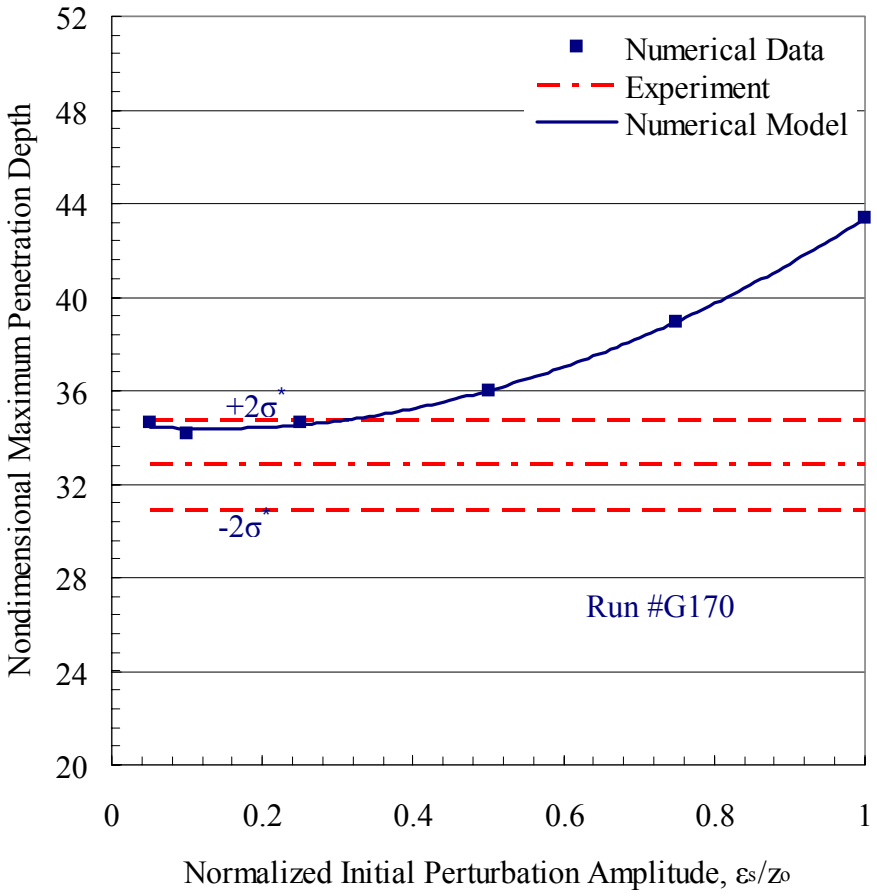

Figure B.62 Numerical and experimental data for the variation of the nondimensional maximum penetration depth with the normalized initial perturbation amplitude carried out for a horizontal surface (Run #G170).

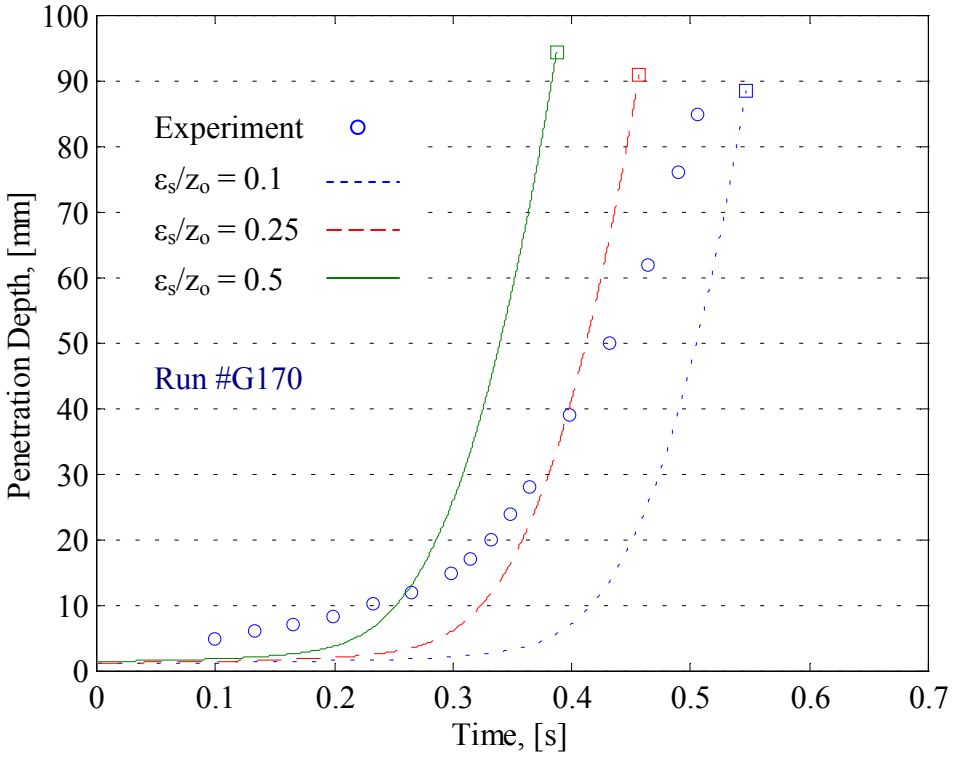

Figure B.63 Numerical and experimental data for the transient variation of the penetration depth carried out for a horizontal surface (Run #G170).

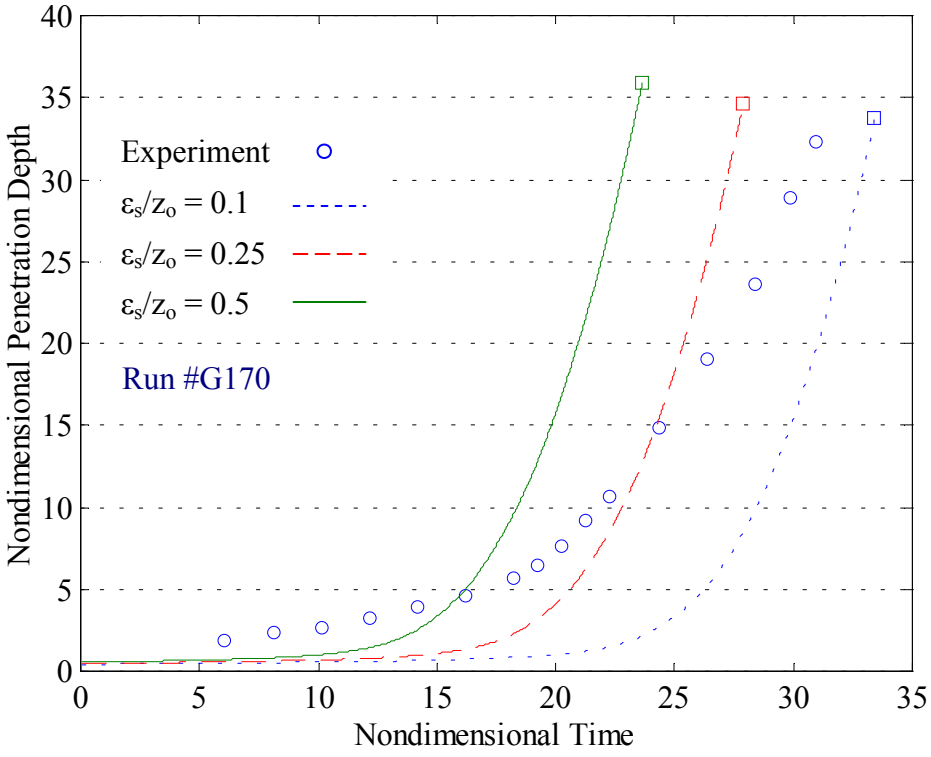

Figure B.64 Numerical and experimental data for the transient variation of the nondimensional penetration depth carried out for a horizontal surface (Run #G170).

B.5 Numerical and Experimental Results for Run #W190

This section details the numerical and experimental results on the characteristic flow field variables for the bounded Rayleigh-Taylor instability with injection through the bounding horizontal surface for Run #W190. These results include: the evolution of the liquid film thickness, the liquid film surface perturbation geometry, the liquid droplet formation and detachment time, the equivalent size for detached droplets, and the time history of the penetration depth.

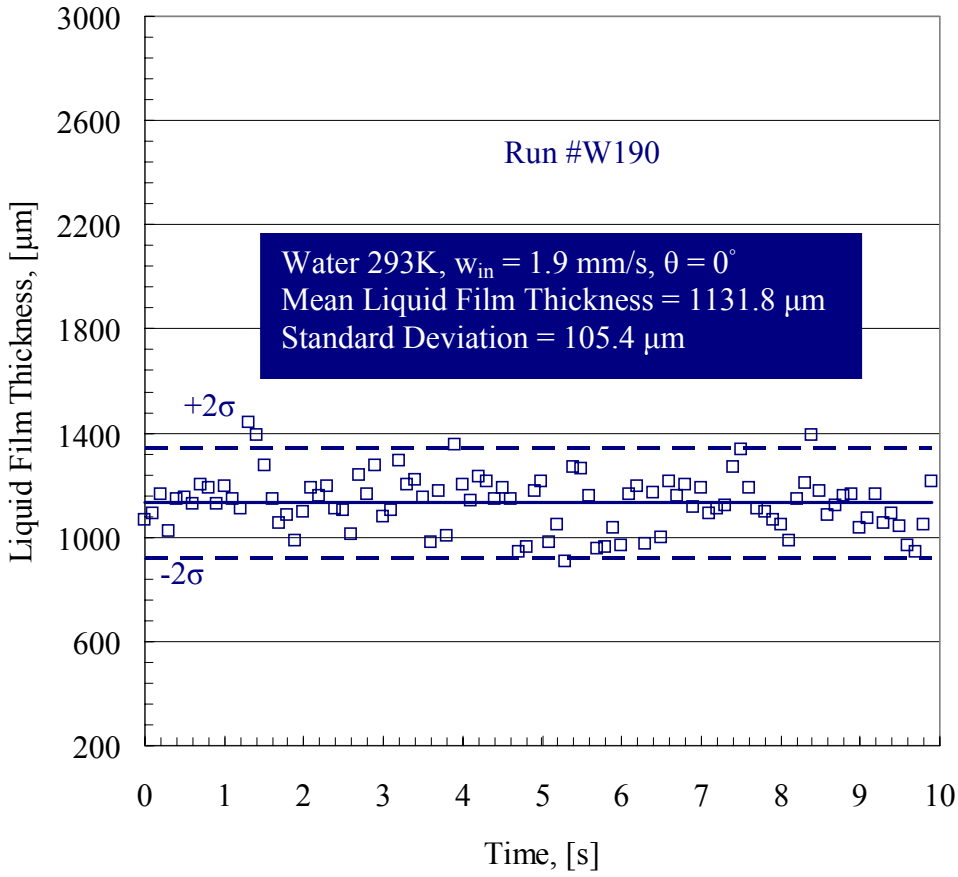

Figure B.65 Transient variation of the unperturbed liquid film thickness for Run #W190.

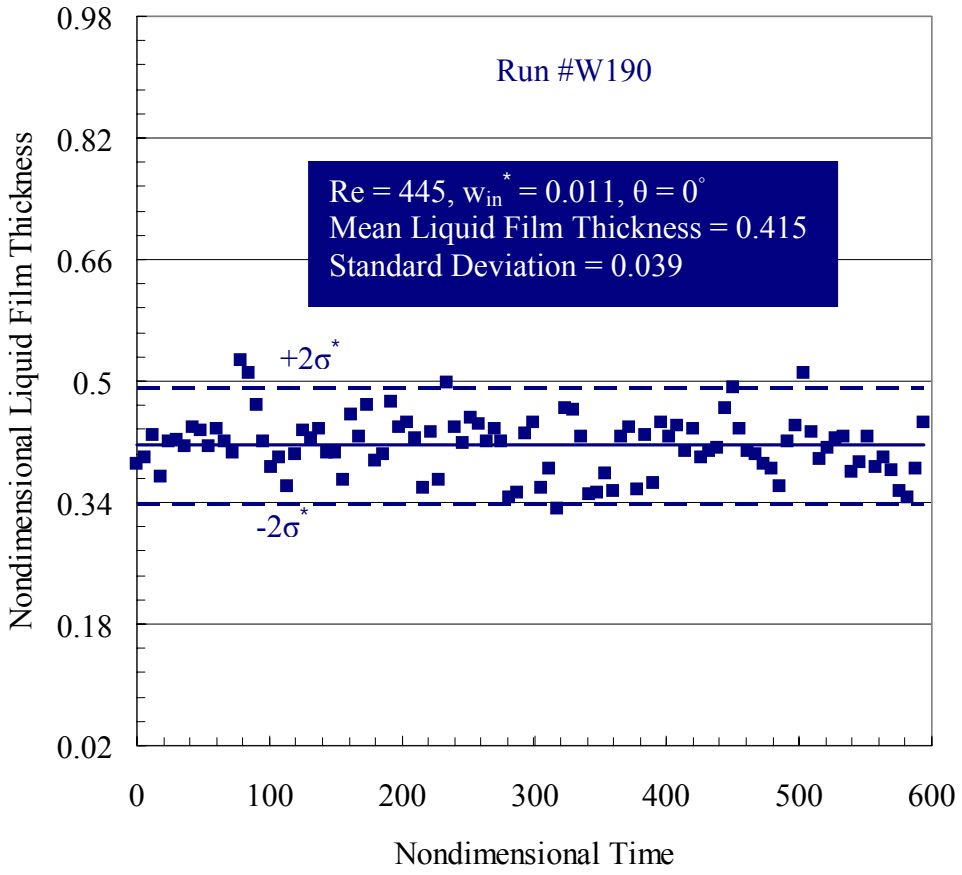

Figure B.66 The unperturbed liquid film thickness normalized by l as a function of time normalized by t_o for Run #W190.

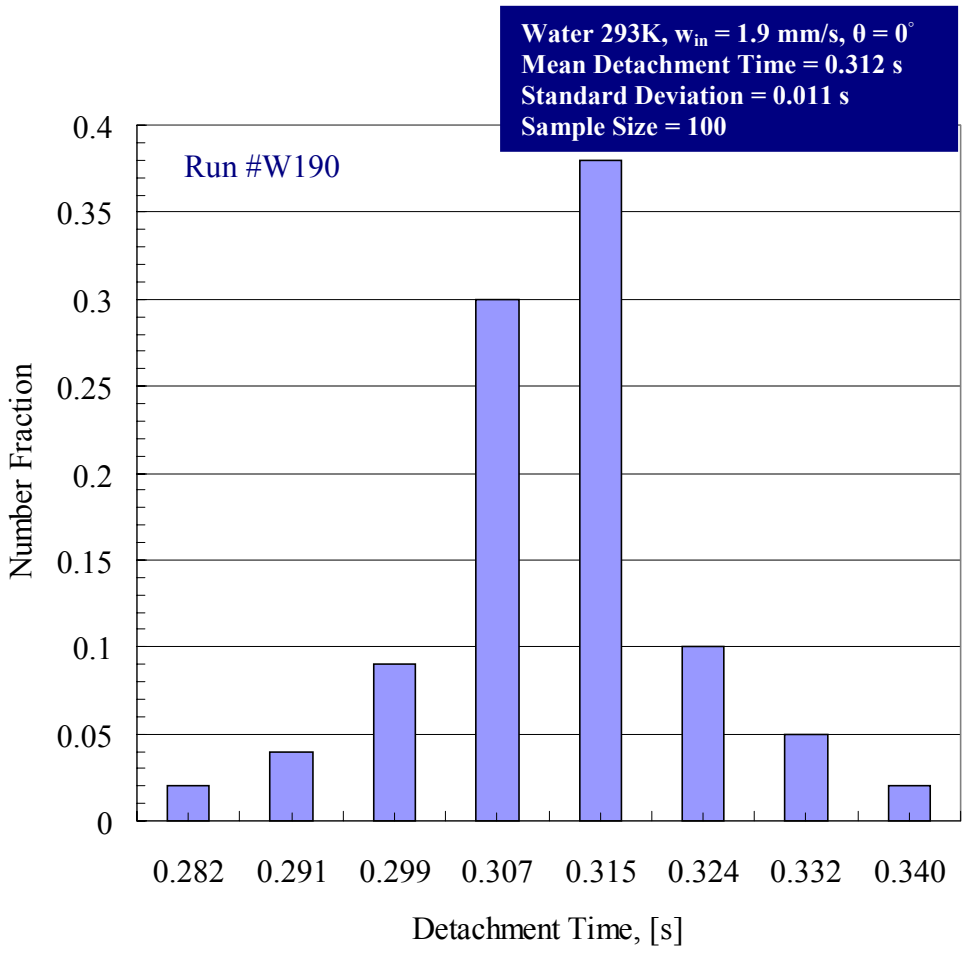

Figure B.67 Experimental data for the distribution of the detachment times carried out for a horizontal surface (Run #W190).

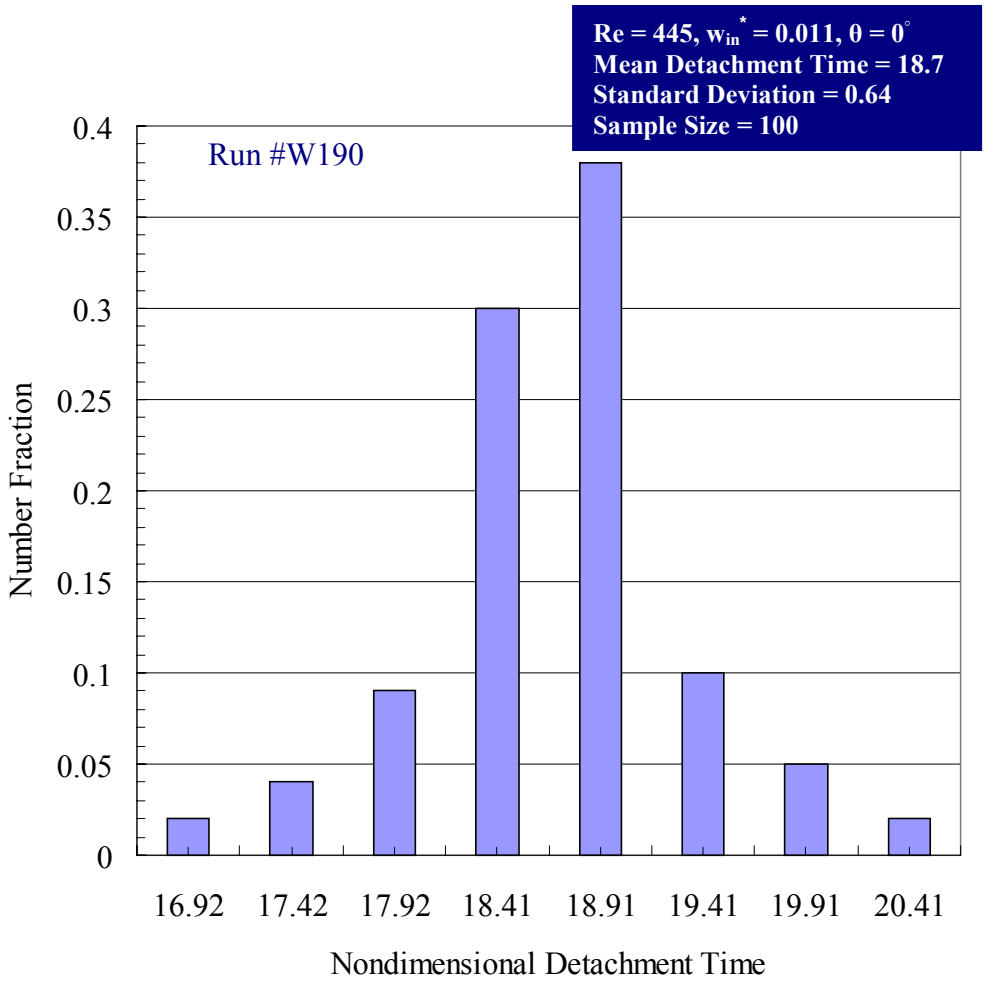

Figure B.68 Experimental data for the distribution of the nondimensional detachment times carried out for a horizontal surface (Run #W190).

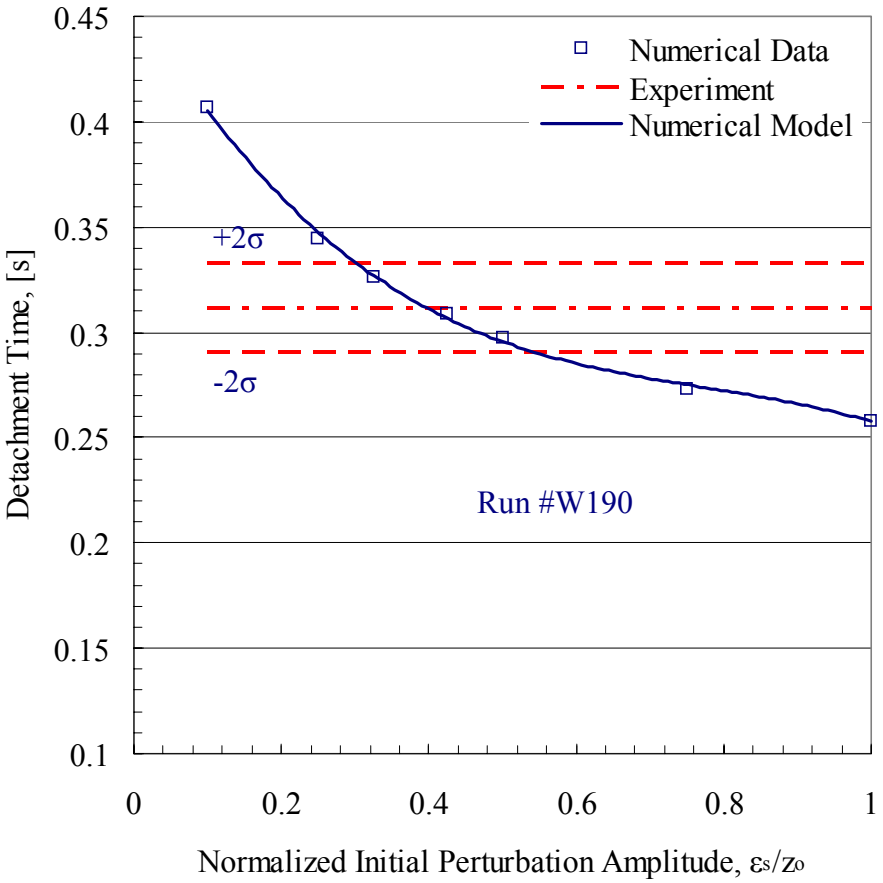

Figure B.69 Numerical and experimental data for the variation of the detachment time with the normalized initial perturbation amplitude carried out for a horizontal surface (Run #W190).

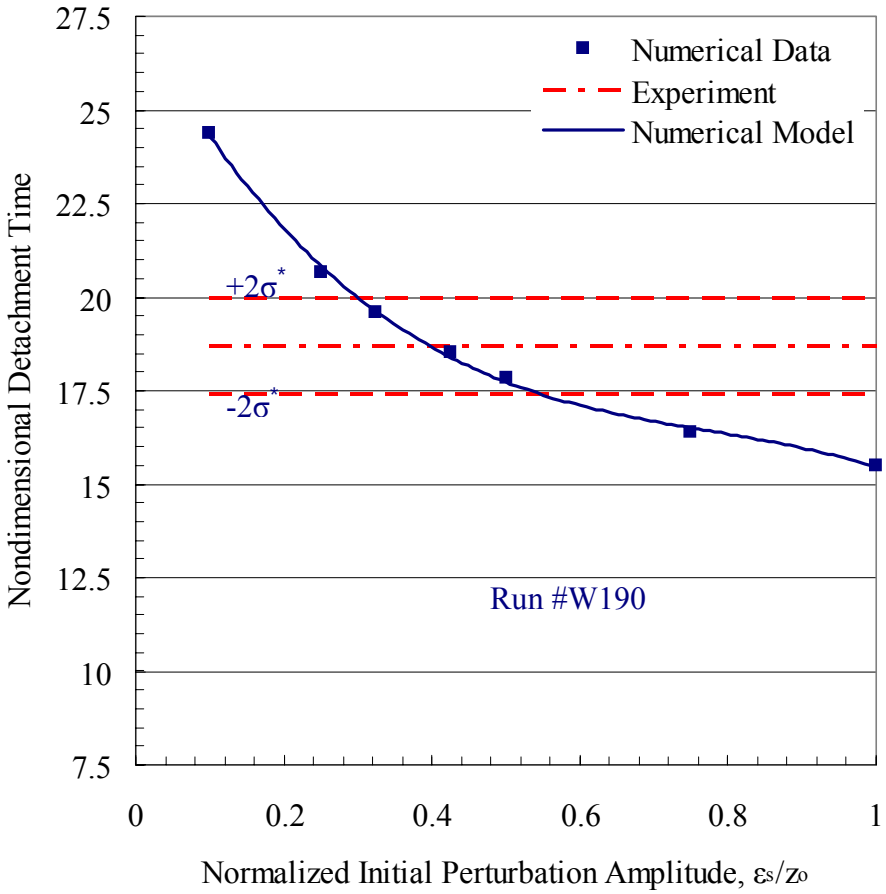

Figure B.70 Numerical and experimental data for the variation of the nondimensional detachment time with the normalized initial perturbation amplitude carried out for a horizontal surface (Run #W190).

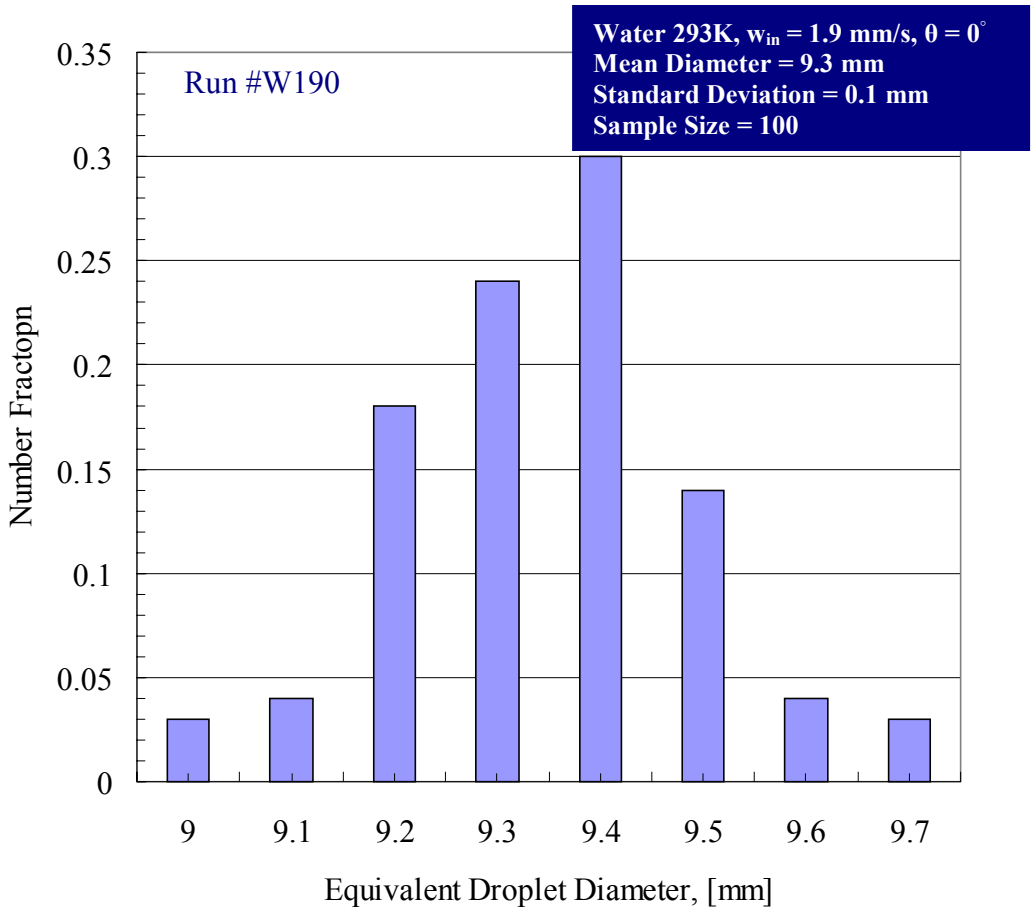

Figure B.71 Experimental data for the distribution of the equivalent droplet diameter carried out for a horizontal surface (Run #W190).

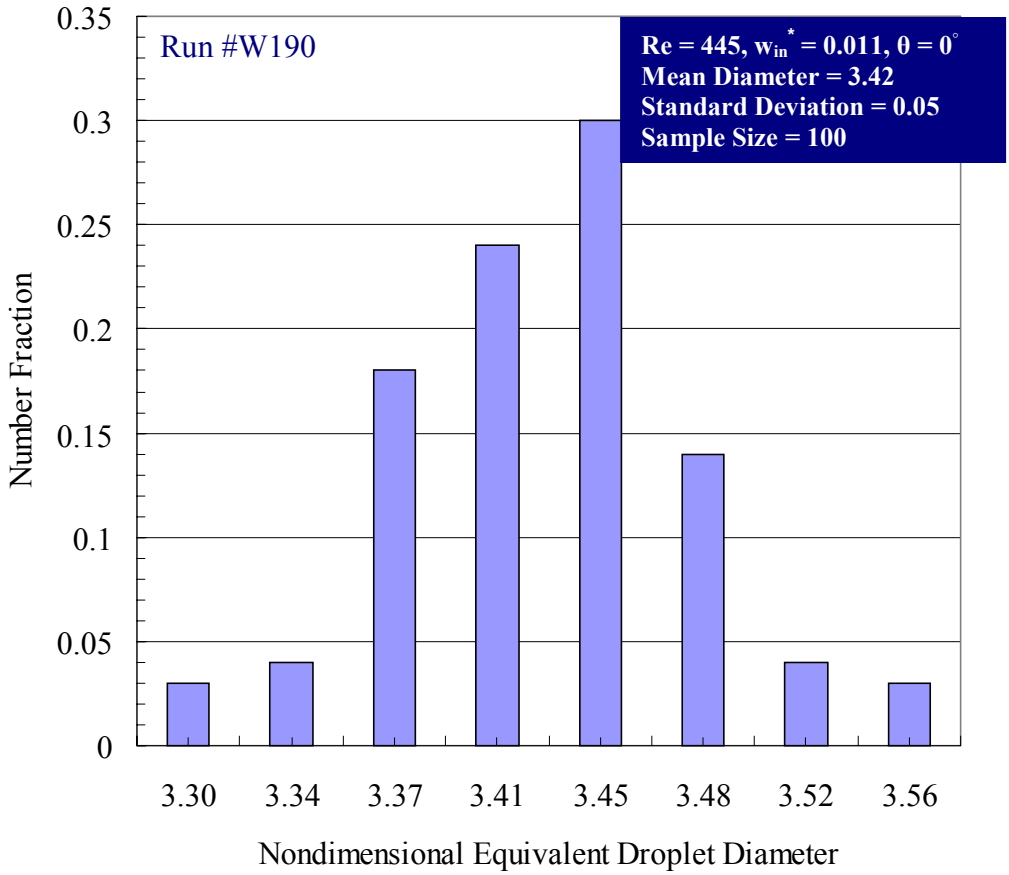

Figure B.72 Experimental data for the distribution of the nondimensional equivalent droplet diameter carried out for a horizontal surface (Run #W190).

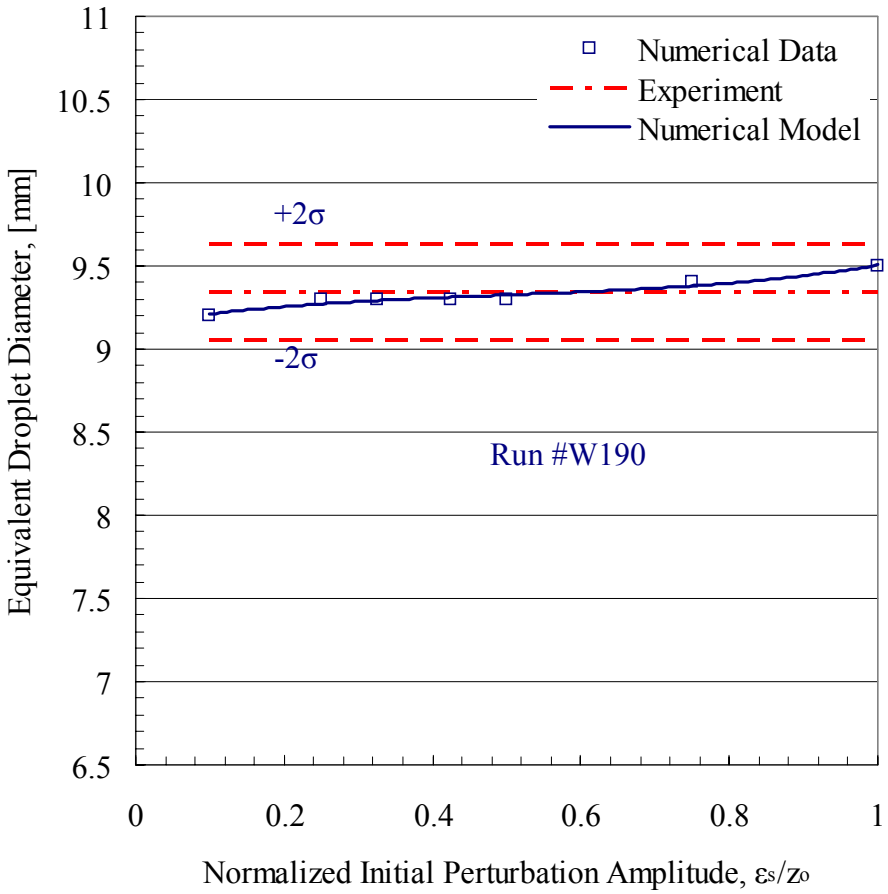

Figure B.73 Numerical and experimental data for the variation of the equivalent droplet diameter with the normalized initial perturbation amplitude carried out for a horizontal surface (Run #W190).

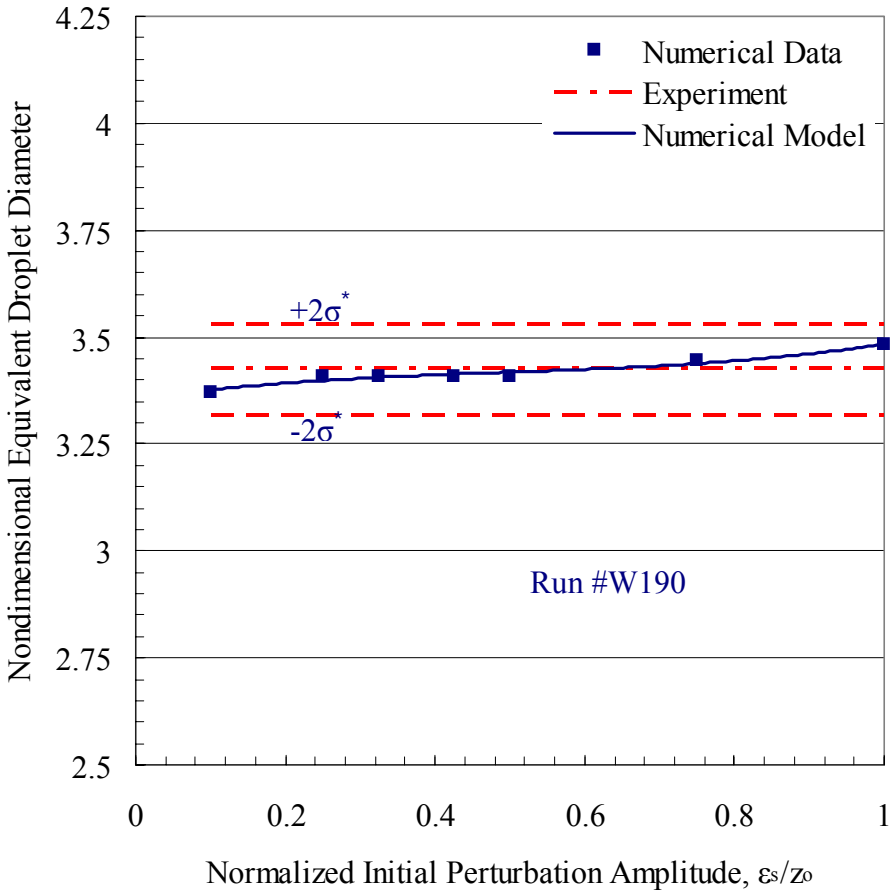

Figure B.74 Numerical and experimental data for the variation of the nondimensional equivalent droplet diameter with the normalized initial perturbation amplitude carried out for a horizontal surface (Run #W190).

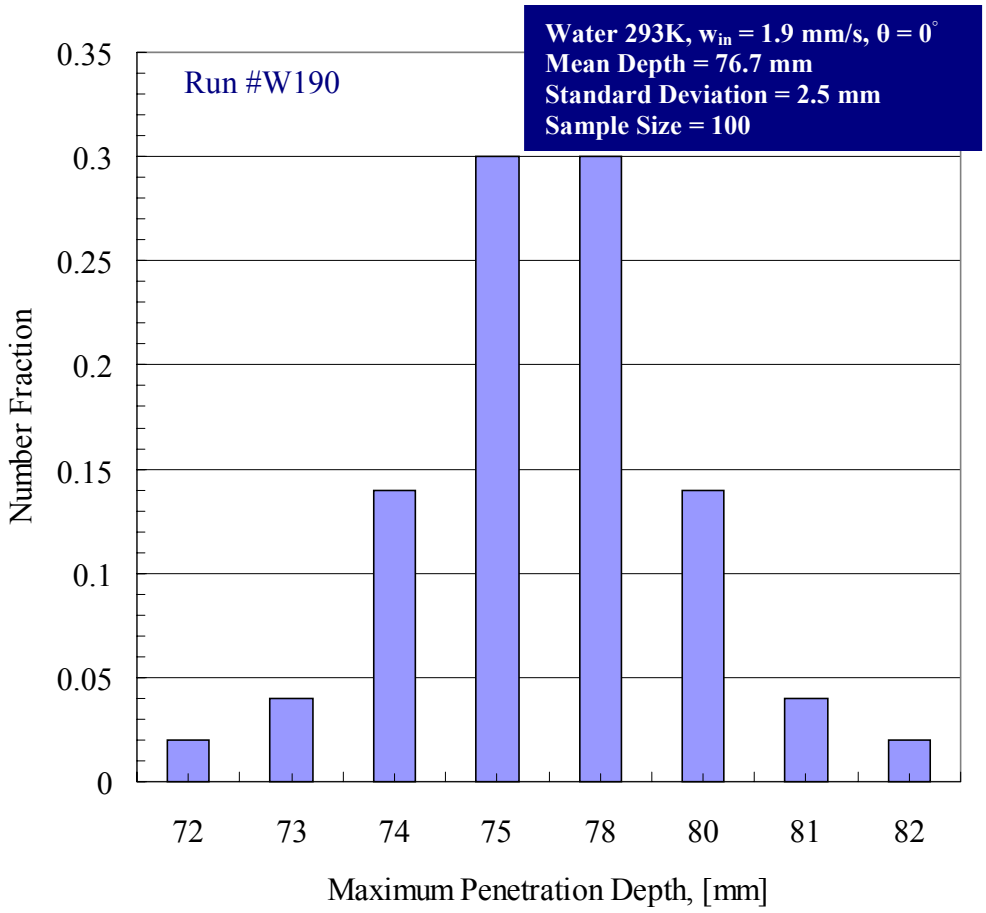

Figure B.75 Experimental data for the distribution of the maximum penetration depth carried out for a horizontal surface (Run #W190).

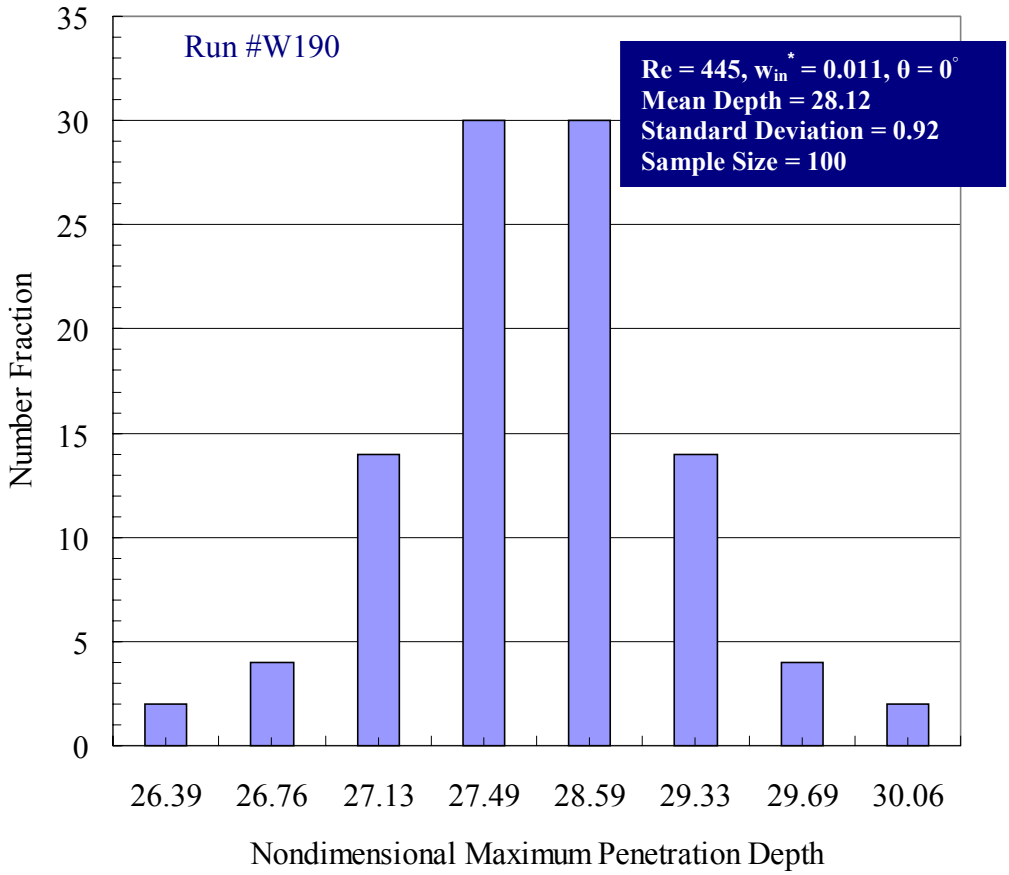

Figure B.76 Experimental data for the distribution of the nondimensional maximum penetration depth carried out for a horizontal surface (Run #W190).

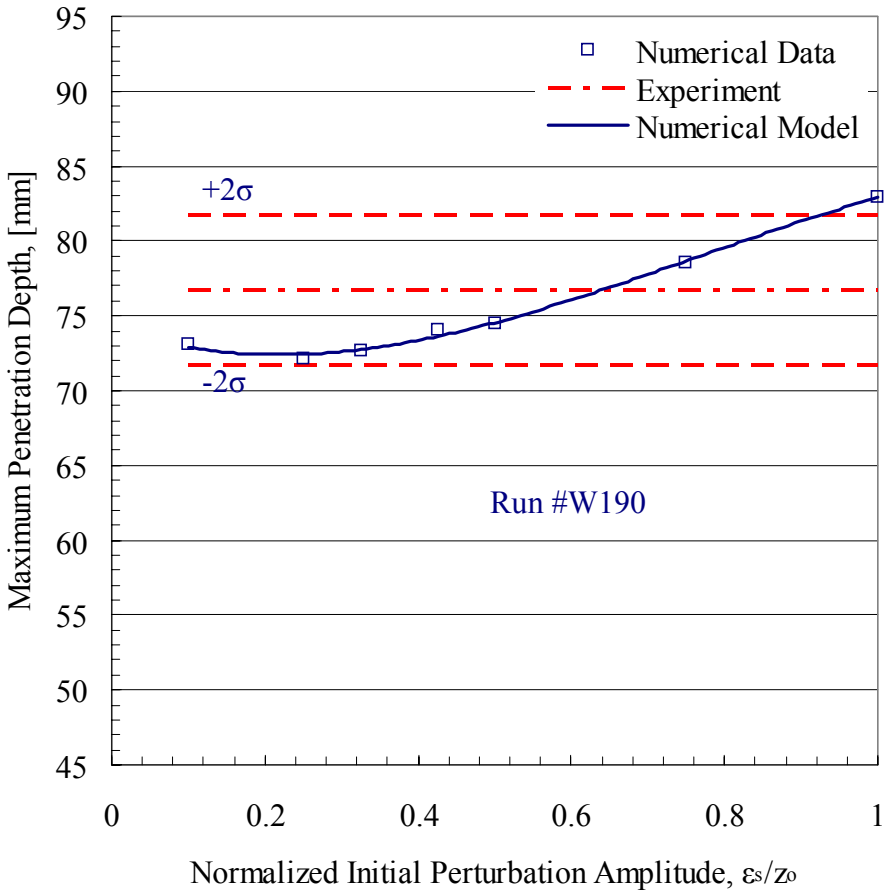

Figure B.77 Numerical and experimental data for the variation of the maximum penetration depth with the normalized initial perturbation amplitude carried out for a horizontal surface (Run #W190).

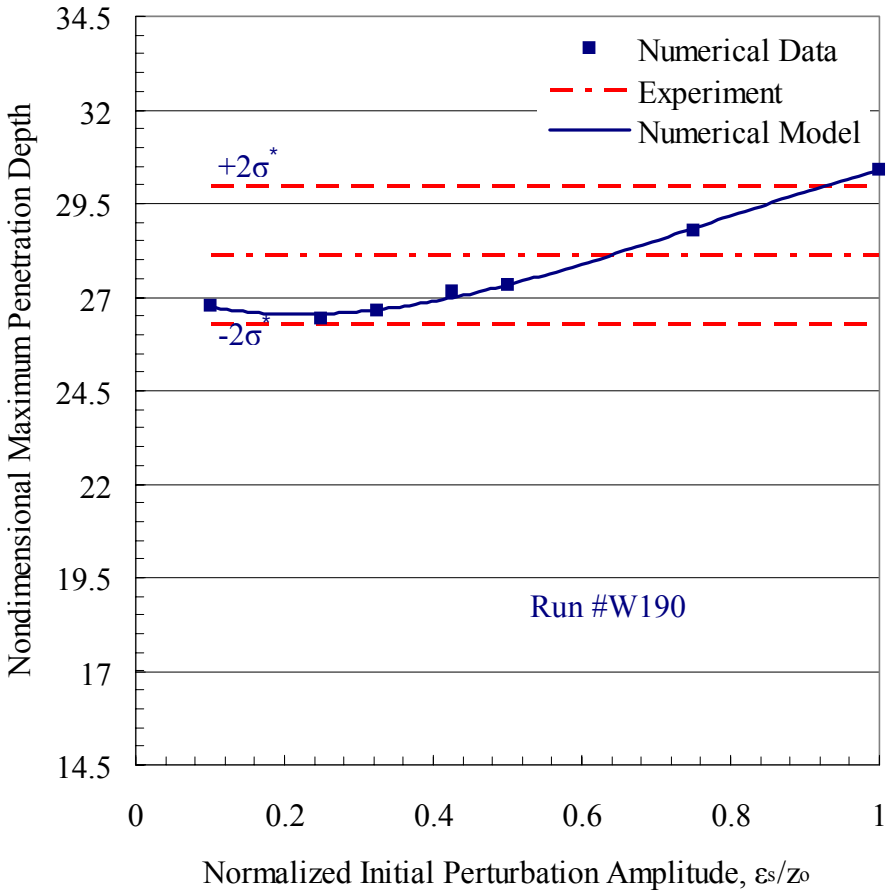

Figure B.78 Numerical and experimental data for the variation of the nondimensional maximum penetration depth with the normalized initial perturbation amplitude carried out for a horizontal surface (Run #W190).

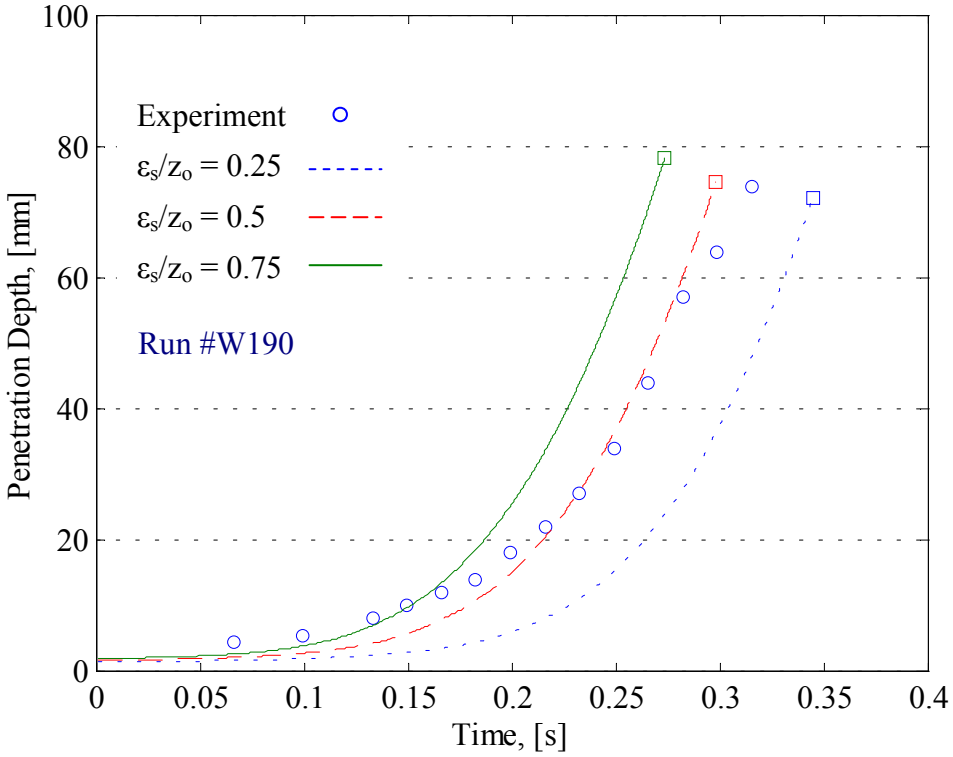

Figure B.79 Numerical and experimental data for the transient variation of the penetration depth carried out for a horizontal surface (Run #W190).

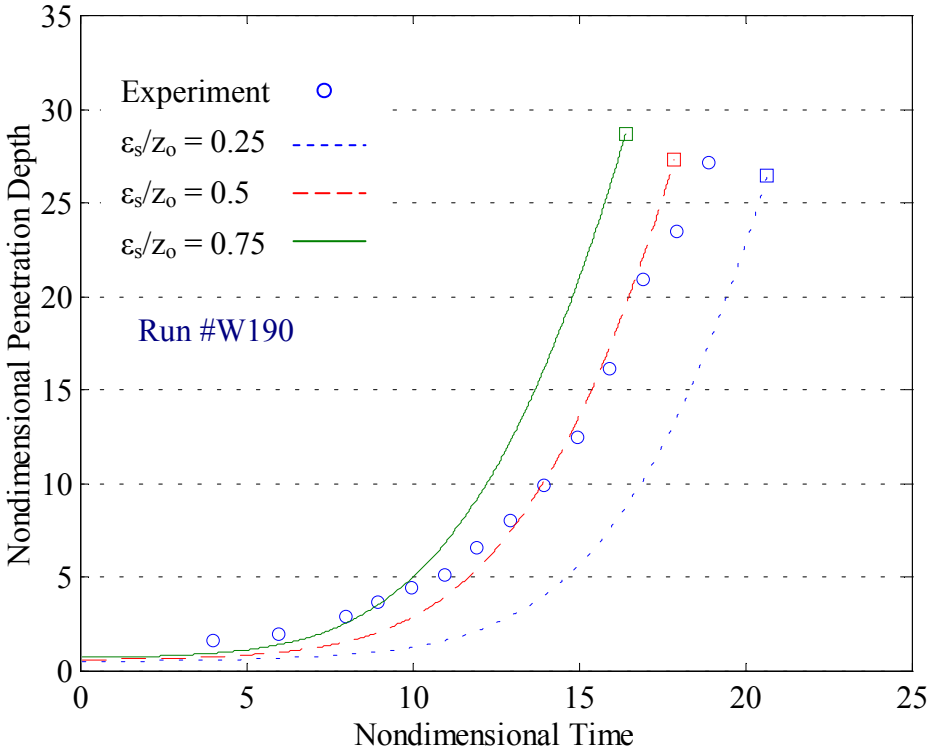

Figure B.80 Numerical and experimental data for the transient variation of the nondimensional penetration depth carried out for a horizontal surface (Run #W190).

APPENDIX C

NUMERICAL AND EXPERIMENTAL RESULTS FOR INCLINED SURFACES

The numerical and experimental results obtained for the characteristic flow field variables of the bounded Rayleigh-Taylor instability with injection through the bounding inclined surfaces are detailed in this appendix. These numerical and experimental runs are listed in Table C.1. Runs W0925 and W2125 are provided in Chapter 5 while the other runs are given in this appendix.

Table C.1 Letter-number designation of the conducted experimental and numerical runs for inclined surfaces.

Experiment Runs	Working Fluid	Injection Velocity, w, [mm/s]	Surface Inclination Angle, θ
W0925	Water	0.9	2.5˚
G0925	20% Glycerol	0.9	2.5˚
W1425	Water	1.4	2.5˚
W1725	Water	1.7	2.5˚
G1725	20% Glycerol	1.7	2.5˚
W1925	Water	1.9	2.5˚
W2125	Water	2.1	2.5˚

C.1 Numerical and Experimental Results for Run #G0925

This section details the numerical and experimental results on the characteristic flow field variables for the bounded Rayleigh-Taylor instability with injection through the bounding inclined surface for Run #G0925. These results include: the evolution of the liquid film thickness, the liquid film surface perturbation geometry, the liquid droplet formation and detachment time, the equivalent size for detached droplets, and the time history of the penetration depth.

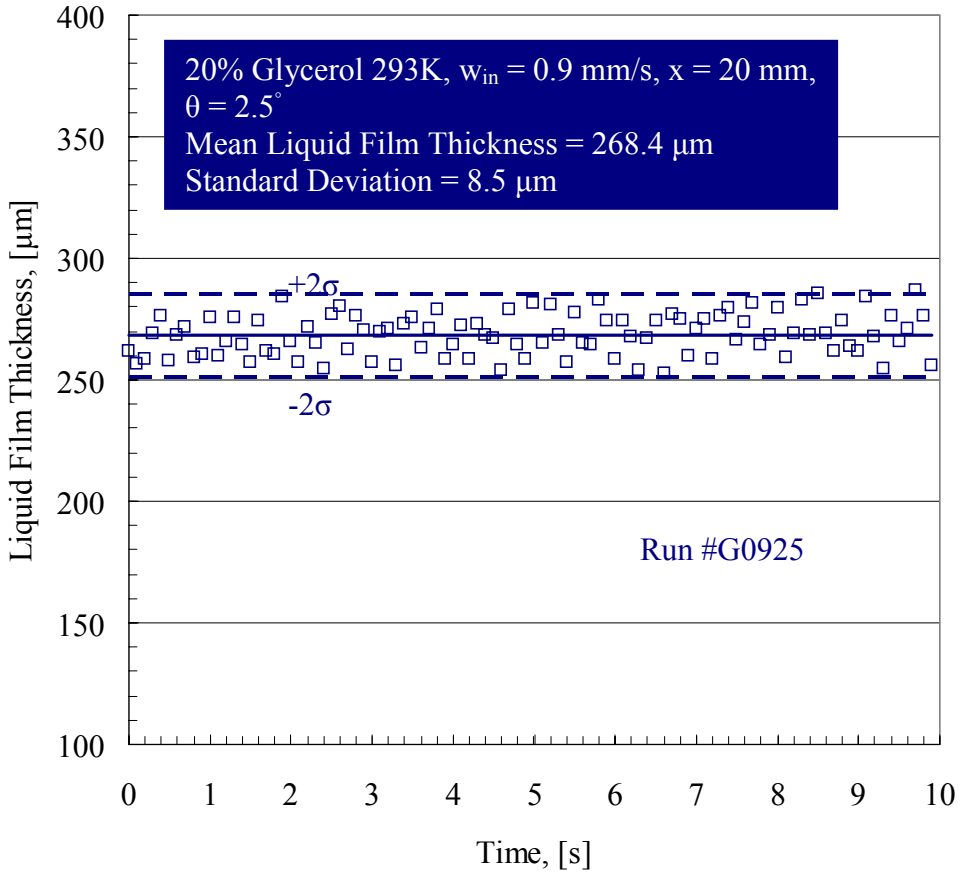

Figure C.1 Transient variation of the unperturbed liquid film thickness measured at an axial position x = 20 mm for Run #G0925.

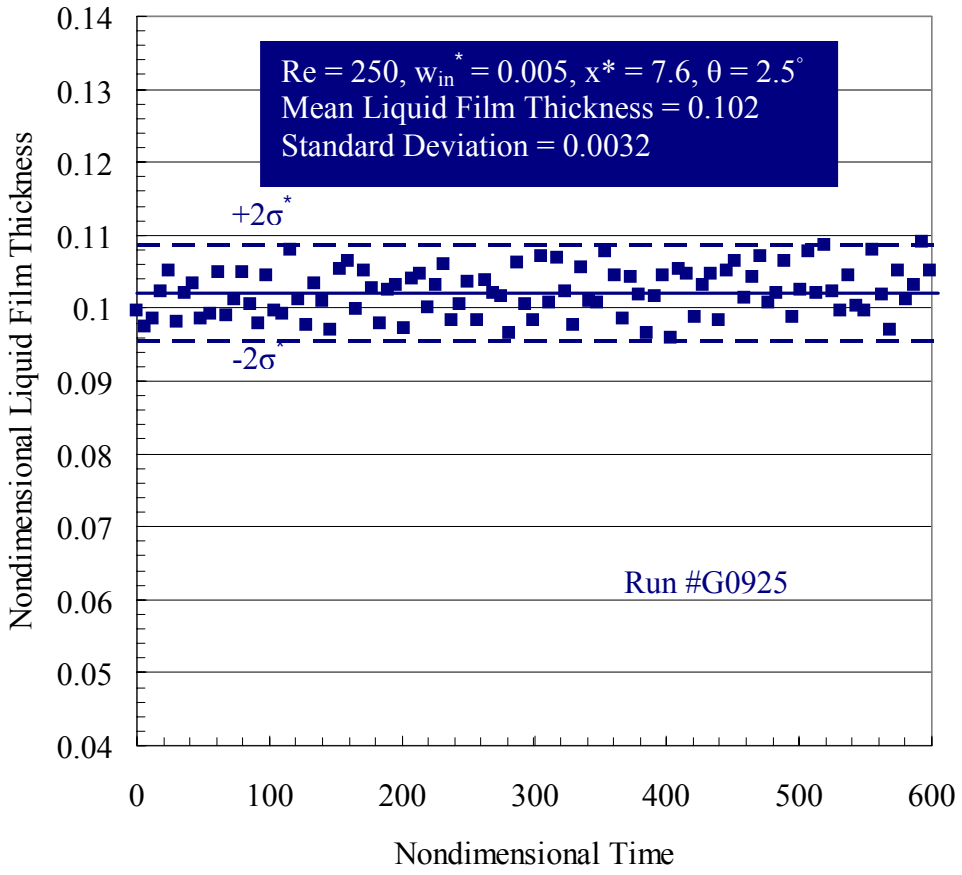

Figure C.2 The unperturbed liquid film thickness normalized by l as a function of time normalized by t_o measured at $x^* = 7.6$ for Run #G0925.

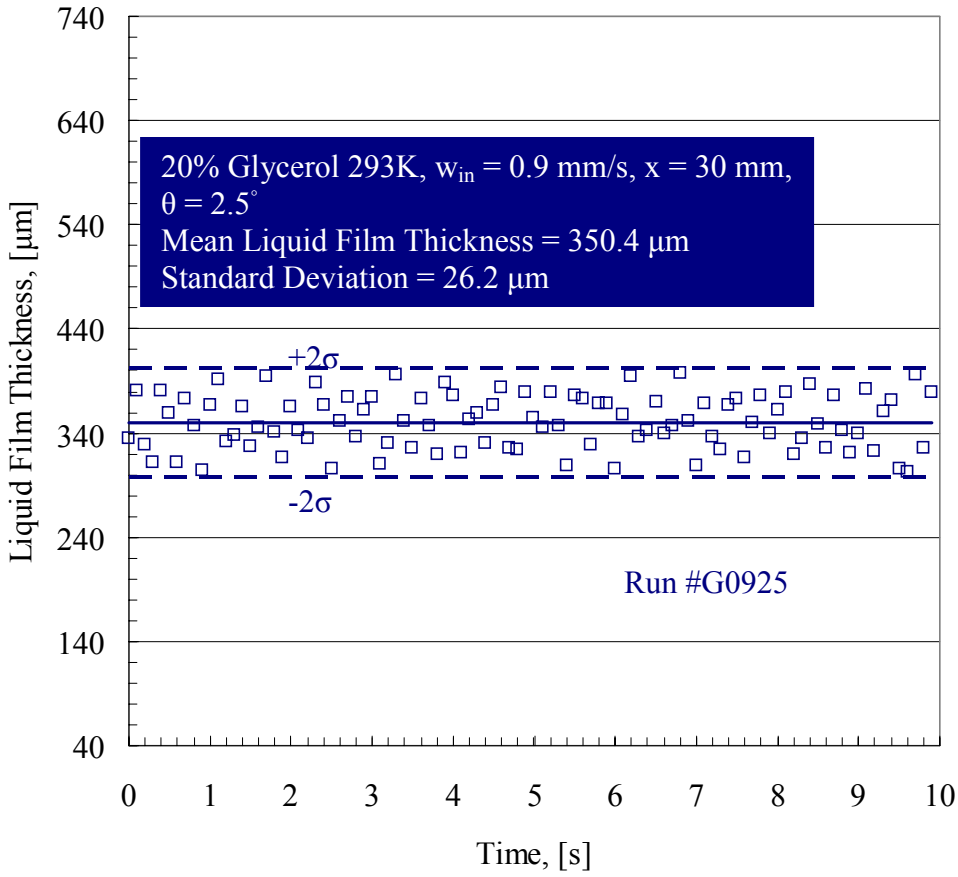

Figure C.3 Transient variation of the unperturbed liquid film thickness measured at an axial position x = 30 mm for Run #G0925.

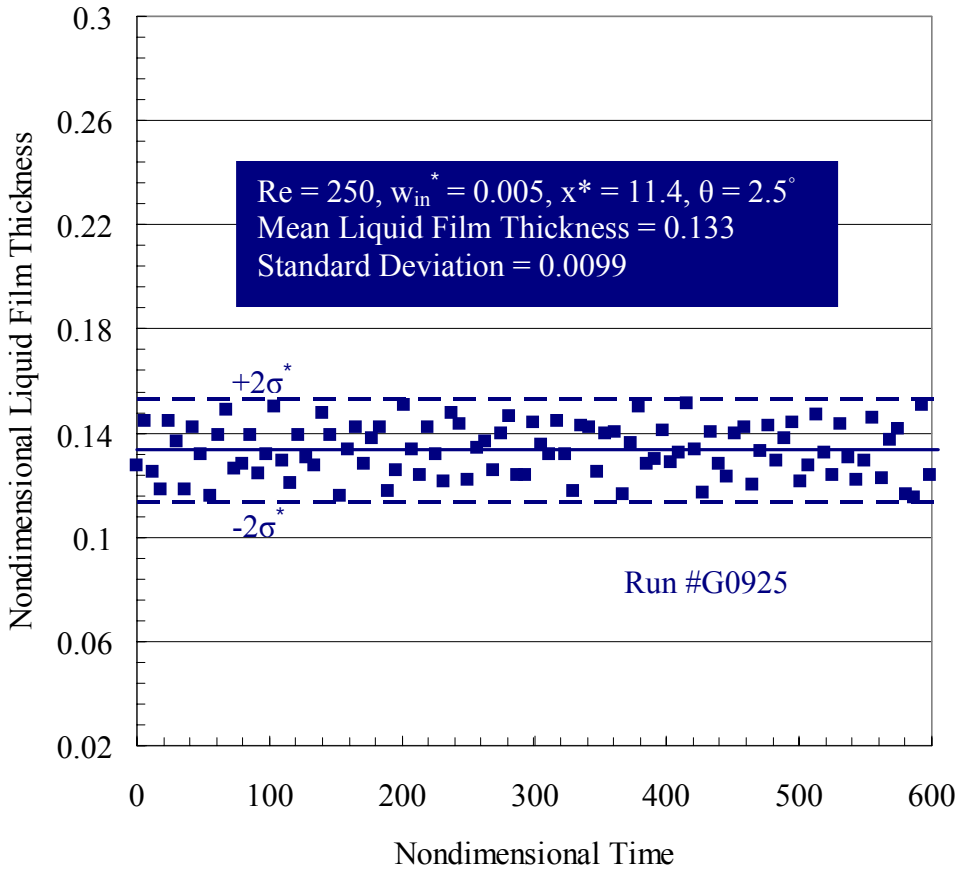

Figure C.4 The unperturbed liquid film thickness normalized by l as a function of time normalized by t_o measured at $x^* = 11.4$ for Run #G0925.

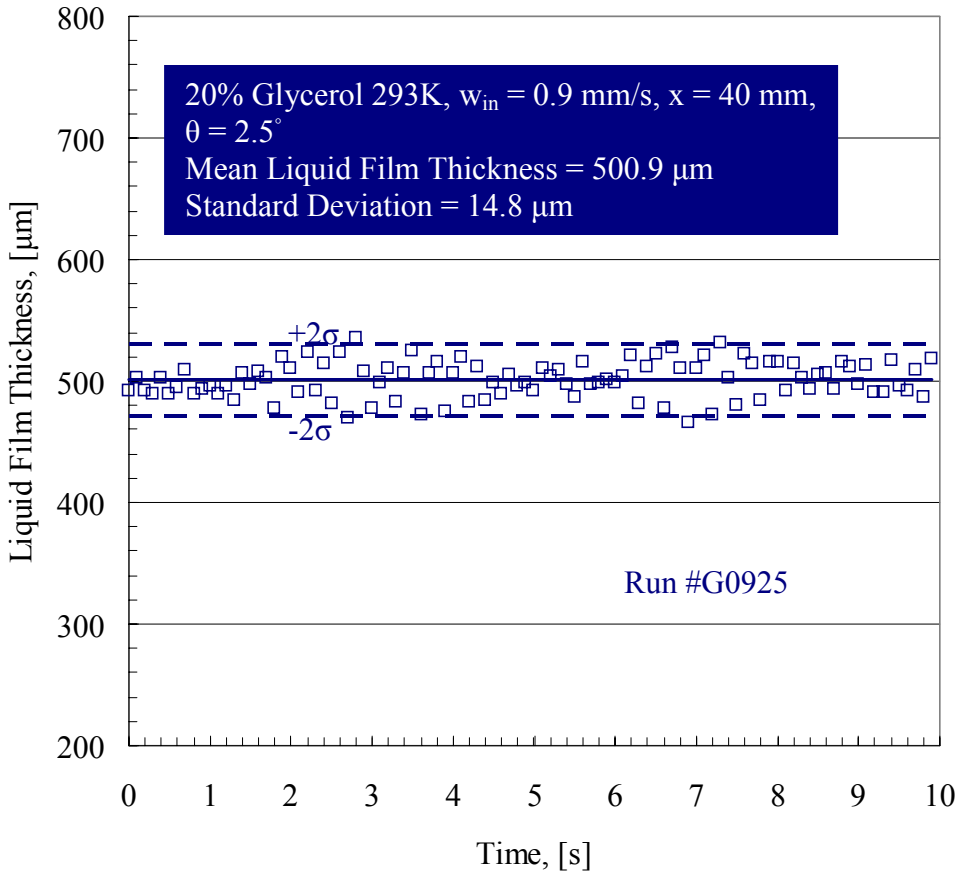

Figure C.5 Transient variation of the unperturbed liquid film thickness measured at an axial position x = 40 mm for Run #G0925.

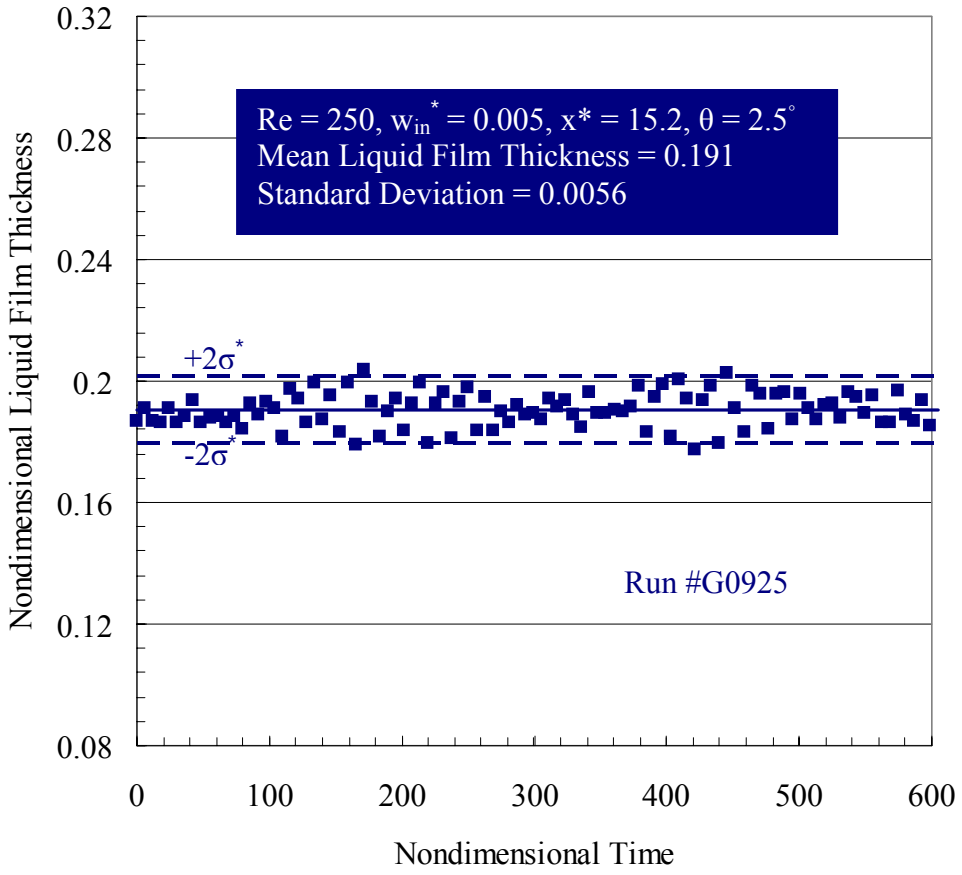

Figure C.6 The unperturbed liquid film thickness normalized by l as a function of time normalized by t_o measured at $x^* = 15.2$ for Run #G0925.

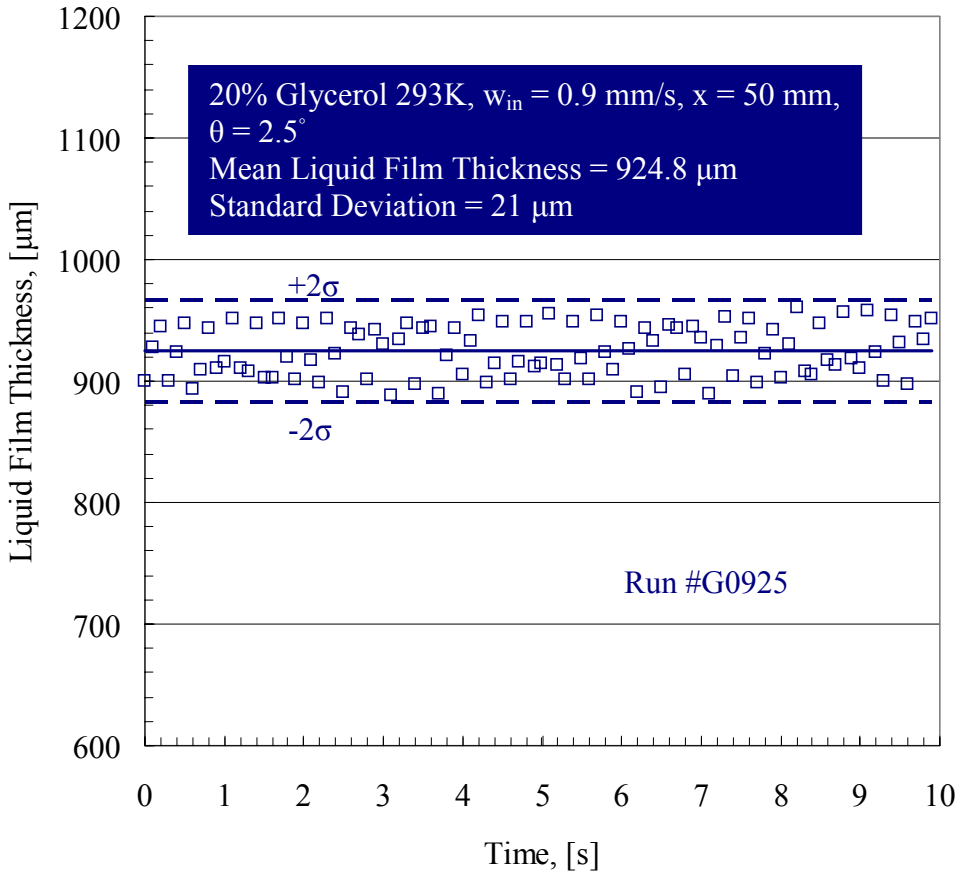

Figure C.7 Transient variation of the unperturbed liquid film thickness measured at an axial position x = 50 mm for Run #G0925.

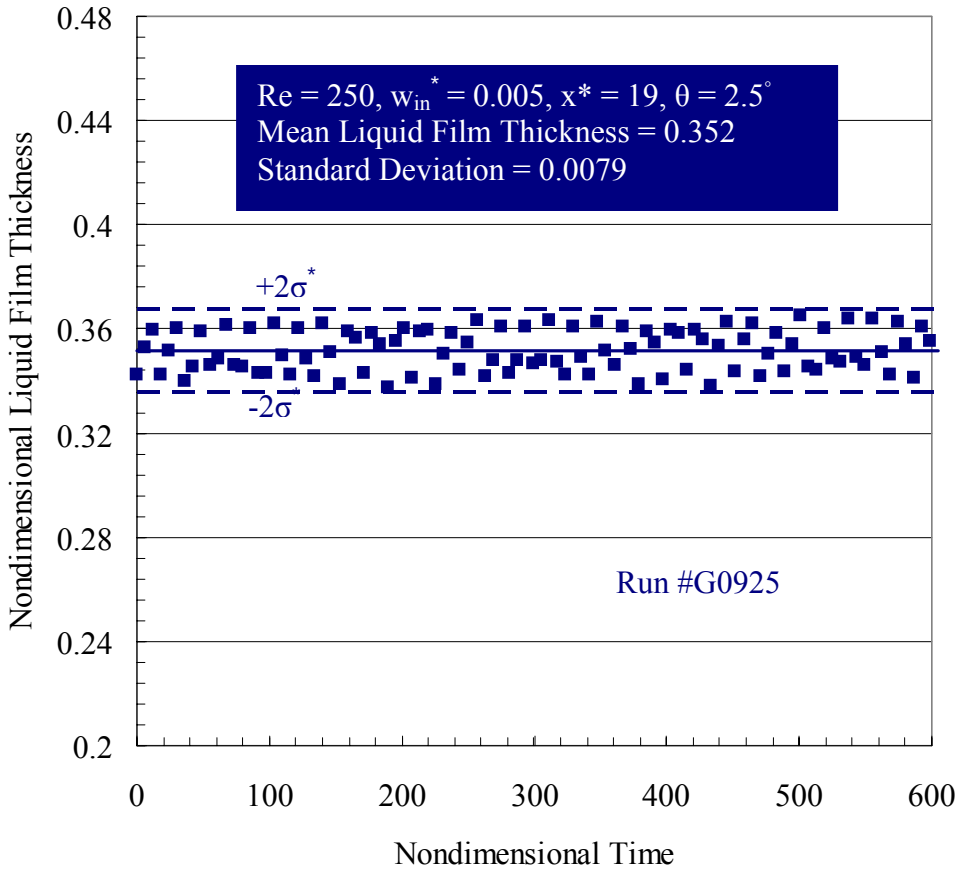

Figure C.8 The unperturbed liquid film thickness normalized by l as a function of time normalized by t_o measured at $x^* = 19$ for Run #G0925.

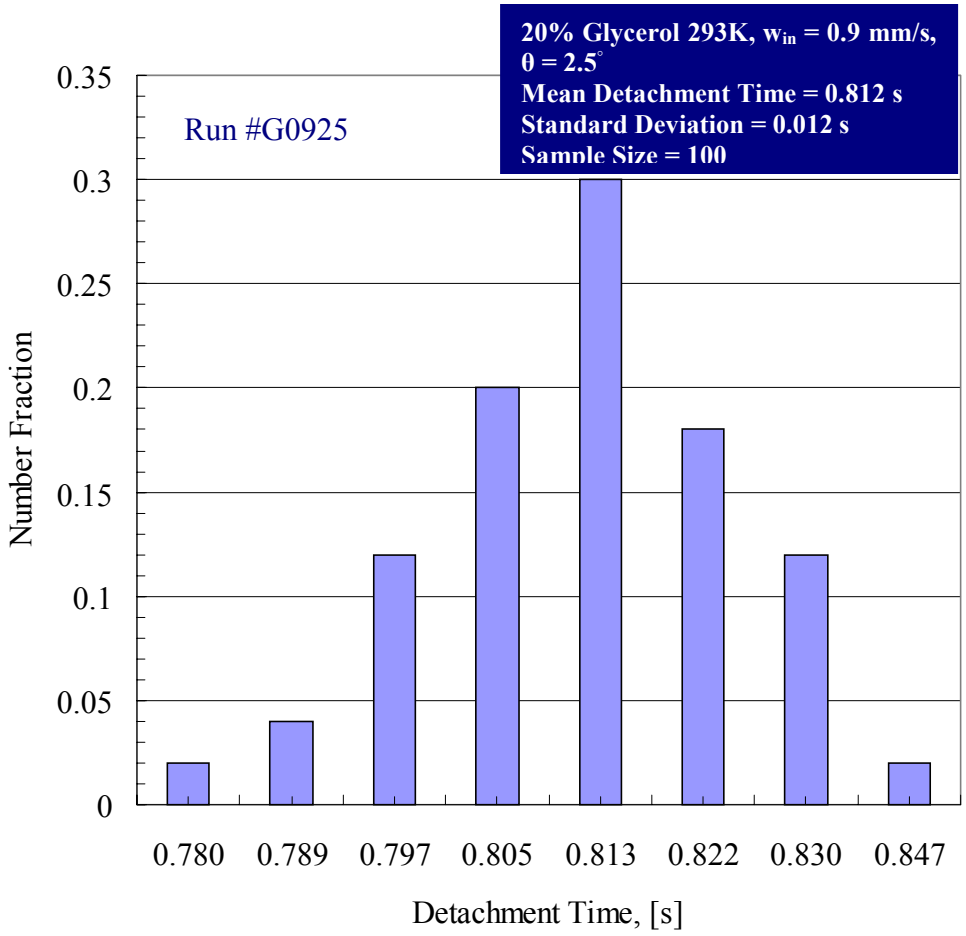

Figure C.9 Experimental data for the distribution of the detachment times carried out for an inclined surface (Run #G0925).

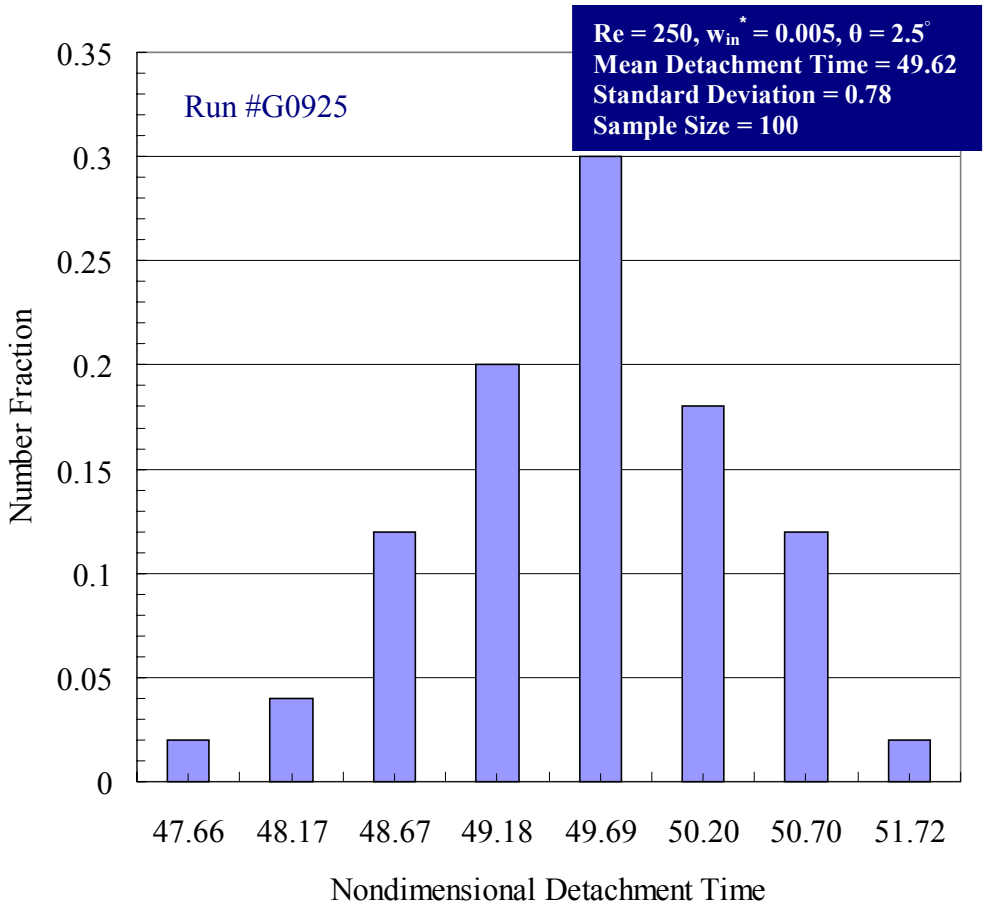

Figure C.10 Experimental data for the distribution of the nondimensional detachment time carried out for an inclined surface (Run #G0925).

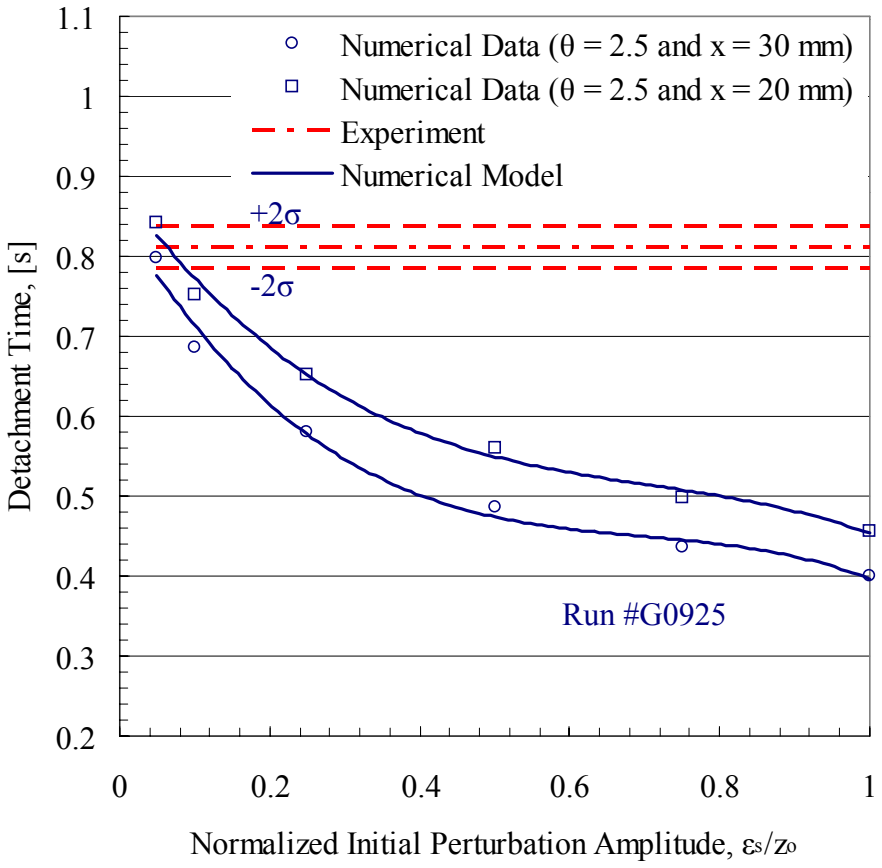

Figure C.11 Numerical and experimental data for the variation of the detachment time with the normalized initial perturbation amplitude carried out for an inclined surface (Run #G0925).

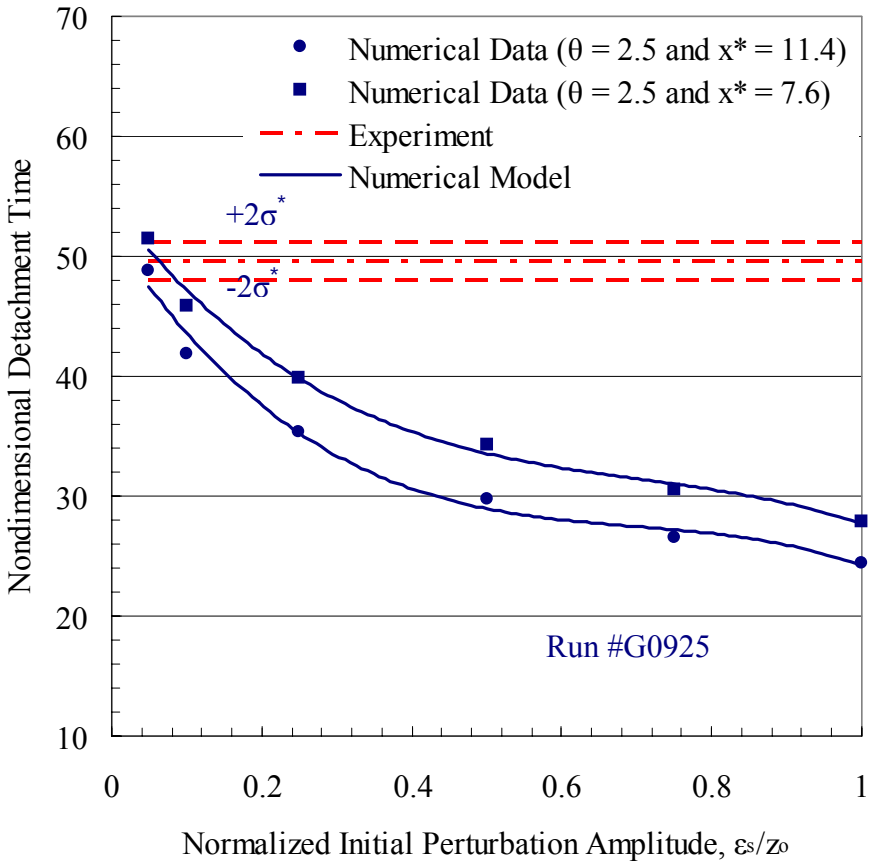

Figure C.12 Numerical and experimental data for the variation of the nondimensional detachment time with the normalized initial perturbation amplitude carried out for an inclined surface (Run #G0925).

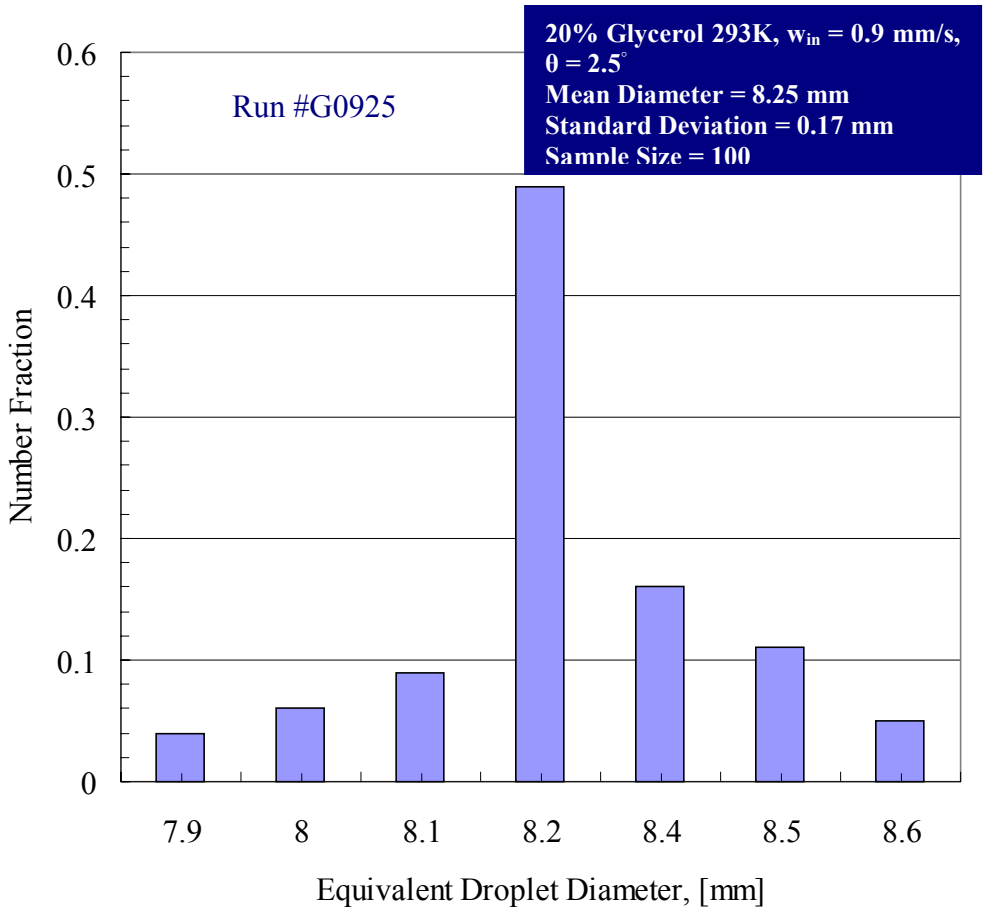

Figure C.13 Experimental data for the distribution of the equivalent droplet diameter carried out for an inclined surface (Run #G0925).

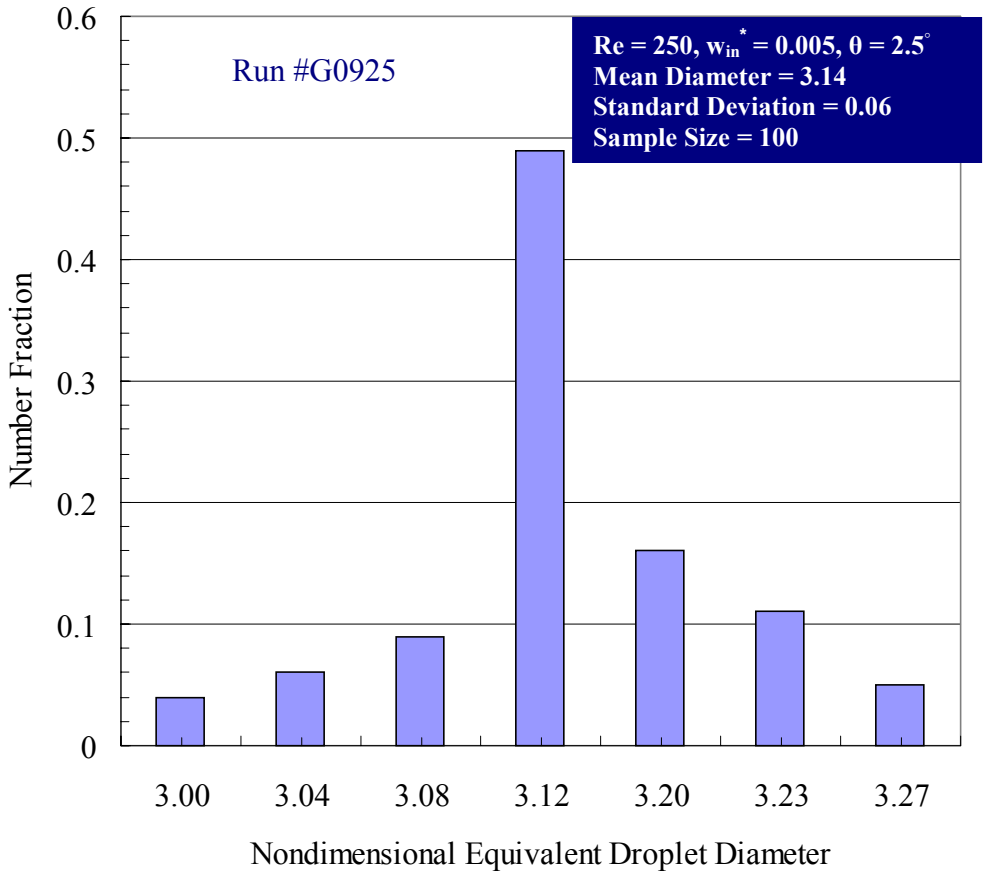

Figure C.14 Experimental data for the distribution of the nondimensional equivalent droplet diameter carried out for an inclined surface (Run #G0925).

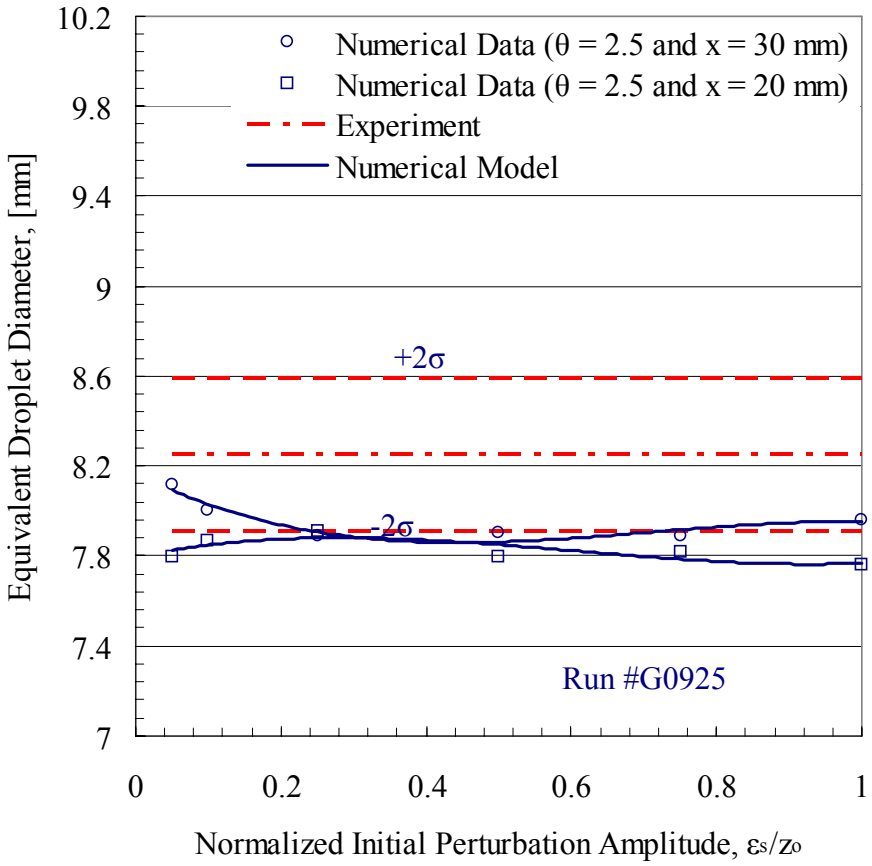

Figure C.15 Numerical and experimental data for the variation of the equivalent droplet diameter with the normalized initial perturbation amplitude carried out for an inclined surface (Run #G0925).

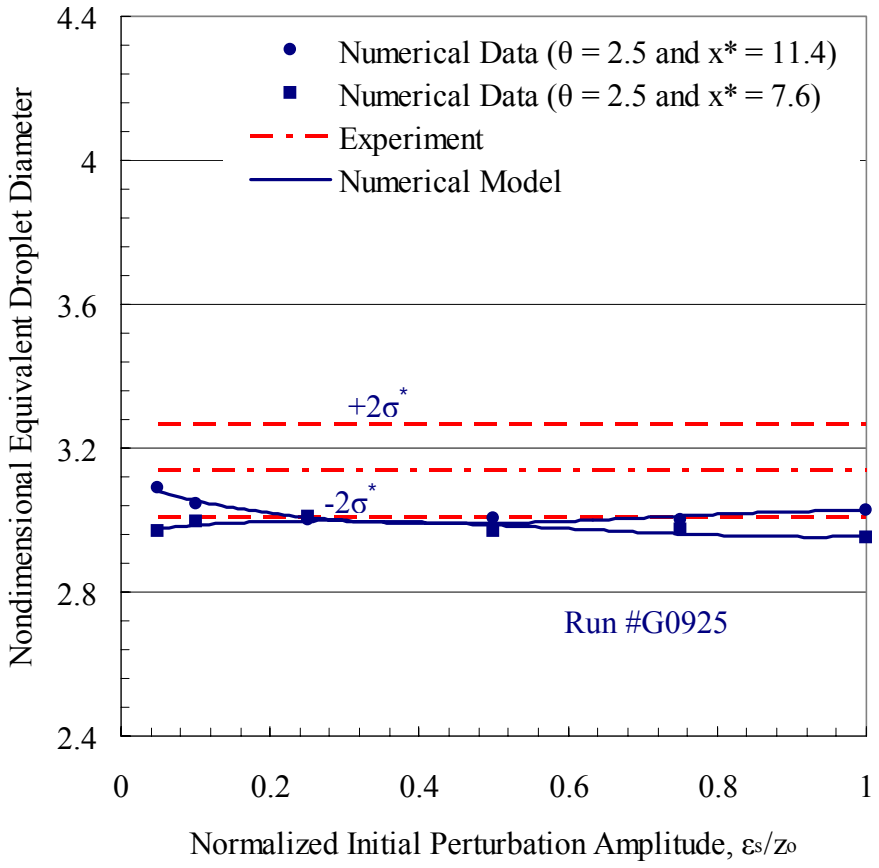

Figure C.16 Numerical and experimental data for the variation of the nondimensional equivalent droplet diameter with the normalized initial perturbation amplitude carried out for an inclined surface (Run #G0925).

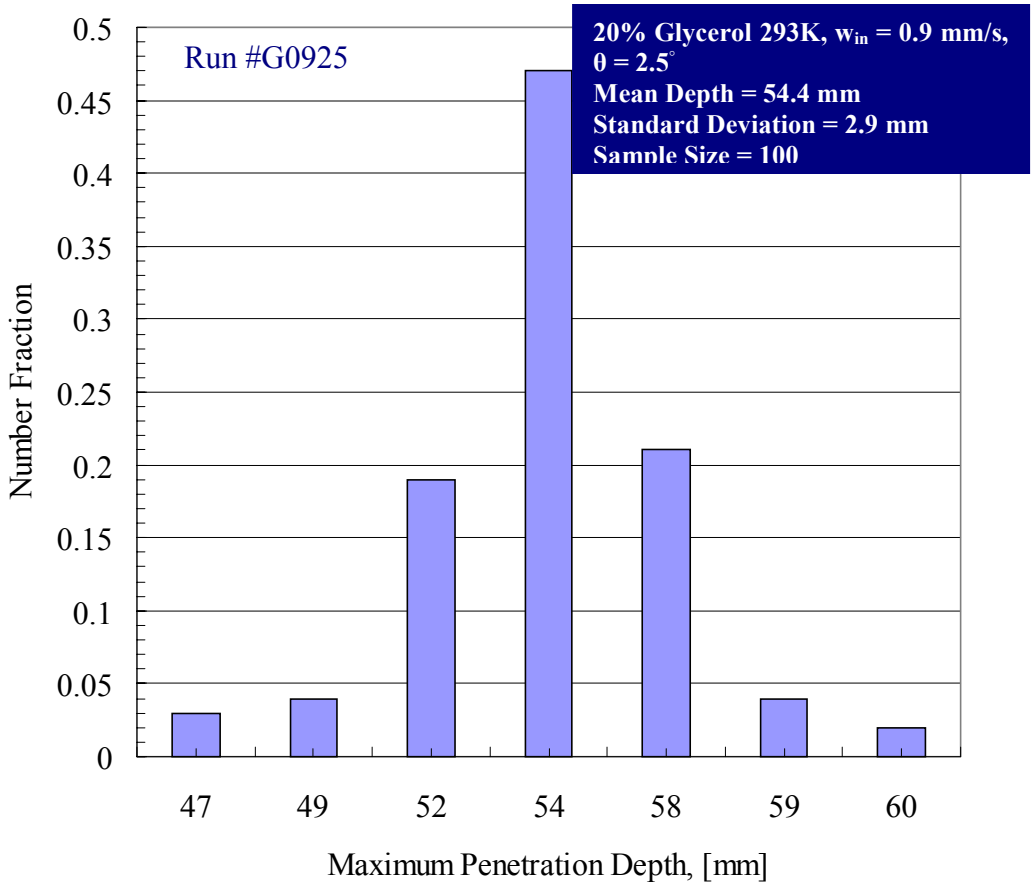

Figure C.17 Experimental data for the distribution of the maximum penetration depth carried out for an inclined surface (Run #G0925).

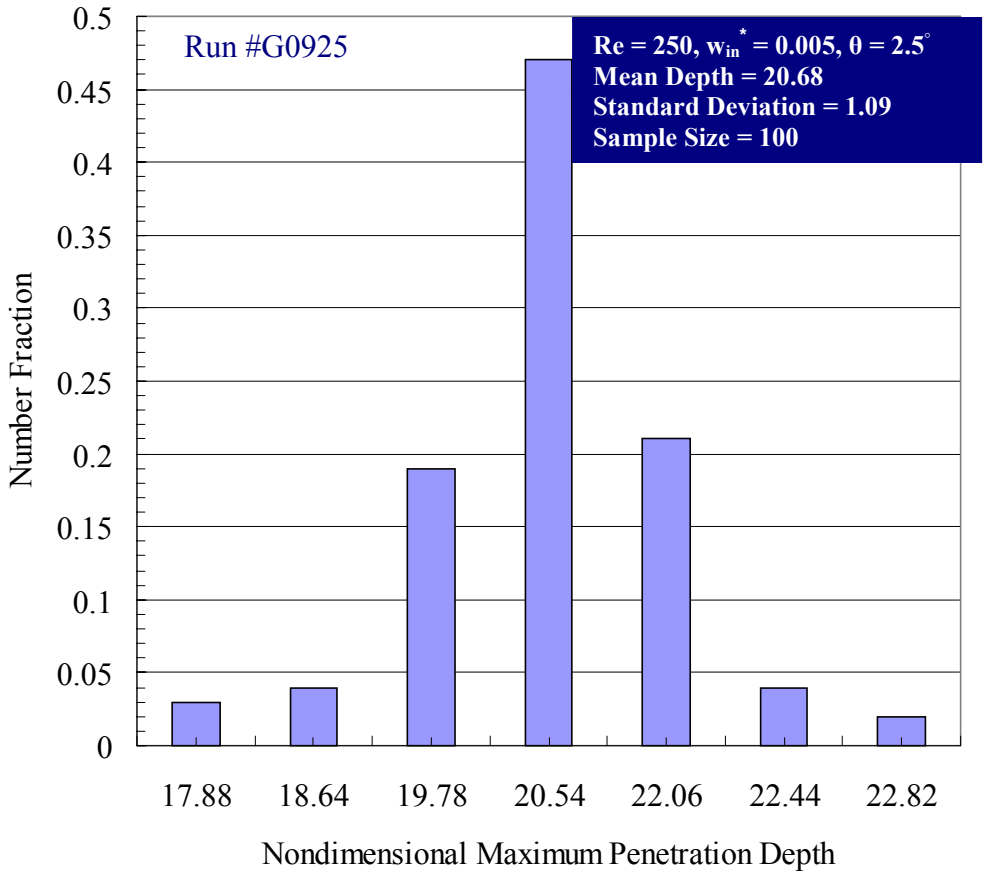

Figure C.18 Experimental data for the distribution of the nondimensional maximum penetration depth carried out for an inclined surface (Run #G0925).

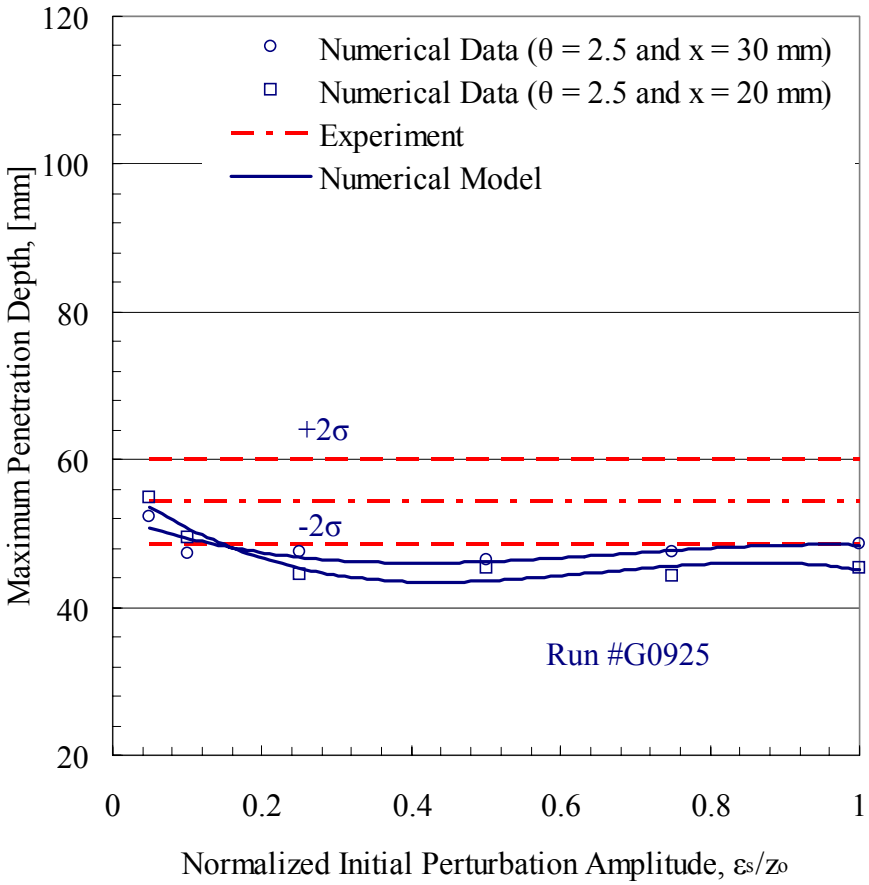

Figure C.19 Numerical and experimental data for the variation of the maximum penetration depth with the normalized initial perturbation amplitude carried out for an inclined surface (Run #G0925).

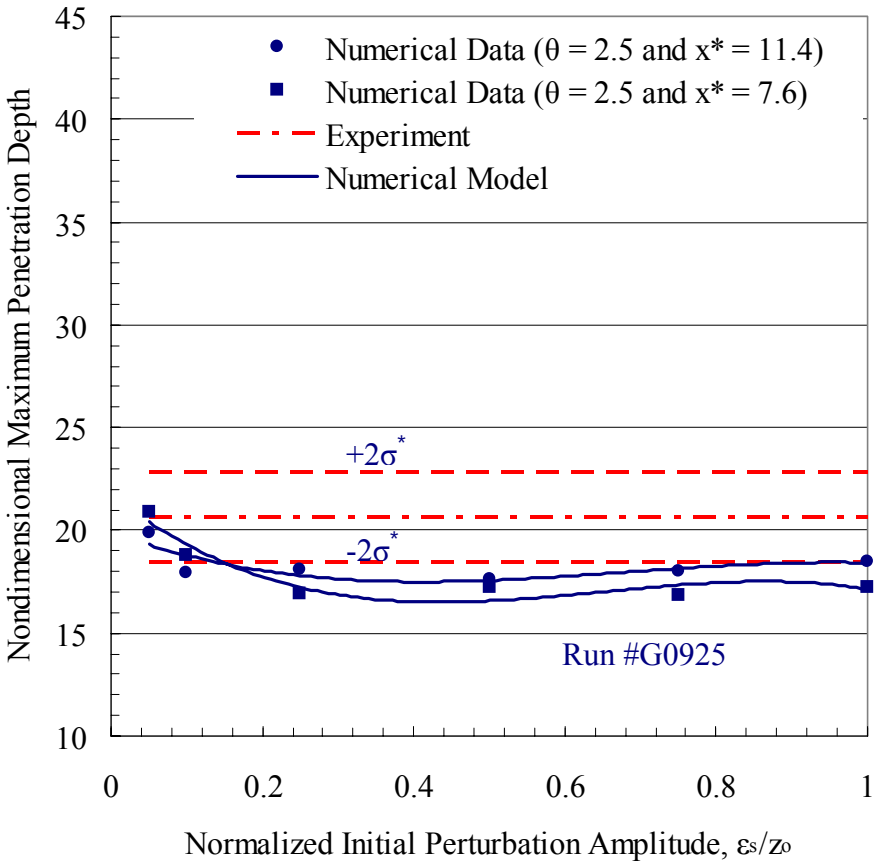

Figure C.20 Numerical and experimental data for the variation of the nondimensional maximum penetration depth with the normalized initial perturbation amplitude carried out for an inclined surface (Run #G0925).

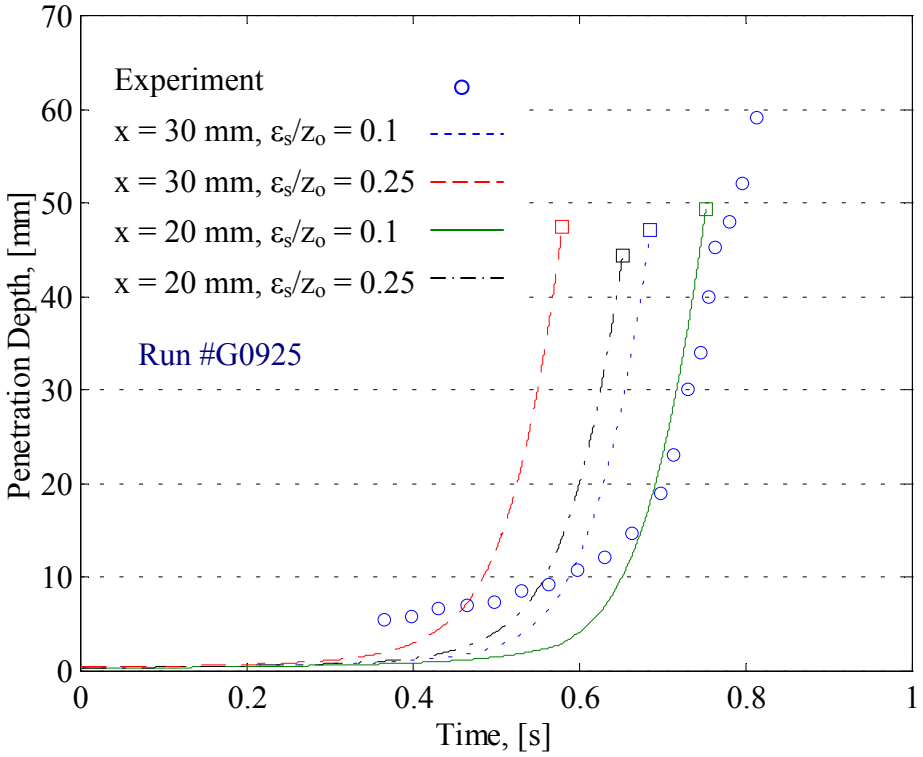

Figure C.21 Numerical and experimental data for the transient variation of the penetration depth carried out for an inclined surface (Run #G0925).

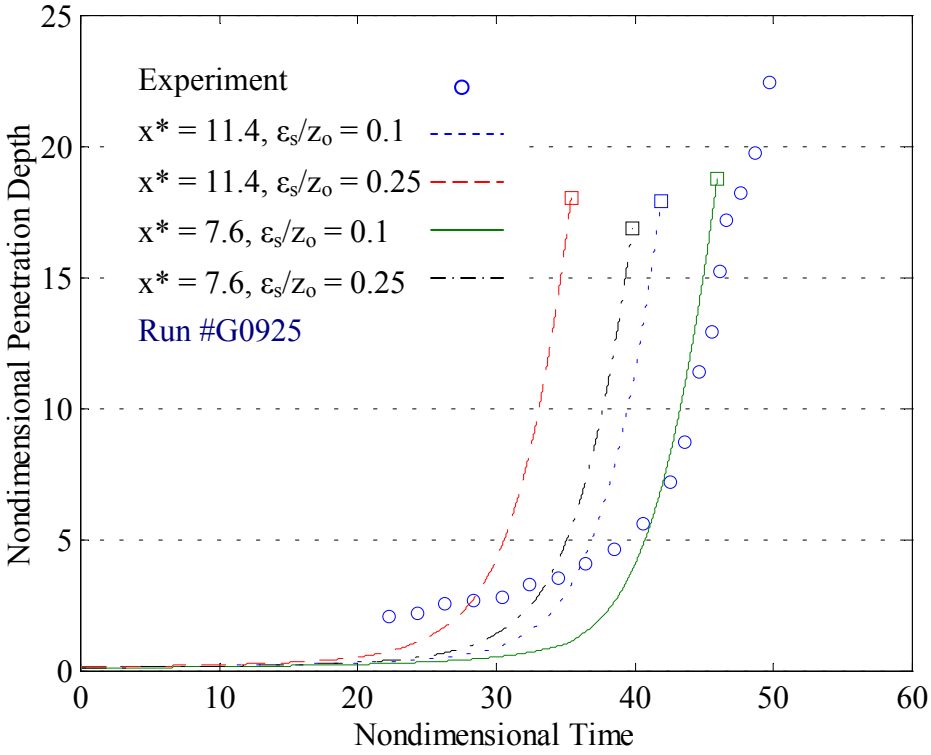

Figure C.22 Numerical and experimental data for the transient variation of the nondimensional penetration depth carried out for an inclined surface (Run #G0925).

C.2 Numerical and Experimental Results for Run #W1425

This section details the numerical and experimental results on the characteristic flow field variables for the bounded Rayleigh-Taylor instability with injection through the bounding inclined surface for Run #W1425. These results include: the evolution of the liquid film thickness, the liquid film surface perturbation geometry, the liquid droplet formation and detachment time, the equivalent size for detached droplets, and the time history of the penetration depth.

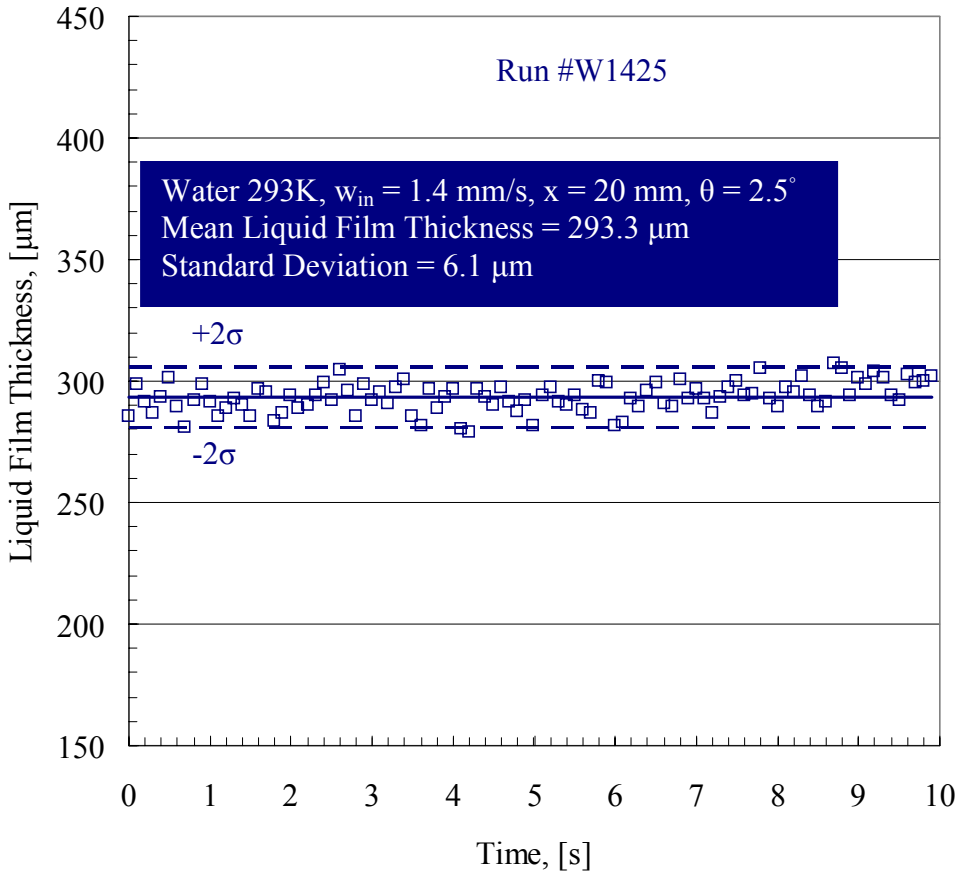

Figure C.23 Transient variation of the unperturbed liquid film thickness measured at an axial position x = 20 mm for Run #W1425.

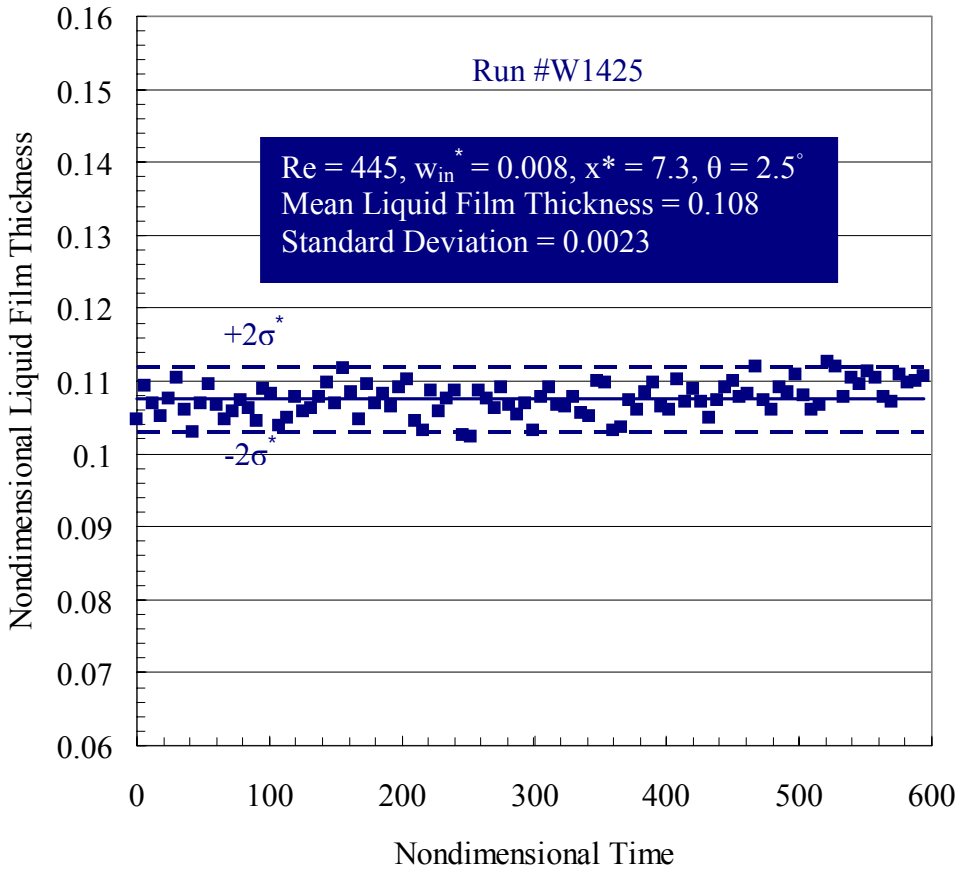

Figure C.24 The unperturbed liquid film thickness normalized by l as a function of time normalized by t_o measured at $x^* = 7.3$ for Run #W1425.

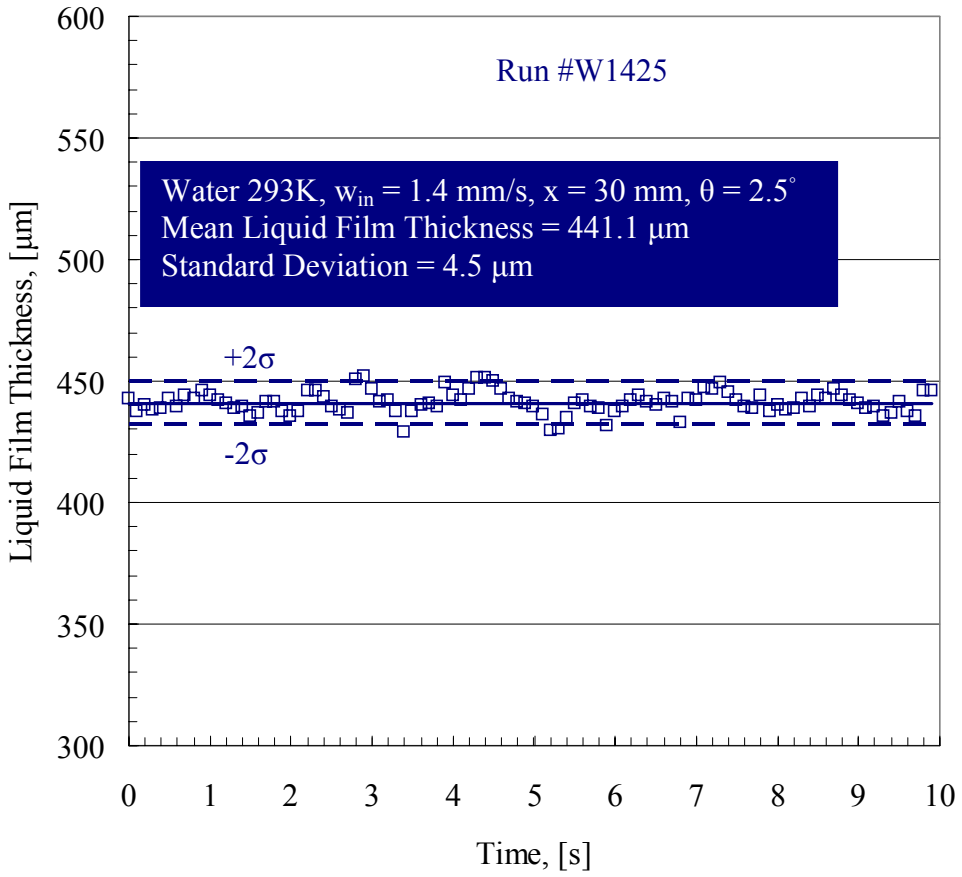

Figure C.25 Transient variation of the unperturbed liquid film thickness measured at an axial position x = 30 mm for Run #W1425.

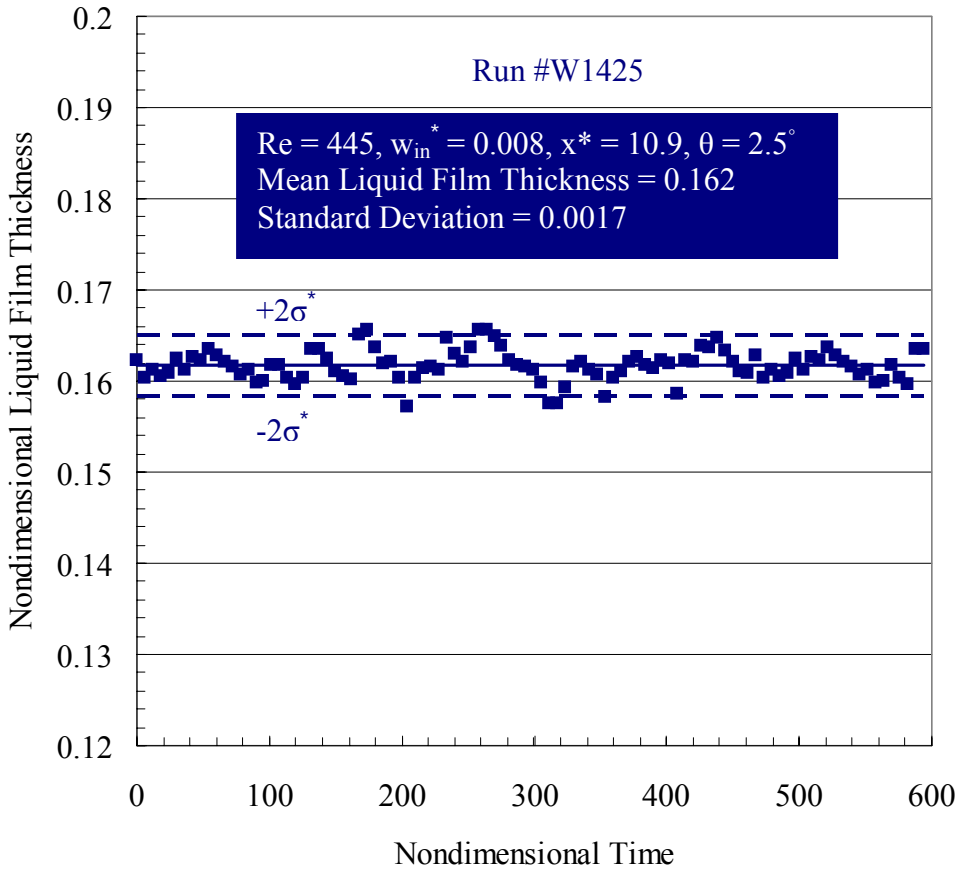

Figure C.26 The unperturbed liquid film thickness normalized by l as a function of time normalized by t_o measured at $x^* = 10.9$ for Run #W1425.

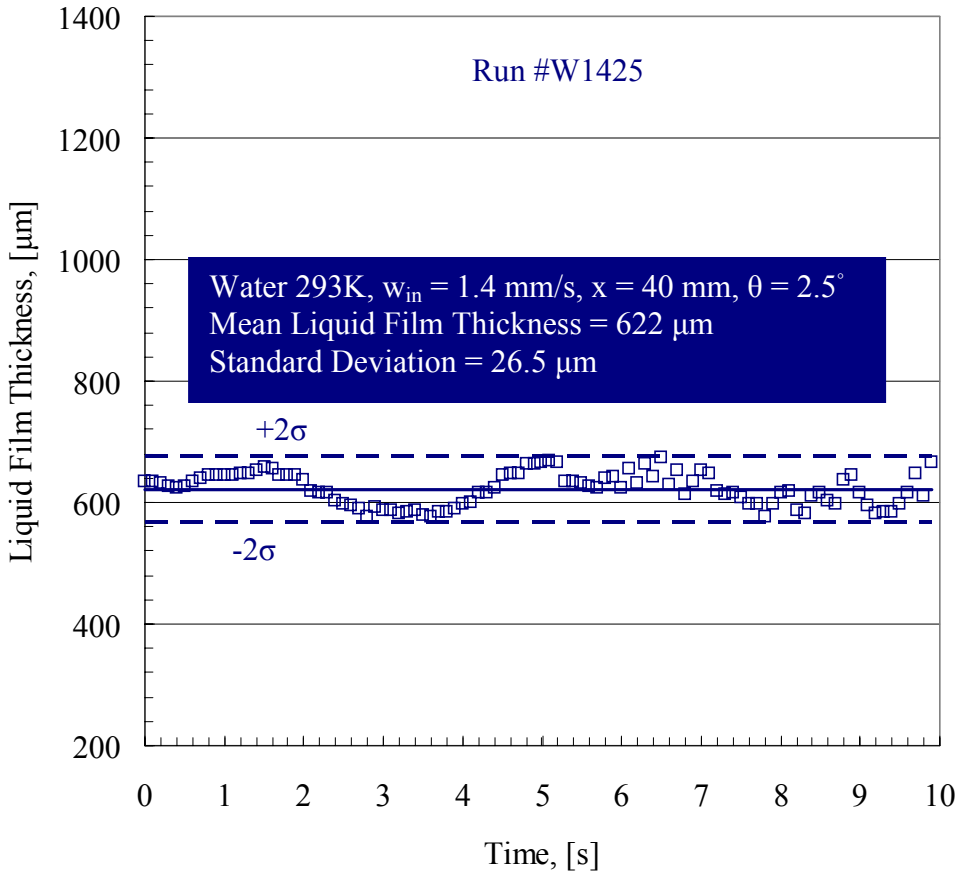

Figure C.27 Transient variation of the unperturbed liquid film thickness measured at an axial position x = 40 mm for Run #W1425.

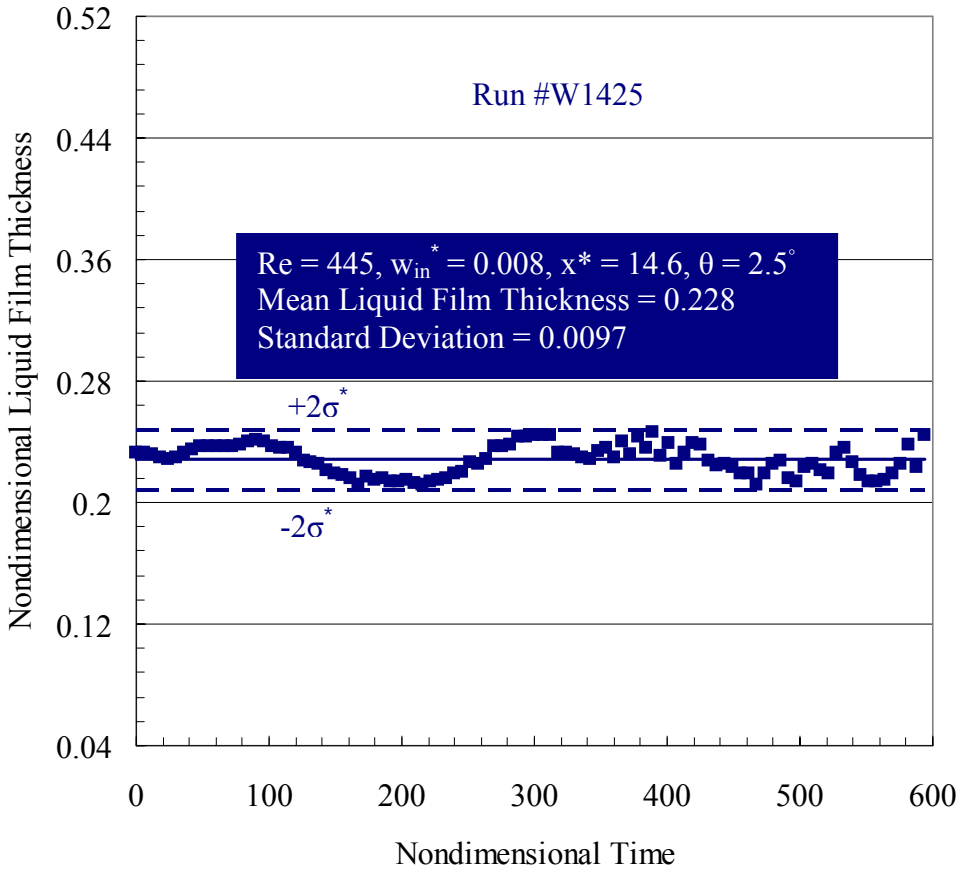

Figure C.28 The unperturbed liquid film thickness normalized by l as a function of time normalized by t_o measured at $x^* = 14.6$ for Run #W1425.

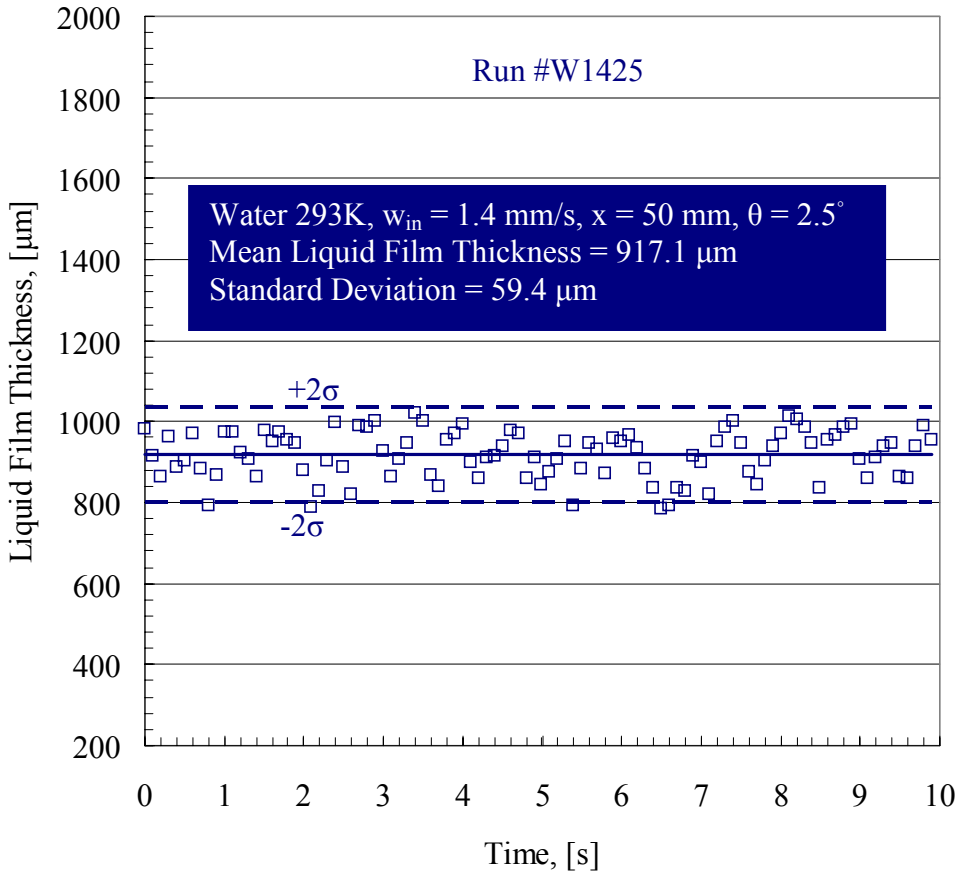

Figure C.29 Transient variation of the unperturbed liquid film thickness measured at an axial position x = 50 mm for Run #W1425.

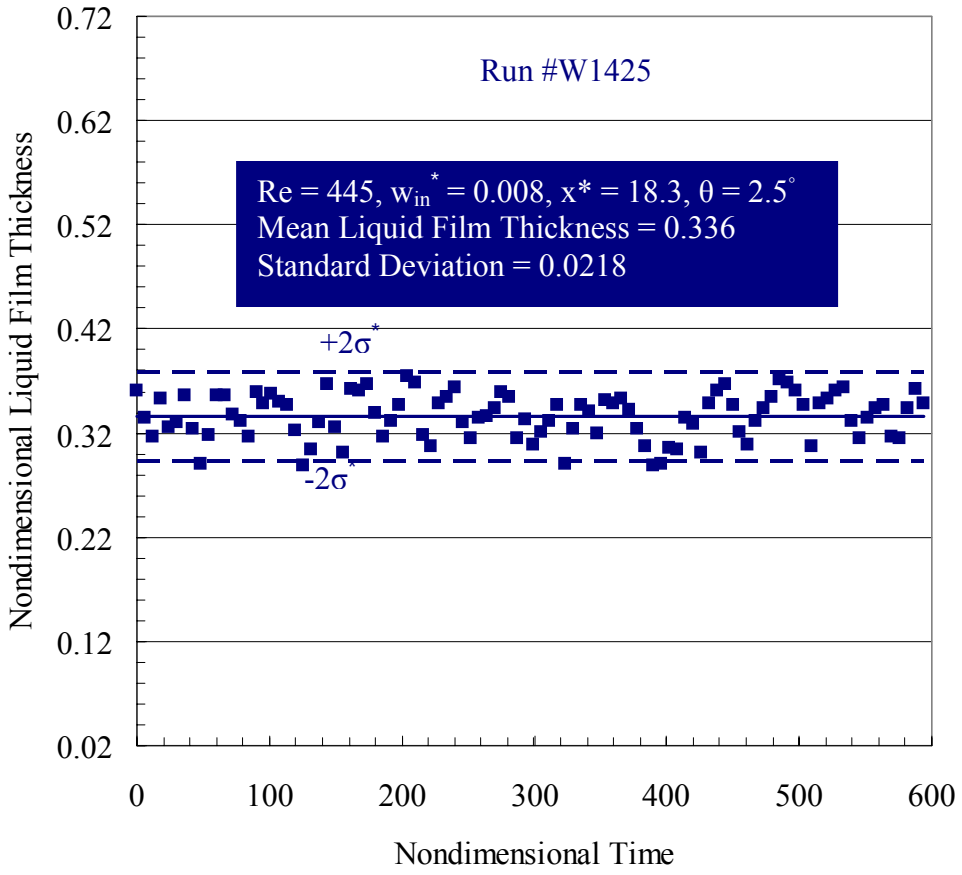

Figure C.30 The unperturbed liquid film thickness normalized by l as a function of time normalized by t_o measured at $x^* = 18.3$ for Run #W1425.

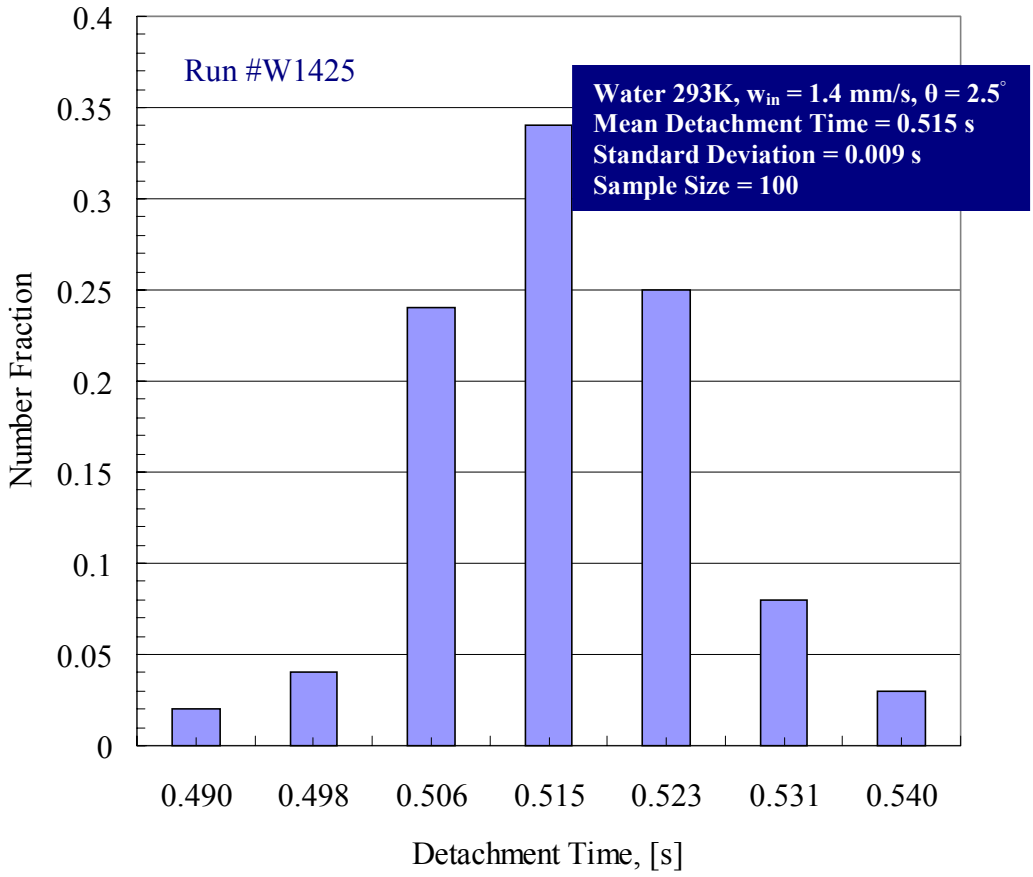

Figure C.31 Experimental data for the distribution of the detachment times carried out for an inclined surface (Run #W1425).

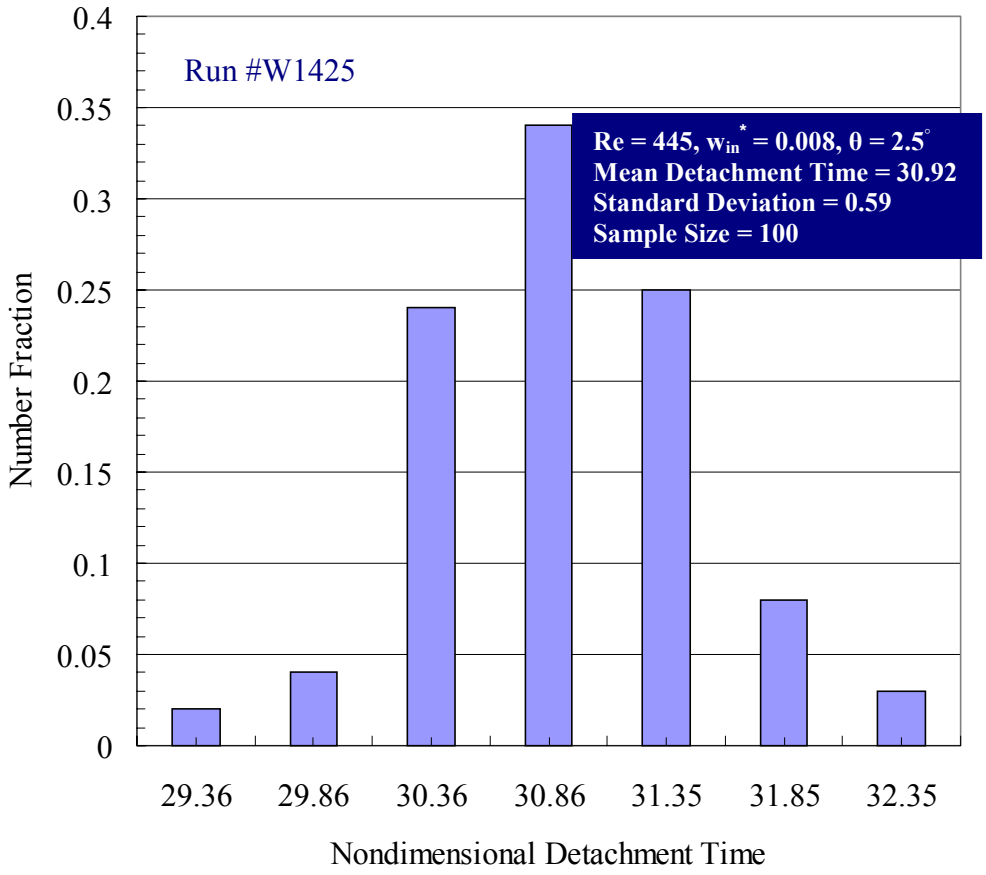

Figure C.32 Experimental data for the distribution of the nondimensional detachment time carried out for an inclined surface (Run #W1425).

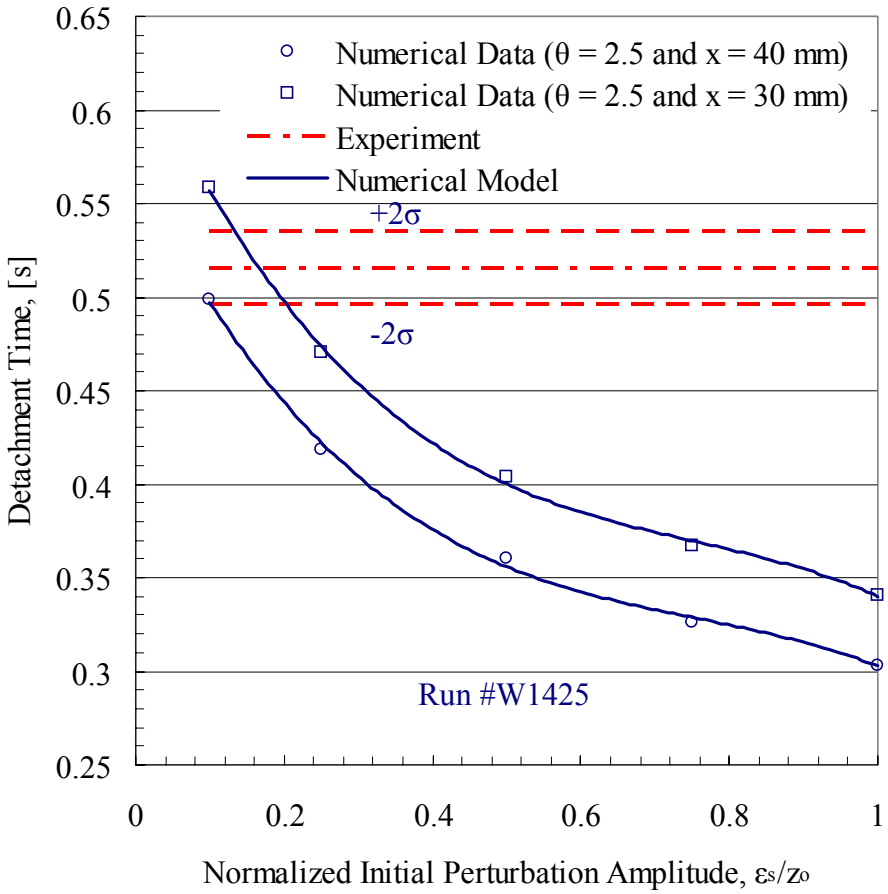

Figure C.33 Numerical and experimental data for the variation of the detachment time with the normalized initial perturbation amplitude carried out for an inclined surface (Run #W1425).

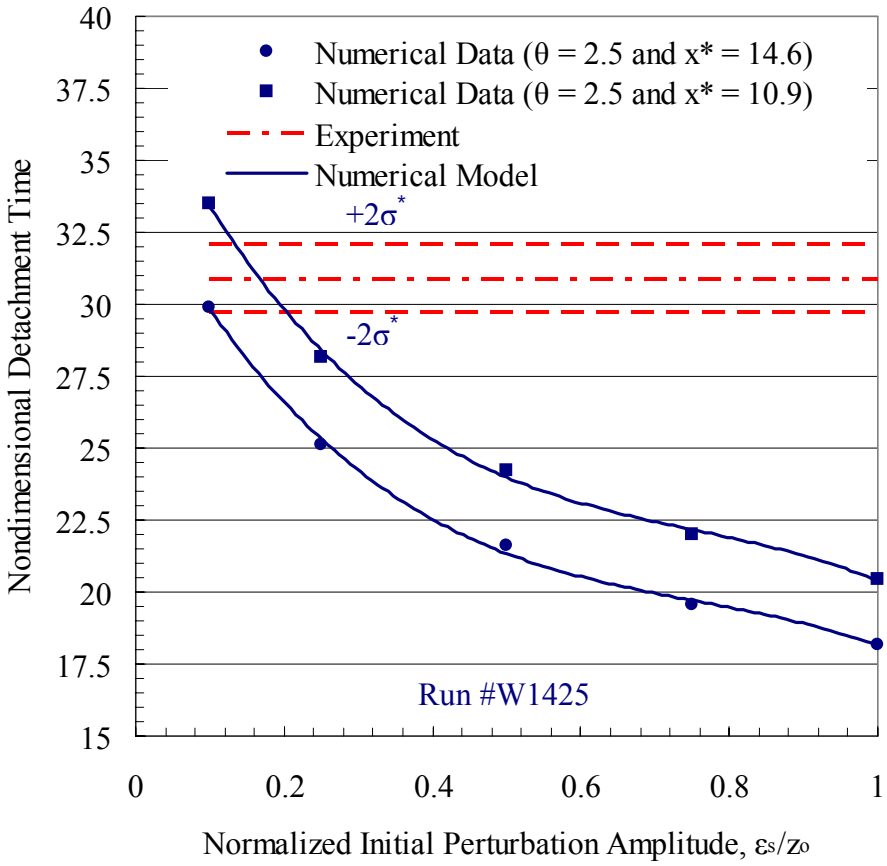

Figure C.34 Numerical and experimental data for the variation of the nondimensional detachment time with the normalized initial perturbation amplitude carried out for an inclined surface (Run #W1425).

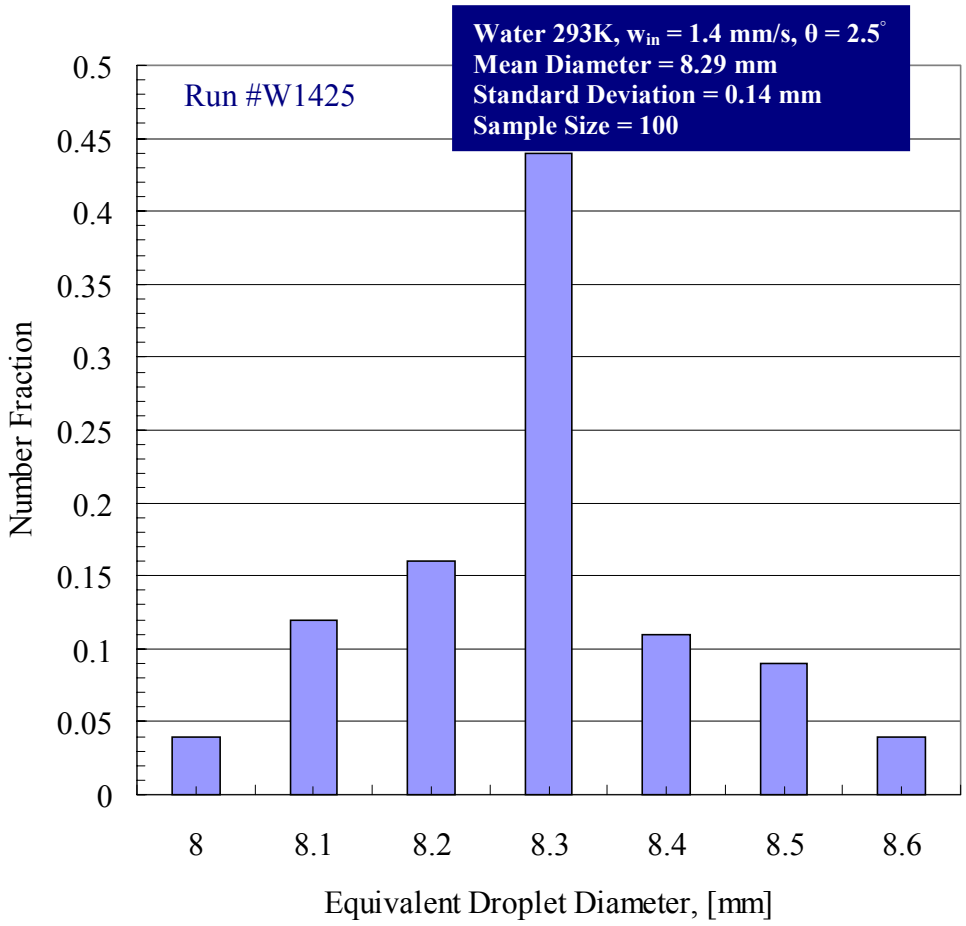

Figure C.35 Experimental data for the distribution of the equivalent droplet diameter carried out for an inclined surface (Run #W1425).

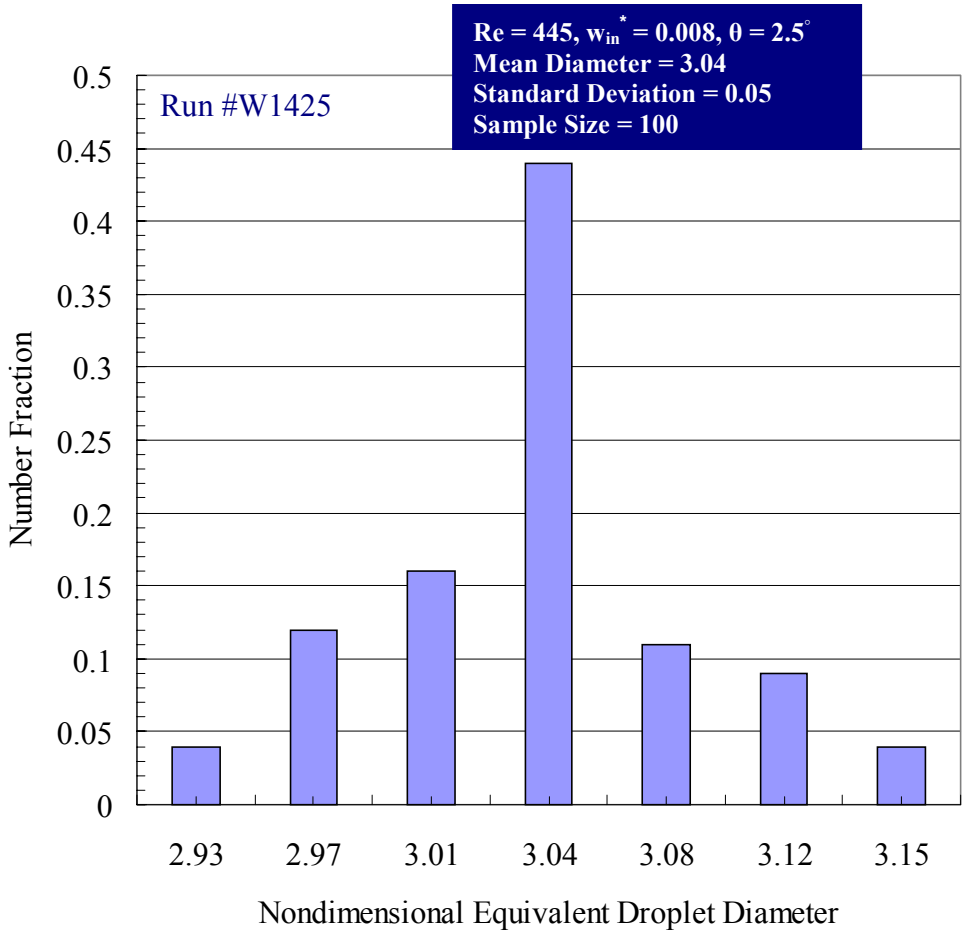

Figure C.36 Experimental data for the distribution of the nondimensional equivalent droplet diameter carried out for an inclined surface (Run #W1425).

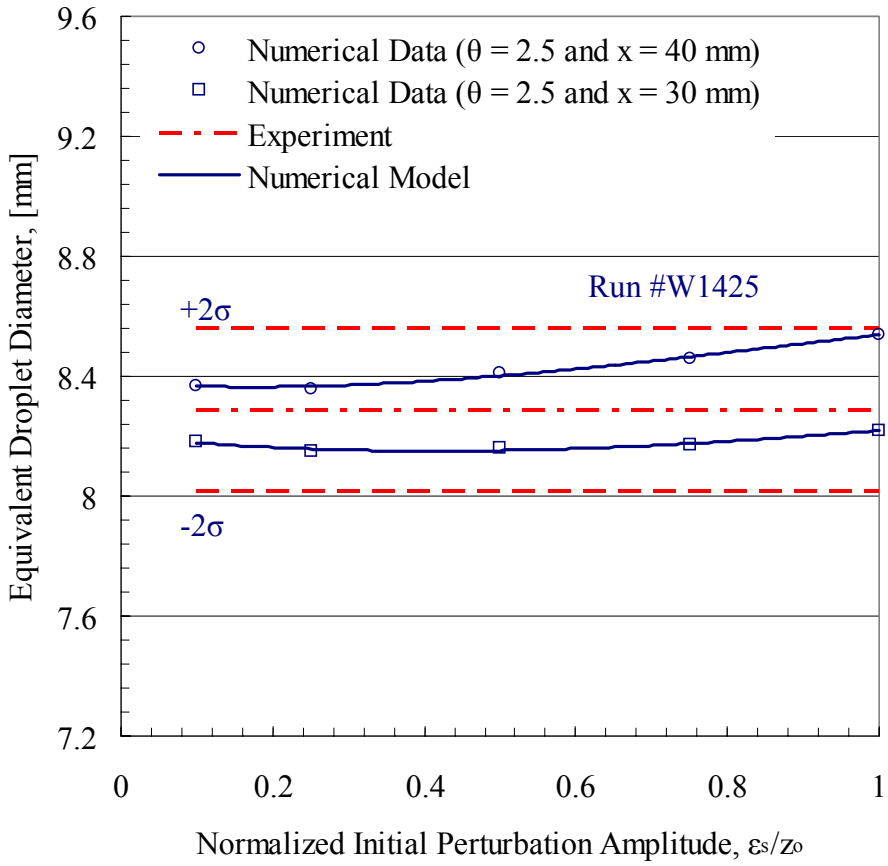

Figure C.37 Numerical and experimental data for the variation of the equivalent droplet diameter with the normalized initial perturbation amplitude carried out for an inclined surface (Run #W1425).

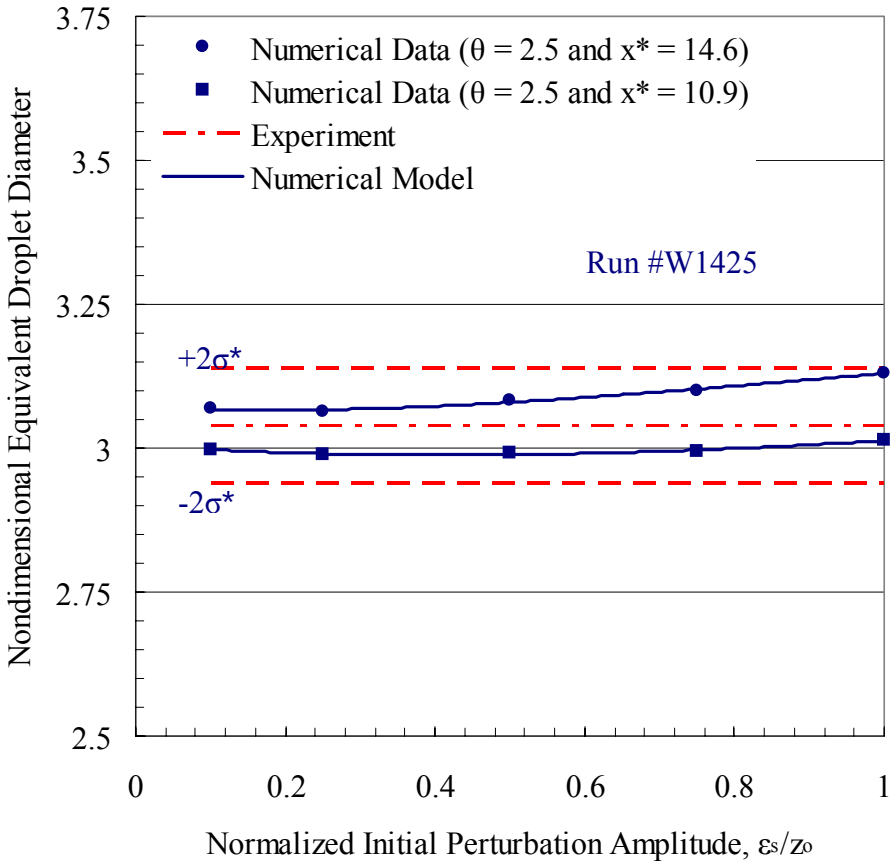

Figure C.38 Numerical and experimental data for the variation of the nondimensional equivalent droplet diameter with the normalized initial perturbation amplitude carried out for an inclined surface (Run #W1425).

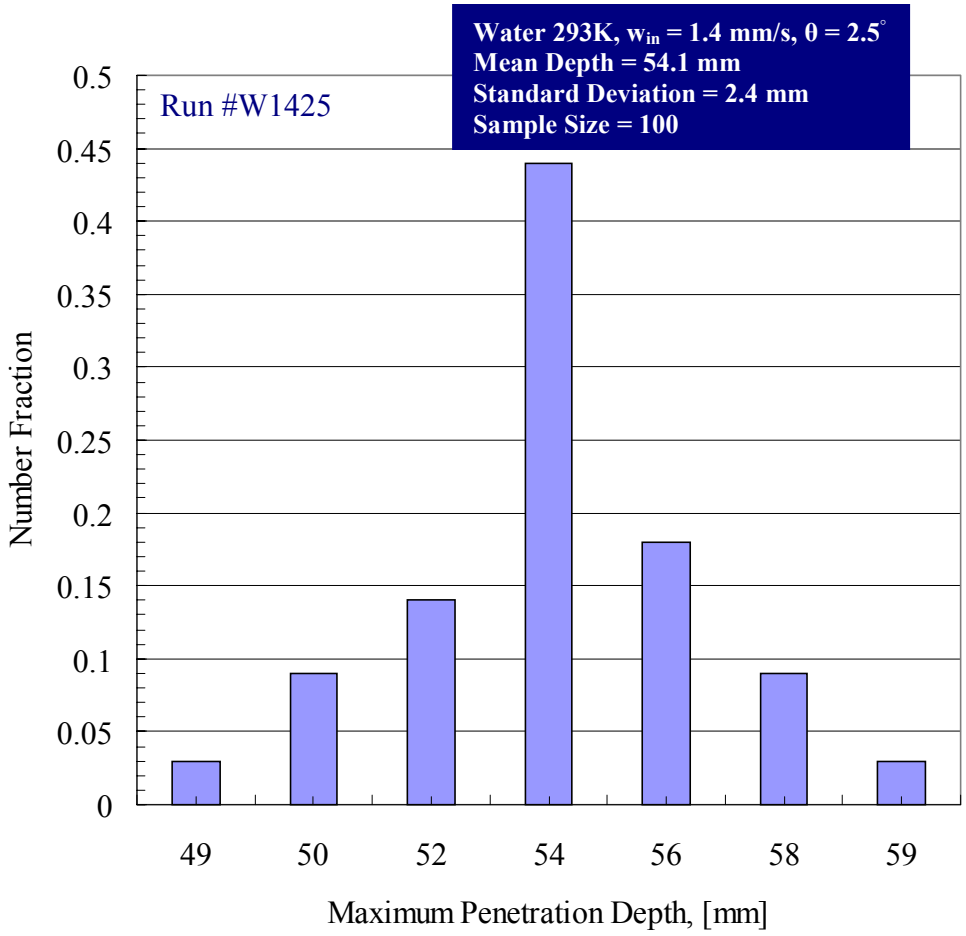

Figure C.39 Experimental data for the distribution of the maximum penetration depth carried out for an inclined surface (Run #W1425).

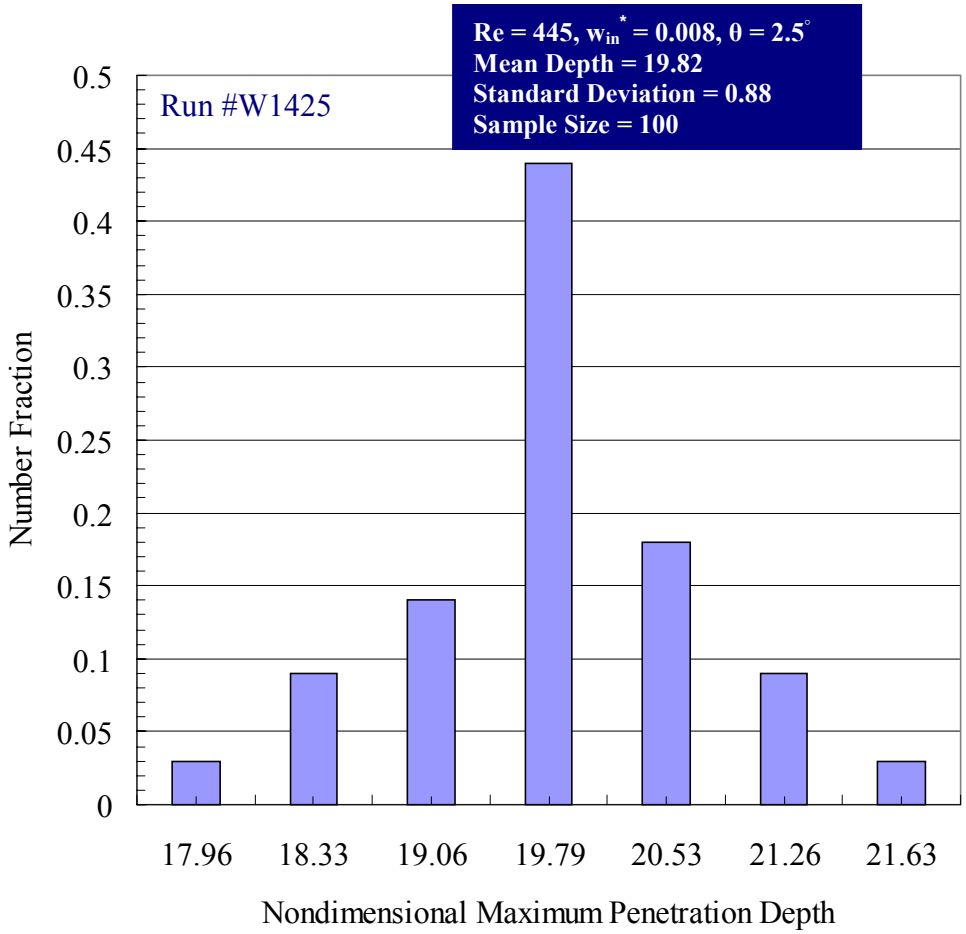

Figure C.40 Experimental data for the distribution of the nondimensional maximum penetration depth carried out for an inclined surface (Run #W1425).

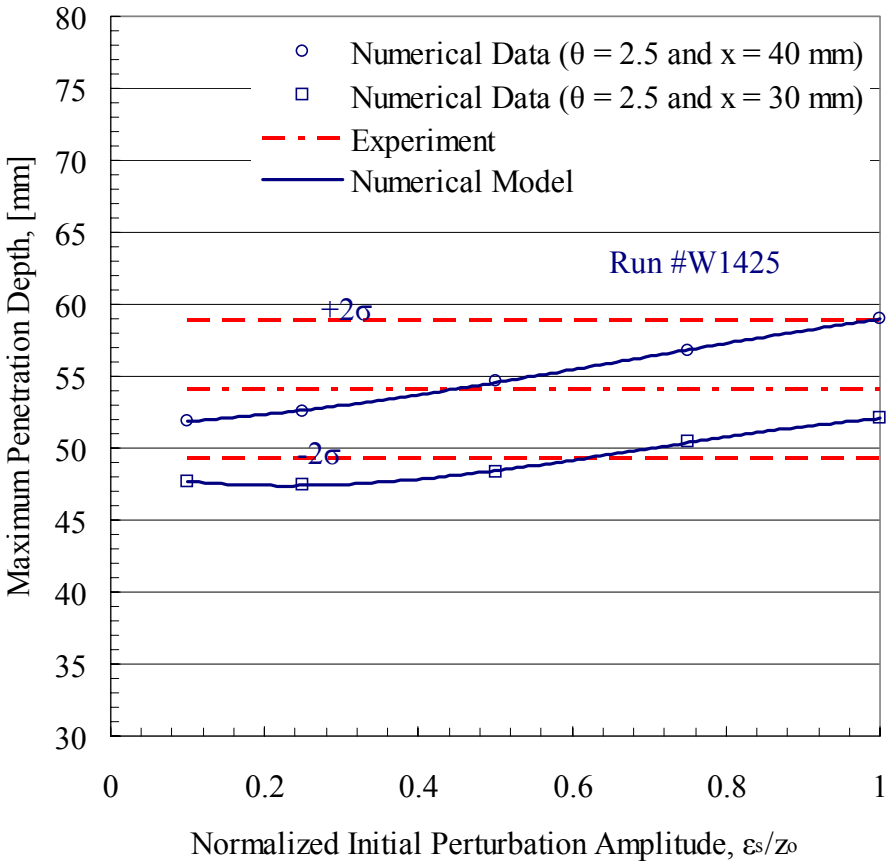

Figure C.41 Numerical and experimental data for the variation of the maximum penetration depth with the normalized initial perturbation amplitude carried out for an inclined surface (Run #W1425).

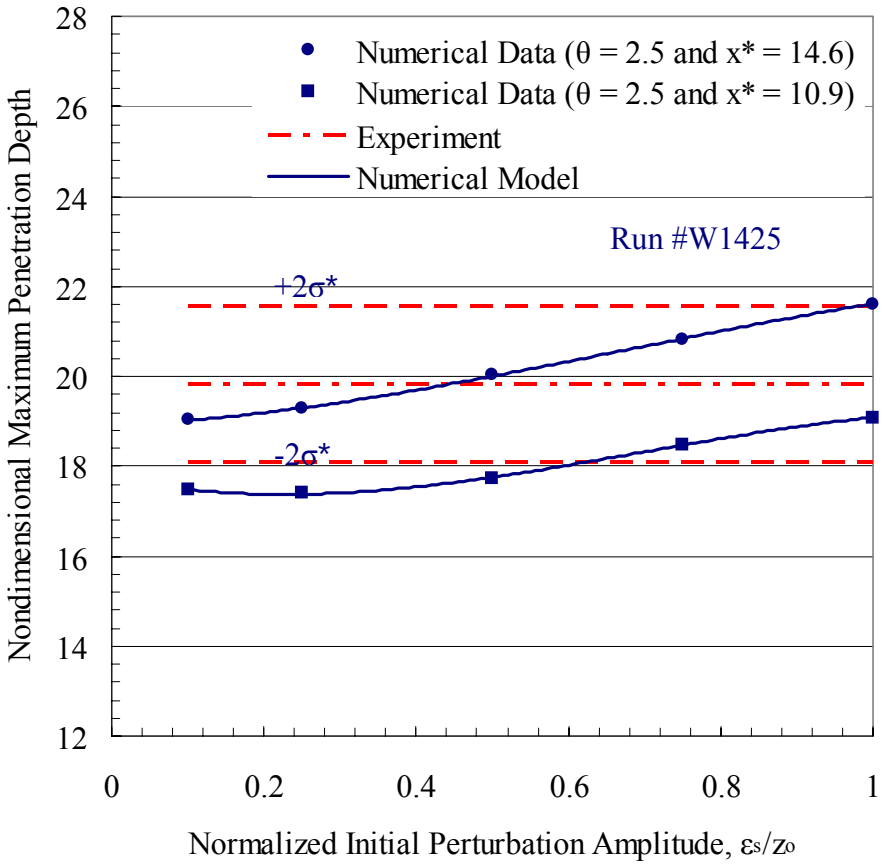

Figure C.42 Numerical and experimental data for the variation of the nondimensional maximum penetration depth with the normalized initial perturbation amplitude carried out for an inclined surface (Run #W1425).

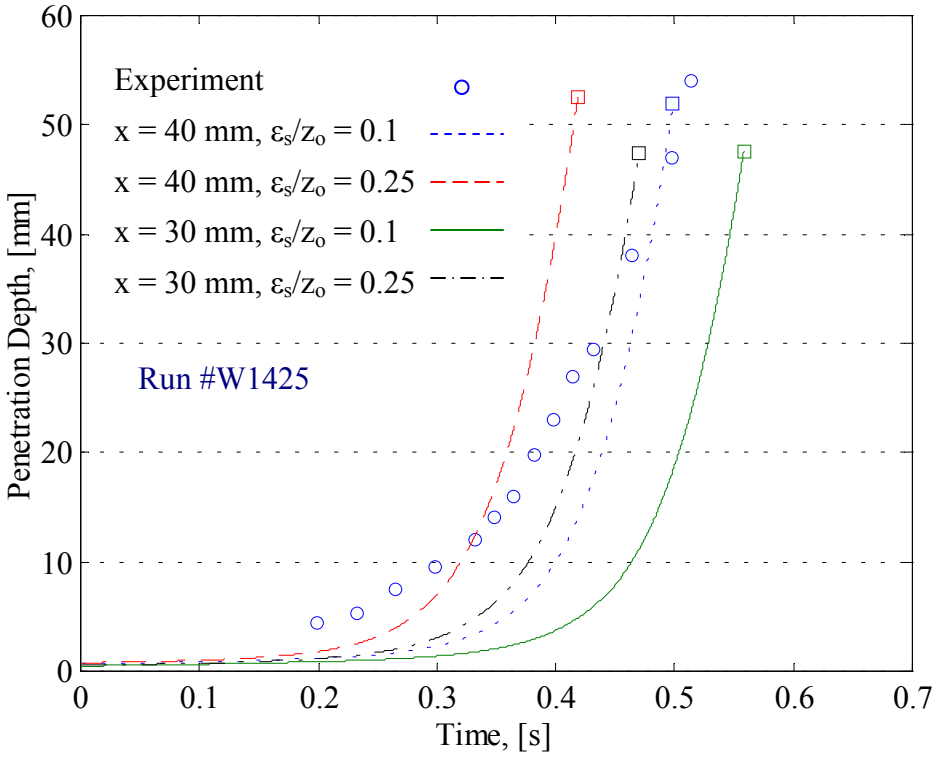

Figure C.43 Numerical and experimental data for the transient variation of the penetration depth carried out for an inclined surface (Run #W1425).

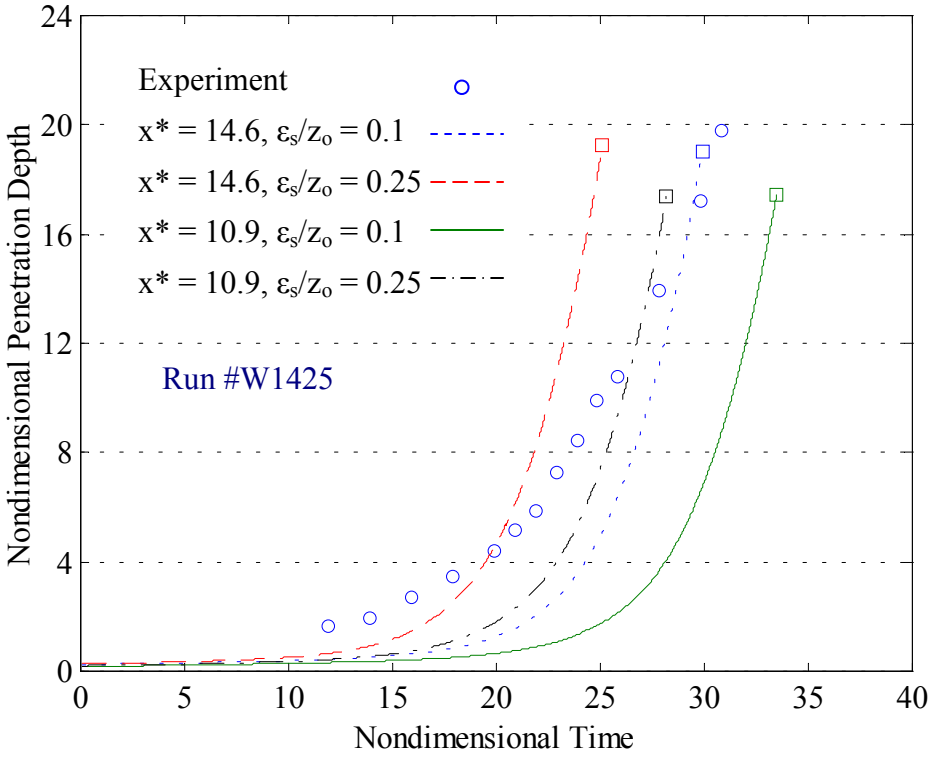

Figure C.44 Numerical and experimental data for the transient variation of the nondimensional penetration depth carried out for an inclined surface (Run #W1425).

C.3 Numerical and Experimental Results for Run #W1725

This section details the numerical and experimental results on the characteristic flow field variables for the bounded Rayleigh-Taylor instability with injection through the bounding inclined surface for Run #W1725. These results include: the evolution of the liquid film thickness, the liquid film surface perturbation geometry, the liquid droplet formation and detachment time, the equivalent size for detached droplets, and the time history of the penetration depth.

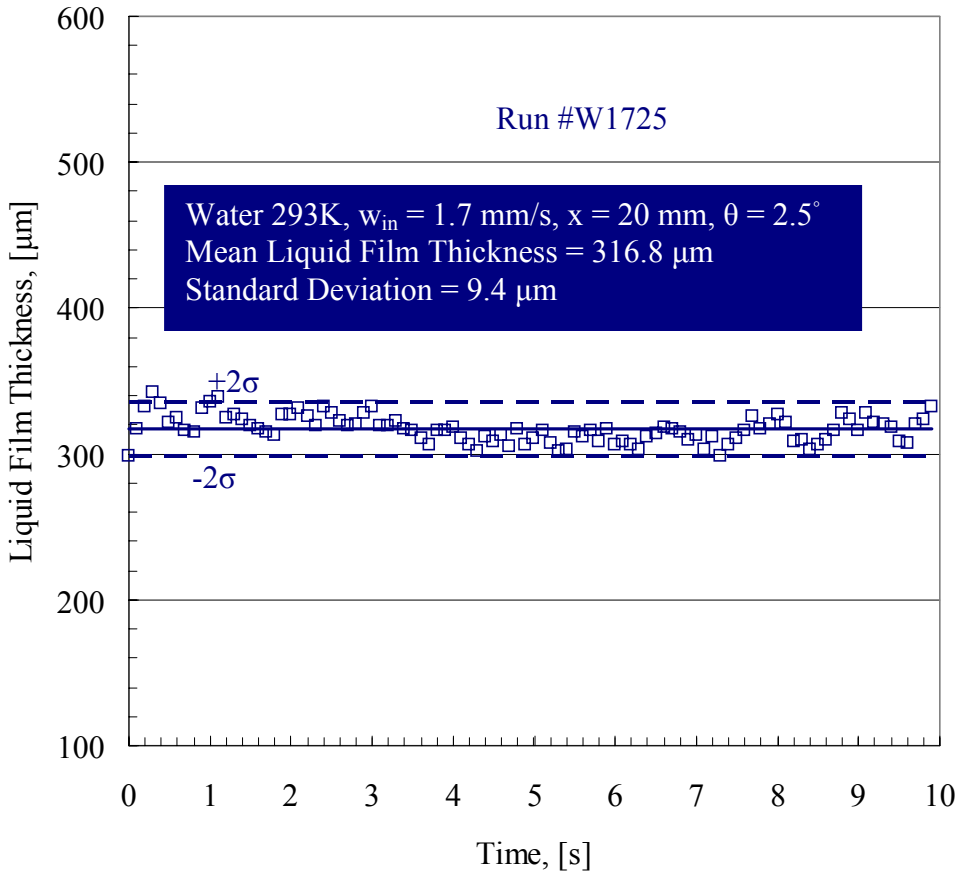

Figure C.45 Transient variation of the unperturbed liquid film thickness measured at an axial position x = 20 mm for Run #W1725.

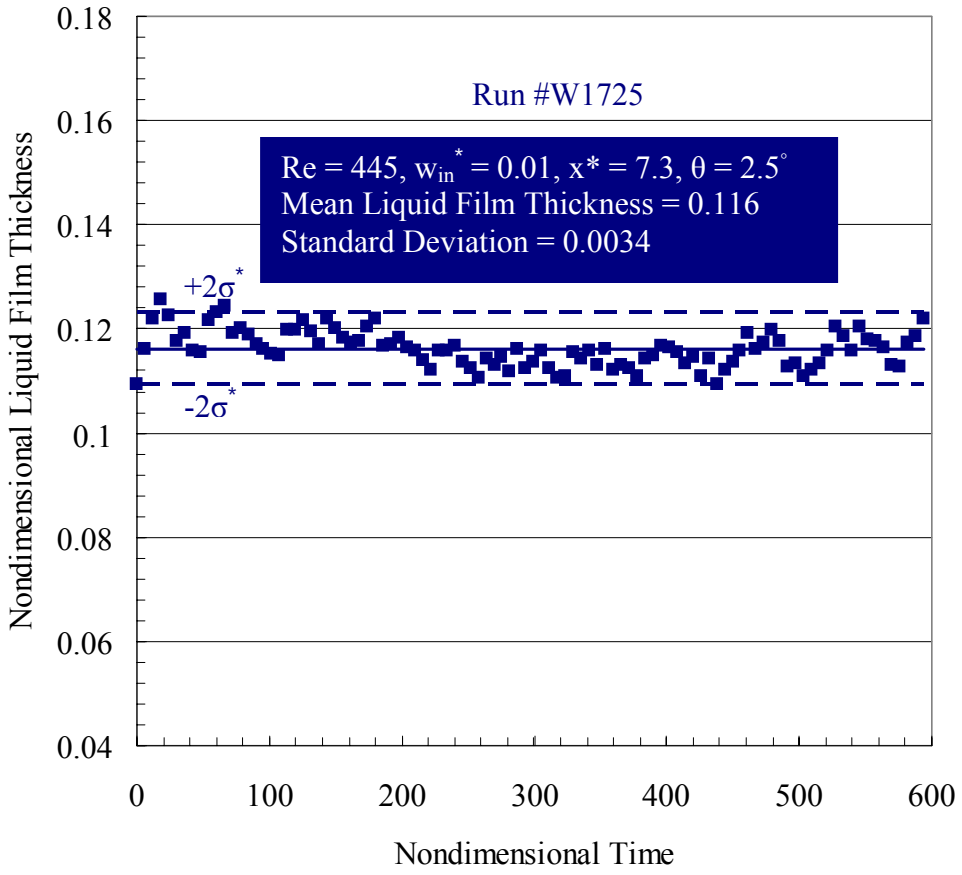

Figure C.46 The unperturbed liquid film thickness normalized by l as a function of time normalized by t_o measured at $x^* = 7.3$ for Run #W1725.

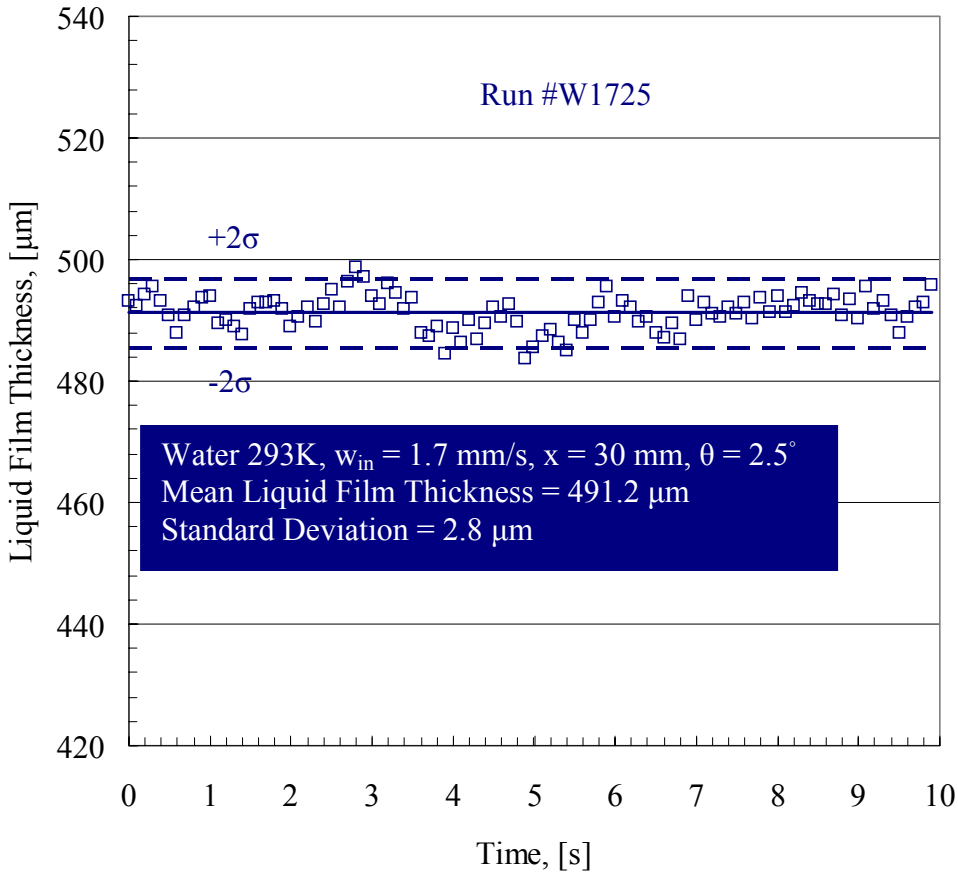

Figure C.47 Transient variation of the unperturbed liquid film thickness measured at an axial position x = 30 mm for Run #W1725.

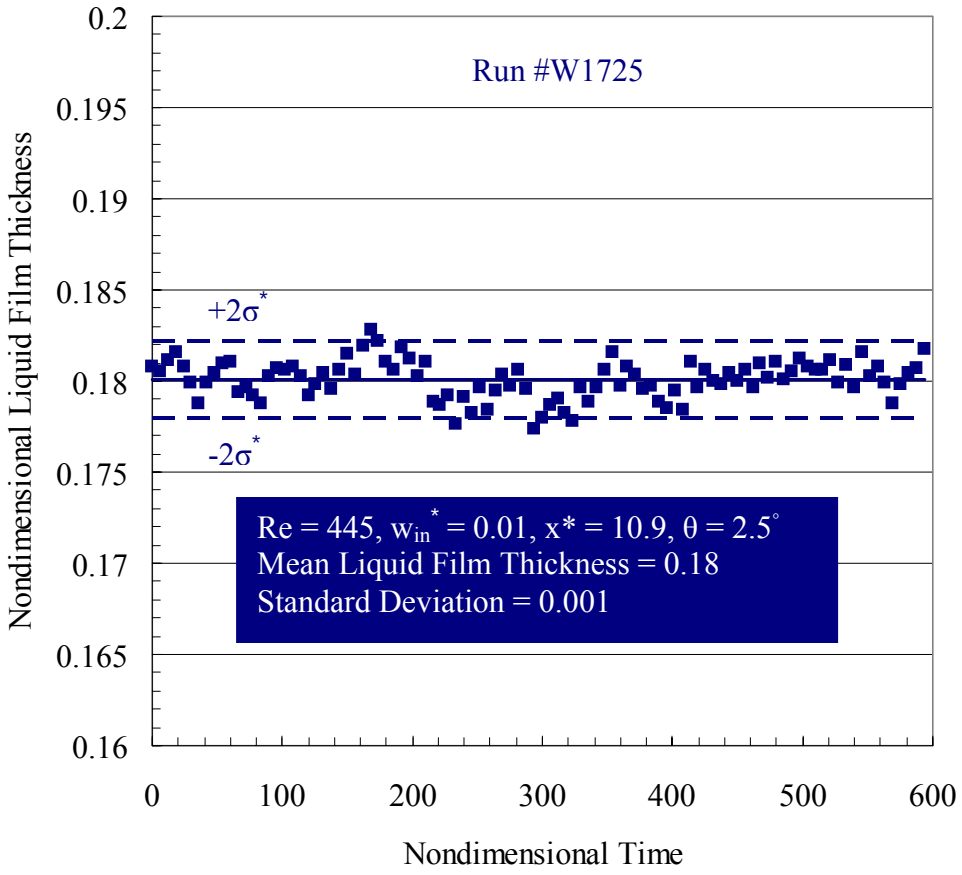

Figure C.48 The unperturbed liquid film thickness normalized by l as a function of time normalized by t_o measured at $x^* = 10.9$ for Run #W1725.

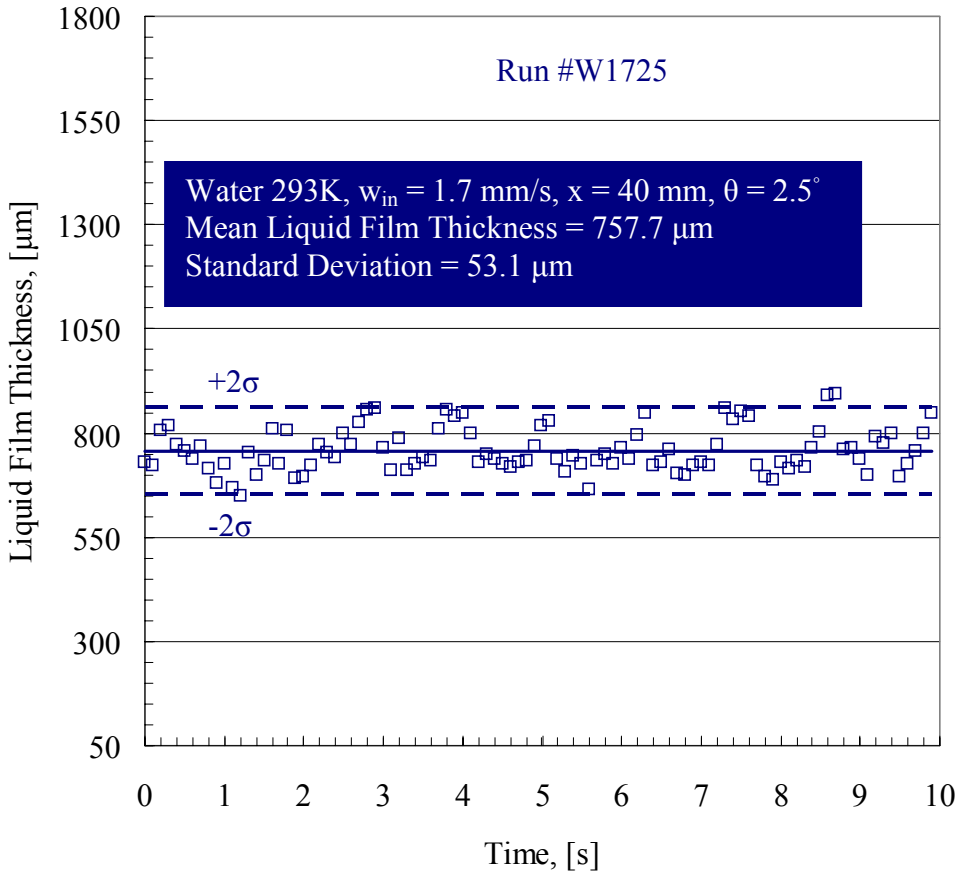

Figure C.49 Transient variation of the unperturbed liquid film thickness measured at an axial position x = 40 mm for Run #W1725.

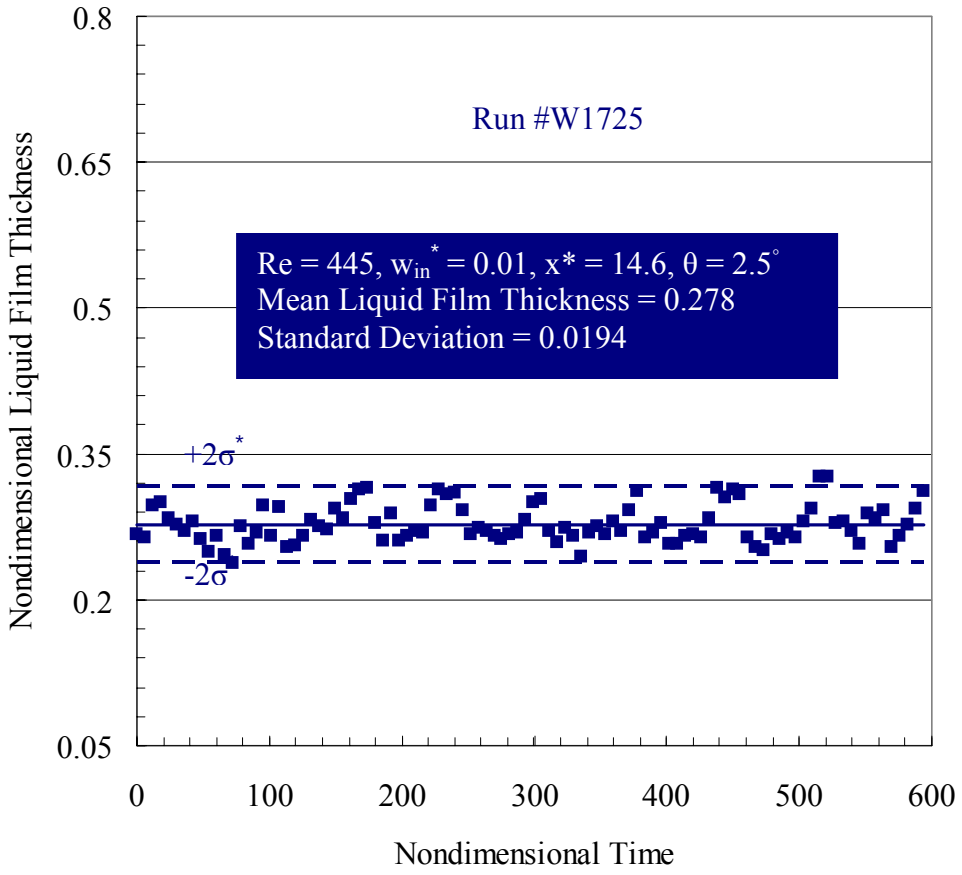

Figure C.50 The unperturbed liquid film thickness normalized by l as a function of time normalized by t_o measured at $x^* = 14.6$ for Run #W1725.

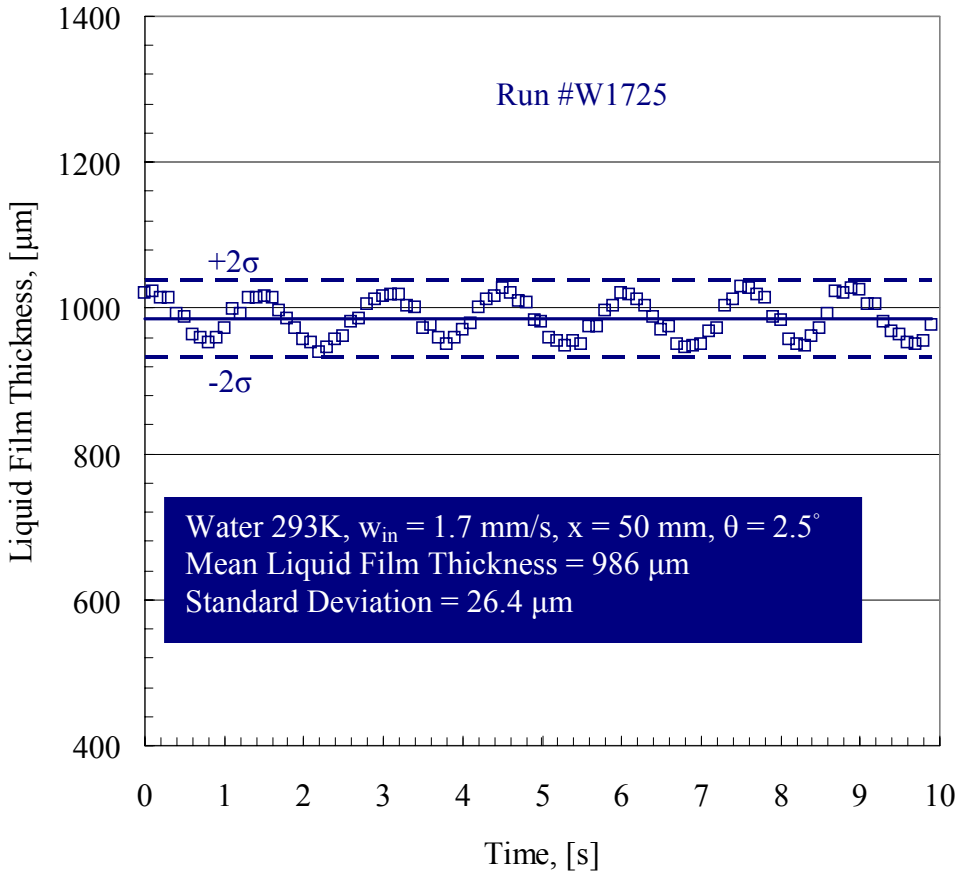

Figure C.51 Transient variation of the unperturbed liquid film thickness measured at an axial position x = 50 mm for Run #W1725.

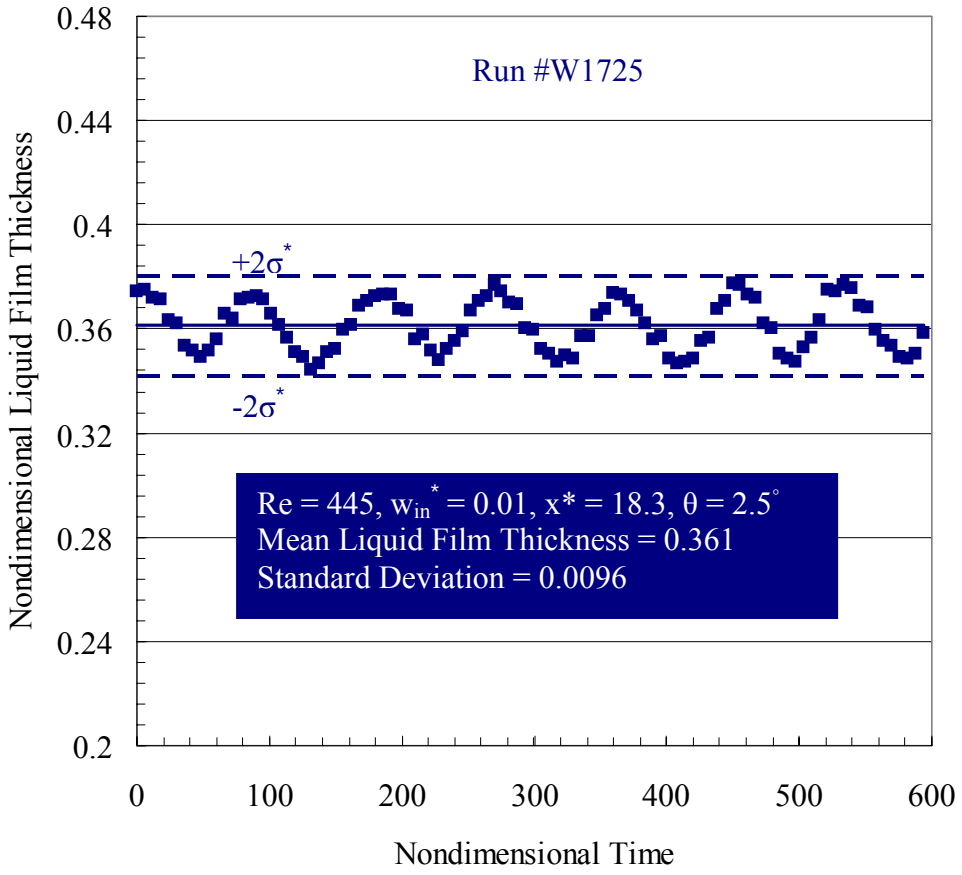

Figure C.52 The unperturbed liquid film thickness normalized by l as a function of time normalized by t_o measured at $x^* = 18.3$ for Run #W1725.

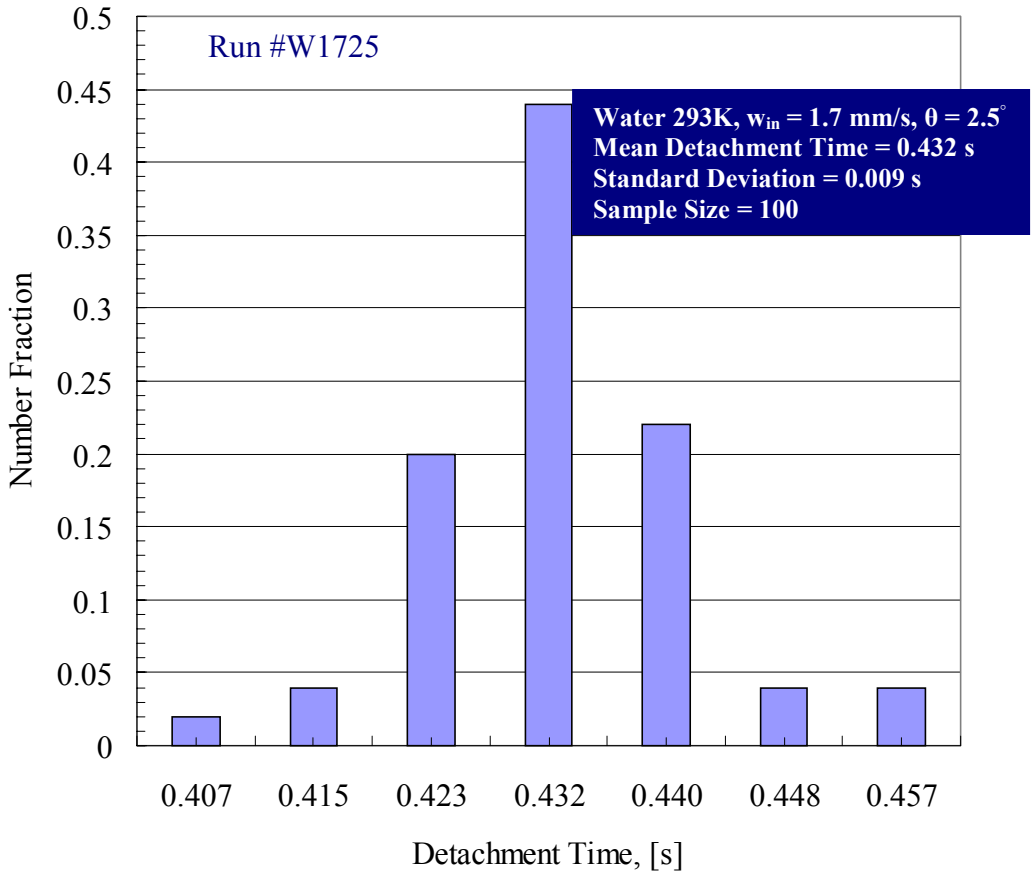

Figure C.53 Experimental data for the distribution of the detachment times carried out for an inclined surface (Run #W1725).

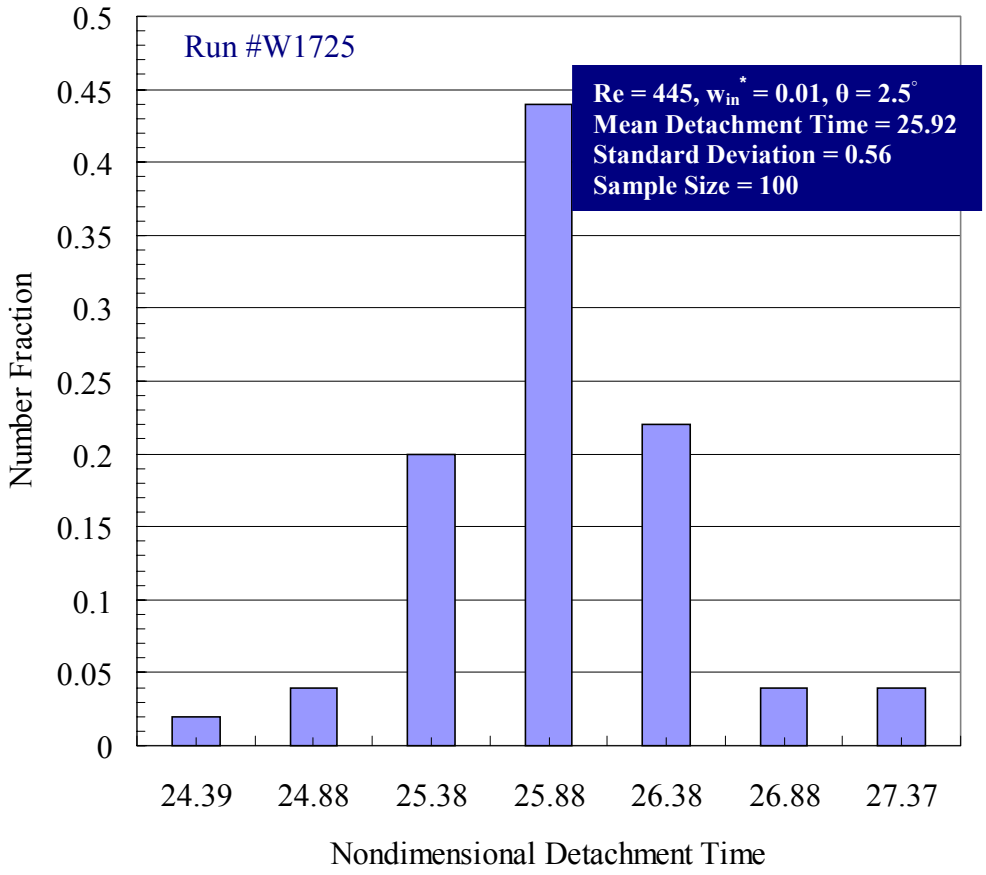

Figure C.54 Experimental data for the distribution of the nondimensional detachment time carried out for an inclined surface (Run #W1725).

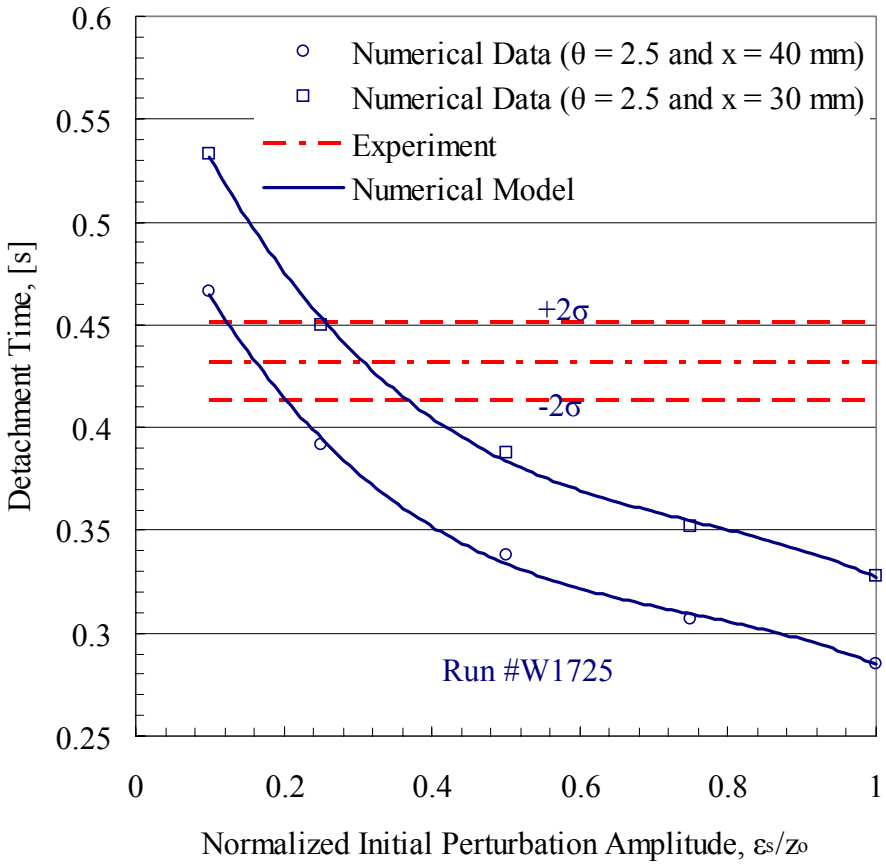

Figure C.55 Numerical and experimental data for the variation of the detachment time with the normalized initial perturbation amplitude carried out for an inclined surface (Run #W1725).

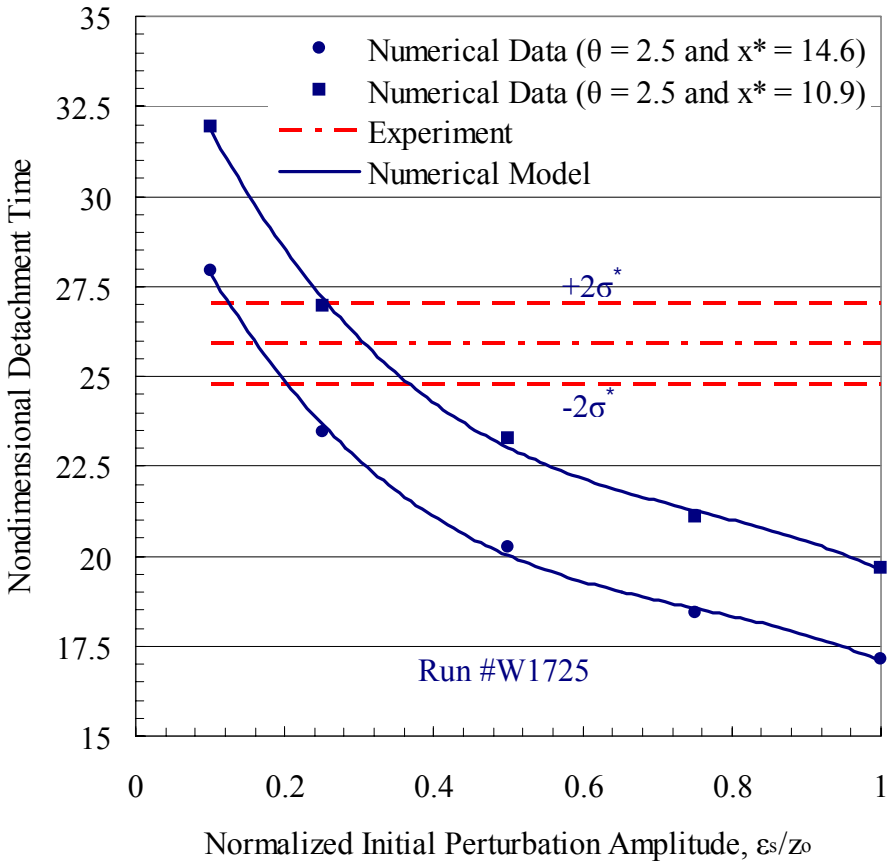

Figure C.56 Numerical and experimental data for the variation of the nondimensional detachment time with the normalized initial perturbation amplitude carried out for an inclined surface (Run #W1725).

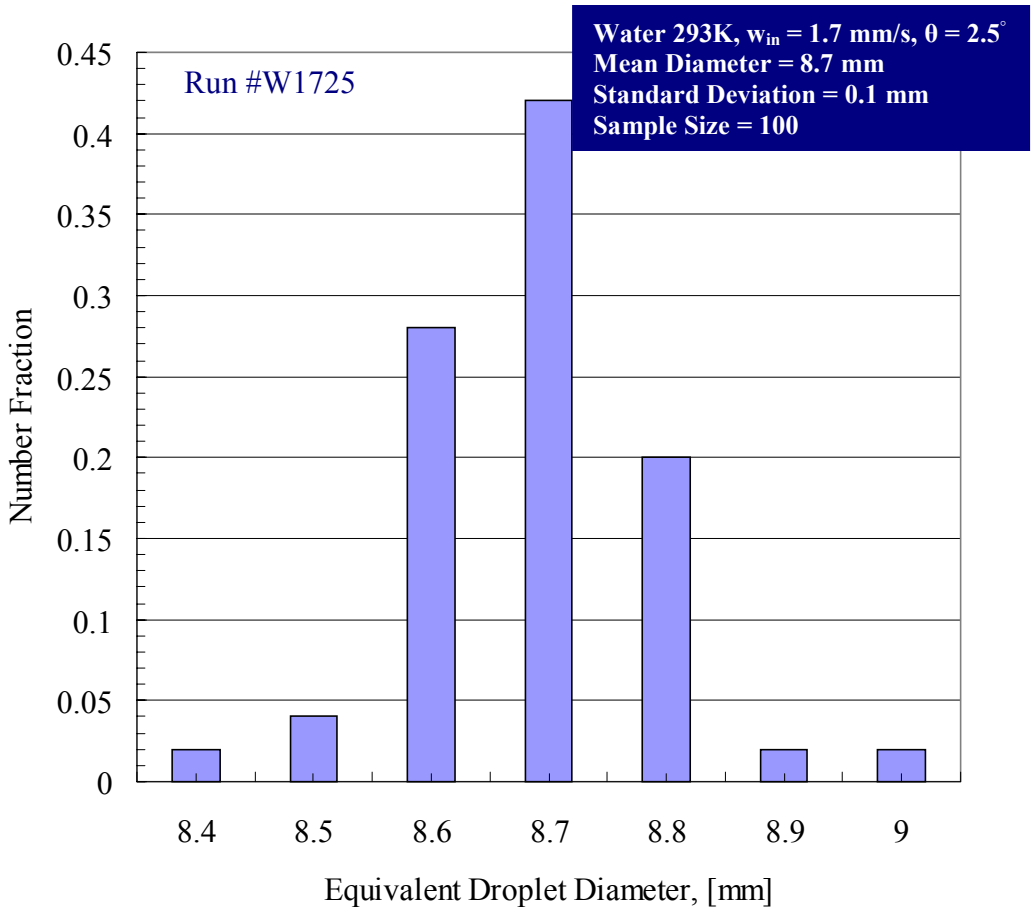

Figure C.57 Experimental data for the distribution of the equivalent droplet diameter carried out for an inclined surface (Run #W1725).

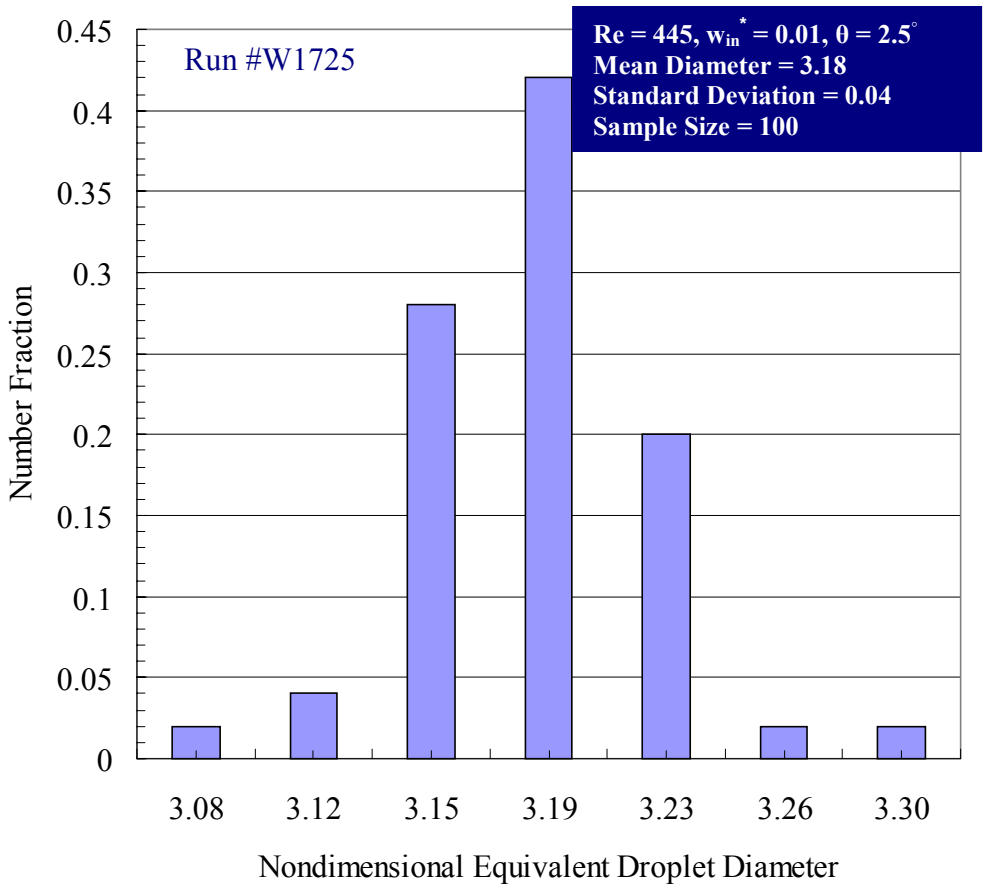

Figure C.58 Experimental data for the distribution of the nondimensional equivalent droplet diameter carried out for an inclined surface (Run #W1725).

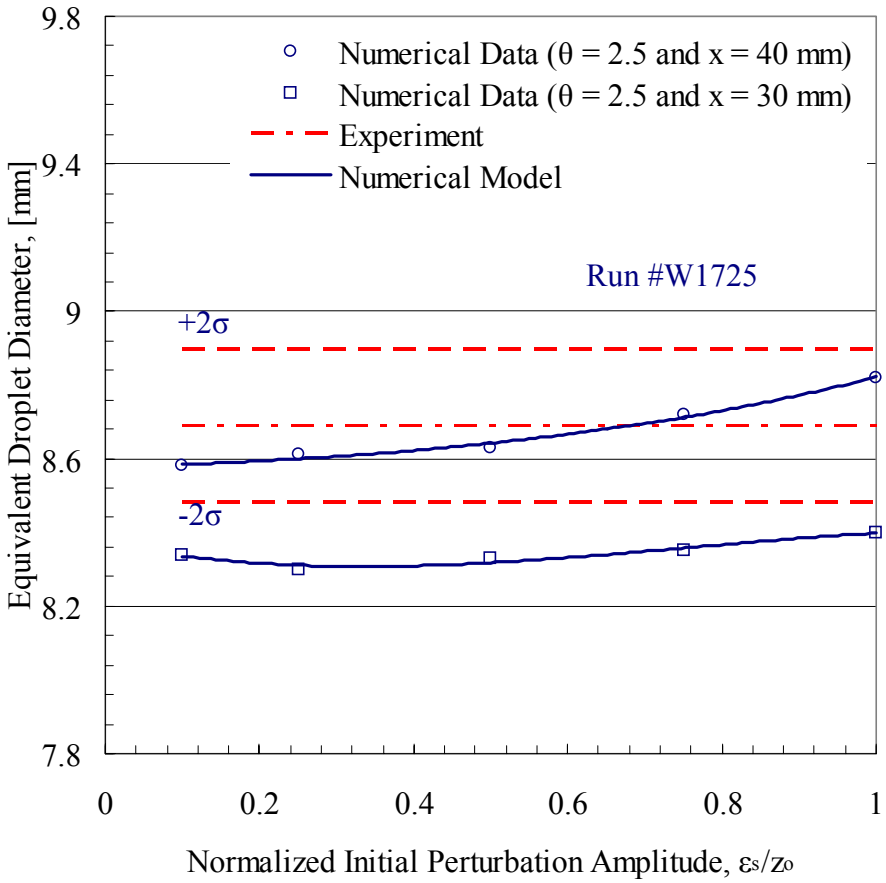

Figure C.59 Numerical and experimental data for the variation of the equivalent droplet diameter with the normalized initial perturbation amplitude carried out for an inclined surface (Run #W1725).

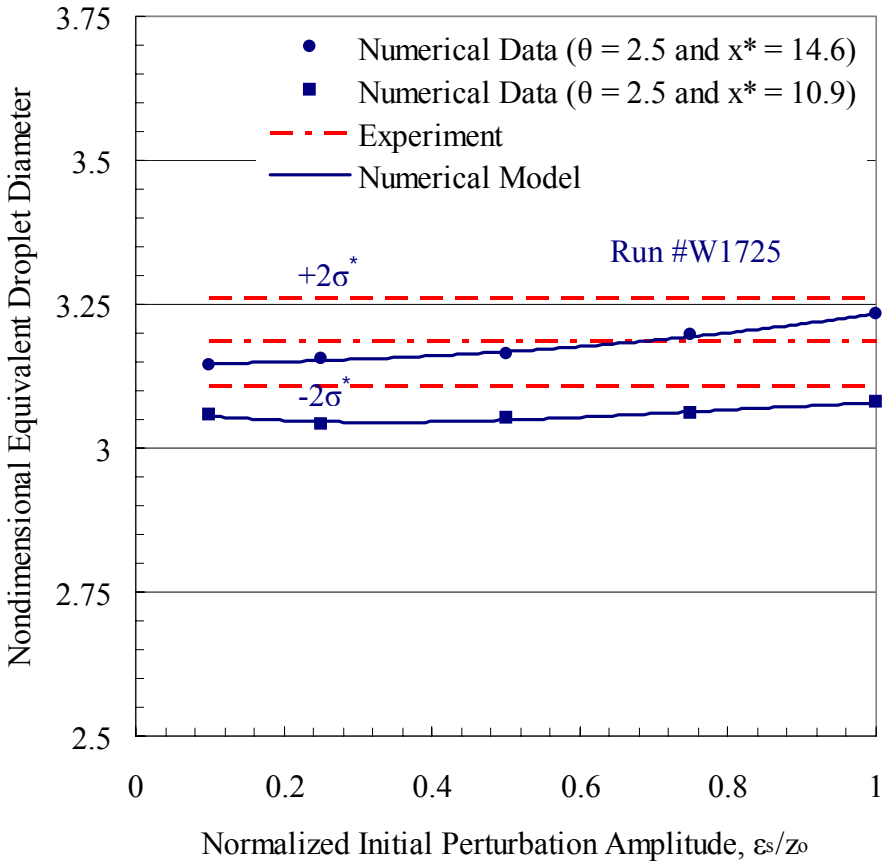

Figure C.60 Numerical and experimental data for the variation of the nondimensional equivalent droplet diameter with the normalized initial perturbation amplitude carried out for an inclined surface (Run #W1725).

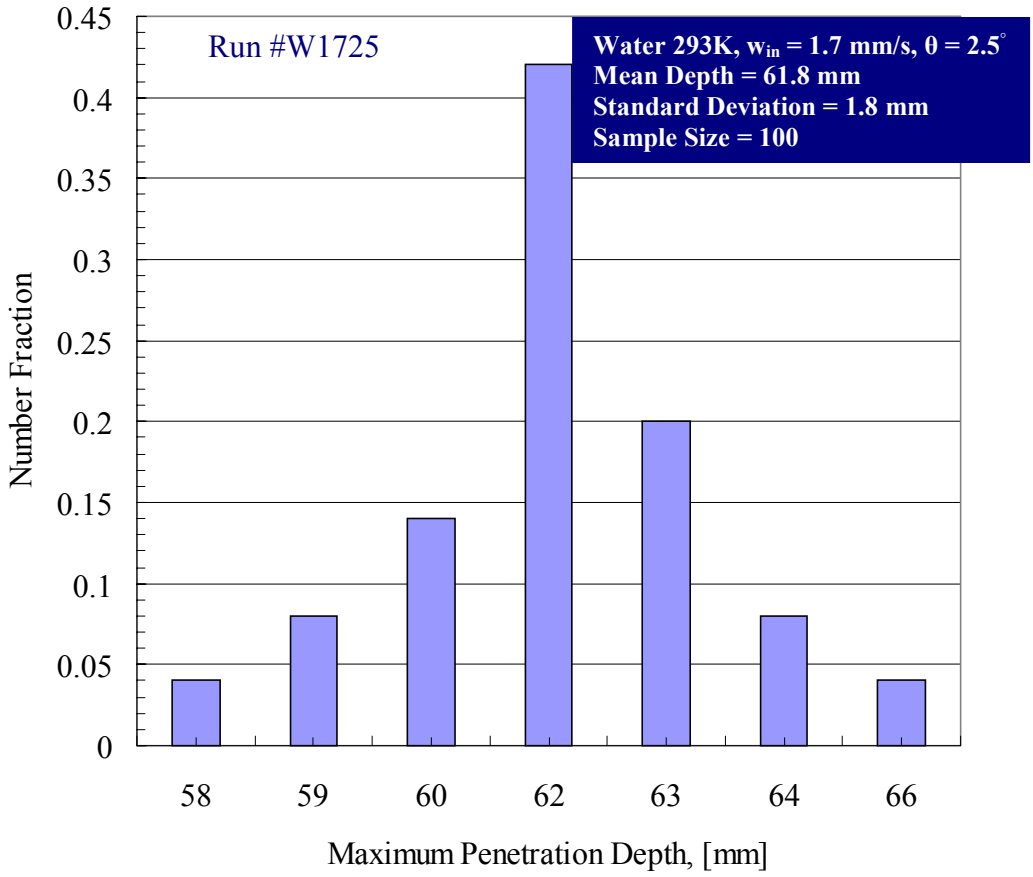

Figure C.61 Experimental data for the distribution of the maximum penetration depth carried out for an inclined surface (Run #W1725).

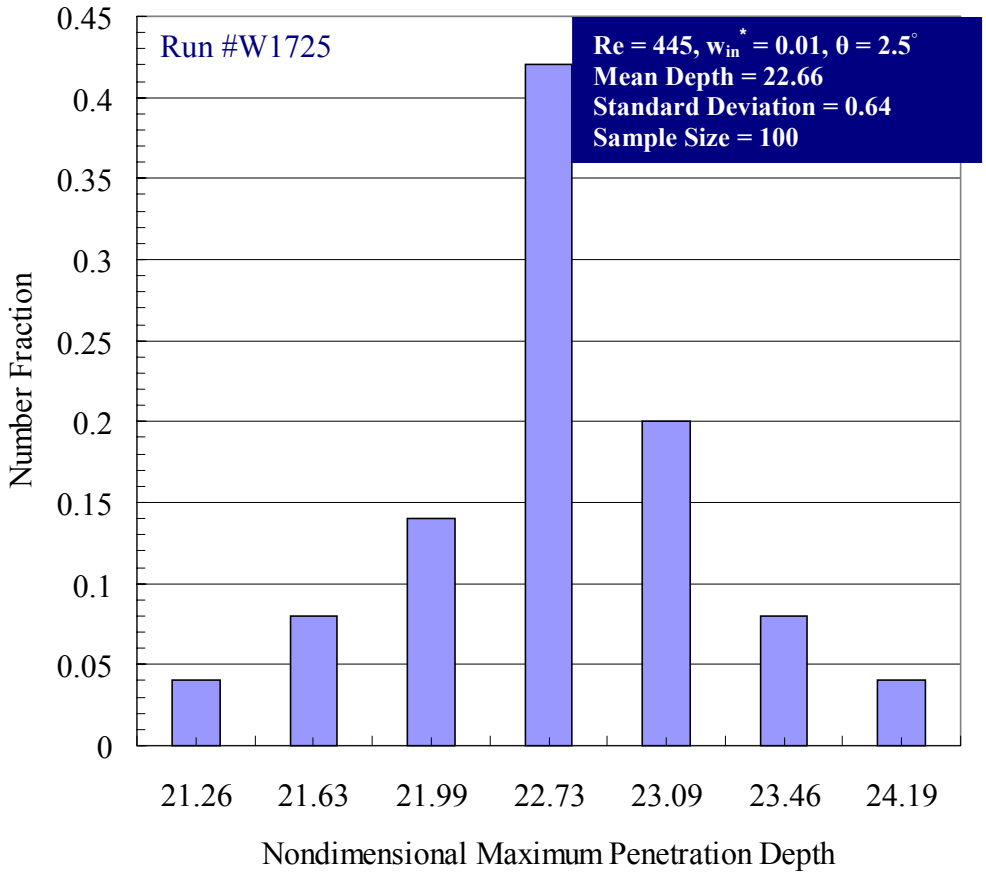

Figure C.62 Experimental data for the distribution of the nondimensional maximum penetration depth carried out for an inclined surface (Run #W1725).

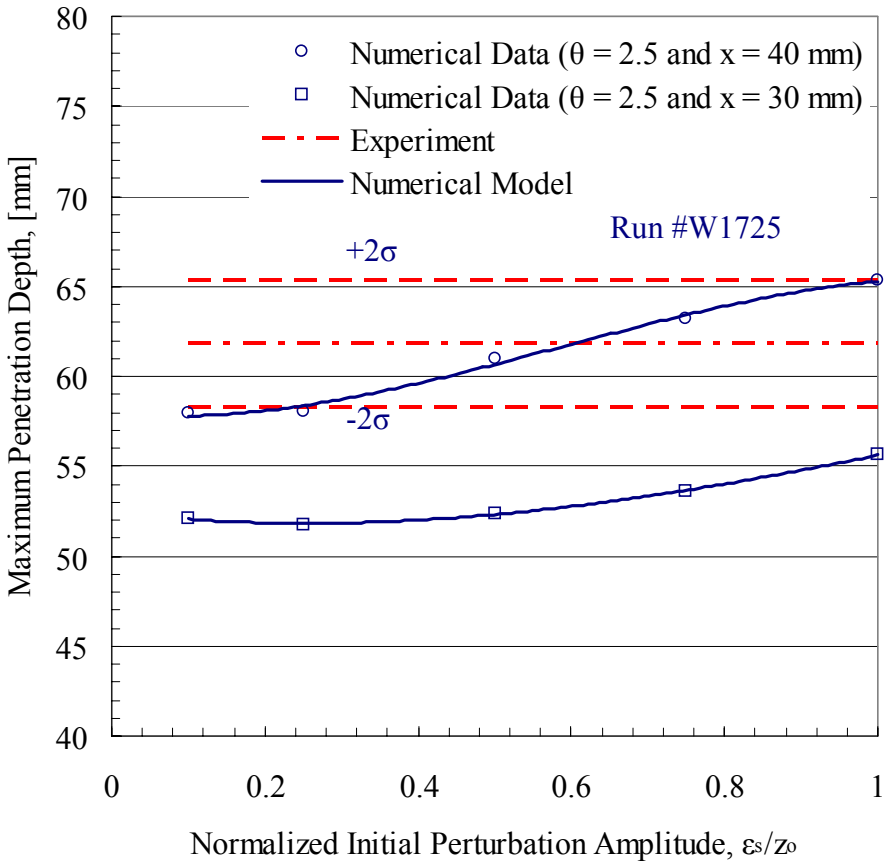

Figure C.63 Numerical and experimental data for the variation of the maximum penetration depth with the normalized initial perturbation amplitude carried out for an inclined surface (Run #W1725).

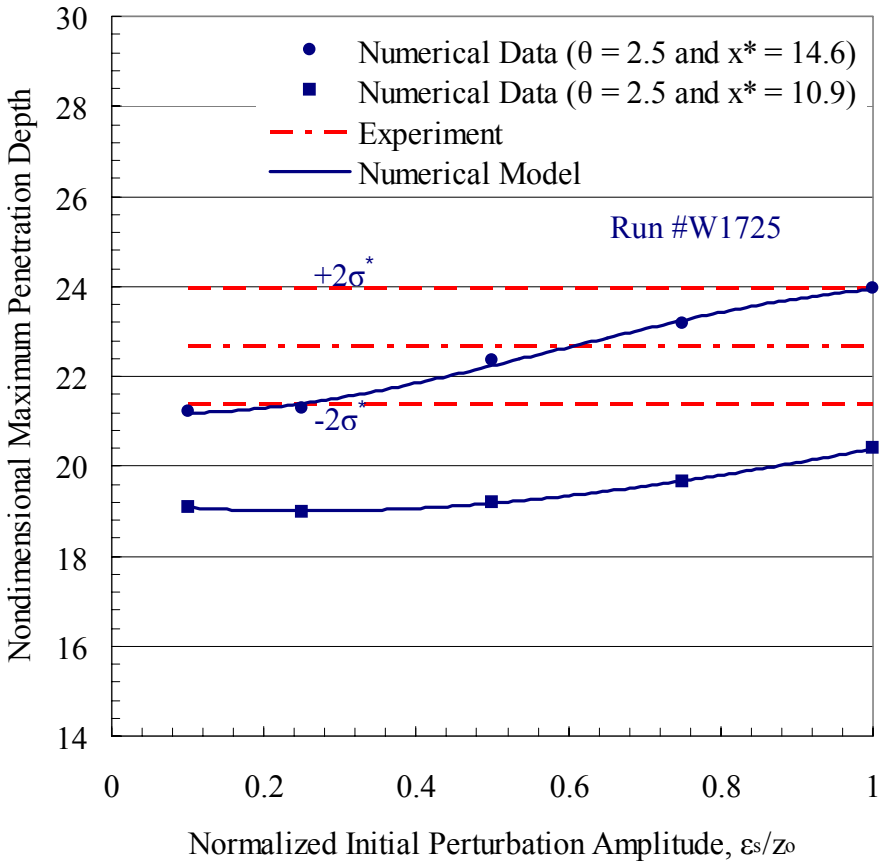

Figure C.64 Numerical and experimental data for the variation of the nondimensional maximum penetration depth with the normalized initial perturbation amplitude carried out for an inclined surface (Run #W1725).

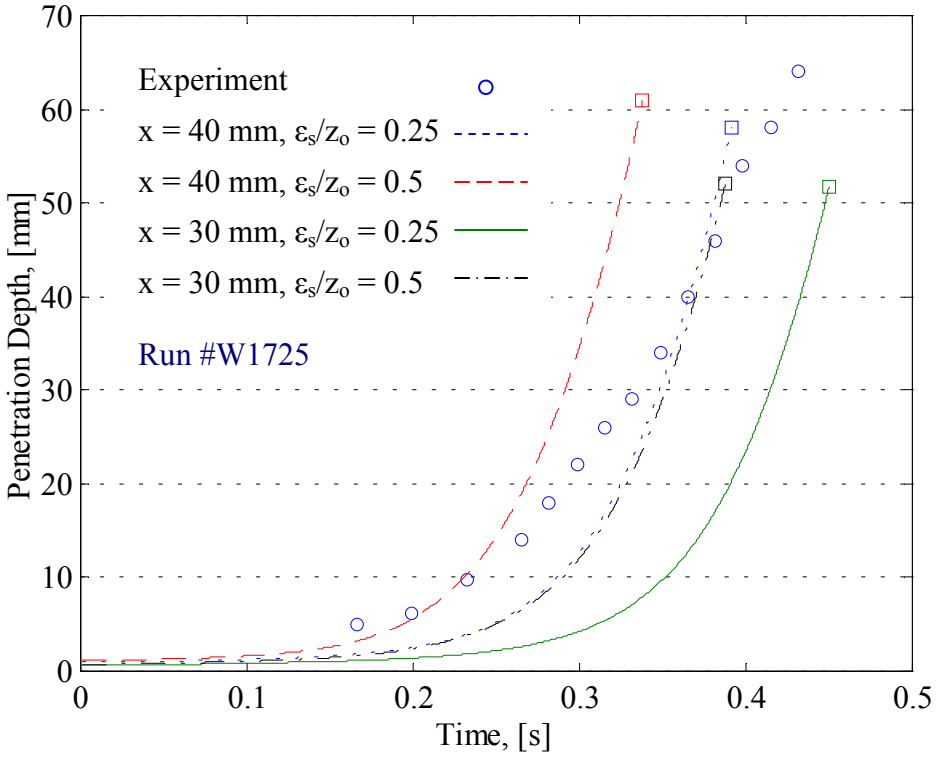

Figure C.65 Numerical and experimental data for the transient variation of the penetration depth carried out for an inclined surface (Run #W1725).

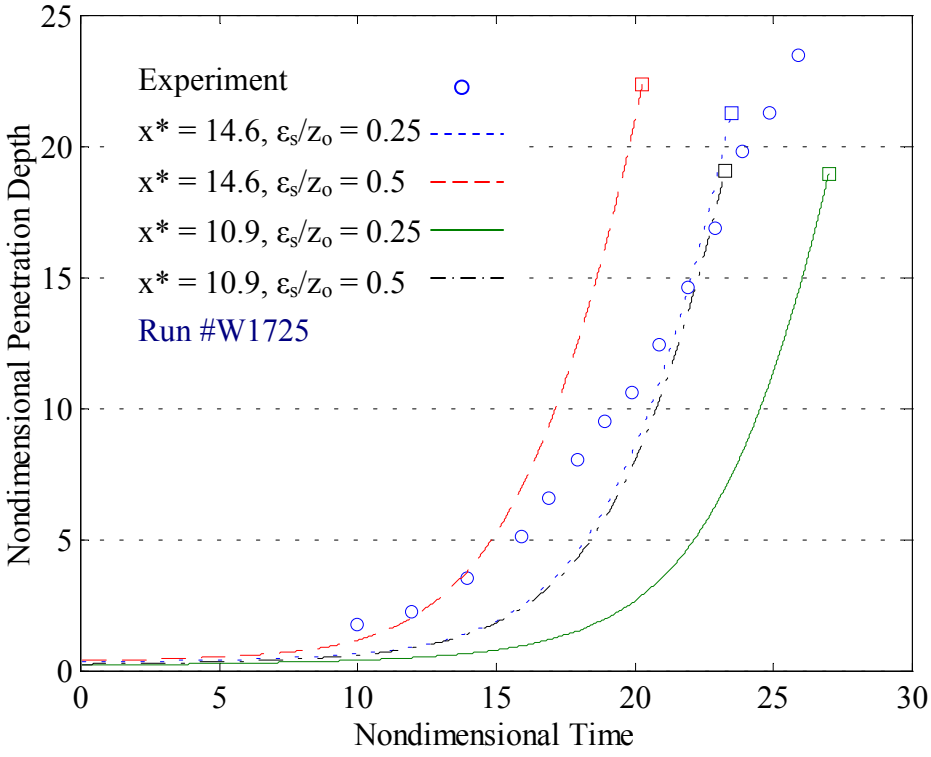

Figure C.66 Numerical and experimental data for the transient variation of the nondimensional penetration depth carried out for an inclined surface (Run #W1725).

C.4 Numerical and Experimental Results for Run #G1725

This section details the numerical and experimental results on the characteristic flow field variables for the bounded Rayleigh-Taylor instability with injection through the bounding inclined surface for Run #G1725. These results include: the evolution of the liquid film thickness, the liquid film surface perturbation geometry, the liquid droplet formation and detachment time, the equivalent size for detached droplets, and the time history of the penetration depth.

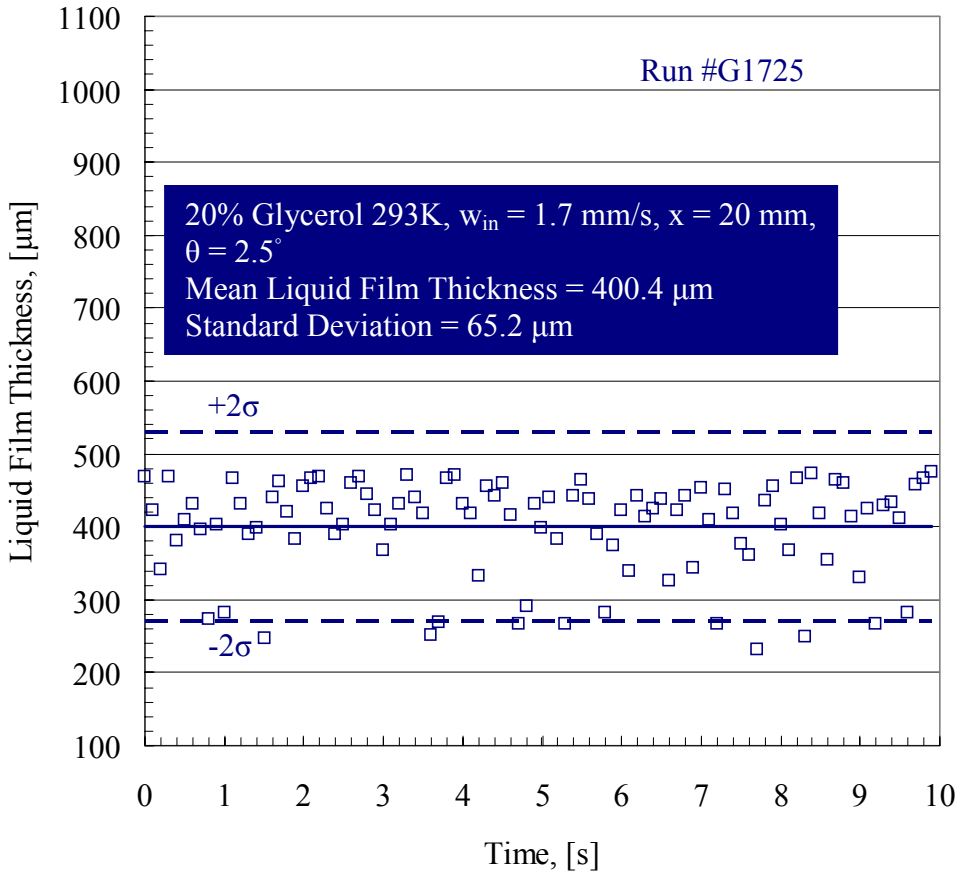

Figure C.67 Transient variation of the unperturbed liquid film thickness measured at an axial position x = 20 mm for Run #G1725.

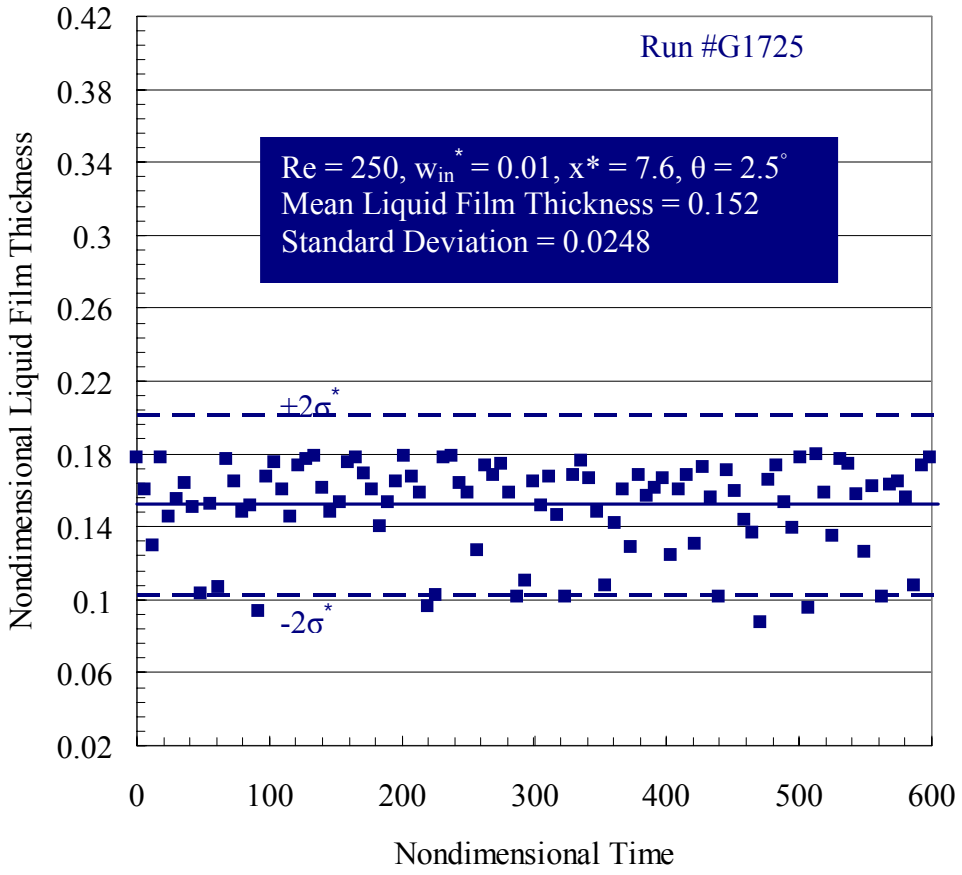

Figure C.68 The unperturbed liquid film thickness normalized by l as a function of time normalized by t_o measured at $x^* = 7.6$ for Run #G1725.

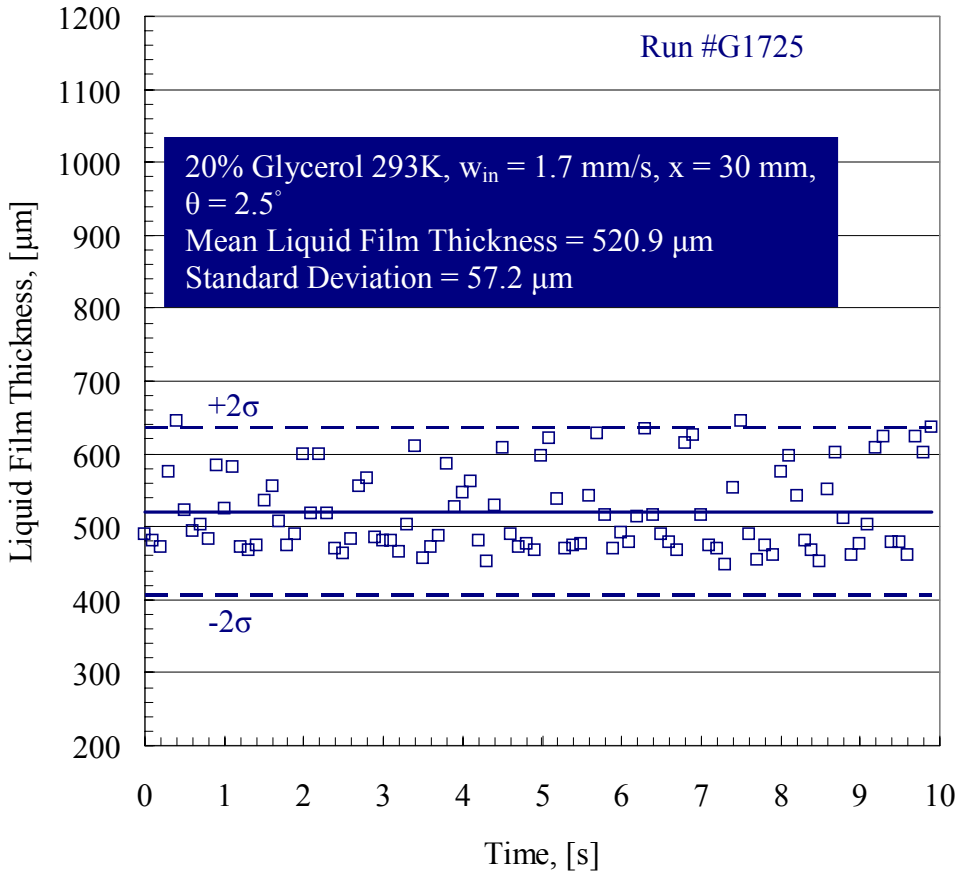

Figure C.69 Transient variation of the unperturbed liquid film thickness measured at an axial position x = 30 mm for Run #G1725.

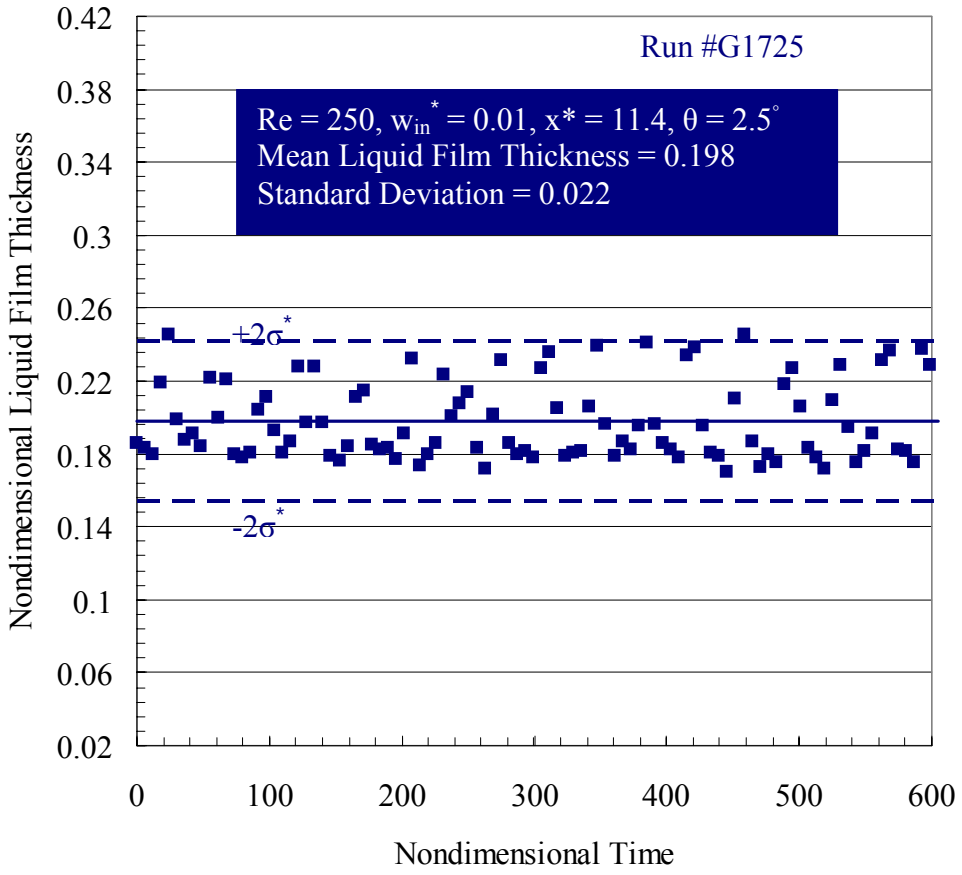

Figure C.70 The unperturbed liquid film thickness normalized by l as a function of time normalized by t_o measured at $x^* = 11.4$ for Run #G1725.

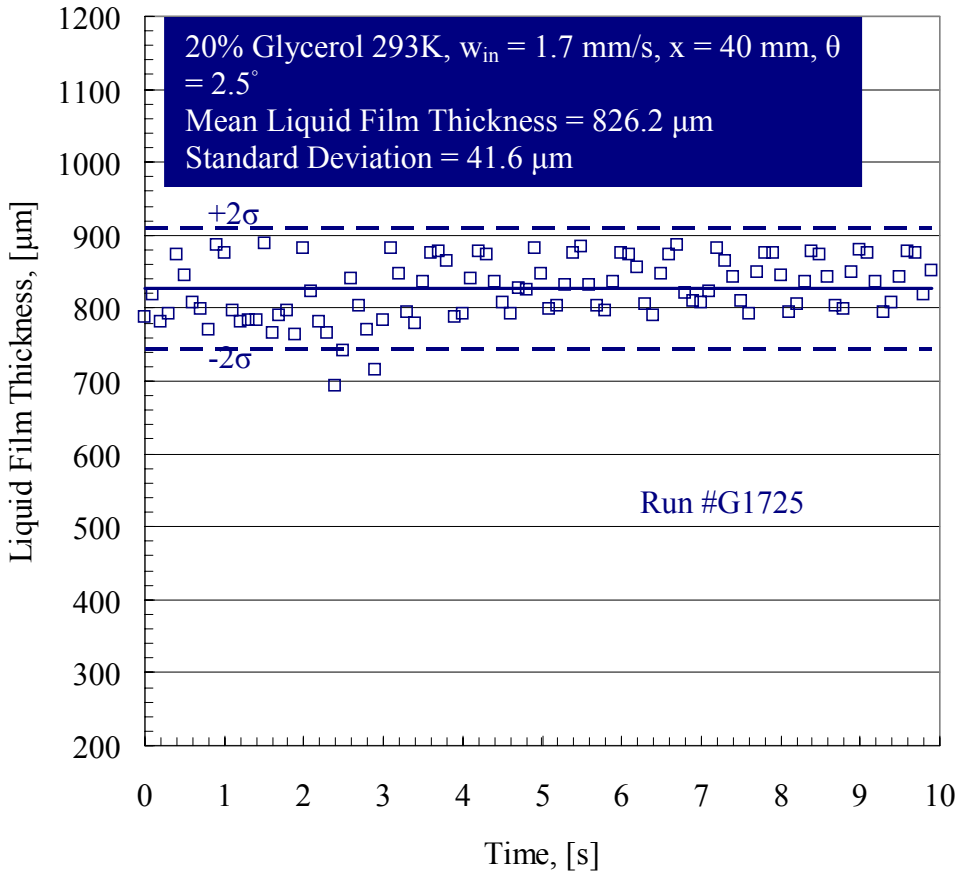

Figure C.71 Transient variation of the unperturbed liquid film thickness measured at an axial position x = 40 mm for Run #G1725.

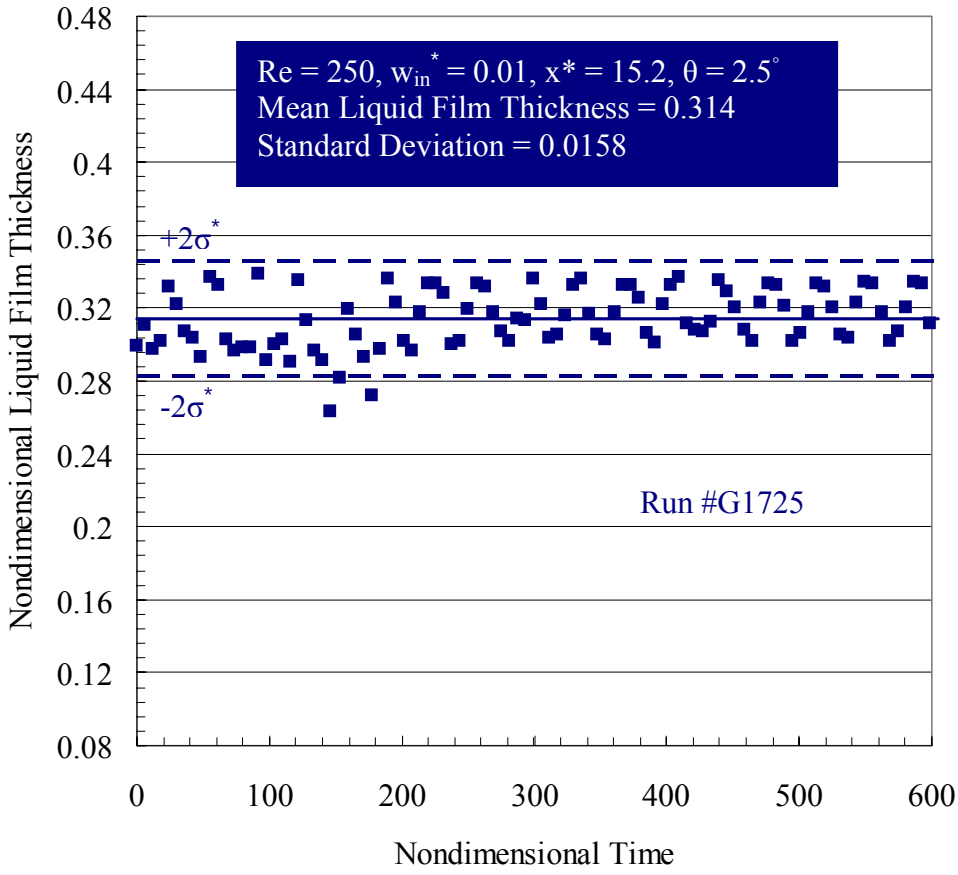

Figure C.72 The unperturbed liquid film thickness normalized by l as a function of time normalized by t_o measured at $x^* = 15.2$ for Run #G1725.

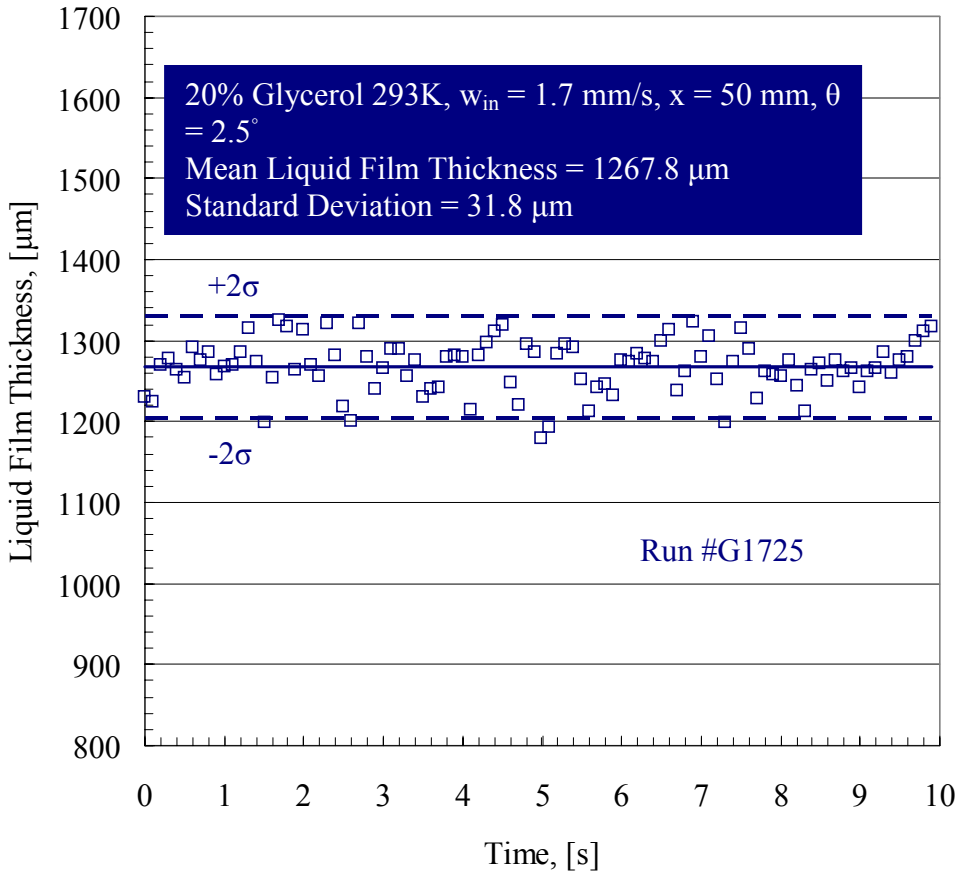

Figure C.73 Transient variation of the unperturbed liquid film thickness measured at an axial position x = 50 mm for Run #G1725.

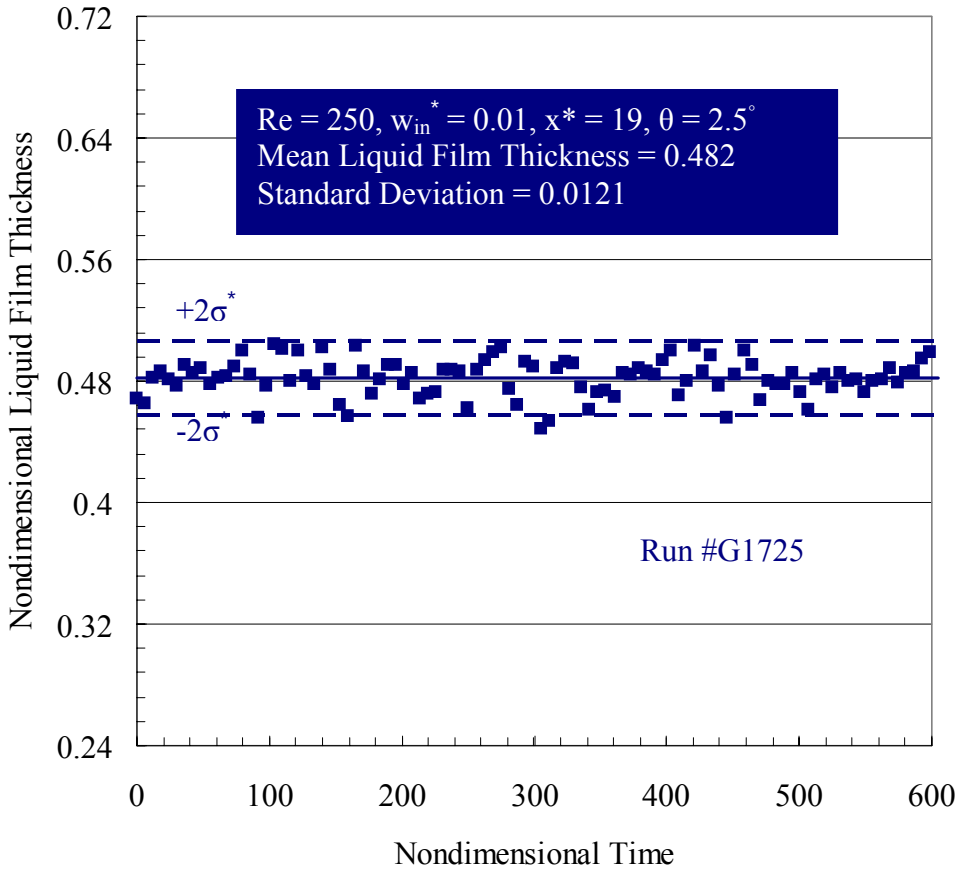

Figure C.74 The unperturbed liquid film thickness normalized by l as a function of time normalized by t_o measured at $x^* = 19$ for Run #G1725.

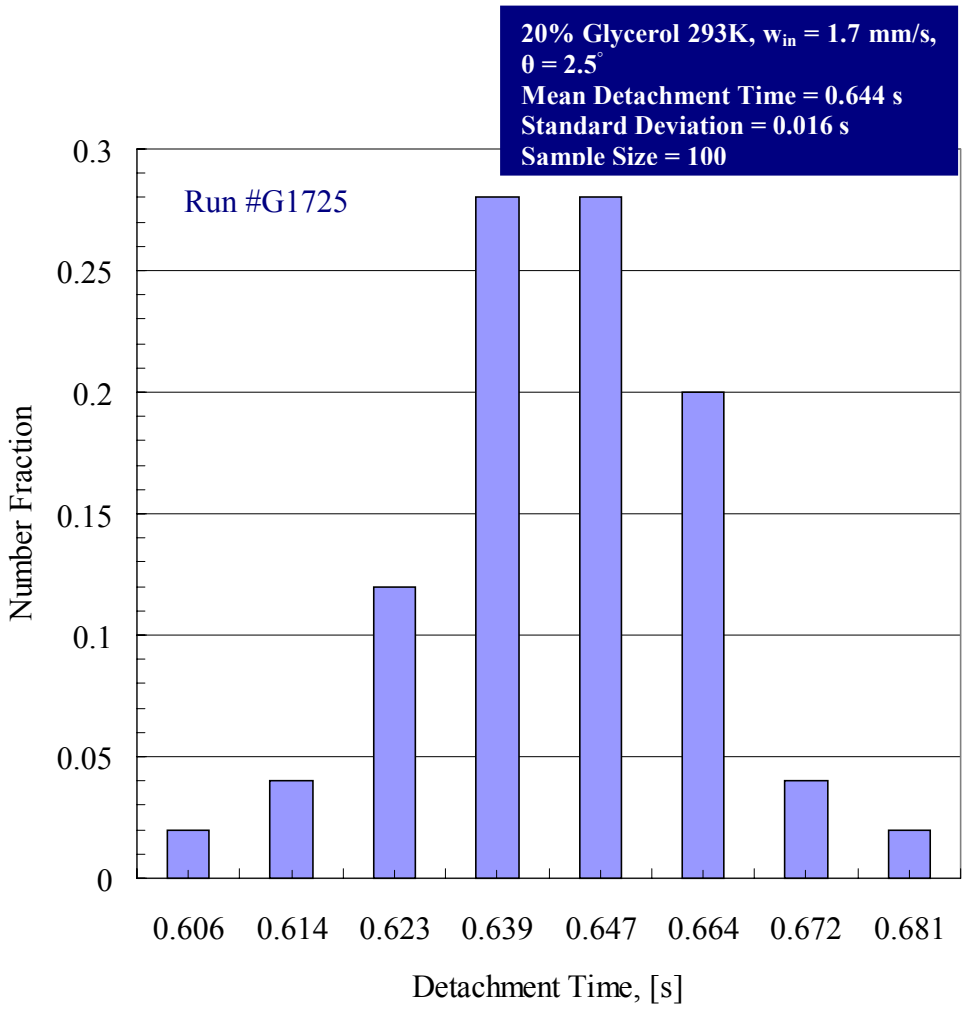

Figure C.75 Experimental data for the distribution of the detachment times carried out for an inclined surface (Run #G1725).

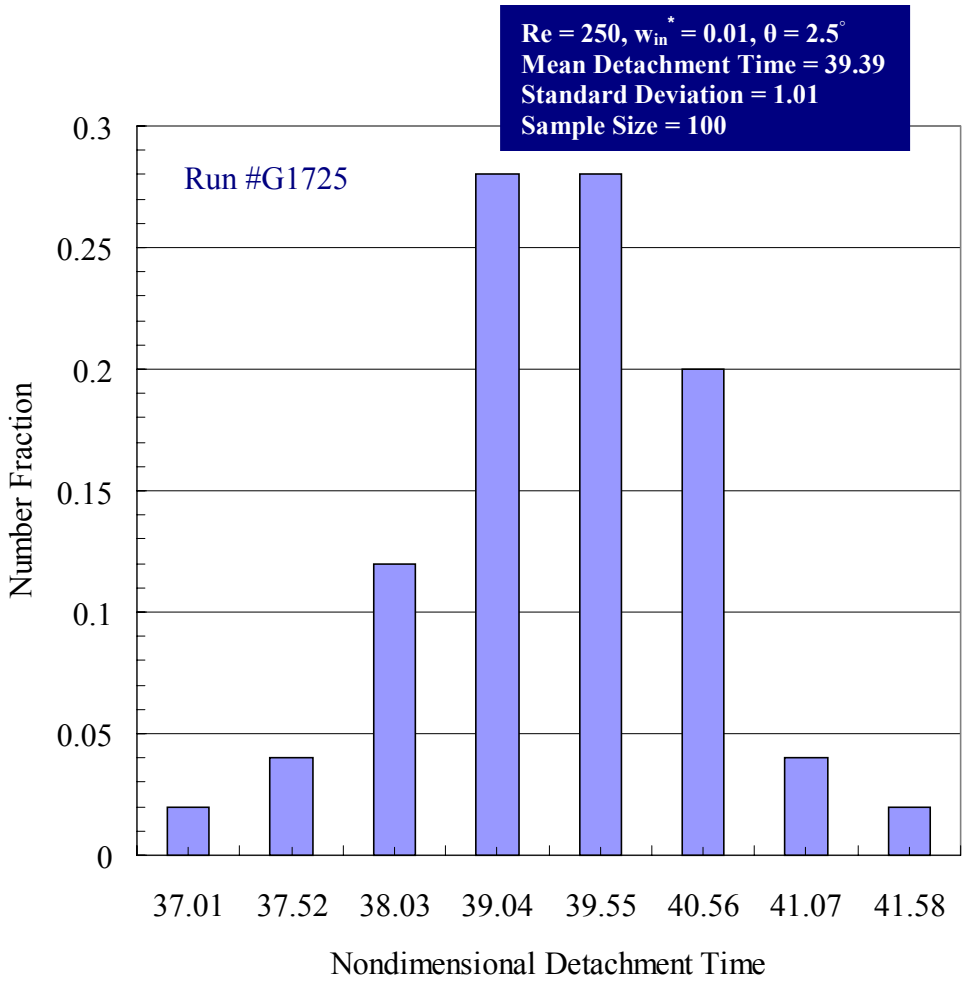

Figure C.76 Experimental data for the distribution of the nondimensional detachment time carried out for an inclined surface (Run #G1725).

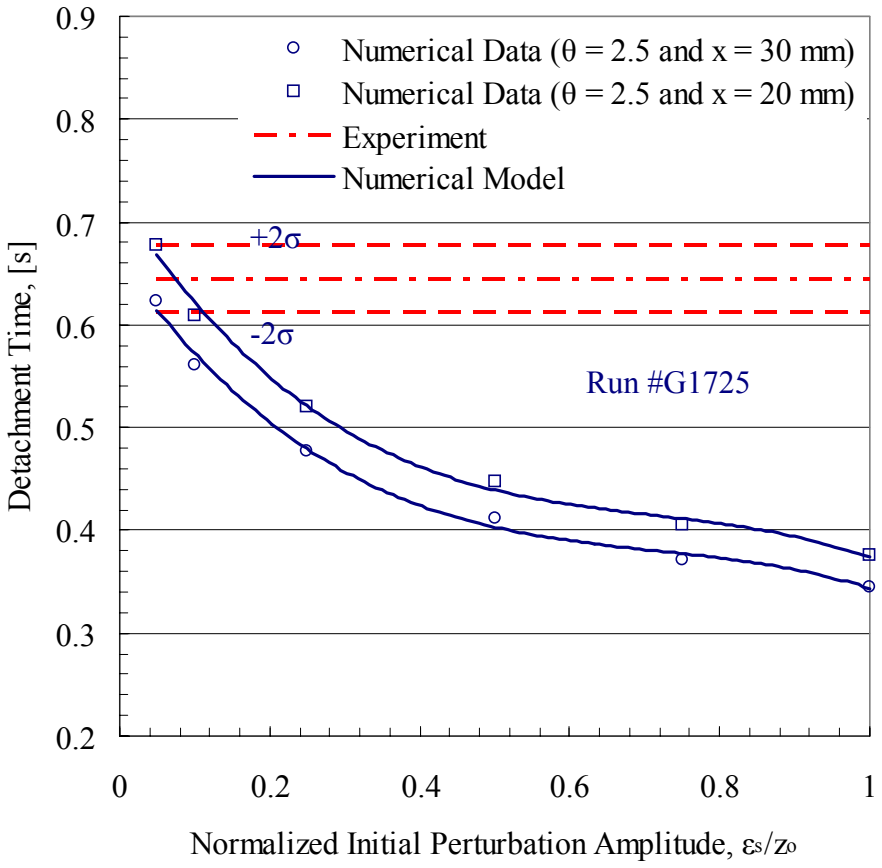

Figure C.77 Numerical and experimental data for the variation of the detachment time with the normalized initial perturbation amplitude carried out for an inclined surface (Run #G1725).

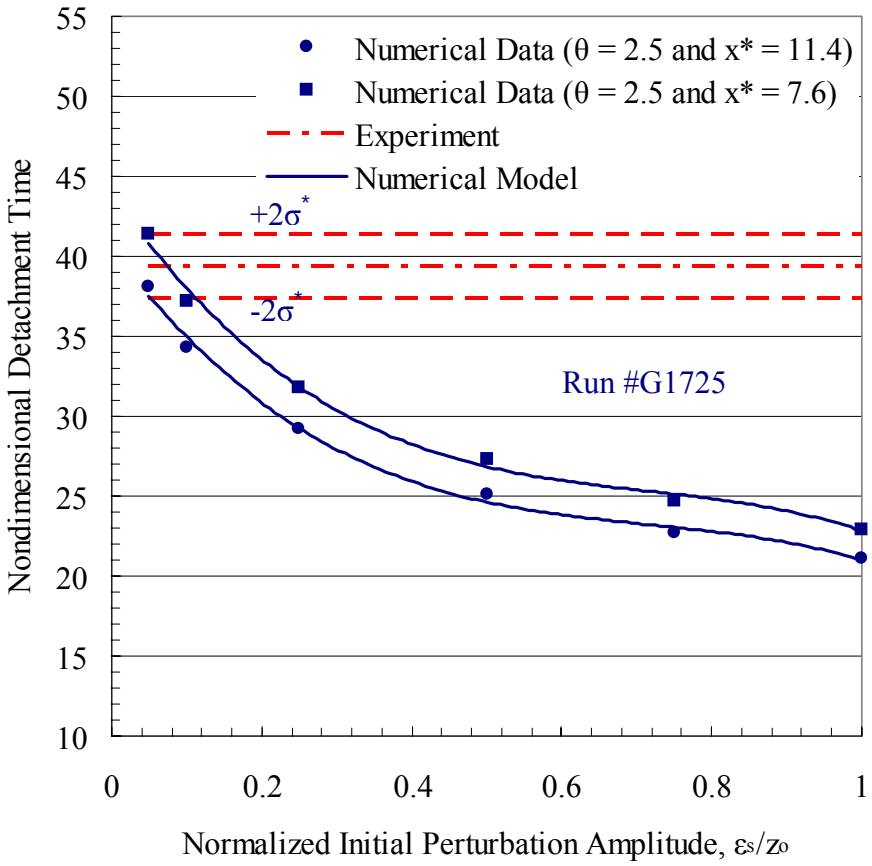

Figure C.78 Numerical and experimental data for the variation of the nondimensional detachment time with the normalized initial perturbation amplitude carried out for an inclined surface (Run #G1725).

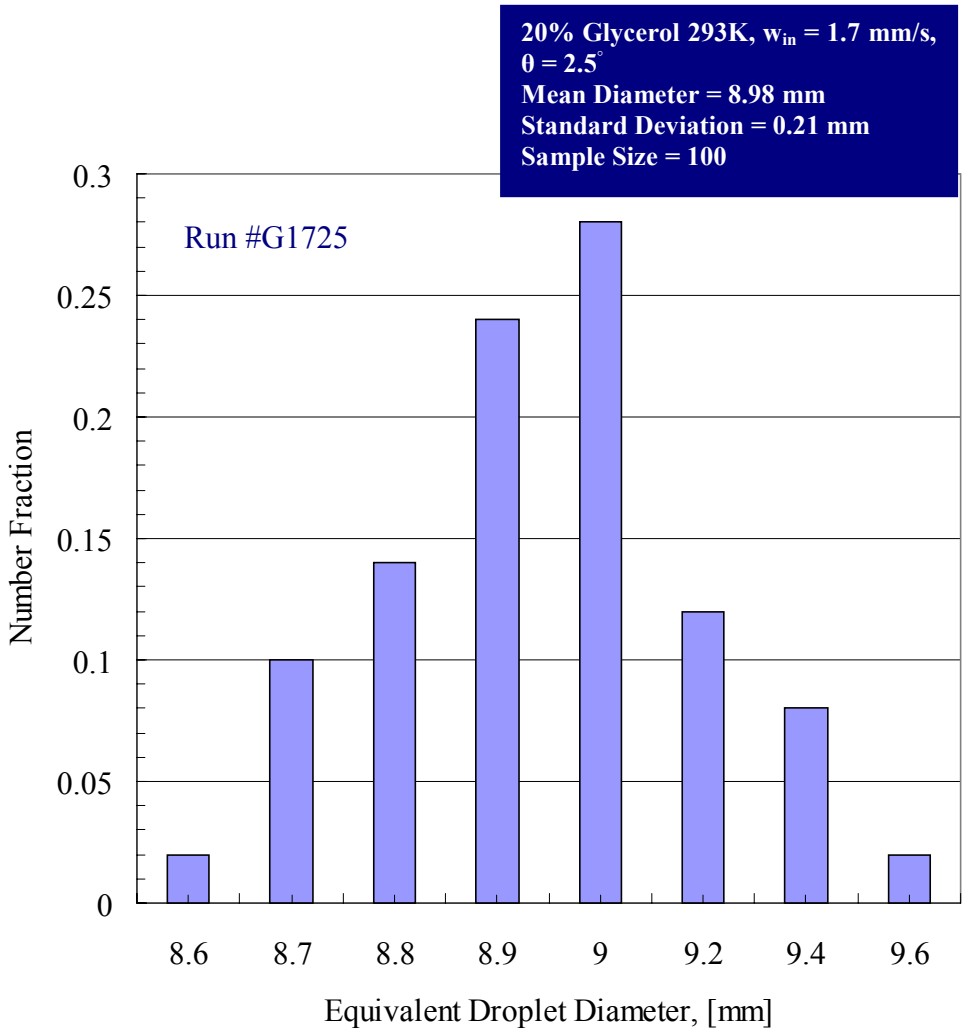

Figure C.79 Experimental data for the distribution of the equivalent droplet diameter carried out for an inclined surface (Run #G1725).

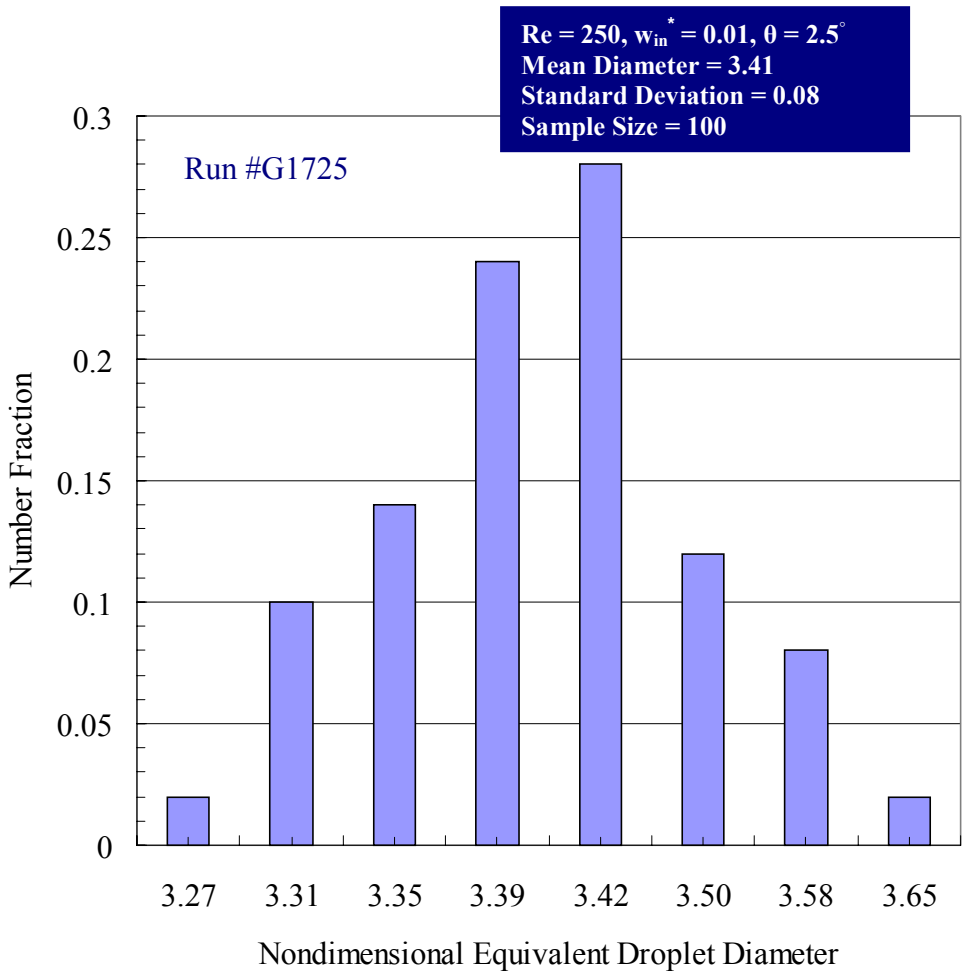

Figure C.80 Experimental data for the distribution of the nondimensional equivalent droplet diameter carried out for an inclined surface (Run #G1725).

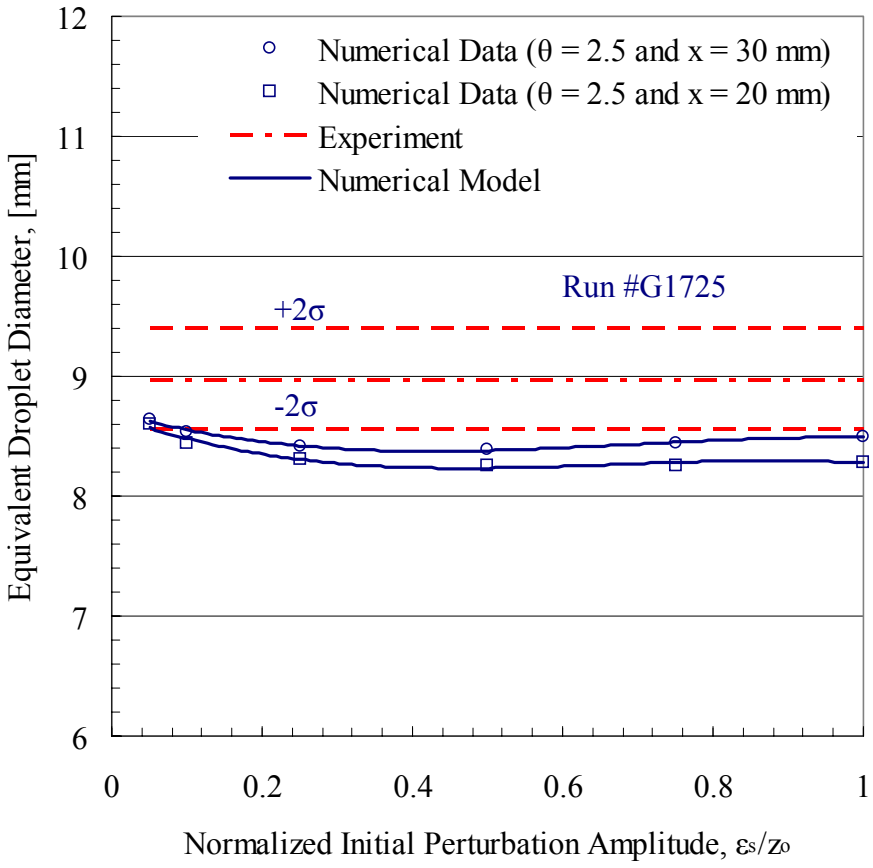

Figure C.81 Numerical and experimental data for the variation of the equivalent droplet diameter with the normalized initial perturbation amplitude carried out for an inclined surface (Run #G1725).

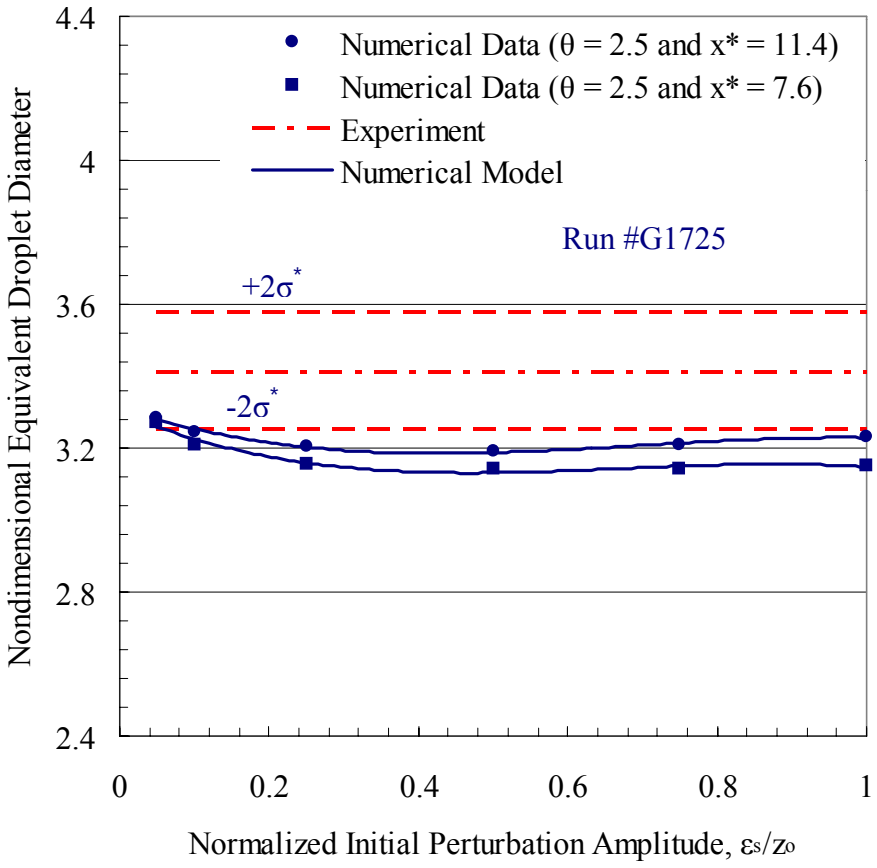

Figure C.82 Numerical and experimental data for the variation of the nondimensional equivalent droplet diameter with the normalized initial perturbation amplitude carried out for an inclined surface (Run #G1725).

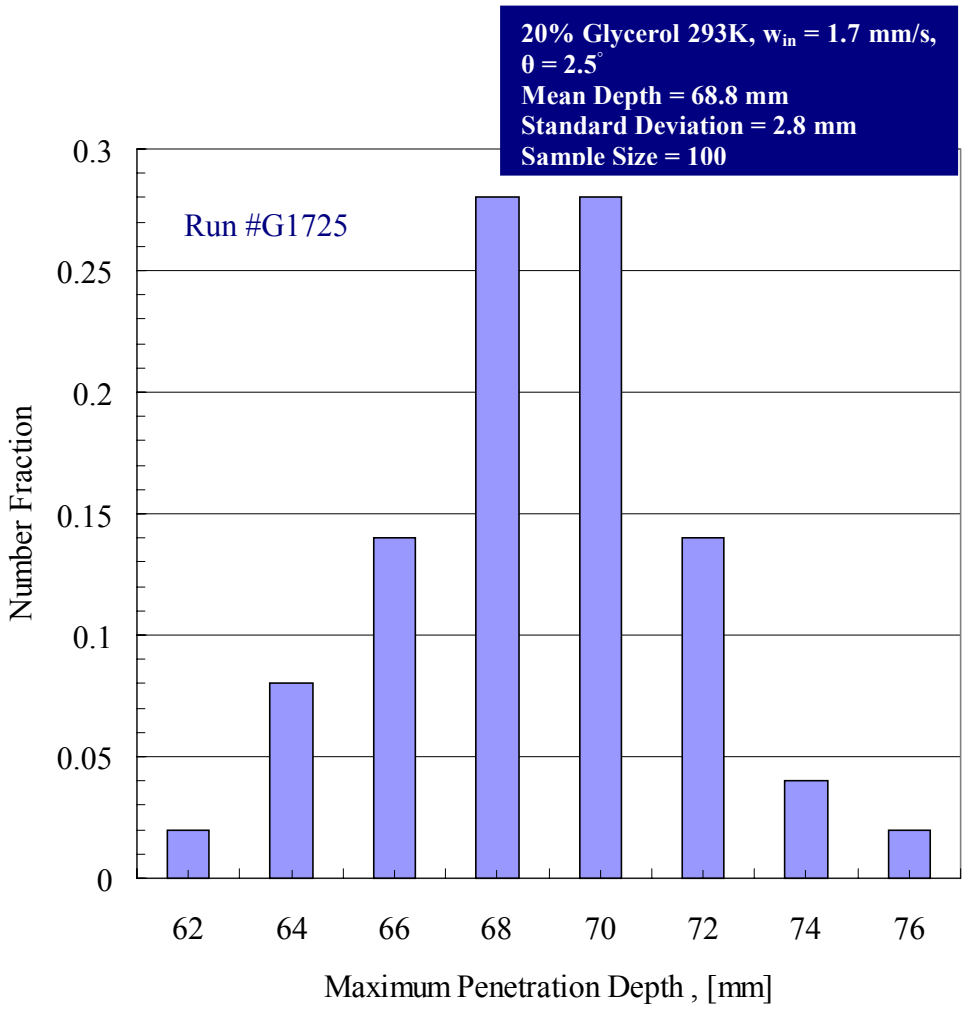

Figure C.83 Experimental data for the distribution of the maximum penetration depth carried out for an inclined surface (Run #G1725).

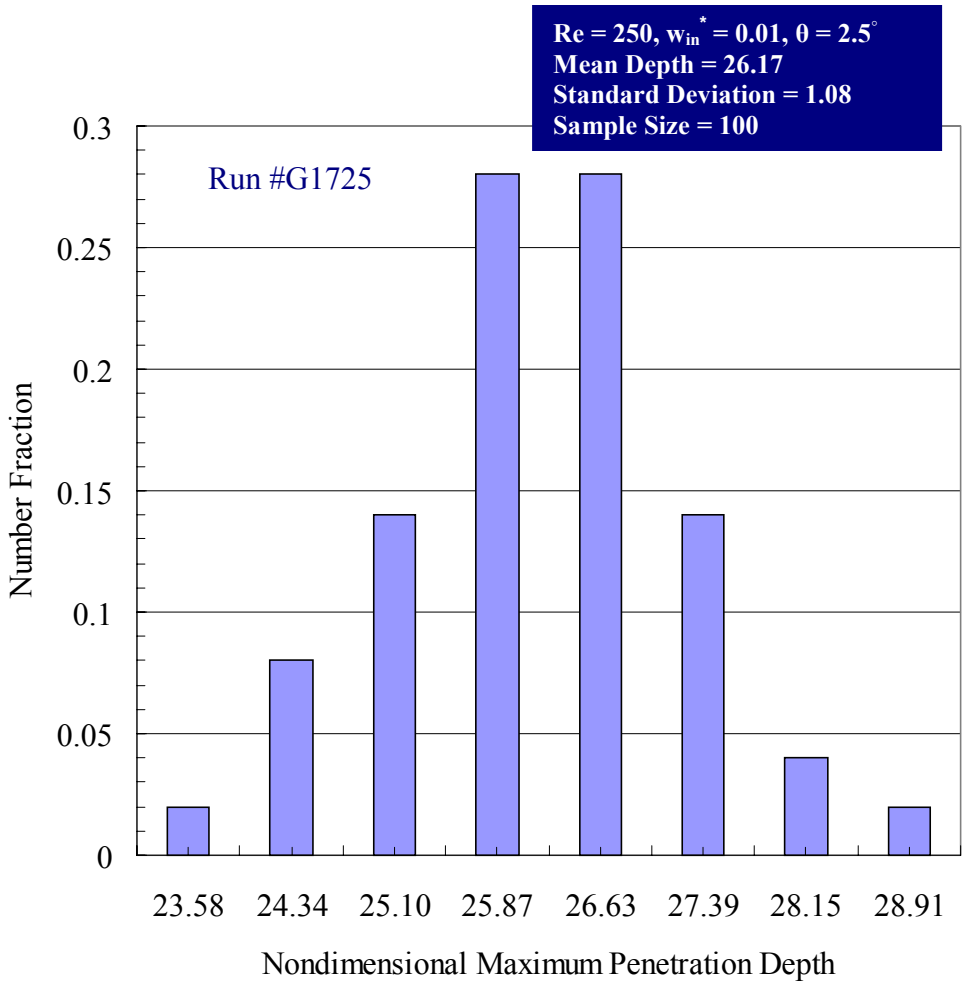

Figure C.84 Experimental data for the distribution of the nondimensional maximum penetration depth carried out for an inclined surface (Run #G1725).

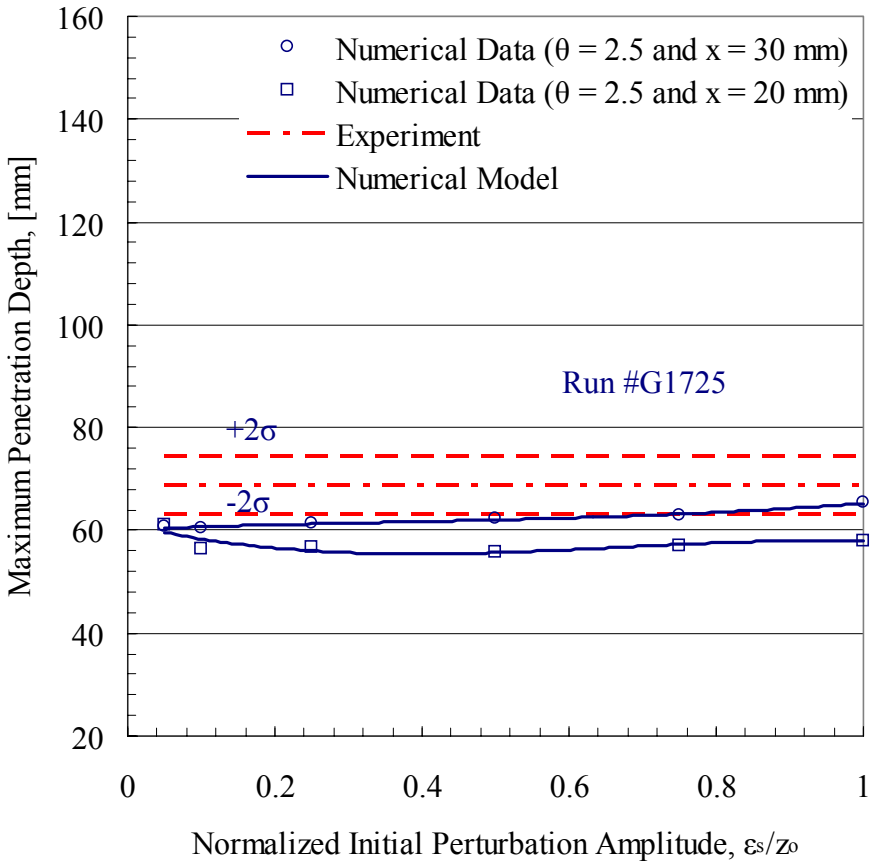

Figure C.85 Numerical and experimental data for the variation of the maximum penetration depth with the normalized initial perturbation amplitude carried out for an inclined surface (Run #G1725).

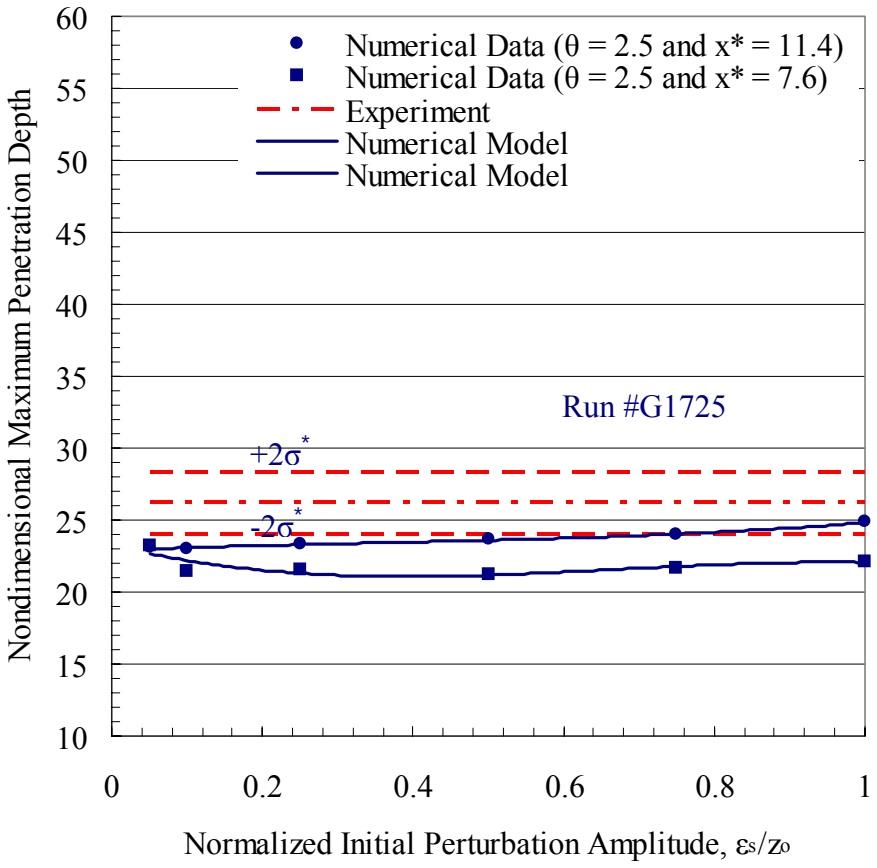

Figure C.86 Numerical and experimental data for the variation of the nondimensional maximum penetration depth with the normalized initial perturbation amplitude carried out for an inclined surface (Run #G1725).

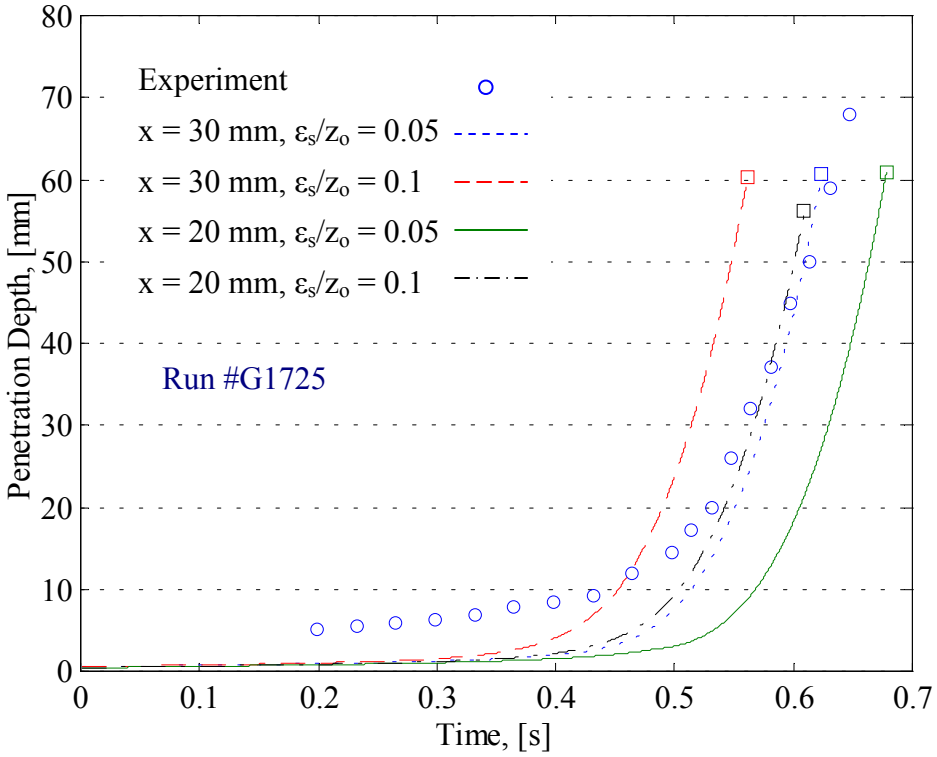

Figure C.87 Numerical and experimental data for the transient variation of the penetration depth carried out for an inclined surface (Run #G1725).

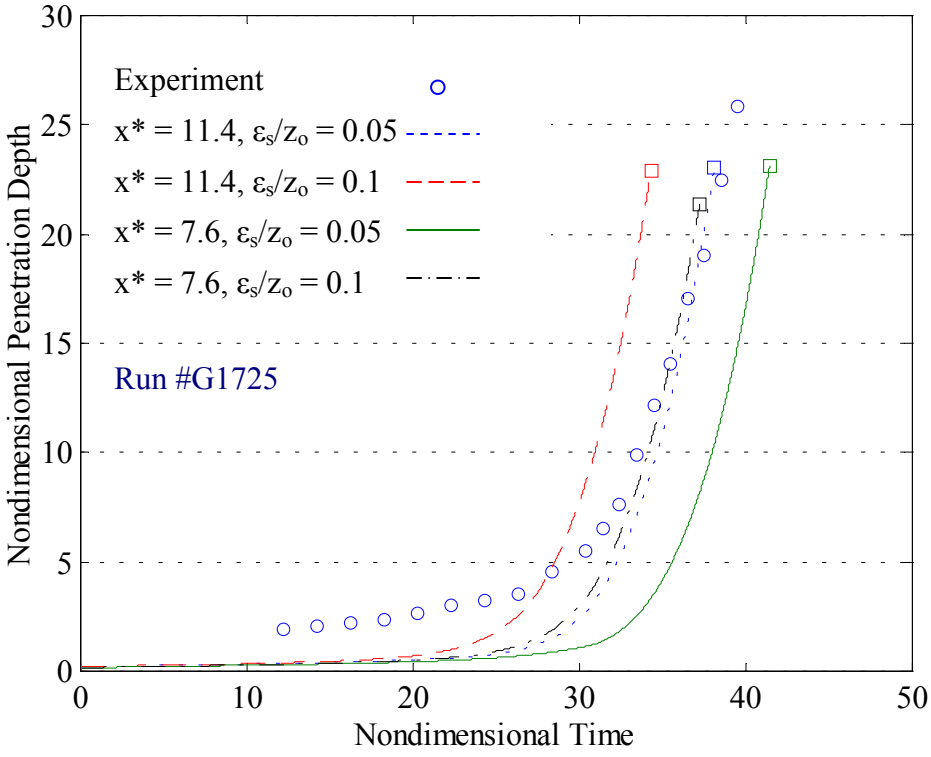

Figure C.88 Numerical and experimental data for the transient variation of the nondimensional penetration depth carried out for an inclined surface (Run #G1725).

C.5 Numerical and Experimental Results for Run #W1925

This section details the numerical and experimental results on the characteristic flow field variables for the bounded Rayleigh-Taylor instability with injection through the bounding inclined surface for Run #W1925. These results include: the evolution of the liquid film thickness, the liquid film surface perturbation geometry, the liquid droplet formation and detachment time, the equivalent size for detached droplets, and the time history of the penetration depth.

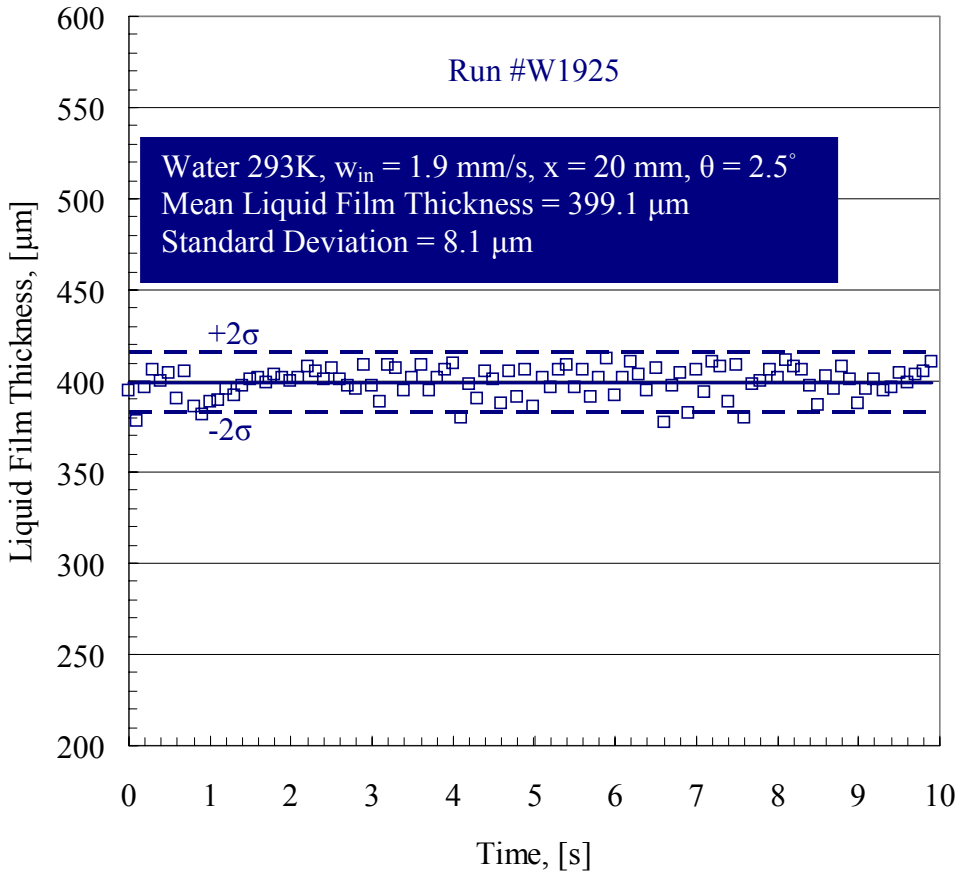

Figure C.89 Transient variation of the unperturbed liquid film thickness measured at an axial position x = 20 mm for Run #W1925.

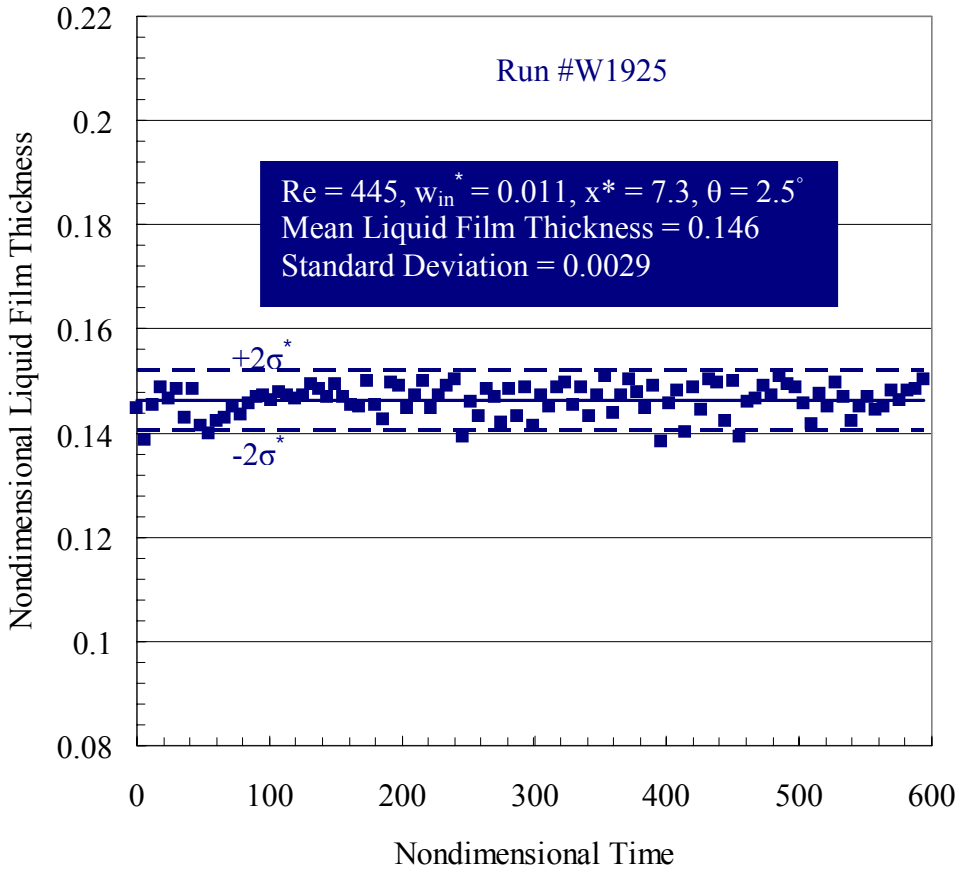

Figure C.90 The unperturbed liquid film thickness normalized by l as a function of time normalized by t_o measured at $x^* = 7.3$ for Run #W1925.

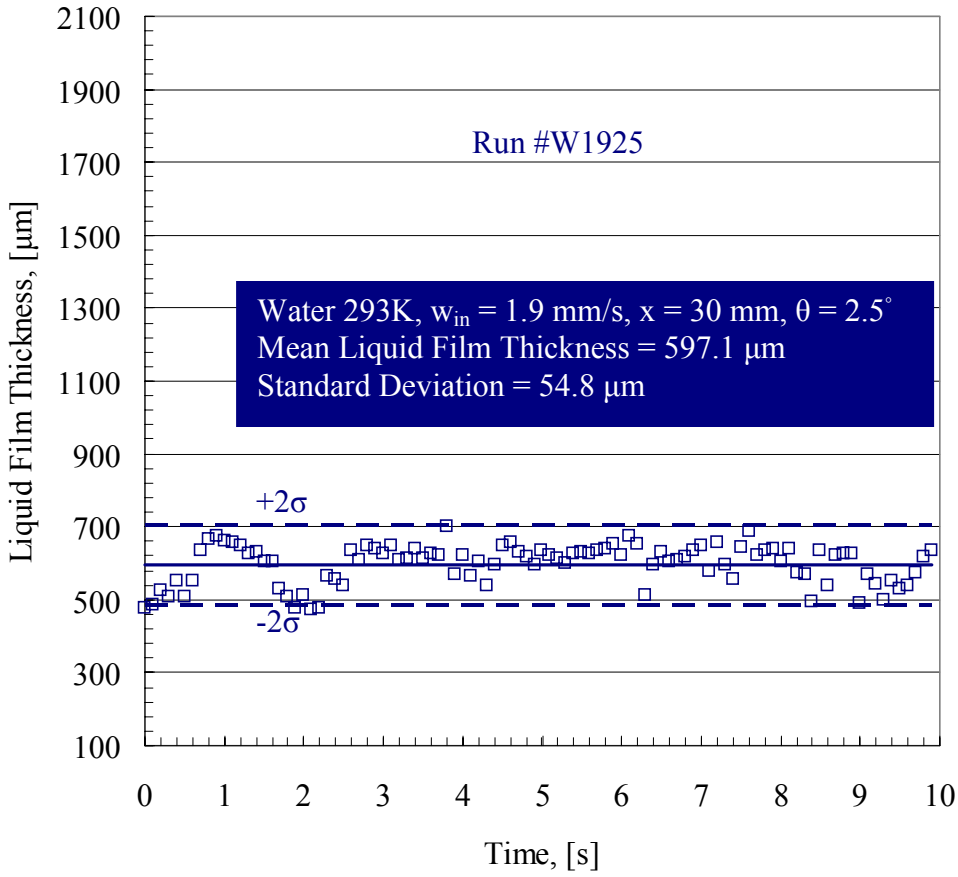

Figure C.91 Transient variation of the unperturbed liquid film thickness measured at an axial position x = 30 mm for Run #W1925.

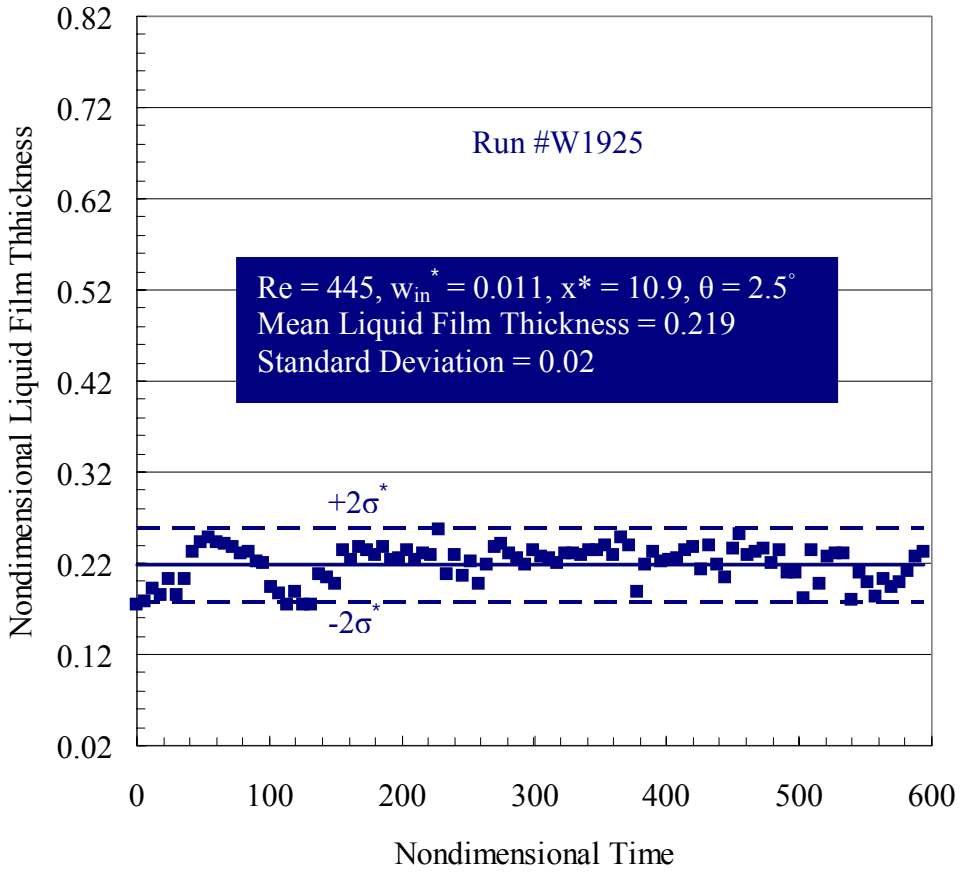

Figure C.92 The unperturbed liquid film thickness normalized by l as a function of time normalized by t_o measured at $x^* = 10.9$ for Run #W1925.

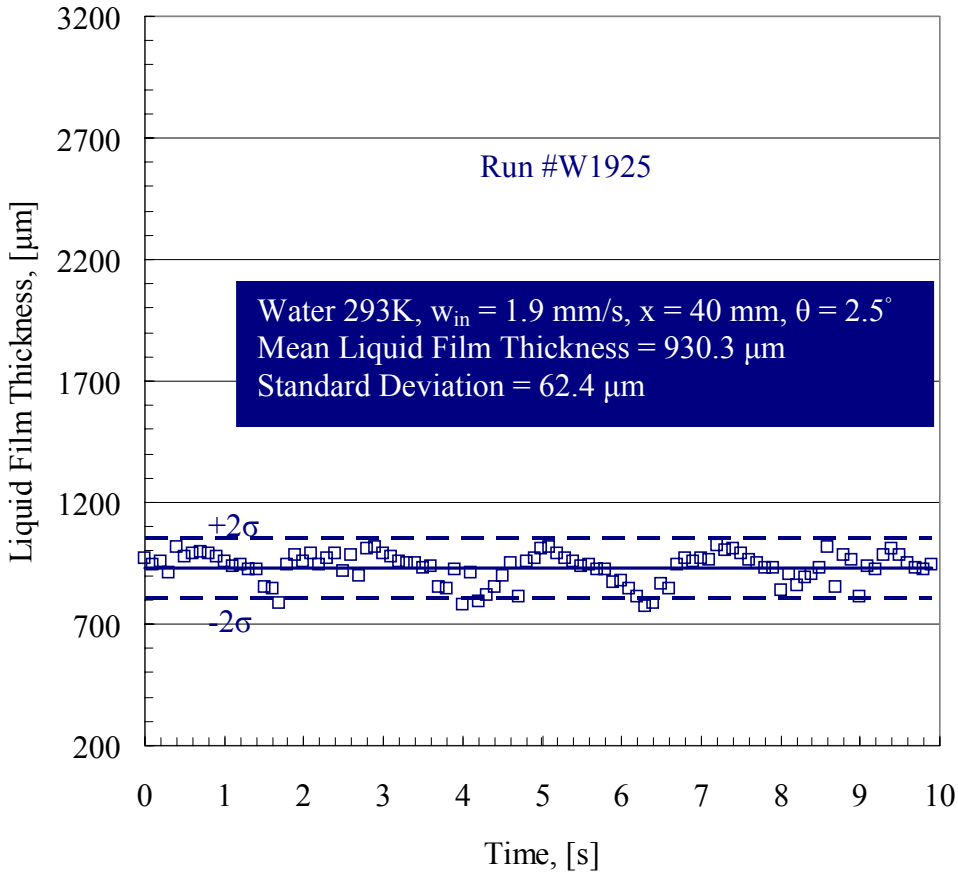

Figure C.93 Transient variation of the unperturbed liquid film thickness measured at an axial position x = 40 mm for Run #W1925.

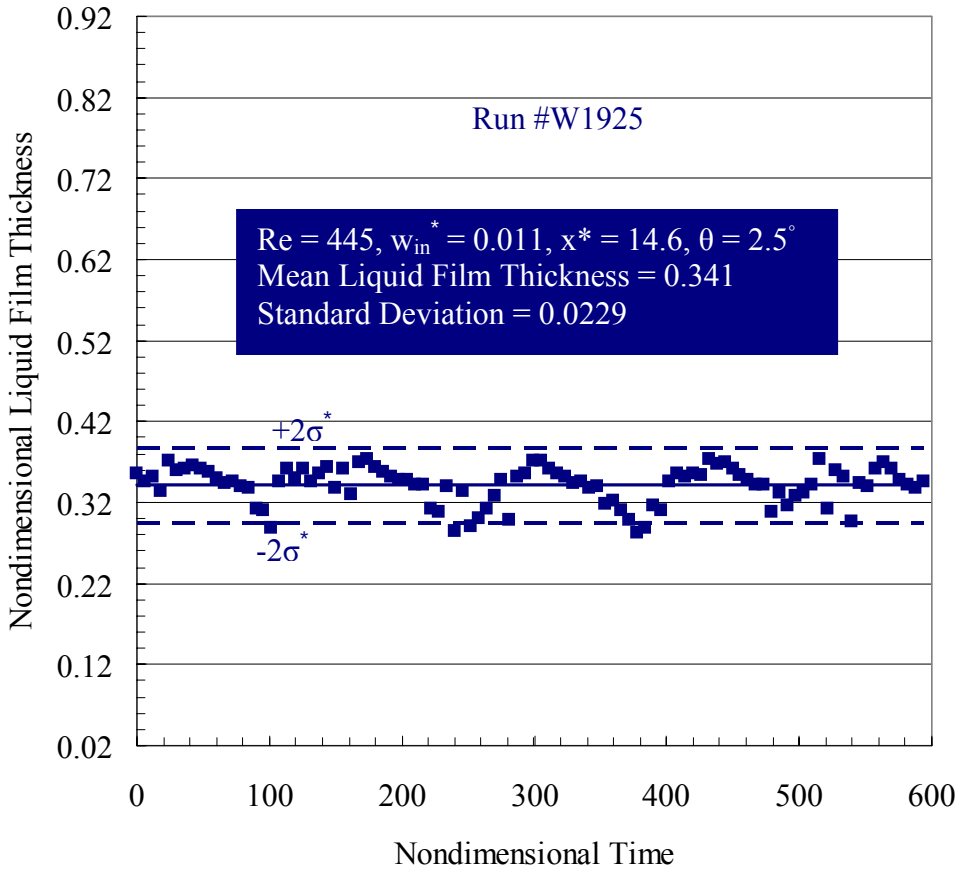

Figure C.94 The unperturbed liquid film thickness normalized by l as a function of time normalized by t_o measured at $x^* = 14.6$ for Run #W1925.

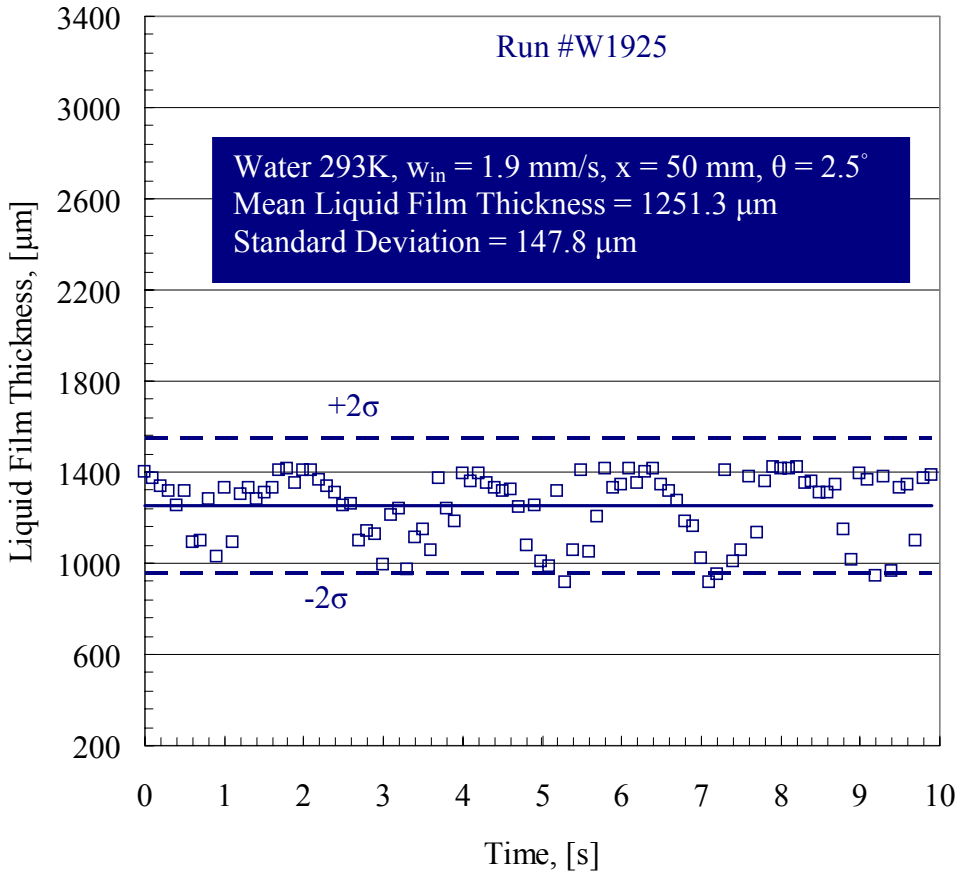

Figure C.95 Transient variation of the unperturbed liquid film thickness measured at an axial position x = 50 mm for Run #W1925.

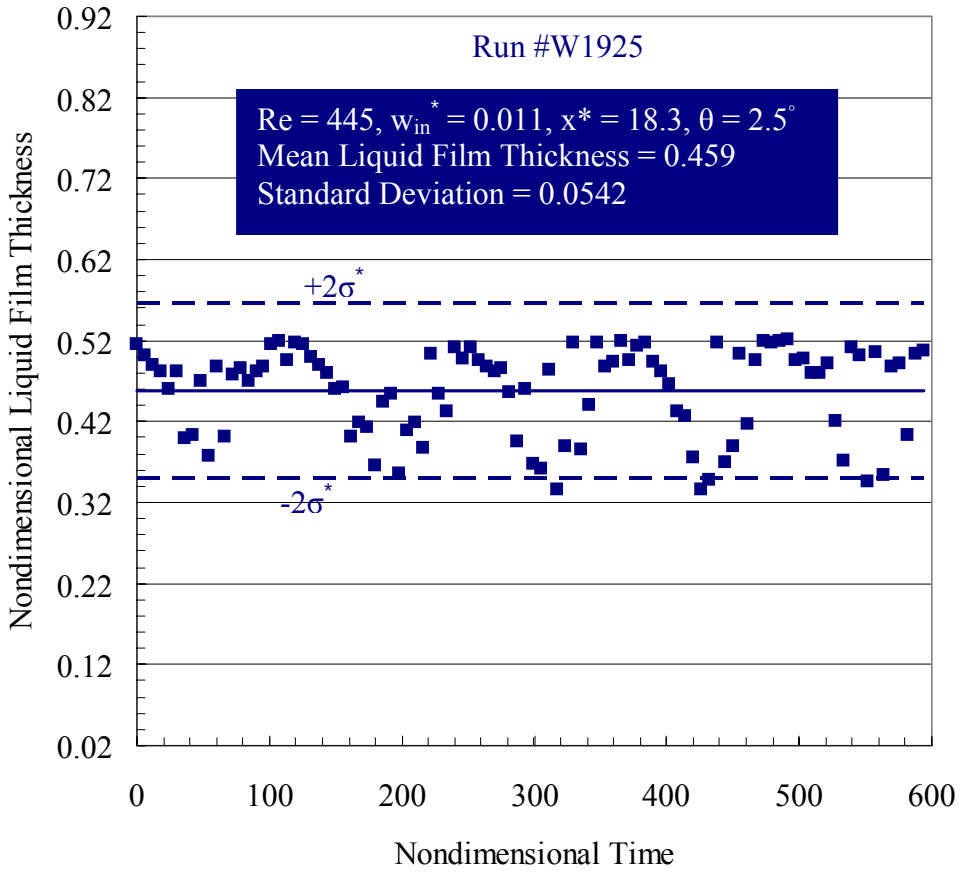

Figure C.96 The unperturbed liquid film thickness normalized by l as a function of time normalized by t_o measured at $x^* = 18.3$ for Run #W1925.

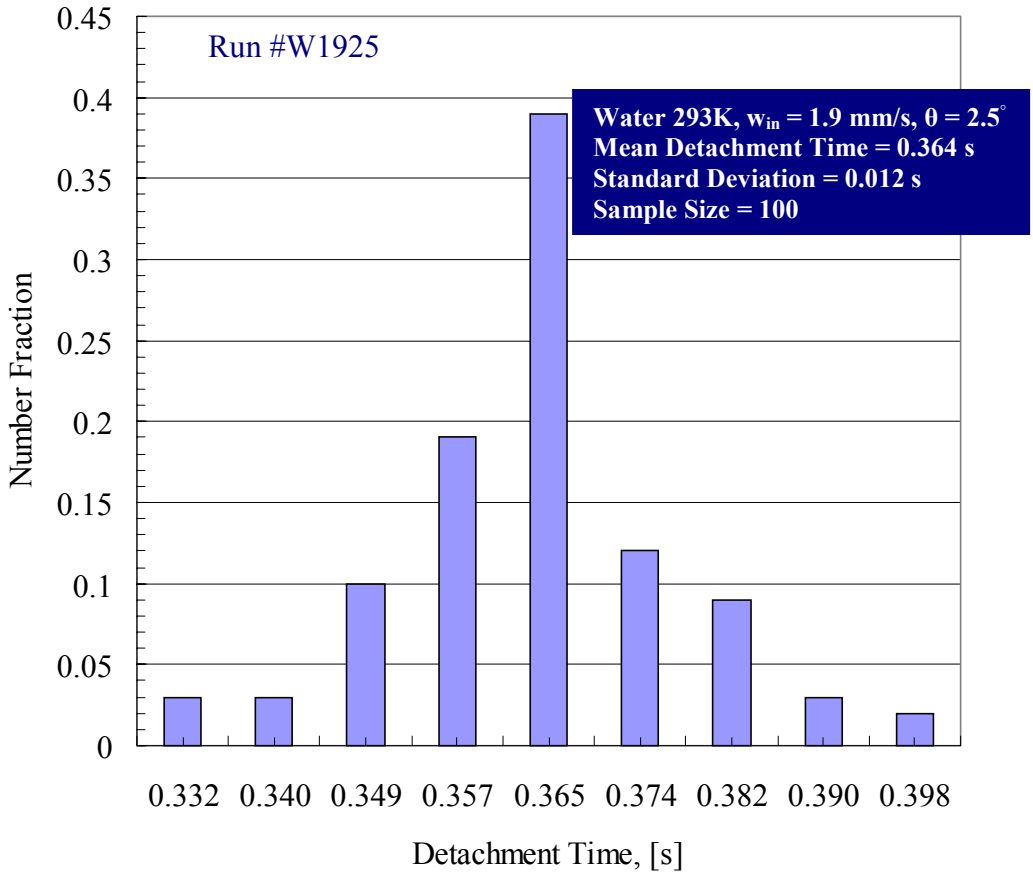

Figure C.97 Experimental data for the distribution of the detachment times carried out for an inclined surface (Run #W1925).

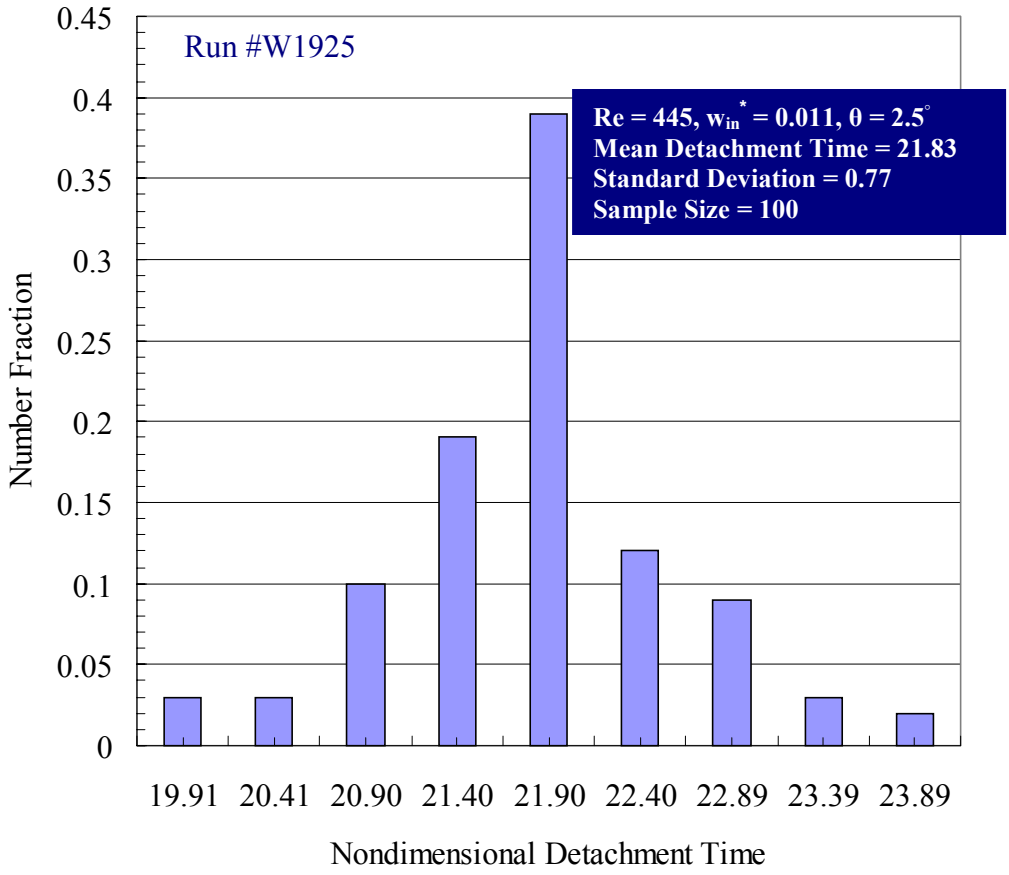

Figure C.98 Experimental data for the distribution of the nondimensional detachment time carried out for an inclined surface (Run #W1925).

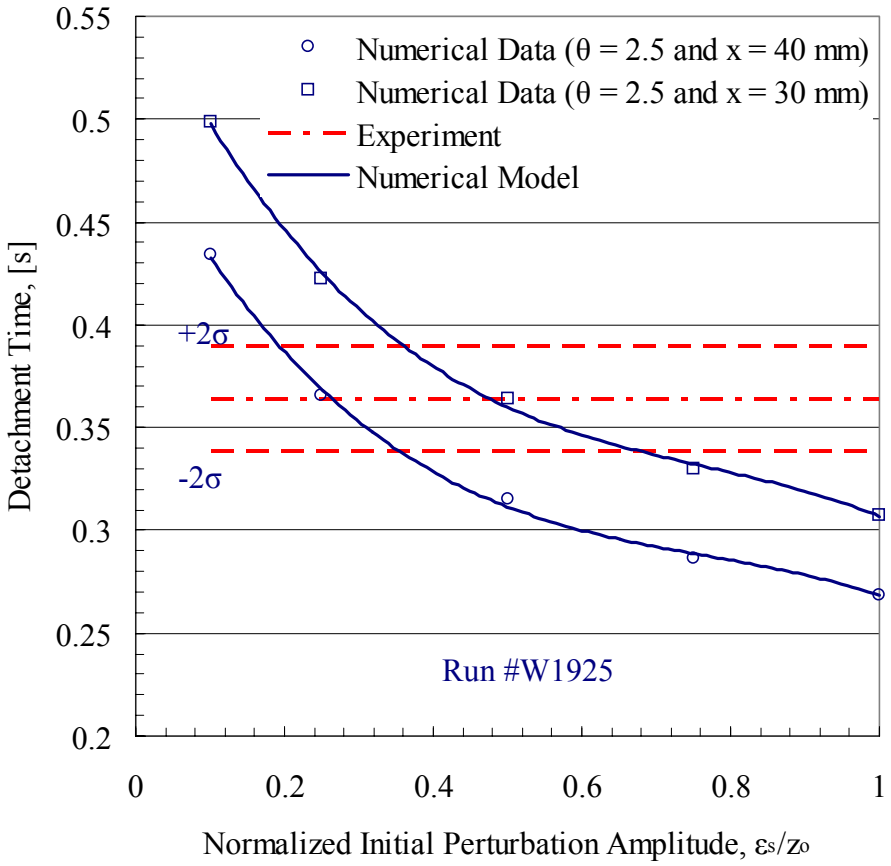

Figure C.99 Numerical and experimental data for the variation of the detachment time with the normalized initial perturbation amplitude carried out for an inclined surface (Run #W1925).

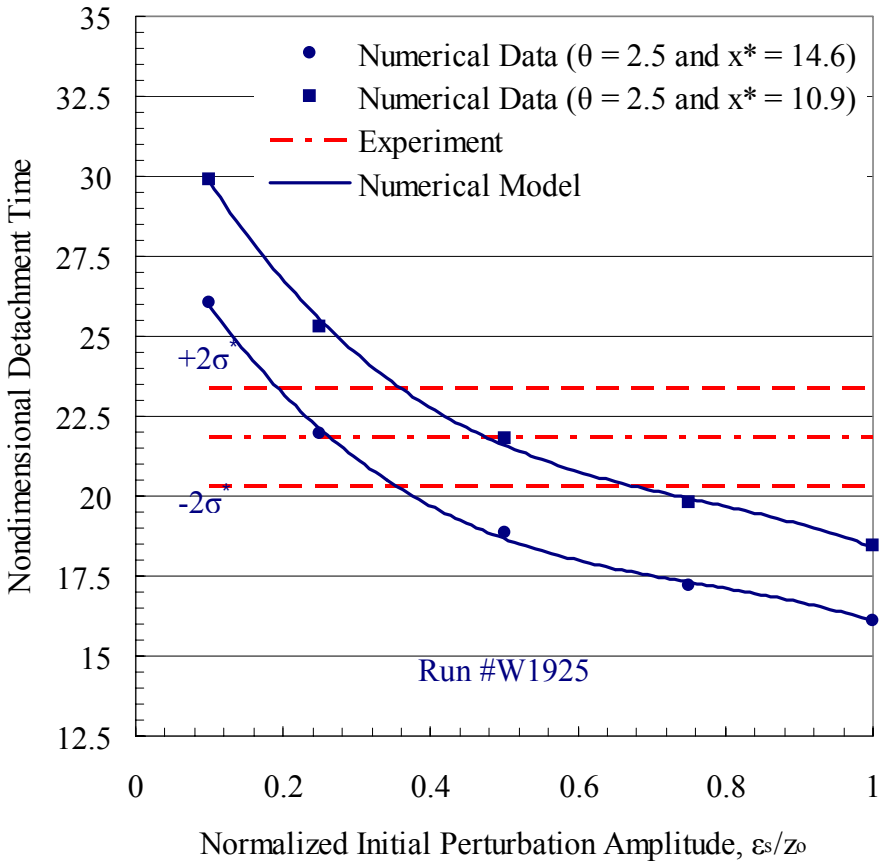

Figure C.100 Numerical and experimental data for the variation of the nondimensional detachment time with the normalized initial perturbation amplitude carried out for an inclined surface (Run #W1925).

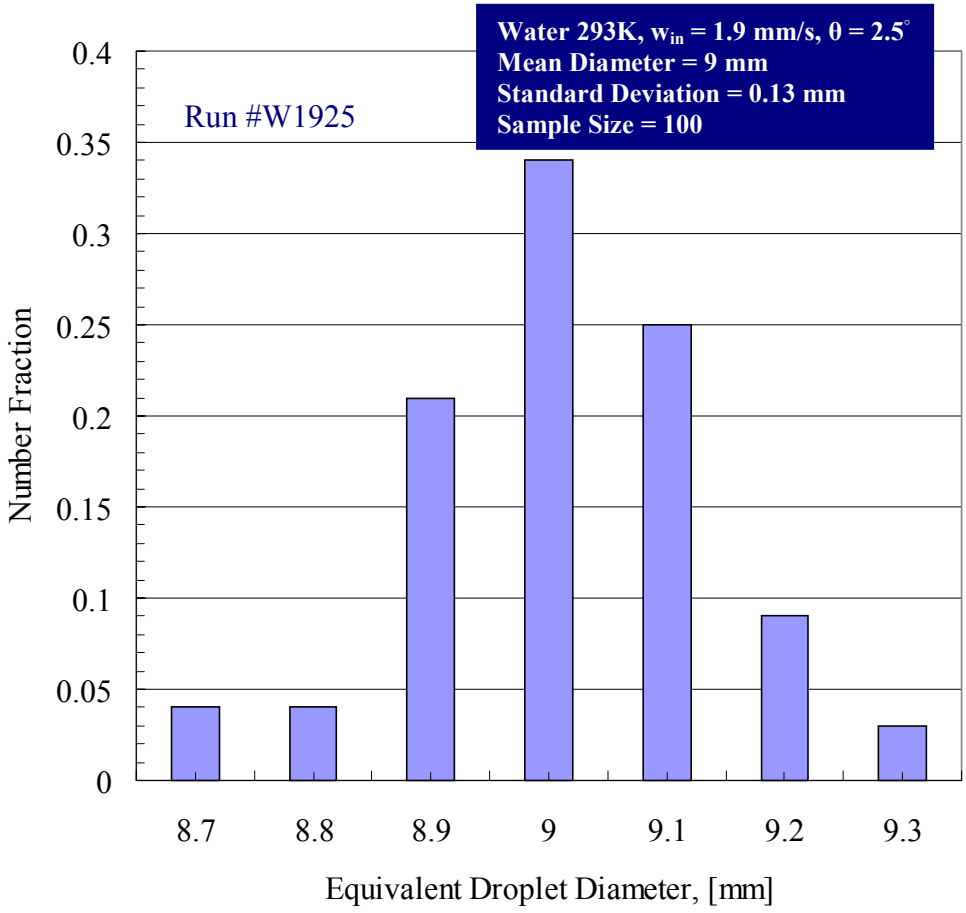

Figure C.101 Experimental data for the distribution of the equivalent droplet diameter carried out for an inclined surface (Run #W1925).

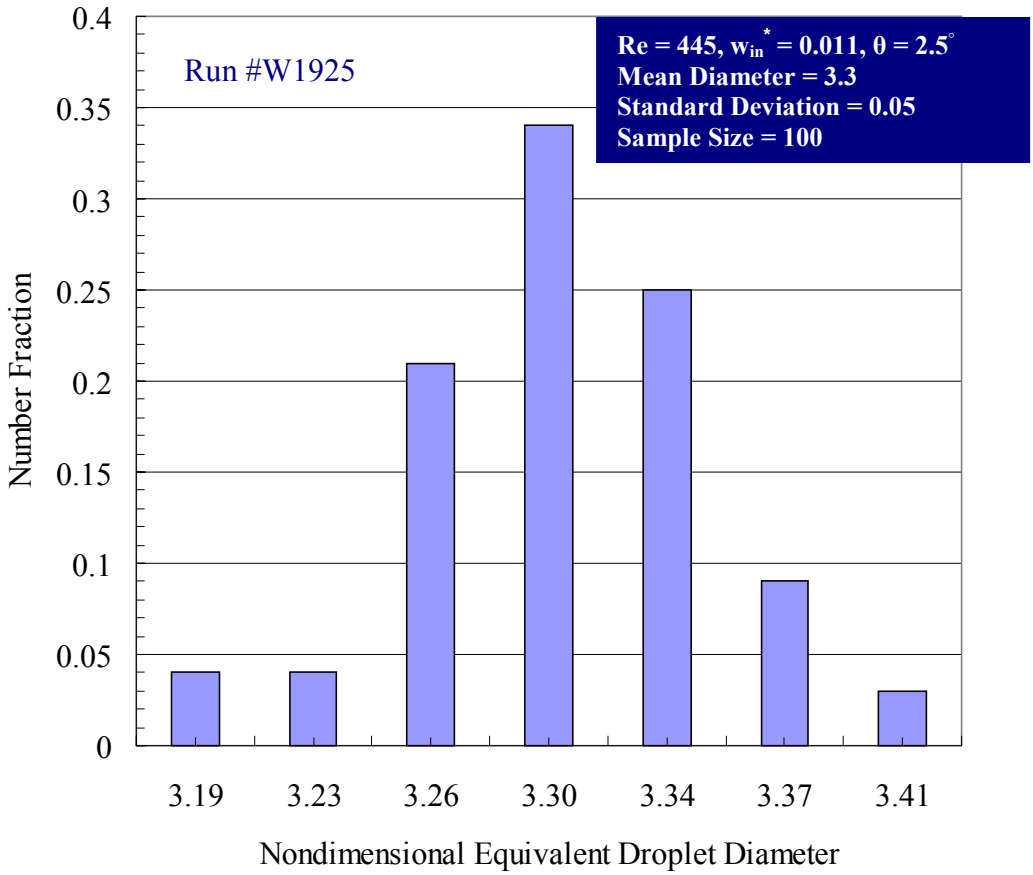

Figure C.102 Experimental data for the distribution of the nondimensional equivalent droplet diameter carried out for an inclined surface (Run #W1925).

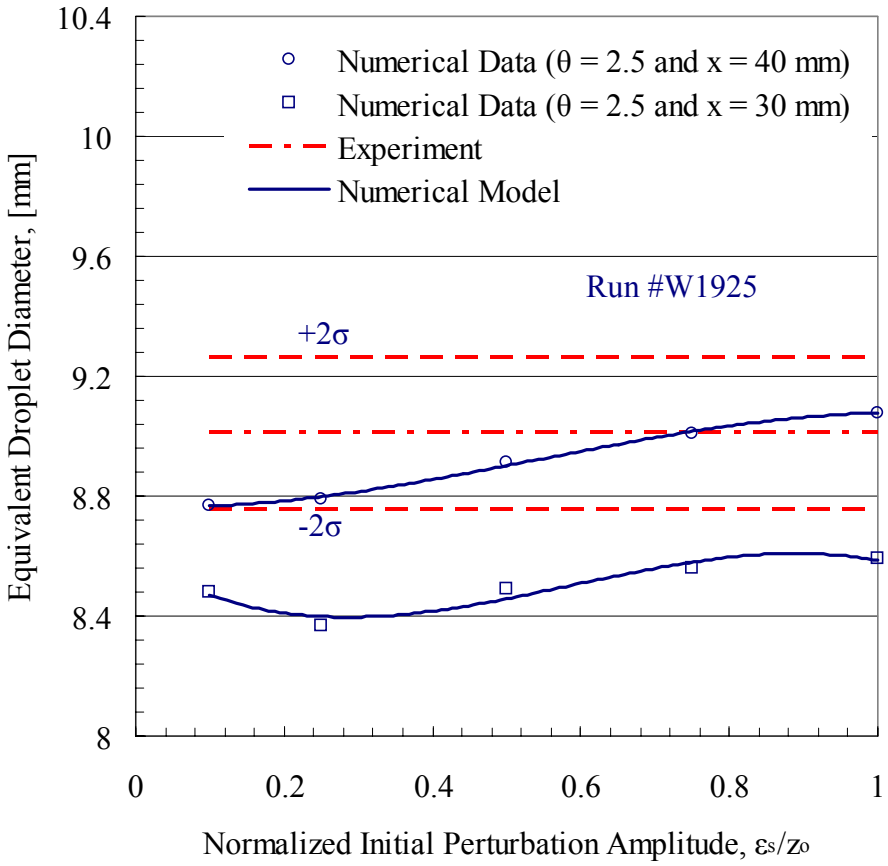

Figure C.103 Numerical and experimental data for the variation of the equivalent droplet diameter with the normalized initial perturbation amplitude carried out for an inclined surface (Run #W1925).

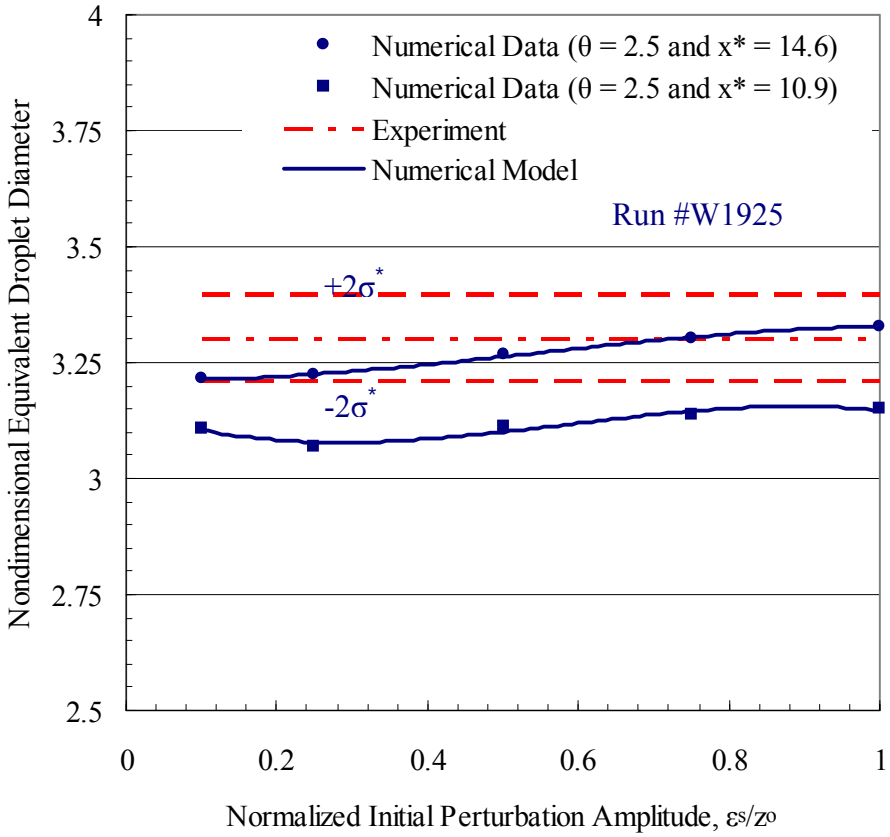

Figure C.104 Numerical and experimental data for the variation of the nondimensional equivalent droplet diameter with the normalized initial perturbation amplitude carried out for an inclined surface (Run #W1925).

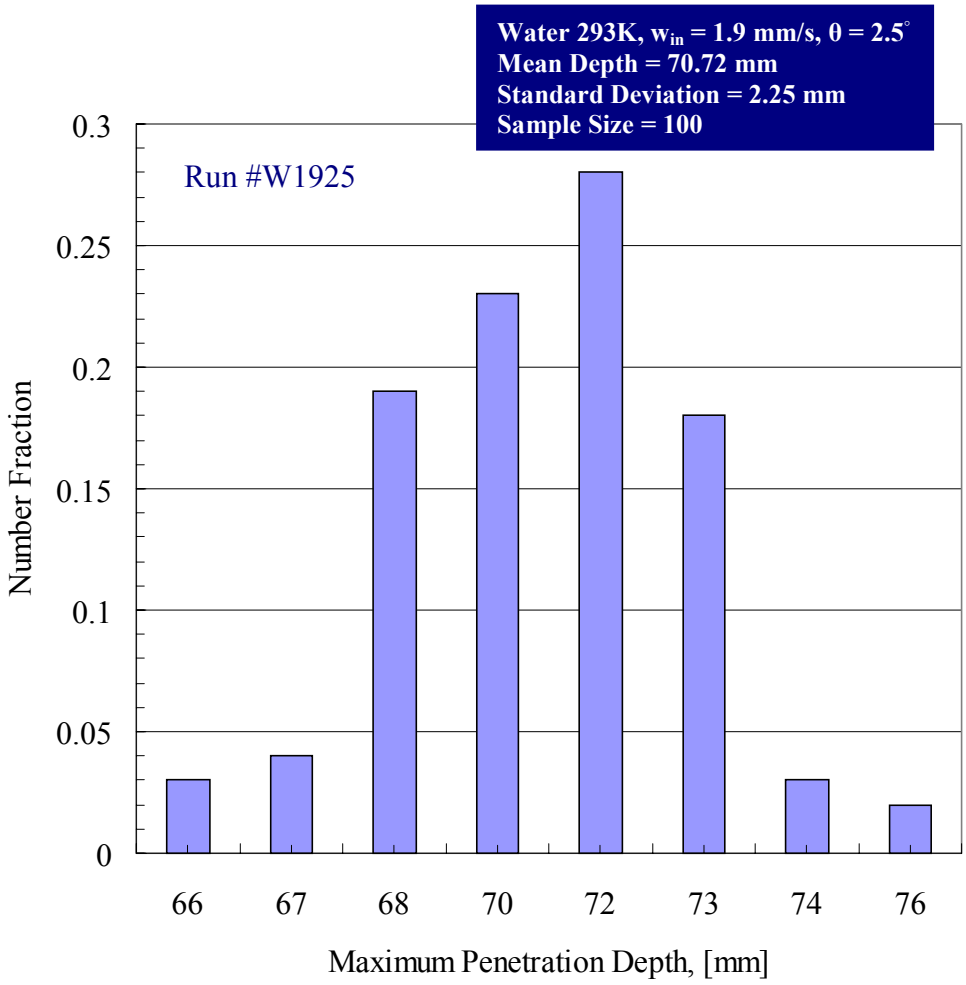

Figure C.105 Experimental data for the distribution of the maximum penetration depth carried out for an inclined surface (Run #W1925).

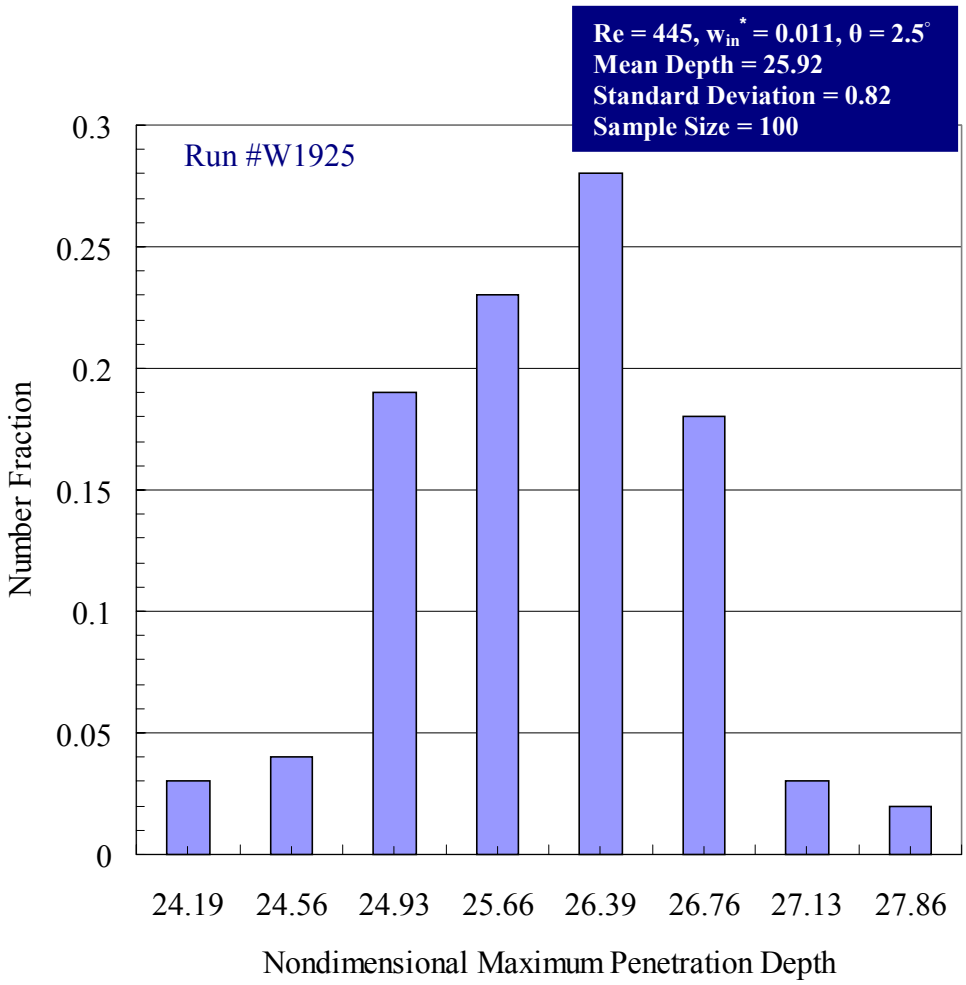

Figure C.106 Experimental data for the distribution of the nondimensional maximum penetration depth carried out for an inclined surface (Run #W1925).

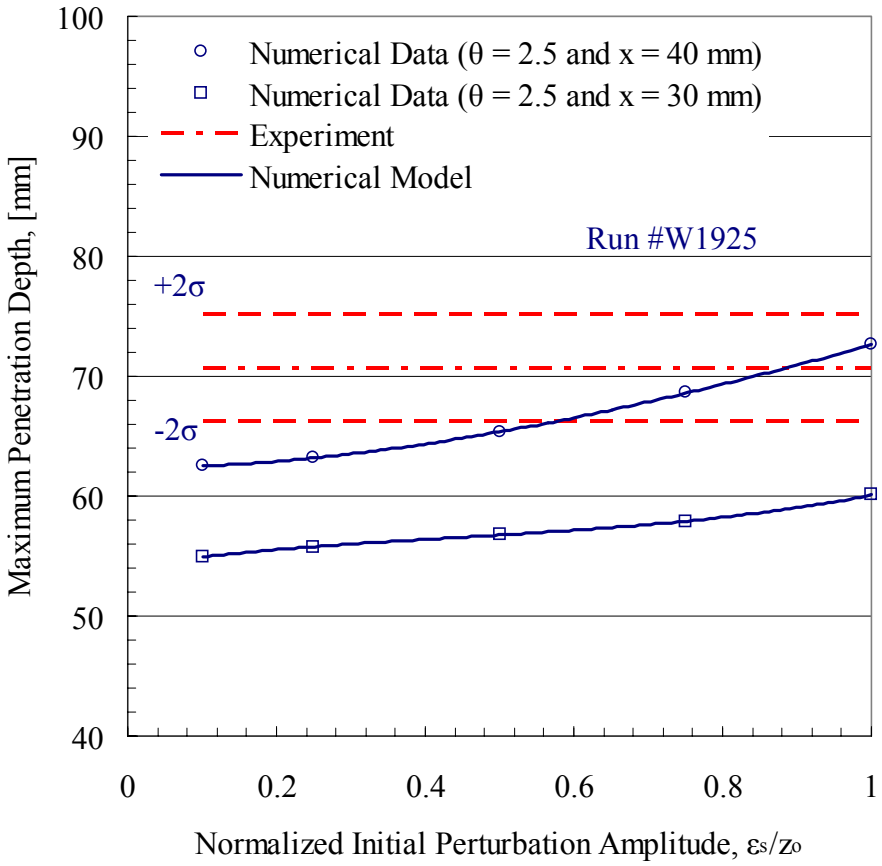

Figure C.107 Numerical and experimental data for the variation of the maximum penetration depth with the normalized initial perturbation amplitude carried out for an inclined surface (Run #W1925).

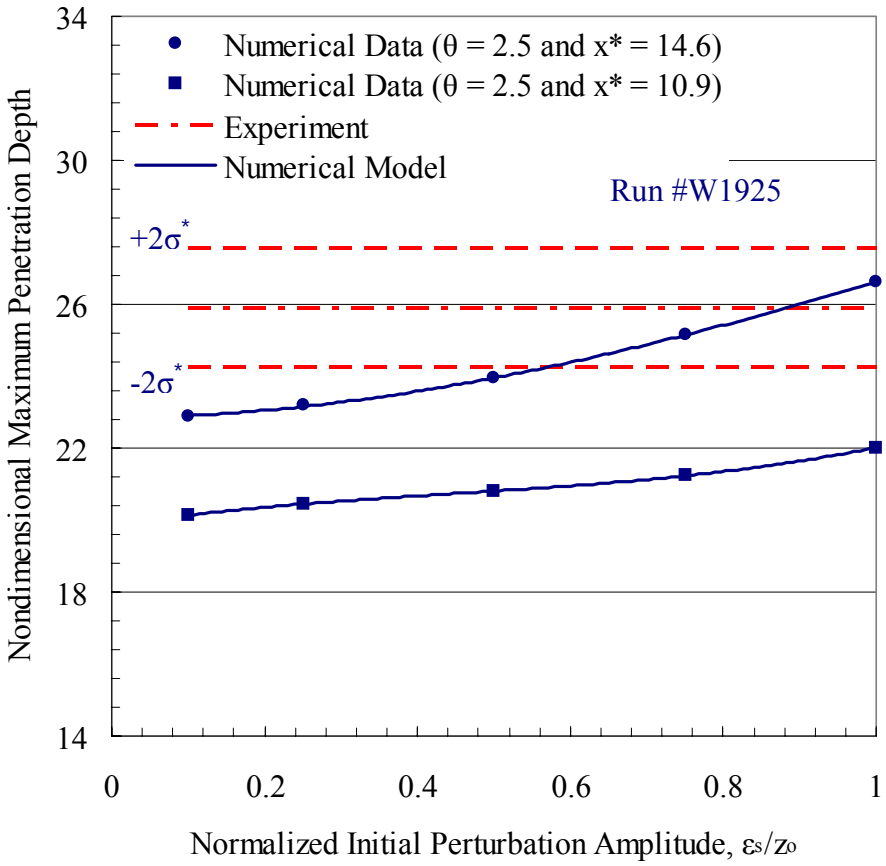

Figure C.108 Numerical and experimental data for the variation of the nondimensional maximum penetration depth with the normalized initial perturbation amplitude carried out for an inclined surface (Run #W1925).

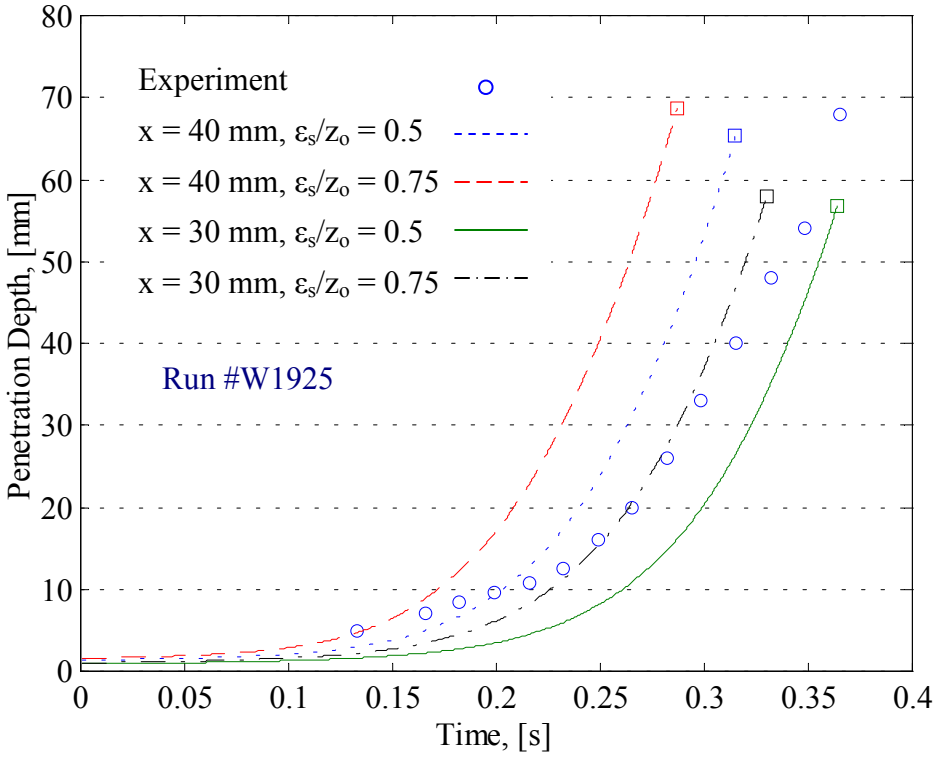

Figure C.109 Numerical and experimental data for the transient variation of the penetration depth carried out for an inclined surface (Run #W1925).

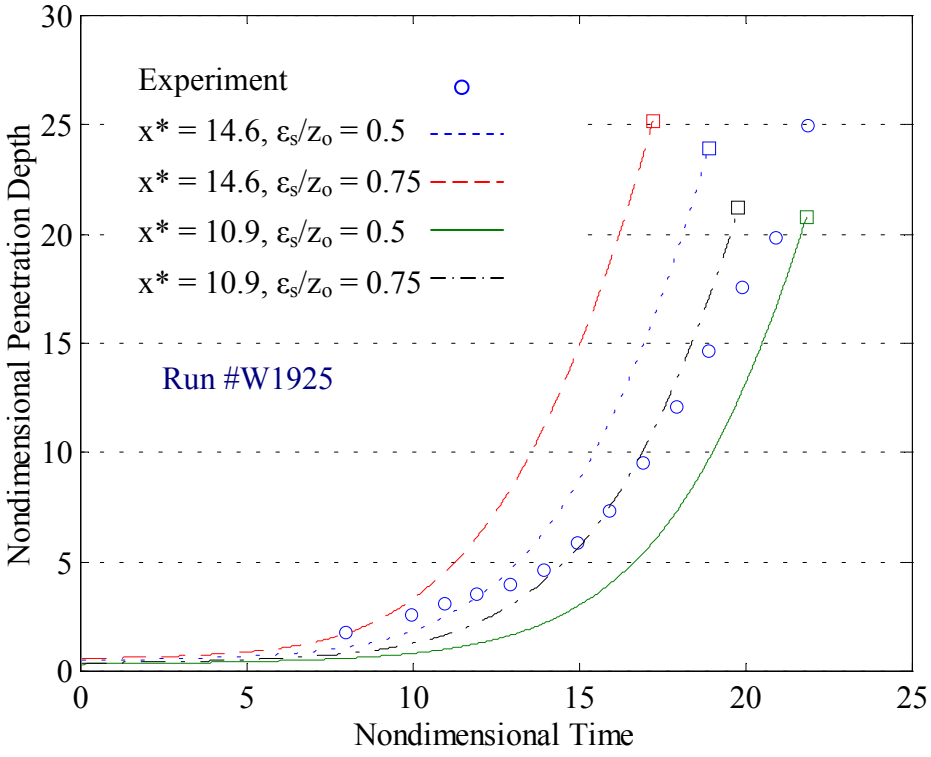

Figure C.110 Numerical and experimental data for the transient variation of the nondimensional penetration depth carried out for an inclined surface (Run #W1925).

REFERENCES

[1] S. I. Abdel-Khalik and T. O. Hunter, Assessment of surface heating problems in laser fusion reactors, ASME J. Heat Transfer 100 (1978) 311-318.

[2] R. R. Peterson, Response of national ignition facility first wall materials to target x-rays and debris, Fusion Technology 30 (1996) 778.

[3] R. R. Peterson, D. A. Haynes, Jr., I. E. Golovkin, and G. A. Moses, Inertial fusion energy target output and chamber response: calculations and experiments, Physics of Plasmas, 9 (2002) 2287-2292.

[4] A. R. Raffray, D. A. Haynes, Jr., and F. Najmabadi, IFE chamber walls: requirements, design options, and synergy with MFE plasma facing components, Presented at PSI-15 Meeting, Gifu, Japan (2002); submitted for publication in Journal of Nuclear materials.

[5] P. F. Peterson and J. M. Scott, The mini-chamber, an advanced protection concept for NIF, Fusion Technology 30 (1996) 442-447.

[6] U. von Möllendorff, M. T. Tobin, Conceptual design considerations for the reaction chamber of a heavy ion driven inertial fusion test facility, Forschungszentrum Karlsruhe, Technik und Umwelt, INR 1945 (July 1996).

[7] G. L. Kulcinski, R. R. Peterson, L. J. Wittenberg, E. A. Mogahed and I. N. Sviatoslavsky, Dry wall issues for the SOMBRERO laser fusion power plant, Fusion Engineering and Design 60 (2002) 3-15.

[8] A. Hassanein and S. I. Abdel-Khalik, Interaction of target debris with liquid-film-protected first walls, Presented at ARIES project Meeting, San Diego, CA (January 2002).

[9] L. A. Booth, Compiler, Central station power generation by laser-driven fusion, LA-4858-MS, Los Alamos Scientific Laboratory report (1972).

[10] J. M. Williams, et al., A conceptual laser controlled thermonuclear reactor power plant, Proceedings First Topical Meeting Technology of Controlled Fusion, San Diego, CA (1974).

[11] L. M. Waganer, et al. Inertial fusion energy reactor design studies, McDonnell Douglas Report, DOE/ER-4101, MDC 92E0008, Volume III (March 1992).

[12] M. A. Abdou, etal. Critical technical issues and evaluation and comparison studies for inertial fusion energy reactors, Fusion Engineering and Design, 23, (1993) 251-297.

[13] L. M. Waganer, Innovation leads the way to attractive inertial fusion energy reactors – Prometheus-L and Prometheus-H, Fusion Engineering and Design, 25, (1994) 125-143.

[14] Osirus and Sombrero Inertial Fusion Power Plant Designs, Final Report, WJSA-9201, DOE/ER/54100-1, March 1992.

[15] HIBALL-A conceptual heavy ion beam driven fusion reactor study preliminary report, University of Wisconsin Report, UWFDM -450, June 1981.

[16] R. W. Moir, Improvements to the HYLIFE-II Inertial Fusion Power Plant Design, Fusion Technology (1994), 26, 1169-1177.

[17] R. W. Moir, The High-Yield Lithium-Injection Fusion- Energy (HYLIFE)-II inertial fusion energy (IFE) power plant concept and implications for IFE, Physics of Plasmas (1995), 2, 2447-2452.

[18] J. E. Eggleston, M. A. Abdou and M. S. Tillack, Analysis of the energy transport and deposition within the reaction chamber of the Prometheus inertial fusion energy reactor, Fusion Engineering and Design, 27, (1995) 226-231.

[19] N. B. Morley, Geometric and blast effects on thin film cavity protection schemes for IFE reactors, Proceedings of the 16th IEEE/NPSS Symposium on Fusion Energy, Champaign, Urbana IL, October 1995.

[20] N. B. Morley, Compressible response of thin liquid film/porous substrate first walls in IFE reactors, Fusion Engineering and Design, 42, (1998) 563-568.

[21] R. L. McCroy, Impact of a target implosion in the OMEGA target chamber, Laboratory of Laser Energetics Annual Report 2002, LLE Publications, University of Rochester (2002).

[22] R. P. Abbott, A fusion chamber for the 2002 robust point design, RPD 2002, Lawrence Livermore National Laboratory, University of California (2002).

[23] A. R. Raffray, D. Haynes, R. R. Peterson, M. S. Tillack, X. Wang, M. Zaghlool, Dry chamber wall thermo-mechanical behavior and lifetime under IFE cyclic energy deposition, IFSA-2, Kyoto (2001).

[24] T. J. Renk, C. L. Olson, T. J. Tanaka, M. A. Ulrickson, G. A. Rochan, R. R. Peterson, I. E. Golovkin, M. O. Thompson, T. R. Knowles, A. R. Raffray, M. S. Tillack, IFE chamber dry wall materials response to pulsed x-rays and ions at power-plant level fluences, Fusion Engineering and Design, volume 65, issue 3, April 2003.

[25] E. A. Mogahed, Thin liquid wall protection concepts for IFE reactors, ARIES meeting in Madison WI, April 2002.

[26] W. R. Meier, R. W. Moir, M. A. Abdou, Chamber technology concepts for inertial fusion energy – three recent examples, Fusion Engineering and Design, 42, (1998) 537-548.

[27] A. Hassanein and I. Konkashbaev, An assessment of disruption erosion in the ITER environment, Fusion Engineering and Design, 28, (1995) 27-33.

[28] ITER EDA Agreement and Protocol 2, ITER EDA Documentation Series No. 5, IAEA, Vienna, 1994.

[29] R. Aymar, W. R. Spears and ITER International Team, Evolution of the ITER project during the CTA, Fusion Engineering and Design, 66-68, (2003) 17-24.

[30] A. Hassanein and I. Konkashbaev, Performance and lifetime assessment of reactor wall and nearby components during plasma instabilities, Journal of Nuclear Materials, 258-263, (1998) 645-652.

[31] A. Hassanein and I. Konkashbaev, Macroscopic erosion of plasma facing and nearby components during plasma instabilities: the droplet shielding phenomenon, Journal of Nuclear Materials, 290-293, (2001) 1074-1078.

[32] A. Hassanein and I. Konkashbaev, Modeling and simulation of fragmentation of suddenly heated liquid metal jets, Argonne National Laboratory Report, ANL-ET/01-13 (June 2001).

[33] R. L. Engelstad, Vibration and stability of vertical tubes conveying fluid subjected to planar excitation, Ph.D. Thesis, University of Wisconsin-Madison (1988).

[34] M. S. El-Genk and H. H. Saber, Minimum thickness of a flowing down liquid film on a vertical surface, Int. J. Heat Mass Transfer 44 (2001) 2809-2825.

[35] D. E. Hartley and W. Murgatroy, Criteria for break-up of thin liquid layers flowing isothermally over a solid surface, Int. J. Heat Mass Transfer 7 (1964) 1003-1015.

[36] A. Oron, S. H. Davis and S. G. Bankoff, Long-scale evolution of thin liquid films, Reviews of Modern Physics, Volume 69, Number 3, (1997) 931-980.

[37] J. Mikielewicz and J. R. Moszynski, Minimum thickness of a liquid film flowing vertically down a solid surface, Int. J. Heat Mass Transfer 19 (1976) 771-776.

[38] A. Doniec, Laminar flow of a liquid rivulet down a vertical solid surface, Canadian J. Chem. Eng. 69 (1991) 198-202.

[39] S. Shin, A level contour reconstruction method for three-dimenional multiphase flows and its applications, Ph.D. Thesis, Georgia Institute of Technology (2002).

[40] S. Shin and D. Juric, Modeling three-dimensional multiphase flow using a level contour reconstruction method for front tracking without connectivity, J. Comput. Phys. 180 (2002) 427-470.

[41] S. Shin, S. I. Abdel-Khalik, D. Juric, M. Yoda, and the ARIES Team, Effects of surface evaporation and condensation on the dynamics of thin liquid films for the porous wetted wall protection scheme in IFE reactors, Presented at Fifteenth Topical Meeting on Technology of Fusion Energy, Washington DC (Nov. 2002), Fusion Science and Technology 44 (2003) 117-126.

[42] S. Shin, F. Abdelall, D. Juric, S. I. Abdel-Khalik, M. Yoda, D. Sadowski, and the ARIES Team, Fluid dynamic aspects of the porous wetted wall protection scheme for inertial fusion energy reactors, Fusion Science and Technology 43 (2003) 366-377.

[43] Lord Rayleigh, Scientific Papers I (1899) 361.

[44] G. I. Taylor, The instability of liquid surfaces when accelerated in a direction perpendicular to their planes. I, Proc. R. Soc. London Ser. A 201 (1950) 192-196.

[45] S. Chandrasekhar, Hydrodynamics and Hydromagnetic Stability, Oxford Univ. Press, Oxford (1961), Chap. X.

[46] E. Fermi and J. von Neumann, Taylor Instability at the Boundary of Two Incompressible Liquids, The Collected Papers of Enrico Fermi, Chicago University Press, Chicago, IL, Volume 2 (1965), p. 821.

[47] D. H. Sharp, An overview of Rayleigh-Taylor instability, Physica D. 12 (1984) 3-18.

[48] D. J. Lewis, The instability of liquid surfaces when accelerated in a direction perpendicular to their planes. II, Proc. R. Soc. London Ser. A 202 (1950) 81-96.

[49] H. W. Emmons, C. T. Chang and B. C. Watson, Taylor instability of finite surface waves, J. Fluid Mech. 7 (1960) 177-193.

[50] R. E. Duff, F. H. Harlow and C. W. Hirt, Effects of diffusion on interface instability between gases, Phys. Fluids 5 (1962) 417-425.

[51] M. Ratafia, Experimental investigation of Rayleigh-Taylor instability, Phys. Fluids 16 (1973) 1207-1210.

[52] R. Popil and F. L. Curzon, Production of reproducible Rayleigh-Taylor instabilities, Rev. Sci. Instr. 50 (1979) 1291-1295.

[53] J. F. Barnes, D. H. Janney, R. K. London, K. A. Meyer and D. H. Sharp, Further experimentation on Taylor instability in solids, J. Appl. Phys. 51 (1980) 4678-4679.

[54] A. Lange, M. Schröter, M. A. Scherer, A. Engel and I. Rehberg, Fingering instability in a water-sand mixture, The European Phys. Journal, B 4 (1998), 475-484.

[55] L. S. Hung and S. C. Yao, Dripping phenomena of water droplets impacted on horizontal wire screens, Int. J. of Multiphase Flow, 28 (2002), 93-104.

[56] S. G. Bankoff, Minimum thickness of a draining liquid film, Int. J. Heat mass Transfer 14 (1971) 2143-2146.

[57] S. G. Bankoff and S. H. Davis, Stability of thin films, PhysChem. Hydrodynamics, 9, (1987) 5-7.

[58] S. G. Yiantsios and B. G. Higgins, Rayleigh-Taylor Instability in thin viscous films, Physics of Fluids A, 1, (1989) 1484-1501.

[59] R. O. Grigoriev, Control of evaporatively driven instabilities of thin liquid films, Physics of Fluids, Volume 14, Number 6, (2002) 1895-1909.

[60] B. D. Nichols, C. W. Hirt and R. S. Hotchkiss, SOLA-VOF: A solution algorithm for transient fluid flow with multiple free boundaries, Technical report LA-8355, Los Alamos Scientific Laboratory (1980).

[61] M. Rudman, Volume-tracking methods for interfacial flow calculations, Int. J. Numer. Methods Fluids 24, 671 (1997).

[62] W. J. Rider and D. B. Kothe, Reconstructing volume tracking, Journal of Computational Physics 141, 112 (1998).

[63] R. Scardovelli and S. Zaleski, Direct numerical simulation of free-surface and interfacial flow, Annual Review of Fluid Mechanics 31, 567 (1999).

[64] J. Glimm, O. Mcbryan, R. Menikoff and D. H. Sharp, Front tracking applied to Rayleigh-Taylor instability, SIAM J. Sci. Stat. Comput. 7 (1986) 230-251.

[65] J. Zhu and J. A. Sethian, Projection methods coupled to level set interface techniques, Journal of Computational Physics 102 (1992) 128.

[66] S. Chen and G. D. Doolen, Lattice Boltzmann method for fluid flows, Annu. Rev. Fluid Mech. 30 (1998) 329.

[67] G. Tryggvason and S. O. Unverdi, Computations of three-dimensional Rayleigh-Taylor instability, Phys. Fluids A. 2 (1990) 656-659.

[68] S. O. Unverdi and G. Tryggvason, A front-tracking method for viscous, incompressible, multi-fluid flows, J. Comput. Phys. 100 (1992) 25-37.

[69] S. O. Unverdi and G. Tryggvason, Computations of multi-fluid flows, Physica D. 60 (1992) 70-83.

[70] J. Glimm, X. L. Li, R. Menikoff, D. H. Sharp and Q. Zhang, A numerical study of bubble interactions in Rayleigh-Taylor instability for compressible fluids, Phys. Fluids A. 2 (1990) 2046-2054.

[71] D. L. Youngs, Three-dimensional numerical simulation of turbulent mixing by Rayleigh-Taylor instability, Phys. Fluids. 3 (1991) 1312-1320.

[72] X. L. Li, Study of three-dimensional Rayleigh-Taylor instability in compressible fluids through level set method and parallel computation, Phys. Fluids A. 5 (1993) 1904-1913.

[73] X. L. Li, A numerical study of three-dimensional bubble merger in Rayleigh-Taylor instability, Phys. Fluids A. 8 (1996) 336-343.

[74] J. Hecht, D. Ofer, U. Alon, D. Shvarts, S. A. Orszag and R. L. Mccrory, Three-dimensional simulations and analysis of the nonlinear stage of the Rayleigh-Taylor instability, Laser and Particle Beams, 13, (1995) 423-440.

[75] A. Elgowainy and N. Ashgriz, The Rayleigh-Taylor instability of viscous fluid layers, Phys. Fluids 9 (1997) 1635-1649.

[76] X. He, S. Chen and R. Zhang, A Lattice Boltzmann Scheme for incompressible multiphase flow and its application in simulation of Rayleigh-Taylor instability, J. Comput. Phys. 152 (1999) 642-663.

[77] X. He, R. Zhang, S. Chen and G. D. Doolen, On the three-dimensional Rayleigh-Taylor instability, Phys. Fluids 11 (1999) 1143-1152.

[78] C. E. Lapple, J. P. Henry and D. E. Blake, Atomization – A Survey and Critique of the Literature, Research Report DA-18-035-AMC-122(A), SRI No. 6, Stanford Research Institute (1967).

[79] C. L. Yaws, Chemical Properties Handbook, McGraw-Hill, New York (1999).

[80] J. W. Cooke and S. Cantor, Physical properties of molten-salt reactor coolant and flush salts, Oak Ridge National Laboratory TM 2316 (1968).

[81] K. Furukawa and H. Ohno, Molten materials I: Molten LiF-BeF_2 (Flibe) System, The Society of Molten-Salt Thermal Technology, Japan Nuclear Energy Information Center (1980).

[82] P. Gierszewski, B. Mikic, N. Todreas, Property calculation for Lithium, Sodium, Helium, Flibe and Water in fusion reactor applications, Research

Report PFC-RR-80-12, Fusion Blanket and Structures Group, Plasma Fusion Center, Massachusetts Institute of Technology (1980).

[83] K. Sheth and C. Pozrikidis, Effects of inertia on the deformation of liquid drops in simple shear flow, Computers and Fluids, 24, (1995) 101-119.

[84] S. Popinet and S. Zaleski, A front-tracking algorithm for accurate representation of surface tension, Int. J. Num. Meth. Fluids, 30, (1999) 493-500.

[85] D. J. Torres and J. U. Brackbill, The point-set method: front-tracking without connectivity, J. Comput. Phys., 165, (2000) 620-644.

[86] Y. C. Chang, T. Y. Hou, B. Merriman and S. Osher, A level set formulation of Eulerian capturing methods for incompressible fluid flows, Journal of Computational Physics, 124, (1996) 449-464.

[87] M. Sussman, P. Smereka and S. Osher, A level set approach for computing solutions to incompressible two-phase flow, Journal of Computational Physics, 114, (1994) 146-159.

[88] G. Tryggvason, B. Bunner, A. Esmaeeli, D. Juric, N. Al-Rawahi, W. Tauber, J. Han, S. Nas and Y. J. Jan, A front tracking method for the computations of multiphase flow, Journal of Computational Physics, 169, (2001) 708-759.

[89] J. Chorin, Numerical solution of the Navier-Stokes equations, Math. Comput. 22 (1968) 745-762.

[90] D. Juric and G. Tryggvason, Computations of boiling flows, Int. J. Multiphase Flow 24 (1998) 387-410.

[91] F. H. Harlow and J. E. Welch, Numerical calculation of time dependent viscous incompressible flow of fluid with free surface, Phys. Fluids 8 (1965)2182-2189.

[92] M. Siddique, The effects of noncondensable gases on steam condensation under forced convection conditions, Ph.D. Thesis, Massachusetts Institute of Technology, 1992.

VITA

Fahd Abdelall, PhD, was born in Alexandria, Egypt in 1975. He received his B.Sc. in mechanical engineering from the American University in Cairo in 1998. He was on the Dean's List graduating with highest honors (Summa Cum Laude). From 1998 to 2000 he was a teaching and research assistant at the University of Toronto, Canada graduating with an M.A.Sc. in mechanical engineering. He then studied for a doctoral degree in the George W. Woodruff School of Mechanical Engineering at the Georgia Institute of Technology, USA. He graduated in May 2004 with a graduate GPA 4.00/4.00. Dr. Abdelall is the recipient of the UAE highest ranking graduating senior award (1993), the AUC highest ranking GPA in mechanical engineering award (1998), the University of Toronto fellowship (1998-2000), and the Woodruff School highest score on the PhD qualifying exams award (2001-2002).